D 2021

U.PORTO
FEUP FACULDADE DE ENGENHARIA
UNIVERSIDADE DO PORTO

OLIVE MILL WASTEWATER VALORIZATION THROUGH STEAM REFORMING REACTION USING A HYBRID SORPTION-ENHANCED MEMBRANE REACTOR FOR HIGH-PURITY HYDROGEN PRODUCTION

CLÁUDIO DA SILVA ROCHA

TESE DE DOUTORAMENTO APRESENTADA
À FACULDADE DE ENGENHARIA DA UNIVERSIDADE DO PORTO EM
ENGENHARIA QUÍMICA E BIOLÓGICA

U.PORTO
FEUP FACULDADE DE ENGENHARIA
UNIVERSIDADE DO PORTO

Olive Mill Wastewater Valorization through Steam Reforming Reaction using a Hybrid Sorption-Enhanced Membrane Reactor for High-Purity Hydrogen Production

Thesis presented to the

University of Porto

for the degree of

Doctor of Philosophy in Chemical and Biological Engineering

by

Cláudio da Silva Rocha

Supervisor: Prof. Dr. Luís Miguel Palma Madeira

Co-Supervisor: Dr. Miguel Angel Soria

lepabe
Laboratory for Process Engineering, Environment, Biotechnology and Energy

Department of Chemical Engineering

Faculty of Engineering

University of Porto

2021

Statement of Originality

I certify that this work does not contain any material that has been used nor will be for the award of any other degree or diploma in my name or anyone, in any university or institution. In addition, I certify that, to the best of my knowledge, this work does not contain any material previously published or written by another person, except where due reference has been made in the text.

_____

Cláudio da Silva Rocha

Abstract

The main objective of this PhD thesis was to valorize the olive oil mill wastewater (OMW), a by-product of olive oil production, by means of H_2 production through OMW steam reforming (OMWSR) with the use of multifunctional hybrid reactors, such as sorption-enhanced reactor (SER), membrane reactor (MR) and sorption-enhanced membrane reactor (SEMR), whose performances were compared with that of a traditional reactor (TR).

To verify if the OMWSR process is thermodynamically feasible to treat a OMW stream, a thermodynamic analysis of the OMWSR was performed for the different reactor configurations - TR, SER, MR and SEMR. The equilibrium compositions were determined employing the Gibbs free energy minimization method. It was found that the H_2 yield increases with the temperature up to a maximum value, while it continuously decreases with the pressure. In opposition, the water content in the feed increases the H_2 yield and decreases the coke formation. The optimum operating conditions for several OMW compositions were also determined. The results were also compared in terms of performance reached for the different reactor configurations. For the SEMR, an H_2 yield very close to the stoichiometric value of 13.54 (for a certain OMW composition) was obtained at 1 bar, 500 °C, water content in the feed of 60-92 wt.% (steam-to-carbon feed ratio, SCFR = 2.1-16.0), $f CO_2$ (removal fraction of CO_2) = 0.99 and $f H_2$ (removal fraction of H_2) = 0.80. Considering a SCFR = 2.1, the H_2 yield obtained in such conditions corresponds to an enhancement of 141% comparatively to the TR.

To use an adsorptive reactor (SER/SEMR) in the OMWSR process, it is essential to choose a suitable CO_2 sorbent. In this way, several hydrotalcites (HTCs) with different compensating anions were prepared. The CO_2 sorption equilibrium isotherms at 300 ºC were determined for all the calcined sorbents and several CO_2 breakthrough runs were carried out. The simultaneous effect of aluminum partial substitution with gallium and impregnation with potassium on their CO_2 sorption capacities was also assessed in these experimental tests. The results indicate that the doping of HTCs with potassium greatly enhanced the sorption capacity when compared with the original materials. Moreover, the sorption kinetics were analysed from CO_2 uptake measurements and two distinct contributions were observed. Lastly, the HTC-CO_3(Ga)_K sample showed the highest CO_2 sorption capacity at 300 °C in the range of p_{CO_2} = 0.1-1 bar (1.45 mmol·g^{-1}, @ p_{CO_2}= 1 bar).

Regardless of the reactor configuration considered, it is always necessary to select one proper catalyst for the OMWSR process. Thus, in this study, several commercial catalysts (Ni-, Cu-Zn- and noble metal-based) and prepared Ni-based catalysts were also tested for the OMWSR process (using a synthetic OMW effluent – a complex mixture of model oxygenates, representative of a real effluent) to compare their performances. A catalytic screening study with all the materials was performed, and stability tests (@ 1 bar and 400 °C) were conducted with the most promising samples. Although there are some materials with good catalytic performance, the commercial Rh-based sample stood out,

exhibiting high catalytic activity and high stability: the H_2 yield (over 9 $mol_{H2} \cdot mol^{-1}_{OMW}$) and total organic carbon (TOC) conversion (> 98 %) were high along all the 24 h of the stability test. Also, the prepared Ni-Ru/SiO_2 sample showed high catalytic activity and stability: the H_2 yield (over 8 $mol_{H2} \cdot mol^{-1}_{OMW}$) and TOC conversion (≈ 75 %) were high along the 24 h of the stability test.

After selecting all the materials required to carry out the proof of concept (catalyst, CO_2 sorbent and H_2 perm-selective membrane), the benefits of the hybrid multifunctional reactors (SER, MR and SEMR) comparatively to a TR for H_2 production were verified (using two types of OMW effluent: synthetic and real). In all reactor configurations, it was used the prepared Ni-Ru/Ce-SiO_2 catalyst, combined in the sorption-enhanced multifunctional reactors with an in-house prepared or a commercial potassium-promoted HTC-based sorbent to capture CO_2. Additionally, in the membrane-based configurations, a commercial Pd-Ag membrane was utilized to separate the formed H_2 from the reaction medium. It was verified an increase in both the H_2 production (before the breakthrough of CO_2) and catalyst stability using the SER in comparison with the TR. However, a higher enhancement of the H_2 yield was observed using the SEMR (again before the breakthrough period), which was less pronounced after the saturation of the adsorbent (which resembles a MR), due to the effect of the H_2 perm-selective membrane. It was also demonstrated that the use of a SEMR in the steam reforming of real OMW effluent allows reducing drastically the pollutant load of this stream, while economically valorizing this waste through the production of H_2.

Finally, a techno-economic analysis of this process, using either a TR or two SERs, was performed. This study focused on key aspects of the process units, such as the reaction and heating/cooling zones. This analysis considered the effect of different water contents in the OMW composition (60-90 wt.%) and the impact of the pressure (1-4 bar), while setting the reformer temperature at 400 ºC. To determine the outlet stream composition of the process and the heat released or required in the reaction, the *Aspen Plus V.10*® software was used. To calculate the cost of the heat exchanger, the *Aspen Exchanger Design & Rating* software was adopted. It was observed that the content of water in the feed, the pressure, the flow rate of the OMW fed and the reactor configuration used affect the economic benefit of the project: lower content of water in the feed, lower pressure, lower OMW flow rate and the utilization of SERs allow to obtain a most economically advantageous project.

Keywords: olive oil mill wastewater valorization; steam reforming; hydrogen; sorption-enhanced membrane reactor; multifunctional reactors.

Resumo

O objetivo principal desta tese de doutoramento foi valorizar as águas ruças (AR), um subproduto poluente da produção de azeite, por meio da produção de H_2 através da reformação a vapor das águas ruças (RVAR) com o uso de reatores híbridos multifuncionais, nomeadamente um reator adsortivo (RA), um reator de membrana (RM) e um reator de membrana com adsorção (RMA), cujos desempenhos foram comparados com o de um reator tradicional (RT).

Para se verificar se o processo de RVAR é termodinamicamente factível para tratar uma corrente de AR, foi efetuada uma análise termodinâmica da RVAR para diferentes configurações de reatores - RT, RA, RM e RMA. As composições de equilíbrio foram determinadas empregando-se o método de minimização de energia livre de Gibbs. Verificou-se que o rendimento de H_2 aumenta com a temperatura até um valor máximo, mas diminui continuamente com a pressão. Em oposição, o teor de água na alimentação aumenta o rendimento de H_2 e diminui a formação de depósitos de carbono. Foram também determinadas as condições operatórias ideais para várias composições de AR. Os resultados foram também comparados, em termos de desempenho alcançado, para as diferentes configurações do reator. Para o RMA, foram determinadas as condições de operação ótimas: um rendimento de H_2 muito próximo do valor estequiométrico de 13,54 (para uma certa composição de AR) foi obtido a 1 bar, 500 ° C, teor de água na alimentação de 60-92 %(m/m) (razão molar entre vapor de água e carbono na alimentação, RVCA = 2,1-16,0), $f$$CO_2$ (fração de remoção de CO_2) = 0,99 e $f$$H_2$ (fração de remoção de H_2) = 0,80. Considerando um RVCA = 2,1, o rendimento de H_2 obtido nessas condições ótimas corresponde a um aumento de 141 % comparativamente ao RT.

Para se utilizar um reator adsortivo (RA/RMA) no processo de RVAR, é essencial escolher um adsorvente de CO_2 adequado. Desta forma, prepararam-se várias amostras de hidrotalcitas (HTCs) com diferentes aniões de compensação. As isotérmicas de equilíbrio de sorção de CO_2 a 300 ºC foram determinadas para todos os adsorventes calcinados, tendo-se realizado vários ensaios de rotura (*breakthrough*) de CO_2. Nestes testes experimentais foi também avaliado o efeito simultâneo da substituição parcial do alumínio por gálio e da impregnação com potássio na capacidade de sorção de CO_2. Os resultados indicam que a dopagem das HTCs com potássio aumentou de forma vincada a capacidade de sorção quando comparada com os materiais originais. Além disso, a cinética de sorção foi analisada a partir dos perfis de captura (*uptake*) de CO_2, tendo sido observadas duas contribuições distintas. Por último, a amostra HTC-CO_3(Ga) _K mostrou a maior capacidade de sorção de CO_2 a 300 ° C na gama de p_{CO_2} = 0,1-1 bar (1,45 mmol·g^{-1}, @ p_{CO_2} = 1 bar).

Independentemente da configuração de reator considerada, é sempre necessário selecionar um catalisador adequado para ser usado no processo de RVAR. Assim, neste estudo, foram testados vários catalisadores comerciais (à base de Ni, Cu-Zn e metais nobres) e foram preparados alguns catalisadores à base de Ni para o processo de RVAR (usando um efluente de AR sintético – mistura

complexa de oxigenados, representativa de um efluente real) com o objetivo de se compararem os seus desempenhos. Foi realizado um estudo de triagem catalítica com todos os materiais, tendo-se ainda realizado testes de estabilidade (@ 1 bar e 400 °C) com as amostras mais promissoras. Embora existam alguns catalisadores com bom desempenho catalítico, o material à base de Rh destacou-se durante os testes, exibindo alta atividade catalítica e alta estabilidade: o rendimento de H_2 (acima de 9 $mol_{H2} \cdot mol^{-1}_{OMW}$) e a conversão de carbono orgânico total (COT - > 98 %) foram altos ao longo das 24 h do teste de estabilidade. Além disso, a amostra Ni-Ru/SiO_2 (preparada laboratorialmente) também exibiu alta atividade catalítica e estabilidade: o rendimento de H_2 (acima de 8 $mol_{H2} \cdot mol^{-1}_{OMW}$) e a conversão de COT (≈ 75 %) foram altos durante as 24 h do teste de estabilidade.

Depois de selecionados todos os materiais necessários para a realização da prova de conceito (catalisador, adsorvente de CO_2 e membrana seletiva a H_2), foram verificados os benefícios dos reatores multifuncionais híbridos (RA, RM e RMA) comparativamente a um RT para a produção de H_2 (utilizando dois tipos de efluente de AR: sintético e real). Em todas as configurações dos reatores foi utilizado um catalisador preparado de Ni-Ru/Ce-SiO_2, combinado nos reatores adsortivos com um adsorvente preparado ou comercial derivado de uma HTC promovido com potássio para capturar CO_2. Além disso, nas configurações dos reatores de membrana, foi utilizada uma membrana comercial de Pd-Ag para separar o H_2 do meio reacional. Verificou-se um aumento tanto na produção de H_2 (antes da rotura do CO_2) como na estabilidade do catalisador utilizando o RA em comparação com o RT. No entanto, foi observado um maior aumento do rendimento de H_2 utilizando o RMA (novamente antes da rotura), que foi menos pronunciado após a saturação do adsorvente, devido ao efeito da membrana seletiva ao H_2. Foi também demonstrado que a utilização de tais reatores multifuncionais na reformação a vapor de um efluente real de AR permite reduzir drasticamente a carga poluente desta corrente, valorizando economicamente este resíduo com a produção de H_2.

Por fim, foi realizada uma análise técnico-económica deste processo, utilizando um RT ou dois RA. Este estudo focou-se nos principais aspetos das unidades processuais, como as zonas de reação e aquecimento/arrefecimento. Esta análise considerou o efeito de diferentes teores de água na composição da AR (60-90 %(m/m)) e o impacto da pressão (1-4 bar), para uma temperatura do reformador de 400 ºC. Para se determinar a composição da corrente de saída e o calor libertado ou necessário na reação, foi utilizado o software *Aspen Plus V.10®*. Para se estimar o custo do permutador de calor, foi utilizado o *Aspen Exchanger Design & Rating*. Observou-se que o teor de água na alimentação, a pressão, o caudal de AR alimentado e a configuração do reator afetam a rentabilidade do projeto: menor teor de água na alimentação, menor pressão, menor caudal de AR e a utilização de um RA permitem obter um projeto economicamente mais vantajoso.

Palavras-chave: valorização das águas ruças; reformação a vapor; hidrogénio; reator de membrana com adsorção; reatores multifuncionais.

Aos meus pais e avós.
À Ana Pereira.

Agradecimentos

Ao Professor Luís Miguel Madeira e ao Doutor Miguel Angel Soria agradeço toda a disponibilidade para orientarem este trabalho de doutoramento, toda a dedicação e disponibilidade para resolverem todos os problemas que foram aparecendo, assim como pela plena confiança que tiveram em mim. Agradeço também toda a força que me foram transmitindo ao longo deste percurso e por todos os bons momentos vividos neste grupo; assim ficou muito mais fácil desenvolver este projeto. Tenho a certeza de que sem o vosso apoio, não tinha adquirido tanto conhecimento e crescido como investigador e como ser Humano. Muito obrigado!

À Professora Arminda Alves agradeço por ser a comandante deste barco chamado LEPABE e por guiar todas os investigadores do nosso grupo a bom porto. Será sempre um gosto trabalhar com a Professora, tanto em assuntos académicos como em assuntos extracurriculares! Obrigado pela confiança que sempre teve em mim.

Ao Professor Fernando Martins quero reconhecer toda a (grande) ajuda na análise técnico-económica e por toda a simpatia que sempre teve comigo.

Ao Professor Alexandre Ferreira agradeço por disponibilizar um cromatógrafo gasoso para deteção de vários hidrocarbonetos de cadeira longa e à Professora Margarida Bastos agradeço por me ter transmitido os seus conhecimentos de Química Orgânica que me foram bastante úteis nesta tese.

Agradeço ao Professor Pedro Tavares a paciência na análise dos resultados de XRD, assim como ao Doutor Auguste Fernandes e à Professora Filipa Ribeiro por todas as análises de TPD-NH_3 efetuadas.

Aos membros da *Tecnalia* reconheço positivamente toda a preocupação que tiveram com as membranas usadas neste trabalho; um especial agradecimento ao Doutor Ekain Fernandez. Agradeço também à *Johnson Matthey* pelo fornecimento de catalisador e ao *Lagar do Parral* e à *Acushla* pela disponibilização de águas ruças.

A todos os Professores do PDEQB que se mostraram solidários com a situação delicada dos estudantes de doutoramento devido à pandemia provocada pela COVID-19, o meu muito obrigado!

Ao Luís Carlos Matos, Zé Luís, Liliana Pereira, Arminda Monteiro, José Avelino, Célia Cerqueira, Joana Sottomayor, Carla Ferreira, Joana Feyo, Marta Ferro, María Gutiérrez, Eugénio Soares, Lina Carvalho, Fátima Ferreira, Alexandre Araújo, Ricardo Vidal, Rui Rocha, Fátima Ribeiro e Diana Paiva quero agradecer por todo o apoio técnico que me foram dando ao longo deste percurso.

Ao Sr. Nelson e Sr. Ricardo por toda a ajuda e disponibilidade na elaboração dos reatores e módulos.

Ao Carlos Miguel agradeço todas as sugestões e ideias dadas durante o trabalho experimental. Agradeço também pela sua preocupação constante ao longo de todo este percurso.

Ao Joel Silva muito agradeço pelas discussões científicas diárias, pelos momentos descontraídos, por todos os jantares e almoços, por todas as músicas partilhadas que tornaram o ambiente de trabalho leve e por todo o apoio que sempre me foi dando ao longo destes anos todos como amigo.

À Catarina Faria e Joana Martins, quero agradecer toda a amizade e ajuda dentro do laboratório -146. Obrigado por todas as discussões científicas (ou não científicas) dentro da FEUP ou com os pés debaixo de uma mesa de jantar que me ajudaram no desenvolvimento profissional e pessoal.

Ao Emanuel Sampaio, Bruno Esteves e Diogo Barros quero agradecer todo o companheirismo e amizade dentro e fora do laboratório. Aos restantes membros (e ex-membros) do grupo de investigação, a *Troop Madeira*, o meu muito obrigado pela vossa presença carinhosa e contínua. Palavra de agradecimento também aos “convidados do grupo”, Carlos Silva e Natasha Rosa.

Obrigado à Sara Pardilhó e à Maria João Romeu pelo apoio nas últimas semanas do doutoramento.

À dupla Tiago Vilas Boas por todo o percurso no MIEQ que me levou a aumentar sempre o nível de conhecimento.

Para com os meus amigos António Teixeira, Rafael Dias, Ana Margarida Silva, Filipe Carvalho, Leonardo Rodrigues, Ruben Sousa, Tiago Canedo, Soraia Neves, Filipa Miranda, Ana Vinhas, Rafael Morais, Joana Costa, Ana Isabel, Marta Barbosa, Jéssica Reis e Pedro Velho expresso o meu grande obrigado geral pela vossa presença persistente e forte na minha vida, visto que a vossa existência me ajudou na superação de vários obstáculos presentes na minha tese! Obrigado por todas as palavras de apoio e toda a vossa amizade.

Ao Filipe Carvalho e ao Leonardo Rodrigues por todos os momentos de lazer e divertimento proporcionados e por estarem sempre presentes quando foi necessário.

Ao Ruben Sousa por ser o amigo mais racional, ponderado e consciente que tenho. Os desabafos no -146 sempre foram muito importantes.

Ao Tiago Canedo por me ensinar que os amigos ficam sempre, em todas as situações.

Ao António Teixeira pelas suas palavras sempre inspiradoras e desafiantes.

Ao Rafael Dias por toda a paciência diária ao longo de 4 anos e por toda a amizade pura e simples.

À Ana Margarida Silva pela sua amizade peculiar, mas não menos importante.

Ao Pedro Velho por me motivar a ser sempre melhor e a pensar fora da caixa.

À Joana Costa, que apesar de estar distante, sempre se preocupou com o meu percurso e doutoramento.

Ao Rafael Morais por ser presença constante e forte, que não vacila nos momentos mais críticos.

À Ana Vinhas por ser o equilíbrio de todo o desequilíbrio que é o PhD; por me transmitir tranquilidade, relativizar a vida e me ajudar em todas as situações.

À Filipa Miranda por ser uma modelo de superação e de esforço. Por ser uma *miga* com a chave dos cadeados das situações.

À Marta Barbosa pela dedicação, paciência e carinho demonstrados em momentos fulcrais deste doutoramento.

À Jéssica Reis por aparecer quando é preciso remar contra a maré e por ser uma importante presença na minha vida. Pela motivação e confiança que sempre me transmitiu.

À Soraia Neves por me dar sempre a mão (sempre!) quando é preciso e pela preocupação constante. Por me mostrar que por mais que o vento mude, o que importa é o objetivo final.

Aos *meus amigos de Aveiro* quero agradecer por todos os momentos de descontração que me ajudaram a encarar a vida de forma mais positiva e tranquila. Por me ensinarem bastante sobre a vida e me recordarem que nunca devemos negar a nossa essência. Obrigado pelos jogos de *padel* que ajudaram a limpar a cabeça quando mais precisava na fase final. A todos vocês que me ensinaram o verdadeiro sentido da palavra amigo! Um obrigado sentido também ao grupo do *mais* que sempre teve uma palavra de motivação. Ao *grupo da feta* um agradecimento por todos os momentos de lazer e de diversão, fundamentais durante este período.

À Ana Pereira, por continuar a ser o suporte do meu catalisador, por estar sempre ao meu lado, nos bons e nos maus momentos; por conseguir pôr-me um sorriso nos piores dias; por potenciar o meu valor e elevar os meus objetivos; por todo o amor e carinho que me tem demonstrado e me ajudou a concluir esta etapa! És a minha luz, a minha motivação, o meu suporte, a minha fase ativa, o meu promotor, o meu catalisador com maior atividade catalítica.

Aos meus avós agradeço a presença contínua, força e muito carinho, fundamentais para ultrapassar os dias menos bons deste caminho.

Aos meus pais, Lino Rocha e Margarida Rocha, por me terem apoiado incondicionalmente ao longo de toda a minha vida e por me terem transmitido os melhores valores! Foram os meus verdadeiros *patrocinadores*, potenciando ao máximo a minha melhor versão e a minha felicidade. Estarei eternamente grato por todo o apoio e amor!

Esta tese foi sustentada financeiramente pelo Financiamento Base - UIDB/00511/2020 da Unidade de Investigação - Laboratório de Engenharia de Processos, Ambiente, Biotecnologia e Energia - LEPABE - financiada por fundos nacionais através da FCT/MCTES (PIDDAC); e pelos projetos NORTE-01-0145-FEDER-000005 e NORTE-01-0247-FEDER-39789, financiados pelo Fundo Europeu de Desenvolvimento Regional (FEDER), através do Programa Operacional Regional do Norte (NORTE 2020). Agradeço também à FCT pela bolsa de doutoramento com a referência SFRH/BD/120179/2016, financiada por fundos nacionais do MCTES e pelo Fundo Social Europeu (FSE), através do Programa Operacional Capital Humano (POCH).

Contents

List of Figures

Chapters

Appendixes

List of Tables

Chapters

Appendixes

Chapter 1. General Introduction

This chapter presents the relevance and motivation behind this PhD work and provides a short introduction to the study. At the end of this chapter, the objectives of this PhD thesis are defined, and the thesis outline is provided.

1.1. Relevance and motivation

In recent years, the problematic related to the production of olive oil mill wastewater (OMW) is becoming progressively more relevant due to the increase in the production and consumption of olive oil around the world - ca. 30 million m^3 of OMW per year are produced worldwide [1-3]. In addition, the OWM is considered to be 200 times more pollutant than urban wastewater [2].

Several treatment processes have been considered to treat OMW, but an effective resolution has not been applied yet. Alternatively, valorization strategies should be envisaged, especially processes that are economically advantageous, given the potential of such streams. In this way, the steam reforming of OMW (OMWSR) was already considered to address this challenge [2-5], which would allow eliminating the pollutants present in the effluents while producing green H_2.

The use of hybrid multifunctional reactor concepts with the aim of suppressing both thermodynamic and kinetic limitations has been studied for several steam reforming processes [6-9]. Since the main products of these processes are H_2 and CO_2, and several reactions are reversible, the application of a sorption-enhanced reactor (SER) with CO_2 capture, a membrane reactor (MR) with selective H_2 permeation, or even a sorption-enhanced membrane reactor (SEMR), with simultaneous in-situ H_2 separation and CO_2 capture, could be promising in the OMWSR process, potentially yielding high-purity streams of H_2.

1.2. Objective and outline of the thesis

The main objective of this PhD thesis was to check whether the OMWSR process is suitable for the treatment and valorization of OMW effluents using different reactor configurations (TR, SER, MR and SEMR). To achieve this, several stages were necessary and are described in the following thesis outline.

Chapter 2 starts by presenting a comprehensive literature review about the OMW composition and about the treatment/valorization processes that have been investigated in the past years to reduce the OMW pollutant load. Besides that, it was presented a summary of the most relevant catalysts reported in the literature for the OMWSR and similar processes. Finally, an overview of the main features (and some results already obtained in previous works) of the multifunctional reactor used in this PhD work are discussed, focusing also on the most promising CO_2 sorbents and H_2 perm-selective membranes that can be applied in these different hybrid reactors.

Chapter 3 describes all the substances, procedures, methods, setups and experimental conditions employed in the runs whose results are presented in the following chapters.

Chapter 4 includes a thermodynamic study of the OMW reaction, carried out in the *Aspen Plus V8.8*® software, performed in different reactor configurations (TR, SER, MR and SEMR). The first subchapter

(4.1) presents a thermodynamic analysis in a TR, to understand the effect of several operation conditions (e.g. pressure, temperature and OMW compositions) in the production of the gaseous products, and particularly H_2. In the second subchapter (4.2), the main results related to the effect of H_2 and/or CO_2 removal from the reaction medium (as occurs in the multifunctional reactors) are presented and discussed.

Chapter 5 addresses the synthesis, characterization and testing of several sorbents derived from hydrotalcites (HTCs) for CO_2 capture. In the first subchapter (5.1), several HTC-based materials were prepared with different interlayer anions, characterized through several techniques, and the CO_2 sorption equilibrium isotherms of all sorbents were determined at 300 ºC. After, several CO_2 breakthroughs were performed and the sorption kinetics during the CO_2 uptakes of the samples was determined. In the second subchapter (5.2), the two sorbents considered previously as the most promising were doped with potassium and modified with gallium, to evaluate the effect of these modifications on the sorption capacity of the materials. Again, the sorbent samples were characterized through several techniques and the sorption kinetics determined. The effect of steam on the sorption capacity/stability of several samples was also assessed.

Chapter 6 presents the results obtained in the catalytic screening performed with commercial and prepared catalysts. In the first subchapter (6.1), the results of the catalytic tests and physicochemical characterization performed with the commercial materials are shown, evidencing some correlations between characterization and catalytic activity. It was also done a long-term test with a commercial sample. In the second subchapter (6.2), the same experimental work was carried out, but with prepared Ni-based catalysts.

Chapter 7 shows the results of the OMWSR obtained using the different reactor configurations (TR, SER, MR and SEMR). First, it was discussed the results obtained in a TR for different operation conditions. OMWSR experiments under the same operating conditions used in the TR were carried out firstly in a SER, where it was used as CO_2 sorbent a commercial potassium-promoted HTC from Sasol or a sorbent prepared in the laboratory derived from a traditional HTC doped with potassium. Then, a Pd-Ag tubular membrane supplied by Tecnalia (Spain) was submitted to H_2 permeation tests at different driving-forces, being followed by the experimental test of OMWSR combined with oxidative regeneration in a SEMR. A comparison between the TR, SER, MR and SEMR is presented in terms of H_2 production. In the last subchapter, it was used a real effluent in a SEMR.

Chapter 8 shows the techno-economic analysis performed for the OMWSR process in a TR or in SERs. The use of a MR/SEMR was not considered, as the cost of a H_2 perm-selective membrane (e.g. Pd-based membrane) remains quite expensive and the degree of maturation of this technology is still low (small TRL). The general considerations/hypotheses adopted are presented. Then, the entire design study defined for the calculation of the costs of the process units is summarized. Finally,

the main conclusions about the economic profitability of the process are discussed, taking into account all the costs and revenues involved, calculated for the different operating conditions considered.

Finally, chapter 9 presents the general conclusions of this PhD thesis, some of its limitations and perspectives of future work.

References

[1] Council, I.O., Economic Affairs & Promotion Unit. 2021 [Acessed 18-02-2021]; Available from: https://www.internationaloliveoil.org/what-we-do/economic-affairs-promotion-unit/#prices.

[2] Tosti, S., M. Fabbricino, L. Pontoni, V. Palma and C. Ruocco, Catalytic reforming of olive mill wastewater and methane in a Pd-membrane reactor. International Journal of Hydrogen Energy, 2016. 41(12): p. 5465-5474.

[3] Tosti, S., C. Accetta, M. Fabbricino, M. Sansovini and L. Pontoni, Reforming of olive mill wastewater through a Pd-membrane reactor. International Journal of Hydrogen Energy, 2013. 38(25): p. 10252-10259.

[4] Alique, D., G. Bruni, R. Sanz, J.A. Calles and S. Tosti, Ultra-Pure Hydrogen via Co-Valorization of Olive Mill Wastewater and Bioethanol in Pd-Membrane Reactors. Processes, 2020. 8(2): p. 219.

[5] Tosti, S., C. Cavezza, M. Fabbricino, L. Pontoni, V. Palma and C. Ruocco, Production of hydrogen in a Pd-membrane reactor via catalytic reforming of olive mill wastewater. Chemical Engineering Journal, 2015. 275(Supplement C): p. 366-373.

[6] Silva, J.M., M.A. Soria and L.M. Madeira, Thermodynamic analysis of Glycerol Steam Reforming for hydrogen production with in situ hydrogen and carbon dioxide separation. Journal of Power Sources, 2015. 273: p. 423-430.

[7] Leal, A.L., M.A. Soria and L.M. Madeira, Autothermal reforming of impure glycerol for H_2 production: Thermodynamic study including in situ CO2 and/or H2 separation. International Journal of Hydrogen Energy, 2016. 41(4): p. 2607-2620.

[8] Montero, C., L. Oar-Arteta, A. Remiro, A. Arandia, J. Bilbao and A.G. Gayubo, Thermodynamic comparison between bio-oil and ethanol steam reforming. International Journal of Hydrogen Energy, 2015. 40(46): p. 15963-15971.

[9] Soria, M.A., C. Mateos-Pedrero, A. Guerrero-Ruiz and I. Rodríguez-Ramos, Thermodynamic and experimental study of combined dry and steam reforming of methane on Ru/ ZrO2-La2O3 catalyst at low temperature. International Journal of Hydrogen Energy, 2011. 36(23): p. 15212-15220.

Chapter 2. Introduction and State of the Art

Abstract:

Olive oil mill wastewater (OMW) is a polluting stream derived from the production of olive oil and is a source of environmental pollution in the Mediterranean countries. In this effluent, several pollutants are present, namely polyphenols, sugars and fatty acids, among others. Nowadays, to reduce the pollutant load, several treatment techniques are applied to this stream, but these technologies have numerous cost and efficiency problems. For this reason, the steam reforming of the OMW (OMWSR) presents as a good alternative to the previous treatments, since this process decreases the pollutant load of the OMW and simultaneously the waste is valorized with the production of green H_2. Currently, the OMWSR is an innovative treatment alternative in the scientific field and with high potential. In the last years, some groups studied the OMWSR and used innovative reactor configurations (namely membrane reactors - MRs - with H_2 perm-selective membranes), aiming to improve the process effectiveness. In this chapter, the OMW treatment/valorization processes, the last developments on catalysis for OMWSR (or steam reforming of similar components present in the OMW), as well as the last advances on OMWSR performed in MRs are addressed. The hypothesis of the use of other multifunctional hybrid reactor configurations (sorption-enhanced reactor or sorption-enhanced membrane reactor) in this process is also discussed.

2.1. Introduction

The olive oil industry is very relevant in Mediterranean countries, both economically and traditionally. Olive oil is often part of the people's diet of this region. Because of its excellent nutritional properties, this oil contributes to cholesterol control and promotes cardiovascular health. This importance is translated into numbers: more than 9 million hectares of cultivated olive tree [1]. It was estimated, for the 2019/2020 crop year, that 70 % of the world's olive oil production is carried out in European Union, with the Iberian Peninsula being a leader zone (76 % of the European Union's total) - see Fig. 2.1 [1, 2]. However, there are other countries with significant olive oil production: Morocco, Tunisia, Syria and the United States of America. Besides that, other countries like Argentina, Australia and South Africa are promoting this type of crop [3].

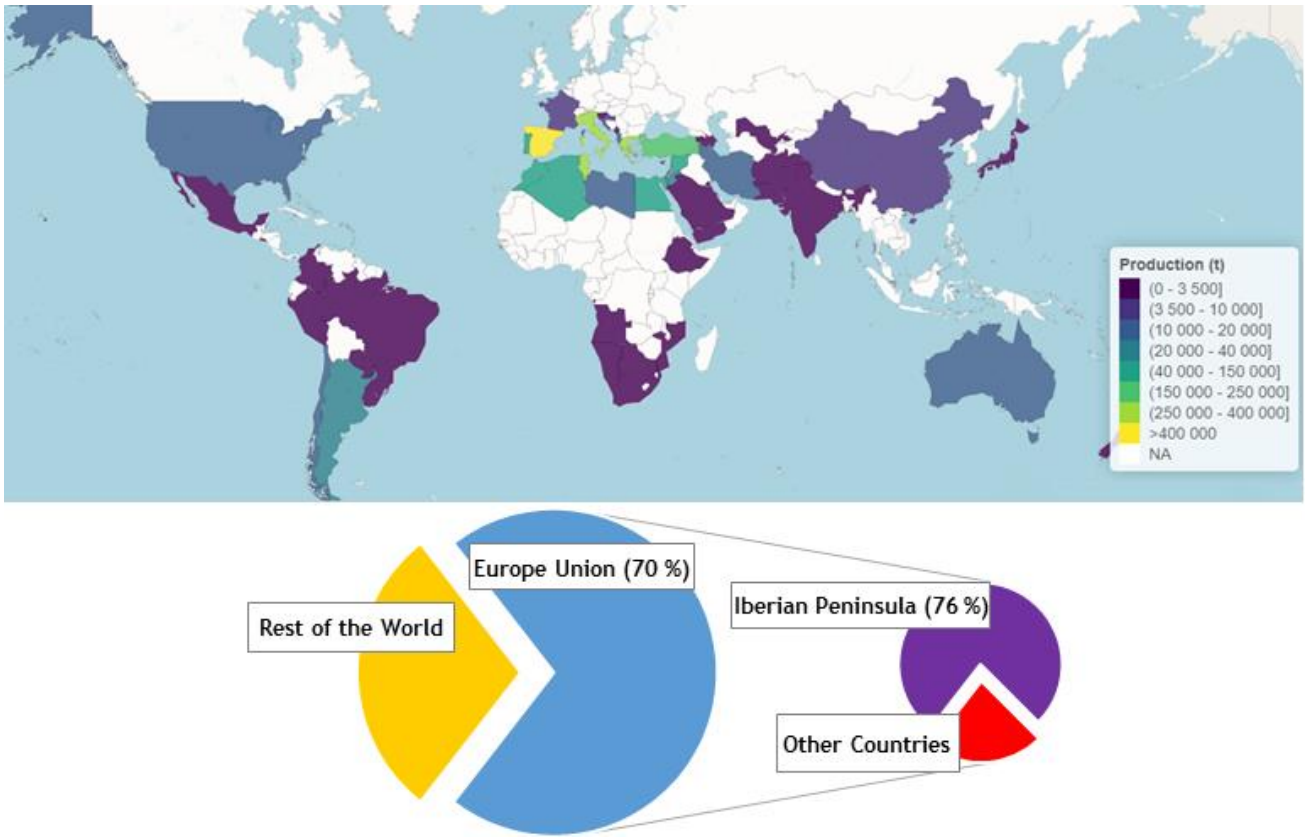

Fig. 2.1. World and Europe Union production of olive oil [2].

In this way, it is observed that these countries are considerably affected by the pollution resulting from the production of olive oil. The process generates massive amounts of solid and liquid waste (olive oil mill wastewater - OMW), which has raised serious disposal problems for producers. In fact, this stream represents a major environmental problem, where large quantities of effluents are generated in a short period. This environmental concern is accentuated by the large amount of olive oil production/consumption (close to 3 million metric tons per year produced/consumed - this value was practically constant in the last 7 years) [2, 4, 5] - see Fig. 2.2.

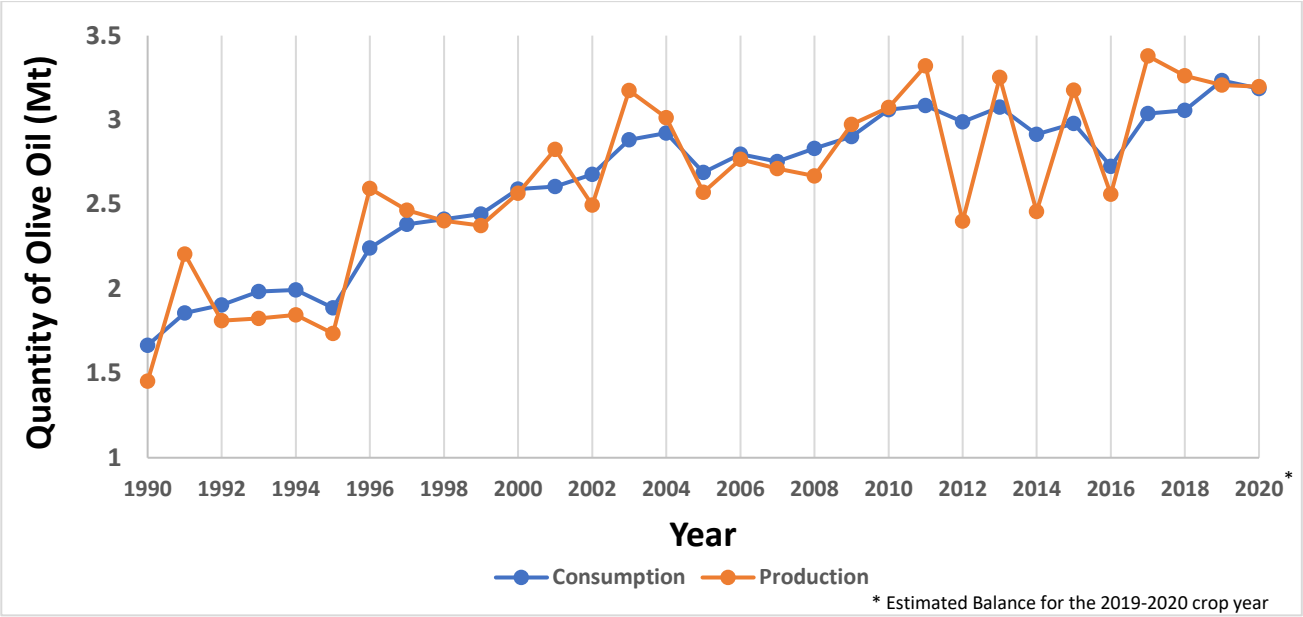

Fig. 2.2. World consumption/production of olive oil [2].

The aqueous residues associated with this agro-industrial activity are generated using either the traditional pressing or the centrifugation systems (three- or two-phase systems) because in all of them water is used to extract the oil from the olive, producing also a residual aqueous phase [1, 6]. In Fig. 2.3 it can be seen a scheme of the main processes of olive oil production [7].

The discontinuous pressing process (traditional method) is the oldest and most widespread method for processing olive. In the traditional pressing (adopted only in small mills/companies) the ground olives are pressed in cloth bags and then the liquid mixer is rested in a sequence of decanters to separate the olive oil. To separate the oil from the other phases, a small quantity of water is added. This traditional process also produces a solid fraction denominated by olive pomace (olive cake) constituted by olive pulp, stone, and water. This traditional method presents several advantages such as cheap equipment and technical simplicity. However, it also has disadvantages, such as process discontinuity and high manpower costs [7]. Besides that, because it adds water in several steps of the production process (previous to the decantation step), a large quantity of OMW (approximately 40-60 L/100 kg olives) is produced in the separation of olive oil from the other components [7].

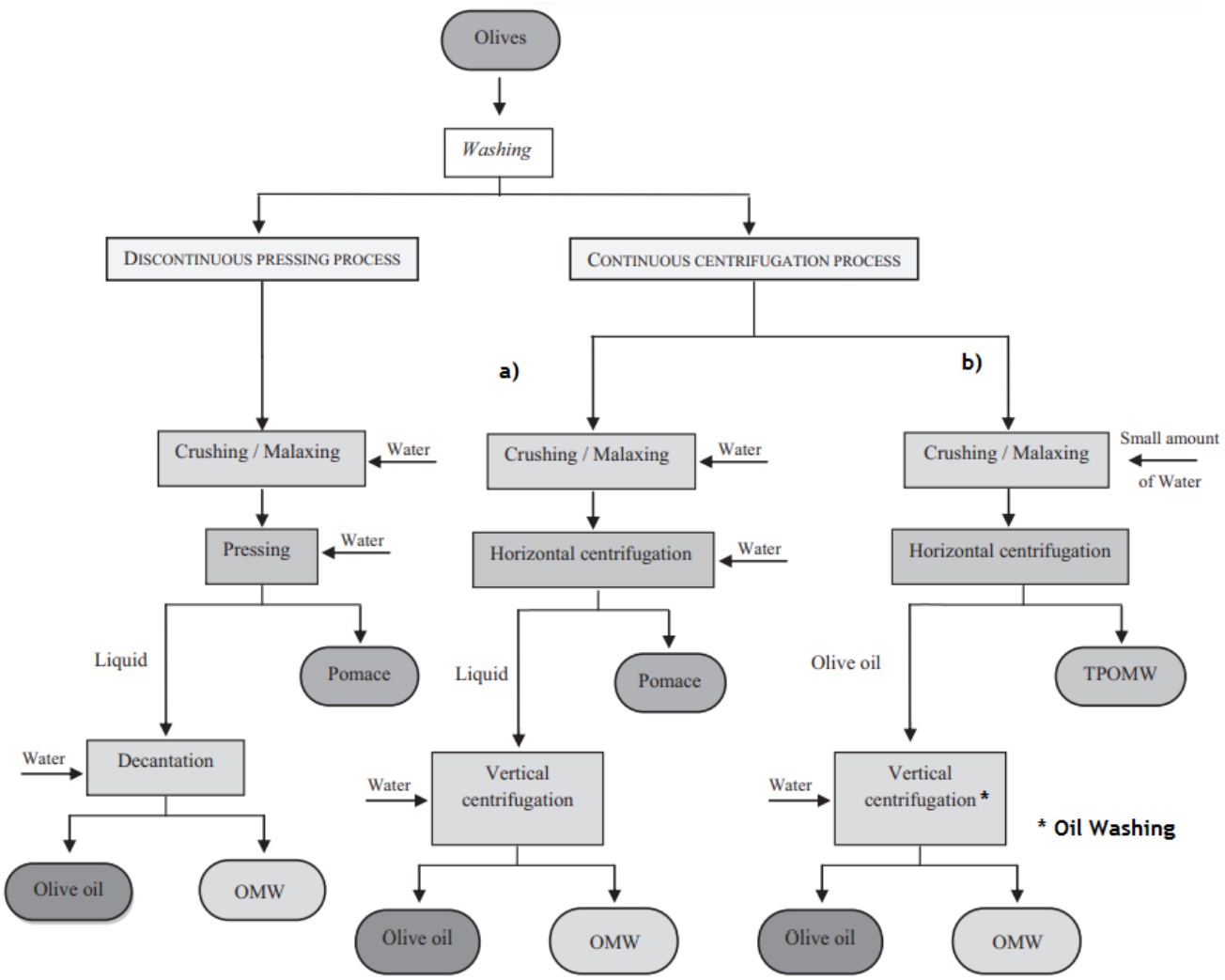

Fig. 2.3. Main processes of olive oil production - traditional (pressing) method, a) three-phase centrifugation process and b) two-phase centrifugation process. Adapted from [7, 8].

The OMW produced has a higher chemical oxygen demand (COD) compared with the OMW generated by the other processes [9]. Until approximately 40 years ago, this was the only process used, although economic problems pushed olive mills to progressively abandon the traditional method [10, 11].

In the centrifugation systems, the crushed olive fruits are pumped into a two-phase/three-phase decanter centrifuge and then the impure oil is centrifuged [12]. These processes are based on the differences in the density of the olive paste components (olive oil, water and solids) and can produce three distinct fractions: pomace, olive oil and OMW - see Fig. 2.3.

Using the three-phase process, the olive paste is divided into three phases in the horizontal centrifugation (water added in this step): olive oil, OMW and pomace [7, 8] - see Fig. 2.3. Then, the liquid fraction generated (olive oil + OMW) is centrifugated (vertical centrifugation) with additional water to recover a high-quality olive oil, producing a high quantity of OMW - see Fig. 2.3. Since the

continuous three-phase centrifugation process (route a) in Fig. 2.3) adds water in the two centrifugation steps, a high volume of OMW is produced (about 100-120 L/100 kg olives - 1.7-3 times more compared to the traditional method) [8]. Nevertheless, this three-phase system has various advantages, such as complete automation and better oil quality. However, this system also presents several disadvantages such a higher level of water and energy consumption, higher volume of OMW produced (as previously mentioned) and more expensive installations [3].

To minimize the impact of OMW, the two-phase centrifugation process (route b) in Fig. 2.3) was developed during the decade of 90 [7]. Using this two-phase process, the olive paste is separated only into two phases in the horizontal centrifugation (no water added in this step): olive oil and wet pomace, the last known as two-phase olive mill waste (TPOMW), a combination of pomace and OMW - see Fig. 2.3 [7]. Then, the olive oil generated is washed (vertical centrifugation - oil washing) with a very small quantity of water, producing only a small OMW stream - see Fig. 2.3 [8]. Despite the lower volume of OMW produced in comparison with the three-phase process, the resulting TPOMW (10 L/100 kg olives) is harder to manage and treat, because its pollutant load is more concentrated [7]. Nevertheless, some quantity of OMW is drained from the TPOMW in the storage tanks and is collected using draining valves. Besides that, it is possible to extract some oil from TPOMW through several techniques (e.g., using solvents), valorizing, in this way, this by-product [7]. In this way, the two-phase system, besides presenting the same advantages of the three-phase system, also produces a lower quantity of OMW (about 8.5-11 L/100 kg olives) and reduced water consumption; thus, this centrifugation system has been called “ecological” [3, 13]. Nevertheless, like the three-phase system, the two-phase system needs expensive installations.

Fig. 2.4 shows a scheme quantifying the formation of OMW (for all extraction processes used in the Mediterranean area) in relation to the quantities of olives and extractive water used, and olive oil/olive husk produced; one can see a big ratio between OMW and olive oil produced [14]. Moreover, it is estimated that 30 Mm^3 of OMW per year are produced worldwide [6]. The OMW results from both the water contained in the olives (mainly) and the water used in the production process of the olive oil, especially with the three-phase centrifugation system and pressing method [1, 6].

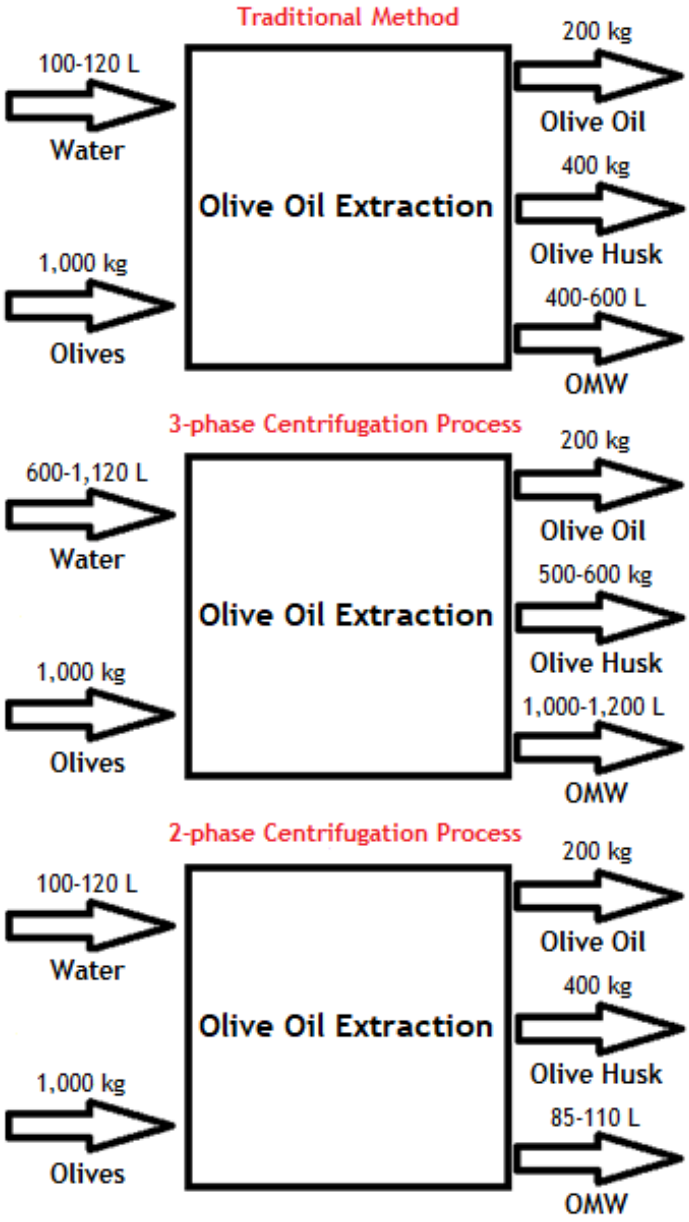

Fig. 2.4. A quantitative relationship between the formation of OMW and the remaining constituents presents in olive oil extraction [14].

These large amounts of OMW cause large environmental impacts, as several studies have already shown [15-18]. It is reported that such residues have an impact on soil and air quality and on the aquatic ecosystems due to the deposition of toxic effluents directly in the receiving bodies. Some of the major negative effects are the increase of the organic charge concentration and the occurrence of phytotoxicity in the water systems. This occurs because of the high values of COD (60-200 $g \cdot L^{-1}$), total organic carbon (TOC - > 9 $g \cdot L^{-1}$) and biochemical oxygen demand (BOD - 14-100 $g \cdot L^{-1}$) present in the OMW [6]. Pollution from OWM was estimated to be 200-400 times higher than from urban wastewater [1, 19, 20]. The uncontrolled disposal of OMW represents a social, economic, and environmental problem, which must be solved.

2.1.1. OMW composition

The composition of OMW is highly variable and suggests that major or minor compounds can be present, depending on several factors which include: the age of the olive tree, the region of cultivation, the maturation level of the olive, the weather conditions that the olive was subjected to in the ripening process, the treatment of the tree and the method of extracting the oil [21]. El-Abbassi *et al.* [22] showed that OMW resulting from the traditional method had a higher phenolic content compared to that obtained from the three-phase centrifugal system. The investigation of these effects in the OMW composition is very important, in order to develop sustainable OMW management strategies.

In general, OMW consists of solid and liquid matter, with a slightly acidic pH. The latter is composed of water, polyphenols, fatty acids and sugars, among other organic and inorganic species [6, 23]. The content of water in this stream is usually between 80-95 wt.% [6, 24-26]. In Table 2.1 is possible to see a typical physico-chemical characterization of the OMW [23].

Table 2.1 - Typical physico-chemical characterization of the OMW [23].

Organic Species		**Inorganic Species**			
Solid Waste ($g \cdot L^{-1}$)	11.5-102.5	Pb ($\mu g \cdot L^{-1}$)	6.7-10	Ca ($g \cdot L^{-1}$)	0.03-0.29
Organic Matter ($g \cdot L^{-1}$)	16.7-81.6	Cd ($\mu g \cdot L^{-1}$)	0.03-10	K ($g \cdot L^{-1}$)	0.73-6.1
Lipids ($g \cdot L^{-1}$)	1.64-9.8	Fe ($mg \cdot L^{-1}$)	0.45-20	Cl ($g \cdot L^{-1}$)	0.76-1
Polyphenols ($g \cdot L^{-1}$)	0.002-11.5	Zn ($mg \cdot L^{-1}$)	1.7-4.98	Na ($g \cdot L^{-1}$)	0.03-0.13
Sugars ($g \cdot L^{-1}$)	1.3-8.79	Cu ($mg \cdot L^{-1}$)	0.49-2.96		
Organic Acids ($g \cdot L^{-1}$)	0.78-1	Mn ($mg \cdot L^{-1}$)	0.46-20		
Total Nitrogen ($g \cdot L^{-1}$)	0.06-0.95	Mg ($mg \cdot L^{-1}$)	0.03-0.17		

The compounds most referenced are the following: vanillic acid, caffeic acid, tyrosol, p-coumaric acid, cinnamic acid, D-arabinose, D-galactose, D-galacturonic acid, syringic acid, gallic acid, protocatechuic acid, phenol, acetic acid, phenethyl alcohol, guaiacol and benzyl alcohol [1, 6, 7, 14, 21, 22, 26, 27-37]. However, it is important to remark that more than 30 polyphenols and sugars have been detected in OMW [38]. In Table 2.2 is represented an example of OMW composition on a dry basis [36].

Table 2.2 - Typical composition (wt.%) on a dry basis of the OMW [36].

Ratio of Polyphenols/Sugars	0.46
Species	
Tyrosol	16.68 %
P-Coumaric acid	14.83 %
D-Arabinose	22.83 %
D-Galactose	22.83 %
D-Galacturonic acid	22.83 %

2.1.2. OMW treatment/valorization

As the substances present in OMW are very toxic, the effluent needs to be correctly treated. A great variety of treatment/valorization processes have been investigated in the past years to reduce OMW pollutant load or to allow their disposal, but research efforts turn nowadays toward other aspects.

However, those methods of OMW load reduction are not generally used due to economic and technical reasons. The trivial management of the OMW consists in the direct discharge into sewer systems and rivers, dilution with other effluents, or disposal in evaporation lagoons, even though such management practices are not allowed in most Mediterranean countries [4, 39]. In addition, the latter practice requires large areas and produces a black foul-smelling sludge that is difficult to remove, with inherent pollutant infiltration into ground water and insect proliferation. Besides that, land disposal is also a common practice considering OMW has a fertilizer if it is well managed. Nevertheless, to avoid soil contamination and a reduction in plant growth, land disposal must be quantitatively controlled by releasing small amounts of wastewater. Thus, nowadays, a controlled release of OMW into the environment (for different ways) is still allowed, according to specific regulations of the different countries.

So, solutions for adding value to OMW or for extracting valuable compounds from it before treatment/discharge are required. Although, in some cases, the OMW is only treated to decrease the pollutant load. The OMW valorization/treatment methods could be organized into several general categories (see Fig. 2.5) and sub-categories:

- **Thermal Processes** [4]**:**
  - *Distillation and Evaporation Processes:* These processes concentrate the organic and inorganic contents of the OMW by evaporation of the water. These processes have high operation costs and the organic content must be treated afterwards;
  - *Combustion:* This process is very efficient but requires a large amount of energy.

- **Membrane Processes** [4, 26, 40-42]**:** These processes separate the organic and inorganic contents of the OMW by the utilization of membranes. However, the cost of the membrane is very high and the process has operation problems (membrane fouling, concentration polarization, etc.). There are several types of membrane-based processes: ultrafiltration, nanofiltration, reverse osmoses and microfiltration.

- **Physicochemical Processes** [43]: These processes consist of physical and chemical reactions involving molecules present in the OMW composition. Sometimes, they are conjugated to maximize efficiency.
  - *Electrochemical Oxidation* [44, 45]*; Ozonation* [46, 47]*; Adsorption* [48-50]*; Ion-Exchange* [51,52]; *Flocculation* [4, 53, 54]*; UV Photocatalysis* [45, 55, 56]*; Wet Oxidation* [57-59]*; Fenton Oxidation* [60-64]*; Photo-Fenton* [38, 65]; *Electro-Coagulation* [66, 67]*; Enzymatic Catalysis* [68]*; Supercritical Water Gasification* [69].

- **Biological Processes** [70]**:** These processes use microorganisms to decrease the pollutant load and, simultaneously, provide products with value (for instance, formation of CH_4 or H_2).
    - *Aerobic Processes* [70-73]; *Anaerobic Processes* [50, 74-76].

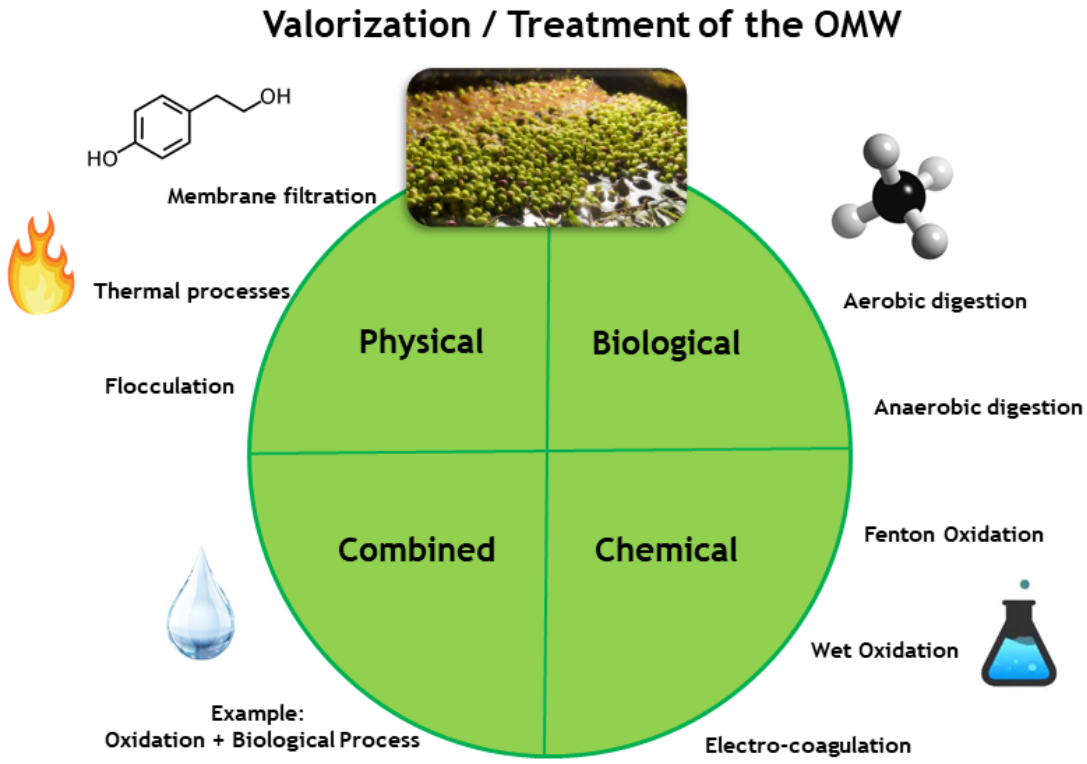

Fig. 2.5. General scheme of different techniques applicable for OMW treatment/valorization [77].

Most of the methods studied aiming OMW valorization include the recovery of the polyphenols fraction owing to their interesting pharmacological properties [78-81]; besides that, OMW phenolic extracts can be used in the food industry, in order to improve the oxidative status of the products [77]. For instance, in recent years, membrane processes have been used for polyphenols recovery [26], namely the following: microfiltration, ultrafiltration, reverse osmosis, nanofiltration, membrane distillation and osmotic distillation [4, 40, 41]. However, membrane processes have a range of limitations; e.g., may be limited by the OMW's high concentration of suspended solids. Besides that, adsorption processes [48, 50] have been also applied to the recovery of phenolic compounds to valorize the OMW effluent.

Concerning the treatment processes, the most commonly utilized physicochemical treatments with this purpose include enzymatic catalysis [68] and electrochemical oxidation with ozonation [71]. Although, there are more physicochemical methods such as electro-coagulation [66], adsorption processes [49] and advanced oxidation processes [43, 82, 83] (particularly Fenton oxidation [60, 61]). Since the polyphenols have strong resistance to bacteria, the physicochemical methods can be extremely important, because these treatment processes can reduce the organic content to make the

effluent suitable for biological processes (two different techniques combined for OMW treatment/valorization).

In general terms, numerous conventional valorization/treatment technologies with varying degrees of success have been proposed. However, most of them require substantial financial input and present low efficiency. In addition, they often focus on removing the polyphenols and end up producing a secondary waste that requires further treatment.

Therefore, it is necessary to develop technological solutions for the treatment and valorization of these wastes to minimize the environmental impacts and to enable sustainable use of resources, in compliance with international waste management practices. In this perspective, the possibility of waste valorization for green energy production has been considered, namely through OMW steam reforming (OMWSR). This technology would allow eliminating the pollutant species present in the OMW while producing H_2, therefore providing added-value. This biofuel is environmentally attractive because it is renewable and reduces the emission of CO_2 into the atmosphere [84]. Unlike fossil fuels, H_2 burns cleanly, without emitting any environmental pollutants (accumulation of CO_2 and other greenhouse gases in the atmosphere). The OMWSR would help reducing the pollution level as well as to economically valorize a by-product of the olive oil sector without any value so far. The H_2 can be used in several applications like in electrochemical cells or combustion engines. Besides the environmental problems, the economics of energy production is also changing. In this way, the global demand for pure H_2 since 1975 has increased about 300 % (see Fig. 2.6); nowadays, about 42 Mt of H_2 are used (per year) [85]. Moreover, a recent publication of the International Energy Agency reported that the global H_2 demand in the Sustainable Development Scenario (between 2019-2070) will increase significantly in the next decades, in order to reach international climate and sustainable energy goals [86] - see Fig. 2.6. To meet this growing demand for H_2, the environmentally friendly production of H_2 has become an important part of the H_2 market.

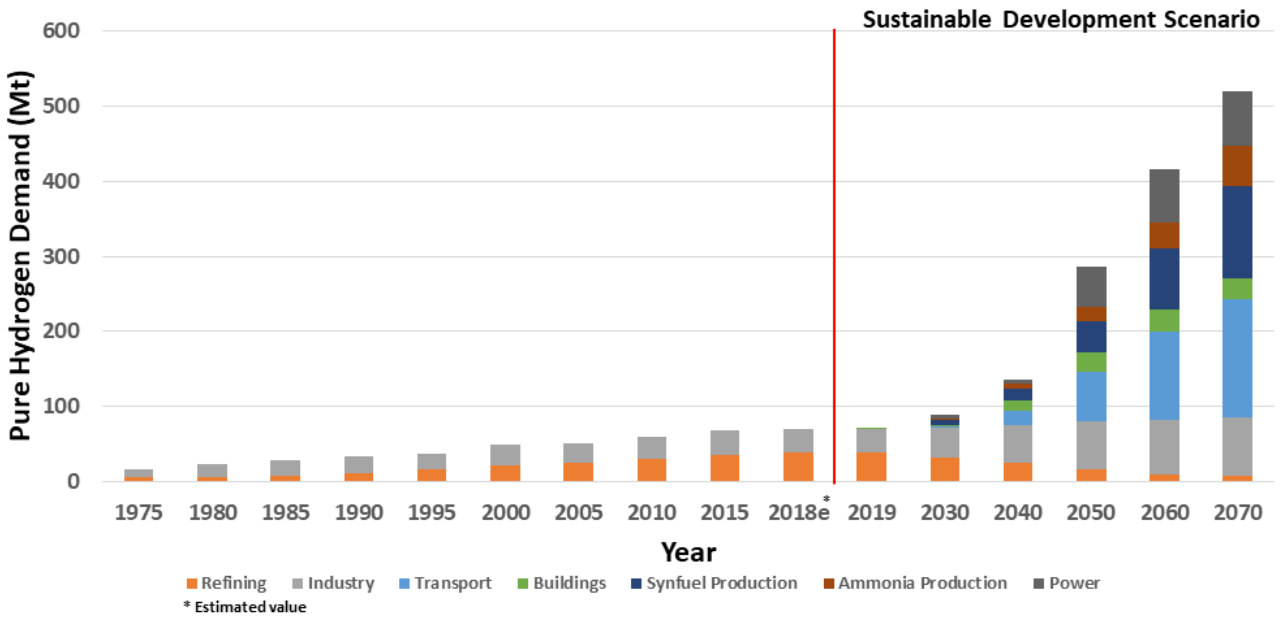

Fig. 2.6. Global demand for pure H_2 along the years - data taken from [85, 86].

2.1.3. Olive mill wastewater steam reforming reaction

The OMWSR (Eq. (2.1)) consists of the sum of two independent reactions: decomposition of high molecular weight molecules in the presence of steam (Eq. (2.2)) and the water-gas shift (WGS - Eq. (2.3)) reaction.

	$\Delta H_r^{25\,°C}$ (kJ·mol^{-1}) [84]	
$C_xH_yO_z + (2x - z)\,H_2O \rightarrow \left(2x - z + {}^{y}/_{2}\right)H_2 + xCO_2$	> 0	(2.1)
$C_xH_yO_z + (x - z)H_2O \rightarrow \left(x - z + {}^{y}/_{2}\right)H_2 + xCO$	> 0	(2.2)
$CO + H_2O \rightleftharpoons H_2 + CO_2$	-41	(2.3)

The reason why the OMWSR was chosen as a method of OMW valorization is mainly due to the fact that the steam reforming process is widely used in industry and for the reasons given above (i.e., environmental concern and production of green H_2). Besides that, syngas (H_2 and CO) produced in this reaction can be used as a resource for the production of valuable chemicals and fuels through Fischer-Tropsch or dimethyl ether synthesis routes [87].

The OMWSR process (in a Traditional Reactor - TR - see Fig. 2.7) has however some challenges that need to be overcome and optimized to be a valid approach for the OMW valorization, namely:

- The OMWSR is an endothermic reaction, thus requiring high temperatures and inherently high operating costs; moreover, producing H_2 by this process also produces CO_2 and CO, whose release is a target of environmental concern and restricted by legislation;

- The WGS reaction is thermodynamically limited (Eq. (2.3));

- This process has several side reactions, which affect both the formation and purity of H_2. The main side reactions are represented by Eq. (2.4) - methanation, Eq. (2.5) [1] - steam reforming of CH_4 - and Eq. (2.6) [2] - dry steam reforming of CH_4;

- Other reaction products apart from the previous ones, such as propane, butane, methanol, acetone, ethanol, benzene, cyclopentadiene, butanol, ethylene and acetaldehyde could be present in the reaction medium. These compounds are referred by many articles as possible secondary products of some reactions (e.g. Eq. (2.7) - cracking of oxygenates) or as intermediates of the reactions involved in the OMWSR process [1, 27, 28];

	$\Delta H_r^{25\,^\circ C}$ (kJ·mol^{-1}) [84]	
$CO + 3H_2 \rightleftharpoons H_2O + CH_4$	-206	(2.4)
$2H_2O + CH_4 \rightleftharpoons CO_2 + 4H_2$	165	(2.5)
$CO_2 + CH_4 \rightleftharpoons 2CO + 2H_2$	247	(2.6)
$C_xH_yO_z \rightarrow C_nH_mO_k + \text{gas}(H_2, CO_2, CO, CH_4, CH_n) + C$	> 0	(2.7)

- The formation of coke is a problem since it deactivates the catalyst (Eqs. (2.7) and (2.8) - cracking of hydrocarbons, Eq. (2.9) - Boudouard reaction, Eq. (2.10) - methane cracking, Eq. (2.11) - carbon monoxide reduction and Eq. (2.12) - carbon dioxide reduction); thus affecting H_2 yield and purity and long-term operation;

	$\Delta H_r^{25\,^\circ C}$ (kJ·mol^{-1}) [84]	
$CH_x \rightarrow \text{coke precursors (alofins + aromatics)} \rightarrow \frac{x}{2}H_2 + C$	> 0	(2.8)
$2CO \rightleftharpoons C + CO_2$	-172	(2.9)
$CH_4 \rightleftharpoons 2H_2 + C$	74	(2.10)
$CO + H_2 \rightleftharpoons H_2O + C$	-131	(2.11)
$CO_2 + 2H_2 \rightleftharpoons 2H_2O + C$	-90	(2.12)

[1] Sum of Eq. (2.3) and reverse of Eq. (2.4).
[2] Sum of reverse of Eq. (2.3) and reverse of Eq. (2.4).

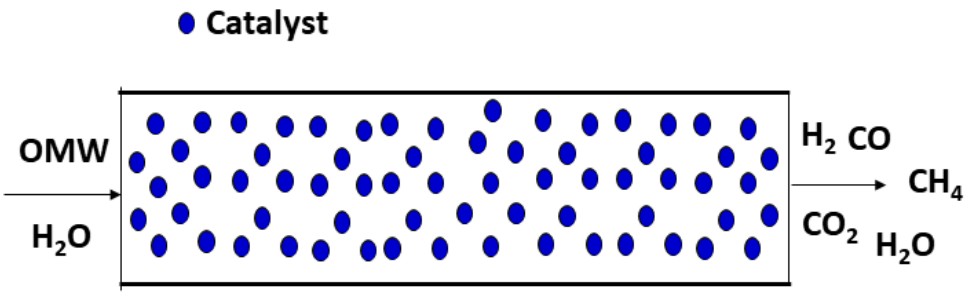

Fig. 2.7. Scheme of the operation of the TR.

With the aim of resolving these problems, new catalysts must be developed. Moreover, new reactor configurations combining the OMWSR process and H_2 and/or CO_2 selective removal should be addressed (actually, they will be a target of research in this PhD work for the first time), due to their potential to solve the limitations previously mentioned. In this chapter, some of the important developments regarding the OMWSR reaction (developed catalysts) and its combination with a H_2 perm-selective membrane (in a Membrane Reactor - MR), in the perspective of process intensification, are reviewed. It is also studied the potential of the utilization of the Sorption-Enhanced Reactor (SER - with a CO_2-selective sorbent) and the Sorption-Enhanced Membrane Reactor (SEMR - combining in the same device the capture of CO_2 and separation of H_2).

2.2. OMWSR catalysts

Heterogeneous catalysis of the OMWSR is not very developed until now. The catalysts investigated until now for this reaction have been Ni-, Pd-, Pt- and Ru-based catalysts. However, several catalysts were extensively studied for the steam reforming of individual components that are similar to the components present in the OMWSR (like acetic acid, or similar molecules). At the moment, the main goal is to prepare catalysts with high catalytic activity and also with high stability.

2.2.1. Catalysts used for steam reforming of OMW

The first group to study this reaction was the group of Tosti *et al.* [1, 6, 88] and then the group of Casanovas *et al.* [28]. Recently, Alique *et al.* [89] also studied the steam reforming of the OMW in a MR, using a prepared catalyst developed and tested in a previous work of Tosti *et al.* [88]. In these works, a previous treatment (filtration and distillation) was applied to the raw and real OMW, to reduce the solid content of the stream and to select the fraction of distilled OMW to be used in the catalytic tests.

In the first study, Tosti *et al.* [6] used a commercial Pt-based catalyst (1 wt.% Pt on Al_2O_3 - BASF SP-01 T) in a MR (150 μm thick Pd-Ag dense tubes). The experimental tests were carried out at 1 bar

and in the range of 600-800 ºC, at different space velocities (4 500-16 000 h^{-1}). The gas chromatographic analysis of the retentate revealed the presence of H_2, CO_2 and CH_4, thus demonstrating the presence of side reactions such as the hydrogenolysis and cracking of high weight molecules. Also, a deactivation of the catalyst due to coke formation was observed. Then, the same research group developed a new noble metals-based catalyst [88] and compared it with the commercial Pt-based catalyst used in the previous work under similar operation conditions (using the same reactor configuration - MR). The noble metals-based catalyst consists of Al_2O_3 pellets coated with a CeO_2-ZrO_2 layer. The active species (Pd, Rh and Pt) loading was lower than 3 wt%. CeO_2-ZrO_2 presents several benefits in the steam reforming reactions: oxidation reactions and WGS reaction are enhanced by the high oxygen mobility, which is also linked to the decrease of the coke formation and sintering prevention. Moreover, when these supports are employed, Rh can exhibit high catalytic stability during the reaction, low Pt loadings (< 1%) are sufficient for limiting deactivation phenomena and Pd can show good stability even at very low steam to carbon ratios (SCFRs). This catalyst exhibited no significant loss of activity after 6-8 h of operation, in contrast with the commercial Pt-based catalyst which activity reduced after 1-2 h of experimental test. When compared to the commercial catalyst, the new catalyst exhibited higher selectivity, allowing it to significantly reduce the formation of CH_4 and coke; thus, it revealed higher H_2 production and greater durability and stability. Regarding the total phenols content, it was possible to visualize that the content was reduced in the retentate by approximately 60 % with the commercial catalyst, while the new catalyst allowed conversion of the phenols of 90 % [88]. This new catalyst was also used in the recent work of Alique *et al.* [89]. This last work reported that, in the MR, higher pressures increased the permeation of H_2, prevailing the membrane shift effect against the negative effect on thermodynamics of the reactions involved in the steam reforming process. In this way, an increase in H_2 production was obtained as the pressure increased.

A. Casanovas and co-workers are another research group that studied this reaction [28] in the last years in a TR. Several catalytic honeycombs loaded with noble metals (Pt, Pd, Rh or Ru) or Ni over La-stabilized CeO_2 were prepared. The experimental tests were carried out at atmospheric pressure and in the range of 600-750 ºC, at different space velocities (4 500-16 000 h^{-1}). Their catalytic performance in terms of H_2 production, selectivity towards reforming products and stability followed a trend: Pt/CeLa > Rh/CeLa > Ru/CeLa >> Ni/CeLa. The trend of coke formation on the surface of these catalysts was: Ru/CeLa > Rh/CeLa > Pt/CeLa, which is the opposite to that of the catalytic performance, strongly suggesting that coke deposition was the cause of catalyst deactivation during OMWSR - see Fig. 2.8. Besides, it was found that the selectivity for secondary reactions increases with time, for all the catalysts, and the catalyst with higher selectivity for H_2 formation was Rh/CeLa. In addition, Ca deposition was also observed after the stability tests in all samples. Calcium comes from OMW and its possible effect on the long-term catalytic performance must be further investigated.

The catalyst 1 wt.% Pt/CeLa showed a very stable distribution of products in long term runs. An increase of the Pt load up to 2 wt.% had a positive effect on the product distribution, particularly on the suppression of CH_4. It was also observed that the temperature influences the production of H_2 as well as the selectivity, as expected. Independent carbon mass balances obtained by COD and gas chromatography analyses showed a 90-95 % of reduction of the organic carbon present in distillated OMW [28].

Besides that, it was also reported several studies regarding the steam reforming of guaiacol (component typically present in the composition of the OMW) using Ni-based catalysts [90-93].

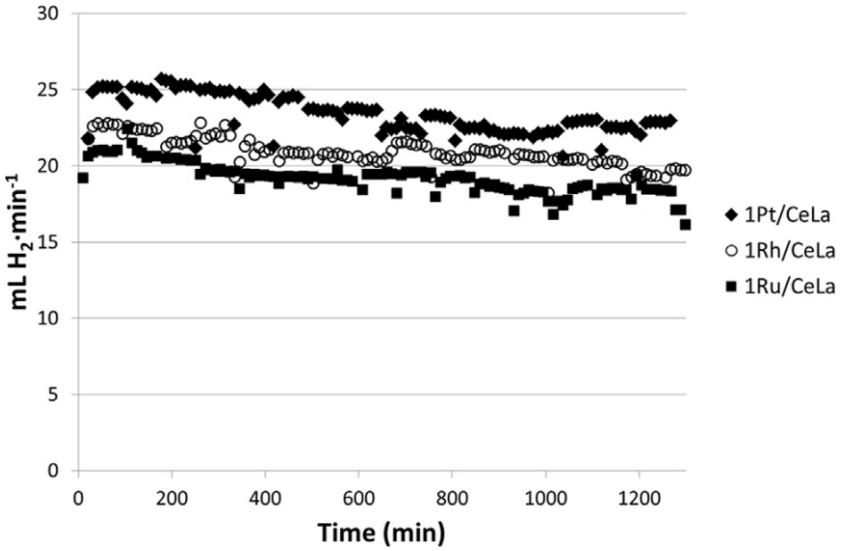

Fig. 2.8. H_2 production at 700 ºC over time on stream, F_{OMW} = 0.6 mL·min^{-1}, GHSV = 9 000 h^{-1}. Taken from [28].

Finally, it is important to emphasize that several works have already studied the steam reforming of effluents (e.g. bio-oil and palm oil mill) with compositions very similar to OMW (oxygenated species), using Ni and Co-based catalysts [94-103].

A summary of some results obtained with the catalysts more relevant reviewed in this subchapter 2.2.1 is presented in Table 2.3.

Table 2.3 - Summary of the catalytic performance and operating conditions of several catalysts on OMWSR.

Catalyst	Temperature (ºC)	Pressure (bar)	Feed Flow Rate	F_{OMW} ($g \cdot h^{-1}$)	Conversion (%)	H_2 Yield (%)	H_2 Purity (%)	Ref.
1 wt.% Pt/Al_2O_3 (commercial)	450	3	WHSV[a] = 5.56×10^{-3} $mol \cdot h^{-1} \cdot g_{cat}^{-1}$	10	n.d.[b]	40[c]	38[d]	[6]
1 wt.% Pt/Al_2O_3 (commercial)	450	5	WHSV[a] = 1.74×10^{-2} $mol \cdot h^{-1} \cdot g_{cat}^{-1}$	15	≈ 60[e]	29[c]	25[d]	[88]
< 3 wt.% Pt-Rh-Pd/$CeZr_2$-Al_2O_3	450	5	WHSV[a] = 1.74×10^{-2} $mol \cdot h^{-1} \cdot g_{cat}^{-1}$	15	>90[e]	35[c]	35[d]	[88]
1 wt.% Pt/CeLa	700	1	GHSV[f] = 13 500 h^{-1}	54	90-96[g]	58[i]	72[h]	[28]
1 wt.% Ru/CeLa	700	1	GHSV[f]= 13 500 h^{-1}	54	90-96[g]	52[i]	72[h]	[28]
1 wt.% Rh/CeLa	700	1	GHSV[f] = 13 500 h^{-1}	54	90-96[g]	44[i]	73[h]	[28]
10 wt.% Ni/CeLa	700	1	GHSV[f] = 13 500 h^{-1}	54	90-96[g]	42[i]	65[h]	[28]

[a] WHSV: weight hourly space velocity. [b] Not defined. [c] Yield (%) = $\frac{H_{2perm}}{TOC_{feed}} \times 100$, in a MR with a H_2 recovery of 80 %. Recovery (%) = $\frac{H_{2perm}}{H_{2perm}+H_{2ret}} \times 100$.

[d] H_2 purity (%) = $\frac{H_2}{H_2+CH_4+CO_2+CO} \times 100$, in a MR, on the retentate side, with a H_2 recovery of 80 %. Recovery (%) = $\frac{H_{2perm}}{H_{2perm}+H_{2ret}} \times 100$.

[e] Conversion of phenols. [f] GHSV: Gas Hourly Space Velocity. [g] Conversion of organic carbon. [h] H_2 purity (%) = $\frac{H_2}{H_2+CH_4+CO_2+CO} \times 100$, in a TR.

[i] Yield (%) = $\frac{H_{2prod}}{TOC_{feed}} \times 100$, in a TR.

New catalysts must be developed for future catalytic screening and improvement. These catalysts will have to increase the catalytic performance. In addition, the new catalysts will need to maximize the reaction conversion, decrease the coke formation and increase the H_2 selectivity at operation temperatures compatible with the properties of the sorbent and membrane (if these materials are present in the reactor configuration).

2.2.2. Catalysts used for steam reforming of model molecules of OMW

Among the above-mentioned, numerous catalysts (Ni, Pt, Ru, Co and Rh-based) have been extensively studied for the steam reforming of individual components similar to the species present in OMW. Thus, in this work, three different molecules were defined as OMW model compounds: acetic acid (detected in an OMW stream [6]), phenol and toluene. The catalytic performances of the catalysts used for the steam reforming of these species were affected by the active phase, support and promoter agents. These topics are discussed in the next subchapters.

2.2.2.1. Effect of the active phase

The active phase is the metal element of the catalyst that catalyzes the reaction. Numerous catalysts (Ni, Pt, Ru, Co and Rh-based) have been extensively studied for the steam reforming of oxygenates.

The Ni-based catalysts are the most used in the steam reforming processes because of their effectiveness (they have the potential to be highly active and stable), commercially available and relatively cheap [104-108]. Nevertheless, it is necessary to be attentive to the Ni loading, support, promoter(s) and synthesis method used in the preparation of the catalyst, since these factors have a crucial impact on both catalytic activity and price [109]. In the study of Zhang *et al*. [110], it was concluded that the increase of Ni loading from 10 wt.% to high values did not significantly increase the activity of the catalysts, but enhanced the stability, and especially the resistivity towards coking in the steam reforming of acetic acid. The coke formed over the catalyst with the lower Ni loading was more amorphous and the coke formed over higher Ni loading was more fibrous, which was possibly the catalytic coke [110]. It was verified by Borges *et al*. [111] that the higher is the Ni loading, the lower will be the temperature and the time necessary for the reduction. The catalyst with a molar ratio of Ni/Co = 3 exhibited the highest activity and the best carbon deposition resistance due to the high density of basic sites for the steam reforming of phenol. In a recent study of Yu *et al*. [112], the effects of type of anion in the Ni precursors in the catalytic behaviors of Ni/Al_2O_3 catalysts in steam reforming of acetic acid were studied. Besides the metal content present in the catalyst is also important for other metal elements, the examples presented were only with Ni-based catalysts, since the studies for other elements are limited.

Besides the Ni-based catalysts, other elements (Pt, Co, Rh, Cu, Fe) were used as catalysts for the steam reforming of similar molecules present in OMW. Since the noble metal-based catalysts are more expensive than the Ni-based catalysts, lower metal contents are usually used in the preparation of the noble metal-based catalysts. Güell *et al.* [113] reported that the Pt catalyst was active for the steam reforming of oxygenates, like shown in the study of Castro *et al.* [114]. Pant *et al.* [115] reported that Ni-Co, Ni-Co/CeO_2-ZrO_2 and Ni/La_2O_3-Al_2O_3 catalysts can catalyze the steam reforming reaction of acetic acid. Among the three catalysts investigated Ni-Co catalyst was found to be more effective for this reaction. Several authors [116-118] found that Rh-based catalysts have a good performance in the steam reforming of oxygenates and several of these catalysts exhibit better performance when compared to a commercial Ni-based catalyst. A series of Ni-Cu bimetallic catalysts supported on sepiolite (Ni_x-Cu_y/SEP) were prepared by Liang *et al.* [119] for the steam reforming of phenol. The results show that the Ni-Cu alloys were successfully synthesized in bimetallic catalysts, and the addition of Cu decreased the Ni particles size, improved the redox ability and metal dispersion of bimetallic catalysts (in this case, Cu can be also considered as a promoter of the catalyst). Hu and co-workers [62] compared the performances of Ni-, Co-, Fe-, and Cu-based catalysts for the steam reforming of acetic acid and observed that the order of decreasing activity could be defined as Ni > Co > Fe > Cu. The study reported that Ni and Co catalysts demonstrated high performance not only in the activation of the cracking of C-C bonds but also in the activation of C-H bonds.

The catalyst Fe_2O_3/SiO_2−Al_2O_3 was used by Adnan *et al.* [120] for the steam reforming of toluene. The results indicate that the Fe_2O_3/SiO_2−Al_2O_3 catalyst is a promising catalyst (in terms of activity and stability) since it is a catalyst with a large quantity of acidic active sites. However, the study of Wang *et al.* [121] (steam reforming of acetic acid), reported that in the Co-Fe catalysts, the component more active is Co rather than Fe.

Furthermore, several authors [122-124] show that multi-metallic catalyst shows high activity and improves the H_2 yield due to synergistic effects of the multiple components of the active phase.

Finally, mixed oxides such as hydrotalcites-type oxides have been reported as promising catalyst precursors for the steam reforming of these types of oxygenates [111, 125].

2.2.2.2. Effect of the support

In several studies, it was verified that the support had a significant effect on the performance of the catalysts. Different catalyst supports significantly influenced the reforming reaction.

Ni-based catalysts supported on various Al_2O_3 supports with different crystalline phases were prepared and tested by Chen *et al.* [107]. The crystalline phases of Al_2O_3 support influenced the interaction intensity between these supports and Ni and the formation of metallic Ni. Besides that, a series of Ni core-shell catalysts with various shell species (SiO_2, Al_2O_3, CeO_2 and TiO_2) were prepared

by Pu *et al.* [126]. By comparing the catalytic activities of the catalysts with various shell materials, it was concluded that the Ni/Al_2O_3 catalyst was the most suitable material for the steam reforming of acetic acid, showing much higher catalytic activity than the other catalysts. It was also observed in the work of Li *et al.* [127] that Al_2O_3 support has a high specific area that can enhance the catalytic activity, but the acidity of Al_2O_3 promotes the carbon deposition, reducing the stability of the materials.

The nature of the support was also studied by Zhang *et al.* [128], using attapulgite (ATTP) and Al_2O_3 as support of Ni-based catalysts. It was verified that ATTP had a lower specific surface area and lower thermal stability than Al_2O_3; this low thermal stability negatively affects the catalytic performance of the material for steam reforming of acetic acid. The stability of the Ni/Al_2O_3 catalyst was higher than Ni/ATTP catalyst, not only due to the higher surface area of Al_2O_3, but also due to the coke formed on the surface of the Ni/Al_2O_3 catalysts (fibrous) instead of the coke formed on Ni/ATTP catalyst (amorphous).

Hoang *et al.* [106] studied the steam reforming of acetic acid using supported Ni on CeO_2 or ZrO_2. Ni/ZrO_2 showed gradual deactivation over the catalytic test due to coke formation. Also Güell *et al.* [113] reported that the Pt-based catalyst using CeO_2 as support is more stable than that using ZrO_2. This improvement was explained by the facile redox properties of CeO_2 which can help the oxidation of coke deposits with water.

Pant *et al.* [115] reported that Ni-Co, Ni-Co/CeO_2-ZrO_2 and Ni/La_2O_3-Al_2O_3 catalysts can catalyze the steam reforming of acetic acid. Among the three catalysts studied, the Ni-Co catalyst was found to be more effective for the steam reforming of acetic acid. In this specific case, the catalyst unsupported presents a higher performance due to the interaction of the alloy Ni-Co.

Chen *et al.* [129] studied the effect of biochar as support in Ni-based catalysts for the steam reforming of acetic acid. The results of the catalyst characterization showed that the porosity of biochar was increased significantly after activation, increasing the surface area of the materials and the dispersion of the Ni particles on the catalysts surface. Besides that, in the work of Wang *et al.* [130] - study of the steam reforming of acetic acid - it was found that the treatment of biochar support with HNO_3 enhanced the quantity and the strength of the acidic active sites as well as the catalytic activity of the Ni/biochar catalysts.

In the work of Savuto *et al.* [108], the Mayenite ($Ca_{12}Al_{14}O_{33}$) was used as support of a Ni catalyst and show excellent oxidation properties that increase the resistance of the catalyst to carbon deposits. Additionally, Yang *et al.* [131] using a NiO/MgO catalyst the interaction between the support and active phase can prevent the material from sintering.

Finally, silicate structured mesoporous materials were reported to be less susceptible to deactivation due to coke formation than the conventional microporous catalyst supports. They also cause less resistance to the diffusion of reactants to the active sites [87].

2.2.2.3. Effect of promoters

In several studies of the steam reforming of oxygenates, the catalysts were doped with promoters. It was reported that Cr inhibited the formation of Ni_3C and can modify the metal sites forming alloys with Ni [132, 133], La_2O_3 led to a decrease in coke formation [105, 132-136], K and MgO improved the stability [105, 117, 132, 133, 136-139] and TiO_2 decreases the conversion [132]. It was also observed that the addition of CeO_2 improved the activity and stability of the catalyst [106, 108, 114, 135, 140-142].

The work of Li *et al.* [143] reported that the presence of CeO_2 in the catalyst increased the support-metal interaction, restricting the growth of metal particles. Besides that, in the same work, it was found that the oxygen vacancies of the CeO_2 are responsible for the activation of the water to generate OH^- groups, which can react with intermediate products to produce CO_2 and H_2. In the study of Iiada *et al.* [118], $Ru/SrCO_3$-Al_2O_3 catalysts with a low Ru loading exhibited higher catalytic activity for steam reforming of toluene compared to a commercial Ru/Al_2O_3 catalyst. In this way, it was possible to see that the $SrCO_3$ increases the performance of the catalyst. Additionally, in the study of Zhang *et al.* [144], it was verify that the addition of KOH to Ni/Al_2O_3 with the lowest Ni loading significantly enhances the catalytic activity and promotes gasification of the reactive intermediates such as methyl group, carbonyl group, etc.. Besides that, it was observed that the activation of ATTP support with KOH enhanced the surface area [93]. The activation of the support with KOH created a high amount of micropores in the ATTP material and increased the dispersion of Ni species via reducing the particle size of Ni [93].

Choi *et al.* [145] studied the steam reforming of acetic acid by using catalysts modified by MgO, LaO_3, Cu, and KOH. Ni/Al_2O_3 modified with Mg showed the best performance at low temperatures. It was possible to verify that to improve the catalytic performance and minimize the coke formation, a catalyst with a large amount of weak basic sites and few middle and strong basic sites is required. Finally, it was observed that the toluene conversion and H_2 yields increased with the addition of alkaline-earth metals [146]. In a general way, the addition of basic oxides (e.g. MgO, CeO_2, La_2O_3, etc.) enhanced the coking resistance, thus improving the catalytic activity and stability. These oxides aim to enhance the redox properties of the catalyst [143, 147-150], which increases the oxidation of surface carbon. For instance, Kumar *et al.* [151] reported that the coke formation was also significantly suppressed by the γ-Al_2O_3-La_2O_3-CeO_2 support.

Finally, Yu *et al.* [152] reported that the addition of Mn enhanced the specific area of the catalyst, by the formation of more pores and the addition of Mn, Fe, La and Ce could enhance the dispersion of Ni particles in the support. Besides that, K, Na, Co, La or Ce enhance the activity of Ni-based catalysts and K or Na addition promoted the reduction of Ni oxides.

However, Galdamez *et al.* [153] in the steam reforming of bio-oil concluded that the addition of La_2O_3 in the Ni catalyst does not increase the H_2 yield. Besides that, it has been reported in one work [105] that the presence of K in the catalyst retards the reduction process by hindering the dissociation of H_2 or by blocking the pores, limiting H_2 accessibility or preventing H_2O to leave the reduced metal site. It was also found that ZrO_2 had a negligible effect on the performance of the catalyst [138].

A summary of the catalysts more relevant for the steam reforming of individual components (or similar) of the OMW reviewed in this subchapter 2.2.2 and their best catalytic performances are presented in Table 2.4. As already mentioned in this subchapter and taking into account the studies referred in Table 2.4, it is possible to verify that Ni-based catalysts are effective for these reactions and relatively cheap. Due to this, more detailed information about the catalytic stability and preparation method of these catalysts is reported in Table 2.5. It is possible to see that several Ni-based catalysts present no deactivation until the end of the experimental test, even though noble metal-based catalysts are less susceptible to coke formation [94, 154, 155]. Furthermore, the most used preparation method of these catalysts is the impregnation of the Ni on the support; however, there are only a few studies about the effect of the preparation method in the catalytic behavior of the materials for the steam reforming of long-chain oxygenates.

Table 2.4 - Summary of the catalytic performance and operating conditions of catalysts on steam reforming reactions of oxygenated compounds.

Catalyst	Temperature (ºC)	Pressure (bar)	Feed Flow Rate	SCFR[a)]	Conversion (%)	H_2 Yield[b)] (%)	H_2 Selectivity[c)] / Purity[d)] (%)	Ref.
3.5 wt.% Ni/5 wt.% La_2O_3-ZrO_2 [1]	700	1	GHSV[e)] = 240 000 h^{-1}	5	100	87	89/64	[105]
(2.5+2.5) wt.% Ni-Cu/Al_2O_3 [1]	750	1	WHSV[f)] = 28 h^{-1}	1.25	100	67	68/57	[156]
15 wt.% Ni/α-Al_2O_3 [1]	600	1	WHSV[f)] = 20 h^{-1}	1	≈ 100	90	90/66	[107]
(15+2) wt.% Ni-Ru/10 wt.% CeO_2-Al_2O_3 [1]	700	1	WHSV[f)] = 21 h^{-1}	3.2	91	67	79/61	[140]
10 wt.% Ni/La_2O_3-Al_2O_3 [1] (La_2O_3/Al_2O_3 = 1:3, weight ratio)	700	1	LHSV[g)] = 10 h^{-1}	1	100	72	71/59	[134]
15 wt.% Ni/Al_2O_3 [1]	700	1	$F_{Acetic\ Acid}$ = 10 g·h^{-1}	1	100	57	58/54	[157]
3.2 wt.% Ni/CeO_2-ZrO_2 [1]	700	1	WHSV[f)] = 25 h^{-1}	14	≈ 84	68	88/64	[106]
0.5 wt.% Pt/CeO_2 [1]	700	n.s. [h)]	GHSV[e)] = 80,000 h^{-1}	5	98	94	≈ 100/67	[113]
28 wt.% Co/7 wt.% K-Al_2O_3 [1]	600	1	LHSV[g)] = 10 h^{-1}	7.5	100	86	87/64	[138]
(6.6+10) wt.% Ni-Fe/$(CeO_2)_{0.4}$-$PG_{0.6}$ [1]	600	1	LHSV[g)] = 14,427 h^{-1}	3	≈ 97	88	84/63	[141]
(35 wt.% NiO) Ni/Hydrotalcite [1]	600	1	n.s.[h)]	1.5	≈ 100	47	67/56	[111]
Ni/BC4 [1]	700	1	LHSV[g)] = 10 h^{-1}	2.5	91.2	71	79/61	[129]
10 wt.% Ni/ATTP [1]	600	1	LHSV[g)] = 7.2 h^{-1}	5	≈ 100	72	91/65	[128]
25 wt.% Ni/Atta [1]	700	1	LHSV[g)] = 10.4 h^{-1}	5	96	89	90/64	[93]
15 wt.% Ni/Al_2O_3-La_2O_3-CeO_2 [1]	650	1	Q_T = 2.5 mL·h^{-1}	6.5	≈ 100	88	90/64	[151]
Co (unsupported)	600	1	LHSV[g)] = 4 h^{-1}	9.2	100	≈ 100	99/66	[121]
3 wt.% Ni/(0.4+5) wt.% K-LaO_2-ZrO_2 [2]	700	1	GHSV[e)] = 950 000 h^{-1}	20	≈ 81	83	98/70	[136]
0.1 wt% Rh/(50+25) wt. % MgO-CeO_2-ZrO_2 [2]	700	1	GHSV[e)] = 80 000 h^{-1}	13	97	90	86/67	[116]
Ni-Fe/olivine [2]	850	1	W/F[i)] = 10.28 kg_{cat}·h·m^{-3}	1	≈ 100	n.d.[h)]	81/63	[158]
1.5 wt.% Pt/CeO_2-Al_2O_3 [3]	700	1	Q_T = 300 mL·min^{-1}	6	≈ 95	n.d.[h)]	81/66	[114]
16.4 wt.% Ni/Al_2O_3	800	1	GHSV[e)] = 61 200 h^{-1}	3	> 94	91	75/66	[159]

[a)] Steam to carbon feed ratio. [b)] Yield (%) = $\frac{H_2}{H_{2_{Máx.}}} \times 100$. [c)] Selectivity (%) = $\frac{H_2}{RR \times (CO_2+CH_4+CO)} \times 100$. RR is H_2/CO_2 reforming ratio. [d)] Purity (%) = $\frac{H_2}{(H_2+CO_2+CH_4+CO)} \times 100$. [e)] GHSV: gas hourly space velocity. [f)] WHSV: weight hourly space velocity. [g)] LHSV: liquid hourly space velocity. [h)] Not determined/specified. [i)] W_{cat}/F_{Phenol}.
[1] Steam reforming of acetic acid. [2] Steam reforming of phenol. [3] Steam reforming of toluene.

Table 2.5 - Stability and preparation methods for Ni-based catalysts used on steam reforming reactions of oxygenated species.

Catalyst	Mass of catalyst (g)	Stability	Preparation Method	Ref.
3.5 wt.% Ni/5 wt.% La_2O_3-ZrO_2	0.050	Lost 7% H_2 yield in 20 h	Impregnation	[105]
(2.5+2.5) wt.% Ni-Cu/Al_2O_3	0.1	Result of 7.5 h (no deactivation)	Impregnation over support prepared by following evaporation induced self-assembly	[156]
15 wt.% Ni/α-Al_2O_3	1.5	n.d.[a)]	Impregnation	[107]
10 wt.% Ni/La_2O_3-Al_2O_3 (La_2O_3/Al_2O_3 = 1:3, weight ratio)	0.2	Result of 30 h (no deactivation)	Co-precipitation	[134]
15 wt.% Ni/Al_2O_3	0.2	n.d.[a)]	Incipient wetness impregnation	[157]
6.6 wt.% Ni - 10 wt.% Fe/$(CeO_2)_{0.4}$-$PG_{0.6}$	n.s.[a)]	Result of 20 h (no deactivation)	Co-precipitation	[141]
Ni/BC4	0.15	n.d.[a)]	Impregnation	[129]
10 wt.% Ni/ATTP	0.5	n.d.[a)]	Impregnation	[128]
16.4 wt.% Ni/Al_2O_3	n.s.[a)]	Result of 5 h (no deactivation)	Impregnation	[159]

[a)] Not determined/specified.

2.2.3. Summary

Until now, only a few catalysts have been developed for the OMWSR process: Ni-, Pd-, Pt-, Rh- and Ru-based. However, several catalysts were studied for the steam reforming of components that are similar to species present in the OMW.

In this subchapter 2.2, it is possible to conclude that Ni-based catalysts have promising results for these reactions (steam reforming of oxygenated species). Almost all catalysts showed conversions close to 100 % and high H_2 yields and selectivities, being difficult to choose the best one. These results show how attractive Ni-based catalysts are for the OMWSR process.

Almost Ni-based catalysts were prepared by impregnation, appearing to be the best method for the preparation of these materials. However, it is still necessary to study the effect of the preparation method on the catalytic behavior of the materials.

In this way, a bi-metallic catalyst with Ni and one noble metal (e.g. Ru) as active phases, supported in an adequate material (e.g. Al_2O_3 or SiO_2) and doped with a promotor (e.g. CeO_2) is a potential catalyst to achieve high catalytic performance (H_2 yield and OMW conversion) for OMWSR during long reaction times.

2.3. Sorption-enhanced reactor

In the last years, alternatives for improving the catalytic steam reforming processes have been investigated and debated, since this reaction has an equilibrium limitation. One of those alternatives is the sorption-enhanced reactor (SER - see Fig. 2.9), which consists of combining the TR and CO_2 capture in the same device. This innovative configuration allows shifting the thermodynamic equilibrium of the steam reforming reaction by removing one of the reaction products from the reaction medium - Le Chatelier principle [160]. This reactor configuration was already used in multiple applications [109, 161-193] in the last decade. The SER allows to shift the equilibrium of the reversible reactions towards higher conversions of the reagents. In this way, this reactor configuration will enhance the production of H_2, since the removal of CO_2 shifts the WGS reaction (Eq. (2.3)) to the forward direction and inhibits CH_4 and coke production (Eq. (2.5) and Eqs. (2.10) and (2.12)).

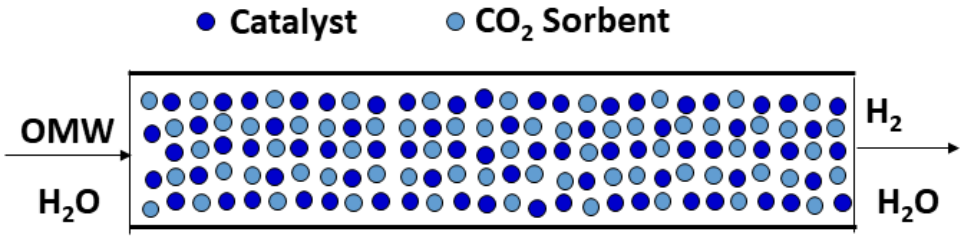

Fig. 2.9. Scheme of the operation of the SER.

However, the drawback of this system is that the CO_2 sorbent gets saturated at some point and then regeneration is necessary. To be possible to run continuously, the system must have two parallel reactors, being that while one of them is used as SER the other is being regenerated. It is possible to distinguish three regimes along time: pre-breakthrough, breakthrough and pos-breakthrough. In the pre-breakthrough region, all of the CO_2 is being removed, thus enhancing H_2 production. In the breakthrough region, the H_2 concentration at the reactor outlet starts decreasing. In the pos-breakthrough region, the sorbent is already saturated and so the enhancement of H_2 production due to CO_2 removal disappears - Fig. 2.10 and Fig. 2.11. The effect of the removal of CO_2 from the reaction medium (thermodynamic work) is discussed for the OMWSR [194] in this PhD thesis (subchapter 4.2); besides that, this effect was already analyzed for other similar reactions [84, 195-197].

Besides that, this reactor configuration intensifies the performance of the process by combining the reaction and CO_2 capture in a single device (avoiding the construction of two different operating units). In this way, a SER leads to smaller dimensions of the plant layout and allows the production of more high-purity products at the outlet (in this case, pure H_2 before the breakthrough time).

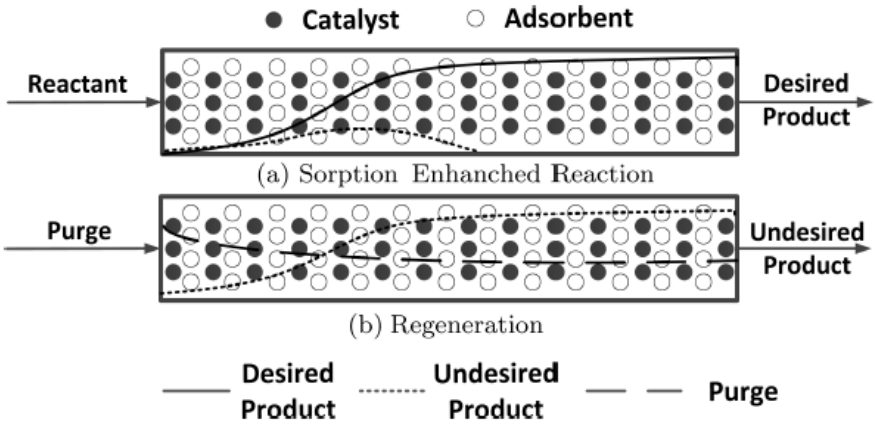

Fig. 2.10. Scheme of the operation of the SER. Taken from [162].

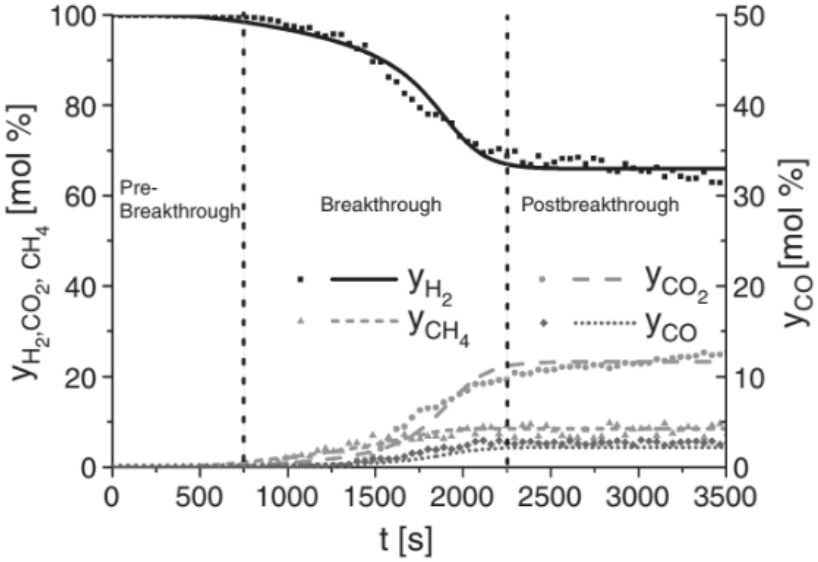

Fig. 2.11. Example of product distribution as a function of time in the outlet of a SER (steam reforming of ethanol). Taken from [162].

In this reactor configuration, the capture of the CO_2 emission also presents a very interesting environmental topic. Since the industrial revolution, the global CO_2 concentration increased from about 280 ppm to 380 ppm in 150 years. The higher concentration of pollutants in the atmosphere increases the greenhouse effect with a huge environmental impact. To avoid irreversible changes in global climate, the United Nations have agreed to establish goals to reduce the CO_2 emissions to limit its concentration in the atmosphere to less than 550 ppm - Kyoto protocol [198]. So, this reactor configuration is also in line with this premise, in order to decrease the environmental impact of CO_2.

2.3.1. CO_2 sorbents

Sorption-enhanced technologies require the combination of a catalyst, that is stable and with high catalytic activity in the temperature range of interest (in this case 300-500 ºC), and a solid sorbent, in this case with high CO_2 sorption capacity and with fast sorption-desorption kinetics.

Several materials like CaO-based materials [199-208], hydrotalcites (HTCs) [209-224], lithium silicates [225-238], lithium cuprate [239] and lithium zirconates [240-242], among others, have been reported in the literature as high-temperature CO_2 sorbents. It is expected from a good CO_2 sorbent to present high CO_2 capture capacity at moderated temperatures (300-500 ºC), adequate sorption-desorption kinetics (fast sorption-desorption kinetics) [243], good hydrothermal and mechanical stability and low cost. A solid with high CO_2 sorption capacity but slow kinetics is not suitable since it is required much time for the gas to get into the particle and long times are needed to reach saturation [244].

Although metal oxides (e.g. CaO) have a higher capacity at high temperatures and can be stabilized when used as a mixture of oxides, they lose their properties very quickly throughout the sorption cycles, a phenomenon that is more marked when the adsorbent is in contact with steam. Besides that, the capacity of these materials decreases because of sintering phenomena [109]. In opposite, HTCs have practically constant capacity over the cycles, increase their capacity in a wet environment and have great thermal and mechanical stability. In addition, compared to other potential sorbents such as CaO and lithium zirconates, HCTs show faster adsorption-desorption kinetics and the energy required in their regeneration is significantly lower [244].

Nevertheless, some research was performed with other sorbents to compete with the HTCs, which is shortly described hereinbelow.

Akgsornpeak *et al.* [245] avoided the sintering phenomena by preparing CaO sorbents through the sol-gel synthesis in the presence of cetyltrimethyl ammonium bromide. Besides that, the incorporation of Y_2O_3 has been recently reported to significantly enhance the carbonation rate and adsorption capacity of CaO-based sorbents [206]. The addition of optimized amounts of K to Li_2ZrO_3 sorbents was reported to enhance their CO_2 sorption capacity, sorption rate and stability in sorption/desorption cycles [226]. Seggiani *et al.* [226] analysed the performance of different doped-Li_4SO_4 sorbents, having observed that the K-doped and Na-doped presented the highest CO_2 sorption capacities and sorption rates. In terms of stability, only the K-doped sorbent was able to keep its properties after 25 sorption/desorption cycles. However, Iwand *et al.* [240] concluded that the traditional preparation method of K-doped materials results in sorbents with slow regeneration step.

The sorption capacities and the sorption/regeneration temperatures of several sorbents are summarized in Table 2.6.

Table 2.6 - Sorption capacities and sorption/regeneration temperatures of several CO_2 sorbents.

Sorbent	Sorption Capacity[a] ($mmol \cdot g^{-1}$)	Temperature (ºC)	Regeneration Temperature (ºC)	p_{CO_2} (bar)	p_{H_2O} (bar)	Ref.
CaO-Y_2O_3 (20 wt.% Y_2O_3)	12.95	850	850	n.s.[b]	-	[206]
CaO	17.30	600	700	0.30	-	[207]
CuO/CaO/$Ca_{12}Al_{14}O_{33}$(19/43/38 wt%)	3.14	650	870	0.15	0.25	[202]
Na_2CO_3-CaO	14.7	800	800	1.00	-	[208]
CaO-Mg	10.22	600	700	0.50	-	[205]
Li_2ZrO_3	5.00	500	n.s.[b]	n.s.[b]	n.s.[b]	[242]
Li_4SiO_4	7.29	600	750	1.00	-	[236]
Li_4SiO_4	6.24	550	700	0.15	-	[229]
K-Li_4SiO_4 (30 wt.% K_2CO_3)	5.23	580	700	0.04	-	[226]
K-Li_4SiO_4	5.00	575	700	1.00	-	[241]
Li_4SiO_4	5.00	550	700	0.15	-	[229]
CaNd75	10.9	650	n.s.[b]	0.15	-	[203]

[a] Sorption capacity of the fresh sorbent.
[b] Not specified (or regeneration step not performed).

Table 2.6 (Continuation) - Sorption capacities and sorption/regeneration temperatures of several CO_2 sorbents.

Sorbent	Sorption Capacity[a] ($mmol \cdot g^{-1}$)	Temperature (ºC)	Regeneration Temperature (ºC)	p_{CO_2} (bar)	p_{H_2O} (bar)	Ref.
cHTC (Mg/Al = 2)	0.81	300	n.s.[b]	1.03	-	[209]
HTC (Mg/Al = 2)	0.54	300	n.s.[b]	0.14	-	[210]
K-HTC	0.79	400	n.s.[b]	1.00	-	[243]
K-HTC (20 wt.% K_2CO_2, Mg/Al = 0.6)	0.28	400	400	0.50	-	[219]
K-HTC (22 wt.% K_2CO_2, Mg/Al ≈ 2)	0.58	400	400	0.47	-	[220]
HTC-20K (20 wt.% K, Mg/Al = 2)	2.14	300	n.s.[b]	1.10	-	[210]
cK-HTC (20 wt.% K, Mg/Al = 2,)	1.42	300	n.s.[b]	1.02	-	[209]
MG30-K^N (20 wt.% K, Mg/Al ≈ 0.5)	1.08	335	435	0.50	0.5	[221]
K-HTC (20 wt.% K_2CO_2 and Mg/Al = 2)	9.40	300	600	0.34	4.5	[215]
K-HTC MW (20 wt.% K_2CO_2, Mg/Al = 2)	1.46	300	n.s.[b]	1.00	-	[223]
cK-HTC MW (20 wt.% K, Mg/Al = 2)	1.51	300	n.s.[b]	1.00	-	[209]
HTC-10Ga(10 wt.% Ga, Mg/Al = 2)	0.58	300	n.s.[b]	1.12	-	[210]
HTC-10Ga-20K (10 wt.% Ga, 20 wt.% K, Mg/Al = 2)	1.82	300	300	1.08	-	[210]
cK-HTCGa MW (20 wt.% K, Mg/(Al+Ga) = 2, Al/Ga = 9)	1.70	300	n.s.[b]	1.05	-	[209]
Li/Na/K-MgAl-C_{16} (55 wt.% Li-Na-K, Mg/Al = 20)	3.21	200	400	1.00	-	[246]
Mg_3Al_1-CO_3	0.53	200	n.s.[b]	1.00	-	[222]
Mg_3Al_1-NO_3	0.21	200	n.s.[b]	1.00	-	[222]
Mg_3Al_1-HNO_3	0.18	200	n.s.[b]	1.00	-	[222]
Mg_3Al_1-SO_4	0.10	200	n.s.[b]	1.00	-	[222]
Mg_3Al_1-Cl	0.18	200	n.s.[b]	1.00	-	[222]
(Mg,Al)(Cl) (Mg/Al = 3)	0.44	330	n.s.[b]	1.00	-	[224]
(Mg,Al)(ClO_4) (Mg/Al = 3)	3.55	330	n.s.[b]	1.00	-	[224]
(Mg,Al)($Fe(CN)_6$) (Mg/Al = 3)	0.75	330	n.s.[b]	1.00	-	[224]
MgAl-C_{16} (Mg/Al = 3)	0.91	200	400	1.00	-	[246]
Mg_3Al-stearate	1.25	300	n.s.[b]	1.00	-	[247]

[a] Sorption capacity of the fresh sorbent.
[b] Not specified (or regeneration step not performed)

2.3.2. Hydrotalcites

HTC is a layered double hydroxide. This synthetic or natural lamellar hydroxide has two kinds of metallic cations (divalent and trivalent) in the main layers and interlayer domains containing anionic species (compensating/interlayer anions) - Fig. 2.12 [248, 249]. These materials are used in a wide range of applications as catalysts, precursors and sorbents [214]. Several thousands of tons of HTCs are produced annually by different chemical companies, such as BASF, SASOL, Clariant, Kisuma Chemicals, Sakai Chemical [250]. The general formula is $[M^{2+}_{1-x}M^{3+}_{x}(OH)_2]^{x+}\left[A^{n-}_{x/n}\cdot yH_2O\right]^{x-}$, where M^{2+} is a divalent metal cation and M^{3+} is a trivalent metal cation. A^{n-} is a charge balancing anion (usually CO_3^{2-}) located in the interlayer space and *x* is generally between 0.2 and 0.4, while *y* is the number of moles of water located in the interlayer space [209, 210]. Similar layered structures of HTCs could be produced with several interlayer anions [222, 224, 246, 247, 250-257].

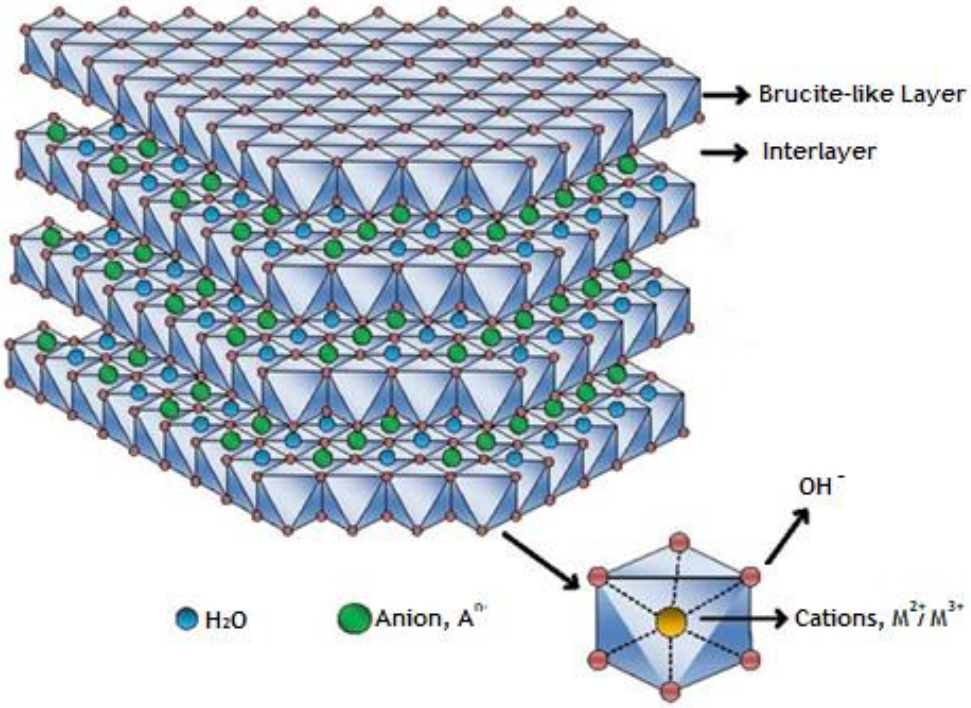

Fig. 2.12. Schematic representation of the hydrotalcite structure. Adapted from [249].

Co-precipitation is the most used method for the preparation of this type of material. It is based on the slow addition of a mixed solution of divalent and trivalent metals salts in adequate proportions into a reactor. An alkaline solution (e.g. NaOH) is added to the reactor in order to maintain the pH at a selected value leading to the co-precipitation of the two metallic salts [248]. So, there is often competition between several anionic species, and the control of experimental conditions can lead to the selective intercalation of one of them as the primary interlamellar anion. Secondary interlamellar

anions can replace them with further treatments such as an anionic exchange. Besides that, it is not obvious that a pure HTC phase is always obtained, while the global composition of the precipitate corresponds to the expected value, but contains secondary phases such as hydroxides or basic salts of the divalent or trivalent metal [248]. HTCs can, however, be synthesized by various techniques depending on the specific requirement and properties of the compounds. Other methods include combustion, recrystallization, urea hydrolysis, ion exchange, reverse-microemulsion, sol-gel, and hydrothermal [209, 258-262].

The morphology and the thermal stability of the synthesized HTCs affect CO_2 sorption performance. The properties of HTCs can be modified by combining adequate cations and anions [222, 224, 246, 247, 250-257, 263, 264], by varying the molar ratio of M^{2+}/M^{3+} [211, 212, 246], by changing the preparation conditions such as pH [222] (pH value between 8-10 can be used to synthesize HTCs [258]), calcination temperature [246, 265, 266] or aging process (e.g. microwave, ultrasonication, etc.) [209, 223, 267] among other parameters. On the other hand, the basicity of the sorbents can be improved by promotion with alkaline species [268], this way increasing their CO_2 sorption capacity.

Fresh HTCs as such are not good CO_2 adsorbents due to poor basic properties and the presence of entities that hinder CO_2 adsorption. This is caused by the presence of adsorbed water and interlayer anions which hinder the access of the adsorptive/reactive gas to the basic sites located on the surface and interlayer region [244]. Hence, they are subjected to thermal treatment (calcination treatment) to obtain a nearly amorphous mixed solid solution - with a poorly defined 3D network - with more stable and favorable properties for CO_2 sorption [248]. HTCs undergo different stages of transition during calcination. These transitions depend on many factors such as nature and relative amounts of cations, type of anions, crystallinity and method of synthesis. Several researchers have systematically investigated the thermal decomposition process [214, 261, 263, 265, 269]. The optimum temperature of calcination is usually 400 ºC, since it allows the decomposition of the compensating anions (and then, the active sites can be occupied by the CO_2) and the formation of the amorphous phase (mixed oxides) with sorption properties, without the complete and irreversible destruction of the structure. Apparently, such optimum temperature results from the balance between surface area and the number of basic active sites [214, 263]. In the calcination program, the first weight loss is detected between 70 °C and 190 °C, attributed to the loss of interlayer water; then, in the temperature range of 190 °C to 280 °C, the OH^- group bonded with Al^{3+} disappears [270]. The OH^- group bonded with Mg^{2+} disappears from the structure of the material in the temperature range 280 °C to 405 °C and the interlayer anions are usually released between 405 °C and 580 °C [270]; in this way, the material becomes an amorphous mixed oxide solution, which is reversible if the calcination temperature is not higher than 550 - 600 °C [270, 271] - see Fig. 2.13. The use of very high calcination temperatures leads to the formation of spinel phases ($MgAl_2O_4$), which should be avoided in order to conserve the

platelet morphology of HTCs and an adequate basicity [244, 246]. The original structures of the calcined samples can be recovered again by exposure to steam and atmospheric CO_2 (or through anion intercalation) - "memory effect" [264, 272-274].

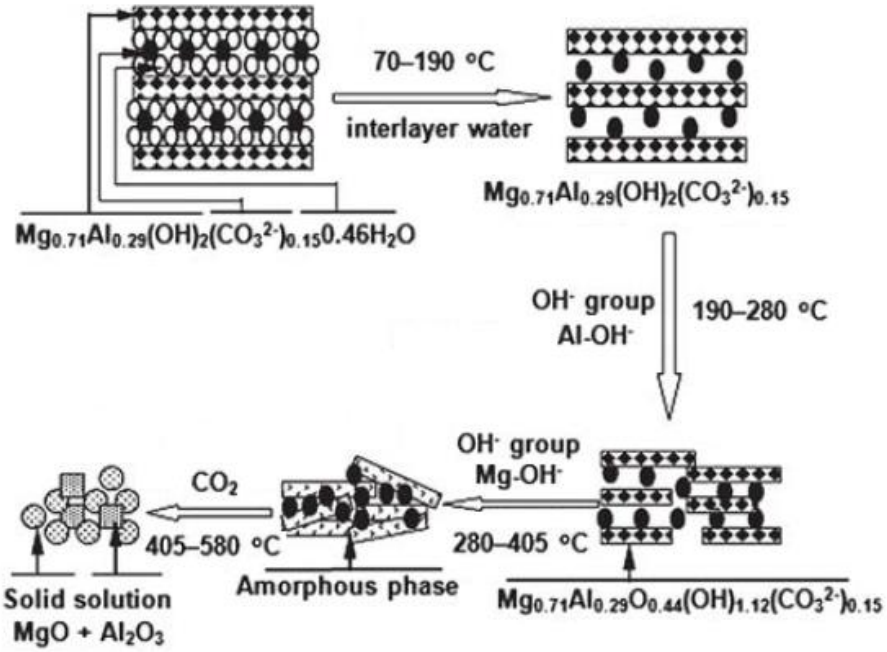

Fig. 2.13. The structural evolution of a typical HTC as a function of calcination temperature. Adapted from [275].

Different optimum Mg^{2+}/Al^{3+} ratios have been reported in the literature, which varies from 1:1 to 3:1 - the optimum ratio depends on the type of interlayer anion used, preparation method, etc. [212, 276, 277]. Although high Mg^{2+} content allows a formation of a higher number of basic active sites in the material, at higher Mg^{2+}/Al^{3+} ratios, $MgCO_3$ may also form at high partial pressures of steam and CO_2, which can lead to mechanical stability issues [278, 279]. In the work of Yong *et al.* [212], the authors studied the effect of different Mg^{2+}/Al^{3+} ratios (0.5, 1.3 and 3.0) in the sorption capacity of three commercial HTCs from SASOL. It was verified that the HTC with Mg^{2+}/Al^{3+} ratio of 1.3 had the highest performance. However, there is a lowest limit of the Mg^{2+}/Al^{3+} ratio (= 2.0) to obtain a crystallographically pure HTC, since this ratio influenced the electrostatic repulsion between neighboring trivalent metals in the layers [280]. Besides that, the optimum Mg^{2+}/Al^{3+} molar ratio reported in several studies is often equal to 2 [209, 210, 212, 255] for the sorbents impregnated with potassium.

As previously mentioned in this subchapter, the CO_2 sorption capacity of the HTCs can be enhanced by impregnating with an alkali metal such as Na, K or Cs [281, 282]. It was verified by several works that HTCs modified with alkali promoters K_2CO_3 (or Na/KNO_3) showed best CO_2 sorption performance than the base HTCs [209, 210, 218, 243, 281-286]. Besides that, several authors [209, 210, 218, 287]

have also shown that the simultaneous impregnation with K and substitution of Al^{3+} with Ga^{3+} markedly improved the sorption capacity of HTCs, the first modification acting as a chemical promoter and the latter providing a superstructure, robust and stable at elevated temperatures. For K_2CO_3 modified HTCs with high Mg^{2+}/Al^{3+} ratios, the doping is mainly localized in the bulk phase and acts as a reactant to form high stable K-Mg double carbonates after sorbed CO_2. With the increase of the Al^{3+} content, surface modifications occur and become the dominant enhancement mechanism via the interaction between the K^+ ions and unsaturated oxygen sites [283].

It has also been found that the physical and chemical properties of HTCs are highly influenced by the interlayer anions used. The anion influences the crystallinity and layer spacing in HTCs. In this way, materials with different interlayer anions present different morphologies and chemical surfaces, influencing the sorption performance of the HTCs-derived mixed oxides. For instance, Yong *et al.* [288] reported that the sorption capacity of HTC containing $Fe(CN)_6^{4-}$ was higher (1.3 $mmol \cdot g^{-1}$) than the one containing NO_3^- (0.3 $mmol \cdot g^{-1}$) at 25 ºC and 1 bar of CO_2. However, Wang *et al.* [222] analysed several charge compensating anions (CO_3^{2-}, HCO_3^-, NO_3^-, SO_4^{2-} and Cl^-) having observed that when using CO_3^{2-}, a spheroidal "sand rose" type of HTC with a very high surface area was produced. On the other hand, the other compensating anions led to the formation of "stone" type HTCs with very low surface areas. For this reason, the HTC with CO_3^{2-} as interlayer anion presented the highest CO_2 capture capacity. However, larger size anions tend to increase the interlayer spacing; this space can help the K ions disperse into the HTC interlayer and, thus, create more Al(Mg)−O−K bonds to enhance the performance of the sorbent [247]. The thermal stability was also found to depend on the interlayer anion used: the Mg_3Al_1-SO_4 was the one that presented the highest thermal stability [222]. Hutson and Attwood also prepared several HTCs with different compensating anions [224] and obtained conclusions similar to those already mentioned - see the CO_2 sorption capacities of all these materials in Table 2.6.

Several studies have shown that the presence of steam in feed gas increases the CO_2 sorption capacity of potassium doped-HTCs by 10-17 % and enhances the stability of these materials (in the temperature range of 200-400 ºC and the pressure range of 1-3.5 bar) [193, 216, 218, 221, 279, 289-291]. It was found that at least four different adsorption sites participate in the sorption/desorption of CO_2 and H_2O and the presence of steam activates some active sites for the CO_2 sorption. Two adsorption sites can be regenerated with N_2, whereas the other adsorption sites require the presence of H_2O to be activated/desorbed [279, 289, 290].

The CO_2 kinetics in dry conditions for these materials were studied by Miguel *et al.* [210] and Silva *et al.* [209] and it was observed that the kinetics are dependent on the morphology/composition of the material, being the physical sorption faster than the chemical one. Besides, the physical sorption is reversible in contrast with the chemical sorption [209, 210], meaning that during cyclic operation a working capacity is obtained, lower than the one measured with the fresh calcined HTC.

The decision on which kind of CO_2 sorbent is more adequate to be used in the SER strongly depends on the operating temperature at which it will be employed. Since one of the main goals is to reduce the temperature of the steam reformer to reduce operation costs, it is desirable to work at relatively low temperatures (300-500 ºC). For such temperatures, HTCs have been reported to present higher CO_2 capacities and faster sorption kinetics, as well as easier regeneration, and lower loss of sorption capacity. HTCs are also better than other sorbents due to nearly infinite selectivity for CO_2 sorption over gases like CH_4, CO, and N_2 [250]. Moreover, the fact that the CO_2 sorption capacity of HTCs is strongly enhanced under wet conditions (steam reforming conditions) makes them an even better candidate for use in the OMWSR process using a SER (for instance, Hong Lu *et al.* [207] reported that the sorption capacity of a CaO sorbent over the carbonation/decarbonation cycles decreased faster when steam was present in the system).

2.3.3. Summary

The OMWSR through a SER consists of combining the reaction and CO_2 capture in the same device. This innovative reactor configuration requires a solid sorbent with high CO_2 sorption capacity, and which must be easy to regenerate and have good performance with steam. There are several materials like CaO-based materials, lithium silicates, lithium cuprate and lithium zirconates, among others, that have been reported in the literature as high-temperature CO_2 sorbents.

However, in this subchapter 2.3, it is possible to conclude that HTCs have the adequate properties to be used in a SER: practically constant and high CO_2 sorption capacity over the cycles, increase their capacity in a wet condition, have adequate sorption-desorption kinetics and present great thermal and mechanical stability.

In this way, a HTC impregnated with potassium is a potential sorbent to be used to capture from the reaction medium the CO_2 produced in the OMWSR (sorption-enhanced process), increasing the purity of the H_2 and shifting the thermodynamic equilibrium to the production of more H_2 (increasing the H_2 yield).

2.4. Membrane reactor

Another alternative to enhance the OMWSR is the utilization of a Membrane Reactor (MR - see Fig. 2.14), which consists of combining the TR and H_2 separation in the same device.

In a MR, the membrane not only selectively separates one or more components but also allows overcoming the thermodynamic boundaries of equilibrium-limited reactions - Le Châtelier principle [292]. Regarding its advantages compared to TRs, they are the same as SERs, except for the reduction of CO_2 emissions in the pre-breakthrough zone, being that the capital costs reduction can

be higher in the case of MRs since only one reactor is needed (instead of the parallel reactors required for the SER), as long as cheap and long-lasting H_2 perm-selective membranes can be obtained. This reactor configuration was already used in other applications [173, 293-304] and for the OMWSR [1, 6, 88, 89] in the last decade.

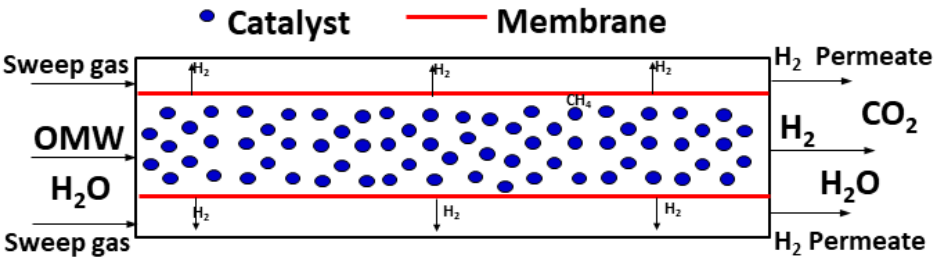

Fig. 2.14. Scheme of the operation of the MR.

Besides that, it is possible to produce ultra-pure H_2 streams if membranes with a nearly infinite H_2 perm-selectivity are used (e.g. dense Pd-based membrane). Thus, a MR is an important technology to increase the energy performance of the process by combining the reaction and recovery stages in a single device (avoiding the construction of two unit operations), leading to considerably smaller dimensions of plant layout, producing one stream with high-purity H_2 (in the permeate side - see a scheme of a MR in Fig. 2.14).The effect of the removal of H_2 from the reaction medium (thermodynamic/modeling study) is analyzed for this reaction [194] in subchapter 4.2. Moreover, this effect was already analyzed for other applications [84, 196, 293, 299, 305-307].

In this particular case, a H_2 perm-selective membrane is considered to selectively separate H_2 from the other gaseous components; however, a CO_2 perm-selective membrane could be used instead. Still, since one of the main goals of using MRs for the OMWSR reaction is to produce ultra-pure H_2 that can be later utilized in other processes, it is preferable to use a H_2 perm-selective membrane to isolate H_2, instead of using CO_2 perm-selective membranes (and consequently have H_2 in the retentate stream with other gaseous species).

In order to use a MR in the OMWSR process, it is fundamental to select an appropriate H_2 perm-selective membrane. Therefore, the following subchapters comprise a short overview of H_2 perm-selective membranes reported in the literature as well as an analysis of experimental tests in MRs for OMWSR. The performance of a MR depends largely on the flux of H_2 extracted and on the purity of the produced H_2. The stability of a membrane is here considered as the ability of a membrane to maintain a constant flux of H_2, as well as a constant perm-selectivity over time.

2.4.1. Hydrogen perm-selective membranes

H_2 perm-selective membranes may be classified as dense metallic membranes, proton-conducting dense ceramic membranes, dense polymeric membranes, microporous ceramic membranes and porous carbon membranes [308, 309]. The main advantage of dense metallic membranes is that usually they withstand high temperatures (e.g., as compared to polymeric ones) and present higher selectivity towards H_2, thus being possible to obtain high purity H_2-permeate streams [308]. Therefore, dense metallic membranes are preferable for ultra-pure H_2 production and will be the main target of focus.

When choosing a membrane to be used in a MR, it is required to consider the operating conditions under which the membrane will be used. In the last years, there has been an incredible effort in order to find suitable membranes for MR applications. Pd-based membranes are currently the most promising for high purity H_2 production in MRs, especially Pd alloys (with transition metals - e.g. Pd-Ag, Pd-Ru, Pd-Cu and Pd-Au) which are less sensitive than pure Pd to embrittlement (caused by the presence of H_2 at temperatures below 300 ºC and H_2 pressures below 20 bar) and poisoning (caused by contact with CO, CO_2 or H_2S) [308, 310-315]. The embrittlement phenomenon may produce pinholes/cracks on the membrane, which will negatively affect the H_2 perm-selectivity of the membrane. In addition, one of the biggest inhibitory factors for H_2 permeation across a Pd membrane is concentration polarization and it is necessary to avoid that (this topic will be more deeply discussed later in this subchapter) [316]. However, although these negative aspects, the ability of Pd to dissociate H_2 to its atomic form makes this metal ideal for H_2 separation applications [317]. Pd-Ag membranes show good stability, relatively lower material costs and better mechanical properties than pure Pd membranes. Besides that, it has been shown that the addition of a third element to the Pd-Ag alloy (e.g. Au) improves the tolerance to poisoning with H_2S [318].

Several studies reported that the Pd alloys allow to obtain high permeances in the experimental tests [319-323]. Moreover, their H_2 permeability increases with the percentage of Ag in the alloy up to a maximum, which occurs at around 23 wt.% Ag [324]. In previous studies, it was found that the maximum recommended operating temperature for long-term stable tests with Pd-Ag membranes was close to 500 ºC [297, 325-328]. Above this temperature, besides the existence of leakages through the sealings, it is observed the formation of surface defects (small pinholes) that leads to the decrease of the membrane performance [325]. Tosti *et al.* [329] verified that self-supported dense Pd-Ag 23 wt.% tubular membranes with finger-type configuration are highly durable and reliable since these membranes allow to attain complete H_2 selectivity and no failures were observed after one year of thermal and hydrogenation cycles. These characteristics, together with high permeability, make such materials very promising for ultra-pure H_2 production in industrial and energetic applications [329]. Nevertheless, several works reported that the H_2 removal fraction never reaches a value higher than 0.80 [305, 324, 330] for low to medium pressures. Besides that, the application of these dense

membranes is still limited; for instance, self-supported Pd membranes are considered by several authors not being suitable in MR processes because of their large thickness required for reaching mechanical stability, and corresponding low fluxes and high costs. Due to these reasons, a strong effort has been put in the preparation of thinner Pd films over different supports and in the development of new membranes with less expensive metals. For instance, group V metals (such as V, Nb and Ta) are promising alternative materials to Pd because of their lower costs and higher H_2 permeabilities. However, the main problem of these elements as membrane materials is their too high solubility to H_2, making the membranes susceptible to severe H_2 embrittlement which can lead to the formation of cracks [331]. Besides that, direct use of these materials as a membrane is hindered due to the formation of oxide layers and the occurrence of surface reactions, which promote the reduction of the H_2 permeability through the membrane. Thus, the main criteria for membrane selection are high permeability, high selectivity and resistance to reactive gases, particularly CO, CO_2, CH_4 and H_2O and resistance to coking [332].

Nowadays, as previously mentioned, many researchers are pursuing the possibility of using supported membranes with as thin as possible Pd-alloy layers [333]. Concerning these supported membranes, it is important to emphasize that metallic supports are mechanically stronger and can be easily assembled into metallic reactors than ceramics supports (lower probability of leakages). However, the metallic supports have low porosity, their pores are larger (with no uniform pore size distribution), the surface is rough and, at this moment, they are much more expensive than ceramics supports [331]. Several works [327, 334] reported that the materials (namely, the support) that contact with the membrane must be meticulously chosen. For instance, Okazaki *et al.* [327] stated that the decrease of the H_2 permeation observed in that work was related to the interaction between the Al_2O_3 support and the Pd layer of the membrane.

In terms of preparation methods of these H_2 selective membranes, namely supported ones, electroless plating (EP) and chemical vapor deposition (CVD) are the most used ones. The EP method normally consists of the production of Pd particles through the reduction of a plating solution containing Pd-amine complexes. This technique allows to obtain high coating adhesion, involves low operation costs and allows simple operation. However, the impurities present in the plating solution may lead to the presence of defects on the Pd layer. The CVD technique allows to very easily deposit a metal film on a support with the utilization of several reactions with water [293].

Usually, the permeation of H_2 through a Pd-based membrane is described by a solution-diffusion mechanism like shown in Fig. 2.15.

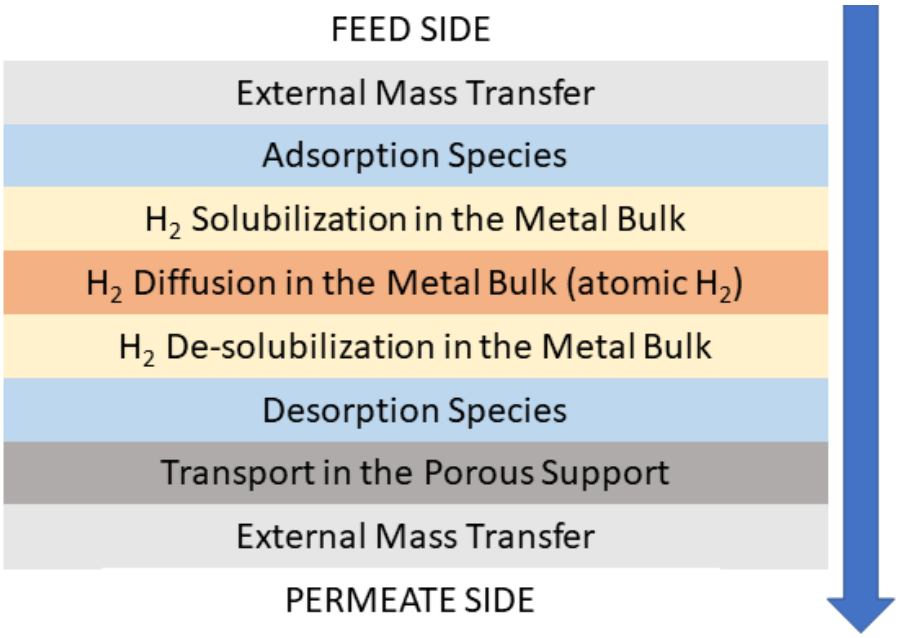

Fig. 2.15. Solution-diffusion mechanism of the permeation of H_2 through a Pd-based membrane [335].

The simplest model used to explain the mass transport of H_2 permeating through a dense membrane assumes that the H_2 diffuses through the membrane according to Fick's first law of diffusion for a pure component [336-338]. Besides that, in the permeation of H_2 through Pd-based membranes is commonly assumed that the diffusion coefficient is constant along the membrane and the mass transport kinetics is controlled by the diffusion step; this implies that the sorption and desorption process should be considered always to be at equilibrium (concentration of H_2 in the surface of the membrane in equilibrium with the gas phase - in the retentate and permeate sides): in the case of Pd-based membranes, the sorption isotherm is generally described by the Sieverts' law [339]. Taking into account all these considerations, the flux of H_2 that permeates through the membrane (J_{H_2}) can be determined by the integration of Fick's first law of diffusion along the thickness of the membrane (Eq. (2.13)) [339-341]:

$$J_{H_2} = \frac{L_{H_2}}{\delta} \times \left(p_{H_2,feed}^{0.5} - p_{H_2,permeate}^{0.5} \right) \quad (2.13)$$

where L_{H_2} is the permeability of the membrane, δ is the membrane thickness, p_{H_2} is the partial pressures of H_2 in the retentate (inlet - feed side) or in the permeate (outlet) side. The ratio $\frac{L_{H_2}}{\delta}$ is normally called permeance.

The permeability is described by an Arrhenius-type dependency on the temperature (*T*) - Eq. (2.14):

$$L_{H_2} = {L_{H_2}}^0 \times e^{\left(-\frac{E_a}{RT}\right)} \quad (2.14)$$

where ${L_{H_2}}^0$ is the pre-exponential factor, E_a is the activation energy of the membrane permeation process and R is the universal gas constant.

Despite the extensive use of Eq. (2.13), it is necessary to emphasize that this equation is valid only for certain operation conditions: for instance, the expression is only applicable to ideal H_2/metal mixtures and when the resistance in the diffusion of the H_2 along the thickness of the membrane is the rate-dominant process [321]. In general, the flux of H_2 can be influenced by several factors such as temperature, partial pressure difference, membrane thickness, membrane diffusivity, adsorption/desorption kinetics and concentration polarization at the surface of the membrane. Ward and Dao [342] reported that for a clean Pd membrane, in the absence of external mass transfer resistance, the diffusion is the dominating step at moderately high temperatures, even for membrane thicknesses close to 1 μm.

However, as also reported by Ward and Dao [342] (and shown in Fig. 2.15), beyond the H_2 diffusion through the membrane, other phenomena occur in the permeation process and the resistances to transport in the external gas phase may also be significant in some cases. For instance, the concentration polarization is related to decreased H_2 concentration in the feed side of the membrane in a multi-component system. In certain cases, due to the fluid dynamics inside the device, there is an accumulation of several species in the adjacent zone to the membrane surface, increasing the concentration of these species in the boundary film nearby to the membrane surface [343]. This causes a H_2 partial pressure gradient in the boundary layer and prevents the H_2 adsorption on the membrane surface (increase of the mass transport resistance). Thus, the H_2 concentration adjacent to the surface of the membrane is lower than that of bulk gas and thus decreases the flux of H_2 permeated through the membrane [344-348]. The concentration polarization is affected not only by the external hydrodynamic conditions of the module but also on the mass transport process inside of the membrane layer [349]. While most of the existing permeation results for thick Pd membranes are consistent with the considerations for the diffusion-limited permeation, significant differences exist for membranes with thickness with less than 10 μm, since the very high fluxes made possible with such thin membranes makes the external mass transfer resistances relevant [342].

In this manner, due to the several possible phenomena that occur in this separation process, it is typical to use the empirical Eq. (2.15) to describe the permeating H_2 flux [340, 341]. It was reported in the literature that the pressure exponent *n*, in a general way, can provide info regarding which transport step(s) control the overall permeation process. Several works studied and evaluated the physical meaning of the exponent *n* [342, 350, 351] for H_2 permeation through Pd-based membranes.

$$J_{H_2} = \frac{L_{H_2}}{\delta} \times \left(p^n_{H_2,\text{feed}} - p^n_{H_2,\text{permeate}} \right) \quad (2.15)$$

As already mentioned, the parameter *n* obtained is near 0.5 for a situation of no mass transfer resistance (and the diffusion through the membrane controls the permeation process) [342, 351, 352]. It was also observed that the required value of the exponent *n* usually varies between 0.5 and 1 in the presence of external mass transfer resistances (effects are particularly strong on the permeate side) [342]. Moreover, it was reported that, in the absence of external mass transfer resistances, the *n* value approaches zero when the H_2 permeation is only desorption-limited and varies between 0 and 0.5 when the desorption and diffusion are both influencing the H_2 flux [342]. It was also stated that (again in the absence of external resistances) the value of the exponent *n* is equal to the unity if only the adsorption process in the feed side limits the H_2 flux and varies between 0.5 and 1 when adsorption and diffusion in the metal bulk are both limiting the permeation [352]. In line with the aforementioned, the study of Caravella *et al.* [351] verified that at low temperature and using a thin membrane the value of the exponent *n* decreases toward values lower than 0.5 - desorption-limited process. However, higher values (> 1) for the pressure exponent have been determined in previous works [352, 353]. Besides that, the H_2 diffusion coefficient may also exhibit a concentration dependence and the membrane may present defects on the membrane films which may lead, for instance, to Knudsen diffusion.

Table 2.7 and Table 2.8 demonstrate a summary of different Pd-based membranes that have been reported in the last years with different parameters and performances.

Table 2.7- Summary of Pd-based membranes' performances and respective characteristics.

Membrane/Support	Temperature (ºC)	δ (μm)	H_2 Permeance ($mol \cdot m^{-2} \cdot s^{-1} \cdot Pa^{-0.5}$)[a)]	Selectivity (H_2/N_2)	Ref.
Pd-25 wt.% Ag/Al_2O_3	300	50	1.15×10^{-4}	∞	[354]
Pd-23-25 wt.% Ag	350	84	2.26×10^{-4}	∞	[355]
Pd-5 wt.% Pt/YSZ	400	6.6	1.18×10^{-3}	994	[356]
Pd/TiO_2/Ti-Al	500	14	1.07×10^{-3}	∞	[357]
Pd-23 wt.% Ag/stainless steel	400	150	1.27×10^{-4}	∞	[6]
Pd-15 wt.% Ag/Al_2O_3	300	5	2.13×10^{-3}	528	[358]
Pd-23 wt.% Ag	400	61	1.46×10^{-4}	∞	[329]
Pd-20 wt.% Ag/Al_2O_3	400	2.5	2.70×10^{-3}	∞	[321]
Pd-8 wt.% Ho	600	100	7.89×10^{-4}	n.d.[b)]	[313]
Pd-Au/PSS	450	12	1.30×10^{-3}	∞	[359]
Pd-1.3 wt.% Ru/Al_2O_3	500	1.8	4.12×10^{-3}	2,611	[360]
Pd-20 wt.% Ag/Al_2O_3	400	2.5	3.90×10^{-3}	≥ 10,000	[361]
Pd-23 wt.% Ag/PSS	400	2.8	3.25×10^{-3}	≥ 2,900	[320]

[a)] H_2 Permeance obtained by Eq. (2.15).
[b)] Not determined.

Table 2.8 - Summary of Pd-based thin membranes' performances and respectability characteristics.

Membrane/Support	Temperature (ºC)	δ (μm)	H_2 Permeance ($mol \cdot m^{-2} \cdot s^{-1} \cdot Pa^{-1}$)[a)]	Selectivity (H_2/N_2)	Ref.
Pd-7 wt.% Ag/Al_2O_3	400	0.78	1.14×10^{-5}	640	[362]
Pd-15 wt.% Ag/Al_2O_3	400	4.0	4.2×10^{-6}	20,000	[363]
Pd-5 wt.% Ag/Al_2O_3	400	1.0	4.6×10^{-6}	25,938	[294]
Pd-23 wt.% Ag/ZrO_2	400	1.0	8.0×10^{-6}	500	[364]
Pd-Ag/Al_2O_3	400	1.3	$9.0\text{-}9.4 \times 10^{-6}$	1,900	[365]
Pd-7-8 wt.% Au/Al_2O_3	500	2-3	6.2×10^{-6}	1,400	[366]

[a)] Permeance values have been calculated for a H_2 partial pressure of 1 bar.

2.4.2. OMWSR in membrane reactors

Just a few experimental studies on OMWSR in MRs were found in the literature [1, 6, 88, 89], which assessed the effects of pressure and gas/weight hourly space velocity (GHSV/WHSV) and will be summarized in this subchapter.

In the first work ofTosti *et al.* [6], filtered and concentrated OMW was used for feeding a MR consisting of a dense Pd-Ag permeator tube filled with a Pt-based catalyst. Reforming tests were performed at 450 ºC in the range of 100-500 kPa total pressure. The experimental tests have demonstrated the capability of the membrane device to selectively separate the H_2 produced and to provide a retentate stream rich in non-permeated H_2, CO_2, and CH_4. A maximum H_2 yield corresponding to 2 kg of H_2 permeated per ton of OMW has been measured, when operating at 300 kPa with a space velocity of 5.56×10^3 $mol \cdot h^{-1} \cdot g^{-1}_{cat}$. The gas chromatographic analysis of the retentate revealed the presence of H_2, CO_2 and CH_4, thus demonstrating the presence of side reactions such as the hydrogenolysis and cracking of alcohols. No detectable amounts of CO were measured due to the completion of the WGS promoted by the presence of the membrane. Also, a deactivation of the catalyst due to coke formation was observed.

In the second work, Tosti *et al.* [88] conducted again the OMWSR process in a MR (using a Pd membrane) to investigate the ability to recover pure H_2 and H_2-rich gas mixtures from OMW. In particular, a Pt-Rh-Pd-based catalyst supported on rare earth oxides was tested in order to verify its capability of maximizing the H_2 yield and reducing side reactions. As a main result, this work allowed verifying the following capabilities of the studied membrane process: the production of H_2 from waste (up to 3.25 kg of H_2 per ton of OMW) and a reduction in the pollution potential of the OMW (phenols and total carbon concentrations are reduced by about 90 %). Compared to a commercial Pt-based catalyst that was tested in the previous work, the novel catalyst showed higher selectivity toward the reforming reaction, allowing a significant reduction in the formation of CH_4 and coke and thus exhibiting a higher H_2 yield and higher stability. In fact, in all tests, low CH_4 concentrations were detected in the retentate stream, while no significant loss of catalyst activity was observed after 6 -8 h of operation. The very low selectivity of the noble metals-based catalyst toward CH_4 formation was related to its intrinsic high reforming activity.

In the last work of the same research group [1], they tested the reforming of OMW and CH_4 in a Pd-membrane reformer and demonstrated that the steam reforming of CH_4 + OMW exhibits about the same H_2 yield of the reforming of the OMW alone. Besides that, the addition of CH_4 to OMW does not affect the ability of the steam reforming process to reduce pollution. Finally, it was possible to verify that the H_2 yield reached in the steam reforming of OMW together with CH_4 was higher than the H_2 yield obtained for the steam reforming of CH_4 alone.

More recently, Alique *et al.* [89], using a catalyst prepared by Tosti *et. al* in a previous work [88], reported that, in a MR, higher pressures were favorable, predominating the membrane shift effect (with increased H_2 permeating fluxes) against the negative effect of thermodynamics on the steam reforming reactions.

2.4.3. Summary

The OMWSR through a MR consists of combining the reaction and H_2 separation in the same device. This innovative reactor configuration requires a H_2 perm-selective membrane.

In this subchapter 2.4, it is shown that Pd-based membranes are currently promising for high purity H_2 production in MRs for ultra-pure H_2 production. Since the cost of these dense membranes is still a limiting factor, a major effort has been put into the preparation of thinner Pd films over different supports, by several techniques. This decrease of the thickness of the membrane will allow the increase of the permeation flux, but the selectivity will be lower.

In this way, a supported Pd membrane with thin thickness is a potential membrane to separate from the reaction medium the H_2 produced in the OMWSR (membrane separation process), in order to increase the H_2 yield (since shifts the thermodynamic equilibrium to the production of more H_2) and produce an ultra-pure H_2 stream. However, it is necessary to study the effect of the species present in the OMW on the performance of the membrane.

2.5. Sorption-enhanced membrane reactor

Another alternative is the multifunctional hybrid reactor combined capture of CO_2 and H_2 separation: sorption-enhanced membrane reactor (SEMR - see Fig. 2.16). This hybrid reactor configuration allows shifting the thermodynamic equilibrium of the steam reforming reaction by removing two of the reaction products from the reaction medium. This reactor configuration intensifies the performance of the process by combining the reaction, H_2 separation and CO_2 capture in a single device. This reactor configuration was not studied in detail until now [166] and the first thermodynamic study is performed for the OMWSR [194] in this PhD thesis (subchapter 4.2). The SEMR combines the advantages of a SER and a MR; however, like in a SER, the CO_2 sorbent gets saturated at some point and then

regeneration is necessary (see details in subchapter 2.3). At this point, this reactor configuration is similar to a MR, since the CO_2 is not captured, but the H_2 is continuously separated from the reaction medium to the permeate side.

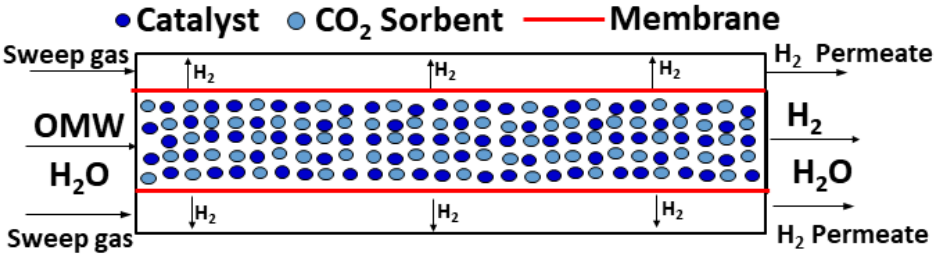

Fig. 2.16. Scheme of the operation of the SEMR.

2.6 Conclusions

OMW is a polluting stream derived from the olive oil industry and is an important source of environmental pollution, particularly in the Mediterranean countries. This stream is typically constituted by polyphenols, sugars, fatty acids and water. Nowadays, in order to reduce the pollutant load, several treatment/valorization techniques are applied, but these technologies have large cost and efficiency problems. Due to this, OMWSR presents as a good alternative, since this process decreases the pollutant load of the OMW and simultaneously the waste is valorized with the production of green H_2.

Currently, the OMWSR is an innovative treatment alternative with high potential. In the last years, a small number of researchers were carried out on OMWSR process using a MR.

Nevertheless, it is expected that several reactor configurations (SER, MR and SEMR) would allow to work at lower temperatures than in the conventional steam reformers and attain similar or even better performances than TRs operating at higher temperatures. However, for the successful implementation of these reactor configurations, CO_2 sorbents with high sorption capacity, easy regeneration and high stability, as well as H_2 perm-selective membranes with high H_2 permeance and selectivity have to be used. Nowadays, HTCs and Pd-based membranes are seen as promising systems for use in the SEMR at temperatures in the range of 300-400 ºC.

Notation and Glossary

List of Variables

E_a	Activation energy (kJ·mol^{-1})
J_{H_2}	Flux of H_2 (mol·m^{-2}·s^{-1})
L_{H_2}	Permeability (mol·m^{-1}·s^{-1}·Pa$^{-0.5}$)
$L_{H_2}{}^0$	Pre-exponential factor (mol·m^{-1}·s^{-1}·Pa$^{-0.5}$)
$p_{H_2}^x$	Partial pressures of H_2 (Pa)
n	Pressure exponent
T	Temperature (ºC or K)
$\Delta H_r^{0\,°C}$	Enthalpy of reaction at standard conditions (kJ·mol^{-1})
δ	Membrane thickness (m)

List of Acronyms

BOD	Biochemical oxygen demand
COD	Carbon oxygen demand
CVD	Chemical vapor deposition
EP	Electroless plating
HTC	Hydrotalcite
MR	Membrane reactor
OMW	Olive oil mill wastewater
OMWSR	Olive oil mill wastewater steam reforming
SCFR	Steam-to-carbon feed ratio
SEMR	Sorption-enhanced membrane reactor
SER	Sorption-enhanced reactor
TOC	Total organic carbon
TPOMW	Two-phase olive mill waste
TR	Traditional reactor
WGS	Water-gas shift

References

[1] Tosti, S., M. Fabbricino, L. Pontoni, V. Palma and C. Ruocco, Catalytic reforming of olive mill wastewater and methane in a Pd-membrane reactor. International Journal of Hydrogen Energy, 2016. 41(12): p. 5465-5474.

[2] Council, I.O., Economic Affairs & Promotion Unit. 2021 [Acessed 18-02-2021]; Available from: https://www.internationaloliveoil.org/what-we-do/economic-affairs-promotion-unit/#prices.

[3] Roig, A., M.L. Cayuela and M.A. Sánchez-Monedero, An overview on olive mill wastes and their valorisation methods. Waste Management, 2006. 26(9): p. 960-969.

[4] Rozzi, A. and F. Malpei, Treatment and disposal of olive mill effluents. International Biodeterioration & Biodegradation, 1996. 38(3): p. 135-144.

[5] Dawson, D., Global Olive Oil Production to Dip in 2018/2019. 2018 [Acessed 25-02-2019]; Available from: https://www.oliveoiltimes.com/olive-oil-business/global-olive-oil-production-to-dip-in-2018-19/66039.

[6] Tosti, S., C. Accetta, M. Fabbricino, M. Sansovini and L. Pontoni, Reforming of olive mill wastewater through a Pd-membrane reactor. International Journal of Hydrogen Energy, 2013. 38(25): p. 10252-10259.

[7] Dermeche, S., M. Nadour, C. Larroche, F. Moulti-Mati and P. Michaud, Olive mill wastes: Biochemical characterizations and valorization strategies. Process Biochemistry, 2013. 48(10): p. 1532-1552.

[8] Alburquerque, J.A., J. Gonzálvez, D. García and J. Cegarra, Agrochemical characterisation of “alperujo”, a solid by-product of the two-phase centrifugation method for olive oil extraction. Bioresource Technology, 2004. 91(2): p. 195-200.

[9] Di Giovacchino, L., S. Sestili and D. Di Vincenzo, Influence of olive processing on virgin olive oil quality. European Journal of Lipid Science and Technology, 2002. 104(9-10): p. 587-601.

[10] Niaounakis, M. and C.P. Halvadakis, Characterization of olive processing waste. Olive Processing Waste Management: Literature Review and Patent Survey, 2006. 5: p. 23-64.

[11] Sanchez Moral, P. and M. Ruiz Méndez, Production of pomace olive oil. 2006.

[12] Aktas, E.S., S. Imre and L. Ersoy, Characterization and lime treatment of olive mill wastewater. Water Research, 2001. 35(9): p. 2336-2340.

[13] Kapellakis, I.E., K.P. Tsagarakis and J.C. Crowther, Olive oil history, production and by-product management. Reviews in Environmental Science and Bio/Technology, 2008. 7(1): p. 1-26.

[14] Caputo, A.C., F. Scacchia and P.M. Pelagagge, Disposal of by-products in olive oil industry: waste-to-energy solutions. Applied Thermal Engineering, 2003. 23(2): p. 197-214.

[15] Paredes, M.J., E. Moreno, A. Ramos-Cormenzana and J. Martinez, Characteristics of soil after pollution with wastewaters from olive oil extraction plants. Chemosphere 16, 1987. 7: p. 1557-1564.

[16] DellaGreca, M., P. Monaco, G. Pinto, A. Pollio, L. Previtera and F. Temussi, Phytotoxicity of low-molecular-weight phenols from olive mill wastewaters. Bulletin of Environmental Contamination and Toxicology 67, 2001: p. 352-359.

[17] Rana, G., M. Rinaldi and M. Introna, Volatilisation of substances alter spreading olive oil waste water on the soil in a Mediterranean environment. Agriculture, Ecosystems and Environment 96, 2003: p. 49-58.

[18] Anzelmo, B., J. Wilcox and S. Liguori, Hydrogen production via natural gas steam reforming in a Pd-Au membrane reactor. Investigation of reaction temperature and GHSV effects and long-term stability. Journal of Membrane Science, 2018. 565: p. 25-32.

[19] Tsagaraki, E., H.N. Lazarides and K.B. Petrotos, Olive Mill Wastewater Treatment, in Utilization of By-Products and Treatment of Waste in the Food Industry. 2007, Springer US: Boston. p. 133-157.

[20] Jaouad, Y., M. Villain-Gambier, L. Mandi, B. Marrot and N. Ouazzani, Comparison of aerobic processes for olive mill wastewater treatment. Water Science and Technology, 2020. 81(9): p. 1914-1926.

[21] Aggoun, M., R. Arhab, A. Cornu, J. Portelli, M. Barkat and B. Graulet, Olive mill wastewater microconstituents composition according to olive variety and extraction process. Food Chemistry, 2016. 209: p. 72-80.

[22] El-Abbassi, A., H. Kiai and A. Hafidi, Phenolic profile and antioxidant activities of olive mill wastewater. Food Chemistry, 2012. 132(1): p. 406-412.

[23] Zbakh, H. and A. El Abbassi, Potential use of olive mill wastewater in the preparation of functional beverages: A review. Journal of Functional Foods, 2012. 4(1): p. 53-65.

[24] Nasr, B., B. Ahmed and G. Abdellatif, Fenton treatment of olive oil mill wastewater-applicability of the method and parameters effects on the degradation process. Journal of Environmental Sciences, 2004. 16: p. 942-944.

[25] Katsoyannos, E., A. Hatzikioseyian, E. Remoundaki and M. Tsezos, Photocatalytic treatment of olive mill wastewaters (OMW) in pilot scale, in 13th International Symposium on Pollution and its Impact on Life in Mediterranean Region. 2005, National Technical University of Athens Greece.

[26] Gebreyohannes, A.Y., R. Mazzei and L. Giorno, Trends and current practices of olive mill wastewater treatment: Application of integrated membrane process and its future perspective. Separation and Purification Technology, 2016. 162: p. 45-60.

.

[27] Montero, C., L. Oar-Arteta, A. Remiro, A. Arandia, J. Bilbao and A.G. Gayubo, Thermodynamic comparison between bio-oil and ethanol steam reforming. International Journal of Hydrogen Energy, 2015. 40(46): p. 15963-15971.

[28] Casanovas, A., A. Galvis and J. Llorca, Catalytic steam reforming of olive mill wastewater for hydrogen production. International Journal of Hydrogen Energy, 2015. 40(24): p. 7539-7545.

[29] Daâssi, D., J. Lozano-Sánchez, I. Borrás-Linares, L. Belbahri, S. Woodward, H. Zouari-Mechichi, T. Mechichi, M. Nasri and A. Segura-Carretero, Olive oil mill wastewaters: Phenolic content characterization during degradation by Coriolopsis gallica. Chemosphere, 2014. 113: p. 62-70.

[30] Fki, I., N. Allouche and S. Sayadi, The use of polyphenolic extract, purified hydroxytyrosol and 3,4-dihydroxyphenyl acetic acid from olive mill wastewater for the stabilization of refined oils: a potential alternative to synthetic antioxidants. Food Chemistry, 2005. 93(2): p. 197-204.

[31] Kyriacou, A., K.E. Lasaridi, M. Kotsou, C. Balis and G. Pilidis, Combined bioremediation and advanced oxidation of green table olive processing wastewater. Process Biochemistry, 2005. 40(3-4): p. 1401-1408.

[32] Araújo, M., F.B. Pimentel, R.C. Alves and M.B.P.P. Oliveira, Phenolic compounds from olive mill wastes: Health effects, analytical approach and application as food antioxidants. Trends in Food Science & Technology, 2015. 45(2): p. 200-211.

[33] Kaleh, Z. and S.U. Geißen, Selective isolation of valuable biophenols from olive mill wastewater. Journal of Environmental Chemical Engineering, 2016. 4(1): p. 373-384.

[34] Vlyssides, A.G., M. Loizides and P.K. Karlis, Integrated strategic approach for reusing olive oil extraction by-products. Journal of Cleaner Production, 2004. 12(6): p. 603-611.

[35] Paredes, C., J. Cegarra, A. Roig, M.A. Sánchez-Monedero and M.P. Bernal, Characterization of olive mill wastewater (alpechin) and its sludge for agricultural purposes. Bioresource Technology, 1999. 67(2): p. 111-115.

[36] Feki, M., N. Allouche, M. Bouaziz, A. Gargoubi and S. Sayadi, Effect of storage of olive mill wastewaters on hydroxytyrosol concentration. European Journal of Lipid Science and Technology, 2006. 108(12): p. 1021-1027.

[37] Hamden, K., N. Allouche, M. Damak and A. Elfeki, Hypoglycemic and antioxidant effects of phenolic extracts and purified hydroxytyrosol from olive mill waste in vitro and in rats. Chemico-Biological Interactions, 2009. 180(3): p. 421-432.

[38] Justino, C.I., K. Duarte, F. Loureiro, R. Pereira, S.C. Antunes, S.M. Marques, F. Gonçalves, T.A.P. Rocha-Santos and A.C. Freitas, Toxicity and organic content characterization of olive oil mill wastewater undergoing a sequential treatment with fungi and photo-Fenton oxidation. Journal of Hazardous Materials, 2009. 172(2-3): p. 1560-1572.

[39] Zghari, B., D. Pierre, R. Abderrahmane and A. Boukir, GC-MS, FTIR and 1H ,13C NMR Structural Analysis and Identification of Phenolic Compounds in Olive Mill Wastewater Extracted from Oued Oussefrou Effluent (Beni Mellal-Morocco. Vol. 8. 2017. 4496-4509.

[40] El-Abbassi, A., M. Khayet, H. Kiai, A. Hafidi and M.C. García-Payo, Treatment of crude olive mill wastewaters by osmotic distillation and osmotic membrane distillation. Separation and Purification Technology, 2013. 104(Supplement C): p. 327-332.

[41] El-Abbassi, A., H. Kiai, A. Hafidi, M.C. García-Payo and M. Khayet, Treatment of olive mill wastewater by membrane distillation using polytetrafluoroethylene membranes. Separation and Purification Technology, 2012. 98(Supplement C): p. 55-61.

[42] Allaoui, S., M. Naciri Bennani, H. Ziyat, O. Qabaqous, N. Tijani and N. Ittobane, Removing polyphenols contained in olive mill wastewater by membrane based on natural clay and Hydrotalcite Mg-Al. 2020, 2020. 8(1).

[43] Ochando-Pulido, J.M., S. Pimentel-Moral, V. Verardo and A. Martinez-Ferez, A focus on advanced physico-chemical processes for olive mill wastewater treatment. Separation and Purification Technology, 2017. 179: p. 161-174.

[44] Un, U.T., U. Altay, A.S. Koparal and U.B. Ogutveren, Complete treatment of olive mill wastewaters by electrooxidation. Chemical Engineering Journal, 2008. 139(3): p. 445-452.

[45] Rioja-Cabanillas, A., D. Valdesueiro, P. Fernández-Ibáñez and J.A. Byrne, Hydrogen from wastewater by photocatalytic and photoelectrochemical treatment. Journal of Physics: Energy, 2020. 3(1): p. 012006.

[46] Cañizares, P., R. Paz, C. Sáez and M.A. Rodrigo, Costs of the electrochemical oxidation of wastewaters: A comparison with ozonation and Fenton oxidation processes. Journal of Environmental Management, 2009. 90(1): p. 410-420.

[47] Lafi, W.K., B. Shannak, M. Al-Shannag, Z. Al-Anber and M. Al-Hasan, Treatment of olive mill wastewater by combined advanced oxidation and biodegradation. Separation and Purification Technology, 2009. 70(2): p. 141-146.

[48] Frascari, D., G. Rubertelli, F. Arous, A. Ragini, L. Bresciani, A. Arzu and D. Pinelli, Valorisation of olive mill wastewater by phenolic compounds adsorption: Development and application of a procedure for adsorbent selection. Chemical Engineering Journal, 2019. 360: p. 124-138.

[49] Al Bsoul, A., M. Hailat, A. Abdelhay, M. Tawalbeh, I. Jum'h and K. Bani-Melhem, Treatment of olive mill effluent by adsorption on titanium oxide nanoparticles. Science of The Total Environment, 2019. 688: p. 1327-1334.

[50] Vavouraki, A.I., M.A. Dareioti and M. Kornaros, Olive Mill Wastewater (OMW) Polyphenols Adsorption onto Polymeric Resins: Part I—Batch Anaerobic Digestion of OMW. Waste and Biomass Valorization, 2020.

[51] Ochando-Pulido, J.M., J.A. Vellido-Pérez, R. González-Hernández and A. Martínez-Férez, Optimization and modeling of two-phase olive-oil washing wastewater integral treatment and phenolic compounds recovery by novel weak-base ion exchange resins. Separation and Purification Technology, 2020. 249: p. 117084.

[52] Ochando-Pulido, J.M., R. González-Hernández and A. Martinez-Ferez, On the Effect of the Operating Parameters for Two-Phase Olive-Oil Washing Wastewater Combined Phenolic Compounds Recovery and Reclamation by Novel Ion Exchange Resins. Separation and Purification Technology, 2018.

[53] Sarika, R., N. Kalogerakis and D. Mantzavinos, Treatment of olive mill effluents: Part II. Complete removal of solids by direct flocculation with poly-electrolytes. Environment International, 2005. 31(2): p. 297-304.

[54] Alver, A., E. Baştürk, A. Kılıç and M. Karataş, Use of advance oxidation process to improve the biodegradability of olive oil mill effluents. Process Safety and Environmental Protection, 2015. 98: p. 319-324.

[55] Uğurlu, M. and İ. Kula, Decolourization and removal of some organic compounds from olive mill wastewater by advanced oxidation processes and lime treatment. Environmental Science and Pollution Research - International, 2007. 14(5): p. 319-325.

[56] Chatzisymeon, E., N.P. Xekoukoulotakis and D. Mantzavinos, Determination of key operating conditions for the photocatalytic treatment of olive mill wastewaters. Catalysis Today, 2009. 144(1): p. 143-148.

[57] Maduna, K., N. Kumar, A. Aho, J. Wärnå, S. Zrnčević and D.Y. Murzin, Kinetics of Catalytic Wet Peroxide Oxidation of Phenolics in Olive Oil Mill Wastewaters over Copper Catalysts. ACS Omega, 2018. 3(7): p. 7247-7260.

[58] Najjar, W., S. Azabou, S. Sayadi and A. Ghorbel, Screening of Fe-BEA catalysts for wet hydrogen peroxide oxidation of crude olive mill wastewater under mild conditions. Applied Catalysis B: Environmental, 2009. 88(3): p. 299-304.

[59] Azabou, S., W. Najjar, M. Bouaziz, A. Ghorbel and S. Sayadi, A compact process for the treatment of olive mill wastewater by combining wet hydrogen peroxide catalytic oxidation and biological techniques. Journal of Hazardous Materials, 2010. 183(1): p. 62-69.

[60] Kallel, M., C. Belaid, R. Boussahel, M. Ksibi, A. Montiel and B. Elleuch, Olive mill wastewater degradation by Fenton oxidation with zero-valent iron and hydrogen peroxide. Journal of Hazardous Materials, 2009. 163(2): p. 550-554.

[61] Maamir, W., Y. Ouahabi, S. Poncin, H.-Z. Li and K. Bensadok, Effect of Fenton pretreatment on anaerobic digestion of olive mill wastewater and olive mill solid waste in mesophilic conditions. International Journal of Green Energy, 2017. 14(6): p. 555-560.

[62] Esteves, B.M., C.S.D. Rodrigues and L.M. Madeira, Synthetic olive mill wastewater treatment by Fenton's process in batch and continuous reactors operation. Environmental Science and Pollution Research, 2018. 25(35): p. 34826-34838.

[63] Hodaifa, G., J.M. Ochando-Pulido, S. Rodriguez-Vives and A. Martinez-Ferez, Optimization of continuous reactor at pilot scale for olive-oil mill wastewater treatment by Fenton-like process. Chemical Engineering Journal, 2013. 220: p. 117-124.

[64] Nieto, L.M., G. Hodaifa, S. Rodríguez, J.A. Giménez and J. Ochando, Degradation of organic matter in olive-oil mill wastewater through homogeneous Fenton-like reaction. Chemical Engineering Journal, 2011. 173(2): p. 503-510.

[65] Hodaifa, G., C. Agabo García and R. Borja, Study of Catalysts' Influence on Photocatalysis/Photodegradation of Olive Oil Mill Wastewater. Determination of the Optimum Working Conditions. Catalysts, 2020. 10(5): p. 554.

[66] Adhoum, N. and L. Monser, Decolourization and removal of phenolic compounds from olive mill wastewater by electrocoagulation. Chemical Engineering and Processing: Process Intensification, 2004. 43(10): p. 1281-1287.

[67] Elkacmi, R., O. Boudouch, A. Hasib, M. Bouzaid and M. Bennajah, Photovoltaic electrocoagulation treatment of olive mill wastewater using an external-loop airlift reactor. Sustainable Chemistry and Pharmacy, 2020. 17: p. 100274.

[68] D'Annibale, A., S.R. Stazi, V. Vinciguerra and G. Giovannozzi Sermanni, Oxirane-immobilized Lentinula edodes laccase: stability and phenolics removal efficiency in olive mill wastewater. Journal of Biotechnology, 2000. 77(2): p. 265-273.

[69] Casademont, P., M.B. García-Jarana, J. Sánchez-Oneto, J.R. Portela and E.J. Martínez de la Ossa, Hydrogen production by catalytic conversion of olive mill wastewater in supercritical water. The Journal of Supercritical Fluids, 2018.

[70] García-Gómez, A., A. Roig and M.P. Bernal, Composting of the solid fraction of olive mill wastewater with olive leaves: organic matter degradation and biological activity. Bioresource Technology, 2003. 86(1): p. 59-64.

[71] Fadil, K., A. Chahlaoui, A. Ouahbi, A. Zaid and R. Borja, Aerobic biodegradation and detoxification of wastewaters from the olive oil industry. International Biodeterioration & Biodegradation, 2003. 51(1): p. 37-41.

[72] Beltran-Heredia, J., J. Torregrosa, J.R. Dominguez and J. Garcia, Treatment of black-olive wastewaters by ozonation and aerobic biological degradation. Water Research, 2000. 34(14): p. 3515-3522.

[73] Hajjouji, H.E., J.R. Bailly, P. Winterton, G. Merlina, J.C. Revel and M. Hafidi, Chemical and spectroscopic analysis of olive mill waste water during a biological treatment. Bioresource Technology, 2008. 99(11): p. 4958-4965.

[74] Bertin, L., S. Berselli, F. Fava, M. Petrangeli-Papini and L. Marchetti, Anaerobic digestion of olive mill wastewaters in biofilm reactors packed with granular activated carbon and “Manville” silica beads. Water Research, 2004. 38(14): p. 3167-3178.

[75] Gonçalves, M.R., J.C. Costa, M.A. Pereira, A.A. Abreu and M.M. Alves, On the independence of hydrogen production from methanogenic suppressor in olive mill wastewater. International Journal of Hydrogen Energy, 2014. 39(12): p. 6402-6406.

[76] Eroğlu, E., İ. Eroğlu, U. Gündüz, L. Türker and M. Yücel, Biological hydrogen production from olive mill wastewater with two-stage processes. International Journal of Hydrogen Energy, 2006. 31(11): p. 1527-1535.

[77] Caporaso, N., D. Formisano and A. Genovese, Use of phenolic compounds from olive mill wastewater as valuable ingredients for functional foods. Critical Reviews in Food Science and Nutrition, 2018. 58(16): p. 2829-2841.

[78] Agalias, A., P. Magiatis, A.-L. Skaltsounis, E. Mikros, A. Tsarbopoulos, E. Gikas, I. Spanos and T. Manios, A New Process for the Management of Olive Oil Mill Waste Water and Recovery of Natural Antioxidants. Journal of Agricultural and Food Chemistry, 2007. 55(7): p. 2671-2676.

[79] Gonçalves, C., M. Lopes, J.P. Ferreira and I. Belo, Biological treatment of olive mill wastewater by non-conventional yeasts. Bioresource Technology, 2009. 100(15): p. 3759-3763.

[80] Servili, M., S. Esposto, G. Veneziani, S. Urbani, A. Taticchi, I. Di Maio, R. Selvaggini, B. Sordini and G. Montedoro, Improvement of bioactive phenol content in virgin olive oil with an olive-vegetation water concentrate produced by membrane treatment. Food Chemistry, 2011. 124(4): p. 1308-1315.

[81] Mazzei, R., E. Drioli and L. Giorno, Enzyme membrane reactor with heterogenized β-glucosidase to obtain phytotherapic compound: Optimization study. Journal of Membrane Science, 2012. 390-391(Supplement C): p. 121-129.

[82] Kestioğlu, K., T. Yonar and N. Azbar, Feasibility of physico-chemical treatment and Advanced Oxidation Processes (AOPs) as a means of pretreatment of olive mill effluent (OME). Process Biochemistry, 2005. 40(7): p. 2409-2416.

[83] Drouiche, M., V. Le Mignot, H. Lounici, D. Belhocine, H. Grib, A. Pauss and N. Mameri, A compact process for the treatment of olive mill wastewater by combining OF and UV/H2O2 techniques. Desalination, 2004. 169(1): p. 81-88.

[84] Leal, A.L., M.A. Soria and L.M. Madeira, Autothermal reforming of impure glycerol for H2 production: Thermodynamic study including in situ CO2 and/or H2 separation. International Journal of Hydrogen Energy, 2016. 41(4): p. 2607-2620.

[85] Agency, I.E., The Future of Hydrogen. 2019 [Accessed 20-02-2021]; Available from: https://www.iea.org/reports/the-future-of-hydrogen.

[86] Agency, I.E., Global hydrogen demand by sector in the Sustainable Development Scenario, 2019-2070. 2020 [Accessed 20-02-2021]; Available from: https://www.iea.org/data-and-statistics/charts/global-hydrogen-demand-by-sector-in-the-sustainable-development-scenario-2019-2070.

[87] Cakiryilmaz, N., H. Arbag, N. Oktar, G. Dogu and T. Dogu, Effect of W incorporation on the product distribution in steam reforming of bio-oil derived acetic acid over Ni based Zr-SBA-15 catalyst. International Journal of Hydrogen Energy, 2018. 43(7): p. 3629-3642.

[88] Tosti, S., C. Cavezza, M. Fabbricino, L. Pontoni, V. Palma and C. Ruocco, Production of hydrogen in a Pd-membrane reactor via catalytic reforming of olive mill wastewater. Chemical Engineering Journal, 2015. 275(Supplement C): p. 366-373.

[89] Alique, D., G. Bruni, R. Sanz, J.A. Calles and S. Tosti, Ultra-Pure Hydrogen via Co-Valorization of Olive Mill Wastewater and Bioethanol in Pd-Membrane Reactors. Processes, 2020. 8(2): p. 219.

[90] Zhang, Z., X. Hu, L. Zhang, Y. Yang, Q. Li, H. Fan, Q. Liu, T. Wei and C.-Z. Li, Steam reforming of guaiacol over Ni/Al2O3 and Ni/SBA-15: Impacts of support on catalytic behaviors of nickel and properties of coke. Fuel Processing Technology, 2019. 191: p. 138-151.

[91] Zhang, Z., X. Zhang, L. Zhang, Y. Wang, X. Li, S. Zhang, Q. Liu, T. Wei, G. Gao and X. Hu, Steam reforming of guaiacol over Ni/SiO2 catalyst modified with basic oxides: Impacts of alkalinity on properties of coke. Energy Conversion and Management, 2020. 205: p. 112301.

[92] Zhang, Z., L. Zhang, F. Liu, Y. Sun, Y. Shao, K. Sun, S. Zhang, Q. Liu, G. Hu and X. Hu, Tailoring the surface properties of Ni/SiO2 catalyst with sulfuric acid for enhancing the catalytic efficiency for steam reforming of guaiacol. Renewable Energy, 2020. 156: p. 423-439.

[93] Zhang, Z., Y. Sun, Y. Wang, K. Sun, Z. Gao, Q. Xu, S. Zhang, G. Hu, L. Xu and X. Hu, Steam reforming of acetic acid and guaiacol over Ni/Attapulgite catalyst: Tailoring pore structure of the catalyst with KOH activation for enhancing the resistivity towards coking. Molecular Catalysis, 2020. 493: p. 111051.

[94] Trane, R., S. Dahl, M.S. Skjøth-Rasmussen and A.D. Jensen, Catalytic steam reforming of bio-oil. International Journal of Hydrogen Energy, 2012. 37(8): p. 6447-6472.

[95] Xie, H., Q. Yu, M. Wei, W. Duan, X. Yao, Q. Qin and Z. Zuo, Hydrogen production from steam reforming of simulated bio-oil over Ce-Ni/Co catalyst with in continuous CO2 capture. International Journal of Hydrogen Energy, 2015. 40(3): p. 1420-1428.

[96] Soria, M.A., D. Barros and L.M. Madeira, Hydrogen production through steam reforming of bio-oils derived from biomass pyrolysis: Thermodynamic analysis including in situ CO2 and/or H2 separation. Fuel, 2019. 244: p. 184-195.

[97] Kechagiopoulos, P.N., S.S. Voutetakis, A.A. Lemonidou and I.A. Vasalos, Hydrogen Production via Steam Reforming of the Aqueous Phase of Bio-Oil in a Fixed Bed Reactor. Energy & Fuels, 2006. 20(5): p. 2155-2163.

[98] Remiro, A., B. Valle, A.T. Aguayo, J. Bilbao and A.G. Gayubo, Operating conditions for attenuating Ni/La2O3-αAl2O3 catalyst deactivation in the steam reforming of bio-oil aqueous fraction. Fuel Processing Technology, 2013. 115: p. 222-232.

[99] Remiro, A., A. Arandia, L. Oar-Arteta, J. Bilbao and A.G. Gayubo, Regeneration of NiAl2O4 spinel type catalysts used in the reforming of raw bio-oil. Applied Catalysis B: Environmental, 2018. 237: p. 353-365.

[100] Valle, B., B. Aramburu, M. Olazar, J. Bilbao and A.G. Gayubo, Steam reforming of raw bio-oil over Ni/La2O3-αAl2O3: Influence of temperature on product yields and catalyst deactivation. Fuel, 2018. 216: p. 463-474.

[101] Yu, N., M.M. Rahman, J. Chen, J. Sun, M. Engelhard, X.I.P. Hernandez and Y. Wang, Steam reforming of simulated bio-oil on K-Ni-Cu-Mg-Ce-O/Al2O3: The effect of K. Catalysis Today, 2019. 323: p. 183-190.

[102] Cheng, Y.W., M.R. Khan, K.H. Ng, S. Wongsakulphasatch and C.K. Cheng, Harnessing renewable hydrogen-rich syngas from valorization of palm oil mill effluent (POME) using steam reforming technique. Renewable Energy, 2019. 138: p. 1114-1126.

[103] Cheng, Y.W., C.C. Chong, S.P. Lee, J.W. Lim, T.Y. Wu and C.K. Cheng, Syngas from palm oil mill effluent (POME) steam reforming over lanthanum cobaltite: Effects of net-basicity. Renewable Energy, 2019.

[104] Medrano, J.A., M. Oliva, J. Ruiz, L. Garcia and J. Arauzo, Catalytic steam reforming of acetic acid in a fluidized bed reactor with oxygen addition. International Journal of Hydrogen Energy, 2008. 33(16): p. 4387-4396.

[105] Matas Güell, B., I.M.T.d. Silva, K. Seshan and L. Lefferts, Sustainable route to hydrogen - Design of stable catalysts for the steam gasification of biomass related oxygenates. Applied Catalysis B: Environmental, 2009. 88(1): p. 59-65.

[106] Hoang, T.M.C., B. Geerdink, J.M. Sturm, L. Lefferts and K. Seshan, Steam reforming of acetic acid - A major component in the volatiles formed during gasification of humin. Applied Catalysis B: Environmental, 2015. 163(Supplement C): p. 74-82.

[107] Chen, G., J. Tao, C. Liu, B. Yan, W. Li and X. Li, Steam reforming of acetic acid using Ni/Al2O3 catalyst: Influence of crystalline phase of Al2O3 support. International Journal of Hydrogen Energy, 2017. 42(32): p. 20729-20738.

[108] Savuto, E., R.M. Navarro, N. Mota, A. Di Carlo, E. Bocci, M. Carlini and J.L.G. Fierro, Steam reforming of tar model compounds over Ni/Mayenite catalysts: effect of Ce addition. Fuel, 2018. 224: p. 676-686.

[109] Silva, J.M., M.A. Soria and L.M. Madeira, Challenges and strategies for optimization of glycerol steam reforming process. Renewable and Sustainable Energy Reviews, 2015. 42: p. 1187-1213.

[110] Zhang, Z., X. Hu, J. Li, G. Gao, D. Dong, R. Westerhof, S. Hu, J. Xiang and Y. Wang, Steam reforming of acetic acid over Ni/Al2O3 catalysts: Correlation of nickel loading with properties and catalytic behaviors of the catalysts. Fuel, 2018. 217: p. 389-403.

[111] Borges, R.P., R.A.R. Ferreira, R.C. Rabelo-Neto, F.B. Noronha and C.E. Hori, Hydrogen production by steam reforming of acetic acid using hydrotalcite type precursors. International Journal of Hydrogen Energy, 2018. 43(16): p. 7881-7892.

[112] Yu, Z., X. Hu, P. Jia, Z. Zhang, D. Dong, G. Hu, S. Hu, Y. Wang and J. Xiang, Steam reforming of acetic acid over nickel-based catalysts: The intrinsic effects of nickel precursors on behaviors of nickel catalysts. Applied Catalysis B: Environmental, 2018. 237: p. 538-553.

[113] Matas Güell, B., I. Babich, K.P. Nichols, J.G.E. Gardeniers, L. Lefferts and K. Seshan, Design of a stable steam reforming catalyst—A promising route to sustainable hydrogen from biomass oxygenates. Applied Catalysis B: Environmental, 2009. 90(1): p. 38-44.

[114] de Castro, T.P., E.B. Silveira, R.C. Rabelo-Neto, L.E.P. Borges and F.B. Noronha, Study of the performance of Pt/Al2O3 and Pt/CeO2/Al2O3 catalysts for steam reforming of toluene, methane and mixtures. Catalysis Today, 2018. 299(Supplement C): p. 251-262.

[115] Pant, K.K., P. Mohanty, S. Agarwal and A.K. Dalai, Steam reforming of acetic acid for hydrogen production over bifunctional Ni-Co catalysts. Catalysis Today, 2013. 207(Supplement C): p. 36-43.

[116] Polychronopoulou, K., J.L.G. Fierro and A.M. Efstathiou, The phenol steam reforming reaction over MgO-based supported Rh catalysts. Journal of Catalysis, 2004. 228(2): p. 417-432.

[117] Constantinou, D.A. and A.M. Efstathiou, Low-temperature purification of gas streams from phenol by steam reforming over novel supported-Rh catalysts. Applied Catalysis B: Environmental, 2010. 96(3): p. 276-289.

[118] Iida, H., A. Fujiyama, A. Igarashi and K. Okumura, Steam reforming of toluene over $Ru/SrCO_3$-Al_2O_3 catalysts. Fuel Processing Technology, 2017. 168(Supplement C): p. 50-57.

[119] Liang, T., Y. Wang, M. Chen, Z. Yang, S. Liu, Z. Zhou and X. Li, Steam reforming of phenol-ethanol to produce hydrogen over bimetallic NiCu catalysts supported on sepiolite. International Journal of Hydrogen Energy, 2017. 42(47): p. 28233-28246.

[120] Adnan, M.A., O. Muraza, S.A. Razzak, M.M. Hossain and H.I. de Lasa, Iron Oxide over Silica-Doped Alumina Catalyst for Catalytic Steam Reforming of Toluene as a Surrogate Tar Biomass Species. Energy & Fuels, 2017. 31(7): p. 7471-7481.

[121] Wang, S., X. Li, L. Guo and Z. Luo, Experimental research on acetic acid steam reforming over Co-Fe catalysts and subsequent density functional theory studies. International Journal of Hydrogen Energy, 2012. 37(15): p. 11122-11131.

[122] Furusawa, T., K. Saito, Y. Kori, Y. Miura, M. Sato and N. Suzuki, Steam reforming of naphthalene/benzene with various types of Pt- and Ni-based catalysts for hydrogen production. Fuel, 2013. 103: p. 111-121.

[123] Wang, S., F. Zhang, Q. Cai, L. Zhu and Z. Luo, Steam reforming of acetic acid over coal ash supported Fe and Ni catalysts. International Journal of Hydrogen Energy, 2015. 40(35): p. 11406-11413.

[124] Nabgan, W., T.A. Tuan Abdullah, R. Mat, B. Nabgan, Y. Gambo and S. Triwahyono, Influence of Ni to Co ratio supported on ZrO2 catalysts in phenol steam reforming for hydrogen production. International Journal of Hydrogen Energy, 2016. 41(48): p. 22922-22931.

[125] Silva, O.C.V., E.B. Silveira, R.C. Rabelo-Neto, L.E.P. Borges and F.B. Noronha, Hydrogen Production Through Steam Reforming of Toluene Over Ni Supported on MgAl Mixed Oxides Derived from Hydrotalcite-Like Compounds. Catalysis Letters, 2018. 148(6): p. 1622-1633.

[126] Pu, J., K. Nishikado, N. Wang, T.T. Nguyen, T. Maki and E.W. Qian, Core-shell nickel catalysts for the steam reforming of acetic acid. Applied Catalysis B: Environmental, 2018. 224: p. 69-79.

[127] Li, J., X. Mei, L. Zhang, Z. Yu, Q. Liu, T. Wei, W. Wu, D. Dong, L. Xu and X. Hu, A comparative study of catalytic behaviors of Mn, Fe, Co, Ni, Cu and Zn-Based catalysts in steam reforming of methanol, acetic acid and acetone. International Journal of Hydrogen Energy, 2020. 45(6): p. 3815-3832.

[128] Zhang, C., X. Hu, Z. Yu, Z. Zhang, G. Chen, C. Li, Q. Liu, J. Xiang, Y. Wang and S. Hu, Steam reforming of acetic acid for hydrogen production over attapulgite and alumina supported Ni catalysts: Impacts of properties of supports on catalytic behaviors. International Journal of Hydrogen Energy, 2018.

[129] Chen, J., M. Wang, S. Wang and X. Li, Hydrogen production via steam reforming of acetic acid over biochar-supported nickel catalysts. International Journal of Hydrogen Energy, 2018. 43(39): p. 18160-18168.

[130] Wang, Y., Z. Zhang, S. Zhang, Y. Wang, S. Hu, J. Xiang and X. Hu, Steam reforming of acetic acid over Ni/biochar catalyst treated with HNO3: Impacts of the treatment on surface properties and catalytic behaviors. Fuel, 2020. 278: p. 118341.

[131] Yang, X., Y. Wang, M. Li, B. Sun, Y. Li and Y. Wang, Enhanced Hydrogen Production by Steam Reforming of Acetic Acid over a Ni Catalyst Supported on Mesoporous MgO. Energy & Fuels, 2016. 30(3): p. 2198-2203.

[132] Bangala, D.N., N. Abatzoglou and E. Chornet, Steam reforming of naphthalene on Ni-Cr/Al2O3 catalysts doped with MgO, TiO2, and La2O3. AIChE Journal, 1998. 44(4): p. 927-936.

[133] Garcia, L.a., R. French, S. Czernik and E. Chornet, Catalytic steam reforming of bio-oils for the production of hydrogen: effects of catalyst composition. Applied Catalysis A: General, 2000. 201(2): p. 225-239.

[134] Wang, M., F. Zhang and S. Wang, Effect of La2O3 replacement on γ-Al2O3 supported nickel catalysts for acetic acid steam reforming. International Journal of Hydrogen Energy, 2017. 42(32): p. 20540-20548.

[135] Li, L., B. Jiang, D. Tang, Q. Zhang and Z. Zheng, Hydrogen generation by acetic acid steam reforming over Ni-based catalysts derived from La1−xCexNiO3 perovskite. International Journal of Hydrogen Energy, 2018. 43(14): p. 6795-6803.

[136] Matas Güell, B., I.V. Babich, L. Lefferts and K. Seshan, Steam reforming of phenol over Ni-based catalysts - A comparative study. Applied Catalysis B: Environmental, 2011. 106(3): p. 280-286.

[137] Frusteri, F., S. Freni, V. Chiodo, L. Spadaro, O. Di Blasi, G. Bonura and S. Cavallaro, Steam reforming of bio-ethanol on alkali-doped Ni/MgO catalysts: hydrogen production for MC fuel cell. Applied Catalysis A: General, 2004. 270(1): p. 1-7.

[138] Hu, X., D. Dong, X. Shao, L. Zhang and G. Lu, Steam reforming of acetic acid over cobalt catalysts: Effects of Zr, Mg and K addition. International Journal of Hydrogen Energy, 2017. 42(8): p. 4793-4803.

[139] Ahmed, T., S. Xiu, L. Wang and A. Shahbazi, Investigation of Ni/Fe/Mg zeolite-supported catalysts in steam reforming of tar using simulated-toluene as model compound. Fuel, 2018. 211(Supplement C): p. 566-571.

[140] Pu, J., F. Ikegami, K. Nishikado and E.W. Qian, Effect of ceria addition on NiRu/CeO2Al2O3 catalysts in steam reforming of acetic acid. International Journal of Hydrogen Energy, 2017. 42(31): p. 19733-19743.

[141] Wang, Y., M. Chen, J. Yang, S. Liu, Z. Yang, J. Wang and T. Liang, Hydrogen Production from Steam Reforming of Acetic Acid over Ni-Fe/Palygorskite Modified with Cerium. 2017. Vol. 12. 2017.

[142] Zhao, X., Y. Xue, Z. Lu, Y. Huang, C. Guo and C. Yan, Encapsulating Ni/CeO2-ZrO2 with SiO2 layer to improve it catalytic activity for steam reforming of toluene. Catalysis Communications, 2017. 101(Supplement C): p. 138-141.

[143] Li, L., D. Tang, Y. Song, B. Jiang and Q. Zhang, Hydrogen production from ethanol steam reforming on Ni-Ce/MMT catalysts. Energy, 2018. 149: p. 937-943.

[144] Zhang, Z., X. Hu, G. Gao, T. Wei, D. Dong, Y. Wang, S. Hu, J. Xiang, Q. Liu and D. Geng, Steam reforming of acetic acid over NiKOH/Al2O3 catalyst with low nickel loading: The remarkable promotional effects of KOH on activity. International Journal of Hydrogen Energy, 2018.

[145] Choi, I.-H., K.-R. Hwang, K.-Y. Lee and I.-G. Lee, Catalytic steam reforming of biomass-derived acetic acid over modified Ni/γ-Al2O3 for sustainable hydrogen production. International Journal of Hydrogen Energy, 2019. 44(1): p. 180-190.

[146] Higo, T., H. Saito, S. Ogo, Y. Sugiura and Y. Sekine, Promotive effect of Ba addition on the catalytic performance of Ni/LaAlO3 catalysts for steam reforming of toluene. Applied Catalysis A: General, 2017. 530: p. 125-131.

[147] Fally, F., V. Perrichon, H. Vidal, J. Kaspar, G. Blanco, J.M. Pintado, S. Bernal, G. Colon, M. Daturi and J.C. Lavalley, Modification of the oxygen storage capacity of CeO2-ZrO2 mixed oxides after redox cycling aging. Catalysis Today, 2000. 59(3): p. 373-386.

[148] Vidal, H., J. Kašpar, M. Pijolat, G. Colon, S. Bernal, A. Cordón, V. Perrichon and F. Fally, Redox behavior of CeO2-ZrO2 mixed oxides: II. Influence of redox treatments on low surface area catalysts. Applied Catalysis B: Environmental, 2001. 30(1): p. 75-85.

[149] Menendez, R.B., C. Graschinsky and N.E. Amadeo, Sorption-Enhanced Ethanol Steam Reforming Process in a Fixed-Bed Reactor. Industrial & Engineering Chemistry Research, 2018. 57(34): p. 11547-11553.

[150] Chen, M., Y. Wang, Z. Yang, T. Liang, S. Liu, Z. Zhou and X. Li, Effect of Mg-modified mesoporous Ni/Attapulgite catalysts on catalytic performance and resistance to carbon deposition for ethanol steam reforming. Fuel, 2018. 220: p. 32-46.

[151] Kumar, A. and A.S.K. Sinha, Hydrogen production from acetic acid steam reforming over nickel-based catalyst synthesized via MOF process. International Journal of Hydrogen Energy, 2020.

[152] Yu, Z., L. Zhang, C. Zhang, G. Gao, Z. Ye, S. Zhang, Q. Liu, G. Hu and X. Hu, Steam reforming of acetic acid over nickel catalysts: Impacts of fourteen additives on the catalytic behaviors. Journal of the Energy Institute, 2020. 93(3): p. 1000-1019.

[153] Galdámez, J.R., L. García and R. Bilbao, Hydrogen Production by Steam Reforming of Bio-Oil Using Coprecipitated Ni−Al Catalysts. Acetic Acid as a Model Compound. Energy & Fuels, 2005. 19(3): p. 1133-1142.

[154] Rostrup-Nielsen, J.R., J. Sehested and J.K. Nørskov, Hydrogen and synthesis gas by steam- and C02 reforming, in Advances in Catalysis. 2002, Academic Press. p. 65-139.

[155] Bengaard, H.S., J.K. Nørskov, J. Sehested, B.S. Clausen, L.P. Nielsen, A.M. Molenbroek and J.R. Rostrup-Nielsen, Steam Reforming and Graphite Formation on Ni Catalysts. Journal of Catalysis, 2002. 209(2): p. 365-384.

[156] Pekmezci Karaman, B., N. Cakiryilmaz, H. Arbag, N. Oktar, G. Dogu and T. Dogu, Performance comparison of mesoporous alumina supported Cu & Ni based catalysts in acetic acid reforming. International Journal of Hydrogen Energy, 2017. 42(42): p. 26257-26269.

[157] Goicoechea, S., E. Kraleva, S. Sokolov, M. Schneider, M.-M. Pohl, N. Kockmann and H. Ehrich, Support effect on structure and performance of Co and Ni catalysts for steam reforming of acetic acid. Applied Catalysis A: General, 2016. 514(Supplement C): p. 182-191.

[158] Meng, J., Z. Zhao, X. Wang, A. Zheng, D. Zhang, Z. Huang, K. Zhao, G. Wei and H. Li, Comparative study on phenol and naphthalene steam reforming over Ni-Fe alloy catalysts supported on olivine synthesized by different methods. Energy Conversion and Management, 2018. 168: p. 60-73.

[159] Zhu, H.L., L. Pastor-Pérez and M. Millan, Catalytic Steam Reforming of Toluene: Understanding the Influence of the Main Reaction Parameters over a Reference Catalyst. Energies, 2020. 13(4): p. 813.

[160] Ni, F. and H.S. Caram, Sorption enhanced reaction for high purity products in reversible reactions. AIChE Journal, 2017. 63(12): p. 5452-5461.

[161] Hufton, J., S. Mayorga, T. Gaffney, S. Nataraj, M. Rao and S. Sircar, Sorption enhanced reaction process (SERP). Proceedings of the 1998 USDOE Hydrogen Program Review, 1998. 2: p. 693-705.

[162] Rodrigues, A.E., L.M. Madeira, R. Faria and Y.J. Wu, Sorption Enhanced Reaction Processes. 2017: World Scientific Publishing Company Pte Limited.

[163] Soria, M.A., S. Tosti, A. Mendes and L.M. Madeira, Enhancing the low temperature water-gas shift reaction through a hybrid sorption-enhanced membrane reactor for high-purity hydrogen production. Fuel, 2015. 159: p. 854-863.

[164] Iliuta, I., H.R. Radfarnia and M.C. Iliuta, Hydrogen Production by Sorption-Enhanced Steam Glycerol Reforming: Sorption Kinetics and Reactor Simulation. AIChE Journal, 2013. 59(6): p. 2105-2118.

[165] Clough, P.T., M.E. Boot-Handford, L. Zheng, Z. Zhang and P.S. Fennell, Hydrogen Production by Sorption Enhanced Steam Reforming (SESR) of Biomass in a Fluidised-Bed Reactor Using Combined Multifunctional Particles. Materials, 2018. 11(5): p. 859.

[166] Park, B.-G., A hybrid adsorbent-membrane reactor (HAMR) system for hydrogen production. Korean Journal of Chemical Engineering, 2004. 21(4): p. 782-792.

[167] Wu, Y.J., F. Díaz Alvarado, J.C. Santos, F. Gracia, A.F. Cunha and A.E. Rodrigues, Sorption-Enhanced Steam Reforming of Ethanol: Thermodynamic Comparison of CO2 Sorbents. Chemical Engineering & Technology, 2012. 35(5): p. 847-858.

[168] Dou, B., V. Dupont, G. Rickett, N. Blakeman, P.T. Williams, H. Chen, Y. Ding and M. Ghadiri, Hydrogen production by sorption-enhanced steam reforming of glycerol. Bioresource Technology, 2009. 100(14): p. 3540-3547.

[169] Martavaltzi, C.S. and A.A. Lemonidou, Hydrogen production via sorption enhanced reforming of methane: Development of a novel hybrid material—reforming catalyst and CO2 sorbent. Chemical Engineering Science, 2010. 65(14): p. 4134-4140.

[170] Aloisi, I., A. Di Giuliano, A. Di Carlo, P.U. Foscolo, C. Courson and K. Gallucci, Sorption enhanced catalytic Steam Methane Reforming: Experimental data and simulations describing the behaviour of bi-functional particles. Chemical Engineering Journal, 2017. 314: p. 570-582.

[171] Reijers, H.T.J., S.E.A. Valster-Schiermeier, P.D. Cobden and R.W. van den Brink, Hydrotalcite as CO2 Sorbent for Sorption-Enhanced Steam Reforming of Methane. Industrial & Engineering Chemistry Research, 2006. 45(8): p. 2522-2530.

[172] Kim, C.-H., J.-Y. Han, H. Lim, K.-Y. Lee and S.-K. Ryi, Hydrogen production by steam methane reforming in membrane reactor equipped with Pd membrane deposited on NiO/YSZ/NiO multilayer-treated porous stainless steel. Journal of Membrane Science, 2018. 563: p. 75-82.

[173] Soria, M.A., C. Mateos-Pedrero, I. Rodríguez-Ramos and A. Guerrero-Ruiz, Catalytic steam reforming of methane under conditions of applicability with Pd membranes over supported Ru catalysts. Catalysis Today, 2011. 171(1): p. 126-131.

[174] S G Adiya, Z.I., V. Dupont and T. Mahmud, Steam reforming of shale gas with nickel and calcium looping. Fuel, 2019. 237: p. 142-151.

[175] Omoniyi, O.A. and V. Dupont, Optimised cycling stability of sorption enhanced chemical looping steam reforming of acetic acid in a packed bed reactor. Applied Catalysis B: Environmental, 2019. 242: p. 397-409.

[176] Diglio, G., P. Bareschino, E. Mancusi, F. Pepe, F. Montagnaro, D.P. Hanak and V. Manovic, Feasibility of CaO/CuO/NiO sorption-enhanced steam methane reforming integrated with solid-oxide fuel cell for near-zero-CO2 emissions cogeneration system. Applied Energy, 2018. 230: p. 241-256.

[177] Xie, H., W. Zhang, X. Zhao, H. Chen, Q. Yu and Q. Qin, Sorption-enhanced reforming of tar: Influence of the preparation method of CO2 absorbent. Korean Journal of Chemical Engineering, 2018. 35(11): p. 2191-2197.

[178] Di Felice, L., S.S. Kazi, M.H. Sørby, I. Martinez, G. Grasa, D. Maury and J. Meyer, Combined sorbent and catalyst material for sorption enhanced reforming of methane under cyclic regeneration in presence of H2O and CO2. Fuel Processing Technology, 2019. 183: p. 35-47.

[179] Di Giuliano, A., F. Giancaterino, K. Gallucci, P.U. Foscolo and C. Courson, Catalytic and sorbent materials based on mayenite for sorption enhanced steam methane reforming with different packed-bed configurations. International Journal of Hydrogen Energy, 2018. 43(46): p. 21279-21289.

[180] Ghungrud, S.A., K.D. Dewoolkar and P.D. Vaidya, Cerium-promoted bi-functional hybrid materials made of Ni, Co and hydrotalcite for sorption-enhanced steam methane reforming (SESMR). International Journal of Hydrogen Energy, 2018.

[181] Dang, C., S. Wu, Y. Cao, H. Wang, F. Peng and H. Yu, Co-production of high quality hydrogen and synthesis gas via sorption-enhanced steam reforming of glycerol coupled with methane reforming of carbonates. Chemical Engineering Journal, 2019. 360: p. 47-53.

[182] Cherbański, R. and E. Molga, Sorption-enhanced steam methane reforming (SE-SMR) - A review: Reactor types, catalysts and sorbents characterization, process modelling. 2018.

[183] Jang, H.M., K.B. Lee, H.S. Caram and S. Sircar, High-purity hydrogen production through sorption enhanced water gas shift reaction using K2CO3-promoted hydrotalcite. Chemical Engineering Science, 2012. 73: p. 431-438.

[184] Xie, H., Q. Yu, H. Lu, L. Ji, H. Chen and Q. Qin, Selection and preparation of CO2 sorbent for sorption-enhanced steam reforming process of raw coke oven gas. Environmental Progress & Sustainable Energy, 2019. 38(1): p. 89-97.

[185] Soria, M.A., C. Rocha, S. Tosti, A. Mendes and L.M. Madeira, COx free hydrogen production through water-gas shift reaction in different hybrid multifunctional reactors. Chemical Engineering Journal, 2019. 356: p. 727-736.

[186] Vanga, G., D.M. Gattia, S. Stendardo and S. Scaccia, Novel synthesis of combined CaO-Ca12Al14O33-Ni sorbent-catalyst material for sorption enhanced steam reforming processes. Ceramics International, 2019. 45(6): p. 7594-7605.

[187] Liu, L., D. Hong, N. Wang and X. Guo, High purity H2 production from sorption enhanced bio-ethanol reforming via sol-gel-derived Ni-CaO-Al2O3 bi-functional materials. International Journal of Hydrogen Energy, 2020.

[188] Wang, X., Y. He, T. Xu, B. Xiao, S. Liu, Z. Hu and J. Li, CO2 sorption-enhanced steam reforming of phenol using Ni-M/CaO-Ca12Al14O33 (M = Cu, Co, and Ce) as catalytic sorbents. Chemical Engineering Journal, 2020. 393: p. 124769.

[189] Dang, C., S. Wu, G. Yang, Y. Cao, H. Wang, F. Peng, S. Wang and H. Yu, Hydrogen Production from Sorption-Enhanced Steam Reforming of Phenol over a Ni-Ca-Al-O Bifunctional Catalyst. ACS Sustainable Chemistry & Engineering, 2020. 8(18): p. 7111-7120.

[190] Nimmas, T., S. Wongsakulphasatch, C. Kui Cheng and S. Assabumrungrat, Bi-metallic CuO-NiO based multifunctional material for hydrogen production from sorption-enhanced chemical looping autothermal reforming of ethanol. Chemical Engineering Journal, 2020. 398: p. 125543.

[191] Li, H., H. Tian, S. Chen, Z. Sun, T. Liu, R. Liu, S. Assabumrungrat, J. Saupsor, R. Mu, C. Peiand J. Gong, Sorption enhanced steam reforming of methanol for high-purity hydrogen production over Cu-MgO/Al2O3 bifunctional catalysts. Applied Catalysis B: Environmental, 2020. 276: p. 119052.

[192] Zhang, W., H. Xie, Z. Yu, P. Wang, Z. Wang and Q. Yu, Steam reforming of tar from raw coke oven gas over bifunctional catalysts: Reforming performance for H2 production. Environmental Progress & Sustainable Energy. n/a(n/a): p. e13501.

[193] Coenen, K., F. Gallucci, P. Cobden, E. van Dijk, E. Hensen and M.V. Annaland, Influence of material composition on the CO2 and H2O adsorption capacities and kinetics of potassium-promoted sorbents. Chemical Engineering Journal, 2018. 334: p. 2115-2123.

[194] Rocha, C., M.A. Soria and L.M. Madeira, Steam reforming of olive oil mill wastewater with in situ hydrogen and carbon dioxide separation - Thermodynamic analysis. Fuel, 2017. 207: p. 449-460.

[195] Lima da Silva, A. and I.L. Müller, Hydrogen production by sorption enhanced steam reforming of oxygenated hydrocarbons (ethanol, glycerol, n-butanol and methanol): Thermodynamic modelling. International Journal of Hydrogen Energy, 2011. 36(3): p. 2057-2075.

[196] Silva, J.M., M.A. Soria and L.M. Madeira, Thermodynamic analysis of Glycerol Steam Reforming for hydrogen production with in situ hydrogen and carbon dioxide separation. Journal of Power Sources, 2015. 273: p. 423-430.

[197] Noppakun, N., S. Wongsakulphasatch, R. Kokoo and S. Assabumrungrat, Hydrogen production from sorption-enhanced steam methane reforming chemical-looping. IOP Conference Series: Materials Science and Engineering, 2020. 736: p. 042009.

[198] Oliveira, E., PhD Thesis: Sorption enhanced steam methane reforming process for continuous production of hydrogen in pressure swing adsorptive reactors, in Department of Chemical Engineering. 2009, Faculty of Engineering of University of Porto: Porto.

[199] Al-Mamoori, A., H. Thakkar, X. Li, A.A. Rownaghi and F. Rezaei, Development of Potassium- and Sodium-Promoted CaO Adsorbents for CO2 Capture at High Temperatures. Industrial & Engineering Chemistry Research, 2017. 56(29): p. 8292-8300.

[200] Martavaltzi, C.S. and A.A. Lemonidou, Development of new CaO based sorbent materials for CO2 removal at high temperature. Microporous and Mesoporous Materials, 2008. 110(1): p. 119-127.

[201] Wang, S., H. Shen, S. Fan, Y. Zhao, X. Ma and J. Gong, Enhanced CO2 adsorption capacity and stability using CaO-based adsorbents treated by hydration. AIChE Journal, 2013. 59(10): p. 3586-3593.

[202] Westbye, A., L. Di Felice, A. Aranda and P.D.C. Dietzel. Efficient calcination of CaCO3 by means of combined Ca-Cu materials for Sorption Enhanced Reforming. in 25th International Conference on Chemical Reaction Engineering. 2018. Florence, Italy.

[203] Zhang, Y., X. Gong, X. Chen, L. Yin, J. Zhang and W. Liu, Performance of synthetic CaO-based sorbent pellets for CO2 capture and kinetic analysis. Fuel, 2018. 232: p. 205-214.

[204] Yoon, H.J. and K.B. Lee, Introduction of chemically bonded zirconium oxide in CaO-based high-temperature CO2 sorbents for enhanced cyclic sorption. Chemical Engineering Journal, 2019. 355: p. 850-857.

[205] Guo, H., Z. Xu, T. Jiang, Y. Zhao, X. Ma and S. Wang, The effect of incorporation Mg ions into the crystal lattice of CaO on the high temperature CO2 capture. Journal of CO2 Utilization, 2020. 37: p. 335-345.

[206] Zhang, X., Z. Li, Y. Peng, W. Su, X. Sun and J. Li, Investigation on a novel CaO-Y2O3 sorbent for efficient CO2 mitigation. Chemical Engineering Journal, 2014. 243(Supplement C): p. 297-304.

[207] Lu, H., E.P. Reddy and P.G. Smirniotis, Calcium Oxide Based Sorbents for Capture of Carbon Dioxide at High Temperatures. Industrial & Engineering Chemistry Research, 2006. 45(11): p. 3944-3949.

[208] Di Giuliano, A. and K. Gallucci, Sorption enhanced steam methane reforming based on nickel and calcium looping: a review. Chemical Engineering and Processing - Process Intensification, 2018. 130: p. 240-252.

[209] Silva, J.M., R. Trujillano, V. Rives, M.A. Soria and L.M. Madeira, High temperature CO2 sorption over modified hydrotalcites. Chemical Engineering Journal, 2017. 325: p. 25-34.

[210] Miguel, C.V., R. Trujillano, V. Rives, M.A. Vicente, A.F.P. Ferreira, A.E. Rodrigues, A. Mendes and L.M. Madeira, High temperature CO2 sorption with gallium-substituted and promoted hydrotalcites. Separation and Purification Technology, 2014. 127(Supplement C): p. 202-211.

[211] Kim, S., S.G. Jeon and K.B. Lee, High-Temperature CO2 Sorption on Hydrotalcite Having a High Mg/Al Molar Ratio. ACS Applied Materials & Interfaces, 2016. 8(9): p. 5763-5767.

[212] Yong, Z., Mata and A.E. Rodrigues, Adsorption of Carbon Dioxide onto Hydrotalcite-like Compounds (HTlcs) at High Temperatures. Industrial & Engineering Chemistry Research, 2001. 40(1): p. 204-209.

[213] Wang, X.P., J.J. Yu, J. Cheng, Z.P. Hao and Z.P. Xu, High-Temperature Adsorption of Carbon Dioxide on Mixed Oxides Derived from Hydrotalcite-Like Compounds. Environmental Science & Technology, 2008. 42(2): p. 614-618.

[214] Ram Reddy, M.K., Z.P. Xu, G.Q. Lu and J.C. Diniz da Costa, Layered Double Hydroxides for CO2 Capture: Structure Evolution and Regeneration. Industrial & Engineering Chemistry Research, 2006. 45(22): p. 7504-7509.

[215] Maroño, M., Y. Torreiro and L. Gutierrez, Influence of steam partial pressures in the CO2 capture capacity of K-doped hydrotalcite-based sorbents for their application to SEWGS processes. International Journal of Greenhouse Gas Control, 2013. 14(Supplement C): p. 183-192.

[216] Coenen, K., F. Gallucci, P. Cobden, E. van Dijk, E. Hensen and M. van Sint Annaland, Chemisorption working capacity and kinetics of CO2 and H2O of hydrotalcite-based adsorbents for sorption-enhanced water-gas-shift applications. Chemical Engineering Journal, 2016. 293: p. 9-23.

[217] Martunus, Z. Helwani, A.D. Wiheeb, J. Kim and M.R. Othman, Improved carbon dioxide capture using metal reinforced hydrotalcite under wet conditions. International Journal of Greenhouse Gas Control, 2012. 7: p. 127-136.

[218] Silva, J.M., R. Trujillano, V. Rives, M.A. Soria and L.M. Madeira, Dynamic behaviour of a K-doped Ga substituted and microwave aged hydrotalcite-derived mixed oxide during CO2 sorption experiments. Journal of Industrial and Engineering Chemistry, 2019.

[219] Boon, J., P.D. Cobden, H.A.J. van Dijk, C. Hoogland, E.R. van Selow and M. van Sint Annaland, Isotherm model for high-temperature, high-pressure adsorption of CO2 and H2O on K-promoted hydrotalcite. Chemical Engineering Journal, 2014. 248: p. 406-414.

[220] Halabi, M.H., M.H.J.M. de Croon, J. van der Schaaf, P.D. Cobden and J.C. Schouten, High capacity potassium-promoted hydrotalcite for CO2 capture in H2 production. International Journal of Hydrogen Energy, 2012. 37(5): p. 4516-4525.

[221] Wu, Y.-J., P. Li, J.-G. Yu, A.F. Cunha and A.E. Rodrigues, K-Promoted Hydrotalcites for CO2 Capture in Sorption Enhanced Reactions. Chemical Engineering & Technology, 2013. 36(4): p. 567-574.

[222] Wang, Q., Z. Wu, H.H. Tay, L. Chen, Y. Liu, J. Chang, Z. Zhong, J. Luo and A. Borgna, High temperature adsorption of CO2 on Mg-Al hydrotalcite: Effect of the charge compensating anions and the synthesis pH. Catalysis Today, 2011. 164(1): p. 198-203.

[223] Hanif, A., S. Dasgupta, S. Divekar, A. Arya, M.O. Garg and A. Nanoti, A study on high temperature CO2 capture by improved hydrotalcite sorbents. Chemical Engineering Journal, 2014. 236(Supplement C): p. 91-99.

[224] Hutson, N.D. and B.C. Attwood, High temperature adsorption of CO2 on various hydrotalcite-like compounds. Adsorption, 2008. 14(6): p. 781-789.

[225] Sanna, A., S. Thompson, K.J. Whitty and M.M. Maroto-Valer, Fly Ash Derived Lithium Silicate for in-situ Pre-combustion CO2 Capture. Energy Procedia, 2017. 114(Supplement C): p. 2401-2404.

[226] Seggiani, M., M. Puccini and S. Vitolo, Alkali promoted lithium orthosilicate for CO2 capture at high temperature and low concentration. International Journal of Greenhouse Gas Control, 2013. 17(Supplement C): p. 25-31.

[227] Seggiani, M., E. Stefanelli, M. Puccini and S. Vitolo, CO2 sorption/desorption performance study on K2CO3-doped Li4SiO4-based pellets. Chemical Engineering Journal, 2018. 339: p. 51-60.

[228] Gao, N., K. Ma, T. Ding, J. Cai, Y. Tian and X. Li, Enhanced carbon dioxide adsorption performance and kinetic study of K and Al co-doped Li4SiO4. Chinese Chemical Letters, 2018. 29(3): p. 482-484.

[229] Hu, Y., W. Liu, Z. Zhou and Y. Yang, Preparation of Li4SiO4 Sorbents for Carbon Dioxide Capture via a Spray-Drying Technique. Energy & Fuels, 2018. 32(4): p. 4521-4527.

[230] Wang, H., J. Zhang, G. Wang, Q. Wang and T. Song, High-temperature capture of CO2 by Li4SiO4 prepared with blast furnace slag and kinetic analysis. Journal of Thermal Analysis and Calorimetry, 2018. 133(2): p. 981-989.

[231] Hu, Y., M. Qu, H. Li, Y. Yang, J. Yang, W. Qu and W. Liu, Porous extruded-spheronized Li4SiO4 pellets for cyclic CO2 capture. Fuel, 2019. 236: p. 1043-1049.

[232] Izquierdo, M.T., A. Saleh, E. Sánchez-Fernández, M.M. Maroto-Valer and S. García, High-Temperature CO2 Capture by Li4SiO4 Sorbents: Effect of CO2 Concentration and Cyclic Performance under Representative Conditions. Industrial & Engineering Chemistry Research, 2018. 57(41): p. 13802-13810.

[233] Hu, Y., W. Liu, Y. Yang, M. Qu and H. Li, CO2 capture by Li4SiO4 sorbents and their applications: Current developments and new trends. Chemical Engineering Journal, 2019. 359: p. 604-625.

[234] Kwon, Y.M., H.J. Chae, M.S. Cho, Y.K. Park, H.M. Seo, S.C. Lee and J.C. Kim, Effect of a Li2SiO3 phase in lithium silicate-based sorbents for CO2 capture at high temperatures. Separation and Purification Technology, 2019. 214: p. 104-110.

[235] Zhang, T., M. Li, P. Ning, Q. Jia, Q. Wang and J. Wang, K2CO3 promoted novel Li4SiO4-based sorbents from sepiolite with high CO2 capture capacity under different CO2 partial pressures. Chemical Engineering Journal, 2020. 380: p. 122515.

[236] Li, H., M. Qu and Y. Hu, Preparation of spherical Li4SiO4 pellets by novel agar method for high-temperature CO2 capture. Chemical Engineering Journal, 2020. 380: p. 122538.

[237] Fang, Y., R. Zou and X. Chen, High-temperature CO2 adsorption over Li4SiO4 sorbents derived from different lithium sources. The Canadian Journal of Chemical Engineering. n/a(n/a).

[238] Fang, Y., R. Zou and X. Chen, High-temperature CO2 adsorption over Li4SiO4 sorbents derived from different lithium sources. The Canadian Journal of Chemical Engineering, 2020. 98(7): p. 1495-1500.

[239] Labajos, F.M., V. Rives and M.A. Ulibarri, Effect of hydrothermal and thermal treatments on the physicochemical properties of Mg-Al hydrotalcite-like materials. Journal of Materials Science, 1992. 27(6): p. 1546-1552.

[240] Iwan, A., H. Stephenson, W.C. Ketchie and A.A. Lapkin, High temperature sequestration of CO2 using lithium zirconates. Chemical Engineering Journal, 2009. 146(2): p. 249-258.

[241] Peltzer, D., J. Mùnera, L. Cornaglia and M. Strumendo, Characterization of potassium doped Li2ZrO3 based CO2 sorbents: Stability properties and CO2 desorption kinetics. Chemical Engineering Journal, 2018. 336: p. 1-11.

[242] Halabi, M.H., M.H.J.M. de Croon, J. van der Schaaf, P.D. Cobden and J.C. Schouten, Reactor modeling of sorption-enhanced autothermal reforming of methane. Part I: Performance study of hydrotalcite and lithium zirconate-based processes. Chemical Engineering Journal, 2011. 168(2): p. 872-882.

[243] Lee, K.B., A. Verdooren, H.S. Caram and S. Sircar, Chemisorption of carbon dioxide on potassium-carbonate-promoted hydrotalcite. Journal of Colloid and Interface Science, 2007. 308(1): p. 30-39.

[244] Iruretagoyena Ferrer, D., PhD Thesis: Supported layered double hydroxides as CO2 adsorbents for sorption-enhanced H2 production, in Chemical Engineering Department. 2014, Imperial College London: London.

[245] Akgsornpeak, A., T. Witoon, T. Mungcharoen and J. Limtrakul, Development of synthetic CaO sorbents via CTAB-assisted sol-gel method for CO2 capture at high temperature. Chemical Engineering Journal, 2014. 237(Supplement C): p. 189-198.

[246] Qin, Q., J. Wang, T. Zhou, Q. Zheng, L. Huang, Y. Zhang, P. Lu, A. Umar, B. Louis and Q. Wang, Impact of organic interlayer anions on the CO2 adsorption performance of Mg-Al layered double hydroxides derived mixed oxides. Journal of Energy Chemistry, 2017. 26(3): p. 346-353.

[247] Li, S., Y. Shi, Y. Yang, Y. Zheng and N. Cai, High-Performance CO2 Adsorbent from Interlayer Potassium-Promoted Stearate-Pillared Hydrotalcite Precursors. Energy & Fuels, 2013. 27(9): p. 5352-5358.

[248] Rives, V., Layered Double Hydroxides: Present and Future. 2001: Nova Publishers.

[249] Tronto, J., A.C. Bordonal, Z. Naal and J.B. Valim, Conducting Polymers / Layered Double Hydroxides Intercalated Nanocomposites, in Materials Science - Advanced Topics, Y. Mastai, Editor. 2013, IntechOpen.

[250] Bhatta, L.K.G., S. Subramanyam, M.D. Chengala, S. Olivera and K. Venkatesh, Progress in hydrotalcite like compounds and metal-based oxides for CO2 capture: a review. Journal of Cleaner Production, 2015. 103(Supplement C): p. 171-196.

[251] Khan, A.I. and D. O'Hare, Intercalation chemistry of layered double hydroxides: recent developments and applications. Journal of Materials Chemistry, 2002. 12(11): p. 3191-3198.

[252] Brindley, G. and S. Kikkawa, A crystal-chemical study of Mg, Al and Ni, N hydroxy-perchlorates and hydroxycarbonates. American Mineralogist, 1979. 64(7-8): p. 836-843.

[253] Meyer, O., F. Roessner, R.A. Rakoczy and R.W. Fischer, Impact of Organic Interlayer Anions in Hydrotalcite Precursor on the Catalytic Activity of Hydrotalcite-Derived Mixed Oxides. ChemCatChem, 2010. 2(3): p. 314-321.

[254] Velu, S., V. Ramjumar, A. Narayana and C.S. Swamy, Effect of interlayer anions on the physicochemical properties of zinc-aluminium hydrotalcite-like compounds. Journal of Materials Science, 1997. 32(4): p. 957-964.

[255] Yamamoto, T., T. Kodama, N. Hasegawa, M. Tsuji and Y. Tamaura, Synthesis of hydrotalcite with high layer charge for CO2 adsorbent. Energy Conversion and Management, 1995. 36(6): p. 637-640.

[256] Tanaka, R., I. Ogino and S.R. Mukai, Synthesis of Mg-Al Mixed Oxides with Markedly High Surface Areas from Layered Double Hydroxides with Organic Sulfonates. ACS Omega, 2018. 3(12): p. 16916-16923.

[257] Wang, Q., H.H. Tay, Z. Zhong, J. Luo and A. Borgna, Synthesis of high-temperature CO2 adsorbents from organo-layered double hydroxides with markedly improved CO2 capture capacity. Energy & Environmental Science, 2012. 5(6): p. 7526-7530.

[258] Othman, M.R., Z. Helwani, Martunus and W.J.N. Fernando, Synthetic hydrotalcites from different routes and their application as catalysts and gas adsorbents: a review. Applied Organometallic Chemistry, 2009. 23(9): p. 335-346.

[259] Zeng, S., X. Xu, S. Wang, Q. Gong, R. Liu and Y. Yu, Sand flower layered double hydroxides synthesized by co-precipitation for CO2 capture: Morphology evolution mechanism, agitation effect and stability. Materials Chemistry and Physics, 2013. 140(1): p. 159-167.

[260] Ezeh, C.I., X. Huang, X. Yang, C.-g. Sun and J. Wang, Sonochemical surface functionalization of exfoliated LDH: Effect on textural properties, CO2 adsorption, cyclic regeneration capacities and subsequent gas uptake for simultaneous methanol synthesis. Ultrasonics Sonochemistry, 2017. 39: p. 330-343.

[261] León, M., E. Díaz, S. Bennici, A. Vega, S. Ordóñez and A. Auroux, Adsorption of CO2 on Hydrotalcite-Derived Mixed Oxides: Sorption Mechanisms and Consequences for Adsorption Irreversibility. Industrial & Engineering Chemistry Research, 2010. 49(8): p. 3663-3671.

[262] Yang, Z.-z., J.-j. Wei, G.-m. Zeng, H.-q. Zhang, X.-f. Tan, C. Ma, X.-c. Li, Z.-h. Li and C. Zhang, A review on strategies to LDH-based materials to improve adsorption capacity and photoreduction efficiency for CO2. Coordination Chemistry Reviews, 2019. 386: p. 154-182.

[263] Wang, Q., H.H. Tay, D.J.W. Ng, L. Chen, Y. Liu, J. Chang, Z. Zhong, J. Luo and A. Borgna, The Effect of Trivalent Cations on the Performance of Mg-M-CO3 Layered Double Hydroxides for High-Temperature CO2 Capture. ChemSusChem, 2010. 3(8): p. 965-973.

[264] Goh, K.-H., T.-T. Lim and Z. Dong, Application of layered double hydroxides for removal of oxyanions: A review. Water Research, 2008. 42(6): p. 1343-1368.

[265] Hutson, N.D., S.A. Speakman and E.A. Payzant, Structural Effects on the High Temperature Adsorption of CO2 on a Synthetic Hydrotalcite. Chemistry of Materials, 2004. 16(21): p. 4135-4143.

[266] Martunus, M.R. Othman and W.J.N. Fernando, Elevated temperature carbon dioxide capture via reinforced metal hydrotalcite. Microporous and Mesoporous Materials, 2011. 138(1): p. 110-117.

[267] Tichit, D., A. Rolland, F. Prinetto, G. Fetter, M. de Jesus Martinez-Ortiz, M.A. Valenzuela and P. Bosch, Comparison of the structural and acid-base properties of Ga- and Al-containing layered double hydroxides obtained by microwave irradiation and conventional ageing of synthesis gels. Journal of Materials Chemistry, 2002. 12(12): p. 3832-3838.

[268] Walspurger, S., P.D. Cobden, O.V. Safonova, Y. Wu and E.J. Anthony, High CO2 Storage Capacity in Alkali-Promoted Hydrotalcite-Based Material: In Situ Detection of Reversible Formation of Magnesium Carbonate. Chemistry - A European Journal, 2010. 16(42): p. 12694-12700.

[269] Othman, M.R., N.M. Rasid and W.J.N. Fernando, Mg-Al hydrotalcite coating on zeolites for improved carbon dioxide adsorption. Chemical Engineering Science, 2006. 61(5): p. 1555-1560.

[270] Yang, W., Y. Kim, P.K.T. Liu, M. Sahimi and T.T. Tsotsis, A study by in situ techniques of the thermal evolution of the structure of a Mg-Al-CO3 layered double hydroxide. Chemical Engineering Science, 2002. 57(15): p. 2945-2953.

[271] Reichle, W.T., S.Y. Kang and D.S. Everhardt, The nature of the thermal decomposition of a catalytically active anionic clay mineral. Journal of Catalysis, 1986. 101(2): p. 352-359.

[272] Mascolo, G. and M.C. Mascolo, On the synthesis of layered double hydroxides (LDHs) by reconstruction method based on the “memory effect”. Microporous and Mesoporous Materials, 2015. 214: p. 246-248.

[273] Yuan, X., Y. Wang, J. Wang, C. Zhou, Q. Tang and X. Rao, Calcined graphene/MgAl-layered double hydroxides for enhanced Cr(VI) removal. Chemical Engineering Journal, 2013. 221: p. 204-213.

[274] Guo, Y., Z. Zhu, Y. Qiu and J. Zhao, Enhanced adsorption of acid brown 14 dye on calcined Mg/Fe layered double hydroxide with memory effect. Chemical Engineering Journal, 2013. 219: p. 69-77.

[275] Wang, Q., J. Luo, Z. Zhong and A. Borgna, CO2 capture by solid adsorbents and their applications: current status and new trends. Energy & Environmental Science, 2011. 4(1): p. 42-55.

[276] Yang, J.-I. and J.-N. Kim, Hydrotalcites for adsorption of CO2 at high temperature. Korean Journal of Chemical Engineering, 2006. 23(1): p. 77-80.

[277] Aschenbrenner, O., P. McGuire, S. Alsamaq, J. Wang, S. Supasitmongkol, B. Al-Duri, P. Styring and J. Wood, Adsorption of carbon dioxide on hydrotalcite-like compounds of different compositions. Chemical Engineering Research and Design, 2011. 89(9): p. 1711-1721.

[278] van Selow, E.R., P.D. Cobden, A.D. Wright, R.W. van den Brink and D. Jansen, Improved sorbent for the sorption-enhanced water-gas shift process. Energy Procedia, 2011. 4: p. 1090-1095.

[279] Coenen, K., F. Gallucci, G. Pio, P. Cobden, E. van Dijk, E. Hensen and M. van Sint Annaland, On the influence of steam on the CO2 chemisorption capacity of a hydrotalcite-based adsorbent for SEWGS applications. Chemical Engineering Journal, 2017. 314(Supplement C): p. 554-569.

[280] De Roy, A., C. Forano and J.P. Besse, Layered Double Hydroxides: Synthesis and post synthesis modification. In Layered Double Hydroxides: Present and Future. Layered Double Hydroxides: Synthesis and Post-Synthesis Modification, in Layered Double Hydroxides: Present and Future, 2001: p. 1-39.

[281] Oliveira, E.L.G., C.A. Grande and A.E. Rodrigues, CO2 sorption on hydrotalcite and alkali-modified (K and Cs) hydrotalcites at high temperatures. Separation and Purification Technology, 2008. 62(1): p. 137-147.

[282] Sun, L., Y. Yang, H. Ni, D. Liu, Z. Sun, P. Li and J. Yu, Enhancement of CO2 Adsorption Performance on Hydrotalcites Impregnated with Alkali Metal Nitrate Salts and Carbonate Salts. Industrial & Engineering Chemistry Research, 2020. 59(13): p. 6043-6052.

[283] Zhu, X., C. Chen, Q. Wang, Y. Shi, D. O'Hare and N. Cai, Roles for K2CO3 doping on elevated temperature CO2 adsorption of potassium promoted layered double oxides. Chemical Engineering Journal, 2019. 366: p. 181-191.

[284] Zheng, Y., Y. Shi, S. Li, Y. Yang and N. Cai, Elevated temperature hydrogen/carbon dioxide separation process simulation by integrating elementary reaction model of hydrotalcite adsorbent. International Journal of Hydrogen Energy, 2014. 39(8): p. 3771-3779.

[285] Ebner, A.D., S.P. Reynolds and J.A. Ritter, Nonequilibrium Kinetic Model That Describes the Reversible Adsorption and Desorption Behavior of CO2 in a K-Promoted Hydrotalcite-like Compound. Industrial & Engineering Chemistry Research, 2007. 46(6): p. 1737-1744.

[286] Ding, Y. and E. Alpay, Equilibria and kinetics of CO2 adsorption on hydrotalcite adsorbent. Chemical Engineering Science, 2000. 55(17): p. 3461-3474.

[287] Yavuz, C.T., B.D. Shinall, A.V. Iretskii, M.G. White, T. Golden, M. Atilhan, P.C. Ford and G.D. Stucky, Markedly Improved CO2 Capture Efficiency and Stability of Gallium Substituted Hydrotalcites at Elevated Temperatures. Chemistry of Materials, 2009. 21(15): p. 3473-3475.

[288] Yong, Z. and A.r.E. Rodrigues, Hydrotalcite-like compounds as adsorbents for carbon dioxide. Energy Conversion and Management, 2002. 43(14): p. 1865-1876.

[289] Lee, C.H., S.W. Choi, H.J. Yoon, H.J. Kwon, H.C. Lee, S.G. Jeon and K.B. Lee, Na2CO3-doped CaO-based high-temperature CO2 sorbent and its sorption kinetics. Chemical Engineering Journal, 2018. 352: p. 103-109.

[290] Coenen, K., F. Gallucci, E. Hensen and M. van Sint Annaland, CO2 and H2O chemisorption mechanism on different potassium-promoted sorbents for SEWGS processes. Journal of CO2 Utilization, 2018. 25: p. 180-193.

[291] Du, H., C.T. Williams, A.D. Ebner and J.A. Ritter, In Situ FTIR Spectroscopic Analysis of Carbonate Transformations during Adsorption and Desorption of CO2 in K-Promoted HTlc. Chemistry of Materials, 2010. 22(11): p. 3519-3526.

[292] Giorno, L., The Principle of Membrane Reactors, in Encyclopedia of Membranes, E. Drioli and L. Giorno, Editors. 2015, Springer Berlin Heidelberg: Berlin, Heidelberg. p. 1-3.

[293] Mendes, D., A. Mendes, L.M. Madeira, A. Iulianelli, J.M. Sousa and A. Basile, The water-gas shift reaction: from conventional catalytic systems to Pd-based membrane reactors—a review. Asia-Pacific Journal of Chemical Engineering, 2010. 5(1): p. 111-137.

[294] Arratibel, A., A. Pacheco Tanaka, I. Laso, M. van Sint Annaland and F. Gallucci, Development of Pd-based double-skinned membranes for hydrogen production in fluidized bed membrane reactors. Journal of Membrane Science, 2018. 550: p. 536-544.

[295] Rahimpour, M.R., F. Samimi, A. Babapoor, T. Tohidian and S. Mohebi, Palladium membranes applications in reaction systems for hydrogen separation and purification: A review. Chemical Engineering and Processing: Process Intensification, 2017. 121: p. 24-49.

[296] Fedotov, A., D. Antonov, V. Uvarov and M. Tsodikov, Syngas and ultrapure hydrogen co-production from biomass products and synthetic fuel using hybrid membrane-catalytic reactor, in 25th International Conference on Chemical Reaction Engineering 2018: Florence, Italy.

[297] Lin, K.-H., W.-H. Lin, C.-H. Hsiao, H.-F. Chang and A.C.C. Chang, Hydrogen production in steam reforming of glycerol by conventional and membrane reactors. International Journal of Hydrogen Energy, 2012. 37(18): p. 13770-13776.

[298] Basile, A., F. Gallucci and L. Paturzo, Hydrogen production from methanol by oxidative steam reforming carried out in a membrane reactor. Catalysis Today, 2005. 104(2-4): p. 251-259.

[299] Mendes, D., S. Sá, S. Tosti, J.M. Sousa, L.M. Madeira and A. Mendes, Experimental and modeling studies on the low-temperature water-gas shift reaction in a dense Pd-Ag packed-bed membrane reactor. Chemical Engineering Science, 2011. 66(11): p. 2356-2367.

[300] Tong, J., L. Su, Y. Kashima, R. Shirai, H. Suda and Y. Matsumura, Simultaneously Depositing Pd−Ag Thin Membrane on Asymmetric Porous Stainless Steel Tube and Application To Produce Hydrogen from Steam Reforming of Methane. Industrial & Engineering Chemistry Research, 2006. 45(2): p. 648-655.

[301] Chang, A.C.C., W.-H. Lin, K.-H. Lin, C.-H. Hsiao, H.-H. Chen and H.-F. Chang, Reforming of glycerol for producing hydrogen in a Pd/Ag membrane reactor. International Journal of Hydrogen Energy, 2012. 37(17): p. 13110-13117.

[302] Didenko, L.P., V.N. Babak, L.A. Sementsova, P.E. Chizhov and T.V. Dorofeeva, Effect of Pd-Ru alloy membrane thickness on H2 flux from steam reforming products. Petroleum Chemistry, 2017. 57(11): p. 935-946.

[303] Coenen, K., F. Gallucci, B. Mezari, E. Hensen and M. van Sint Annaland, An in-situ IR study on the adsorption of CO2 and H2O on hydrotalcites. Journal of CO2 Utilization, 2018. 24: p. 228-239.

[304] Lytkina, A.A., N.V. Orekhova and A.B. Yaroslavtsev, Methanol Steam Reforming in Membrane Reactors. Petroleum Chemistry, 2018. 58(11): p. 911-922.

[305] Gallucci, F., L. Paturzo and A. Basile, Hydrogen Recovery from Methanol Steam Reforming in a Dense Membrane Reactor: Simulation Study. Industrial & Engineering Chemistry Research, 2004. 43(10): p. 2420-2432.

[306] Macedo, M.S., M.A. Soria and L.M. Madeira, Glycerol steam reforming for hydrogen production: Traditional versus membrane reactor. International Journal of Hydrogen Energy, 2019. 44(45): p. 24719-24732.

[307] Parente, M., M.A. Soria and L.M. Madeira, Hydrogen and/or syngas production through combined dry and steam reforming of biogas in a membrane reactor: A thermodynamic study. Renewable Energy, 2020. 157: p. 1254-1264.

[308] Gallucci, F., E. Fernandez, P. Corengia and M. van Sint Annaland, Recent advances on membranes and membrane reactors for hydrogen production. Chemical Engineering Science, 2013. 92(Supplement C): p. 40-66.

[309] Adhikari, S. and S. Fernando, Hydrogen Membrane Separation Techniques. Industrial & Engineering Chemistry Research, 2006. 45(3): p. 875-881.

[310] Miguel, C.V., A. Mendes, S. Tosti and L.M. Madeira, Effect of CO and CO2 on H2 permeation through finger-like Pd-Ag membranes. International Journal of Hydrogen Energy, 2012. 37(17): p. 12680-12687.

[311] O'Brien, C.P. and I.C. Lee, CO Poisoning and CO Hydrogenation on the Surface of Pd Hydrogen Separation Membranes. The Journal of Physical Chemistry C, 2017. 121(31): p. 16864-16871.

[312] Pérez, P., C.A. Cornaglia, A. Mendes, L.M. Madeira and S. Tosti, Surface effects and CO/CO2 influence in the H2 permeation through a Pd-Ag membrane: A comprehensive model. International Journal of Hydrogen Energy, 2015. 40(20): p. 6566-6572.

[313] Shirasaki, Y., T. Tsuneki, T. Seki, I. Yasuda, T. Sato and N. Itoh, Improvement in Hydrogen Permeability of Palladium Membrane by Alloying with Transition Metals. JOURNAL OF CHEMICAL ENGINEERING OF JAPAN, 2018. 51(1): p. 123-125.

[314] Dalla Fontana, A., N. Sirini, L.M. Cornaglia and A.M. Tarditi, Hydrogen permeation and surface properties of PdAu and PdAgAu membranes in the presence of CO, CO2 and H2S. Journal of Membrane Science, 2018. 563: p. 351-359.

[315] Lewis, F.A., The palladium-hydrogen system: Structures near phase transition and critical points. International Journal of Hydrogen Energy, 1995. 20(7): p. 587-592.

[316] Nakajima, T., T. Kume, Y. Ikeda, M. Shiraki, H. Kurokawa, T. Iseki, M. Kajitani, H. Tanaka, H. Hikosaka, Y. Takagiand M. Ito, Effect of concentration polarization on hydrogen production performance of ceramic-supported Pd membrane module. International Journal of Hydrogen Energy, 2015. 40(35): p. 11451-11456.

[317] Al-Mufachi, N.A., N.V. Rees and R. Steinberger-Wilkens, Hydrogen selective membranes: A review of palladium-based dense metal membranes. Renewable and Sustainable Energy Reviews, 2015. 47: p. 540-551.

[318] Peters, T.A., T. Kaleta, M. Stange and R. Bredesen, Development of ternary Pd-Ag-TM alloy membranes with improved sulphur tolerance. Journal of Membrane Science, 2013. 429: p. 448-458.

[319] Mejdell, A.L., M. Jøndahl, T.A. Peters, R. Bredesen and H.J. Venvik, Experimental investigation of a microchannel membrane configuration with a 1.4μm Pd/Ag23wt.% membrane—Effects of flow and pressure. Journal of Membrane Science, 2009. 327(1): p. 6-10.

[320] Peters, T.A., M. Stange and R. Bredesen, On the high pressure performance of thin supported Pd-23%Ag membranes—Evidence of ultrahigh hydrogen flux after air treatment. Journal of Membrane Science, 2011. 378(1): p. 28-34.

[321] Pizzi, D., R. Worth, M. Giacinti Baschetti, G.C. Sarti and K.-i. Noda, Hydrogen permeability of 2.5μm palladium-silver membranes deposited on ceramic supports. Journal of Membrane Science, 2008. 325(1): p. 446-453.

[322] Maneerung, T., K. Hidajat and S. Kawi, Ultra-thin (<1μm) internally-coated Pd-Ag alloy hollow fiber membrane with superior thermal stability and durability for high temperature H2 separation. Journal of Membrane Science, 2014. 452(Supplement C): p. 127-142.

[323] Babak, V.N., L.P. Didenko, Y.P. Kvurt and L.A. Sementsova, Studying the Operation of a Membrane Module Based on Palladium Foil at High Temperatures. Theoretical Foundations of Chemical Engineering, 2018. 52(2): p. 181-194.

[324] Mendes, D., PhD thesis: Use of Pd-Ag Membrane Reactors in the Water-Gas Shift Reaction for Producing Ultra-Pure Hydrogen. 2010, FEUP.

[325] Nooijer, N.d., A. Arratibel Plazaola, J. Meléndez Rey, E. Fernandez, D.A. Pacheco Tanaka, M.v. Sint Annaland and F. Gallucci, Long-Term Stability of Thin-Film Pd-Based Supported Membranes. Processes, 2019. 7(2): p. 106.

[326] Gallucci, F., J. Medrano, E. Fernandez, J. Melendez, M. van Sint Annaland and A. Pacheco, Advances on High Temperature Pd-Based Membranes and Membrane Reactors for Hydrogen Purification and Production. Journal of Membrane Science and Research, 2017. 3(3): p. 142-156.

[327] Okazaki, J., T. Ikeda, D.A.P. Tanaka, K. Sato, T.M. Suzuki and F. Mizukami, An investigation of thermal stability of thin palladium-silver alloy membranes for high temperature hydrogen separation. Journal of Membrane Science, 2011. 366(1): p. 212-219.

[328] Gallucci, F., E. Fernandez Gesalaga, J.A. Medrano Jimenez, D.A. Pacheco Tanaka and M. van Sint Annaland, Pd-based membranes for high temperature applications: current status. Austin Chemical Engineering, 2016. 3(1).

[329] Tosti, S., A. Basile, L. Bettinali, F. Borgognoni, F. Chiaravalloti and F. Gallucci, Long-term tests of Pd-Ag thin wall permeator tube. Journal of Membrane Science, 2006. 284(1): p. 393-397.

[330] Jokar, S., M. Rahimpour, A. Shariati, A. Iulianelli, G. Bagnato, A. Vita, F. Dalena and A. Basile, Pure Hydrogen Production in Membrane Reactor with Mixed Reforming Reaction by Utilizing Waste Gas: A Case Study. Processes, 2016. 4(3): p. 33.

[331] Pacheco Tanaka, D.A., J.A. Medrano, J.L. Viviente Sole and F. Gallucci, 1 - Metallic membranes for hydrogen separation, in Current Trends and Future Developments on (Bio-) Membranes, A. Basile and F. Gallucci, Editors. 2020, Elsevier. p. 1-29.

[332] Patil, C., PhD thesis: Membrane reactor technology for ultrapure hydrogen production 2005, University of Twente.

[333] Brunetti, A., A. Caravella, E. Fernandez, D.A. Pacheco Tanaka, F. Gallucci, E. Drioli, E. Curcio, J.L. Viviente and G. Barbieri, Syngas upgrading in a membrane reactor with thin Pd-alloy supported membrane. International Journal of Hydrogen Energy, 2015. 40(34): p. 10883-10893.

[334] Fernandez, E., A. Helmi, K. Coenen, J. Melendez, J.L. Viviente, D.A. Pacheco Tanaka, M. van Sint Annaland and F. Gallucci, Development of thin Pd-Ag supported membranes for fluidized bed membrane reactors including WGS related gases. International Journal of Hydrogen Energy, 2015. 40(8): p. 3506-3519.

[335] Li, H., A. Caravella and H.Y. Xu, Recent progress in Pd-based composite membranes. Journal of Materials Chemistry A, 2016. 4(37): p. 14069-14094.

[336] Barrie, J.A. and K. Munday, Gas transport in heterogeneous polymer blends: I. Polydimethylsiloxane-g-polystyrene and polydimethylsiloxane-b-polystyrene. Journal of Membrane Science, 1983. 13(2): p. 175-195.

[337] Shah, M.R., R.D. Noble and D.E. Clough, Analysis of transient permeation as a technique for determination of sorption and diffusion in supported membranes. Journal of Membrane Science, 2006. 280(1): p. 452-460.

[338] Koros, W.J., A.H. Chan and D.R. Paul, Sorption and transport of various gases in polycarbonate. Journal of Membrane Science, 1977. 2: p. 165-190.

[339] Campo, M., A. Tanaka, A. Mendes and J.M. Sousa, 3 - Characterization of membranes for energy and environmental applications, in Advanced Membrane Science and Technology for Sustainable Energy and Environmental Applications, A. Basile and S.P. Nunes, Editors. 2011, Woodhead Publishing. p. 56-89.

[340] Basile, A., F. Gallucci and S. Tosti, Synthesis, Characterization, and Applications of Palladium Membranes, in Membrane Science and Technology. 2008, Elsevier. p. 255-323.

[341] Yun, S. and S. Ted Oyama, Correlations in palladium membranes for hydrogen separation: A review. Journal of Membrane Science, 2011. 375(1): p. 28-45.

[342] Ward, T.L. and T. Dao, Model of hydrogen permeation behavior in palladium membranes. Journal of Membrane Science, 1999. 153(2): p. 211-231.

[343] Musket, R.G., Effects of contamination on the interaction of hydrogen gas with palladium: A review. Journal of the Less Common Metals, 1976. 45(2): p. 173-183.

[344] Zhang, X.-L., 7 - Effect of poisoning on metallic membranes, in Current Trends and Future Developments on (Bio) Membranes, A. Basile and F. Gallucci, Editors. 2020, Elsevier. p. 169-187.

[345] Hara, S., K. Sakaki and N. Itoh, Decline in Hydrogen Permeation Due to Concentration Polarization and CO Hindrance in a Palladium Membrane Reactor. Industrial & Engineering Chemistry Research, 1999. 38(12): p. 4913-4918.

[346] Hou, K. and R. Hughes, The effect of external mass transfer, competitive adsorption and coking on hydrogen permeation through thin Pd/Ag membranes. Journal of Membrane Science, 2002. 206(1): p. 119-130.

[347] Zhang, J., D. Liu, M. He, H. Xu and W. Li, Experimental and simulation studies on concentration polarization in H2 enrichment by highly permeable and selective Pd membranes. Journal of Membrane Science, 2006. 274(1): p. 83-91.

[348] Mori, N., T. Nakamura, K.-i. Noda, O. Sakai, A. Takahashi, N. Ogawa, H. Sakai, Y. Iwamoto and T. Hattori, Reactor Configuration and Concentration Polarization in Methane Steam Reforming by a Membrane Reactor with a Highly Hydrogen-Permeable Membrane. Industrial & Engineering Chemistry Research, 2007. 46(7): p. 1952-1958.

[349] Nagy, E. and E. Kulcsár, The effect of the concentration polarization and the membrane layer mass transport on membrane separation. Desalination and Water Treatment, 2010. 14(1-3): p. 220-226.

[350] Caravella, A., S. Hara, E. Drioli and G. Barbieri, Sieverts law pressure exponent for hydrogen permeation through Pd-based membranes: Coupled influence of non-ideal diffusion and multicomponent external mass transfer. International Journal of Hydrogen Energy, 2013. 38(36): p. 16229-16244.

[351] Caravella, A., F. Scura, G. Barbieri and E. Drioli, Sieverts Law Empirical Exponent for Pd-Based Membranes: Critical Analysis in Pure H2 Permeation. The Journal of Physical Chemistry B, 2010. 114(18): p. 6033-6047.

[352] Gielens, F.C., H.D. Tong, C.J.M. van Rijn, M.A.G. Vorstman and J.T.F. Keurentjes, Microsystem technology for high-flux hydrogen separation membranes. Journal of Membrane Science, 2004. 243(1): p. 203-213.

[353] Keurentjes, J.T.F., F.C. Gielens, H.D. Tong, C.J.M. van Rijn and M.A.G. Vorstman, High-Flux Palladium Membranes Based on Microsystem Technology. Industrial & Engineering Chemistry Research, 2004. 43(16): p. 4768-4772.

[354] Mendes, D., V. Chibante, J.-M. Zheng, S. Tosti, F. Borgognoni, A. Mendes and L.M. Madeira, Enhancing the production of hydrogen via water-gas shift reaction using Pd-based membrane reactors. International Journal of Hydrogen Energy, 2010. 35(22): p. 12596-12608.

[355] Santucci, A., F. Borgognoni, M. Vadrucci and S. Tosti, Testing of dense Pd-Ag tubes: Effect of pressure and membrane thickness on the hydrogen permeability. Journal of Membrane Science, 2013. 444(Supplement C): p. 378-383.

[356] Lewis, A.E., D.C. Kershner, S.N. Paglieri, M.J. Slepicka and J.D. Way, Pd-Pt/YSZ composite membranes for hydrogen separation from synthetic water-gas shift streams. Journal of Membrane Science, 2013. 437(Supplement C): p. 257-264.

[357] Zhang, D., S. Zhou, Y. Fan, N. Xu and Y. He, Preparation of dense Pd composite membranes on porous Ti-Al alloy supports by electroless plating. Journal of Membrane Science, 2012. 387-388(Supplement C): p. 24-29.

[358] Pacheco Tanaka, D.A., M.A. Llosa Tanco, S.-i. Niwa, Y. Wakui, F. Mizukami, T. Namba and T.M. Suzuki, Preparation of palladium and silver alloy membrane on a porous α-alumina tube via simultaneous electroless plating. Journal of Membrane Science, 2005. 247(1): p. 21-27.

[359] Anzelmo, B., J. Wilcox and S. Liguori, Hydrogen production via natural gas steam reforming in a Pd-Au membrane reactor. Comparison between methane and natural gas steam reforming reactions. Journal of Membrane Science, 2018. 568: p. 113-120.

[360] Liu, J., S. Bellini, N.C.A. de Nooijer, Y. Sun, D.A. Pacheco Tanaka, C. Tang, H. Li, F. Gallucci and A. Caravella, Hydrogen permeation and stability in ultra-thin PdRu supported membranes. International Journal of Hydrogen Energy, 2020. 45(12): p. 7455-7467.

[361] Catalano, J., M. Giacinti Baschetti and G.C. Sarti, Influence of the gas phase resistance on hydrogen flux through thin palladium-silver membranes. Journal of Membrane Science, 2009. 339(1): p. 57-67.

[362] Melendez, J., E. Fernandez Gesalaga, A. Helmi Siasi Farimani, F. Gallucci, P.L. Arias and D.A. Pacheco Tanaka. Preparation and characterization of ultra-thin (<1 micron) Pd-Ag membranes on porous alumina support (100 nm pore size). in 12th International Conference on Catalysis in Membrane Reactors (ICCMR12). 2015. Szczecin, Poland.

[363] Helmi, A., E. Fernandez, J. Melendez, D.A. Pacheco Tanaka, F. Gallucci and M. Van Sint Annaland, Fluidized Bed Membrane Reactors for Ultra Pure H2 Production—A Step forward towards Commercialization. Molecules, 2016. 21(3): p. 376.

[364] Fernandez, E., J.A. Sanchez-Garcia, J. Melendez, V. Spallina, M. van Sint Annaland, F. Gallucci, D.A. Pacheco Tanaka and R. Prema, Development of highly permeable ultra-thin Pd-based supported membranes. Chemical Engineering Journal, 2016. 305: p. 149-155.

[365] Fernandez, E., A. Helmi, J.A. Medrano, K. Coenen, A. Arratibel, J. Melendez, N.C.A. de Nooijer, V. Spallina, J.L. Viviente, J. Zuñiga, M. van Sint Annaland, D.A. Pacheco Tanakaand F. Gallucci, Palladium based membranes and membrane reactors for hydrogen production and purification: An overview of research activities at Tecnalia and TU/e. International Journal of Hydrogen Energy, 2017. 42(19): p. 13763-13776.

[366] Shi, L., A. Goldbach and H. Xu, High-flux H2 separation membranes from (Pd/Au)n nanolayers. International Journal of Hydrogen Energy, 2011. 36(3): p. 2281-2284

Chapter 3. Materials and Methods

This chapter describes all substances, procedures, methods, setups and experimental conditions employed in the runs whose results are presented in the following chapters of this PhD thesis.

3.1. Thermodynamic analysis of olive mill wastewater steam reforming process

For the olive oil mill wastewater (OMW) steam reforming (OMWSR) simulation, the *Aspen Plus V8.8*® software was used, employing a non-stoichiometric method: the Gibbs free energy minimization. This method determines the equilibrium composition by minimizing the total Gibbs free energy (G^{T}) - Eq. (3.1):

$$G^{\mathrm{T}} = \sum_{\mathrm{i}=1}^{N} n_i \mu_i \tag{3.1}$$

where n_i is the number of moles of component *i* in the system and μ_i is the chemical potential for each of them. A more detailed description of the methodology is available elsewhere [1]. Although this method requires the resolution of non-linear equations and detailed information about the possible components present in the mixture (Gibbs free formation energy and standard formation enthalpy), there are several advantages for using this approach such as fast convergence to the solution and no pre-set selection of possible chemical reactions; estimation of initial equilibrium compositions are also not required [2]. Ideal gas mixtures were considered due to the high temperatures and low pressures applied in this study [3]. It was considered that all components are in the vapor phase in the reactor (except coke, CaO, $Ca(OH)_2$ and $CaCO_3$, which are in solid state - whenever applicable).

Fig. 3.1 shows a process flow diagram as implemented in the Aspen Plus® software. For the simulations of a traditional reactor (TR), a GIBBS reactor (RGIBBS - represented as REAT in Fig. 3.1) was used, which calculates the composition of the compounds considered in equilibrium at a determined temperature and pressure (with a given input feed composition). These inputs are required for the simulation to be performed. For these simulations, it was assumed that the reactor is isothermal and the feed composition is at the same conditions as the reactor. With this method applied, it is not necessary to define the stoichiometry of the involved reactions, which are detailed below - see Table 3.1.

In cases of systems with H_2 separation, it is necessary to use a more complex model than just one Gibbs reactor. To simulate a H_2 perm-selective membrane, the modular approach used to represent a membrane reactor (MR) or a sorption-enhanced membrane reactor (SEMR) is represented by (N+1) sub-reformers (represented as REAT in Fig. 3.1) and N H_2 sub-separators (represented as SEPAR in Fig. 3.1). The sub-reformer consists of Gibbs reactors, as mentioned above, which determine the thermodynamic equilibrium. The sub-separator is a process unit that yields two streams with different compositions; one of them is introduced into the next RGIBBS while the other, which is constituted only by H_2, represents the permeate stream of a H_2 perm-selective membrane. This separation is realized based on a specified split fraction or flow (removal fraction of H_2 - *f*H_2), which is related to

factors like membrane's selectivity, permeability, thickness, area and temperature/pressure across the membrane [4]. To calculate fH_2 it was used Eq. (3.2):

$$fH_2 = \frac{\sum_{k=1}^{N} m_{H_2,k}}{\sum_{k=1}^{N} m_{H_2,k} + m_{H_2,N+1}} \quad (3.2)$$

where $m_{H_2,k}$ is the molar flow rate of H_2 in the permeate stream of sub-separator *k* and $m_{H_2,N+1}$ is the molar flow rate of H_2 in the output of the sub-reformer N+1 [4]. The number of sub-separators needed in the model depends on the H_2 removal fraction set for the simulation. The higher the removal fraction, the higher the number of sub-separators needed, because the separator can only remove the H_2 from the previous reactor. This method has been implemented in other studies [4, 5]. In order to achieve the pretended removal fraction, a *Design Spec* is created in the simulation. Thus, the software iterates its calculation sequence through a multiple of values provided for the independent variable (in this case the fraction of H_2), in order to obtain a specified spec [5].

To simulate the sorption-enhanced process [case of a sorption-enhanced reactor (SER) or SEMR], the CO_2 sorption was represented through its reactions with CaO to form calcium hydroxide ($Ca(OH)_2$) and calcium carbonate ($CaCO_3$) - Eqs. (3.17) and (3.18), respectively. CaO was chosen because it is one of the most common sorbents reported, and it has a good sorption capacity in the temperature range of the reforming [6]. To calculate the removal (captured) fraction of CO_2 (fCO_2) it was used Eq. (3.3):

$$fCO_2 = \frac{m_{CaCO_3,N+1}}{m_{CaCO_3,N+1} + m_{CO_2,N+1}} \quad (3.3)$$

where $m_{CaCO_3,N+1}$ is the molar flow rate of $CaCO_3$ in the output of the sub-reformer N+1 and $m_{CO_2,N+1}$ is the molar flow rate of CO_2 in the same stream (not converted into $CaCO_3$.).

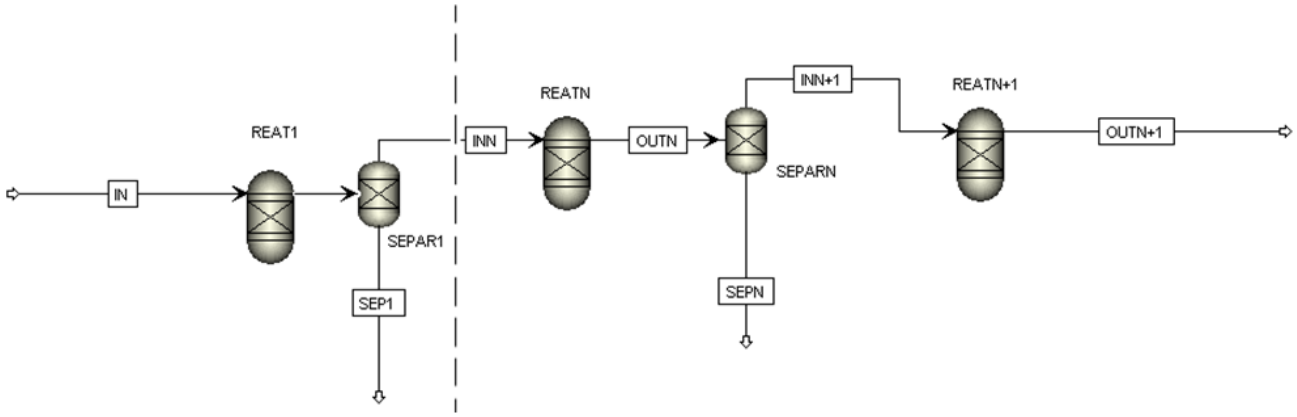

Fig. 3.1. Sequential modular approach diagram of the MR/SEMR with the *Aspen Plus*® software.

The components which were assumed to be present in the system were set according to possible reactions occurring during the simulations [7]. The overall OMWSR process (Table 3.1, Eq. (3.5))

involves the steam reforming of each effluent species present in the OMW (Table 3.1, Eq. (3.6)) and the water-gas shift reaction (WGS) (Eq. (3.7)) - multiplied by the number of carbon atoms in the compound). In this type of process secondary reactions (e.g. methanation reaction, Eq. (3.8)) - and coke formation - Eq. (3.12)-(3.15) - that limit H_2 production should also be taken into account, as considered in previous thermodynamic studies [4, 5]. The enthalpies of reaction ($\Delta H_r^{0\,°C}$) for the steam reforming and overall reaction of the OMWSR process of different chemical species that might be present in OMW are presented in Table 3.2 and were calculated according to Eq. (3.4).

$$\Delta H_r^{0\,°C} = \sum_{i=1}^{N} \nu_i \Delta H_f^{0\,°C} \tag{3.4}$$

In Eq. (3.4), ν_i is the stoichiometric coefficient of component *i* (positive value when related with products and negative when related with reagents) and $\Delta H_f^{0\,°C}$ is the enthalpy of formation at standard conditions for each component *i* - data are taken from the *Aspen Plus V.8.8*® software and literature [8-11].

This thermodynamic analysis in subchapter 4.1 was performed at temperatures between 300-1000 °C, 1-20 bar, and water content in the feed between 20-92 wt.% using the Sensibility Analysis Tool available in the *Aspen Plus*® software. In this thermodynamic analysis, 17 different compositions of OMW were considered and are expressed in Table 3.3. It should be noted that an average proportion of polyphenols/sugars (0.46) [12-21] was used when this information did not exist for a given composition.

Table **3.1 -** Possible reactions occurring during the OMWSR.

Reactions	$\Delta H_r^{25\,°C}$ (kJ·mol^{-1}) [5]	Equation number
Steam Reforming of high molecular weight molecules		
$C_xH_yO_z + (2x - z)\ H_2O \rightleftharpoons \left(2x - z + {}^{y}/_{2}\right)H_2 + xCO_2$ [1]	> 0 [a)]	(3.5)
Decomposition of high molecular weight molecules		
$C_xH_yO_z + (x - z)H_2O \rightleftharpoons \left(x - z + {}^{y}/_{2}\right)H_2 + xCO$	> 0 [a)]	(3.6)
Water-gas shift		
$CO + H_2O \rightleftharpoons H_2 + CO_2$	-41	(3.7)
CO Methanation		
$CO + 3H_2 \rightleftharpoons H_2O + CH_4$	-206	(3.8)
Steam reforming of methane		
$2H_2O + CH_4 \rightleftharpoons CO_2 + 4H_2$ [2]	165	(3.9)
Dry reforming of methane		
$CO_2 + CH_4 \rightleftharpoons 2CO + 2H_2$ [3]	247	(3.10)
Carbon formation		
$CH_x \rightarrow \text{coke precursors (olefins + aromatics)} \rightarrow \frac{x}{2}H_2 + C$	> 0	(3.11)
$2CO \rightleftharpoons C + CO_2$	-172	(3.12)
$CH_4 \rightleftharpoons 2H_2 + C$	74	(3.13)
$CO + H_2 \rightleftharpoons H_2O + C$	-131	(3.14)
$CO_2 + 2H_2 \rightleftharpoons 2\,H_2O + C$	-90	(3.15)
Cracking of oxygenates		
$C_xH_yO_z \rightleftharpoons C_nH_mO_k + \text{gas}(H_2, CO_2, CO, CH_4, CH_n) + C$	> 0	(3.16)
CO_2 Sorption		
$CaO + H_2O \rightleftharpoons Ca(OH)_2$	-109	(3.17)
$CO_2 + Ca(OH)_2 \rightleftharpoons H_2O + CaCO_3$	-70	(3.18)

[1] Sum of Eq. (3.6) and Eq. (3.7).
[2] Sum of Eq. (3.7) and the reverse of Eq. (3.8).
[3] Sum of the reverse of Eq. (3.7) and reverse of Eq. (3.8).
[a)] View Table 3.2.

Table 3.2 - Enthalpies of reactions, at standard conditions, in which each species present in OMW can be involved.

Species	Decomposition (kJ·mol^{-1})	Steam Reforming (kJ·mol^{-1})
Vanillic acid[a)]	640	312
Caffeic acid[a)]	708	339
Tyrosol[a)]	867	539
P-Coumaric acid[a)]	772	403
Cinnamic acid[a)]	1 014	645
D-Arabinose[a)]	303	98
D-Galactose[a)]	622	376
D-Galacturonic acid[a)]	588	342
Syring acid[a)]	693	324
Gallic acid[a)]	457	170
Protocatechuic acid[a)]	521	234
Guaiacol[b)]	695	408
Benzyl alcohol[b)]	790	503
Phenethyl alcohol[b)]	932	604
Acetic acid[b)]	654	572
Phenol[b)]	642	396

[a)] Thermodynamic properties are taken from the literature [8-11].
[b)] Thermodynamic properties are taken from the Aspen Plus® software.

The thermodynamic analysis in subchapter 4.2 was performed at temperatures between 300-500 °C, total pressures in the range 1-11 bar and contents of water in the feed between 20-92 wt.% (corresponding to steam-to-carbon feed ratios, SCFRs, of 0.35-16), using the Sensibility Analysis Tool available in the *Aspen Plus*® software. For the SER and SEMR, the removal fraction of CO_2 was varied between 0-0.99 (corresponding to CaO/OMW molar ratios in the range of 0-6.5, depending on the temperature, pressure and feed composition, namely water content); one should remark that in practice all CO_2 is sorbed until the sorbent reaches the saturation - pre-breakthrough, that is why fCO_2 values close to 1 were considered. In the case of the MR and SEMR, the removal fraction of H_2 ranged between 0-0.80. In previous studies, it was found that the maximum operational temperature permitted by the Pd-Ag membranes was close to 500 °C [22, 23] and that the H_2 removal fraction never reaches a value higher than 0.80 [24-26] for low to medium pressures. Therefore, a maximum H_2 removal of 80 % is considered much more realistic while operating at feed pressures close to 1 bar [27]. The above-mentioned range of water content in the OMW was considered due to the maximum values found in the literature (80-92 wt.%) [28-31] and the potential need to distill the feed OMW to avoid operation problems (when it contains large quantities of water). This treatment will also minimize several operational problems (reactors with larger dimensions, low concentrations of organic species, etc.) and operation costs (water vaporization, reactor heating, etc.). For subchapter 4.2, a typical composition of OMW is considered (Composition #11 of Table 3.3). An average proportion of polyphenols/sugars = 0.46 was also considered [12-21] as well as the same content for each sugar (D-arabinose, D-galactose and D-galacturonic acid).

Besides the compounds present in the OMW already mentioned above, H_2, CO_2, CO, CH_4 and coke were also considered as possible species present throughout the simulations. Other reaction products apart from the previous ones, such as benzene, cyclopentadiene, propane, butane, methanol, ethanol, butanol, ethylene, acetaldehyde and acetone have been also considered. These last compounds are referred by several authors as possible secondary products of some reactions (not considered in Table 3.1) or as intermediates of the reactions involved in the OMWSR process [32-34]. However, the results showed that these compounds are absent in the reactor outlet stream in all simulations carried out, and the only reaction products observed, in the range of the conditions analysed, were H_2, CO_2, CO, CH_4 and coke. For this reason, Eq. (3.16) was not considered for the analysis of the results.

For all possible cases, the yield of H_2, CO_2, CO and CH_4 are calculated according to Eq. (3.19):

$$Y_{\mathrm{i}} = \frac{\sum_{\mathrm{k}=1}^{\mathrm{N}} m_{i,\mathrm{k}} + m_{\mathrm{i,N+1}}}{m_{\mathrm{OMW,feed}}} \tag{3.19}$$

where $m_{i,\mathrm{k}}$ is the molar flow rate of species *i* in the permeate stream of sub-separator *k* (only for H_2 and for the MR and SEMR), $m_{\mathrm{i,N+1}}$ is the molar flow rate of that species in the output of the sub-reformer N+1, and $m_{\mathrm{OMW,feed}}$ is the molar flow rate of organic species in the OMW feed. It is important

to note that H_2 was the only component considered to be present in the permeate stream, which corresponds to a membrane with infinity selectivity (e.g. dense metallic Pd-based membranes). In the case of the SER and SEMR, the fraction of CO_2 that is removed from the system (by reaction with $Ca(OH)_2$) is not considered in the calculation of the CO_2 yield, since it is not present in the retentate stream.

Table 3.3 - Compositions of the OMW taken from the literature (dry basis wt.%).

	Composition number and source of information.								
	#1[a] [35]	**#2[a] [35]**	**#3[a] [35]**	**#4[a] [35]**	**#5[a] [35]**	**#6[a] [35]**	**#7[a] [14]**	**#8[a] [14]**	**#9[a] [19]**
Polyphenols/Sugars	0.46	0.46	0.46	0.46	0.46	0.46	0.43	0.51	0.32
Species									
Vannilic acid	3.88	3.87	4.31	6.09	3.00	5.01	0	0	7.09
Caffeic acid	2.87	3.85	12.06	5.00	7.00	7.40	1.87	1.39	0
Tyrosol	24.35	23.41	14.95	19.72	20.85	18.61	5.07	5.84	0
P-Coumaric acid	0.00	0.00	0.00	0.00	0.00	0.00	11.23	18.65	17.16
Cinnamic acid	0.00	0.00	0.00	0.00	0.00	0.00	0.00	0.00	0.00
D-Arabinose	22.83	22.83	22.83	22.83	22.83	22.83	23.31	22.08	25.25
D-Galactose	22.83	22.83	22.83	22.83	22.83	22.83	23.31	22.08	25.25
D-Galacturonic acid	22.83	22.83	22.83	22.83	22.83	22.83	23.31	22.08	25.25
Syring acid	0.00	0.00	0.00	0.00	0.00	0.00	0.00	0.00	0.00
Gallic acid	0.41	0.38	0.19	0.70	0.66	0.49	11.90	7.88	0
Protocatechuic acid	0.00	0.00	0.00	0.00	0.00	0.00	0.00	0.00	0.00
Guaiacol	0.00	0.00	0.00	0.00	0.00	0.00	0.00	0.00	0.00
Benzyl alcohol	0.00	0.00	0.00	0.00	0.00	0.00	0.00	0.00	0.00
Phenethyl alcohol	0.00	0.00	0.00	0.00	0.00	0.00	0.00	0.00	0.00
Acetic acid	0.00	0.00	0.00	0.00	0.00	0.00	0.00	0.00	0.00
Phenol	0.00	0.00	0.00	0.00	0.00	0.00	0.00	0.00	0.00
	#10[a] [36]	**#11[a] [37]**	**#12[a] [38]**	**#13[b] [16]**	**#14[b] [39]**	**#15[b] [39]**	**#16[b] [39]**	**#17[b] [40]**	
Polyphenols/Sugars	0.46	0.46	0.46	0.46	0.46	0.46	0.46	0.46	
Species									
Vannilic acid	0.00	0.00	0.00	0.02	3.18	2.95	2.86	2.29	
Caffeic acid	6.88	0.00	9.83	0.00	9.98	10.09	10.12	0	
Tyrosol	18.24	16.68	12.45	0.00	8.98	9.03	9.06	15.25	
P-Coumaric acid	6.39	14.83	1.67	0.00	9.37	9.44	9.47	1.78	
Cinnamic acid	0.00	0.00	0.00	0.00	0.00	0.00	0.00	7.37	
D-Arabinose	22.83	22.83	22.83	23.81	22.83	22.83	22.83	22.83	
D-Galactose	22.83	22.83	22.83	23.81	22.83	22.83	22.83	22.83	
D-Galacturonic acid	22.83	22.83	22.83	23.81	22.83	22.83	22.83	22.83	
Syring acid	0.00	0.00	0.00	0.00	0.00	0.00	0.00	0.25	
Gallic acid	0.00	0.00	0.00	0.00	0.00	0.00	0.00	0.00	
Protocatechuic acid	0.00	0.00	7.56	0.00	0.00	0.00	0.00	4.57	
Guaiacol	0.00	0.00	0.00	0.08	0.00	0.00	0.00	0.00	
Benzyl alcohol	0.00	0.00	0.00	0.07	0.00	0.00	0.00	0.00	
Phenethyl alcohol	0.00	0.00	0.00	0.10	0.00	0.00	0.00	0.00	
Acetic acid	0.00	0.00	0.00	28.28	0.00	0.00	0.00	0.00	
Phenol	0.00	0.00	0.00	0.02	0.00	0 %	0 %	0.00	

[a] Real effluents.
[b] Simulated effluents.

3.2. Synthesis, characterization and testing of sorbents derived from hydrotalcites for CO_2 capture

3.2.1. Chemicals and gases

Aluminum nitrate 9-hydrate, magnesium nitrate 6-hydrate and gallium nitrate hydrate (Panreac, highest purity degree available) were used as Al^{3+}, Mg^{2+} and Ga^{3+} precursors, respectively. Sodium salts (sodium carbonate and sodium triacetoxyborohydride) were used as compensating anion precursors (Panreac, highest purity degree available). Sodium hydroxide (Panreac, highest purity degree available) was used to maintain an alkaline pH during the synthesis. Potassium carbonate (Panreac, highest purity degree available) was used as a promoter to modify the hydrotalcites (HTCs). CO_2 (≥ 99.8 %) and N_2 (≥ 99.999 %), from Linde, were used in the experimental sorption tests. Several commercially available sorbents were also used for comparison purposes: commercial HTC, MgO and CaO (all from Sigma-Aldrich), PURAL MG 30 K (herein called MG30_K), PURAL MG 63 (herein called MG63), PURAL MG 70 (herein called MG70) and Al_2O_3 ("Extrudates") (all from Sasol) [41].

3.2.2. Sorbents preparation

HTCs with molar ratios Mg^{2+}/Al^{3+} = 2 or $Mg^{2+}/(Al^{3+}+Ga^{3+})$ = 2 and (Al^{3+}/Ga^{3+} = 9) were synthesized using a co-precipitation method. These ratios were selected taking into account previous studies reported in the literature [42-45], being suggested as the optimum for higher performance in terms of CO_2 capture at high temperatures. A higher Mg^{2+}/Al^{3+} ratio can be beneficial for the adsorption of acid gases because of the higher basicity of the resulting HTCs, however, mechanical stability issues have been reported due to the formation of $MgCO_3$ at high partial pressures of CO_2 and H_2O [46].

A series of HTCs-A samples with different compensating anions [A = CO_3^{2-}, Cl^-, SO_4^{2-}, BrO_3^-, ClO_4^- or $(CH_3COO)_3BH^-$ - the latter denominated herein by "long"], used in subchapter 5.1, were prepared by adding the $Mg(NO_3)_2{\cdot}6H_2O$ and $Al(NO_3)_3{\cdot}9H_2O$ solutions (total volume of 200 mL with an excess mass of precursor anion of 25 %) drop-wise into an anion precursor solution (total volume of 400 mL). Nevertheless, sodium triacetoxyborohydride used as compensating anion precursor is very reactive with water and undergoes a hydrolytic decomposition. Hence, the material described as HTC-long in this study does not include the triacetoxyborohydride anions in the interlayer layer. It was necessary to consider the products of triacetoxyborohydride decomposition in water, to identify the true intercalating species. Besides the formation of H_2 (breakdown of the B-H bond), the $B(OH)_4^-$ anion could be formed by hydrolysis of the B-O bond, since there is excess water, and that will give B-OH bonds formation [47, 48]. However, since this anion is mainly formed only when the pH is higher than 11 and the pH used for the co-precipitation is 9.5, the species most likely to be present in the solution are triborate $[B_3O_3(OH)_4]^-$ or/and tetraborate $[B_4O_5(OH)_4]^{2-}$ anions [49]. The rest of the original chain

was probably in the form of acetate anions and would be left in free solution or partially regenerating the acetic acid.

The pH of the precipitation was controlled at 9.5 (as already mentioned) using a 1 M NaOH solution. After, the mixture was stirred for 20 h at room temperature. Then, the solid was filtered (vacuum filter) and washed several times (until the pH of the residual water was constant) in order to eliminate nitrate ions, and finally, it was dried at 40 ºC for 48 h. With this procedure, it was possible to produce ca. 30 g of each HTC. To obtain a HTC-based sorbent, the respective dry HTC was calcined in air (at 400 ºC for 2 h - heating ramp of 5 ºC·min^{-1}). This temperature program was used taking into account the results of the thermogravimetric (TG) analysis and the work of Reddy *et al.* [50], where it was observed that calcination of HTC materials at 400 ºC allows obtaining higher CO_2 sorption capacities.

In subchapter 5.2, besides the samples HTC-CO_3 and HTC-long, HTCs with partial substitution of Al^{3+} by Ga^{3+} (herein called HTC-A(Ga)) were also evaluated, which were prepared using the procedure already described above (but adding also $Ga(NO_3)_3 \cdot xH_2O$ into the initial cation solution). A portion of these HTCs (with and without Ga^{3+} substitution) was impregnated with an aqueous solution of K_2CO_3 (herein called HTC-A_K or HTC-A(Ga)_K), dissolved in the minimum possible amount of water, to achieve a final K loading of 20 wt.%, which is the optimum percentage found in previous works [42, 45, 51-54]. The loss of mass during calcination of each sample was determined and accounted to prepare the potassium modified samples. To study the effect of the potassium loading in the new herein prepared HTC-long_K samples, different contents of potassium were also used - Table 3.4. These materials were dried again (at 40 ºC for 48 h) and calcined in air (400 ºC for 2 h - a heating rate of 5 ºC·min^{-1}). Lastly, two of the commercial HTCs analysed in subchapter 5.2 (MG63 and MG70) were doped with potassium for comparison purposes with the reference MG30_K sample (doped-HTC). These sorbents were doped with 20 wt.% of potassium and treated like mentioned before for the prepared HTCs.

Table 3.4 summarizes the conditions employed during the synthesis of all the prepared materials.

Table 3.4 - Synthesis conditions for the different HTCs.

Sorbent	$Mg^{2+}/(Al^{3+}+Ga^{3+})$	Al^{3+}/Ga^{3+}	K (wt.%)
HTC-ClO_4	2	-	-
HTC-Cl	2	-	-
HTC-SO_4	2	-	-
HTC-BrO_3	2	-	-
HTC-CO_3	2	-	-
HTC-CO_3(Ga)	2	9	-
HTC-CO_3_K	2	-	20
HTC-CO_3(Ga)_K	2	9	20
HTC-long	2	-	-
HTC-long(Ga)	2	9	-
HTC-long_$K_{10wt.\%}$	2	-	10
HTC-long_$K_{20wt.\%}$	2	-	20
HTC-long_$K_{30wt.\%}$	2	-	30
HTC-long(Ga)_K	2	9	20
MG63_K	2	-	20
MG70_K	3	-	20

3.2.3. Characterization of the HTCs

The materials were characterized by several techniques. The thermogravimetric (TG and derivative thermogravimetric - DTG) analyses were performed in a NETZSCH apparatus, Model STA 449 F3 Jupiter, to study their thermal stability and calculate the loss of mass in the process of calcination. All these analyses were carried out under N_2 flow (60 $mL_{NTP}\cdot min^{-1}$). Three different programs were used to study the decomposition of the HTCs:

1) Each dry sample was heated at 10 $ºC\cdot min^{-1}$ up to 1000 ºC, in a N_2 atmosphere.
2) Each dry sample was heated at 10 $ºC\cdot min^{-1}$ up to 400 ºC and maintained at this temperature for 4 h, in a N_2 atmosphere (calcination program used in dry HTCs).
3) The HTCs used in the sorption-desorption experiments were heated at 10 $ºC\cdot min^{-1}$ up to 300 or 400 ºC and maintained at this temperature during 2 h, in a N_2 atmosphere (pre-treatment in the breakthrough tests).

Powder X-ray diffraction (XRD) patterns were obtained in a PAN'alytical X'Pert MPD unit equipped with a X'Celerator detector and a secondary monochromator using Cu$K\alpha$ (0.15418 nm) radiation, 40 kV, 30 mA; data was recorded at a step size of 0.017◦ and 100 s/step.

The Fourier transformed infrared (FTIR) spectra were recorded in the 4000-400 cm^{-1} range in a Perkin-Elmer Spectrum-One spectrometer with a MIR TGS detector. About 2 mg of sample and 300 mg of KBr were used in the preparation of the discs.

N_2 adsorption-desorption at -196 ºC was recorded, after degassing the samples for 2 h at 110 ºC in a FlowPrep 060 accessory (Micromeritics), in a Micromeritics Instrument, model Gemini II.

Scanning electron microscopy (SEM) coupled with energy dispersive spectroscopy (EDS) was performed in a FEI Quanta 400 FEG ESEM/EDAX Pegasus X4M instrument.

Lastly, the content of potassium in the calcined materials was determined by atomic absorption spectrophotometry (AAS) using a UNICAM 939 AA Spectrometer. It was used an oxidizing air-acetylene flame (1.2 $L_N \cdot min^{-1}$) to atomize the sample and a potassium alumina hollow cathode lamp. The samples were completely digested in a small quantity of HCl (37 wt.%) and diluted several times in water to be analysed.

3.2.4. Sorption experiments

The CO_2 sorption capacities (static tests) were assessed for both subchapters 5.1 and 5.2 using a magnetic suspension balance (CI Microbalance) with a mass measurement precision of $\pm$ 0.001 mg. Before each test, the magnetic suspension microbalance was calibrated. Subsequently, the samples were heated up to 300 ºC under vacuum (pressure ≈ 0.001 bar) and remained for 24 h (pre-treatment at the maximum possible temperature reached by the resistance). The temperature of the balance head was kept constant, the vacuum pump was turned off and then CO_2 was introduced into the chamber until reaching a given pressure of CO_2. The equilibrium was assumed to be reached in 24 h (variation lower than 0.030 mg in 5 h). After the equilibrium has been reached, new equilibrium data in the isotherm was determined. Since buoyancy caused by the gas in the microbalance chamber affects the measured mass, buoyancy correction was done for each pressure according to the methodology used by Miguel *et al.* [42]. For this, it was necessary to assess the density of the sorbents, determined by He picnometry for each sample (data not shown).

For HTC-CO_3 and HTC-long samples, the desorption equilibrium isotherms were also determined at 300 ºC in subchapter 5.1. After the determination of the sorption capacity at p_{CO_2} = 3 bar, the vacuum pump was turned on and then CO_2 was removed from the chamber until reaching a given pressure of CO_2. Again, the equilibrium was assumed to be reached in 24 h (variation lower than 0.030 mg in 5 h). After the equilibrium has been reached, new data in the desorption isotherm was measured. The last point of the desorption isotherms was determined under vacuum.

Afterwards, some sorbents were submitted to sorption-desorption cycles (dynamic tests) at 300 ºC and 1 bar of total pressure (in both subchapters 5.1 and 5.2). Even though the samples were calcined before the tests (400 ºC for 2 h), it was performed a pre-treatment in-situ (@ 300 or 400 ºC) in order to remove some water and atmospheric CO_2 sorbed after the calcination - similar pre-treatment in-situ after calcination was already used in the study of Quin *et al.* [55]. The mass was not kept constant

over the different dynamic tests with different samples (the column was completely filled with the sorbent, however, the samples had different densities). The tests were performed at different experimental conditions in order to study different effects - see Table 3.5. In the experimental work considered in subchapter 5.1, *Exps. 1.1* and *1.2* were carried out, while in the experimental research discussed in subchapter 5.2, *Exps. 1.1*, *1.3* and *1.4* were performed.

For these breakthrough tests, the gas feeding system consisted of Bronkhorst mass flow controllers (MFC) and a Bronkhorst Controlled Evaporator Mixer (CEM) were respectively used to feed the gases and introduce the desired content of steam into the mixture. Experiments were performed in a stainless steel packed-bed unit with 12 cm of length and 7.75 mm i.d., which was placed inside a tubular oven (model Split from Termolab, Fornos Eléctricos, Lda.) equipped with a 3-zone PID temperature controller (model MR13 from Shimaden). The gases were fed upwardly to the reactor using mass flow controllers (model F201 from Bronkhorst-High Tech). Type-K thermocouples allowed recording the temperature histories in two axial positions of the column - see Fig. 3.2 to visualize the experimental setup. This column was positioned inside the oven to keep the temperature constant. The molar concentration in the outlet of the column was measured with a CO and CO_2 infrared analyzer. More details about the infrared analyzer and the experimental setup can be found elsewhere [56].

Blank experiments were performed under the same conditions, in order to correct the dispersion effects in the system and the space-time on the tubes. Replicates of either the dynamic or static tests have shown that the difference between the CO_2 sorption capacities was < 2 %.

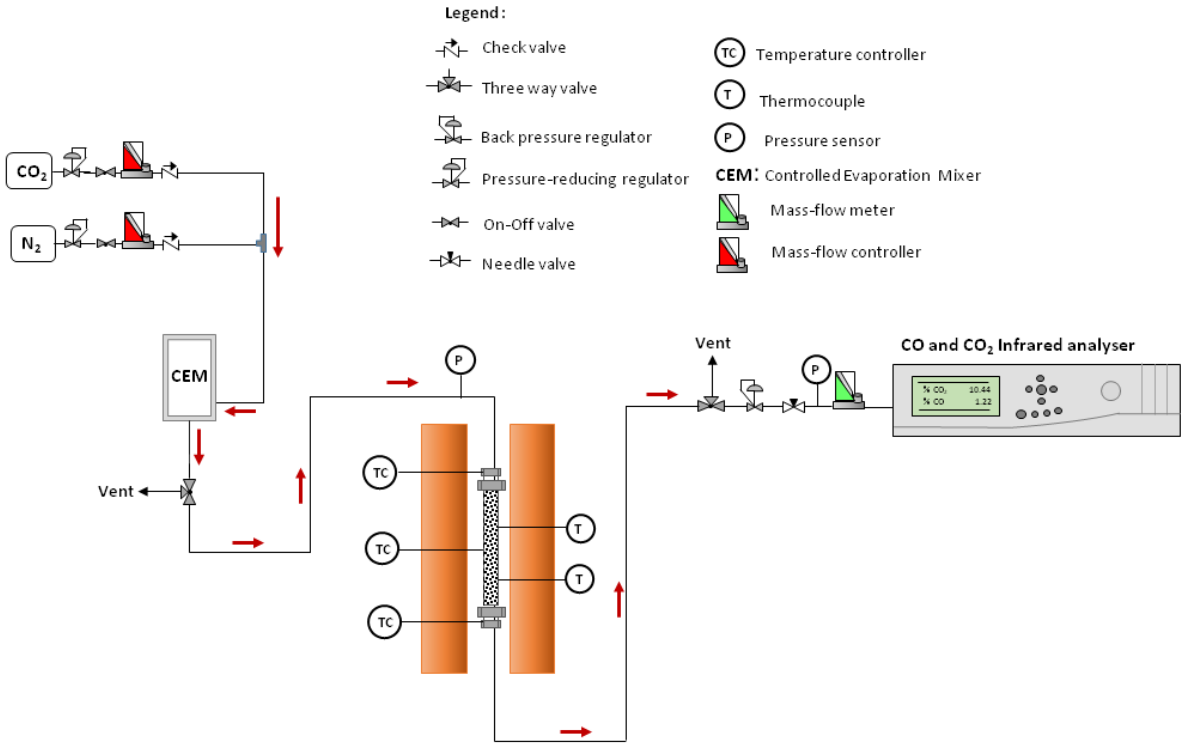

Fig. 3.2. Schematic diagram of the experimental setup for the breakthrough tests.

Table 3.5 - Experimental conditions used during the breakthrough experiments.

Exp. Runs	Temperature (ºC)	Pressure (bar)	Pre-treatment Temperature (ºC)	Sorption Step ($mL_{NTP} \cdot min^{-1}$)	Regeneration Step* ($mL_{NTP} \cdot min^{-1}$)	Sorption Time (min)
Exp. 1.1	300	1	300	85 N_2 + 15 CO_2	95 N_2	20
Exp. 1.2	200					
	400					
Exp. 1.3	300		400			60
						480
Exp. 1.4			300	70 N_2 + 15 CO_2 + 15 H_2O	85 N_2 + 15 H_2O	20

* Regeneration time of 30 min for all the experimental runs.

3.3. Screening of catalysts for steam reforming of olive oil mill wastewater

3.3.1. Chemicals and gases

Several commercial catalysts were used: 1 wt.% Pt/Al_2O_3 (from Merck), 50 wt.% CuO - 40 wt.% ZnO/Al_2O_3 (from REB Research & Consulting), Rh/Al_2O_3 promoted with a rare-earth metal (supplied by Johnson Matthey - this has no reference about the loading of the metal due to the confidentiality agreement), 64 wt.% CuO - 25 wt.% $ZnO/MgO\text{-}Al_2O_3$ (trade mark HiFUEL® W230), 0.5 wt.% Pd/Al_2O_3, 66 wt.% $Ni/SiO_3\text{-}Al_2O_3$, 0.5 wt.% Rh/Al_2O_3, 5 wt.% Pd/Al_2O_3, 0.5 wt.% Pt/Al_2O_3 and 2 wt.% Ru/Al_2O_3 (all from Alfa Aesar). Hereafter, to simplify the discussion and the writing of the thesis, all commercial and prepared materials are re-named with a short name - see Table 3.6 - with the general information about the catalysts used in subchapter 6.1.

Magnesium nitrate 6-hydrate, aluminum nitrate 9-hydrate, sodium carbonate anhydrous (all from Panreac, high purity), ruthenium (III) chloride hydrate (from Merck, ≥ 99.9 % purity) and nickel (II) nitrate 6-hydrate (Alfa Aesar, with 98 % purity) were utilized as Al^{3+}, Mg^{2+}, CO_3^{2-}, Ru^{3+} and Ni^{2+} precursors, respectively, for the preparation of the catalysts. Sodium hydroxide (Panreac, high purity) was used in the synthesis of the HTCs while commercial SiO_2 was used as support of the prepared catalysts (silica gel from Fluka, highest purity degree). An aqueous solution of HCl (Sigma-Aldrich, ≥ 37 wt.%) and an aqueous solution of HNO_3 (JMGS, ≥ 65 wt.%) were used in the inductively coupled plasma (ICP) technique. The results obtained with these catalysts are present in subchapter 6.2.

All components present in the synthesized OMW (vanillic, gallic, cinnamic, 4-hydroxybenzoic and syringic acids, L-arabinose and D-galactose), were purchased from Alfa Aesar except the veratric and protocatechuic acids, from Acros Organics, and tyrosol, from Sigma-Aldrich.

Nitrogen (≥ 99.999 % - used as a carrier gas in the catalytic experiments and makeup gas in the gas chromatograph number 1 (GC_1)), argon (≥ 99.999 % - used as a carrier, reference and makeup gas in the GC_1), helium (≥ 99.999 % - used as a carrier and makeup gas in the GC_2), hydrogen (≥ 99.999 % - used for catalyst activation and as fuel gas in the $GC_{1/2}$) and reconstituted air (20 vol.% O_2/N_2 - used as oxidizing gas in temperature-programmed oxidation analyses and the $GC_{1/2}$) were all supplied from Linde.

Table 3.6 - General information about the commercial catalysts used.

Short Name	Composition	Active Phase	Theoretical Metal(s) Loading (wt.%)	Promoter/Support
Cu-Zn[1]	$CuO-ZnO/MgO-Al_2O_3$	CuO-ZnO	64-25[a)]	$MgO-Al_2O_3$
Cu-Zn[2]	$CuO-ZnO/Al_2O_3$	CuO-ZnO	50-40[a)]	Al_2O_3
Ni	$Ni/SiO_2-Al_2O_3$	Ni	66 ± 5	$SiO_2-Al_2O_3$
Pd[1]	Pd/Al_2O_3	Pd	0.5	Al_2O_3
Pd[2]	Pd/Al_2O_3	Pd	5	Al_2O_3
Pt[1]	Pt/Al_2O_3	Pt	0.5	Al_2O_3
Pt[2]	Pt/Al_2O_3	Pt	1	Al_2O_3
Rh	$Rh/M-Al_2O_3$[b)]	Rh	2[c)]	Al_2O_3
Ru	Ru/Al_2O_3	Ru	2	Al_2O_3

[a)] Content of the metal oxides.
[b)] *M* is a rare-earth metal (promoter).
[c)] Value provided by the supplier.

3.3.2. Catalysts preparation and OMW composition

In this thesis, a series of HTC-based materials (herein called HTC^x) and Ni and Ni-Ru bimetallic supported catalysts were prepared and tested - discussion in subchapter 6.2. The detailed information about the catalysts prepared in this work is provided in Table 3.7.

The samples HTC^1, HTC^2 and HTC^3 were synthesized using a co-precipitation method by adding dropwise a solution of $Mg(NO_3)_2 \cdot 6H_2O$, $Ni(NO_3)_2 \cdot 6H_2O$ and $Al(NO_3)_3 \cdot 9H_2O$ into a Na_2CO_3 solution. The pH (8.5) of the co-precipitation solution was kept constant during preparation by adding, whenever necessary, a 1 M NaOH solution with a peristaltic pump (Minipuls 3 from Gilson) connected to a pH controller (BL 931700-1 BlackStone from HANNA Instruments). Then, the resulting precipitated was aged, at room temperature for 24 h with stirring, filtered and washed to remove the nitrates; finally, it was dried at 60 ºC for 24 h. The HTC^1, HTC^2 and HTC^3 dry samples were calcined in air (at 500 ºC for 5 h - with a heating ramp of 5 ºC·min^{-1}) to obtain a mixed oxide material. The support of the HTC^4 catalyst was also prepared using a co-precipitation method by adding dropwise a solution of $Mg(NO_3)_2 \cdot 6H_2O$ and $Al(NO_3)_3 \cdot 9H_2O$ into a Na_2CO_3 solution - again, the pH of the solution (9.5) was controlled using a solution of 1 M NaOH. The obtained solid was filtered and washed to remove the nitrates and dried at 60 ºC for 24 h. Then, this support was loaded with an aqueous solution of $Ni(NO_3)_2 \cdot 6H_2O$, dissolved in the minimum amount of water, to attain a final nickel content of 15 wt.%. Finally, the HTC^4 catalyst was also dried (60 ºC for 24 h) and calcined in air (500 ºC for 5 h - heating ramp of 5 ºC·min^{-1}). The temperature (500 ºC) selected for the calcination of all these catalysts (HTC^1,

HTC^2, HTC^3 and HTC^4) was based on the fact that it allows to destroy completely the typical structure of the HTC and obtain a mixed oxide material [50, 57, 58]: see section 1 of Appendix F for further details.

Finally, two other Ni-based catalysts were prepared using SiO_2 as support (Ni-Ru/SiO_2 and Ni/SiO_2, herein called as Ni-Ru and Ni, respectively - cf. Table 3.7). Before the metal loading, SiO_2 was calcined for 5 h at 500 ºC (heating ramp of 5 ºC·min^{-1}) to activate the support [59, 60]. Then, the Ni/SiO_2 sample containing 10 wt.% of nickel was prepared by impregnation using $Ni(NO_3)_2 \cdot 6H_2O$ as a precursor, dissolved in the minimum amount of water. Lastly, a similar procedure was carried out to obtain the Ni-Ru/SiO_2 catalyst. In this case, an aqueous solution of $Ni(NO_3)_2 \cdot 6H_2O$ and $RuCl_3 \cdot H_2O$ was used to reach a final nickel and ruthenium content of 10 and 1 wt.%, respectively. Both catalysts were dried at 60 ºC (24 h) and calcined at 250 ºC for 5 h (heating ramp of 5 ºC·min^{-1}). To determine the calcination temperature, thermogravimetric analysis (TGA) was carried out to verified the thermal decomposition of the dry sample of Ni-Ru (see Fig. F.2 in section 1 of Appendix F). It was possible to verify that at high temperatures (> 270 ºC), the catalyst decomposes due to the volatilization of Ru (formation of volatile oxides during the calcination under oxidizing atmosphere) [61-65]; in this way, the calcination temperature of Ni-Ru/SiO_2 must be lower than 270 ºC. A similar temperature (250 ºC) was used in the calcination of a Ru-based catalyst by Wang *et al*. [65].

In this study, a synthetic OMW composed of a mixture of six different phenolic acids and two sugars typically present in most abundance in real OMW streams was used. The phenolic compounds concentrations used for simulating the wastewater were adjusted according to works reported in the literature [14, 19, 66, 67] as follows: 50 mg·L^{-1} of vanillic ($C_8H_8O_4$), gallic ($C_7H_6O_5$), cinnamic ($C_9H_8O_2$) and syringic ($C_9H_{10}O_5$) acids, and 100 mg·L^{-1} of tyrosol ($C_8H_{10}O_2$), veratric ($C_9H_{10}O_4$), 4-hydroxybenzoic ($C_7H_6O_3$) and protocatechuic ($C_7H_6O_4$) acids. About the sugars, it was used 1050 mg·L^{-1} of L-arabinose ($C_5H_{10}O_5$) and 450 mg·L^{-1} of D-galactose ($C_6H_{12}O_6$). The compounds were dissolved in distilled water and then the solution was submitted to ultrasounds (Sonorex Super RK255H) for 15 min, to ensure full dissolution. The SCFR was equal to 694. Before the catalytic tests, the initial effluent was characterized in terms of pH (3.5) and total organic carbon (TOC - 960 $mg_C \cdot L^{-1}$).

Table 3.7 - Data about the prepared materials.

Name	Chemical Formula	Active Metal(s)	Theoretical Active Metal(s) Loading (wt.%)	Support	Ni^{2+}/Mg^{2+} a)	$Al^{3+}/(Al^{3+}+Ni^{2+}+Mg^{2+})$ a)	$(Ni^{2+}+Mg^{2+})/Al^{3+}$ a)	Calcination Temperature (ºC)
HTC[1]	$[(Mg_{2.14}Ni_{0.86})Al(OH)_8(CO_3)_{0.5}\cdot yH_2O]$	Ni	30[b]	n.a.[c]	0.4	0.25	3	500
HTC[2]	$[(Mg_{0.5}Ni_{1.5})Al(OH)_8(CO_3)_{0.5}\cdot yH_2O]$	Ni	53[b]	n.a.[c]	3	0.33	2	500
HTC[3]	$[(Mg_{2.38}Ni_{0.62})Al(OH)_8(CO_3)_{0.5}\cdot yH_2O]$	Ni	22[b]	n.a.[c]	0.26	0.25	3	500
HTC[4]	$[(Mg_2Al(OH)_6(CO_3)_{0.5}\cdot yH_2O]$	Ni	15[b]	$MgO\text{-}Al_2O_3$	n.a.[c]	0.33	2	500
Ni-Ru	n.a.[c]	Ni-Ru	10-1[b]	SiO_2	n.a.[c]	n.a.[c]	n.a.[c]	250
Ni	n.a.[c]	Ni	10[b]	SiO_2	n.a.[c]	n.a.[c]	n.a.[c]	250

[a] Molar ratio.
[b] In the calcined sample.
[c] Not applicable.

3.3.3. OMW and catalysts characterization

The pH of the initial OMW solution was measured by a pH meter (HI 2211, HANNA instruments) and calibrated with a buffer with pH = 10/4 (ChemLab). During the catalytic experiments, several samples of the reactor outlet stream condensable phase (obtained in the peltiers located after the reactor) were collected and characterized in terms of TOC, which was determined with a TC/TOC analyzer equipped with an auto-sampler (Shimadzu TOC-L), operated at a maximum coefficient of variation ≤ 2%. The TOC values were determined by catalytic oxidation at 698 °C (method 5310 D) [68].

To characterize physic and chemically the catalysts (before and after the catalytic tests), several techniques were used: temperature-programmed reduction (TPR), temperature-programmed desorption of CO_2 (TPD-CO_2), temperature-programmed oxidation (TPO), temperature-programmed desorption of NH_3 (TPD-NH_3), N_2 adsorption-desorption isotherms recorded at -196 ºC, H_2 or CO chemisorption, transmission electron microscopy (TEM), SEM/EDS, TGA and inductively coupled plasma - optical emission spectrometry (ICP-OES).

TPR of the fresh catalyst (around 1 g) was carried out after thermal treatment at 150 ºC (heating from room temperature, at a rate of 5°C·min^{-1}) for 1.5 h under N_2 flow (100 mL_{NTP}·min^{-1}). Thereafter, the sample was cooled down to room temperature and then was heated up to 820 ºC at 10 ºC·min^{-1} under a flow rate of 10 mL_{NTP}·min^{-1} of H_2 diluted with 90 mL_{NTP}·min^{-1} of N_2. The quantity of H_2 consumed in these analyses was calculated, upon integration of the total flow rate measured in the mass-flow meter (model F111 from Bronkhorst-High Tech) at the outlet of the setup.

For the TPD-CO_2, the fresh catalyst (around 300 mg) was first treated at 150 ºC (heating from room temperature, at a rate of 5°C·min^{-1}) for 1.5 h under N_2 flow (100 mL_{NTP}·min^{-1}) and then reduced (see in subchapter 3.3.5 the reduction program applied). After this, the catalyst was saturated with CO_2 at room temperature for 1 h under pure CO_2 flow (30 mL_{NTP}·min^{-1}). The setup was flushed with N_2 for 30 min, and then the catalyst was heated up to 820 ºC at 10 ºC·min^{-1} (under a flow rate of 30 mL_{NTP}·min^{-1} of pure N_2).

For the in situ TPO, the sample of the spent catalyst used in the long-term test was heated up from room temperature up to 820 ºC at 10 ºC·min^{-1} under a flow rate of 100 mL_{NTP}·min^{-1} of reconstituted air (20 vol.% O_2/N_2 stream). The CO and CO_2 outlet concentrations obtained during the TPO, TPD-CO_2 and TPR runs were monitored by an online infrared analyzer (Servomex, model 4210).

For the TPD-NH_3, the fresh catalyst (around 150 mg) was first treated and then reduced with the same procedures used in the TPD-CO_2 analyses. After this, the catalyst was pre-treated again at 350 ºC for 1 h under He (50 mL_{NTP}·min^{-1} - 10 ºC·min^{-1}). Then, the materials were saturated with a stream of 15 vol.% NH_3/He at 125 ºC for 1 h (total flow rate of 50 mL_{NTP}·min^{-1}). The setup was flushed with He for 1 h (@ 150 ºC), and then the catalyst was heated up to 600 ºC at 10 ºC·min^{-1} (under a flow rate of

50 $mL_{NTP}·min^{-1}$ of pure He). The outlet concentration of NH_3 during the TPD-NH_3 analyses was measured with a micro TCD detector from Vici.

N_2 adsorption-desorption isotherms were recorded at -196 ºC, after degassing the samples under vacuum (using an MVP 015-2 pump from Pfeiffer) at 150 ºC for 2 h, in an ASAP 2420 apparatus (from Micromeritics).

H_2 or CO chemisorption was performed at 30 ºC, after reducing the samples at 350 ºC for 2 h, in an ASAP 2020C apparatus (from Micromeritics). The metal dispersion and metallic surface area were calculated as described elsewhere [69]. The metallic surface area per mass of catalyst (S_{M}) was calculated according to Eq. (3.20) and the metal dispersion (D_{M}) with Eq. (3.21); in such equations, n_{m} is the quantity of chemisorbed molecules per mass of catalyst, $\mathrm{N_A}$ is the Avogadro's number, s is the chemisorption stoichiometry (2 for H_2 and 1 for CO), n_{s} is the number of atoms at the surface per unit area (taken from [70]), $\mathrm{M_{Metal}}$ is the molar mass of the active phase and y_{Metal} is the mass fraction of metal in the catalyst.

$$S_{\mathrm{M}}\ (m^2 \cdot \mathrm{g}_{\mathrm{catalyst}}^{-1}) = \frac{n_{\mathrm{m}} \cdot \mathrm{N_A} \cdot s}{n_{\mathrm{s}}} \tag{3.20}$$

$$D_{\mathrm{M}}\ (\%) = \frac{n_{\mathrm{m}} \cdot s \cdot \mathrm{M_{Metal}}}{y_{\mathrm{Metal}}} \times 100 \tag{3.21}$$

TEM was performed on reduced and spent catalysts employed in the stability tests using a STEM Hitachi HD2700 operated at 200 kV. The samples were grounded, suspended in methanol, ultrasonicated and deposited on a copper grid coated with carbon film.

SEM/EDS analyses were performed in a FEI Quanta 400 FEG ESEM/EDAX Pegasus X4M instrument. The samples of the catalysts analysed by SEM/EDS were deposited on carbon tape (on top of metallic support).

TGA was performed under 60 $mL_{NTP}·min^{-1}$ of N_2, in a NETZSCH apparatus (Model STA 449 F3 Jupiter) to assess the decomposition of the catalysts and determine the loss of mass during the thermal treatment.

Lastly, the metal(s) content of the materials was determined ICP-OES using an iCAP 7000 spectrophotometer from Thermo Scientific. Before analysis, the catalysts were dissolved in a mixture of HCl and HNO_3 (10:1), using a START D microwave digestion system from Milestone.

3.3.4. Experimental setup

The catalytic tests were carried out in the experimental setup shown in Fig. 3.3. Experiments were performed in a stainless steel packed-bed reactor with 12 cm of length and 7.75 mm i.d., which was placed inside a tubular oven (model Split from Termolab, Fornos Eléctricos, Lda.) equipped with a 3-zone PID temperature controller (model MR13 from Shimaden). N_2 was fed upwardly to the reactor using mass-flow controllers (model F201 from Bronkhorst-High Tech) while the OMW solution was fed by an HPLC pump (Eldex, 1LMP) and forced to pass through an evaporation/mixing zone at 350 ºC before entering the reactor. The reactor was placed inside the oven so that the temperature throughout the bed was fairly uniform before the catalytic tests. Type-K thermocouples allowed recording the temperature histories in two axial positions of the reactor. The pressure drop was measured by means of two pressure transducers (model PMP 4010 from Druck) placed before and after the packed-bed unit; no significant pressure drop was detected in the catalytic tests (< 0.05 bar).

The liquid phase produced during the reaction was condensed in a home-assembled Peltier cold-trap located after the reactor (cf. Fig. 3.3). The tube between the reactor outlet and the first Peltier condenser was kept at 150 ºC. A system of two Peltier-based cold-traps, a coalescence filter and a filter were used between the reactor and the analysis system to retain all condensable species and any solid particles.

The GC_1 (Agilent 7820A), equipped with a thermal conductivity detector (TCD - using argon as makeup and reference gas), a CO/CO_2 methanizer fed with hydrogen and a flame ionization detector (FID -using nitrogen as makeup gas, hydrogen as fuel gas and reconstituted air as oxidizing gas), was used to analyze the gas phase produced in the reaction experiments. The Agilent 7820A is also equipped with two columns (Plot Q (30 m × 0.32 mm) and Plot 5A (30 m × 0.32 mm)). The formed H_2 was analysed by TCD with argon as a carrier gas to achieve a better response owing to the higher difference in thermal conductivity. CO and CO_2 were detected in the FID detector in the CH_4 form (through the utilization of the methanizer). Besides that, the GC_2 (GC-2010 Plus from Shimazu), equipped with an FID (using helium as makeup gas, hydrogen as fuel gas and reconstituted air as oxidizing gas), was utilized to detect the hydrocarbons present in the gas phase produced in the reaction experiments. The GC-2010 Plus is equipped with a GS-Alumina 115-3532 column (30 m x 0.53 mm).

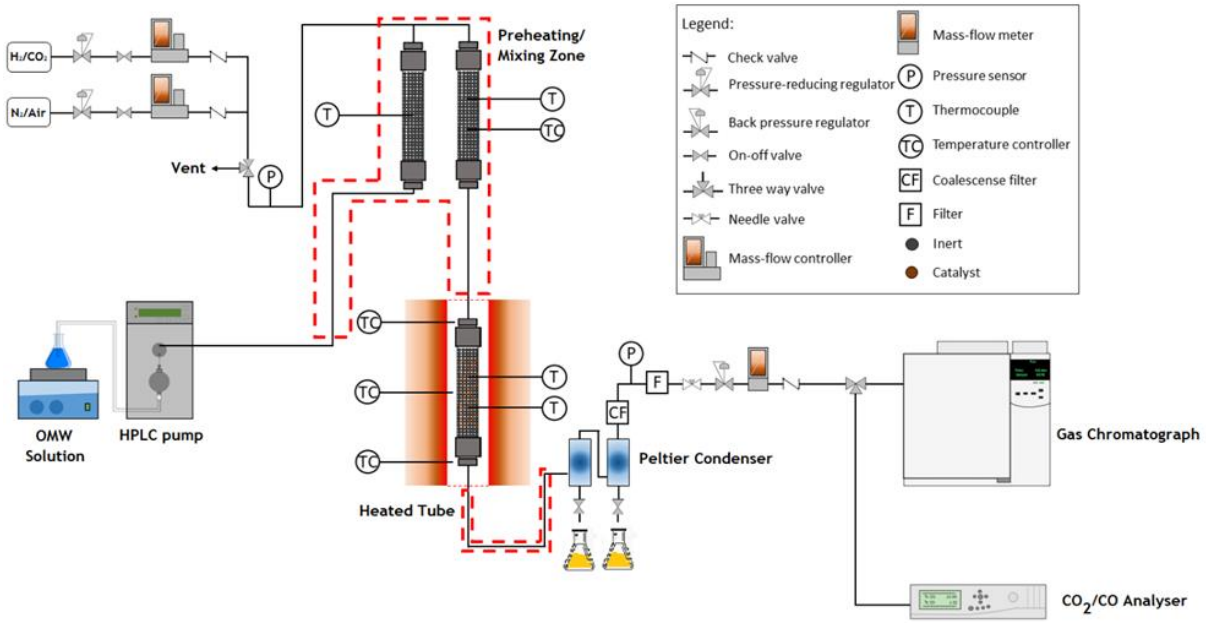

Fig. 3.3. Experimental setup used for the catalytic tests. Adapted from [71].

3.3.5. Catalytic experiments and performance indicators

Before the OMW steam reforming tests, the commercial and prepared catalysts were activated (at 350/650 ºC for 2 h under a 10 % H_2/N_2 stream - total flow rate of 100 $mL_{NTP}{\cdot}min^{-1}$) taking into account the TPR-H_2 results.

All the experiments were performed at atmospheric pressure. The catalyst pellets were crushed and sieved to the same particle size range (350-600 μm). The catalytic tests were not performed with the pellets because the gas-solid wall effects cannot be neglected when $D_{reactor}/d_{particle}$ ratio is below 10 [72]. On the other hand, the pellets were not crushed and sieved to a smaller particle size range (< 350 μm) due to the excessive pressure drop verified in a preliminary test (> 0.5 bar).

The catalyst particles were then mixed with inert silicon carbide particles with similar size. Dilution of the catalyst with inert silicon carbide enhances the heat transfer and minimizes temperature gradients, which was confirmed through direct measurement of the bed temperature (it remained nearly constant during the experimental tests, i.e. ± 1 ºC).

A blank test, herein called *Exp. 2.0*, in which the reactor was filled only with inert (SiC) was carried out at two different temperatures (350 ºC and 400 ºC). For all catalysts, an initial experimental test (*Exp. 2.1*) was carried out during 3h and 45 min (1h and 30 min at 350 ºC and 2h and 15 min at 400 ºC). The effect of the reduction temperature in the catalytic performance of the HTC-based catalysts was also studied in *Exp. 2.1* (wherein the prepared materials were also reduced at 650 ºC - in subchapter 6.2). The last experimental run, herein called *Exp. 2.2*, consisted of a 24 h test carried out over 3 days, ≈ 8 h each day, being that after each 8 h of reaction the catalyst was kept under N_2

atmosphere overnight. In *Exp. 2.2*, the catalysts with better catalytic performances shown in *Exp. 2.1* were used.

Samples of the condensable phase were collected during all the experimental tests (every ≈ 30 min) and analysed as already described in terms of TOC. All these runs are summarized in Table 3.8.

Table 3.8 - Operation conditions for the different experimental tests.

Exp. Runs	Temperature (ºC)	Catalyst Mass (g)	Reduction Temperature (ºC)	Total duration (h)	τ [a] (s)	WHSV [b] ($mol \cdot h^{-1} \cdot g_{cat}^{-1}$)
Exp. 2.0	350 and 400	-	-	-	0.13	-
Exp. 2.1	350 and 400	0.950	350/650	3.75		1.75
Exp. 2.2	400	0.650	350/650	24		2.56

[a] Residence Time.
[b] Weight hourly space velocity.

The stainless steel reactor was filled with ≈ 950 mg (for *Exp. 2.1*) or ≈ 650 mg (for *Exp. 2.2*) of catalyst homogeneously diluted with SiC (≈ 4.6 g). The catalyst's mass used in this *Exp. 2.2* was lower than that of the other experimental runs, to be simpler to detect a possible catalyst deactivation during the long-term test. At the bottom and upper parts of the reactor, a layer of inert particles allows to even out the reaction mixture flow. The temperature profile along the column length under an inert atmosphere was uniform (differences < 1 ºC). The OMW was fed to the evaporation system at a constant flow rate (Q_{OMW}) of 0.5 $mL \cdot min^{-1}$. Then, the vaporized OMW was carried into the reactor by the carrier gas (25 $mL_{NTP} \cdot min^{-1}$ of N_2).

The conversion of OMW during OMWSR was analysed by the TOC conversion and was calculated according to Eq. (3.22), where the subscripts "initial" and "final" stand for the feed and outlet liquid streams, respectively.

$$\mathrm{TOC\ Conversion}\ (\%) = \left(1 - \frac{\mathrm{TOC}_{\mathrm{final}}}{\mathrm{TOC}_{\mathrm{initial}}}\right) \times 100 \tag{3.22}$$

The H_2 purity (excluding nitrogen) obtained in the catalytic tests was calculated according to Eq. (3.23), where $F_{\mathrm{H_2}}$ is the molar flow rate of H_2 produced in the reactor (and therefore present in the outlet stream) and $F_{\mathrm{CO_2+\ CO+\ CH_4}}$ is the total molar flow rate of the carbon-containing gaseous products (CO_2, CO and CH_4) measured in the outlet stream.

$$\mathrm{H_2\ Purity}\ (\%) = \frac{F_{\mathrm{H_2}}}{F_{\mathrm{H_2}} + F_{\mathrm{CO_2+\ CO+\ CH_4}}} \times 100 \tag{3.23}$$

The selectivity of a catalyst for the formation of H_2 (through the OMWSR reaction - Eq. (3.5) comparatively to other gaseous products produced in the process was determined by Eq. (3.24); therein, RR is the H_2/CO_2 reforming ratio, which is equal to 2.03 for the OMWSR process (for the effluent considered in this study) [73]. The H_2 selectivity is equal to 100 % when only the reaction represented by Eq. (3.5) (steam reforming of oxygenates) occurs in the OMWSR process. When other secondary reactions involving H_2 consumption take place (for instance, the methanation reaction -

Eq. (3.8)), the value of H_2 selectivity is lower than 100 %. However, this parameter can be higher than 100 % due to the formation of products not considered in Eq. (3.24), namely coke (therefore decreasing the moles of carbon-containing gas products in the outlet stream), and other gaseous carbon species not considered in Eq. (3.24) and not analysed; still, H_2 selectivity can be above 100% due to the cracking of oxygenates and hydrocarbons (Eq. (3.11) and (3.16)) that can produce H_2 without the formation of other gaseous carbon-containing products.

$$\mathrm{H_2\ Selectivity\ (\%)} = \frac{F_{\mathrm{H_2}}}{\mathrm{RR} \cdot \left(F_{\mathrm{CO_2 + CO + CH_4}}\right)} \times 100 \tag{3.24}$$

The yield of the products was calculated according to Eq. (3.25), where F_i stands for the molar flow rate of components *i* at the outlet of the reactor (CO, CO_2, CH_4 or H_2), and $\mathrm{F_{OMW}}$ is the molar flow rate of organic compounds present in the OMW flowed to the system.

$$\mathrm{Yield}_i\ (\mathrm{mol}_i \cdot \mathrm{mol}_{\mathrm{OMW}}^{-1}) = \frac{F_{i_{\mathrm{outlet}}}}{F_{\mathrm{OMW_{inlet}}}} \tag{3.25}$$

The carbon balance (Eq.(3.26)) was also accounted during all the experimental tests. The molar flow rate of carbon fed to the reactor ($F_{\mathrm{C_{inlet}}}$) was compared with the molar flow rate of the carbon species (CH_4, CO or CO_2) detected at the reactor outlet plus the molar flow rate of carbon identified in the condensate phase. The flow rate of the condensate phase was considered equal to Q_{OMW} due to the very high concentration of H_2O in the feed and low conversion of steam in these experimental tests.

$$Carbon\ balance\ (\%) = \frac{F_{\mathrm{CO_2 + CO + CH_4}} + (\mathrm{TOC_{Condensable\ phase}} \times Q_{\mathrm{OMW}})}{F_{\mathrm{C_{inlet}}}} \times 100 \tag{3.26}$$

Finally, to better evaluate the performance of the catalysts used in this study, the turnover frequency (*TOF*) of several samples (with higher and lower H_2 yields) were calculated and compared at 350 and 400 ºC - Eq. (3.27). In this equation, W_{Catalyst} is the catalyst mass used in the catalytic experiment.

$$TOF\ (\mathrm{mol_{H_2}} \cdot \mathrm{mol_{Metal}^{-1}} \cdot \mathrm{min^{-1}}) = \frac{F_{\mathrm{H_2}}}{\frac{W_{\mathrm{Catalyst}} \times y_{\mathrm{Metal}}}{\mathrm{M_{Metal}}} \times \frac{D_{\mathrm{M}}}{100}} \tag{3.27}$$

3.4. Multifunctional reactors

3.4.1. Chemicals and gases

One prepared catalyst - Ni-Ru-based supported on SiO_2 and doped with CeO_2 (herein called Ni-Ru/Ce) - was used in this study; this material is very similar to the prepared catalyst Ni-Ru mentioned in subchapter 3.3 (and tested in subchapter 6.2). However, the Ni-Ru/Ce catalyst was doped with cerium oxide (catalyst promoter) to increase its resistance against coking [74-76]. Ruthenium (III) chloride hydrate (from Merck, ≥ 99.9 % purity), cerium (III) nitrate 6-hydrate (from Fluka, ≥ 99.0 % purity) and nickel (II) nitrate 6-hydrate (Alfa Aesar, with 98 % purity) were used as Ru^{3+}, Ce^{4+} and Ni^{2+} precursors, respectively; commercial SiO_2 (silica gel from Fluka, highest purity degree) was used as support of the prepared catalyst.

Nitrogen (≥ 99.999 % purity - used as carrier/sweep gas in the catalytic experiments and makeup gas in the gas chromatograph (GC)), reconstituted air (20 vol.% O_2/N_2, ≥ 99.999 % purity - used as oxidant agent employed during oxidative regeneration of the catalyst and in the GC), argon (≥ 99.999 % purity - used as a carrier, reference and makeup gas in the GC) and hydrogen (≥ 99.999 % purity - used for catalyst/membrane activation, permeation tests and as fuel gas in the GC) were supplied from AirLiquid.

Ultra-pure H_2O (slightly acidified with orthophosphoric acid) and methanol (≥ 99.8 %, Fischer Chemicals) were used as mobile phases in the high-performance liquid chromatography system equipped with a diode-array detector (HPLC-DAD).

All components present in the synthetic OMW effluent (vanillic, gallic, cinnamic, 4-hydroxybenzoic, p-coumaric and syringic acids, L-arabinose and D-galactose), were purchased from Alfa Aesar except the veratric, caffeic and protocatechuic acids, which were from Acros Organics, and tyrosol, from Sigma-Aldrich.

A commercial CO_2 sorbent - PURAL MG30K (herein called MG30_K) - and an in-house prepared sorbent - HTC-CO_3_K (prepared by the team in previous work [77]) - were used in this study for comparison purposes.

3.4.2. Catalyst synthesis and OMW preparation

The Ni-Ru/Ce catalyst was prepared using SiO_2 as support and CeO_2 as promotor. Before the metals loading, SiO_2 was calcined for 5 h at 500 ºC (heating rate of 5 ºC·min^{-1}) to activate the support [78]. Then, the activated support was impregnated with an aqueous solution of $Ni(NO_3)_2 \cdot 6H_2O$, $RuCl_3 \cdot H_2O$ and $Ce(NO_3)_3 \cdot 6H_2O$, to achieve a final loading of 10 wt.% Ni, 1 wt.% Ru and 3 wt.% Ce. The catalyst was dried at 60 ºC (24 h) and calcined at 250 ºC (5 h - heating rate of 5 ºC·min^{-1}). The calcination

temperature was chosen considering the TGA results obtained in this thesis; particularly, it was taken into account that at high temperatures (> 270 ºC) the catalyst decomposes due to volatilization of Ru, as also verified in other studies [61-65]. The calcination treatment applied for the material was performed to remove volatile species (e.g., H_2O and NO_3^{2-}) and promote the formation of metal oxides (e.g. NiO).

The synthetic OMW was composed of a mixture of ten different phenolic acids and two sugars typically present in real OMW effluents. The concentrations of the components were established according to several previous works [14, 19, 66] and can be seen in Table 3.9 - SCFR = 58. The compounds were partially dissolved in distilled water and then the solution was submitted to ultrasounds (Sonorex Super RK255H) for 30 min to ensure full dissolution.

A real effluent, generated from the 2-phase process of olive oil production (direct drainage of the wet pomace), was also used. After the drainage, the liquid was filtered to remove the suspended solids. The initial sample was collected from an olive oil producer in Portugal.

Table 3.9 - Synthetic OMW composition.

Chemical Compound	Concentration ($mg \cdot L^{-1}$)
Vanillic acid	600
Tyrosol	450
Gallic acid	1 400
Cinnamic acid	150
Syringic acid	650
Veratric Acid	200
4-hydroxybenzoic acid	750
Protocatechuic acid	1 500
L-Arabinose	10 000
D-Galactose	10 000
Caffeic acid	50
p-Coumaric acid	300

3.4.3. Experimental setup

The catalytic tests were performed in a stainless steel module that consists of two tubes with different diameters, being the catalyst, inert and sorbent placed in the annular region (see detail in Fig. 3.4) - the tube with a higher diameter is a stainless steel tube with 320 mm in length and 30 mm i.d.. For the TR and SER configurations, the tube with lower diameter is a stainless steel tube (length of 280 mm and 13 mm o.d.), which was closed at both ends; this tube has been used so that the flow pattern and hydrodynamics is identical in all reactor configurations. For the SEMR, the tube with a lower diameter contains the Pd-Ag membrane (length of 91 mm, 14 mm o.d. and ≈ 5 μm of selective film thickness), which was sealed in one end with a Swagelok plug to form the permeator tube (total length of 280 mm - see Fig. G.1 in Appendix G). A counter-current configuration for the utilization of a sweep-gas was adopted for the SEMR. The module was placed inside a tubular oven (model Split from Termolab, Fornos Eléctricos, Lda.) equipped with a 3-zone PID temperature controller (model MR13

from Shimaden). A type-K thermocouple was used to continuously measure the temperature in the bed, which remained nearly constant along the catalytic tests (± 2 ºC). N_2 was fed to the reaction medium and to the permeate zone of the membrane-based reactors as sweep gas using mass flow controllers (model F201 from Bronkhorst-High Tech), while the OMW solution was fed by an HPLC pump (Eldex, 1LMP) and forced to pass through an evaporation/mixing zone at 400 ºC before entering the reactor. The pressure in the system was measured utilizing three pressure transducers (model PMP 4010 from Druck) placed before and after the packed-bed unit and in the permeate side. The condensable phase produced during the reaction was condensed in a home-assembled Peltier cold-trap (at around 0.5 ºC) located after the reactor (cf. Fig. 3.4). The tube between the module outlet and the first Peltier condenser was kept at 150 ºC. A system of two Peltier based cold-traps, a coalescence filter and a filter were used between the reactor and the analysis system in order to retain all condensable species and any solid particles.

A GC (Agilent 7820A), equipped with a thermal conductivity detector (TCD, using argon as makeup and reference gas), a CO/CO_2 methanizer fed with H_2 and a flame ionization detector (FID, using N_2 as makeup gas, H_2 as fuel and reconstituted air as an oxidizing agent), was used to analyze the gas phase of the permeate zone. The GC is also equipped with two columns (Plot Q (30 m × 0.32 mm) and Plot 5A (30 m × 0.32 mm)). H_2 was analysed by the TCD with argon as a carrier gas to achieve a better response owing to the higher difference in thermal conductivity. The dry composition (H_2, CO_2, CO and CH_4) at the outlet of the retentate side was monitored by an online analyzer (AwiFlex Cool+).

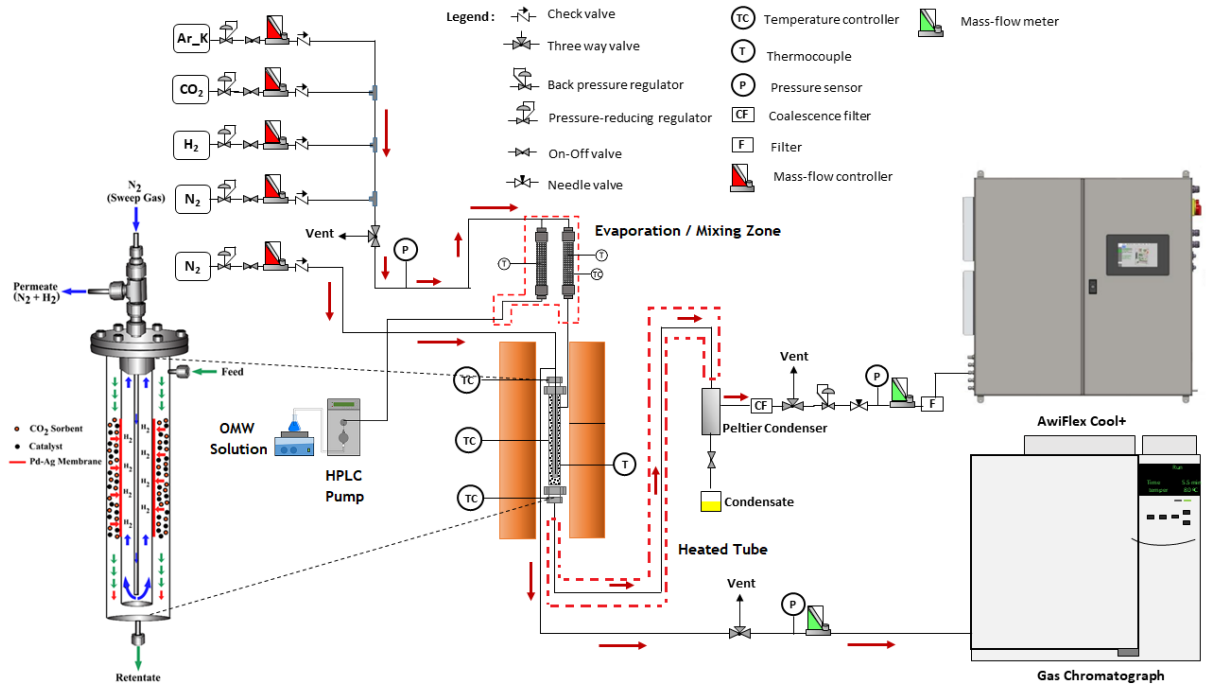

Fig. 3.4. Experimental setup used for the catalytic tests and TPD-CO_2 analyses, and detail of the SEMR.

3.4.4. Liquid samples characterization and catalysts oxidative regeneration

Liquid samples were periodically collected from the outlet of the reactor (in the Peltiers condenser) and then characterized by several techniques. TOC was determined by catalytic oxidation at 698 °C (method 5310 D [68]) with a TC/TOC analyzer (Shimadzu TOC-L apparatus equipped with auto-sampler, which was operated at a maximum coefficient of variation ≤ 2 %). The determination of the presence of phenolic species was performed with a HPLC-DAD, consisting of an L-2310 pump, L2200 auto-sampler, and L-2455 DAD. The separation was achieved using a Purospher STAR RP-18 column (240 mm × 4 mm, 5 µm), operating at a flow rate of 1 mL/min, at 50 °C. The volume of injection was 20 µL and the spectra were recorded at 280 nm. Mobile phases consisted of 70 vol.% of ultra-pure H_2O (slightly acidified with orthophosphoric acid) and 30 vol.% of methanol (≥ 99.8 %, Fischer Chemicals), at isocratic conditions. The total phenolic content (TPh) of the samples was estimated using the Folin-Ciocalteau reagent (Panreac), as described elsewhere [67]. For such determinations, gallic acid (GA) was used as the standard compound and, in this way, the TPh values are reported as $mg_{GAeq}{\cdot}L^{-1}$. The method 5220 D (closed reflux method) was applied for chemical oxygen demand (COD) determinations [68].

The catalyst oxidative regeneration was employed in all tests (among periods/cycles) since it was observed that this treatment (coke gasification) allowed to recover almost completely the catalytic activity [79]. Besides that, air treatment is usually used to stabilize and increase the H_2 permeation in Pd-based membranes [80, 81]. In several previous studies [71, 82-86] it was noticed the existence of two different combustion peaks during oxidation of spent catalysts, below and above 500/550 ºC, which were related to the formation of amorphous and graphitic carbon, respectively. For the in situ oxidative regeneration (application of a temperature program oxidation - TPO) in the TR and SER, the samples of spent catalysts were treated with a flow rate of 25 $mL_N{\cdot}min^{-1}$ of reconstituted air (20 vol.% O_2 in N_2) diluted with 75 $mL_N{\cdot}min^{-1}$ of N_2, first at 400 ºC and then at 500 ºC and 1 bar; the air was diluted to avoid the temperature gradients observed in previous work [71]. For the SEMR, the oxidative regeneration (catalyst and membrane) was carried out under 2.5 $mL_N{\cdot}min^{-1}$ of reconstituted air diluted with 97.5 $mL_N{\cdot}min^{-1}$ of N_2 always at 400 ºC and 1 bar; once again, such procedure was used to avoid the damage of the membrane. The temperature program employed for the oxidation was chosen based on TPO results obtained with this catalyst (data not shown for brevity). The coke produced during the tests was always fully oxidized in the TPO runs (the concentration of CO_2 measured at the reactor outlet was equal to zero at the end of the oxidation). The amount of carbon gasified in the form of CO_2 was measured with an online infrared-based analyzer (AwiFlex Cool+) - CO and CH_4 were not detected in these analyses. After this procedure, the catalyst was exposed to a reducing atmosphere (H_2). Besides that, the system was always flushed with N_2 (100 $mL_{NTP}{\cdot}min^{-1}$) for 15/20 min between the treatment programs and before and after the catalytic tests.

3.4.5. Experimental runs and performance indicators

Before the OMW steam reforming catalytic tests or after the oxidative regenerations, the catalyst was activated (@ 400 ºC under a 10 % H_2/N_2 stream - total flow rate of 100 $mL_{NTP} \cdot min^{-1}$) until its complete reduction. Prior to the experimental tests in the membrane-based reactor configurations, the Pd-Ag membrane (ca. 5 µm-thick Pd-Ag membrane supported on a porous Al_2O_3 tube, from Tecnalia) was activated until the permeate H_2 flow rate was constant, following the activation conditions suggested by the supplier: first, the MR/SEMR was heated up to 400 ºC under N_2 atmosphere (100 $mL_{NTP} \cdot min^{-1}$); then, the membrane activation was performed feeding 200 $mL_{NTP} \cdot min^{-1}$ of pure H_2 (@ 1 bar and 400 °C), using 100 $mL_{NTP} \cdot min^{-1}$ of N_2 as sweep gas in the permeate side. Atmospheric pressure was always maintained in the permeate side of the membrane during the tests. This activation procedure of the membrane also allowed, simultaneously, to reduce the Ni-Ru catalyst.

The catalyst (and sorbent when applicable) was crushed, sieved (350-600 µm) and mixed with inert silicon carbide particles with the same particle size. Using this range of particle size is possible to neglect the pressure drop in the reactor (< 0.05 bar).

The operating conditions used in the different reactor configurations are shown in Table 3.10. The experimental tests were carried out at two different sets of operations conditions, where one of them (higher temperature and pressure, i.e. @ 400 ºC and 4 bar) favors the kinetics of the reactions, the H_2 permeation and the CO_2 sorption; the other conditions were 350 ºC and 1 bar. At the bottom and upper parts of the module, a layer of SiC allows to smooth the flow of the reaction mixture. In all the experimental runs, the OMW was fed to the evaporation system at a constant flow rate of 0.5 $mL \cdot min^{-1}$. Then, the vaporized OMW was carried into the reactor by the carrier gas (90 $mL_{NTP} \cdot min^{-1}$ of N_2).

The blank tests, herein called *Exp. 3.0*, in which the TR was filled only with inert (SiC), were carried out for both operation conditions studied in this work. Besides that, other four different sets of experimental runs were carried out: one set for each reactor configuration (TR, SER and SEMR) and another with real effluents using a SEMR - see Table 3.10 for further details. Along this work, the performance reached with the MR corresponds to that of the SEMR at steady-state, i.e., when the CO_2 sorbent is saturated.

The conversion of OMW during the reaction was analysed by the TOC conversion - Eq. (3.22) and the yield of the reaction products was calculated by Eq.(3.25).

Table 3.10 - Operation conditions for the different catalytic tests.

Exp. Runs	Temperature (ºC)	P_{ret} [a] (bar)	Catalyst Mass (g)	Sorbent Mass (g)	P_{perm} [b] (bar)	Sweep Gas ($mL_{NTP} \cdot min^{-1}$)	OMW	τ [c] (s)	WHSV [d] ($mol \cdot h^{-1} \cdot g_{cat}^{-1}$)
Exp. 3.0 (TR)	350	1	-	-	-	-	Synthetic	0.80	-
	400	4							
Exp. 3.1 (TR)	350	1	40						4.18×10^{-2}
	400	4							
Exp. 3.2 (SER)	350	1		40					
	400	4							
Exp. 3.3 (SEMR)	350	1			1	100			
	400	4							
Exp. 3.4 (SEMR)	400	4					Real		

[a] Total pressure in the retentate side.
[b] Total pressure in the permeate side.
[c] Residence Time.
[d] Weight hourly space velocity.

Notation and Glossary

List of Variables

D_{M}	Metal dispersion (dimensionless)
$D_{reactor}$	Internal diameter of the reactor (mm)
$d_{particle}$	Particle diameter (mm)
fCO_2	Removal fraction of CO_2 (dimensionless)
fH_2	Removal fraction of H_2 (dimensionless)
F_i / m_i	Molar flow rate of component *i* ($mol \cdot min^{-1}$)
G^{T}	Total Gibbs free energy (J)
M_{Metal}	Molecular weight of the metal ($g \cdot mol^{-1}$)
N_{A}	Avogadro's number (mol^{-1})
n_i	Number of moles of specie *i* (mol)
n_{s}	Number of atoms at surface per unit area (m^{-2})
n_{m}	Quantity of chemisorbed molecules ($mol \cdot g^{-1}_{catalyst}$)
p_{CO2}	Partial pressure of CO_2 (bar)
Q_{OMW}	Volumetric flow rate of OMW ($mL \cdot min^{-1}$)
s	Chemisorption stoichiometry (dimensionless)
S_{M}	Metallic surface area per mass of catalyst ($m^2 \cdot g^{-1}_{catalyst}$)
TOF	Turnover frequency (min^{-1})
μ_i	Chemical potential of specie *i* ($J \cdot mol^{-1}$)
ν_{i}	Stoichiometric coefficient of specie *i* (dimensionless)
W_{Catalyst}	Mass of catalyst (g)
y_{Metal}	Mass fraction of the metal in the catalyst (dimensionless)
Y_i	Yield of specie *i* ($mol_{specie\ i} \cdot mol^{-1}_{OMW}$)
ΔH_{f}	Enthalpy of formation of specie *i* ($kJ \cdot mol^{-1}$)
ΔH_{r}	Enthalpy of reaction ($kJ \cdot mol^{-1}$)

List of Acronyms

COD	Chemical oxygen demand
DTG	Derivative thermogravimetric
EDS	Energy dispersive spectroscopy
GC	Gas chromatograph
HTC	Hydrotalcite
ICP-OES	Inductively coupled plasma - optical emission spectrometry
MR	Membrane reactor
OMW	Olive oil mill wastewater

OMWSR	Olive oil mill wastewater steam reforming
RGIBBS	GIBBS reactor
SCFR	Steam-to-carbon feed ratio
SEM	Scanning electron microscopy
SEMR	Sorption-enhanced membrane reactor
SER	Sorption-enhanced reactor
TEM	Transmission electron microscopy
TGA	Thermogravimetric analysis
TOC	Total organic carbon
TPD	Temperature-programmed desorption
TPh	Total phenolic content
TPR	Temperature-programmed reduction
TPO	Temperature-programmed oxidation
TR	Traditional reactor
WGS	Water-gas shift

References

[1] Soria, M.A., C. Mateos-Pedrero, A. Guerrero-Ruiz and I. Rodríguez-Ramos, Thermodynamic and experimental study of combined dry and steam reforming of methane on Ru/ ZrO2-La2O3 catalyst at low temperature. International Journal of Hydrogen Energy, 2011. 36(23): p. 15212-15220.

[2] Chen, H., T. Zhang, B. Dou, V. Dupont, P. Williams, M. Ghadiri and Y. Ding, Thermodynamic analyses of adsorption-enhanced steam reforming of glycerol for hydrogen production. International Journal of Hydrogen Energy, 2009. 34(17): p. 7208-7222.

[3] KhanAcademy, Non-ideal behavior of gases. 2016 [Accessed 7-11-2016]; Available from: https://www.khanacademy.org/science/chemistry/gases-and-kinetic-molecular-theory/ideal-gas-laws/a/non-ideal-behavior-of-gases.

[4] Silva, J.M., M.A. Soria and L.M. Madeira, Thermodynamic analysis of Glycerol Steam Reforming for hydrogen production with in situ hydrogen and carbon dioxide separation. Journal of Power Sources, 2015. 273: p. 423-430.

[5] Leal, A.L., M.A. Soria and L.M. Madeira, Autothermal reforming of impure glycerol for H2 production: Thermodynamic study including in situ CO2 and/or H2 separation. International Journal of Hydrogen Energy, 2016. 41(4): p. 2607-2620.

[6] Avasthi, K.S., R.N. Reddy and S. Patel, Challenges in the Production of Hydrogen from Glycerol - A Biodiesel Byproduct Via Steam Reforming Process. Procedia Engineering, 2013. 51: p. 423-429.

[7] Li, Y., W. Wang, B. Chen and Y. Cao, Thermodynamic analysis of hydrogen production via glycerol steam reforming with CO2 adsorption. International Journal of Hydrogen Energy, 2010. 35(15): p. 7768-7777.

[8] Wildman, S.A. and G.M. Crippen, Prediction of Physicochemical Parameters by Atomic Contributions. Journal of Chemical Information and Computer Sciences, 1999. 39(5): p. 868-873.

[9] Technology, N.I.o.S.a., Standard Reference Data. 2016 [Acessed 20-10-2016]; Available from: https://webbook.nist.gov/cgi/cbook.cgi?ID=B6009950&Mask=80.

[10] Chin, K.-J. and P.H. Janssen, Propionate Formation by Opitutus terrae in Pure Culture and in Mixed Culture with a Hydrogenotrophic Methanogen and Implications for Carbon Fluxes in Anoxic Rice Paddy Soil. Applied and Environmental Microbiology, 2002. 68(4): p. 2089-2092.

[11] Stephenson, R.M., Handbook of the thermodynamics of organic compounds. 2012: Springer Science & Business Media.

[12] Roig, A., M.L. Cayuela and M.A. Sánchez-Monedero, An overview on olive mill wastes and their valorisation methods. Waste Management, 2006. 26(9): p. 960-969.

[13] Caputo, A.C., F. Scacchia and P.M. Pelagagge, Disposal of by-products in olive oil industry: waste-to-energy solutions. Applied Thermal Engineering, 2003. 23(2): p. 197-214.

[14] El-Abbassi, A., H. Kiai and A. Hafidi, Phenolic profile and antioxidant activities of olive mill wastewater. Food Chemistry, 2012. 132(1): p. 406-412.

[15] Vlyssides, A.G., M. Loizides and P.K. Karlis, Integrated strategic approach for reusing olive oil extraction by-products. Journal of Cleaner Production, 2004. 12(6): p. 603-611.

[16] Tosti, S., C. Accetta, M. Fabbricino, M. Sansovini and L. Pontoni, Reforming of olive mill wastewater through a Pd-membrane reactor. International Journal of Hydrogen Energy, 2013. 38(25): p. 10252-10259.

[17] Dermeche, S., M. Nadour, C. Larroche, F. Moulti-Mati and P. Michaud, Olive mill wastes: Biochemical characterizations and valorization strategies. Process Biochemistry, 2013. 48(10): p. 1532-1552.

[18] Aktas, E.S., S. Imre and L. Ersoy, Characterization and lime treatment of olive mill wastewater. Water Research, 2001. 35(9): p. 2336-2340.

[19] Daâssi, D., J. Lozano-Sánchez, I. Borrás-Linares, L. Belbahri, S. Woodward, H. Zouari-Mechichi, T. Mechichi, M. Nasri and A. Segura-Carretero, Olive oil mill wastewaters: Phenolic content characterization during degradation by Coriolopsis gallica. Chemosphere, 2014. 113: p. 62-70.

[20] Bouknana, D., B. Hammouti, R. Salghi, S. Jodeh, Z. A., I. Warad, A. Aouniti and M. Sbaa, Physicochemical Characterization of Olive Oil Mill Wastewaters in the eastern region of Morocco. Journal of Materials and Environmental Science, 2014. 4: p. 1039-1058.

[21] Erog˘lu, E., I. Erog˘lu, U. Gu¨ndu¨z and M. Yu¨cel, Effect of clay pretreatment on photofermentative hydrogen production from olive mill wastewater. Bioresource Technology, 2008. 99: p. 6799-6808.

[22] Lin, K.-H., W.-H. Lin, C.-H. Hsiao, H.-F. Chang and A.C.C. Chang, Hydrogen production in steam reforming of glycerol by conventional and membrane reactors. International Journal of Hydrogen Energy, 2012. 37(18): p. 13770-13776.

[23] Chang, A.C.C., W.-H. Lin, K.-H. Lin, C.-H. Hsiao, H.-H. Chen and H.-F. Chang, Reforming of glycerol for producing hydrogen in a Pd/Ag membrane reactor. International Journal of Hydrogen Energy, 2012. 37(17): p. 13110-13117.

[24] Gallucci, F., L. Paturzo and A. Basile, Hydrogen Recovery from Methanol Steam Reforming in a Dense Membrane Reactor: Simulation Study. Industrial & Engineering Chemistry Research, 2004. 43(10): p. 2420-2432.

[25] Jokar, S., M. Rahimpour, A. Shariati, A. Iulianelli, G. Bagnato, A. Vita, F. Dalena and A. Basile, Pure Hydrogen Production in Membrane Reactor with Mixed Reforming Reaction by Utilizing Waste Gas: A Case Study. Processes, 2016. 4(3): p. 33.

[26] Mendes, D., PhD thesis: Use of Pd-Ag Membrane Reactors in the Water-Gas Shift Reaction for Producing Ultra-Pure Hydrogen. 2010, FEUP.

[27] Mendes, D., S. Sá, S. Tosti, J.M. Sousa, L.M. Madeira and A. Mendes, Experimental and modeling studies on the low-temperature water-gas shift reaction in a dense Pd-Ag packed-bed membrane reactor. Chemical Engineering Science, 2011. 66(11): p. 2356-2367.

[28] Wiesman, Z., Desert Olive Oil Cultivation: Advanced Bio Technologies. 2009: Elsevier.

[29] Katsoyannos, E., A. Hatzikioseyian, E. Remoundaki and M. Tsezos, Photocatalytic treatment of olive mill wastewaters (OMW) in pilot scale, in 13th International Symposium on Pollution and its Impact on Life in Mediterranean Region. 2005, National Technical University of Athens Greece.

[30] Nasr, B., B. Ahmed and G. Abdellatif, Fenton treatment of olive oil mill wastewater-applicability of the method and parameters effects on the degradation process. Journal of Environmental Sciences, 2004. 16: p. 942-944.

[31] Gebreyohannes, A.Y., R. Mazzei and L. Giorno, Trends and current practices of olive mill wastewater treatment: Application of integrated membrane process and its future perspective. Separation and Purification Technology, 2016. 162: p. 45-60.

[32] Montero, C., L. Oar-Arteta, A. Remiro, A. Arandia, J. Bilbao and A.G. Gayubo, Thermodynamic comparison between bio-oil and ethanol steam reforming. International Journal of Hydrogen Energy, 2015. 40(46): p. 15963-15971.

[33] Tosti, S., M. Fabbricino, L. Pontoni, V. Palma and C. Ruocco, Catalytic reforming of olive mill wastewater and methane in a Pd-membrane reactor. International Journal of Hydrogen Energy, 2016. 41(12): p. 5465-5474.

[34] Casanovas, A., A. Galvis and J. Llorca, Catalytic steam reforming of olive mill wastewater for hydrogen production. International Journal of Hydrogen Energy, 2015. 40(24): p. 7539-7545.

[35] Aggoun, M., R. Arhab, A. Cornu, J. Portelli, M. Barkat and B. Graulet, Olive mill wastewater microconstituents composition according to olive variety and extraction process. Food Chemistry, 2016. 209: p. 72-80.

[36] Fki, I., N. Allouche and S. Sayadi, The use of polyphenolic extract, purified hydroxytyrosol and 3,4-dihydroxyphenyl acetic acid from olive mill wastewater for the stabilization of refined oils: a potential alternative to synthetic antioxidants. Food Chemistry, 2005. 93(2): p. 197-204.

[37] Feki, M., N. Allouche, M. Bouaziz, A. Gargoubi and S. Sayadi, Effect of storage of olive mill wastewaters on hydroxytyrosol concentration. European Journal of Lipid Science and Technology, 2006. 108(12): p. 1021-1027.

[38] Hamden, K., N. Allouche, M. Damak and A. Elfeki, Hypoglycemic and antioxidant effects of phenolic extracts and purified hydroxytyrosol from olive mill waste in vitro and in rats. Chemico-Biological Interactions, 2009. 180(3): p. 421-432.

[39] Justino, C.I., K. Duarte, F. Loureiro, R. Pereira, S.C. Antunes, S.M. Marques, F. Gonçalves, T.A.P. Rocha-Santos and A.C. Freitas, Toxicity and organic content characterization of olive oil mill wastewater undergoing a sequential treatment with fungi and photo-Fenton oxidation. Journal of Hazardous Materials, 2009. 172(2-3): p. 1560-1572.

[40] Kyriacou, A., K.E. Lasaridi, M. Kotsou, C. Balis and G. Pilidis, Combined bioremediation and advanced oxidation of green table olive processing wastewater. Process Biochemistry, 2005. 40(3-4): p. 1401-1408.

[41] Sasol, Hydrotalcites and Spinels Pural MG / PURALOX MG 2019 [Acessed 14-07-2019]; Available from: https://www.sasolgermany.de/index.php?id=hydrotalcites0.

[42] Miguel, C.V., R. Trujillano, V. Rives, M.A. Vicente, A.F.P. Ferreira, A.E. Rodrigues, A. Mendes and L.M. Madeira, High temperature CO2 sorption with gallium-substituted and promoted hydrotalcites. Separation and Purification Technology, 2014. 127(Supplement C): p. 202-211.

[43] Yong, Z., Mata and A.E. Rodrigues, Adsorption of Carbon Dioxide onto Hydrotalcite-like Compounds (HTlcs) at High Temperatures. Industrial & Engineering Chemistry Research, 2001. 40(1): p. 204-209.

[44] Yamamoto, T., T. Kodama, N. Hasegawa, M. Tsuji and Y. Tamaura, Synthesis of hydrotalcite with high layer charge for CO2 adsorbent. Energy Conversion and Management, 1995. 36(6): p. 637-640.

[45] Silva, J.M., R. Trujillano, V. Rives, M.A. Soria and L.M. Madeira, High temperature CO2 sorption over modified hydrotalcites. Chemical Engineering Journal, 2017. 325: p. 25-34.

[46] Coenen, K., F. Gallucci, B. Mezari, E. Hensen and M. van Sint Annaland, An in-situ IR study on the adsorption of CO2 and H2O on hydrotalcites. Journal of CO2 Utilization, 2018. 24: p. 228-239.

[47] Milea, C.A., C. Bogatu and A. DuŢĂ, The influence of Parameters in Silica Sol-Gel Process. Bulletin of the Transilvania University of Brasov, Series I: Engineering Sciences, 2011. 4(1): p. 59-66.

[48] Speight, J.G., Chapter 3 - Industrial Organic Chemistry, in Environmental Organic Chemistry for Engineers, J.G. Speight, Editor. 2017, Butterworth-Heinemann. p. 87-151.

[49] Bhattacharyya, A. and D.B. Hall, New triborate-pillared hydrotalcites. Inorganic Chemistry, 1992. 31(18): p. 3869-3870.

[50] Ram Reddy, M.K., Z.P. Xu, G.Q. Lu and J.C. Diniz da Costa, Layered Double Hydroxides for CO2 Capture: Structure Evolution and Regeneration. Industrial & Engineering Chemistry Research, 2006. 45(22): p. 7504-7509.

[51] Oliveira, E.L.G., C.A. Grande and A.E. Rodrigues, CO2 sorption on hydrotalcite and alkali-modified (K and Cs) hydrotalcites at high temperatures. Separation and Purification Technology, 2008. 62(1): p. 137-147.

[52] Hanif, A., S. Dasgupta, S. Divekar, A. Arya, M.O. Garg and A. Nanoti, A study on high temperature CO2 capture by improved hydrotalcite sorbents. Chemical Engineering Journal, 2014. 236(Supplement C): p. 91-99.

[53] Boon, J., P.D. Cobden, H.A.J. van Dijk, C. Hoogland, E.R. van Selow and M. van Sint Annaland, Isotherm model for high-temperature, high-pressure adsorption of CO2 and H2O on K-promoted hydrotalcite. Chemical Engineering Journal, 2014. 248: p. 406-414.

[54] Wu, Y.-J., P. Li, J.-G. Yu, A.F. Cunha and A.E. Rodrigues, K-Promoted Hydrotalcites for CO2 Capture in Sorption Enhanced Reactions. Chemical Engineering & Technology, 2013. 36(4): p. 567-574.

[55] Qin, Q., J. Wang, T. Zhou, Q. Zheng, L. Huang, Y. Zhang, P. Lu, A. Umar, B. Louis and Q. Wang, Impact of organic interlayer anions on the CO2 adsorption performance of Mg-Al layered double hydroxides derived mixed oxides. Journal of Energy Chemistry, 2017. 26(3): p. 346-353.

[56] Diglio, G., P. Bareschino, E. Mancusi, F. Pepe, D. Hanak and V. Manovic, Packed bed sorption enhanced methane reforming on CaO/CuO/Al2O3(NiO) catalyst, in Computer Aided Chemical Engineering, A. Friedl, et al., Editors. 2018, Elsevier. p. 1389-1394.

[57] van Bokhoven, J.A., J.C.A.A. Roelofs, K.P. de Jong and D.C. Koningsberger, Unique Structural Properties of the Mg-Al Hydrotalcite Solid Base Catalyst: An In Situ Study Using Mg and Al K-Edge XAFS during Calcination and Rehydration. Chemistry - A European Journal, 2001. 7(6): p. 1258-1265.

[58] Rocha, C., M.A. Soria and L.M. Madeira, Effect of interlayer anion on the CO2 capture capacity of hydrotalcite-based sorbents. Separation and Purification Technology, 2019. 219: p. 290-302.

[59] West, P.B., G.L. Haller and R.L. Burwell, The catalytic activity of silica gel. Journal of Catalysis, 1973. 29(3): p. 486-493.

[60] Soria, M.A., C. Mateos-Pedrero, I. Rodríguez-Ramos and A. Guerrero-Ruiz, Catalytic steam reforming of methane under conditions of applicability with Pd membranes over supported Ru catalysts. Catalysis Today, 2011. 171(1): p. 126-131.

[61] Ragaini, V., C. Pirola, S. Vitali, G. Bonura, C. Cannilla and F. Frusteri, Stability of Metallic Ruthenium in Ru-Co Supported Silica Catalysts. Catalysis Letters, 2012. 142(12): p. 1452-1460.

[62] Zou, W. and R.D. Gonzalez, The chemical anchoring of noble metal amine precursors to silica. Catalysis Today, 1992. 15(3): p. 443-453.

[63] Goodwin, J.G., D.O. Goa, S. Erdal and F.H. Rogan, Reactive metal volatilization from Ru/Al2O3 as a result of ruthenium carbonyl formation. Applied Catalysis, 1986. 24(1): p. 199-209.

[64] Girardon, J.S., A. Constant-Griboval, L. Gengembre, P.A. Chernavskii and A.Y. Khodakov, Optimization of the pretreatment procedure in the design of cobalt silica supported Fischer-Tropsch catalysts. Catalysis Today, 2005. 106(1): p. 161-165.

[65] Wang, S., E.T. Schrunk, H. Mahajan, Farrauto and R. J., The Role of Ruthenium in CO2 Capture and Catalytic Conversion to Fuel by Dual Function Materials (DFM). Catalysts, 2017. 7(3): p. 88.

[66] Allouche, N., I. Fki and S. Sayadi, Toward a High Yield Recovery of Antioxidants and Purified Hydroxytyrosol from Olive Mill Wastewaters. Journal of Agricultural and Food Chemistry, 2004. 52(2): p. 267-273.

[67] Esteves, B.M., C.S.D. Rodrigues and L.M. Madeira, Synthetic olive mill wastewater treatment by Fenton's process in batch and continuous reactors operation. Environmental Science and Pollution Research, 2018. 25(35): p. 34826-34838.

[68] Rice, E.W., R.B. Baird and A.D. Eaton, Standard Methods for the Examination of Water and Wastewater. 23rd ed. 2017, Washington, DC: American Public Health Association, American Water Works Association, Water Environment Federation.

[69] Webb, P., C. Orr and C. Micromeritics Instrument, Analytical methods in fine particle technology. 1997, Norcross, Ga.: Micromeritics Instrument Corp.

[70] Figueiredo, J.L. and F.R. Ribeiro, Catálise Heterogénea. 1989: Fundação Calouste Gulbenkian. Serviço de Educação.

[71] Silva, J.M., L.S. Ribeiro, J.J.M. Órfão, M.A. Soria and L.M. Madeira, Low temperature glycerol steam reforming over a Rh-based catalyst combined with oxidative regeneration. International Journal of Hydrogen Energy, 2019. 44(5): p. 2461-2473.

[72] Froment, G.F., K.B. Bischoff and J. De Wilde, Chemical reactor analysis and design. Vol. 2. 1990: Wiley New York.

[73] Cortright, R.D., R.R. Davda and J.A. Dumesic, Hydrogen from catalytic reforming of biomass-derived hydrocarbons in liquid water. Nature, 2002. 418(6901): p. 964-967.

[74] Pu, J., F. Ikegami, K. Nishikado and E.W. Qian, Effect of ceria addition on NiRu/CeO2Al2O3 catalysts in steam reforming of acetic acid. International Journal of Hydrogen Energy, 2017. 42(31): p. 19733-19743.

[75] Savuto, E., R.M. Navarro, N. Mota, A. Di Carlo, E. Bocci, M. Carlini and J.L.G. Fierro, Steam reforming of tar model compounds over Ni/Mayenite catalysts: effect of Ce addition. Fuel, 2018. 224: p. 676-686.

[76] Li, L., B. Jiang, D. Tang, Q. Zhang and Z. Zheng, Hydrogen generation by acetic acid steam reforming over Ni-based catalysts derived from La1−xCexNiO3 perovskite. International Journal of Hydrogen Energy, 2018. 43(14): p. 6795-6803.

[77] Rocha, C., M.A. Soria and L.M. Madeira, Doping of hydrotalcite-based sorbents with different interlayer anions for CO2 capture. Separation and Purification Technology, 2020. 235: p. 116140.

[78] Soria, M.A., C. Mateos-Pedrero, P. Marín, S. Ordóñez, A. Guerrero-Ruiz and I. Rodríguez-Ramos, Kinetic analysis of the Ru/SiO2-catalyzed low temperature methane steam reforming. Applied Catalysis A: General, 2012. 413-414: p. 366-374.

[79] Silva, J.M., L.S. Ribeiro, J.J.M. Órfão, S. Tosti, M.A. Soria and L.M. Madeira, From sorption-enhanced reactor to sorption-enhanced membrane reactor: A step towards H2 production optimization through glycerol steam reforming. Chemical Engineering Journal, 2019. 368: p. 795-811.

[80] Mejdell, A.L., H. Klette, A. Ramachandran, A. Borg and R. Bredesen, Hydrogen permeation of thin, free-standing Pd/Ag23% membranes before and after heat treatment in air. Journal of Membrane Science, 2008. 307(1): p. 96-104.

[81] Peters, T.A., M. Stange and R. Bredesen, On the high pressure performance of thin supported Pd-23%Ag membranes—Evidence of ultrahigh hydrogen flux after air treatment. Journal of Membrane Science, 2011. 378(1): p. 28-34.

[82] Wu, C., L. Dong, J. Huang and P.T. Williams, Optimising the sustainability of crude bio-oil via reforming to hydrogen and valuable by-product carbon nanotubes. RSC Advances, 2013. 3(42): p. 19239-19242.

[83] Tan, R., A. Alir, S. Mohamad, K. Md Isa, T. Amran and T.A. Tuan Abdullah, Ni-based catalysts for steam reforming of tar model derived from biomass gasification. 2019.

[84] Galetti, A.E., M.F. Gomez, L.A. Arrúa and M.C. Abello, Hydrogen production by ethanol reforming over NiZnAl catalysts: Influence of Ce addition on carbon deposition. Applied Catalysis A: General, 2008. 348(1): p. 94-102.

[85] Calles, J.A., A. Carrero, A.J. Vizcaíno and L. García-Moreno, Hydrogen production by glycerol steam reforming over SBA-15-supported nickel catalysts: Effect of alkaline earth promoters on activity and stability. Catalysis Today, 2014. 227: p. 198-206.

[86] Charisiou, N.D., K.N. Papageridis, L. Tzounis, V. Sebastian, S.J. Hinder, M.A. Baker, M. AlKetbi, K. Polychronopoulou and M.A. Goula, Ni supported on CaO-MgO-Al2O3 as a highly selective and stable catalyst for H2 production via the glycerol steam reforming reaction. International Journal of Hydrogen Energy, 2019. 44(1): p. 256-273.

Chapter 4. Thermodynamic Analysis

This chapter is divided into two parts: in the first one (subchapter 4.1) the thermodynamic analysis of the olive mill wastewater steam reforming is carried out in a traditional reactor. In the second (subchapter 4.2), the effect of multifunctional reactors on the thermodynamic equilibrium of the process is studied.

Subchapter 4.1. Thermodynamic analysis of olive mill wastewater steam reforming *

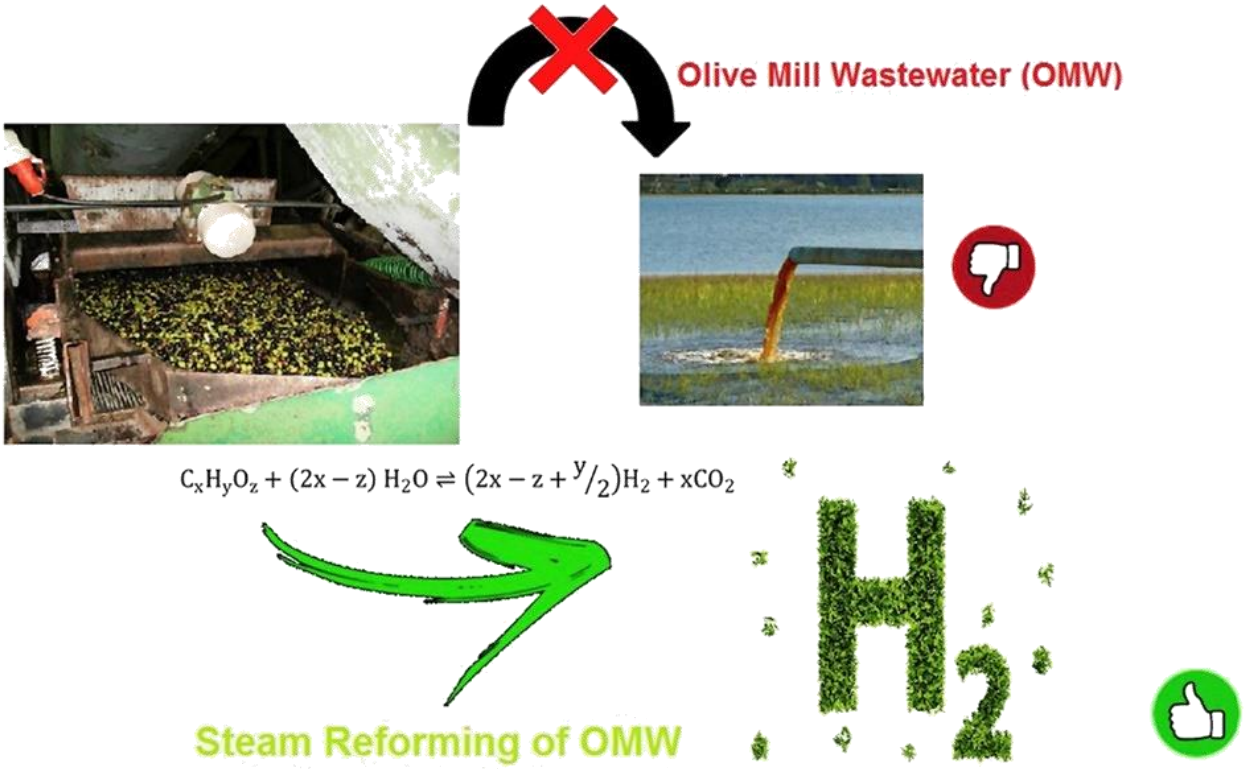

Highlights:

- OMW valorization for H_2 production via steam reforming.
- A thermodynamic analysis of a TR was performed.
- The more favorable operating conditions for each composition were determined.
- The initial composition of OMW influences the H_2 yield.

* The contents of this subchapter were adapted from Rocha, C., M.A. Soria and L.M. Madeira, Thermodynamic analysis of olive oil mill wastewater steam reforming. Journal of the Energy Institute, 2019. 92(5): p. 1599-1609. (https://doi.org/10.1016/j.joei.2018.06.017)

Abstract:

A thermodynamic analysis of the steam reforming of olive oil mill wastewater (OMW) was performed in a traditional reactor (TR). The equilibrium compositions are calculated employing the Gibbs free energy minimization method (using the Aspen Plus V8.8® software). The simulations were performed at different temperatures (300-1000 °C), different pressures (1-20 bar) and different compositions of the OMW, which might differ considerably. It was found that the H_2 yield increases with the temperature up to a maximum value, while it continuously decreases with the pressure. In opposition, the water content in the feed increases the H_2 yield, thus providing an opportunity to take advantage of the waste aqueous matrix. The optimum operating conditions for several OMW compositions, corresponding to either real or simulated effluents from different areas, were determined; this is a very important aspect that allows to assess, in advance, the potential of such waste valorization into green H_2 production. Moreover, it was found a good agreement between the maximum H_2 yield obtained for each wastewater and the ones predicted based on their compositions. Coke formation was also accounted, which increases when decreasing either temperature or water content in the feed. However, for water content in the feed greater than 60 wt.% (which is the case of most OMWs), there is no coke formation whatever the temperature and pressure (within the ranges used in this study) and for all the effluent compositions considered.

4.1.1. Introduction

In this subchapter 4.1, a thermodynamic analysis of the olive oil mill wastewater (OMW) steam reforming (OMWSR) is performed in a traditional reactor (TR) for several sources of OMW, which involve different compositions and oxygenated species. This aspect is very important because the maximum possible H_2 production for a given waste can be estimated based on its composition. To the best of our knowledge, such analysis is done herein for the first time. For this purpose, the effect of the initial composition of the OMW, of the temperature, pressure and the content of water in the feed are assessed.

This work will allow drawing primary conclusions about the feasibility of applying the steam reforming reaction (from a thermodynamic point of view) in several effluents of OMW (i.e., with different compositions), as well as to point out the more favorable operation conditions for each effluent analysed, to maximize the H_2 yield. An advantage of the effluents herein considered, as compared to other oxygenates (e.g. glycerol, acetic acid or ethanol), is that the expected yields obtained (defined as the moles of H_2 produced per mole of organics fed) should be much higher (e.g. maximum theoretical H_2 yield is 7 for the steam reforming of glycerol [1]), thus further highlighting the advantages of using OMW for H_2 generation.

The methods used in this subchapter are described in subchapter 3.1.

4.1.2. Results and discussion

For the analysis of the effect of pressure, temperature and content of water in the feed, only one of the compositions of those mentioned in Table 3.3 is shown (Composition #9), since the other compositions follow the same trends. The effect of the OMW composition is then analysed in a subsequent section.

4.1.2.1. Total pressure effect

Firstly, it was done a thermodynamic analysis of the effect of the pressure in OMWSR. This analysis was performed in the range of 1-20 bar. This variable has been studied at 600 °C varying the content of water in the feed in the range of 20-92 wt.% (which is equivalent to a variation of the molar steam-to-carbon feed ratio (SCFR) between 0.37 and 17 for Composition #9). This last variable was varied because the OMW usually contains a large quantity of water (80-92 wt.%) [2, 3], being a hypothesis to consider at industrial scale the use of an initial pre-treatment to remove the water excess (distillation or membrane process), concentrating the organic load. High water content in the feed implies several operational problems (reactors with larger dimensions, low concentrations of organic species, etc.) and additional operating costs (water vaporization, reactor heating, etc.). So, the treatments will

reduce the reactor size designed for OMWSR and will minimize the amount of energy used to vaporize the feed.

As can be seen in Fig. 4.1a) pressure has a negative effect on the H_2 yield. This trend has been observed because the increase of the total pressure in the system leads to a shift in the equilibrium to the side with a lesser number of moles to counter the pressure rise. Despite OMWSR has a smaller number of moles in the reagents side (whatever component of the OMW stream undergoing steam reforming), it is important to note that total conversion of all organic species occurs, in all simulations (data not shown). So, other reactions have to be considered to account for the observed trend. The water-gas shift (WGS) reaction (Eq. (3.7)) is not affected by the total pressure since both sides have the same number of moles. Thus, the methanation reaction (Eq. (3.8)), which is favored at high pressures, is responsible for both the decrease in H_2 production and the increase of the CH_4 yield (Fig. 4.1b)). The yield of CO_2 varies in the same way as for H_2 and CO (the latter with a much lower decrease, because the variation of H_2 is three times higher than for CO; cf. stoichiometric coefficients of the methanation reaction - 3 mol of H_2 per 1 mol of CO). The CO_2 yield decreases because the CO concentration in the system decreases, inhibiting the formation of CO_2 by the WGS reaction (Eq. (3.7)). The H_2/CO ratio does not vary significantly due to the small content of CO in the system in this range of pressure (ratio equal to 21-25). This ratio is very important since this mixture is the so-called synthesis gas, which may be used in several industrial applications.

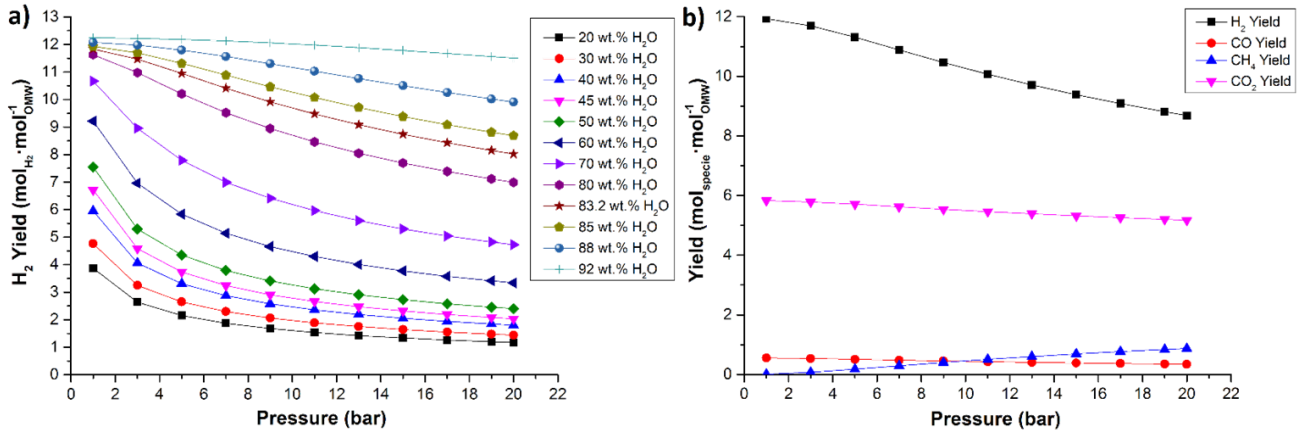

Fig. 4.1. Yield of H_2 in the thermodynamic equilibrium as a function of total pressure and content of water in the feed (wt.%) at 600 °C a) and yield of reaction products in the thermodynamic equilibrium as a function of pressure at 600 °C and 85 wt.% (SCFR = 8.41) of water in the feed b) for Composition #9.

4.1.2.2. Temperature effect

The effect of temperature in this process was studied in the range of 300-1000 °C and at a pressure of 1 bar (which provided a higher yield of H_2). In this analysis, the amount of water in the feed was also varied. Again, it was found complete conversion of all the organic species present in the OMW, in the entire range of conditions considered. From Fig. 4.2a) it can be seen the effect of the reformer

temperature in the yields of the gaseous species (CO, CH_4, H_2 and CO_2) with 85 wt.% of water in the feed (SCFR = 8.41). The yield of H_2 and the yield of CO_2 increase with the temperature up to a maximum point, then starting to decrease slightly from that point on. The yield of CO increases monotonically with temperature as opposed to the yield of CH_4. These behaviors can be explained considered methanation (Eq. (3.8)) and WGS (Eq. (3.7)) reactions (both exothermic). The first reaction explains the decrease in the yield of CH_4 and the increase in the yield of H_2 with the temperature, because it is an exothermic process and therefore more favorable at low temperatures. However, the yield of H_2 starts to decrease at higher temperatures when the endothermic reverse water-gas shift reaction (RWGS: $CO_2 + H_2 = CO + H_2O$) begins to predominate. The variation of the CO_2 yield with temperature follows a trend very similar to that of H_2, because at low temperatures WGS reaction (Eq. (3.7)) promotes its formation, which is however consumed at high temperatures via RWGS. Though, the CO yield increases with the temperature, because it is not further consumed by the reactions that are being inhibited (methanation reaction - Eq. (3.8)) and is inclusively formed via RWGS (reverse of Eq. (3.7)). Due to these different effects, the H_2/CO ratio varies significantly, from 562.29 (300 °C) to 6.27 (1000 °C).

As stated above, since the temperature has opposite effects in the WGS reaction (Eq. (3.7)) and methanation reaction (Eq. (3.8) in relation to H_2 production, there is an optimum temperature in terms of H_2 yield, whatever the water content in the mixture feed. It is however possible to observe that the water content in the feed influences the optimum point and the corresponding value of H_2 yield - Fig. 4.2b), which tends to lower temperatures for higher water concentrations. This phenomenon will be explained in the following subchapter.

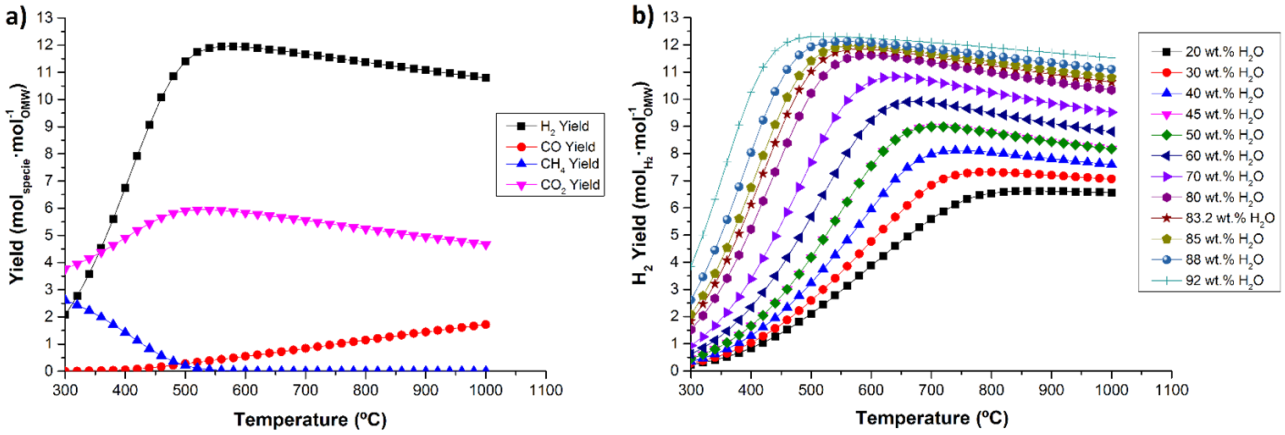

Fig. 4.2. Yield of reaction products in the thermodynamic equilibrium as a function of temperature at 1 bar and 85 wt.% (SCFR = 8.41) of water in the feed a) and yield of H_2 in the thermodynamic equilibrium as a function of temperature and water content in the feed (wt.%) at 1 bar b) for Composition #9.

4.1.2.3. Effect of water content in the feed

It was also analysed the effect of the amount of water present in the feed at 1 bar of total pressure. As already indicated the composition of water in the feed stream was varied from 20 wt.% to 92 wt.%. The range of water content in the OMW varies between 80-92 wt.% [2-5]. However, it was considered the possibility of applying other processes (for instance distillation) to reduce the content of water (until 20 wt.%, but always above the stoichiometric value).

As shown in Fig. 4.3a), the maximum yield of H_2 increases with the increasing amount of water fed (please notice that the figure shows the maximum H_2 yield for different percentages of water, which are reached at different temperatures - cf. Fig. 4.3b). This increased production of H_2 occurs because the increment of the water content causes the shift of the equilibrium of both the methanation and WGS reactions (Eqs. (3.8) and (3.7), respectively) according to the Le Chatelier's principle, inhibiting the first reaction and promoting the latter. Thus, the CO_2 yield also increases, in contrast with the yield of CO that shows the opposite trend (CO reacts in the WGS reaction, Eq. (3.7) - Fig. 4.3a). Therefore, the H_2/CO ratio increases significantly with the increasing wt.% of water in the feed. In this case the H_2/CO ratio increases from 1.13 (20 wt.% of water) to 69.96 (92 wt.% of water). The CH_4 yield is practically zero in the optimal temperatures (those that provided higher H_2 yields - usually high temperatures) for every wt.% of water in the feed.

Although the amount of water does not affect the optimum operation pressure, the opposite occurs in relation to the optimum operation temperature - Fig. 4.3b). As mentioned above, increasing the amount of water in the feed inhibits the methanation reaction - Eq. (3.8) - (strongly exothermic) and promotes the WGS reaction - Eq. (3.7) - (slightly exothermic) by shifting the optimum point to lower temperatures. This is also visible in Fig. 4.3b). As already mentioned, to implement the process industrially it may be necessary to remove some water from the OMW (raw OMW) because of the reforming/vaporization costs.

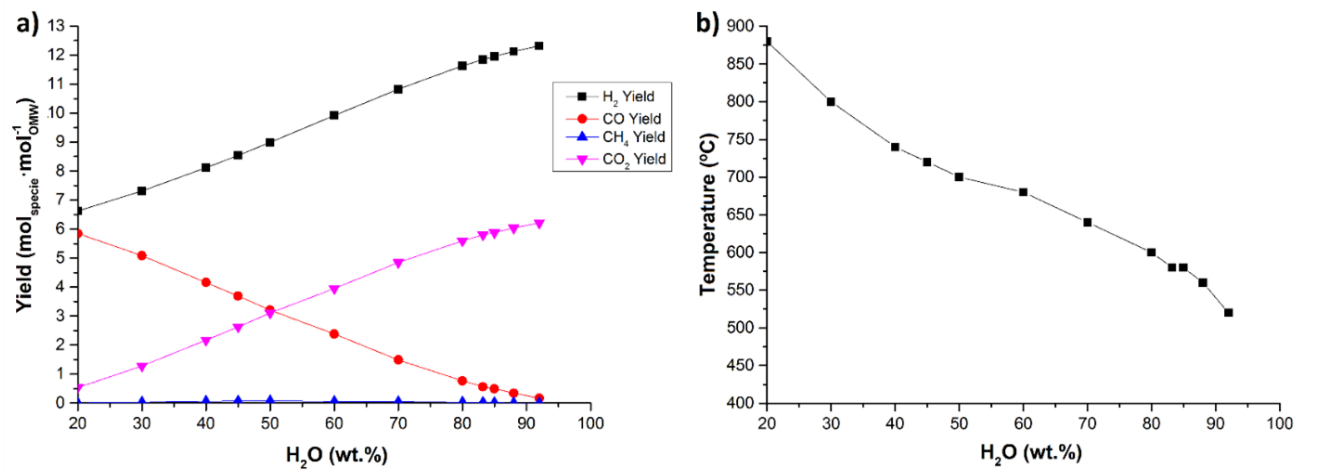

Fig. 4.3. Yield of reaction products in the thermodynamic equilibrium as a function of the water content in the feed (wt.%) at 1 bar a) and variation of the optimum temperature with the water content at 1 bar b); in both cases, the values correspond to the maximum H_2 yield for the OMW Composition #9.

4.1.2.4. Initial OMW composition effect

Several articles refer to different OMW compositions, as mentioned previously in subchapter 3.1 [6-15]. In this way, it is important to understand the effect of the OMW composition in the OMWSR process, namely on the yield of H_2 as well as on the best operating conditions for each effluent (i.e., optimum temperature, because it was fixed the operating pressure of 1 bar). We considered 17 different compositions in terms of concentration and species involved, as detailed in Table 3.3.

It was found that Composition #13 provides the lower yields of H_2 (Fig. 4.4a)), which is due to the high concentration of acetic acid, since this component has the lowest number of moles of hydrogen in its molecular structure. The acetic acid appears in the OMW composition studied by Tosti *et al*. [10], probably due to the anaerobic digestion that the effluent suffered from the microorganisms while it was stored before being analysed [16-20]. The acetic acid is not present in any other OMW (Table 3.3). Regarding the other compositions, it was possible to verify that the yields of H_2 as a function of water content in the feed are within the range of 6.5-13.5 mol of H_2 per mol of OMW_{feed} and all follow the same trend (i.e., more water provides a higher H_2 yield, for the reasons described in subchapter 4.1.2.3). It should be noticed that while changing the water content for each effluent, the proportions among the other components were kept constant. In Fig. 4.4a) is also shown the maximum H_2 yield vs. SCFR in the feed for Compositions #9 and #11, which limit the mentioned range for all the other OMW compositions. Again, it was found that increasing the amount of water in the feed shifts the optimum temperatures towards lower values, whatever the OMW composition (Fig. 4.4b)).

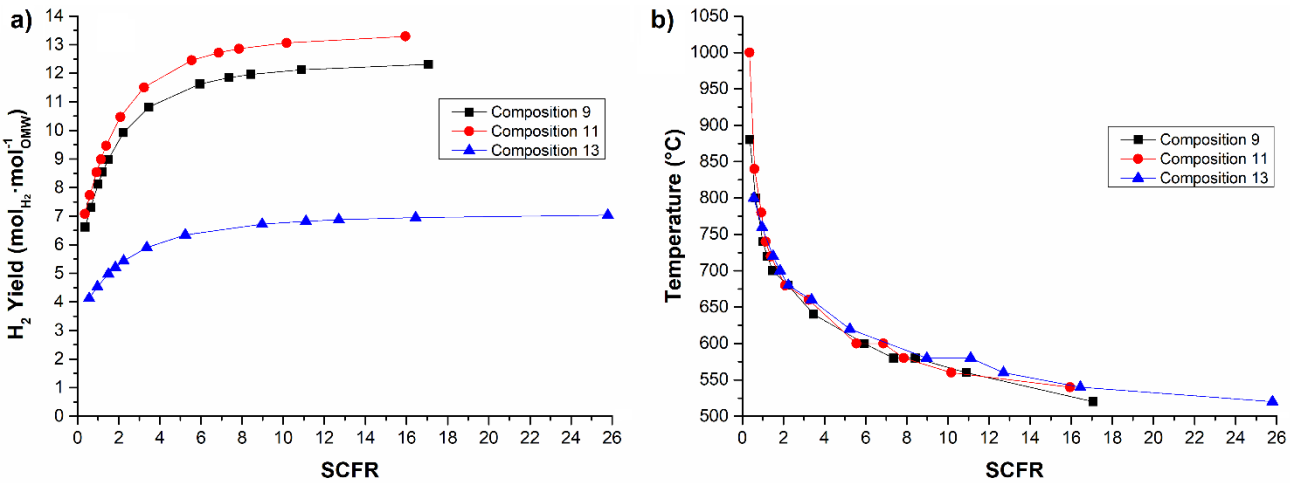

Fig. 4.4. Maximum yields of H_2 in the thermodynamic equilibrium at 1 bar for different steam-to-carbon feed ratios (SCFRs) in the feed a) and operation temperatures that correspond to the maximum H_2 yield b) for Compositions #9, #11 and #13.

In Fig. 4.4a) and Fig. 4.5 it is possible to differentiate the yields of the output products of Compositions #9, #11 and #13 respectively. As the yield of H_2, the yields of CO_2, CO and CH_4 are higher in the case of Composition #11. In terms of the H_2/CO ratio, it was observed that for the composition with higher H_2 yields this ratio is lower for the same content of water in the feed (wt.%) (Fig. A.1 in Appendix A), that is, the purity of H_2 at the reformer outlet stream is lower. However, for similar SCFRs, the H_2/CO ratio is lower for the composition with lower H_2 yield - Fig. A.2 in Appendix A. It was found that for OMW compositions that exhibit higher maximum yields, the optimal operating temperatures are higher - see Fig. 4.4b).

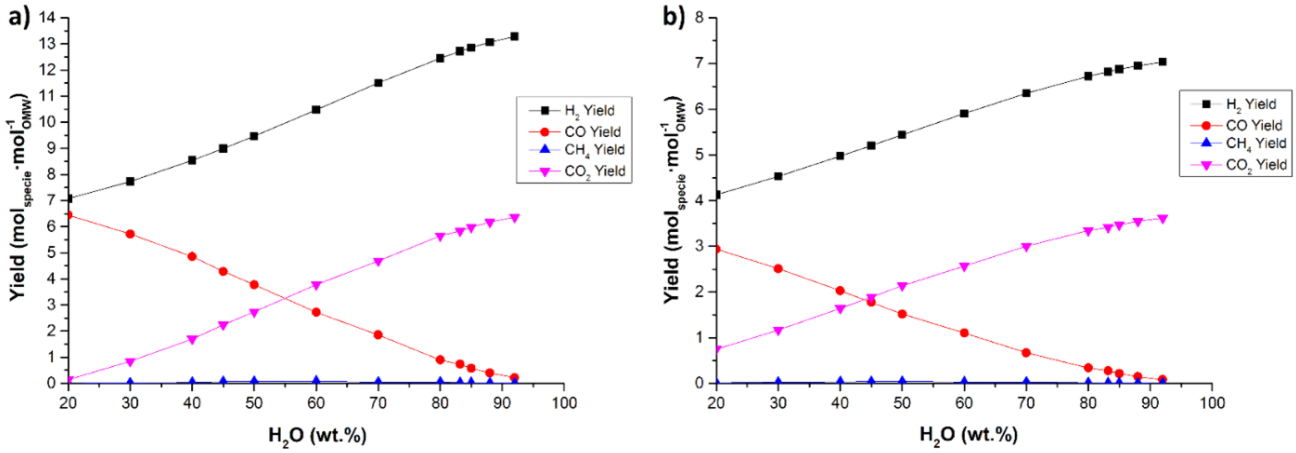

Fig. 4.5. Yield of reaction products in the thermodynamic equilibrium as a function of the water content in the feed (wt.%) at 1 bar for a) Composition #11 and b) Composition #13. Data obtained at optimum temperatures that maximize H_2 production.

The maximum H_2 yield obtained in the simulations was compared with the maximum theoretical yield. This theoretical yield was calculated using Eq. (3.5) taking into account the molar fraction of each chemical species in the feed, while assuming that no secondary reactions occurred. The results obtained are shown in Table 4.1. It can be seen that in almost all compositions an efficiency value (η - Eq. (4.1) close to 98 % is reached, but it is important to note that this simulated maximum yield is

obtained at undesired operating conditions (large amounts of water, which leads to reactor size problems and vaporization costs). This small deviation to 100 % efficiency, of less than 2 %, is due to the small formation of secondary products like CH_4, because the values of maximum simulated yields were obtained under conditions that inhibit the production of secondary products.

$$\eta = \frac{\text{Maximum Simulated Yield of Hydrogen}}{\text{Maximum Theoretical Yield of Hydrogen}} \times 100 \quad (4.1)$$

However, for a more realistic water content (60 wt.%) in the feed (for which the maximum H_2 yield obtained in the simulations is different from the previous scenario with 92 wt.%), it is possible to see in Table 4.2 that the efficiency is much lower. In this way, it is possible to improve the process by using for instance a sorption-enhanced membrane reactor [21], with simultaneous CO_2 capture and H_2 removal (through a CO_2 selective sorbent and an H_2 perm-selective membrane), in order to increase the efficiency.

Table 4.1 - Optimum operating conditions, maximum theoretical yield and maximum simulated yield for all OMW compositions with 92 wt.% of water in the feed.

Composition	Optimum Operation Conditions	Maximum Theoretical Yield ($mol_{H_2} \cdot mol^{-1}_{OMW}$)	Maximum Simulated Yield ($mol_{H_2} \cdot mol^{-1}_{OMW}$)	η (%)
#1	1 bar / 529 ºC	13.44	13.19	98.14
#2	1 bar / 530 ºC	13.41	13.17	98.21
#3	1 bar / 527 ºC	13.21	12.98	98.26
#4	1 bar / 528 ºC	13.27	13.03	98.19
#5	1 bar / 529 ºC	13.35	13.11	98.20
#6	1 bar / 528 ºC	13.27	13.04	98.27
#7	1 bar / 522 ºC	12.42	12.22	98.39
#8	1 bar / 526 ºC	13.04	12.81	98.24
#9	1 bar / 522 ºC	12.52	12.32	98.40
#10	1 bar / 529 ºC	13.46	13.22	98.22
#11	1 bar / 530 ºC	13.54	13.29	98.15
#12	1 bar / 526 ºC	12.90	12.68	98.29
#13	1 bar / 511 ºC	7.13	7.04	98.74
#14	1 bar / 526 ºC	13.22	12.99	98.26
#15	1 bar / 526 ºC	13.23	12.99	98.19
#16	1 bar / 527 ºC	13.23	13.00	98.26
#17	1 bar / 529 ºC	13.30	13.06	98.20

Table 4.2 - Optimum operating conditions, maximum theoretical yield and maximum simulated yield for all OMW compositions with 60 wt.% of water in the feed.

Composition	Optimum Operation Conditions	Maximum Theoretical Yield ($mol_{H_2} \cdot mol^{-1}_{OMW}$)	Maximum Simulated Yield ($mol_{H_2} \cdot mol^{-1}_{OMW}$)	η (%)
#1	1 bar / 689 ºC	13.44	10.43	77.60
#2	1 bar / 688 ºC	13.41	10.42	77.70
#3	1 bar / 683 ºC	13.21	10.31	78.05
#4	1 bar / 686 ºC	13.27	10.34	77.92
#5	1 bar / 686 ºC	13.35	10.39	77.83
#6	1 bar / 685 ºC	13.27	10.34	77.92
#7	1 bar / 675 ºC	12.42	9.81	78.99
#8	1 bar / 681 ºC	13.04	10.16	77.91
#9	1 bar / 674 ºC	12.52	9.92	79.23
#10	1 bar / 684 ºC	13.46	10.45	77.64
#11	1 bar / 689 ºC	13.54	10.48	77.40
#12	1 bar / 682 ºC	12.90	10.09	78.22
#13	1 bar / 656 ºC	7.13	5.91	82.89
#14	1 bar / 683 ºC	13.22	10.31	77.99
#15	1 bar / 683 ºC	13.23	10.31	77.93
#16	1 bar / 683 ºC	13.23	10.32	78.00
#17	1 bar / 687 ºC	13.30	10.32	77.59

4.1.2.5. Comparison with thermodynamic studies using different oxygenates and future perspectives

It is possible to compare the results obtained in simulations with results reported in the literature. Silva *et al.* [1], in their thermodynamic study of the steam reforming of glycerol, defined the H_2 yield in the same way that was defined in this study. In this way, it is viable to directly compare the yields obtained at the following operation conditions: ≈ 430 °C, 1 bar, ≈ 40 wt.% of water in the feed (molar water-to-glycerol feed ratio = 9; SCFR = 3). The study of the steam reforming of glycerol reported a value of 2.21 for the H_2 yield (η = 31.57 %) at the conditions previously mentioned. In the present study, for Composition #9 and at the same conditions, the H_2 yield was ≈ 2.88 (η = 23.00 %).

In the work by Montero *et al*. [22] (thermodynamic study of the steam reforming of ethanol) it is visible that the maximum efficiency of H_2 production (η ≈ 100 %), for a water content of ≈ 92 wt.% (SCFR = 16) and at 1 bar, was obtained at 530 °C. A similar temperature (522 °C) was necessary to obtain the maximum efficiency of H_2 (η = 98.40 %) in the OMWSR under the same conditions (for Composition #9). Still in the study of Montero *et al.* [22], it was possible to notice that, for both processes, the maximum H_2 yield per mole of OMW increases with SCFR, being very noticeable up to SCFR = 5. A similar situation occurs in this study for all compositions - see Fig. 4.4.

The simulations of Leal *et al.* [23] (steam reforming of glycerol) provide a maximum value of H_2 yield of 4.79 (η = 68.43 %) at 1 bar, 620 ºC and SCFR = 3 (approx. 40 wt.% of water in feed). At the same conditions, the H_2 yield in this study (for Composition #9) is equal to 6.52 (η = 52.08 %).

In conclusion, the H_2 yield per mole of organics in the feed obtained in this work (with OMW) was higher than for the other works (with different oxygenate compounds), under similar operation conditions.

In future works it will be necessary to study the effect of kinetics (catalysts), the sustainability of the process, the energy analysis (particularly taking into account how the water content affects the energy efficiency) and the possible combination of OMW with other components (like methane, methanol, ethanol, etc.) in the steam reforming process to enhance the energy efficiency of the process.

4.1.2.6. Coke formation

During the analysis of the effects of the variables under study, it was possible to verify the presence/absence of carbon in the equilibrium mixture. The formation of coke is a very important aspect, which influences the functioning of the reactor, as it affects the performance of the catalyst in a conventional reactor. It is possible to observe that coke formation decreases with increasing temperature and water content in the feed and with decreasing pressure - Fig. 4.6, although the effect of the latter variable is much less notorious. These effects can be explained based on Eq. (3.12)-(3.15) reported in Table 3.1. Coke formation also depends on the initial composition of OMW. In order to avoid coke formation, it is necessary to use at least 60 wt.% of water in the feed whatever the temperature or pressure (for all OMW compositions tested).

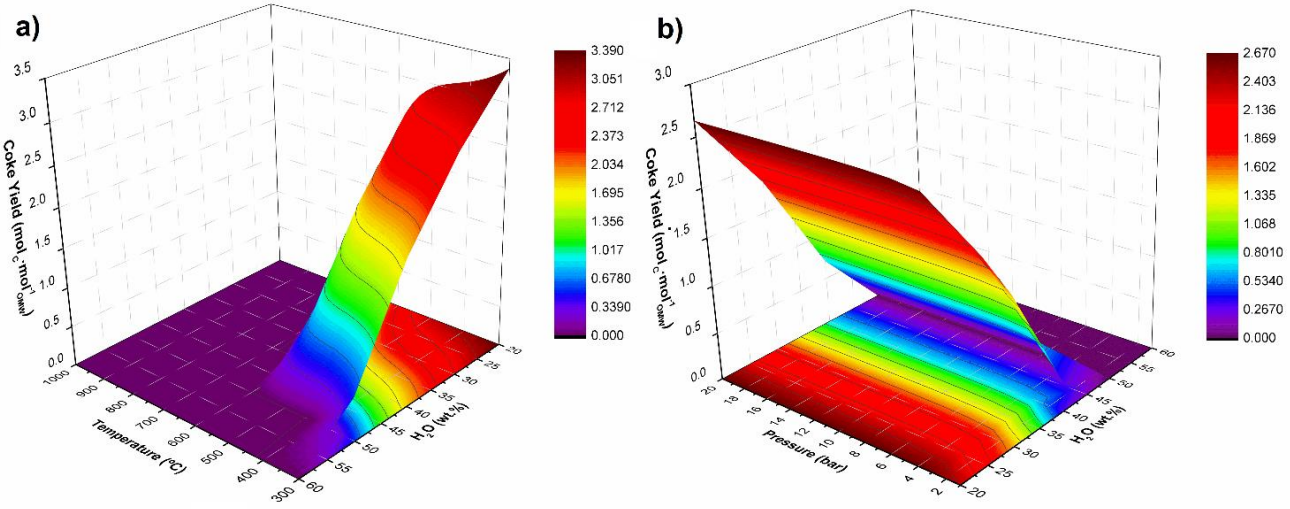

Fig. 4.6. Yield of coke as function of temperature and water content in the feed (wt.%) at 1 bar a) and as function of the pressure and water content in the feed (wt.%) at 600 °C b), in both cases for Composition #9.

4.1.3. Conclusions

A thermodynamic analysis was performed in order to study the effects of several variables on the OMWSR process. These variables were the temperature, the pressure, the weight content of water in the feed and the initial OMW composition, the latter being also a crucial parameter to take into account for industrial implementation.

The H_2 yield increases with the temperature up to a maximum value and then decreases, while it continuously decreases with the pressure, being 1 bar the optimum value. In opposition, higher water content in the feed allows to reach a higher yield of H_2, but it implies several operational problems (reactors with larger dimensions, low concentrations of organic species, etc.) and additional operating costs (water vaporization, reactor heating, etc.).

The optimum operating conditions for each OMW composition were determined. Despite each effluent allows achieving high yields of H_2, the optimum operating temperature must necessarily be high. It was also found a good agreement between the maximum H_2 yield obtained for each wastewater and the ones predicted based on their compositions. This allows in practice to predict how much H_2 can be obtained from a given waste of this agro-industrial activity. This work will allow a proper selection of the operating conditions for experimental tests, taking into consideration the initial composition of the OMW.

It is possible to conclude that coke formation increases with decreasing temperature and water content in the feed. Moreover, using a water content in the feed higher than 60 wt.% there is no limitation in terms of coking, whatever the temperature and pressure range used for the OMW compositions considered. So, it can be observed that by using the amount of water present in the effluent, without any pre-treatment, there is no limitation of coke formation.

Finally, since in the thermodynamic studies reported in the literature for other oxygenates the initial compositions were constituted by molecules with lower amounts of hydrogen atoms, the H_2 yields obtained were smaller as compared to those obtained herein with OMW, putting into evidence another important advantage of valorizing these agro-industrial effluents through steam reforming.

Subchapter 4.2. Steam reforming of olive mill wastewater with in situ hydrogen and carbon dioxide separation - thermodynamic analysis *

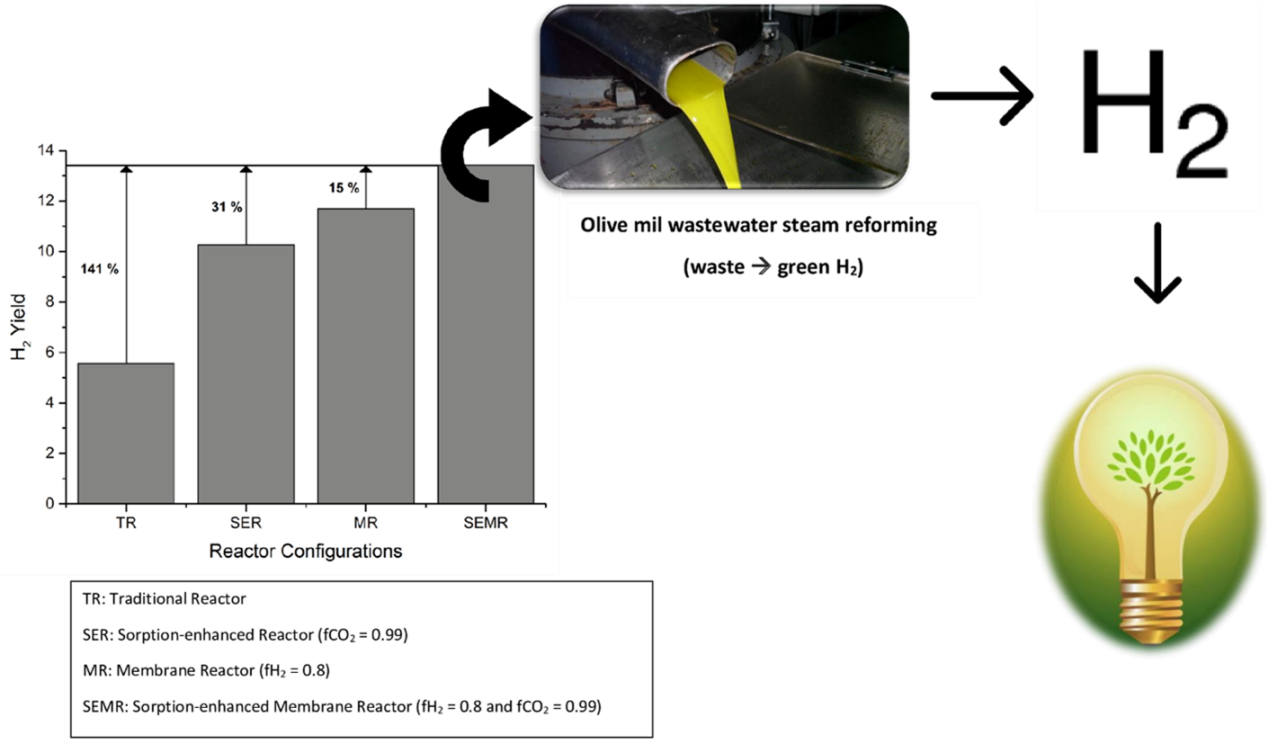

Highlights:

- OMW valorization for H_2 production via steam reforming.
- A thermodynamic analysis of a SEMR was performed.
- Higher temperatures and contents of water and lower pressures increase H_2 yield.
- Higher H_2/CO_2 removal fractions increase H_2 yield.
- Higher water content in the feed inhibits coke formation.

* The contents of this subchapter were adapted from: Rocha, C., M.A. Soria and L.M. Madeira, Steam reforming of olive oil mill wastewater with in situ hydrogen and carbon dioxide separation – Thermodynamic analysis. Fuel, 2017. 207: p. 449-460. (http://dx.doi.org/10.1016/j.fuel.2017.06.111)

Abstract:

A thermodynamic analysis of the steam reforming reaction of olive oil mill wastewater (OMW) with in situ carbon dioxide and hydrogen simultaneous removal was performed. The idea behind this is the integration of the reformer with a H_2 perm-selective membrane and a CO_2-sorbent in a hybrid multifunctional reactor. The simulations were performed at different temperatures (300-500 °C), pressures (1-11 bar), removal fractions of H_2 (0-0.8), removal fractions of CO_2 (0-0.99) and also for different water contents in the feed (20-92 wt.%). The results were compared in terms of performance reached for the different reactor configurations: traditional reactor (TR), membrane reactor (MR) with H_2 separation, sorption-enhanced reactor (SER) with CO_2 capture and sorption-enhanced membrane reactor (SEMR). For the SEMR, the optimum operation conditions were determined. An H_2 yield very close to the stoichiometric value of 13.54 was obtained at 1 bar, 500 °C, water content in the feed of 60-92 wt.% (steam-to-carbon feed ratio, SCFR = 2.1-16.0), $fCO_2 = 0.99$ and $fH_2 = 0.80$. The H_2 yield obtained in such optimum conditions corresponds to an enhancement of 141 % comparatively to the TR. Moreover, under these operation conditions, there is no significant production of CO_2, CO, CH_4 and coke.

4.2.1. Introduction

In this subchapter 4.2, a thermodynamic analysis of the OMWSR is done in a traditional reactor (TR), in a membrane reactor (MR), in a sorption-enhanced reactor (SER) and also in a sorption-enhanced membrane reactor (SEMR). For this purpose, the effect of the temperature, pressure, content of water in the feed, removal fraction of CO_2 and/or H_2 was assessed. In parallel, the study of the coke formation at different conditions was also performed.

This work will allow to draw primary conclusions about the sustainability of this technology for valorizing OMW using multifunctional reactors, as well as to drive the path for finding the best operation conditions for a typical composition of the effluent, in order to obtain the highest H_2 production.

The methods used in this subchapter are described in subchapter 3.1.

4.2.2. Results and discussion

4.2.2.1. Traditional reactor

Firstly, it was done a thermodynamic analysis of the effect of pressure, temperature and content of water in the feed in OMWSR without separation of any reaction product (H_2 and/or CO_2), i.e., considering a traditional reformer. This analysis was performed in the range of 1-11 bar and 300-500 °C. These effects have been studied modifying the content of water in the feed in the range of 20-92 wt.% (SCFR = 0.35-16).

Effect of pressure and temperature

The results obtained showed complete conversion of the organic components present in the OMW in the whole range of temperatures and pressures herein studied. For that reason, results will be presented in terms of yields for reaction products. Fig. 4.7 shows the variation of the yields for the gaseous species present in the outlet stream (CO, CH_4, H_2 and CO_2) as a function of the total pressure (Fig. 4.7a)) and temperature (Fig. 4.7b)). The H_2 yield increases with temperature and decreases with pressure. This last effect results from the fact that increased pressure in the system leads to a shift in the equilibrium to the side of the lesser number of gas moles to counter the pressure rise. Despite OMWSR has a smaller number of gas moles in the reagents side, it is very important to note that total conversion of all organic species has occurred; therefore, other reactions described in Table 3.1 have to be considered. The WGS reaction (Eq. (3.7)) is not affected by pressure. However, the methanation reaction (Eq. (3.8)), which is favored at high pressures, is responsible for the decrease in the H_2 production, increasing the yield of CH_4, as observed in Fig. 4.7a). The yield of CO_2 varies in the same

way as the one for H_2, the same occurring with CO - results with 60 wt.% of water in the feed (SCFR = 2.1). The CO_2 yield decreases because the CO concentration in the system decreases, as already mentioned, inhibiting the formation of CO_2 by the WGS reaction. The H_2/CO molar ratio (which is important to take into account for syngas applications) does not vary significantly with the total pressure (see Fig. B.1 in Appendix B).

Concerning the effect of temperature, and contrarily to the yield of CH_4, the yield of H_2, CO and CO_2 increase with the temperature. These behaviors can be explained considering both the methanation and the WGS, which are exothermic reactions, and thus favorable at low temperatures. With the temperature increase, the reaction that is more considerably inhibited (and consequently further shifted in the direction of the reactants) is the methanation one, which has a higher (absolute value) enthalpy of reaction: $\Delta H_r^{0\,°C}$ = -206 kJ·mol^{-1}. This explains the decrease in the yield of CH_4 and the increase of both H_2 and CO.

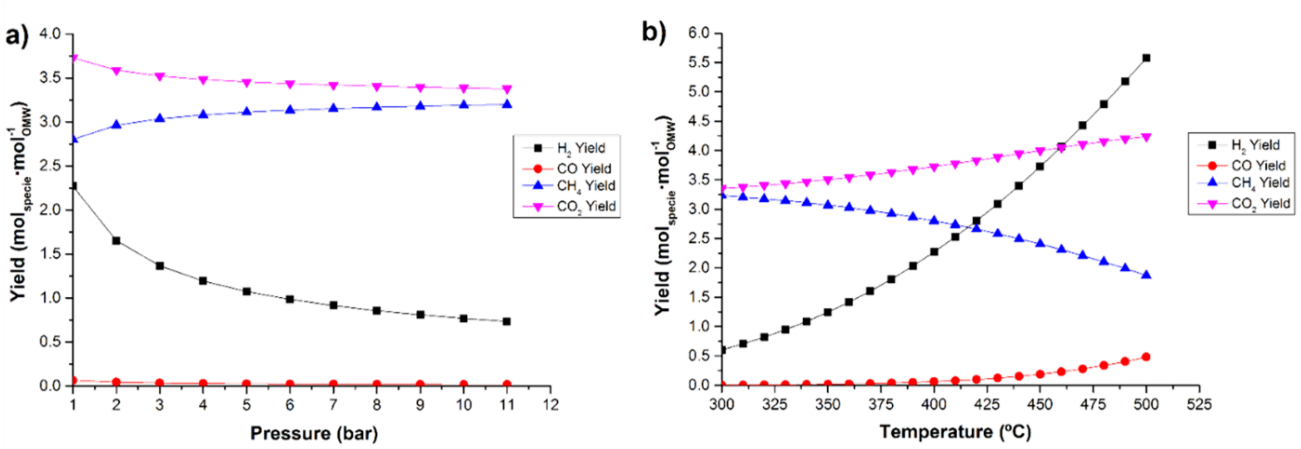

Fig. 4.7. Yield of H_2, CO, CH_4 and CO_2 in the thermodynamic equilibrium as a function of a) pressure at 400 °C with 60 wt.% of water in the feed (SCFR = 2.1) and b) temperature at 1 bar with 60 wt.% of water in the feed (SCFR = 2.1).

The variation of the CO_2 yield with temperature follows a trend similar to that of H_2, because the inhibition of methanation reaction (lower consumption of CO) allows a higher consumption of CO by mean of WGS reaction, increasing the CO_2 yield. The H_2/CO molar ratio decreases significantly with temperature (see Fig. B.2 in Appendix B).

Effect of water content in the feed

The yield of H_2 increases with increasing amounts of water in the feed (assessed in terms of SCFR) at any given pressure or temperature (Fig. 4.8). This phenomenon occurs because the increase of this variable causes the equilibrium shift of both the reverse of the methanation and WGS reactions according to Le Chatelier's principle. Thus, the CH_4 yield as well as the CO yield decrease at high contents of the water in the feed; consequently, the CO_2 yield also increases. Thus, the H_2/CO molar

ratio increases significantly with the increasing of water content in the feed (see Fig. B.3 in Appendix B). CH_4 production is low but it can be seen that there is a peak of CH_4 production for a given content of water in the feed (SCFR = 2.1 - see Fig. B.4 in Appendix B), which is due to the balance between the two reactions: WGS and methanation.

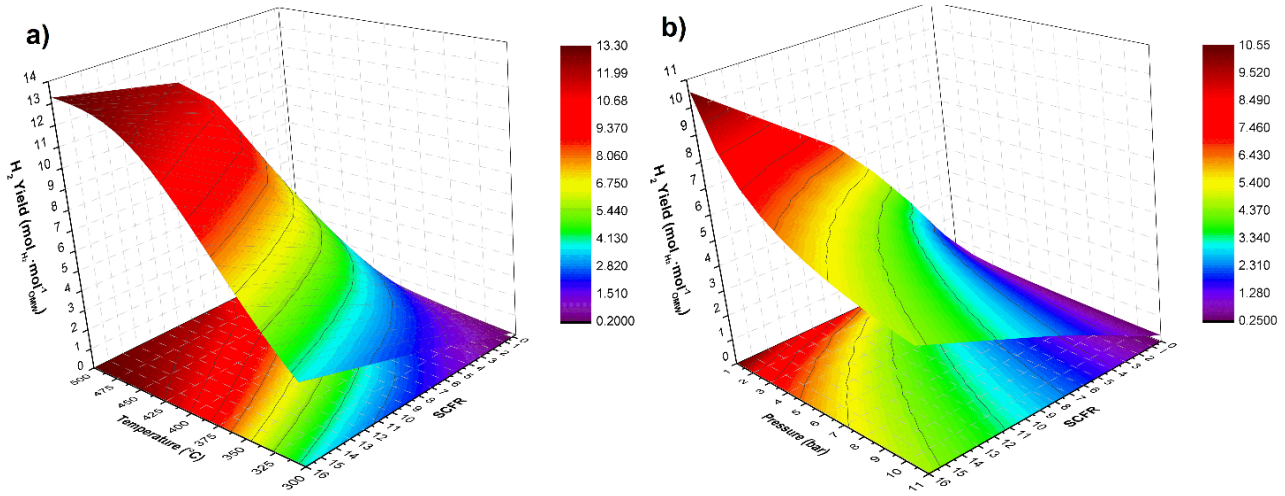

Fig. 4.8. Yield of H_2 in the thermodynamic equilibrium as function of a) temperature and content of water in the feed (SCFR) at 1 bar and b) pressure and content of water in the feed (SCFR) at 400 °C.

It can be seen in Fig. 4.8 that for low SCFR, the pressure/temperature effect in the hydrogen production is very low since the extent of the WGS and (reverse) methanation reactions is mainly controlled by the amount of water present in the system.

Coke formation

The formation of coke is a very important aspect, which influences the functioning of the reactor, as it affects the performance of the catalyst. In order to avoid coke formation, it is necessary to use at least 60 wt.% of water in the feed (SCFR = 2.1) whatever the temperature or pressure.

On the other hand, when the content of water fed is lower than 60 wt.% (SCFR = 2.1) it is possible to observe that coke formation increases although it decreases with increasing temperature (Fig. B.5a) in Appendix B) and with increasing pressure (Fig. B.5b) in Appendix B). In the range of temperatures (300-500 ºC) and pressures (1-11 bar) studied, CH_4 was always observed and therefore it can be anticipated that coke is formed from the reaction represented by Eq. (3.13). With the increase of the temperature, the reaction of Eq. (3.13) is more favored (while the other exothermic reactions for coke formation (Eq. (3.12)-(3.15) are less favored), apparently against the results obtained. However, it is important to emphasize that with the increase of temperature, the CH_4 formation (methanation reaction - Eq. (3.8) is inhibited, decreasing the extent of the reaction Eq. (3.13) and therefore the coke formation. In relation to pressure, it was also found that with the increase of pressure (Eq. (3.13)) is

not favored, decreasing the coke formation (in fact, this is the only coke formation reaction detrimentally affected by the total pressure). Thus, since coke formation decreases with temperature and pressure, one can infer that the reaction represented by Eq. (3.13) is predominant.

4.2.2.2. Membrane reactor or sorption-enhanced reactor

A thermodynamic analysis of the effect of separating H_2 or CO_2 was performed (through an H_2 perm-selective membrane - MR - or CO_2 sorbent - SER -, respectively). The removal of one of these two components (reaction products) aims to increase the H_2 yield at low temperatures and inhibit the production of by-products, which are limitations in the case of a TR. This analysis was performed in the same ranges of conditions as before, H_2 removal fractions of 0-0.80 and CO_2 removal fractions of 0-0.99. Again, complete conversion of all organic species present in the OMW was observed for all the range of conditions analysed.

Effect of the H_2 or CO_2 removal fractions

The variation of the yield of H_2 with temperature/pressure and the H_2 removal fraction (for a membrane reactor) or fed CaO/OMW molar ratio (for a sorption-enhanced reactor) is represented in Fig. 4.9 and Fig. 4.10, respectively. The yield of H_2 increases with the fraction of H_2 or CO_2 removal, whatever the temperature and pressure. It can be observed that for 60 wt.% (SCFR = 2.1) of water in the feed, higher H_2 yields can be achieved by separating H_2 from the reaction medium instead of CO_2 (with the same removal fraction), at the same temperature and pressure. This behavior is associated with the inhibition of the production of CH_4 (always lower than in a TR) by means of the methanation reaction where H_2 is involved as a reactant. However, since CO_2 is not present in this reaction, its removal does not directly influence the methanation. When CO_2 is captured, the equilibrium of the WGS reaction is shifted towards the production of more CO_2, and inherently H_2, with CO consumption, and thus the yield of CH_4 is higher in a SER than in a MR (data not shown). When H_2 is removed from the reactor, it does not only directly affect the WGS reaction but also the methanation reaction. Therefore, higher H_2 yields were obtained in the MR than in the SER. For example, at 500 °C, 1 bar, with a content of water in the feed of 60 wt.%, a H_2 yield of 11.70 was obtained in a MR with fH_2 = 0.8 while it was only 6.99 in a SER with fCO_2 = 0.8 (CaO/OMW = 4).

In Fig. 4.9 and Fig. 4.10 it is possible to verify the effect of the H_2/CO_2 removal from the system in the H_2 yield, for different temperatures (Fig. 4.9a) and Fig. 4.10a)) and pressures (Fig. 4.9b) and Fig. 4.10b)). It is important to emphasize that there are some plateaus in the graphs of Fig. 4.10, since from a certain value of the CaO/OMW molar ratio in the feed, fCO_2 is always close to 1. This happens because, for different temperatures/pressures, different molar ratios of CaO/OMW are required to obtain the same fCO_2. As shown in Fig. 4.10, higher temperatures/lower pressures required higher

molar ratios of CaO/OMW to obtain a determined fCO_2. In the operating zones defined by such plateaus, and for a given temperature/pressure, the increase of the amount of the CaO in the feed does not influence the H_2 yield because all the CO_2 produced is removed from the reactor with a lower molar ratio of CaO/OMW.

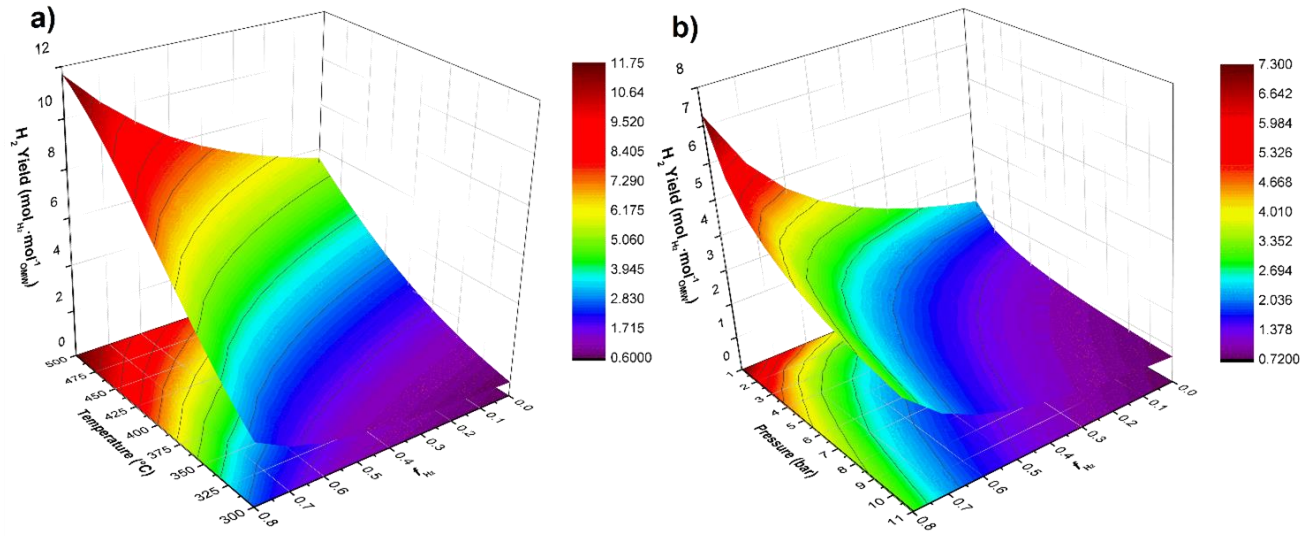

Fig. 4.9. Yield of H_2 in the thermodynamic equilibrium as function of: a) temperature and hydrogen removal fraction at 1 bar, with 60 wt.% of water in the feed (SCFR = 2.1) and b) pressure and hydrogen removal fraction at 400 °C, with 60 wt.% of water in the feed (SCFR = 2.1).

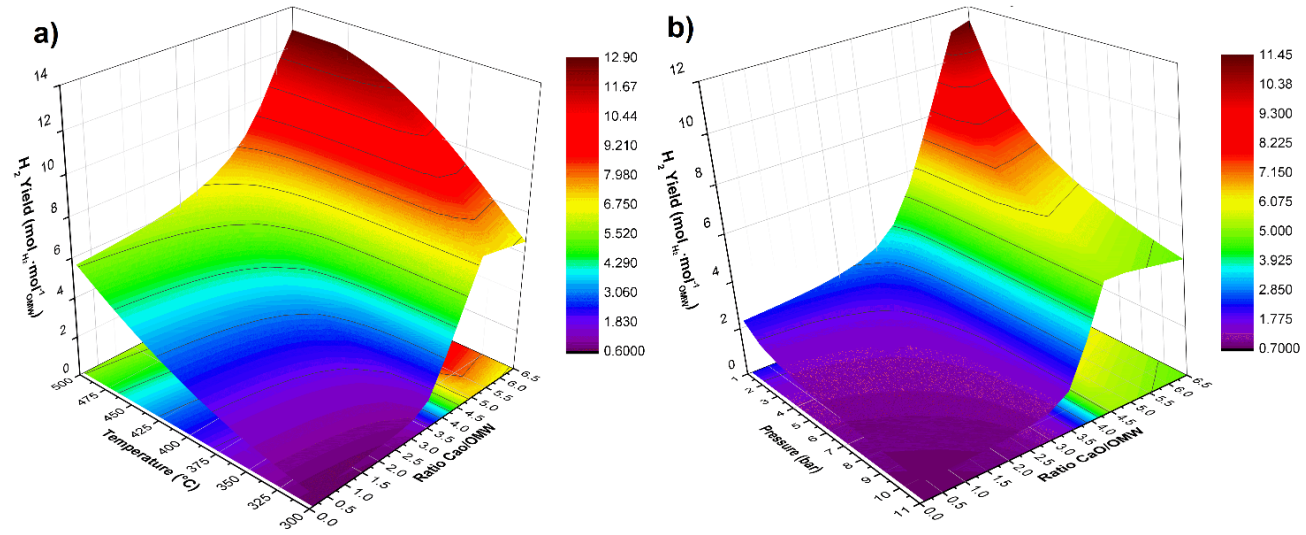

Fig. 4.10. Yield of H_2 in the thermodynamic equilibrium as function of a) temperature and molar ratio of CaO/OMW in the feed at 1 bar, with 60 wt.% of water in the feed (SCFR = 2.1) and b) pressure and molar ratio of CaO/OMW in the feed at 400 °C, with 60 wt.% of water in the feed (SCFR = 2.1).

Finally, it is possible to say that when higher H_2 or CO_2 removals are applied, more CO is consumed through WGS and so lower CO yields are obtained (data not shown). It is possible to verify that the purity of H_2 in the retentate stream increases with CO_2 removal and decreases with H_2 removal.

Coke formation

The formation of coke was a target of study as well, since it is an undesired product that may affect the performance of the catalyst, membrane or sorbent during operation of the MR or SER. When H_2 or CO_2 were removed from the reaction medium, opposite effects were observed - Fig. 4.11. The formation of coke decreases with the fraction of CO_2 removed from the system (Fig. 4.11a)) - thus reaction in Eq. (3.12) is not predominant) while when H_2 is removed more coke is produced (Fig. 4.11b)) - and so reactions in Eqs. (3.14) and (3.15) are also not predominant). So, most of the coke is formed from CH_4 through the reaction described in Eq. (3.13), as anticipated above, in the range of conditions where the formation of CH_4 is not completely inhibited.

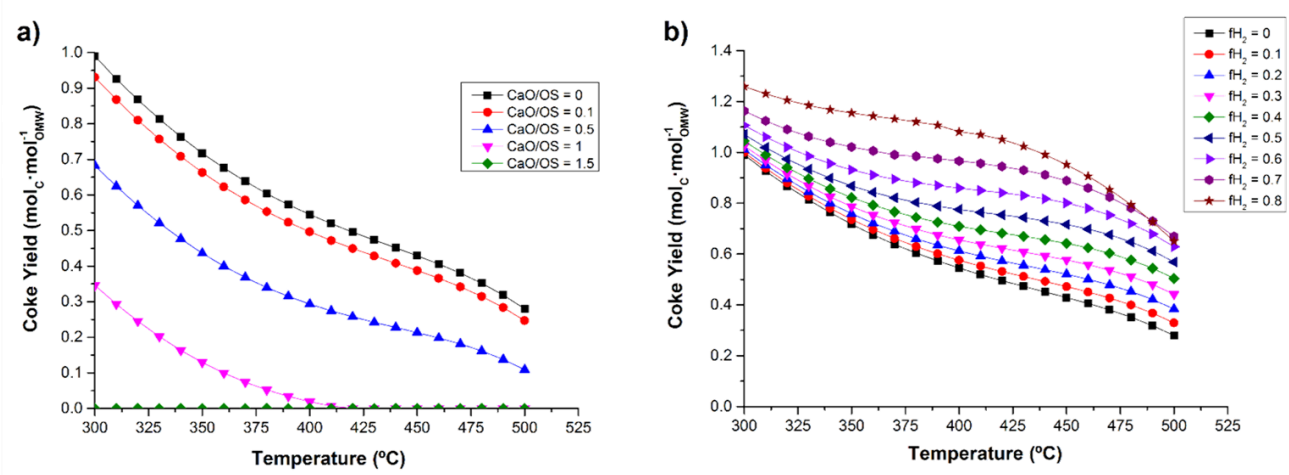

Fig. 4.11. Yield of coke as function of a) temperature and molar ratio of CaO/OMW at 1 bar with 50 wt.% of water in the feed (SCFR = 1.4) and as function of b) temperature and fH_2 at 1 bar with 50 wt.% of water in the feed (SCFR = 1.4).

4.2.2.3. Sorption-enhanced membrane reactor

In this subchapter the effect of the simultaneous removal of H_2 and CO_2 during OMWSR, in a SEMR, as well as the influence of the operating conditions is determined. In addition, an analysis of the limits of operation conditions for coke formation is carried out. During the simulations for the SEMR, the CO_2 removal fraction was kept at 0.99 (implying, however, different molar ratios of CaO/OMW for different contents of water in the feed) and the H_2 removal was kept at 0.80 (maximum admissible removal fraction possible in practice) for different operation conditions. Once again, complete organic species conversion was observed for all the range of conditions analysed.

Effect of temperature

For H_2 removal of 80 % and CO_2 removal of 99 % (pre-breakthrough of CO_2 in a continuous sorption-enhanced reactor), the theoretical maximum H_2 yield of 13.54 is almost obtained in cases where the water content in the feed is higher than 60 wt.% (SCFR = 2.1) - Fig. 4.12a).

As in the case of the MR, between 300 and 500 ºC it is observed that the H_2 yield reaches a maximum and then decreases when the content of water fed is higher than 83.2 % wt. (SCFR = 6.9) (see Fig. B.6 in Appendix B). This maximum happens because the WGS reaction is inhibited by the increase of the temperature as well as the methanation reaction. However, the methanation reaction is completely inhibited at lower temperatures as compared to the WGS. Thus, the yield of H_2 increases until the WGS reaction is inhibited as well. At this point, the RWGS is predominant and the formation of H_2 decreases. The temperature at which such maximum occurs depends on the water content as this species contributes to the inhibition of the RWGS reaction [24].

Therefore, from the thermodynamic point of view, the use of such reactor configuration permits to operate at temperatures around 400 °C, although higher contents of water in the feed are required (Fig. 4.12b)).

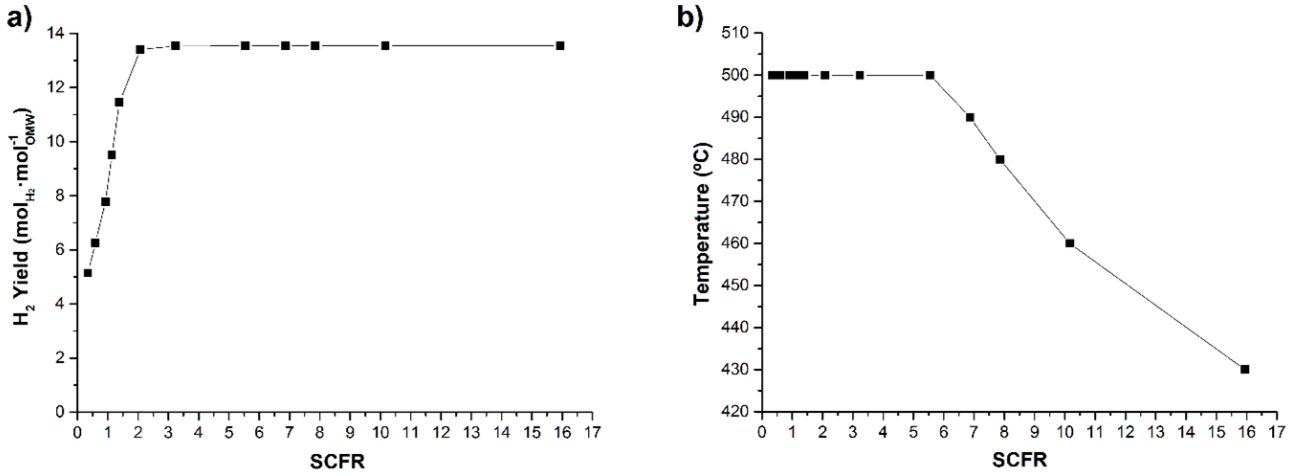

Fig. 4.12. Yield of H_2 in the thermodynamic equilibrium as a function of the content of water in the feed (SCFR) at 1 bar, fH_2 = 0.80 and fCO_2 = 0.99 a) and optimum temperature as a function of the content of water in the feed (SCFR) at 1 bar, fH_2 = 0.80 and fCO_2 = 0.99 b); in both cases the values correspond to the maximum H_2 yield.

By comparing the SEMR with the other reactor configurations in terms of H_2 yield, it was found that the SEMR presents better performance than both the MR and SER and much better performance than the TR. For example, in the TR, at 500 °C, 1 bar and 60 wt.% of water in the feed (SCFR = 2.1), a H_2 yield of 5.58 was reached. Under the same conditions, in the SER with fCO_2 = 0.99, MR with fH_2 = 0.80, and SEMR with fCO_2 = 0.99 and fH_2 = 0.80, H_2 yields of 10.26, 11.70, and 13.42 were observed, respectively. This corresponds to an enhancement of the H_2 yield of approximately 141 %

when the SEMR is used instead of the TR, an enhancement of approximately 31 % when the SEMR is used instead of the SER and an increase of about 15 % when the SEMR is used instead of the MR - see Fig. 4.13a).

However, these differences become much bigger at lower temperatures. For example, at 300 °C, 1 bar and 60 wt.% of water in the feed (SCFR = 2.1), a H_2 yield of 12.83 (CO yield = 0.00 ; CO_2 yield = 0.00 ; CH_4 yield = 0.18) was obtained in the SEMR with fCO_2 = 0.99 and fH_2 = 0.80 while an H_2 yield of 2.03 (CO yield = 0.00 ; CO_2 yield = 0.01 ; CH_4 yield = 2.88) and 2.60 (CO yield = 0.01 ; CO_2 yield = 0.00 ; CH_4 yield = 2.73) were observed in the SER (fCO_2 = 0.99) and MR (fH_2 = 0.80), respectively, corresponding to improvements of 532 % and 393 % when using the hybrid SEMR. Although improvements reached with the SEMR are more noticeable at lower temperatures, under such conditions longer reactors and longer and/or more permeable membranes are required to compensate the decreased reaction and permeation rates [25].

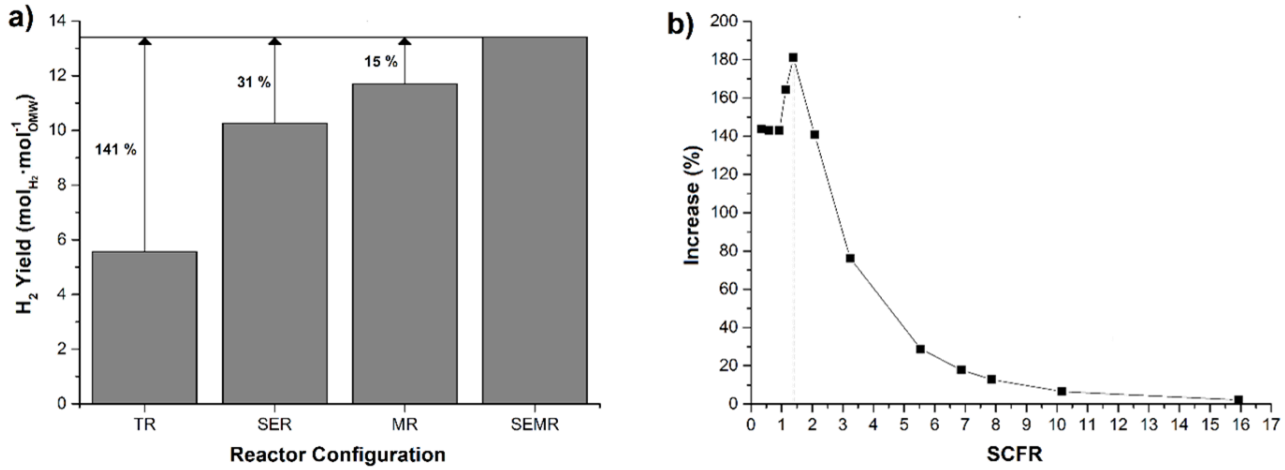

Fig. 4.13. Enhancement of the H_2 yield with the SEMR as compared to the other reactor configurations at 500 °C, 1 bar and 60 wt.% of water in the feed (SCFR = 2.1) a) and the percentage increase of maximum yield of H_2 from TR to SEMR (fCO_2 = 0.99 and fH_2 = 0.80) as a function of the content of water in the feed (SCFR) at 1 bar with different optimum temperatures b).

Effect of the content of water in the feed

In terms of H_2 production, the increase of the content of water in the feed enhances the production of H_2 as described above; this is particularly noticed at lower H_2 and CO_2 removal fractions (data not shown).

Concerning the effect of increasing H_2 and CO_2 removal fractions, for a given water content, higher removal fractions of H_2 and CO_2 lead to higher H_2 production and low CH_4 formation. Moreover, this enhancement is more pronounced for less favorable conditions, for example, low content of water in the feed. In Fig. 4.13b) it is possible to visualize the percentage increase of maximum yield of H_2 from

the TR to the SEMR (1 bar, with fCO_2 = 0.99 and fH_2 = 0.80) as function of the content of water in the feed. Note that for different SCFR, different optimum temperatures are defined.

In summary, considering again the case in which fCO_2 = 0.99 and fH_2 = 0.80, when the content of water in the feed increases from 20 wt.% (SCFR = 0.35) to 92 wt.% (SCFR = 15.9) (at 500 °C and 1bar), the H_2 yield increased from 5.15 to 13.54, while the CH_4 yield decreased from 0.94 to 0.00 (see Fig. B.7 in Appendix B). However, high water contents may lead to catalyst and sorbent deactivation due to pore blocking [26] and diminution of the surface area [27-29], as well as to higher operation costs due to steam generation.

Effect of pressure

When high pressures are used, the yield of H_2 suffers a negative effect (as mentioned before in previous subchapters for TR, SER and MR). However, for very high H_2 and CO_2 removal fractions, the H_2 yield remains practically constant for all the range of pressures considered [content of water higher than 50 wt.% (SCFR = 1.4) at 400 °C, with fCO_2 = 0.99 and fH_2 = 0.80 - Fig. 4.14].

For the SEMR, a high H_2 yield is observed even at high pressures. It is important to refer that the simulations do not take into account the effect of pressure on the removal of both H_2 (through a membrane) and CO_2 (by mean of CaO) as well as in the reaction rate. It is known that pressure influences the capacity for CO_2 sorption and the driving-force for H_2 permeation through a H_2 perm-selective membrane [30]. Thus, higher pressures lead to higher CO_2 and H_2 removal fractions in a real system, meaning that higher H_2 and CO_2 removals could be attained and inherently higher H_2 yields. In the case of fCO_2= 0.99 and fH_2 = 0.80 (SEMR), when the pressure increases from 1 to 11 bar, the H_2 yield decreases much less (actually it is practically constant) than for lower H_2 and/or CO_2 removals. Consequently, the use of high pressures becomes advantageous in a SEMR.

Therefore, the advantages of the SEMR are far more perceptible at lower temperatures (300-400 °C) and also at higher pressures (5-11 bar), which brings several advantages when membranes are used because the H_2 driving-force for permeation increases.

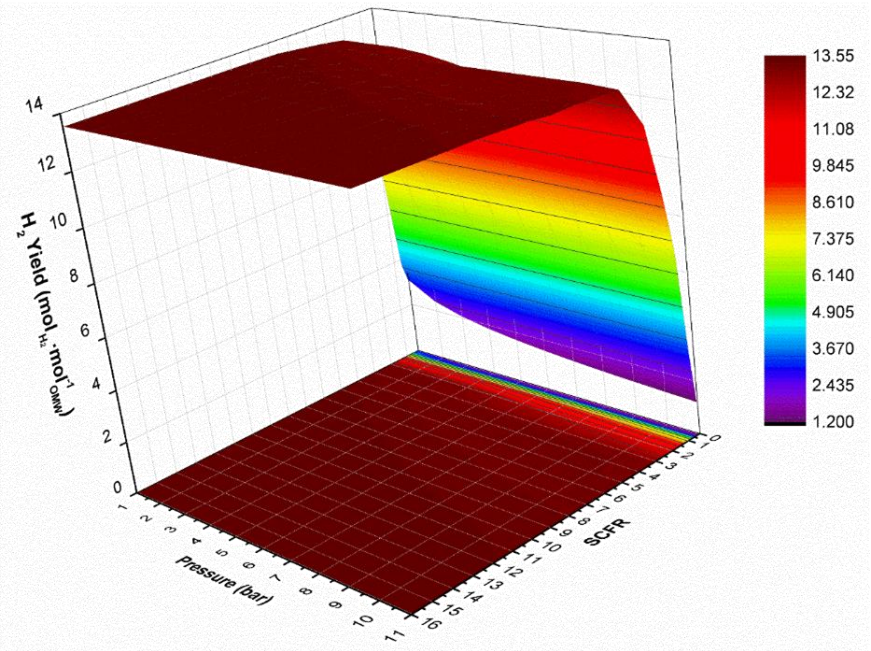

Fig. 4.14. Yield of H_2 in the thermodynamic equilibrium as a function of the content of water in the feed (SCFR) and pressure at 400 °C, with fH_2 = 0.80 and fCO_2 = 0.99 (SEMR).

Coke formation

For coke formation in the SEMR it is expected that when both products (H_2 and CO_2) are removed from the reaction medium, an equilibrium between opposite effects is reached (cf. explanation in subchapter 4.2.2.2). That was in fact observed, being that at fCO_2 = 0.99 and fH_2= 0.80 a 40 wt.% (SCFR = 0.92) of water content in the feed was enough to completely inhibit coke formation for all the range of temperatures and pressures analysed. The content of water required for the same purpose was 30 wt.% for a SER (fCO_2 = 0.99) and 60 wt.% for a MR (fH_2 = 0.8).

Optimum operation conditions

The maximum H_2 yields obtained in the simulations (for all water contents in the feed and 1 bar) for the TR, SER (fCO_2 = 0.99), MR (fH_2 = 0.80) and SEMR (fCO_2 = 0.99 and fH_2 = 0.80) were compared with the maximum yield theoretically calculated (H_2 yield = 13.54) assuming that there are no secondary reactions. Such maximum yield was obtained from Eq. (3.5) and taking into account the molar fraction of each chemical species present in the OMW feed - Table 3.3. Results for the maximum H_2 yields for each reactor configuration are compiled in Table 4.3. It can be seen that an efficiency value $\left(\eta = \frac{\text{Maximum Simulated Yield}}{\text{Maximum Theoretical Yield}} \times 100\right)$ close to 100 % is reached for the SEMR when the content of water in the feed is higher than 50 wt.% (SCFR = 1.4). However, it is important to note that this simulated maximum yield is sometimes obtained at uncomfortable operation conditions (large amounts of water - thus leading to reactor size problems, low concentrations of organic species) and large operations costs (due to reactor heating, water vaporization). The largest increase of H_2 yield

from the TR to SEMR (fCO_2 = 0.99 and fH_2 = 0.80) is reached when the content of water in the feed is 50 wt.% (SCFR = 1.4) - Fig. 4.13b). However, it is possible to verify that for this content of water in the feed, the efficiency value in the SEMR is only 85 % and the purity of H_2 in the retentate stream is 79.44 % - Table 4.3. Analyzing such table, it is possible to determine the best operation conditions (from a thermodynamic point of view) for the OMWSR in a SEMR: fCO_2 = 0.99 and fH_2 = 0.80, 500 °C, 1 bar and content of water of 60 wt.% (SCFR = 2.1). With these conditions, the efficiency and the H_2 purity in the retentate stream are very high and the increase of the H_2 yield from the TR to the SEMR is 141 %. However, to obtain, in practice, fH_2 = 0.80, and to minimize the energy cost of the process, it is suggested to use a pressure between 4-7 bar and a temperature between 400-500 °C. The OMWSR in a SEMR (fCO_2 = 0.99 and fH_2 = 0.80) with a 60 wt.% of water in the feed (SCFR = 2.1) reaches the following efficiencies and purities at 400 °C and 7 bar: η_{SEMR} = 91.86 % and $H_{2\,(Purity)}$ in the retentate stream = 90.02 %. It is also worth saying that practically all CO_2 is sorbed until the sorbent reaches saturation, so fCO_2 = 0.99 is a real condition, and with a content of water in the feed close to 60 wt% (SCFR = 2.1), it is not necessary to vaporize a large amount of water of the initial OMW stream (low energy cost with the pre-treatment). Despite this decrease in the content of water is small (compared to the typical initial content of water in the raw OMW - 80-92 wt.%), the hypothetical pre-treatment will minimize several operational problems (reactors with larger dimensions) and minimize additional operation costs after the use of this technology (water vaporization).

As the purity of H_2 in a SEMR is affected by the removals of CO_2 and H_2, it was verified the following order of purity in the retentate side, for a content of water in the feed between 50-80 wt.%: $H_{2\,Purity\text{-}MR} < H_{2\,Purity\text{-}TR} < H_{2\,Purity\text{-}SER} < H_{2\,Purity\text{-}SEMR}$. For the other contents of water in the feed, it was observed the following order: $H_{2\,Purity\text{-}MR} < H_{2\,Purity\text{-}TR} < H_{2\,Purity\text{-}SEMR} < H_{2\,Purity\text{-}SER.}$ However, it is worth remembering that in the case of MR and SEMR there is a permeate stream that could be free of CH_4 and COx using a membrane completely selective towards H_2.

The optimum operation conditions that were herein identified provide helpful information because they allow determining, after comparison with experimental data (collected or reported in the literature), how far from the thermodynamic equilibrium one is; this way one can perceive how to modify the conditions to improve the process performance.

In addition, the energy analysis of the overall process (i.e. comprising both wastewater concentration and steam reforming) is suggested as future work in order to address the practical application of the technology. With this analysis, it will be possible to assess the best operation conditions in order to have an economically viable process.

Table 4.3 - Maximum simulated yield of H_2 and operation temperature for TR, SER, MR and SEMR. η and H_2 purity in SEMR.

Maximum Theoretical Yield 13.54						
Pressure 1 bar						
wt.% of water in the feed (SCFR)	**Simulated Yield of TR**	**OT* of TR (°C)**	**Simulated Yield of SER[a)]**	**OT* of SER (°C)**	**Simulated Yield of MR[b)]**	**OT* of MR (°C)**
20 (0.35)	2.11	500	2.36	500	4.81	500
30 (0.59)	2.60		3.29		5.87	
40 (0.92)	3.20		5.36		7.29	
45 (1.1)	3.60		6.25		8.20	
50 (1.4)	4.08		7.47		9.28	
60 (2.1)	5.57		10.26		11.70	
70 (3.2)	7.68		12.63		13.05	
80 (5.6)	10.51		13.43		13.40	
83.2 (6.9)	11.49		13.48		13.47	
85 (7.9)	12.00		13.51		13.47	480
88 (10)	12.71		13.53		13.49	460
92 (16)	13.26		13.54		13.52	430
wt.% of water in the feed (SCFR)	**Simulated Yield of SEMR[c)]**	**OT* of SEMR (°C)**	**η_{SEMR} (%)**	**H_2 $_{PuritySEMR}$ (%)[d)]**		
20 (0.35)	5.14	500	37.99	51.26		
30 (0.59)	6.27		46.27	51.49		
40 (0.92)	7.78		57.46	51.51		
45 (1.1)	9.51		70.24	63.54		
50 (1.4)	11.46		84.61	79.44		
60 (2.1)	13.42		99.05	96.64		
70 (3.2)	13.53		99.91	96.67		
80 (5.6)	13.54		100	96.67		
83.2 (6.9)	13.54		100	96.67		
85 (7.9)	13.54	480	100	96.67		
88 (10)	13.54	460	100	96.67		
92 (16)	13.54	430	100	96.67		

* Operation Temperature;

[a)] fCO_2 = 0.99. [b)] fH_2 = 0.80. [c)] fCO_2 = 0.99, fH_2 = 0.80. [d)] In the retentate stream (dry basis).

4.2.3. Conclusions

A thermodynamic analysis was performed in order to study the effects of several variables on the OMWSR with in situ H_2 and CO_2 separation. These variables were the temperature, the pressure, the content of water in the feed, the removal fractions of H_2 and/or CO_2. The optimum operation conditions were determined in a SEMR to maximize the H_2 production via steam reforming of OMW, in the perspective of its valorization (from waste to energy).

The H_2 yield increases with the temperature up to a maximum value (in the case of the SEMR) while the pressure has a negative effect, with the optimum pressure being the minimum possible (1 bar in this case). In opposition, the content of water in the feed, the H_2 removal and the CO_2 removal increase H_2 yield. The optimum temperature depends on the water content in the feed and the H_2 and CO_2 removal.

At 500 °C, 1 bar, 60 wt.% of water in the feed (SCFR = 2.1) an fCO_2 = 0.99 and fH_2 = 0.80, the H_2 yield was 13.42 (very close to the maximum theoretical value). Regarding CH_4 and CO, no considerable production was observed under such conditions. Even though the SEMR presents higher H_2 production than the SER and the MR, the difference is not very high at 500 ºC; an increase of 31 and 15 % respectively. Nevertheless, compared to the TR the H_2 yield increases by 141% at the same temperature. Also, at high temperatures, the yields of the by-products are similar for the different reactor configurations. However, these differences become much bigger with the decrease of temperature. At 300 °C, 1 bar and 60 wt.% of water in the feed (SCFR = 2.1), a H_2 yield of 12.83 was obtained in the SEMR with fCO_2 = 0.99 and fH_2 = 0.80, while H_2 yields of 2.03 and 2.60 were observed in the SER (fCO_2 = 0.99) and MR (fH_2 = 0.80), respectively, corresponding to improvements of 532 % and 393 % when using the hybrid SEMR. Therefore, the advantages of the SEMR are more perceptible at lower temperatures and so, this hybrid reactor configuration can be operated at lower operation temperatures for the OMWSR. However, at lower temperatures, longer reactors and longer and/or more permeable membranes would be necessary to compensate the decreased reaction and permeation rates.

Although in a TR lower pressures are preferable (from the thermodynamic point of view), high pressures almost do not affect the H_2 yield in a SEMR, which is advantageous due to the increased driving-force for H_2 permeation.

To have no formation of coke in the SEMR it is necessary a minimum content of water in the feed of 40 wt.% (SCFR = 0.92). The use of the SEMR in OMWSR allows reaching high H_2 yields with low operation temperatures and high pressures, along with the production of H_2 with high purity.

Notation and Glossary

List of Variables

fCO_2	Removal fraction of CO_2 (dimensionless)
fH_2	Removal fraction of H_2 (dimensionless)
Y_i	Yield of species *i* ($mol_{component\ i} \cdot mol^{-1}_{OMW}$)

List of Acronyms

MR	Membrane reactor
OMW	Olive oil mill wastewater
OMWSR	Olive oil mill wastewater steam reforming
RWGS	Reverse water-gas shift
SCFR	Steam-to-carbon feed ratio
SEMR	Sorption-enhanced membrane reactor
SER	Sorption-enhanced reactor
TR	Traditional reactor
WGS	Water-gas shift

References

[1] Silva, J.M., M.A. Soria and L.M. Madeira, Thermodynamic analysis of Glycerol Steam Reforming for hydrogen production with in situ hydrogen and carbon dioxide separation. Journal of Power Sources, 2015. 273: p. 423-430.

[2] Katsoyannos, E., A. Hatzikioseyian, E. Remoundaki and M. Tsezos, Photocatalytic treatment of olive mill wastewaters (OMW) in pilot scale, in 13th International Symposium on Pollution and its Impact on Life in Mediterranean Region. 2005, National Technical University of Athens Greece.

[3] Nasr, B., B. Ahmed and G. Abdellatif, Fenton treatment of olive oil mill wastewater-applicability of the method and parameters effects on the degradation process. Journal of Environmental Sciences, 2004. 16: p. 942-944.

[4] Gebreyohannes, A.Y., R. Mazzei and L. Giorno, Trends and current practices of olive mill wastewater treatment: Application of integrated membrane process and its future perspective. Separation and Purification Technology, 2016. 162: p. 45-60.

[5] Wiesman, Z., Desert Olive Oil Cultivation: Advanced Bio Technologies. 2009: Elsevier.

[6] Roig, A., M.L. Cayuela and M.A. Sánchez-Monedero, An overview on olive mill wastes and their valorisation methods. Waste Management, 2006. 26(9): p. 960-969.

[7] Caputo, A.C., F. Scacchia and P.M. Pelagagge, Disposal of by-products in olive oil industry: waste-to-energy solutions. Applied Thermal Engineering, 2003. 23(2): p. 197-214.

[8] El-Abbassi, A., H. Kiai and A. Hafidi, Phenolic profile and antioxidant activities of olive mill wastewater. Food Chemistry, 2012. 132(1): p. 406-412.

[9] Vlyssides, A.G., M. Loizides and P.K. Karlis, Integrated strategic approach for reusing olive oil extraction by-products. Journal of Cleaner Production, 2004. 12(6): p. 603-611.

[10] Tosti, S., C. Accetta, M. Fabbricino, M. Sansovini and L. Pontoni, Reforming of olive mill wastewater through a Pd-membrane reactor. International Journal of Hydrogen Energy, 2013. 38(25): p. 10252-10259.

[11] Dermeche, S., M. Nadour, C. Larroche, F. Moulti-Mati and P. Michaud, Olive mill wastes: Biochemical characterizations and valorization strategies. Process Biochemistry, 2013. 48(10): p. 1532-1552.

[12] Aktas, E.S., S. Imre and L. Ersoy, Characterization and lime treatment of olive mill wastewater. Water Research, 2001. 35(9): p. 2336-2340.

[13] Daâssi, D., J. Lozano-Sánchez, I. Borrás-Linares, L. Belbahri, S. Woodward, H. Zouari-Mechichi, T. Mechichi, M. Nasri and A. Segura-Carretero, Olive oil mill wastewaters: Phenolic content characterization during degradation by Coriolopsis gallica. Chemosphere, 2014. 113: p. 62-70.

[14] Bouknana, D., B. Hammouti, R. Salghi, S. Jodeh, Z. A., I. Warad, A. Aouniti and M. Sbaa, Physicochemical Characterization of Olive Oil Mill Wastewaters in the eastern region of Morocco. Journal of Materials and Environmental Science, 2014. 4: p. 1039-1058.

[15] Erog˘lu, E., I. Erog˘lu, U. Gu¨ndu¨z and M. Yu¨cel, Effect of clay pretreatment on photofermentative hydrogen production from olive mill wastewater. Bioresource Technology, 2008. 99: p. 6799-6808.

[16] Gameiro, T., F. Sousa, F.C. Silva, C. Couras, M. Lopes, V. Louros, H. Nadais and I. Capela, Olive Oil Mill Wastewater to Volatile Fatty Acids: Statistical Study of the Acidogenic Process. Water, Air, & Soil Pollution, 2015. 226(4): p. 115.

[17] Alsafadi, D. and O. Al-Mashaqbeh, A one-stage cultivation process for the production of poly-3-(hydroxybutyrate-co-hydroxyvalerate) from olive mill wastewater by Haloferax mediterranei. New Biotechnology, 2017. 34: p. 47-53.

[18] Campanari, S., F.A. e Silva, L. Bertin, M. Villano and M. Majone, Effect of the organic loading rate on the production of polyhydroxyalkanoates in a multi-stage process aimed at the valorization of olive oil mill wastewater. International Journal of Biological Macromolecules, 2014. 71: p. 34-41.

[19] Faraloni, C., A. Ena, C. Pintucci and G. Torzillo, Enhanced hydrogen production by means of sulfur-deprived Chlamydomonas reinhardtii cultures grown in pretreated olive mill wastewater. International Journal of Hydrogen Energy, 2011. 36(10): p. 5920-5931.

[20] Hajjouji, H.E., J.R. Bailly, P. Winterton, G. Merlina, J.C. Revel and M. Hafidi, Chemical and spectroscopic analysis of olive mill waste water during a biological treatment. Bioresource Technology, 2008. 99(11): p. 4958-4965.

[21] Rocha, C., M.A. Soria and L.M. Madeira, Steam reforming of olive oil mill wastewater with in situ hydrogen and carbon dioxide separation - Thermodynamic analysis. Fuel, 2017. 207: p. 449-460.

[22] Montero, C., L. Oar-Arteta, A. Remiro, A. Arandia, J. Bilbao and A.G. Gayubo, Thermodynamic comparison between bio-oil and ethanol steam reforming. International Journal of Hydrogen Energy, 2015. 40(46): p. 15963-15971.

[23] Leal, A.L., M.A. Soria and L.M. Madeira, Autothermal reforming of impure glycerol for H2 production: Thermodynamic study including in situ CO2 and/or H2 separation. International Journal of Hydrogen Energy, 2016. 41(4): p. 2607-2620.

[24] Rocha, C., M.A. Soria and L.M. Madeira, Thermodynamic analysis of olive oil mill wastewater steam reforming. Journal of the Energy Institute, 2019. 92(5): p. 1599-1609.

[25] Chang, A.C.C., W.-H. Lin, K.-H. Lin, C.-H. Hsiao, H.-H. Chen and H.-F. Chang, Reforming of glycerol for producing hydrogen in a Pd/Ag membrane reactor. International Journal of Hydrogen Energy, 2012. 37(17): p. 13110-13117.

[26] Martunus, Z. Helwani, A.D. Wiheeb, J. Kim and M.R. Othman, Improved carbon dioxide capture using metal reinforced hydrotalcite under wet conditions. International Journal of Greenhouse Gas Control, 2012. 7: p. 127-136.

[27] Freidlin, L.K., A.A. Balandin, N.V. Borunova and A.E. Agronomov, Mechanism of the deactivation of nickel catalysts by steam under pressure. Bulletin of the Academy of Sciences of the USSR, Division of chemical science, 1956. 5(8): p. 935-942.

[28] Laurent, E. and B. Delmon, Influence of water in the deactivation of a sulfided NiMoγ-Al2O3 catalyst during hydrodeoxygenation. Journal of Catalysis, 1994. 146(1): p. 281-291.

[29] Bartholomew, C.H., Mechanisms of catalyst deactivation. Applied Catalysis A: General, 2001. 212(1-2): p. 17-60.

[30] Silva, J.M., M.A. Soria and L.M. Madeira, Challenges and strategies for optimization of glycerol steam reforming process. Renewable and Sustainable Energy Reviews, 2015. 42: p. 1187-1213.

Chapter 5. Synthesis, Characterization and Testing of Sorbents derived from Hydrotalcites for CO_2 Capture

This chapter is divided into two parts: in the first one (subchapter 5.1), several hydrotalcite-based materials were prepared with different compensating anions - the CO_2 sorption capacity of these sorbents was determined through dynamic and static tests. In the second (subchapter 5.2), the two materials considered the most promising in subchapter 5.1 were doped with potassium and modified with gallium to evaluate the effect of these modifications on the sorption performance of the sorbents.

Subchapter 5.1. Effect of interlayer anion on the CO_2 capture capacity of hydrotalcite-based sorbents *

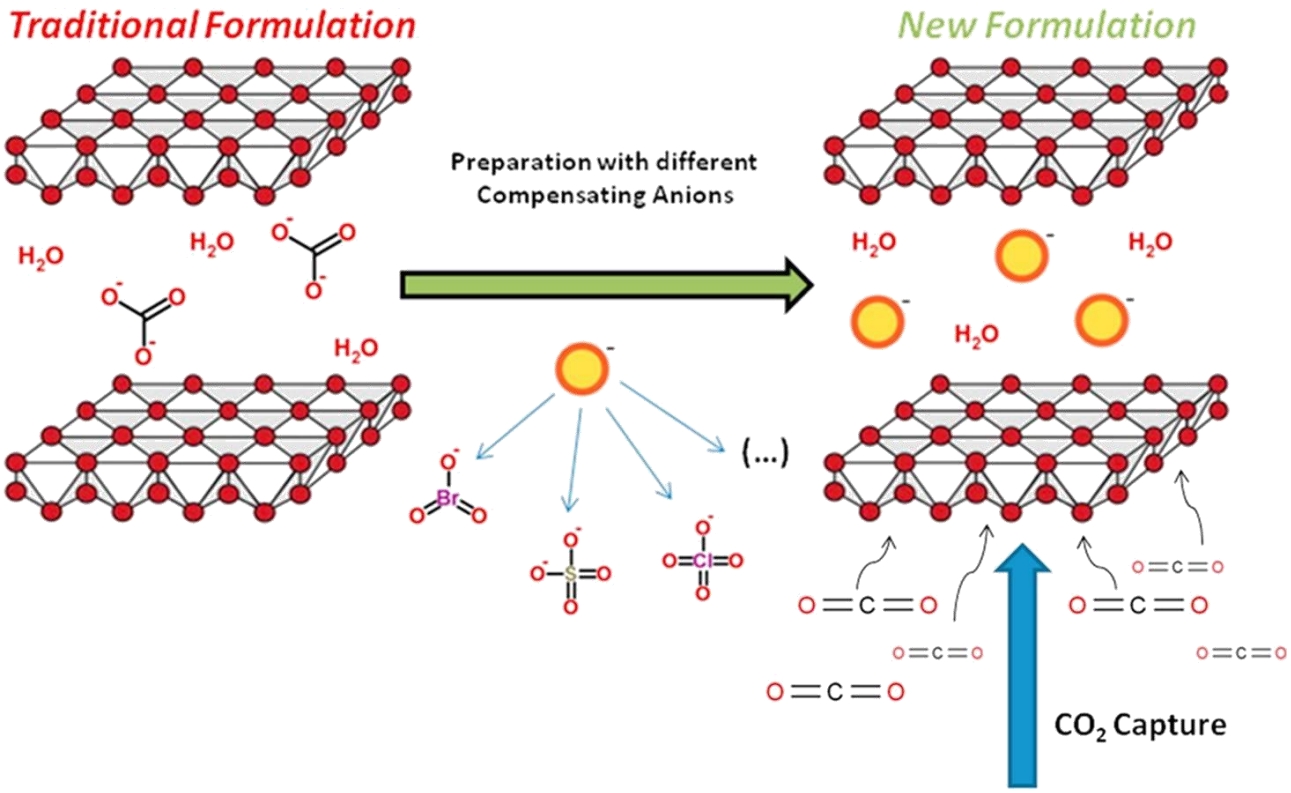

Highlights:

- Several HTCs with different interlayer anions were prepared.
- CO_2 sorption isotherms were determined at 300 °C.
- HTC-CO_3 showed the highest CO_2 sorption capacity of 1.05 mmol·g^{-1}, which was much higher than other similar HTCs.
- The CO_2 sorption capacities were related with the interlayer space of the HTCs.
- The kinetic model proposed adequately fitted CO_2 sorption/desorption uptakes.

* The contents of this subchapter were adapted from Rocha, C., M.A. Soria and L.M. Madeira, Effect of interlayer anion on the CO_2 capture capacity of hydrotalcite-based sorbents. Separation and Purification Technology, 2019. 219: p. 290-302. (https://doi.org/10.1016/j.seppur.2019.03.026)

Abstract:

A series of hydrotalcite (HTC) samples with different compensating anions was prepared (several anions never used before). The physicochemical characterization of these materials was realized through several techniques (including X-ray diffraction (XRD) and scanning electron microscopy coupled with energy dispersive spectroscopy (*SEM/EDS)). The CO_2 sorption capacities of the HTCs were assessed using a magnetic suspension balance (static tests) and CO_2 breakthrough runs in a packed column (dynamic tests). The HTC-CO_3 sample presents the highest CO_2 sorption capacity (1.05 mmol·g^{-1}, @ p_{CO_2} = 1 bar and 300 ºC) in comparison with the other materials. The sorption kinetics were analysed from CO_2 uptake measurements and two distinct contributions were observed. Besides, the effect of temperature on the CO_2 sorption capacity was studied for HTC-CO_3. The efficiency of the column (in the breakthrough tests) was higher for the HTC-CO_3 formulation (20 %).*

5.1.1. Introduction

As already mentioned, hydrotalcites (HTCs) are layered double hydroxides, whose general formula is $[M^{2+}_{1-x}M^{3+}_{x}(OH)_2]^{x+}\left[A^{n-}_{x/n}\cdot yH_2O\right]^{x-}$, where M^{2+} is a divalent metal cation and M^{3+} is a trivalent metal cation. A^{n-} is a charge balancing anion located in the interlayer space and *x* is generally between 0.2 and 0.4 [1, 2], while *y* is the number of moles of water located in the interlayer space. Although similar layered structures of HTCs could be produced with several compensating anions, it was found that their physicochemical properties are highly influenced by these anions, like the sorption capacity [3-12].

Taking this aspect into account, several HTCs with different interlayer anions were prepared in this work. Besides the physicochemical characterization of the materials, the CO_2 sorption equilibrium isotherms were determined at 300 ºC; the CO_2 sorption kinetics was determined as well. Finally, several of the obtained materials were also characterized by breakthrough cycling tests. The main aim of this work was to study the influence of different compensating anions on the sorbents precursors and especially on the CO_2 sorption capacity of the derived mixed oxides aiming at their potential application in processes capable of being enhanced with the removal of the CO_2 (e.g. steam reforming or water-gas shift reactions). The main novelty of this work is the utilization of different types of compensating anions (some of them never used before) in the interlayer space of the HTCs, in opposition with the commercial materials that have always the carbonate as compensating anion. Besides this, the materials with different compensating anions were never studied in dynamic studies (sorption-desorption cycles).

The materials and methods used in this subchapter are described in subchapter 3.2.

5.1.2. Results and discussion

5.1.2.1. Sorbents physicochemical characterization

X-ray diffraction

In order to verify if the prepared materials present typical structures of HTCs, the powder X-ray diffraction (XRD) pattern of each dry sample was analysed - see Table 5.1. XRD is the more suitable technique for determining the interlayer space of the HTCs by means of their lattice parameters. Thus, XRD analyses were carried out for non-calcined samples (Table 5.1) where the compensating anion is hosted in the interlayer space.

Table 5.1 - XRD results for the dry samples.

		Lattice Parameters (Å)		
Sorbent	**Grain Size (nm)**	*a* and *b*	*c*	**Identified phases**
HTC-CO_3	8.7 ± 1	3.034 ± 0.002	22.78 ± 0.02	Hydrotalcite
HTC-long	n.d.	n.d.	n.d.	2 phases of HTCs
HTC-ClO_4	7.0 ± 1	3.03 ± 0.01	26.9 ± 0.1	Hydrotalcite
HTC-Cl	7.0 ± 1	3.04 ± 0.01	26.9 ± 0.1	Hydrotalcite
HTC-BrO_3	7.0 ± 1	3.05 ± 0.01	27.7 ± 0.1	Hydrotalcite
HTC-SO_4	7.0 ± 1	2.99 ± 0.01	25.99 ± 0.04	Hydrotalcite

It was verified that all samples present structures of HTCs (Fig. 5.1 and Fig. C.1 in Appendix C) and that the lattice parameters *a* and *b* are equal for each structure (not possible to calculate in the case of the HTC-long sample). However, for the HTC-long the existence of two different phases may be considered, connected with the existence of triborate $[B_3O_3(OH)_4]^-$ and/or tetraborate $[B_4O_5(OH)_4]^{2-}$ anions: both interlayer anions generated characteristics peaks in the XRD patterns at the same 2θ: ≈ 9, 16 and 24º [13, 14] - c.f. Fig. 5.1; thus, it was not possible to discard the existence of any of such anions. The values of cell parameter *a* for the samples are similar and close to the values reported in the literature for HTCs with Mg^{2+} and Al^{3+} as metal cations [15].

It can be seen from Table 5.1 that the sample with the anion CO_3^{2-} has a higher grain size in comparison with the other samples and a lower lattice parameter *c*. It is possible to associate this cell parameter to the distance of the interlamellar layer (where is present the compensating anion), once the Brucite-like layer is present/equal in all samples. It was reported by Rives *et al.* [15] that the theoretical thickness of the interlamellar layer for distinct compensating anions has the following trend: $(CH_3COO)_3BH^-$ > ClO_4^- > BrO_3^- > SO_4^{2-} > Cl^- > CO_3^{2-}. However, in this work the trend was different: $(CH_3COO)_3BH^-$ > BrO_3^- > ClO_4^- ≈ Cl^- > SO_4^{2-} > CO_3^{2-}. The charge density seems to have a big effect on the thickness of the interlamellar layer and seems to be predominant in comparison to the size of the anions. This result is consistent with the previous findings of Meyer *et al.* [7]. It is important to emphasize that the utilization of compensating anions different from CO_3^{2-} had the objective of increasing the spacing of the interlamellar layer (and to see how it affects the CO_2 sorption capacity); so the objective was fulfilled (as the interlamellar layer thickness was increased), as reported in previous studies [5, 8, 10, 12]. Even though the lattice parameter *c* has not been calculated for the HTC-long sample, it is expectable that this parameter is higher than for the other samples, since the peak $d_{(003)}$ (2θ ≈ 10º) was present at a lower diffraction angle [16].

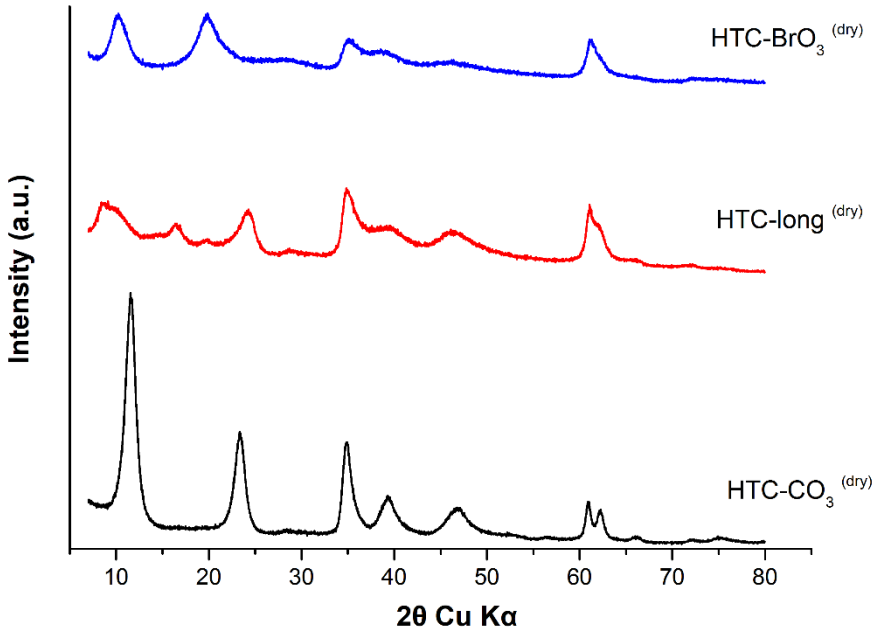

Fig. 5.1. XRD patterns of dry samples of HTC-CO_3, HTC-BrO_3 and HTC-long. The curves have been vertically displaced for clarity.

Thermogravimetric and derivative thermogravimetric analysis

Dry HTC itself does not have basic sites. Upon thermal treatment, HTC gradually loses interlayer water, and then dehydroxylates and decarbonates to a large extent, leading to the formation of a mixed oxide [8]. Thermogravimetric analysis (TGA) was performed to study the thermal decomposition (to determine the calcination temperature) and the mass loss in the calcination for all prepared HTCs. Three different programs were used to study the decomposition of the HTCs (see subchapter 3.2.3).

As for program 1), it was analysed the decomposition of the dried samples in the range of 30-1000 ºC, in order to determine the optimum calcination temperature - Fig. 5.2 and Fig. C.2 in Appendix C. The total mass loss is displayed in Table 5.2, together with the temperatures at which derivative thermogravimetric (DTG) peaks appear. All samples show at least two DTG peaks: one (or two) related to the removal of water (water at surface and interlayer water) as discussed in detail elsewhere [1, 2]. The other DTG peak is related with the removal of the interlayer anion: depending on the compensating anion used, the DTG peak related to its decomposition was shifted to high or low temperatures - see Table 5.2. The removal of water and hydroxyl groups appears in only one peak (in the range of 115-150 ºC) or two peaks (the second peak appears in the range of 180-250 ºC), since the samples have different morphologies and different chemical bonds. For the HTC-BrO_3 it was also possible to identify the possible presence of NO_3^{2-} in the interlayer (peak at ≈ 300 ºC) [17, 18], demonstrating that the NO_3^{2-} competes with BrO_3^- to occupy the interlayer. For the HTC-CO_3 it was possible to see a small peak related to the presence of NO_3^{2-} (since the anion was present in the composition of the Al^{3+} and Mg^{2+} precursors), but with a lower intensity than for HTC-BrO_3. For the

HTC-long it was also possible to identify a small peak at 440 ºC, probably due to the small presence of CO_3^{2-} or NO_3^{2-} in interlayer (anions with more affinity than $[B_3O_3(OH)_4]^-$ and $[B_4O_5(OH)_4]^{2-}$ anions to form the HTC structure); this peak was shifted probably due to molecular interactions with the $[B_3O_3(OH)_4]^-$ and/or $[B_4O_5(OH)_4]^{2-}$ anions.

As mentioned, the dry samples were calcined at 400 ºC for 2 h, as this treatment ensures that water and the anions are removed and that the sample has not a relatively small surface area and few basic sites, which would lead to a low CO_2 sorption capacity [19]. This calcination temperature is in line with previous works [2, 20-22] and was also chosen herein following the study by Reddy *et al.* [19] and Qin *et al.* [12], where it was observed that samples calcined at 400 ºC provided mixed oxides with a higher CO_2 sorption capacity. Moreover, this is the highest temperature expected to be used in most final applications (e.g. steam reforming reactions).

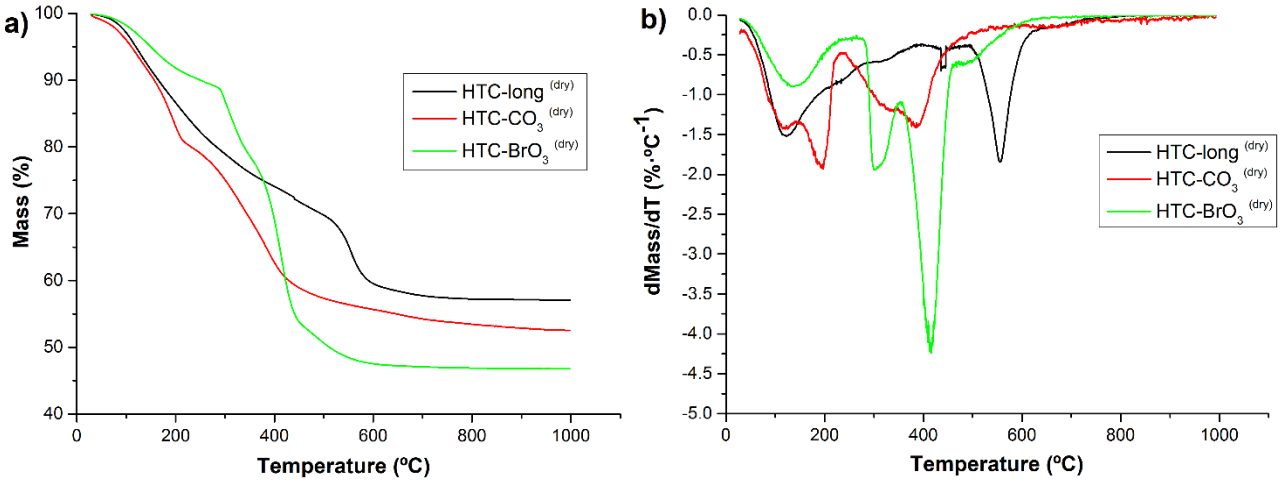

Fig. 5.2. Thermogravimetric a) and derivative thermogravimetric b) analysis of the dry samples HTC-long, HTC-CO_3 and HTC-BrO_3.

Regarding program 2), it was analysed the mass loss in the simulation of a calcination procedure - Fig. 5.3. It was verified that the loss of mass after 2 h of calcination is lower than 2 % for all samples (although Fig. 5.3 shows data only for HTC-BrO_3); in this way, the calcination is stopped after 2 h at 400 ºC.

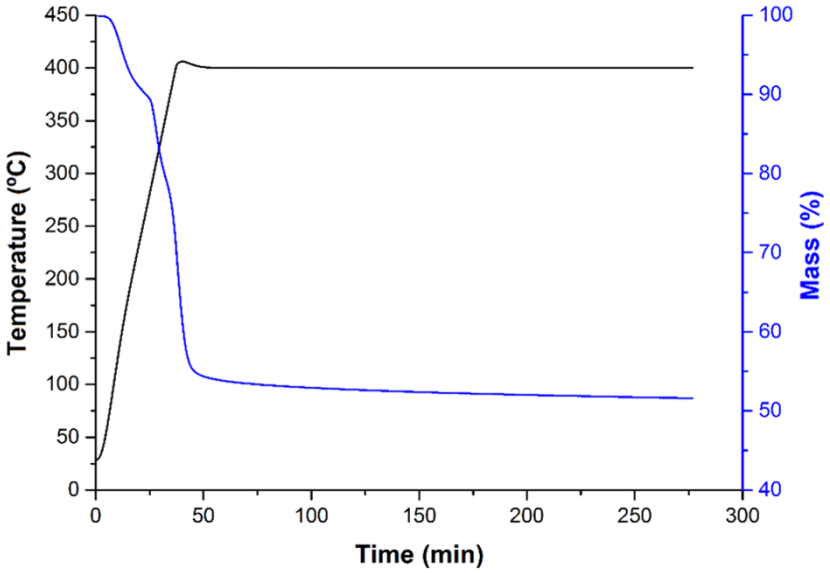

Fig. 5.3. Thermogravimetric analysis of the dry sample HTC-BrO_3 - calcination program.

As for program 3), it was simulated the losses of mass in the pre-treatments realized (at 300 ºC) previously to the sorption-desorption experiments in the dynamic tests. It was possible to conclude that the loss of mass was related to the removal of water and atmospheric CO_2 from the sorbent.

Table 5.2 - TG/DTG results for the as-prepared samples.

Sorbent	Total Mass Lost (%)	Temperature Peaks (ºC)
HTC-CO_3	47	115 / 190 / 380
HTC-long	43	125 / 440/ 555
HTC-ClO_4	50	150 / 440
HTC-Cl	50	140 / 450
HTC-BrO_3	53	140 / 300 / 410
HTC-SO_4	39	110 / 225 / 505

Scanning electron microscopy / Energy dispersive spectroscopy

The analysis of the scanning electron microscopy (SEM) images and the energy dispersive spectroscopy (EDS) analyses were performed only for two HTCs (the two samples with higher sorption capacity): dry samples of HTC-CO_3 and HTC-long (Fig. 5.4). The samples show the existence of a not defined morphology, although the presence of thin slabs is clearly observed (Fig. 5.4b)). The existence of these structures had already been reported for similar samples of HTC with CO_3^{2-} as interlayer anion [1, 2, 20]. It was possible to observe that the sample of dry HTC-CO_3 appears to be an aggregate of particles. Lastly, it was possible to see that the porosity is very low for HTC-long (the surface is similar to a smooth surface), which presents some particles with filaments - Fig. 5.4c-e).

EDS analysis showed that the global Mg^{2+}/ Al^{3+} ratio for the two samples (analysis done for a large amount of sample) was not constant in the particles (it varies from zone to zone in the HTCs, but is close to 2 in the overall sample; in HTC-CO_3 the ratio is 2.06 and in HTC-long the ratio is 2.05) and does not coincide with the molar ratio of cations in the starting solution, as previously observed in

others works [1, 2, 20]. For instance, the Z1 zone in the HTC-CO_3 sample (Fig. 5.4a)) presented a different Mg^{2+}/ Al^{3+} molar ratio in comparison with the global molar ratio calculated for the sample. For all dry samples, high content of carbon and oxygen was detected in these analyses, since the HTCs have water, carbonate groups (more for the HTC-CO_3), and hydroxyl groups in their composition. For the HTC-long it was possible to identify a small quantity of Boron, due to the presence of the $(CH_3COO)_3BH^-$ anion. Besides that, the filaments present in the HTC-long (see Fig. 5.4d) - Z1 zone - and Fig. C.3 in Appendix C) corresponded to solid $NaNO_3$. However, the content of this component in the sample was low and only appears in a few particles.

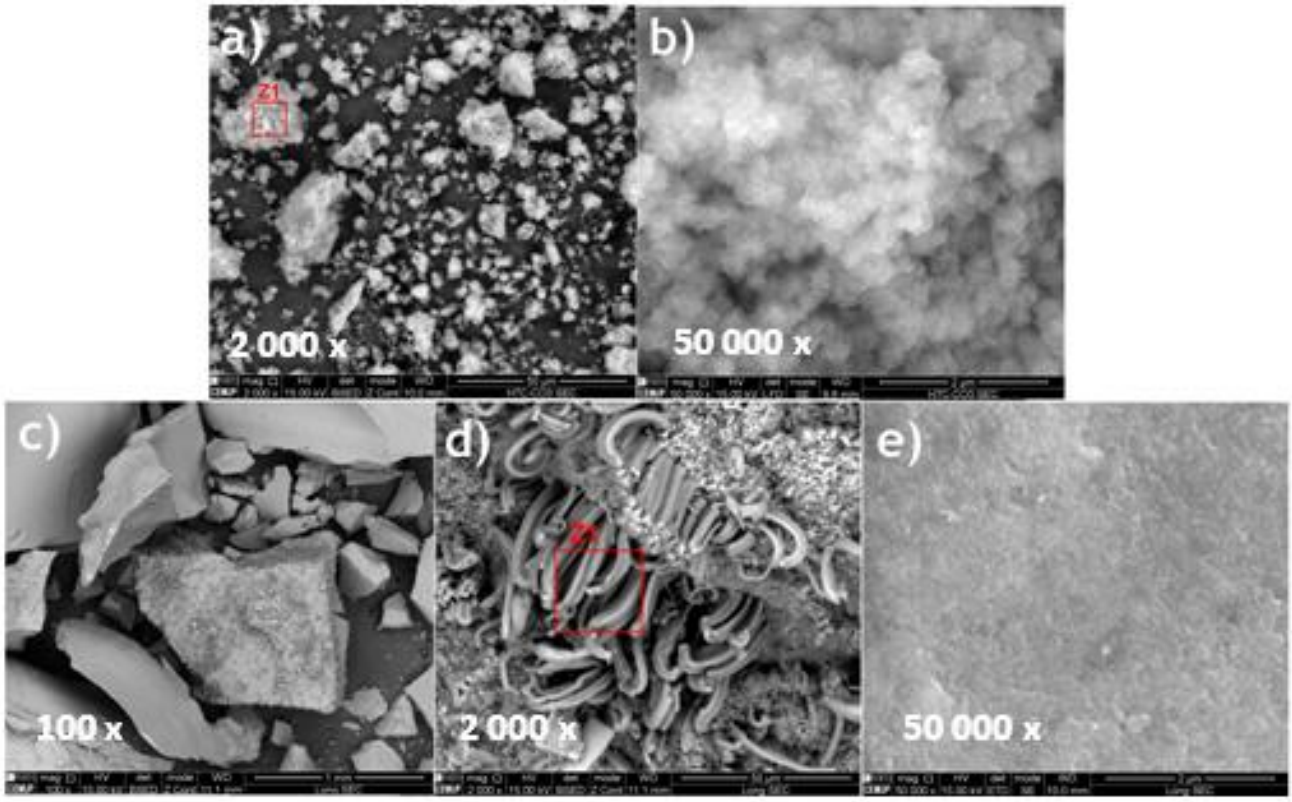

Fig. 5.4. SEM images for dry samples of HTC-CO_3 a) and b) and HTC-long c), d) and e).

Physical adsorption of nitrogen at -196 ºC

The specific Brunauer-Emmet-Teller (BET) surface area was determined for all calcined (@ 400ºC, 2h) samples by physical adsorption of N_2 at -196 ºC - Table 5.3. This technique was used to determine textural properties (e.g. surface area), being that the samples used to determine the BET surface were previously calcined (anions are removed as shown by TG/DTG), and therefore the common interlayer space of hydrotalcites is not present in these samples.

According to the IUPAC classification, isotherms of Type II (HTC-SO_4) and Type IV(a) (HTC-CO_3, HTC-BrO_3, HTC-Cl, HTC-ClO_4 and HTC-long) were obtained - see Fig. 5.5 (for the 2 HTCs with higher sorption capacities) and Fig. C.4 in Appendix C (for the other materials). The volume of micropores (< 0.009 $cm^3 \cdot g^{-1}$ - determined by the t-plot method) can be neglected for all calcined samples.

The Type II and Type IV(a) isotherms obtained for these materials mean that the resulting materials are macroporous/mesoporous solids [23]. The Type II isotherm (only for HTC-SO_4) does not present the phenomenon of hysteresis (see Fig. C.4d) in Appendix C), as expected for this type of isotherm. This material is macroporous or nonporous and the sorption mechanism involves the production of multilayers in the HTC [23]. However, for the N_2 adsorption isotherms of HTC-CO_3, HTC-BrO_3, HTC-Cl, HTC-ClO_4 and HTC-long (Type IV(a) isotherms - see Fig. 5.5 and Fig. C.4 in Appendix C), the process of N_2 sorption-desorption was not reversible, indicating the presence of hysteresis. Besides the production of multilayers, capillary condensation is present in the mesoporous filling mechanism in these materials. When the capillary condensation is different from the capillary evaporation (desorption step), the hysteresis occurs [23-25]. The type of the isotherm was confirmed with the diameter of the pores in the samples (verified by BJH desorption and t-plot methods), since only the HTC-SO_4 presents a large fraction of macropores (data not shown).

For HTC-BrO_3 the hysteresis that occurred was of the H2(b) type, linked with the existence of not well-defined pores (format and distribution) [23, 25]. The type H2(b) loop is related to pore blocking, where the size distribution of neck widths is larger [23]. However, for HTC-Cl, HTC-ClO_4 and HTC-long the hysteresis that occurred was of the H3 type, related with the occurrence of slit-shaped pores [23, 25]. Loops of this type are produced by non-rigid aggregates of plate-like particles, but also if the pore network consists of macropores that are not completely filled with condensate [23].

The total mesoporous and macroporous volume, in the calcined HTCs, follows the order: HTC-CO_3 > HTC-BrO_3 > HTC-ClO_4 > HTC-long > HTC-Cl > HTC-SO_4 - see Table 5.3.

Table 5.3 - Surface area for several calcined samples.

Sorbent	BET Surface Area ($m^2 \cdot g^{-1}$)	Total Pore Volume ($cm^3 \cdot g^{-1}$)
HTC-CO_3	138	0.630
HTC-long	29	0.107
HTC-ClO_4	44	0.144
HTC-Cl	23	0.0595
HTC-BrO_3	126	0.214
HTC-SO_4	2	0.00565

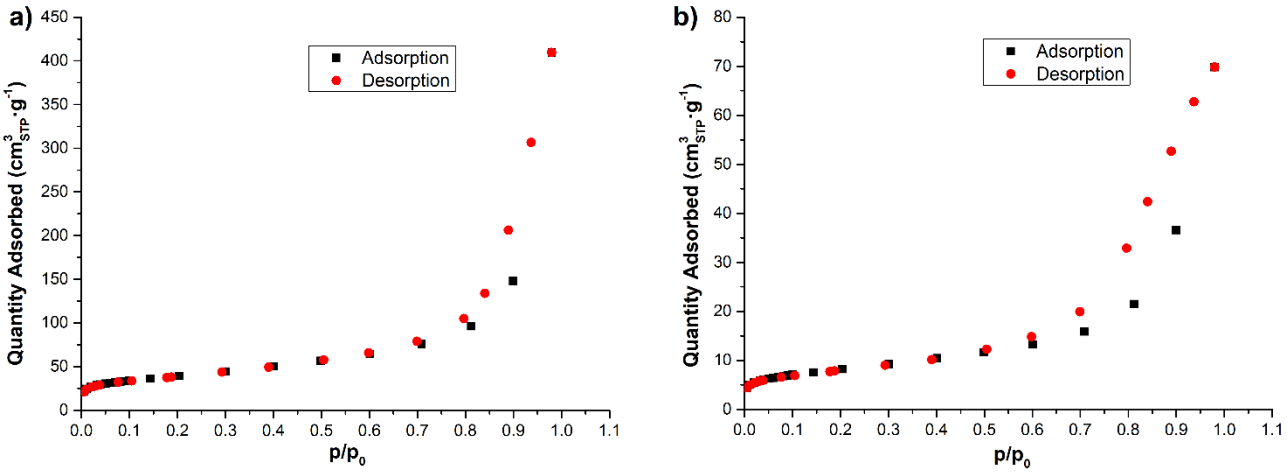

Fig. 5.5. Adsorption/desorption isotherms of N_2 over calcined samples: a) HTC-CO_3 and b) HTC-long.

Fourier-transform infrared spectroscopy

Fourier-transform infrared spectroscopy (FTIR) spectra for dry samples are shown in Fig. 5.6 (the two HTCs with higher sorption capacities and HTC-SO_4, as it presents very different peaks) and Fig. C.5 in Appendix C. All spectra show an intense, broad band centered at 3460 cm^{-1}, due to the stretching mode of the hydroxyl groups, present in the Brucite-like layers, and the water molecules in the interlayer, as well as the water molecules present on the external surface of the sorbent. The shoulder at 2900-3000 cm^{-1} present in HTC-CO_3 has been ascribed [26] to the stretching mode of interlayer hydroxyl groups hydrogen-bonded to the interlayer species (CO_3^{2-} anions). The bending mode of the water molecules is responsible for the rather weak band at ca. 1630 cm^{-1}, also recorded for all dry samples. The v_3 mode of the interlayer anions (carbonate group could be also present in the samples with other interlayer anions) was responsible for the unique intense band at 1384 cm^{-1} in all dry samples, except for the HTC-SO_4 and HTC-ClO_4, where the presence/effect of interlamellar species appeared in the spectra in one more different peak. As seen in previous work [2], it can be noticed that the band at 1384 cm^{-1} shows a clearly identified shoulder at 1500 cm^{-1} for the HTC-CO_3, which can be ascribed to carbonate species in two sites with different interactions. In the spectra of the HTC-SO_4 sample, it was possible to identify a peak at 1110 cm^{-1} related to the presence of the SO_4^{2-} group [27]. In the HTC with ClO_4^- as compensating anion, the spectrum shows a peak at 1100 cm^{-1} related to the presence of the ClO_4^- anion [28]. In the spectra of the sample HTC-long there are no traces of methyl group vibrations (range 2750-3000 cm^{-1}), which proves that no acetate anions have been retained by the material and, in this way, the only compensating anions present in the HTC-long sample was $[B_3O_3(OH)_4]^-$ and/or $[B_4O_5(OH)_4]^{2-}$ anions. Besides that, it was possible to identify a characteristic band, already mentioned in this discussion, related to the presence of $[B_4O_5(OH)_4]^{2-}$ in the structure at 1384 cm^{-1} [14]. However, it was impossible to deny the presence of one of the two possible anions, since the two anions have similar functional groups. Furthermore, other characteristic peaks of these anions located below 1000 cm^{-1} could be overlapped with peaks related to the presence of lattice bonds [14].

The other weaker bands detected in all samples below 1000 cm^{-1} correspond to the presence of the lattice bonds (Al-OH, Mg-OH, etc.) [1, 2]. Finally, it was possible to see that the interlayer anions influenced the positions and the intensities of the peaks related to Al-O and Mg-O vibrations, in agreement with a previous study of Wang *et al.* [8].

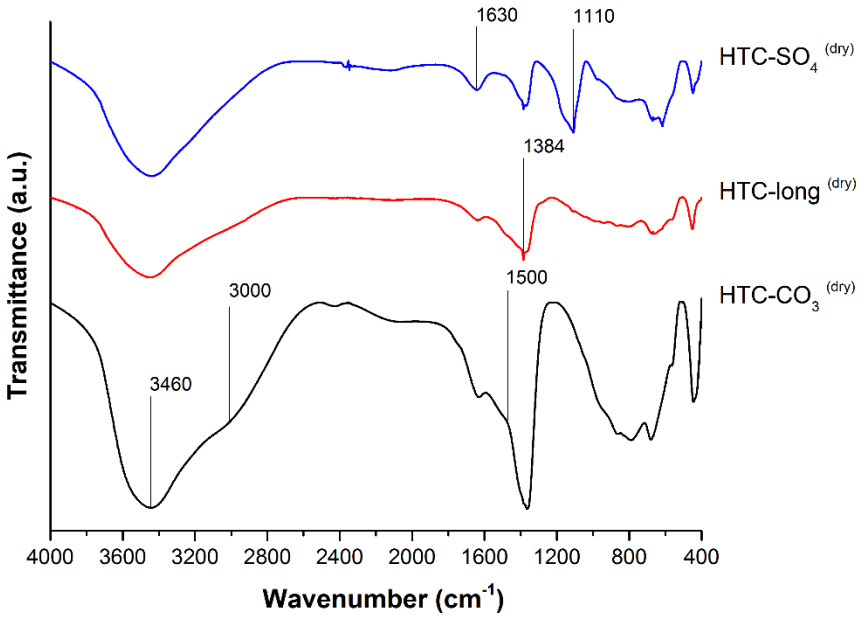

Fig. 5.6. FTIR spectra of dry samples of HTC-SO_4, HTC-CO_3 and HTC-long.

5.1.2.2. CO_2 sorption experiments

In this work, it was firstly realized a screening of the prepared sorbents for CO_2 capture. After the determination of the equilibrium sorption capacities, it was possible to compare the performance and select the best for a sorption-enhanced process. The two best materials in terms of CO_2 sorption capacity were also used in the dynamic tests.

Determination of sorption equilibrium isotherms at 300 ºC for the prepared sorbents

The equilibrium CO_2 sorption capacities of the calcined HTCs, determined at 300 ºC under dry conditions for different total pressures of CO_2 (pure CO_2), are shown in Fig. 5.7. Among the HTCs prepared, HTC-CO_3 showed the highest CO_2 capture capacity of 1.05 mmol·g^{-1} (p_{CO_2} = 1 bar), which was much higher than other similar HTCs reported in the literature under dry conditions - see Table 5.4.

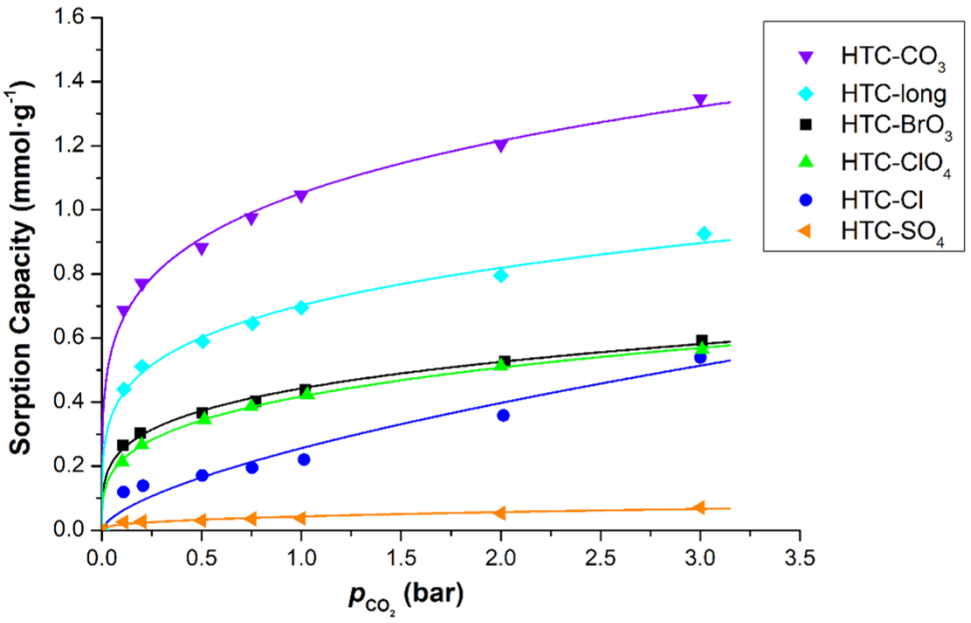

Fig. 5.7. Sorption isotherms for different HTCs (with different compensating anions) at 300 ºC - fitting with the Freundlich model.

Table 5.4 - Effect of the compensating anions in the sorption capacity of HTCs.

Sorbent	Sorption Capacity (mmol·g^{-1})	Temperature (ºC)	p_{CO_2} (bar)	Ref.
HTC	0.54	300	0.14	[2]
cHTC	0.81	300	1.03	[1]
Mg_3Al-CO_3	0.53	200	1	[8]
HTC-CO_3	1.05	300	1	This work
HTC-CO_3	0.69	300	0.11	This work
Mg_3Al-SO_4	0.10	200	1	[8]
HTC-SO_4	0.04	300	1	This work
Mg_3Al-Cl	0.18	200	1	[8]
(Mg,Al)(Cl)	0.44	330	1	[4]
HTC-Cl	0.22	300	1.01	This work
HTC-BrO_3	0.44	300	1.02	This work
HTC-ClO_4	0.42	300	1.03	This work
HTC-long	0.69	300	1	This work

It can be seen in Table 5.5 the adjusted parameters calculated for the sorption isotherms for different HTCs with the maximization of the following equations (Eqs. (5.1) and (5.2)), methodology used by Chen [29] - Eq. (5.1) - and Brandão *et al.* [30] - Eq. (5.2):

$$R^2 = \frac{\sum_{i=1}^{m}\left(q_{m_i} - \overline{q_e}\right)^2}{\sum_{i=1}^{m}\left(q_{m_i} - \overline{q_e}\right)^2 + \sum_{i=1}^{m}\left(q_{m_i} - q_{e_i}\right)^2} \tag{5.1}$$

$$MSC = \ln\left[\frac{\sum_{i=1}^{m}\left(q_{e_i} - \overline{q_e}\right)^2}{\sum_{i=1}^{m}\left(q_{e_i} - q_{m_i}\right)^2}\right] - \frac{2f}{m} \tag{5.2}$$

where, q_m is the sorption capacity obtained from the Freundlich model (Eq. (5.3)), q_e is the equilibrium capacity obtained from experimental data, $\overline{q_e}$ is the average of all q_e data, m is the number of experimental points, f is the number of fitting parameters. Almost all experimental data of

CO_2 sorption isotherms present a good fitting to the Freundlich model - Eq. (5.3) (see Fig. 5.7) - where K_F is the Freundlich constant (mmol·g^{-1}·bar$^{1/n}$), p_{CO_2} is the partial pressure of CO_2 (bar) and n is an exponential constant.

$$q_m = K_F \times {p_{CO_2}}^{1/n} \quad (5.3)$$

The sorption data of each sample was fitted to the Freundlich equation (Eq. (5.3)), which has also been proposed in the literature to describe CO_2 sorption on HTCs [21, 31]; the parameter $1/n$ is normally lower than the unity and as it decreases the isotherm approaches to the alleged irreversible isotherm.

Table 5.5 - Adjusted parameters calculated for the isotherms for the different HTCs - Freundlich model.

Sorbent	K_F[a] (mmol·g^{-1}·bar$^{1/n}$)	n[a]	R^2	K_F[b] (mmol·g^{-1}·bar$^{1/n}$)	n[b]	*MSC*
HTC-CO_3	1.05	4.81	1.00	1.05	4.82	5.61
HTC-BrO_3	0.44	4.04	1.00	0.44	4.04	5.51
HTC-Cl	0.26	1.58	0.96	0.26	1.66	2.55
HTC-ClO_4	0.42	3.54	1.00	0.42	3.54	7.29
HTC-SO_4	0.04	2.55	0.95	0.04	2.69	2.49
HTC-long	0.70	4.49	1.00	0.70	4.51	4.99

[a] Parameters calculated with maximization of R^2 (Eq. (5.1)).
[b] Parameters calculated with maximization of *MSC* (Eq. (5.2)).

The sorption capacities of the sorbents (HTC-CO_3 > HTC-long > HTC-BrO_3 ≈ HTC-ClO_4 > HTC-Cl > HTC-SO_4), in a general way, seems to be related to the interlayer anion space in the dry samples ($(CH_3COO)_3BH^-$ > BrO_3^- > ClO_4^- ≈ Cl^- > SO_4^{2-} > CO_3^{2-}) calculated by XRD analyses (section 5.1.2.1). Thus, the CO_2 sorption capacity was higher for sorbents with HTCs precursors with higher interlamellar layer, except for the HTC-CO_3, as nicely illustrated in Fig. 5.8. The *c* lattice parameter was not calculated for the HTC-long sample, but is expectable that this parameter is higher than for the other samples, since the peak $d_{(003)}$ was present at lower diffraction angle - see Fig. 5.1. In Fig. 5.8, in the dashed region, it is possible to see probable values that the lattice parameter for such sample could have.

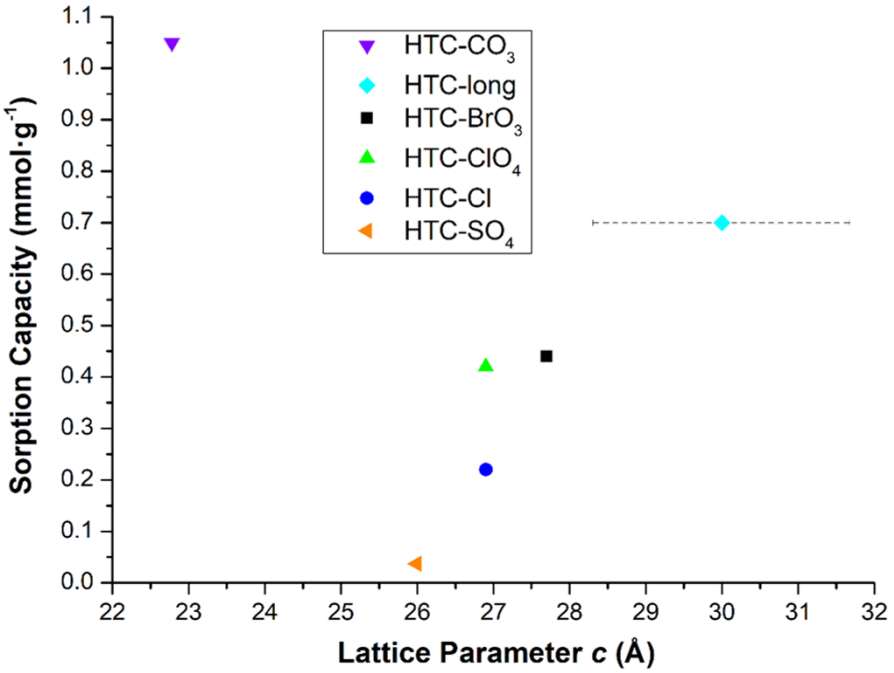

Fig. 5.8. Effect of the lattice parameter c (interlayer distance) in the sorption capacity of the sorbents (@ 300 ºC and 1 bar of CO_2).

Although calcined HTCs - i.e. derived mixed oxides (without the interlayer anions) - have been used to determine the CO_2 sorption capacity of the materials, it was possible to verify that the compensating anion influenced the morphology of the mixed oxides.

The sorption capacity of the materials can be affected by their specific surface areas (cf. Table 5.3). However, in this case, the sorption capacity seems to be more connected to the chemical nature and crystallographic parameters of the materials. In fact, in other works, it was reported that the available surface area does not play a crucial role on the CO_2 sorption capacities [2, 4, 20]. Besides that, Wang *et al.* [8] analysed the effect of different charge compensating anions (CO_3^{2-}, HCO_3^-, NO_3^-, SO_4^{2-} and Cl^-) and observed that when the HTC-CO_3 was prepared, a spherical “sand rose” type of HTC with very high surface area was produced. However, the other compensating anions led to the formation of “stone” type HTCs with very low surface areas. This phenomenon was also verified in this study.

It was also compared the sorption capacities with other textural/morphologic properties of the sorbents (total volume of the pores, pores sizes, etc.), although it was not found any relation between these variables.

Besides the determination of the sorption capacities for the different samples calcined at 400 ºC, the HTC-long was also calcined at 500 ºC and 550 ºC, since the DTGA shows a peak at 550 ºC. After the calcination at these temperatures (for 2 h), the sorption capacities of these materials were determined at 300 ºC and 0.10 bar pressure of CO_2. Both materials present a lower performance than the material

calcined at 400 ºC (500 ºC - 0.12 mmol·g^{-1} and 550 ºC - 0.20 mmol·g^{-1}). These results are in the line with the work of Reddy *et al.* [19], where it was reported that calcination at 400 ºC allows obtaining higher sorption capacities (due to destruction of the structure and low number of basic sites for higher temperatures).

For HTC-CO_3 and HTC-long samples, the desorption equilibrium isotherms were also determined - see Fig. 5.9. This way, kinetic issues are ruled out from the possible decrease in the CO_2 uptake upon reuse of the samples in cyclic processes, as observed in other studies and hereinbelow. The results are presented in relation to the maximum sorption capacity obtained at p_{CO_2} = 3 bar (herein called Relative Sorption Capacity = $\frac{\text{Sorption Capacity}}{\text{Sorption Capacity at } p_{CO_2} = 3 \text{ bar}}$). It is possible to see the existence of irreversible CO_2 sorption in both materials assessed (because there is a difference between the relative sorption capacity determined in the adsorption and the desorption tests), which is however more pronounced for the HTC-long sample. For example, for $p_{CO_2} \approx 0$ bar the relative sorption capacity for HTC-CO_3 was close to 0, but for the HTC-long the relative sorption capacity was equal to 0.1.

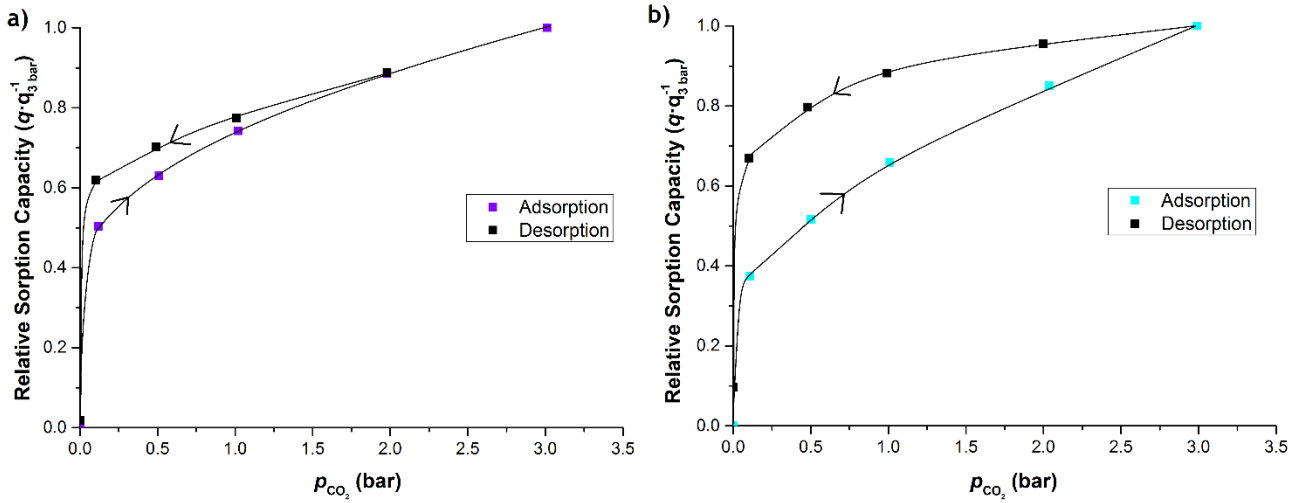

Fig. 5.9. Adsorption and desorption isotherms for a) HTC-CO_3 and b) HTC-long, both at 300 ºC.

Lastly, for the sample with higher sorption capacity (HTC-CO_3), a study of temperature effect on the sorption isotherms was performed - see Fig. 5.10. It is noticed that the increase of the temperature from 200-270 ºC decreases the CO_2 sorption capacity; however, the capacity was very similar for 270 ºC and 300 ºC. For this HTC and in this range of temperature, the exothermic process of adsorption is the main route in the capture of CO_2; nevertheless, for temperatures close to 300 ºC and above some other processes (of endothermic nature) may be present and start to become important [20]. For this reason, and due to limitations of the used magnetic suspension balance, a study of the effect of temperature in the dynamic breakthrough tests was performed in a larger range (200-400 ºC).

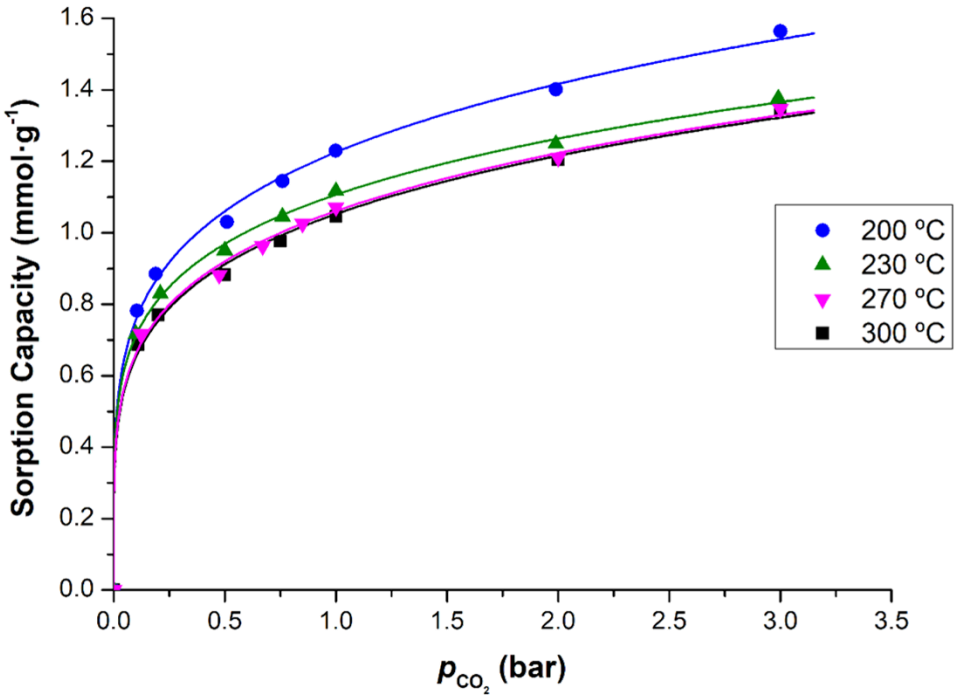

Fig. 5.10. Effect of temperature in the sorption isotherms for HTC-CO_3 - fitting with Freundlich model.

For the HTC-CO_3, the isosteric heat of adsorption was calculated for different sorption capacities - Fig. C.6 in Appendix C. To obtain the variation of the isosteric heat of adsorption with the loading of CO_2 (Eq. (5.4)), individual regression curves were adjusted to experimental data at different temperatures (200, 230, 270 and 300 ºC).

$$(\Delta H_{\mathrm{Ads}})_q = -\mathrm{R}\left(\frac{d\left(\ln p_{\mathrm{CO_2}}\right)}{d\left({}^{1}/_{T}\right)}\right)_q \tag{5.4}$$

In Eq. (5.4), ΔH_{Ads} is the isosteric heat of adsorption for a certain loading of CO_2 in the HTC (q), R is the ideal gases constant, T is the absolute temperature of the experimental tests and p_{CO_2} is the pressure of CO_2.

The isosteric heat is higher for low sorption capacities, but the values are very close to each other (in the range of 3.5 to 4.0 kJ·mol^{-1}). So, the affinity for CO_2 sorption is nearly constant at these loadings. Low values (in the range of 5 to 10 kJ·mol^{-1} for sorption capacities between 0-0.5 mmol·g^{-1}) were also seen in the work of Gil *et al.* [32] for similar HTCs. Nevertheless, in other works with similar sorbents but different ranges of temperature (e.g., between 400 and 520 ºC [33]), the values of the isosteric heat were higher [11, 33, 34].

As stated above, the variation of the sorption capacity with the temperature was herein found to be very low, justifying the low values found for the isosteric heat of adsorption. Probably, exothermic and endothermic phenomena occur simultaneously in the limited range of temperature considered, being

the exothermic processes slightly predominant (once the overall sorption capacity decreases with the temperature).

Determination of CO_2 uptake kinetics

The kinetics of CO_2 sorption on the HTCs was analysed based on the work of Du *et al.* [35], who explained the formation of different carbonate species during the sorption in this type of sorbents. With in situ FTIR spectroscopic analysis, four different carbonate species were found to be formed: uni-, bi-, polydentate and bridged carbonate species. The formation of bridged, uni- and bidentate carbonates was associated with the fast reversible uptakes observed, while the formation of polydentate species was related to the slow irreversible CO_2 sorption observed later in the process. In another work [36], it has also been observed that the sorption of CO_2 over HTC-based sorbents presents very fast kinetics followed by slower sorption. Considering the mechanism proposed by Du *et al.* [35], it was possible to use a model that describes the total amount of CO_2 sorbed in the particle, as proposed by Silva *et al.* [1] and Miguel *et al.* [2]. Eq. (5.5) describes the total amount of CO_2 that has diffused into the sorbent particle [37]:

$$F = \frac{q(t) - q(t=0)}{q(\infty) - q(t=0)} = \left(1 - \frac{6}{\pi^2}\sum_{i=1}^{\infty}\frac{1}{i^2}e^{\left(-i^2\pi^2\frac{D_1}{r^2}t\right)}\right)\frac{q_1}{q_\infty} + \left(1 - \frac{6}{\pi^2}\sum_{i=1}^{\infty}\frac{1}{i^2}e^{\left(-i^2\pi^2\frac{D_2}{r^2}t\right)}\right)\frac{q_2}{q_\infty} = \\ = F_1\frac{q_1}{q_\infty} + F_2\frac{q_2}{q_\infty} \quad (5.5)$$

This transient state model assumes constant surface concentration of CO_2 in the particles, which are assumed to be spherical, uniform initial concentration within the particles and two kinetic contributions occurring at the same time, one responsible for the fast uptake that is observed at the beginning and, the other one, by the slow increase observed for longer times. The kinetics of these two contributions is related with the $\frac{D_i}{r^2}$ parameters. In Eq. (5.5), F is the total CO_2 uptake fraction, F_1 and F_2 are the partial uptake fractions related to the fast and slow stages, respectively, $q(t)$ is the CO_2 sorption capacity measured at time t, $q(t=0)$ is the sorption capacity measured at the beginning of the sorption tests, $q(\infty)$ is the sorption capacity measured at the equilibrium and $\frac{D_1}{r^2}$, $\frac{D_2}{r^2}$ and q_1 (sorption capacity related to the fast uptake) are model parameters that were obtained through non-linear fitting of Eq. (5.5) to the experimental data. The parameter q_2 is the sorption capacity related to the slow uptake and is the difference between $q(\infty)$ and q_1. Fig. 5.11 shows the experimental fractional uptakes at 0.10 bar of CO_2 pressure for the two best sorbents (HTC-CO_3 and HTC-long samples) and the model curves fitted to the respective experimental data. The obtained parameters are shown in Table 5.6. From Fig. 5.11 it is possible to conclude that the model predicts accurately the experimental CO_2 sorption uptake on these calcined HTCs, which is in line with the very good fittings obtained by Miguel *et al.* [2] and Silva *et al.* [1]. By analyzing Fig. 5.12 (which represents the model for all samples

prepared), it is observed that the overall uptake for the sample with the anion SO_4^{2-} is faster than for the other anions. Moreover, a higher relative amount (as compared to the equilibrium) of CO_2 is adsorbed on samples HTC-CO_3 (65 %), HTC-BrO_3 (87 %), HTC-Cl (59%) and HTC-SO_4 (96 %) than for sample HTC-long (45 %) during the fast uptake (Table 5.6). From these results, and for the two sorbents with higher sorption capacities, it can be also concluded that the HTC-CO_3 sample saturates faster than HTC-long (the saturation is the slowest).

Table 5.6 - Parameters obtained through fitting of the experimental CO_2 uptakes for the samples at 0.10 bar and 300 ºC.

Sorbent	$\frac{D_1}{r^2}$ × 10^{-4} (s^{-1})	$\frac{D_2}{r^2}$ × 10^{-5} (s^{-1})	$\frac{q_1}{q_\infty}$ × 100
HTC-$CO_3^{300\ ºC*}$	10.00	0.58	65
HTC-$CO_3^{200ºC*}$	9.52	0.41	63
HTC-long	6.50	0.65	45
HTC-BrO_3	5.24	1.00	87
HTC-Cl	1.90	2.60	59
HTC-ClO_4	2.95	1.33	54
HTC-SO_4	7.12	1.00	96

* For HTC-CO_3, it was calculated the kinetic parameters of the CO_2 uptake at 200 and 300 ºC (@p_{CO_2} = 0.10 bar).

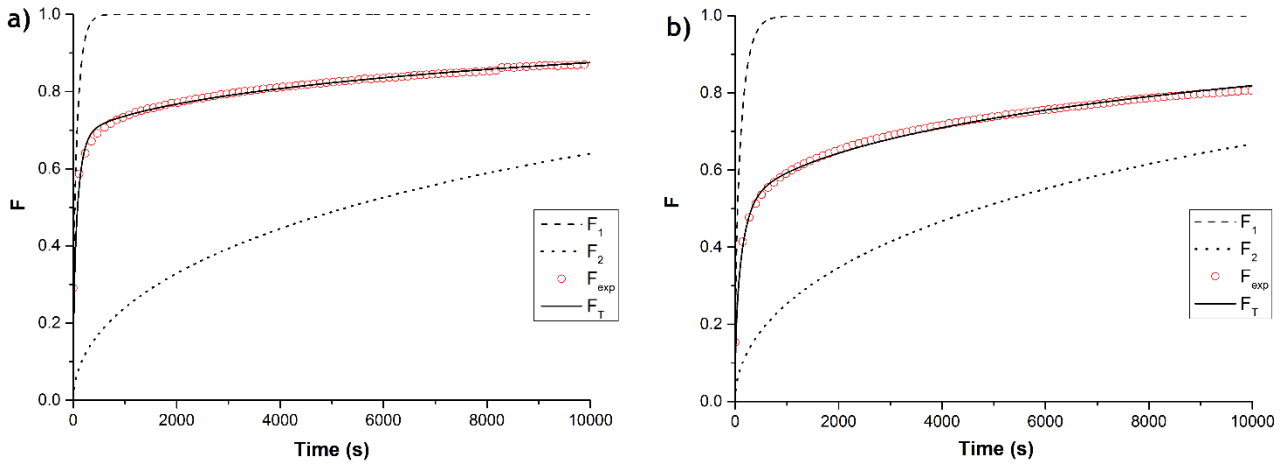

Fig. 5.11. Uptake curves for CO_2 sorption at 0.10 bar and 300 ºC for a) HTC-CO_3 and b) HTC-long.

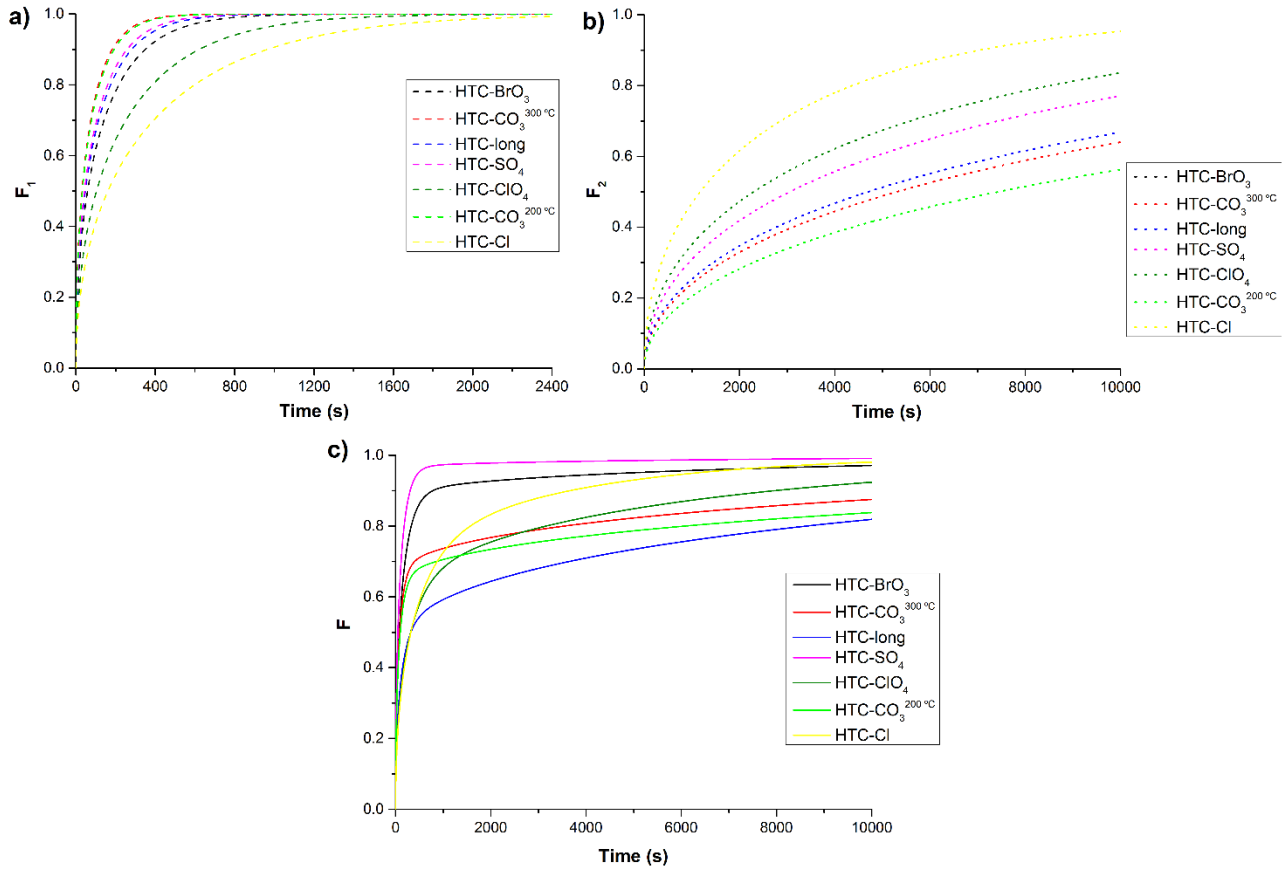

Fig. 5.12. Comparison of the uptake curves at 0.10 bar and 300 ºC (except for HTC-$CO_3^{200\ ºC}$) obtained through the model for the different samples: a) F_1, b) F_2 and c) F.

In relation to the effect of temperature in the uptake mechanism, Table 5.6 shows that, for the two temperatures analysed, the kinetics parameters of the model were different. At lower temperature, it was observed that the values for the kinetic parameters for both fast and slow uptake steps were lower. This phenomenon is related to the kinetic energy of the molecules, which influences the sorption kinetics.

Sorption-desorption dynamic experiments

In order to determine the performance of the two sorbents with higher sorption capacities (HTC-CO_3 and HTC-long samples) in dynamic tests, a series of sorption-desorption cycles were performed in a packed column.

The sorption capacities in the dynamic tests were calculated by Eq. (5.6). In this equation, q_{CO_2} is the sorption capacity, W is the sorbent mass, F_{CO_2} is the CO_2 inlet molar flow rate, t is the sorption time (20 minutes) and $\frac{y_{CO_2}^{out}}{y_{CO_2}^{in}}$ is the fraction between the CO_2 outlet and inlet molar fractions.

$$q_{CO_2} = \frac{F_{CO_2} \int_0^t \left(1 - \frac{y_{CO_2}^{out}}{y_{CO_2}^{in}}\right) dt}{W} \quad (5.6)$$

The efficiency of the column was calculated by Eq. (5.7); in this equation, t_∞ is the time to achieve the total saturation and t_{bp} is the breakthrough time. In this calculation, the value considered for $q_{CO_2\,total}$ was taken from the sorption capacity for a certain partial pressure of CO_2 calculated in the static tests (sorption equilibrium isotherms), since the sorption time (20 min) was not enough to achieve the saturation of the sorbent. This procedure was adopted because an additional test was carried out with a very high sorption time (8h - data not shown) and the sorption capacity calculated for this dynamic test differed only ≈ 5 % (absolute difference of 0.05 mmol·g^{-1}) from the value taken from the sorption equilibrium isotherm. For *Exp. 1.2*, the results are presented in relation to the sorption capacity obtained for HTC-CO_3 at 300 ºC (Relative Sorption Capacity = $\frac{\text{Sorption Capacity}}{\text{Sorption Capacity for the 1}^{st}\text{ cycle @ 300 ºC}}$).

$$\eta = \frac{q_{CO_2 bp}}{q_{CO_2 total}} = \frac{\int_0^{t_{bp}} \left(1 - \frac{y_{CO_2}^{out}}{y_{CO_2}^{in}}\right) dt}{\int_0^{t_\infty} \left(1 - \frac{y_{CO_2}^{out}}{y_{CO_2}^{in}}\right) dt} \quad (5.7)$$

In the *Exp. 1.1* (Fig. 5.13a-b) - see more details about this experimental run in Table 3.5), it is possible to see that the first cycle shows a higher CO_2 sorption capacity than the last cycles for both samples analysed and that none of the sorbents is completely saturated after 20 minutes of sorption (the value of $\frac{y_{CO_2}^{out}}{y_{CO_2}^{in}}$ never reached 1). In addition, it can be seen that the sorption capacity and the shape of the breakthrough curves are different for the different samples. As seen above, the CO_2 sorption kinetics for the HTC-CO_3 is faster in comparison with the HTC-long and, for this reason, the efficiency of the column (η) is higher for the HTC-CO_3 formulation (20 % vs. 9 %)). The reason for that is that the formulation HTC-long, after the breakthrough point, still sorbs a large quantity of CO_2 compared to the amount of CO_2 that has already been sorbed until that instant. This behavior can also be seen in the shape of the breakthrough curves (the HTC-CO_3 sample presents, in a general way, a more vertical curve, where dispersive effects are less notorious). It was expected and confirmed that the sorption capacity (calculated by Eq. (5.6) was higher for the sample HTC-CO_3, as seen previously in this subchapter (Table 5.4). Nevertheless, from the cycling tests, it was observed that the HTC-long sample presents a lower absolute decrease in the sorption capacity over the cycles, while the HTC-CO_3 sample had a worse stability performance. The absolute decrease in the sorption capacity between two consecutive breakthrough cycles was slightly lower for the HTC-long, but the relative decrease was very similar for both HTC samples. To check the reproducibility of the experiments and the possible influence of the irreversible CO_2 sorption capacity during the first cycles, one sample

(HTC-CO_3) was tested twice, in the same conditions (average difference between results of ≈ 5 %). It was checked that the sorption capacity also decreases in the repeated test.

The decrease of the sorption capacities in the cyclic runs may be either due to kinetic effects or to irreversible CO_2 sorption. As stated in this subchapter, the desorption equilibrium isotherms for HTC-long and HTC-CO_3, in which kinetic issues were ruled out, showed that the quantity of CO_2 irreversibly sorbed for HTC-long is higher than that for HTC-CO_3. In this way, since the relative decrease of the sorption capacities was similar for both materials (Fig. 5.13b)), it can be concluded that during the cyclic tests, kinetics issues were also important in the decrease of the sorption capacity for HTC-CO_3.

In the *Exp. 1.2*, a study of temperature effect on the breakthrough tests for the calcined HTC-CO_3 sample was performed - see the results in Fig. 5.13c-d). It was possible to see that the increase of the temperature from 200 ºC to 300 ºC decreases the sorption capacity (results in Fig. 5.13d)). Again, for this HTC and in this temperature range, the exothermic process of adsorption was the main route in the capture of CO_2. Nevertheless, at 400 ºC other processes are present and start to become important, as also reported elsewhere [20, 36, 38]; in this way, the sorption capacity increases again at 400 ºC. However, from the consecutive cycling tests, it was observed that at 200 ºC the sorption capacity after the second breakthrough cycle presents a lower decrease (both relative decrease between two consecutive sorption-desorption cycles and absolute decrease) while at other temperatures the sample had a worse stability performance. This could be related to the type of processes of CO_2 capture that are predominant at each temperature. For instance, at 300 ºC, the process of sorption could involve the formation of polydentate species (irreversible sorption) [35]. As mentioned in the previous paragraph, besides the irreversible reactions, kinetic issues may have influenced the decrease of the performances in the sorption-desorption cycles.

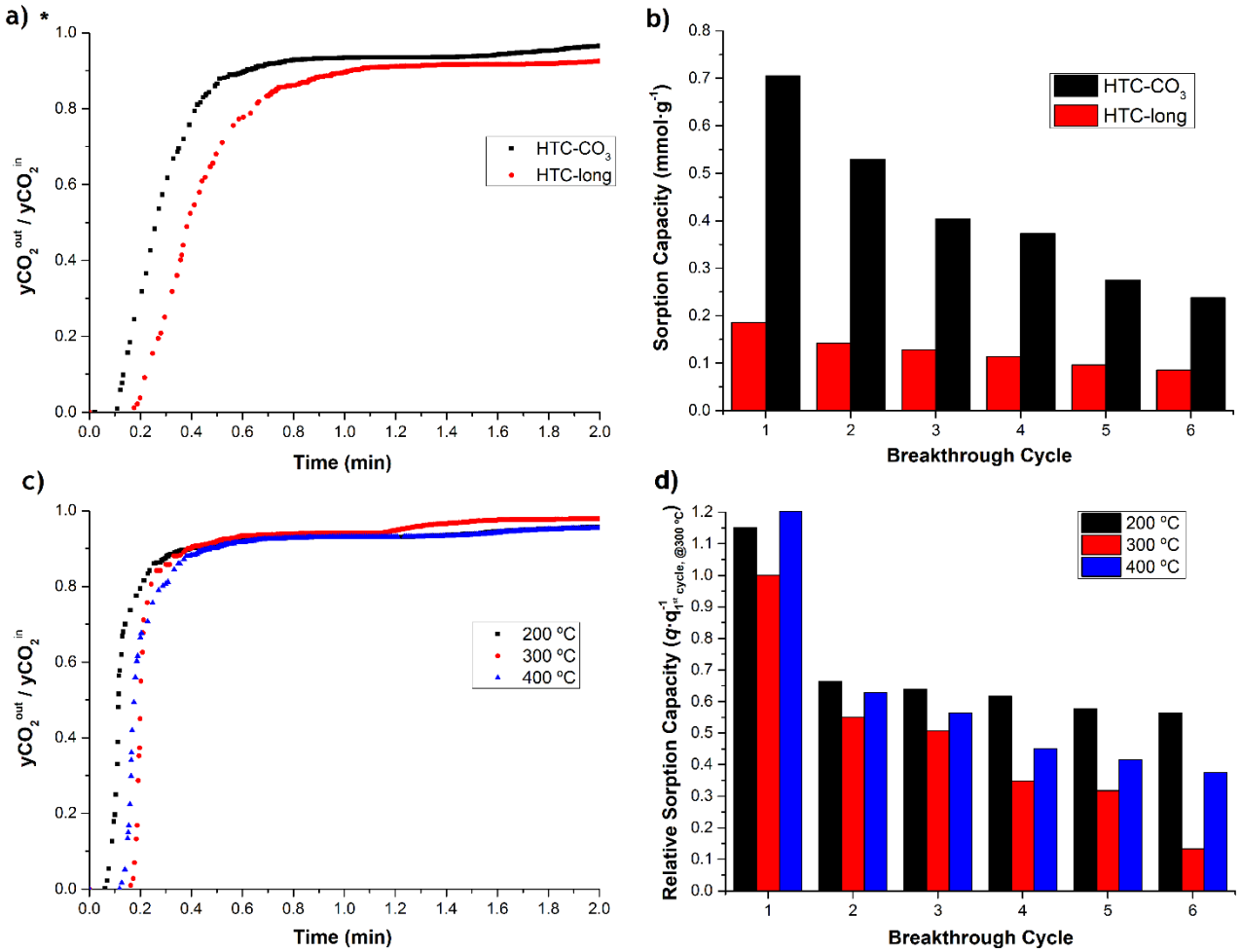

Fig. 5.13. Breakthrough curves for a) *Exp. 1.1* (sorption step: 20 min, 15 vol.% of CO_2 [total flow of 100 $mL_{NTP} \cdot min^{-1}$], 1 bar, 300 ºC; regeneration step: 30 min under N_2 flow [95 $mL_{NTP} \cdot min^{-1}$], 1 bar, 300 ºC) and c) *Exp. 1.2* (same conditions of *Exp. 1.1* at different temperatures (200-300 ºC). CO_2 sorption capacities for b) *Exp. 1.1* and d) *Exp. 1.2*. * The mass in *Exp. 1.1* was not kept constant (the samples had different densities).

5.1.3. Conclusions

This work reports an investigation on how the compensating anion affects the CO_2 sorption capacity of HTC-based sorbents (after their calcination). The anions have an effect on the structural properties, thermal stability and morphology of the hydrotalcite, modifying the CO_2 sorption capacity of the sorbents. Among the prepared HTCs, HTC-CO_3 showed the highest CO_2 sorption capacity of 1.05 $mmol \cdot g^{-1}$ (@ p_{CO_2} = 1 bar and 300 ºC), which was much higher than other similar HTCs reported in the literature under dry conditions. The sorption equilibrium isotherms for all the materials were fitted using a Freundlich-type equation, reaching a very good adherence to experimental data in most of the cases. The CO_2 sorption capacities were related with the interlayer space of the HTCs (before the calcination). Besides that, no correlation was found between the sorption capacity of the materials and properties like their surface area, the total volume of pores, pores size, etc. The better performance of the HTC-CO_3 sample in terms of CO_2 capture in comparison with the other materials

can be attributed to its chemical and morphological properties, namely the spherical “sand rose” structure formed in this HTC, since the presence of other interlayer anions led to the formation of “stone” type HTCs. In this way, the morphology (well defined and similar to the natural form of HTC) and the chemical surface of the HTC-CO_3 allow obtaining the highest performance among all samples.

The sorption kinetics for all the samples was evaluated considering a model which involves two kinetic contributions (fast and slow). It was clearly observed that the CO_2 uptake for the sample with the anion SO_4^{2-} is faster than for the other anions. Moreover, the temperature influenced the rate of CO_2 uptake (kinetic parameters).

Finally, it was found that the HTC-long sample presents a lower decrease in the sorption capacity (absolute decrease) in the breakthrough cycles but HTC-CO_3 always showed a higher sorption capacity. From the sorption-desorption experiments performed at 200-400 ºC it was also concluded that the HTC-CO_3 has a minimum sorption capacity at 300 ºC. At 200 ºC the decrease of the sorption capacity over the sorption-desorption cycles was lower than for the dynamic tests performed at 300 and 400 ºC.

Subchapter 5.2. Doping of hydrotalcite-based sorbents with different interlayer anions for CO_2 capture *

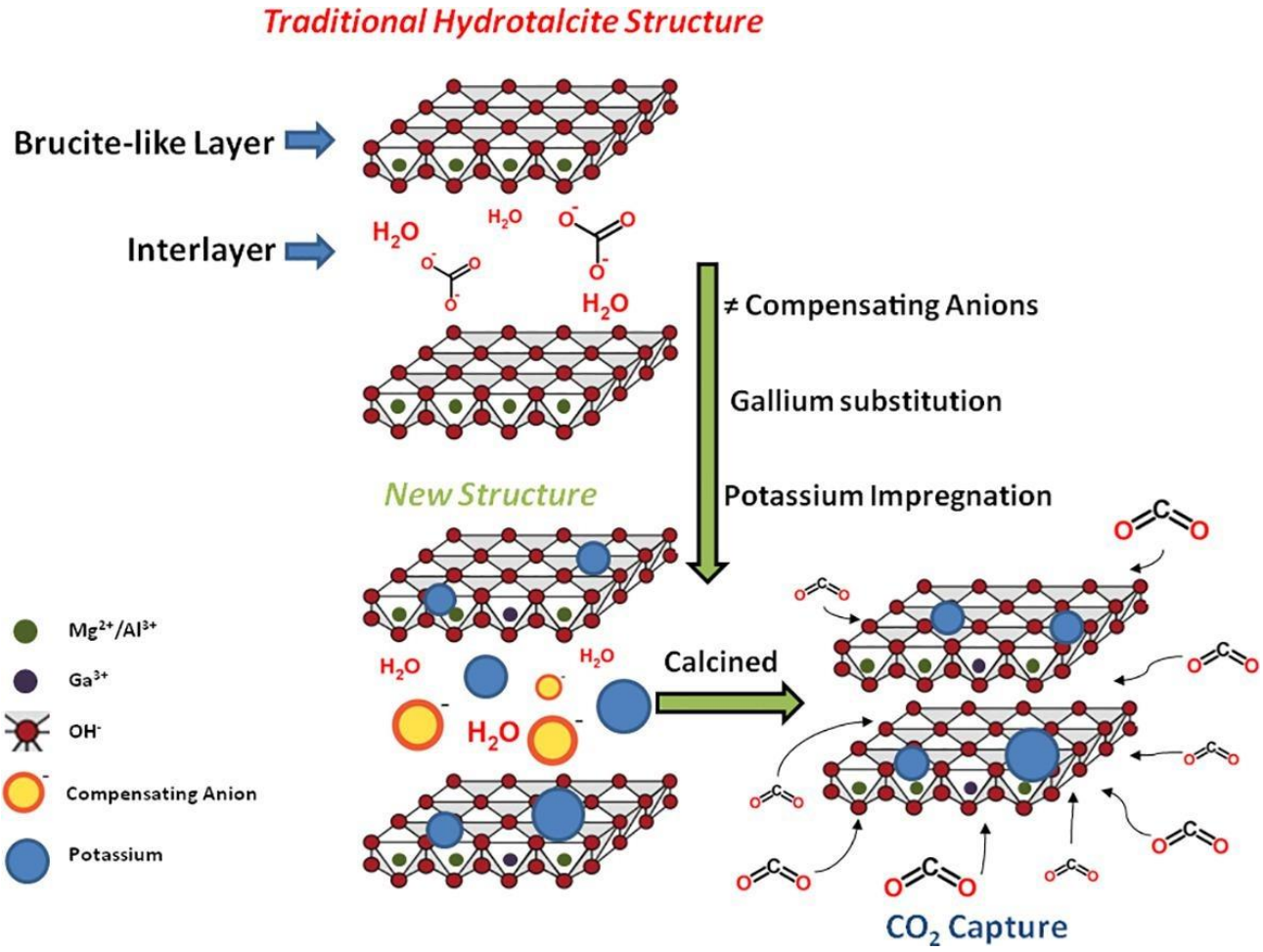

Highlights:

- Several K impregnated and/or Ga^{3+} substituted HTCs were prepared.
- Different interlayer anions were used in the preparation of the materials.
- HTC-CO_3(Ga)_K showed the highest CO_2 sorption capacity at 300 °C in the range of p_{CO_2} = 0.1-1 bar.
- The kinetic/equilibrium models proposed adequately fitted CO_2 uptakes/isotherms.
- The effect of steam during CO_2 capture with the new HTC-based sorbents was studied.

* The contents of this subchapter were adapted from Rocha, C., M.A. Soria and L.M. Madeira, Doping of hydrotalcite-based sorbents with different interlayer anions for CO_2 capture. Separation and Purification Technology, 2020. 235: p. 116140. (https://doi.org/10.1016/j.seppur.2019.116140)

Abstract:

Hydrotalcites (HTCs) with a molar ratio Mg^{2+}/Al^{3+} = 2 or $Mg^{2+}/(Al^{3+}+Ga^{3+})$ = 2 and (Al^{3+}/Ga^{3+} = 9) were synthesized using a co-precipitation method with two different interlayer anions: carbonate (CO_3^{2-}) and triacetoxyborohydride ($(CH_3COO)_3BH^-$). The simultaneous effect of aluminum partial substitution with gallium and impregnation with potassium on their CO_2 sorption capacity was assessed. The physicochemical characterization of the sorbents was performed through different techniques. The CO_2 sorption equilibrium isotherms at 300 ºC were determined for all the calcined sorbents and CO_2 breakthrough runs carried out. Sorption isotherms under dry conditions were well described by the Freundlich model for all samples. The results indicate that the doping of HTCs with potassium greatly enhanced the sorption capacity when compared with the original materials. It was seen in the dynamic tests that steam affects negatively the sorption performance of the HTCs prepared with the compensating anion $(CH_3COO)_3BH^-$, in opposition to what happens with the HTCs containing the CO_3^{2-} anion.

5.2.1. Introduction

After the experimental results obtained in the previous subchapter 5.1 [39], two hydrotalcites (HTCs) with different compensating anions and high sorption capacities were chosen to be modified and doped in order to enhance their CO_2 capture performances. Besides the physicochemical characterization of the modified and doped HTCs (i.e., after Al^{3+} partial substitution with Ga^{3+} and impregnation with K), the CO_2 sorption equilibrium isotherms at 300 ºC were determined for the new sorbents and for several commercial materials, for screening purposes. These results were compared with the performances of the two original HTCs (without K or Ga^{3+}), namely: i) HTC-CO_3 - where carbonate (CO_3^{2-}) is used as interlayer anion; and ii) HTC-long - where triacetoxyborohydride ($(CH_3COO)_3BH^-$) is the interlayer anion precursor. Different models were used to describe the equilibrium conditions and the CO_2 uptake kinetics in the static tests. Finally, all these materials were characterized by breakthrough (dynamic) cycling tests. The effect of steam on the sorption and regeneration steps was studied for the first time for the K-doped HTCs with base formulation HTC-long, in order to assess the performance of these materials in similar operating conditions as those applied in sorption-enhanced steam reforming processes.

In this way, the aims of this work were to develop several materials with different compensating anions that were modified and doped in an attempt to improve their CO_2 capture performance. The main novelty of this work was the preparation of modified or/and doped HTCs with triacetoxyborohydride anion as interlayer compensating precursor, which, as far as we know, were never prepared before. It is important to emphasize that the utilization of different interlayer anions has the purpose of enhancing the performance of the sorbent; the enlarged interlayer distance caused by the utilization of a long chain anion should help the dopant (potassium) to be dispersed into the material and, thus, create more basic sites to enhance the CO_2 sorption capacity [10]. The sample HTC-CO_3 and the doped/modified (with K^+/Ga^{3+}) samples derived from HTC-CO_3 were used as reference materials for comparison purposes with the new HTC-long sample (and its derivations), which were characterized not only by different physical-chemical techniques, but also through several static and dynamic CO_2 capture experiments.

The materials and methods used in this work are described in subchapter 3.2.

5.2.2. Results and discussion

5.2.2.1. Physicochemical characterization

The physicochemical characterization of the sorbents was performed through different techniques (XRD, FTIR, TGA-DTG, SEM/EDS, BET surface area and atomic absorption spectrophotometry (AAS)). The main results/conclusions of the characterization are summarized along this subchapter. For further details, please see Appendix D.

TGA and DTG analysis was performed to study the thermal decomposition and the loss of mass during calcination of the HTCs (see Fig. D.1 and Fig. D.2 in Appendix D). It was possible to verify that the samples present several peaks in the DTG analysis related to the removal of water (close to 100 ºC), hydroxyl groups (in the range of 100-250 ºC) and interlayer anions (higher than 250 ºC) - see Table D.1 in Appendix D. Besides that, the dry samples were calcined at 400 ºC for 2 h before the CO_2 sorption experiments because this pre-treatment removes efficiently water and the interlayer anions while yielding hydrotalcite-derived mixed oxides (HDMOs) - see section 1 of Appendix D for more details.

From the XRD results, it was verified that the dry samples present typical structures of HTCs (diffractograms in Fig. D.3 in Appendix D). However, for several HTCs more than 1 phase was observed (see Table 5.7). The values of the cell parameter *a* shown in Table 5.7 are close to the values reported in the literature for HTCs with Mg^{2+} and Al^{3+} as metal cations (with molar ratio Mg^{2+}/Al^{3+} = 2) [15]. The interlayer distance is related with the lattice parameter *c*, as discussed elsewhere [39], being possible to verify that the utilization of the *long* anion enhanced the interlayer space of HTC-long - Table 5.7 and Fig. D.3 in Appendix D.

Table 5.7 - XRD results for the dry samples.

		Lattice Parameters[a] (Å)		
Sorbent	**Grain Size[b] (nm)**	**a**	**c**	**Identified phases**
HTC-CO_3 dry	8.7 ± 1	3.034 ± 0.002	22.78 ± 0.02	HTC
HTC-CO_3(Ga) dry	9.7 ± 1	3.034 ± 0.002	22.80 ± 0.02	HTC
HTC-long dry	n.d.[c]	n.d.[c]	n.d.[c]	HTC(s)
HTC-long(Ga) dry	n.d.[c]	n.d.[c]	32.0 ± 0.5	HTC(s)
HTC-long_K dry	n.d.[c]	n.d.[c]	n.d.[c]	$KHCO_3$ + HTC
HTC-long_K calcined	n.d.[c]	n.d.[c]	n.d.[c]	$K_2CO_3 \cdot 6H_2O$
HTC-long_K spent[d]	n.d.[c]	n.d.[c]	n.d.[c]	$Mg(OH)_2$
HTC-CO_3(Ga)_K spent[d]	n.d.[c]	n.d.[c]	n.d.[c]	MgO + $MgCO_3$

[a] Calculated from Bragg's law [40]. [b] Calculated from Scherrer equation [41].
[c] Not determined.
[d] Used in the static tests.

FTIR spectra show the typical bands of HTC material for all prepared sorbents (Fig. D.4 in Appendix D). The presence of Ga^{3+} and the impregnation with K did not change significantly the position of the characteristic bands of the HTCs. It is worth noting that in the FTIR spectrum of the

HTC-long material there are no traces of methyl group vibrations in the range 2750-3000 cm^{-1}, which proves that no acetate anions have been retained by the sorbent and, in this way, the only interlayer anions present are CO_3^{2-} and $[B_3O_3(OH)_4]^-$ and/or $[B_4O_5(OH)_4]^{2-}$ (see more details in Appendix D, section 1).

The specific surface area was determined for all calcined samples as well as for some spent and dry samples, namely of HTC-CO_3(Ga)_K and HTC-long_K - see results in Table 5.8, Fig. D.5 and Fig. D.6 in Appendix D. The samples with the HTC-long base formulation have lower surface areas than the samples with base formulation HTC-CO_3, demonstrating that the interlayer anion influences the surface area of the HTCs. It can also be seen that the presence of Ga^{3+} (in substitution of Al^{3+}) slightly increases the surface area of both sample series. Lastly, it is noticed that the surface area decreases with the impregnation of potassium, which blocks the pores, in agreement with the results of other studies [1, 2]. The specific surface area of the samples decreases after calcination (please compare dry and calcined samples), which is related to the collapse of the structure. However, it was almost not affected by the use of the materials or even slightly increased. This is probably due to the "memory effect" that these types of sorbents present [42-44]; in this way, the structure of the dry samples was partially recovered after the tests (contact with CO_2 in the experiments and water from the atmosphere).

Table 5.8 - Surface area for several prepared samples.

Sorbent	BET Surface Area ($m^2 \cdot g^{-1}$)	Sorbent	BET Surface Area ($m^2 \cdot g^{-1}$)
HTC-$CO_3^{calcined}$	138	HTC-long ^{calcined}	29
HTC-CO_3(Ga)^{calcined}	152	HTC-long(Ga) ^{calcined}	54
HTC-CO_3(Ga)_K^{dry}	43	HTC-long_K^{dry}	6
HTC-CO_3(Ga)_$K^{calcined}$	28	HTC-long_$K^{calcined}$	2
HTC-CO_3(Ga)_K^{spent}	29	HTC-long_K^{spent}	7

None of the dry samples shows a well-defined morphology in the SEM images, although the presence of thin slabs is clearly verified (for instance, see Fig. D.8a) in Appendix D). The surface of the samples prepared with the *long* anion is smooth and the porosity was very low in opposition with the samples with CO_3^{2-} as interlayer anion - see Fig. D.8a) and Fig. D.8f) in Appendix D. Besides, it is possible to see that potassium-doped HTC samples present a honey structure in the materials with base formulation HTC-CO_3 and cubic structures in materials with base formulation HTC-long - see Fig. D.8e) and Fig. D.8i) in Appendix D.

EDS analyses showed that the $Mg^{2+}/(Al^{3+}+Ga^{3+})$ ratio for all samples was not constant in the particles (it varies from zone to zone but is close to 2). Furthermore, the boron element was detected several times (data not shown), which demonstrates that $[B_3O_3(OH)_4]^-$ and/or $[B_4O_5(OH)_4]^{2-}$ is present in the structure. Moreover, it was found that several zones did not present Ga^{3+} on the surface and that the

impregnation with K was not homogeneous - see figures about the SEM/EDS analysis in Appendix D, section 1.

The AAS technique was used to determine the real content of potassium in the calcined samples (see Table 5.9), since in the SEM/EDS analyses it was only possible to determine the metal concentration on the surface.

Table 5.9 - Loading of potassium in the calcined samples.

Sorbent	Content of Potassium (wt.%)	Sorbent	Content of Potassium (wt.%)
HTC-CO_3_K	17	HTC-long(Ga)_K	17
HTC-CO_3(Ga)_K	17	MG30_K	17
HTC-long_$K^{10\ wt.\%}$	12	MG63_K	17
HTC-long_$K^{20\ wt.\%}$	17	MG70_K	16
HTC-long_$K^{30\ wt.\%}$	25		

The real content in the samples follows the intended order, since the HTC-long_$K^{30\ wt.\%}$ sample should have the highest potassium content and the HTC-long_$K^{10\ wt.\%}$ the lowest. It can be seen in Table 5.9 that the potassium loading in the calcined HTCs sorbents as well as in the commercial impregnated sorbents (MG30_K, MG70_K and MG63_K) was close to the nominal values.

5.2.2.2. CO_2 sorption experiments

In this work, a screening of both commercial and prepared doped-sorbents for CO_2 capture was realized. After the determination of the sorption capacities (moles of CO_2 sorbed per mass of sorbent), the performances in dynamic tests should be compared to select the best for a sorption-enhanced process.

Determination of sorption equilibrium isotherms at 300 ºC for commercial sorbents

The equilibrium CO_2 sorption capacities of the calcined commercial materials, determined under dry conditions at 300 ºC for different pressures of CO_2, are shown in Fig. 5.14. As already mentioned in subchapter 3.2.2, two commercial HTCs (MG63 and MG70) were doped with potassium for comparison with the reference MG30_K sample; in such materials, the number refers to the magnesium oxide content (wt.%). Potassium-doped MG63 and MG70 materials present higher sorption capacities in comparison with the other commercial sorbents (Fig. 5.15), which can be ascribed to the fact that the Mg^{2+}/Al^{3+} molar ratio influences the CO_2 sorption capacity [45].

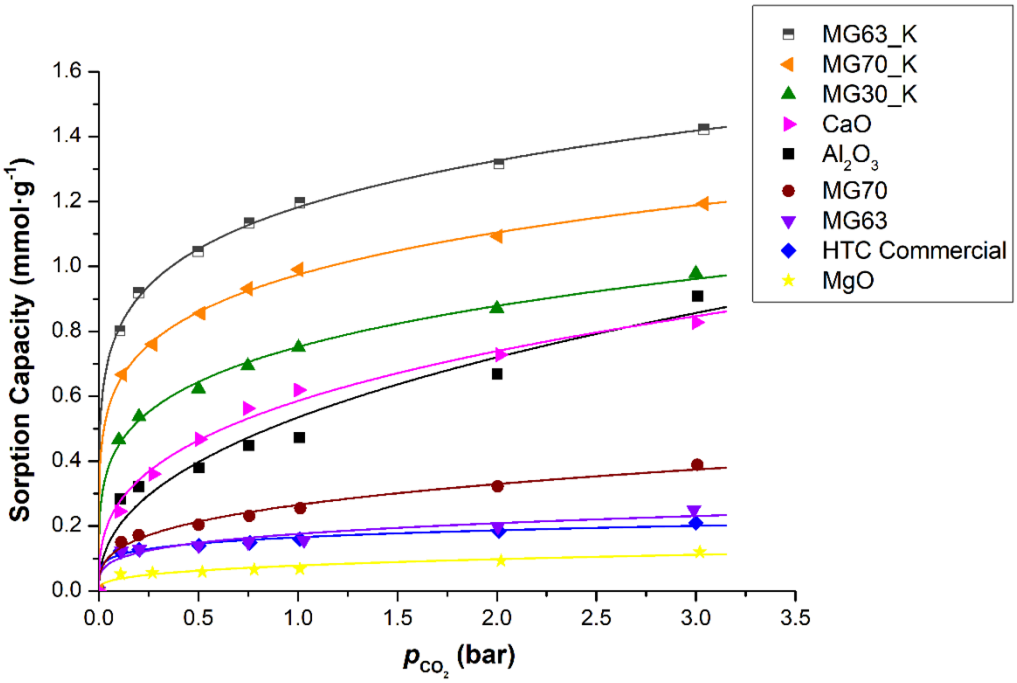

Fig. 5.14. Sorption equilibrium isotherms for different commercial sorbents at 300 ºC - fitting with Freundlich model.

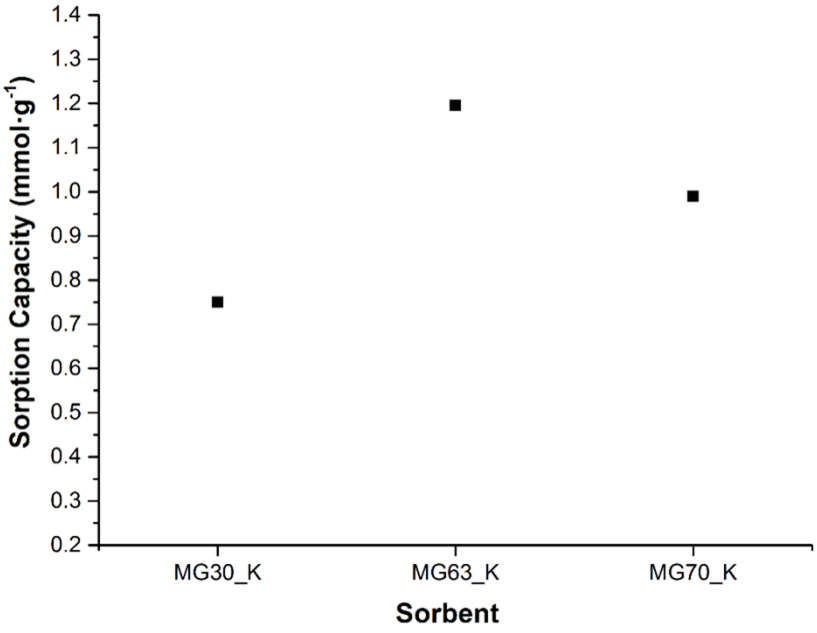

Fig. 5.15. Sorption capacities for different commercial impregnated HTCs at p_{CO_2} = 1 bar and 300 ºC. The molar ratios Mg^{2+}/Al^{3+} are: ≈ 0.5 for MG30_K, ≈ 2 for MG63_K and ≈ 3 for MG70_K.

Fig. 5.15 shows that the optimum ratio for Mg^{2+}/Al^{3+} is around 2 (MG63_K) for the doped-HTCs (impregnated with potassium). For this reason and based on the previous results reported in the literature [45, 46], the synthesized HTCs were prepared with this ratio.

Determination of sorption equilibrium isotherms at 300 ºC for the prepared sorbents

The equilibrium CO_2 sorption capacities of the calcined HTCs, determined under dry conditions at 300 ºC for different pressures of CO_2 (pure CO_2), are shown in Fig. 5.16. Among the two HTC-A samples prepared, HTC-CO_3 showed the highest CO_2 capture capacity of 1.05 mmol·g^{-1} (p_{CO_2} = 1 bar) in comparison with the HTC-long (0.69 mmol·g^{-1} @ p_{CO_2} = 1 bar) - see Table 5.10 and Fig. 5.16.

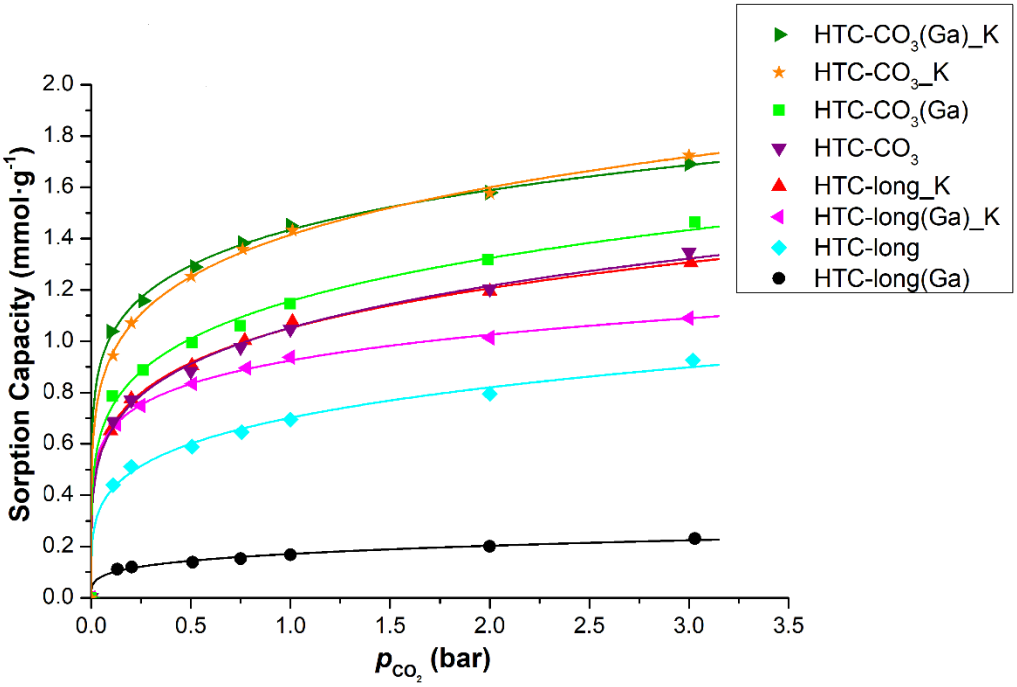

Fig. 5.16. Sorption isotherms for different HTCs at 300 ºC - fitting with Freundlich model.

It was verified that the Al^{3+} partial substitution by Ga^{3+} in the HTC-CO_3 material slightly enhanced the sorption capacity (1.15 mmol·g^{-1} for HTC-CO_3(Ga) at p_{CO_2} = 1 bar), and by doping the starting HTC with 20 wt.% of potassium (HTC-CO_3_K), the CO_2 sorption capacity was increased up to 1.43 mmol·g^{-1} (p_{CO_2}= 1 bar). The combination of the 2 modifications (HTC-CO_3(Ga)_K sample) only very slightly further enhanced the sorption capacity to 1.45 mmol·g^{-1} (p_{CO_2} = 1 bar). However, the combination of these effects is more pronounced at lower partial pressures of CO_2 - see Fig. 5.16. The results for HTC-CO_3(Ga)_K material herein presented are in line with the ones obtained in previous works [1, 2, 22], where it was shown that the impregnation with potassium along with the substitution of Al^{3+} by Ga^{3+} improved the sorption capacity of HTCs, the first acting as a chemical promoter and the second probably providing a double effect, improving the structure and the basicity of the HTC. These effects were however not observed for the HTC-long(Ga)_K sample (in this series, the CO_2 sorption capacity increases with the impregnation of potassium but considerably decreases with the Ga^{3+} partial substitution) - see Table 5.10 and Fig. 5.16.

For both HTC-CO_3 and HTC-long samples the increase of the sorption capacity normalized by the amount of impregnated potassium was the same, i.e., 0.09 $mmol_{CO_2}$·$mmol_K^{-1}$ at p_{CO_2} = 1 bar

(calculations based on the real wt.% of K - Table 5.9). However, for HTC-CO_3(Ga) and HTC-long(Ga), the increase was 0.07 and 0.18 $mmol_{CO_2}{\cdot}mmol_K^{-1}$, respectively. In the work of Silva *et al.* [1], the increase of the performance with the impregnation of K in the base HTC was similar to the one found in this work (0.10 $mmol_{CO_2}{\cdot}mmol_K^{-1}$). Nevertheless, in the work of Miguel *et al.* [2], the increase of the sorption capacity with the impregnation of K in the HTC modified with Ga^{3+} was higher (0.24 $mmol_{CO_2}{\cdot}mmol_K^{-1}$). It seems therefore that there is a consensus in the literature about the positive promoting effect resulting from potassium doping, but such effect, in quantitative terms, changes from sample to sample.

The sample HTC-long_K was also calcined at higher temperatures (500 and 550 ºC); however, the performance of the material was lower than for the sample calcined at 400 ºC (data not shown). This is probably related to the total destruction of the HDMO structure, in line with the work of Reddy *et al.* [19].

The experimental data of CO_2 sorption isotherms present a good fitting to the Freundlich model - Eq. (5.3) (see Fig. 5.14 and Fig. 5.16) - where q is the sorption capacity ($mmol{\cdot}g^{-1}$), K_F is the Freundlich constant ($mmol{\cdot}g^{-1}{\cdot}bar^{1/n}$), p_{CO_2} is the partial pressure of CO_2 (bar) and n is an exponential constant.

In Table 5.11, it is possible to see the adjusted parameters upon maximization of either R^2 (Eq. (5.1)) or *MSC* (Eq. (5.2)), a methodology used in previous works [29, 30] and in the previous subchapter 5.1. It was found that the sorption capacity of the materials was not closely linked to their specific surface areas. In other works, it was also reported that the available surface area does not play a crucial role on the CO_2 sorption capacities [2, 4, 20], which is more related to the chemical nature of the exposed surface. In addition, it was verified that the sorption capacities are also not directly related to the total pore volume in the sorbents, size of pores neither to other parameters reported above for these materials.

Table 5.10 - Sorption capacities of CO_2 sorbents and respective experimental conditions.

Sorbent	Sorption Capacity ($mmol \cdot g^{-1}$)	Temperature (ºC)	p_{CO_2} (bar)	Reference	Sorbent	Sorption Capacity ($mmol \cdot g^{-1}$)	Temperature (ºC)	p_{CO_2} (bar)	Reference
cHTC	0.81	300	1.03	[1]	HTI-K-Na	1.10*	300	0.40	[47]
cK-HTC	1.42	300	1.02	[1]	MG61-K_2CO_3	1.31	300	0.34	[48]
HTC-10Ga	0.58	300	1.12	[2]	MG30-K^N	1.08*	335	0.50	[49]
HTC-10Ga-20K	1.82	300	1.08	[2]	K-HTC	0.28	400	0.50	[50]
cK-HTCGa MW	1.70	300	1.05	[1]	K-HTC	0.58	400	0.47	[21]
K-HTC MW	1.46	300	1.00	[51]	HTC-CO_3	0.88	300	0.50	This work
K-HTC	0.79	400	1.00	[33]	HTC-CO_3(Ga)	0.99	300	0.51	This work
HTC-CO_3	1.05	300	1.00	This work	HTC-CO_3_K	1.25	300	0.50	This work
HTC-CO_3(Ga)	1.15	300	1.00	This work	HTC-CO_3(Ga)_K	1.29	300	0.52	This work
HTC-CO_3_K	1.43	300	1.01	This work	HTC-long	0.59	300	0.51	This work
HTC-CO_3(Ga)_K	1.45	300	1.00	This work	HTC-long(Ga)	0.14	300	0.51	This work
HTC-long	0.69	300	1.00	This work	HTC-long_K	0.90	300	0.51	This work
HTC-long(Ga)	0.17	300	1.00	This work	HTC-long(Ga)_K	0.83	300	0.51	This work
HTC-long_K	1.08	300	1.01	This work					
HTC-long(Ga)_K	0.94	300	1.00	This work					

* Under wet conditions.

Table **5.11 -** Parameters calculated for the Freundlich isotherms for different HTCs.

Sorbent	K_F[a] (mmol·g^{-1}·bar$^{1/n}$)	n[a]	R^2	K_F[b] (mmol·g^{-1}·bar$^{1/n}$)	n[b]	*MSC*
HTC-CO_3	1.05	4.81	1.00	1.05	4.82	5.61
HTC-CO_3(Ga)	1.16	5.12	1.00	1.16	5.13	5.37
HTC-CO_3_K	1.41	5.64	1.00	1.41	5.65	7.05
HTC-CO_3(Ga)_K	1.43	6.79	1.00	1.43	6.79	6.90
HTC-long	0.70	4.49	1.00	0.70	4.51	4.99
HTC-long(Ga)	0.17	4.06	0.99	0.17	4.08	4.51
HTC-long_K	1.05	5.04	1.00	1.05	5.04	6.49
HTC-long(Ga)_K	0.92	6.70	1.00	0.92	6.71	7.26

[a] Parameters calculated with maximization of R^2 (Eq. (5.1)).
[b] Parameters calculated with maximization of *MSC* (Eq. (5.2)).

Effect of the K content

The performance of CO_2 sorbents can be enhanced by promotion with alkaline species [52]. Particularly, K_2O_3-modified HTCs (with CO_3^{2-} as compensating anion) have shown excellent sorption capacities [1, 2, 10, 21, 38, 49]. Several papers [53-55] reported that the optimum content of potassium in HTCs with CO_3^{2-} as compensating anion is 20 wt.%. Since the HTC-long materials present a different morphology and surface chemistry, the effect of the potassium content was studied, which was done for the first time.

The sorption equilibrium isotherms of the calcined potassium-doped HTC-long samples, determined under dry conditions at 300 ºC for different partial pressures of CO_2, are shown in Fig. 5.17. The sorption capacity of CO_2 increased with the amount of potassium until 20 wt.%, indicating that the number of basic sites for CO_2 sorption was increased. Although with a loading of 30 wt.% the number of basic sites could have been increased, the CO_2 sorption capacity decreases (till lower values than the sorption capacity of the bare sample - HTC-long), probably due to the pore blocking caused by the K_2CO_3 impregnation (see surface areas in Table 5.12); such overdoping effect has also been observed in other areas (e.g. [56, 57]). Therefore, among the HTC-long samples containing different potassium loadings, that with 20 wt.% showed the highest CO_2 sorption capacity.

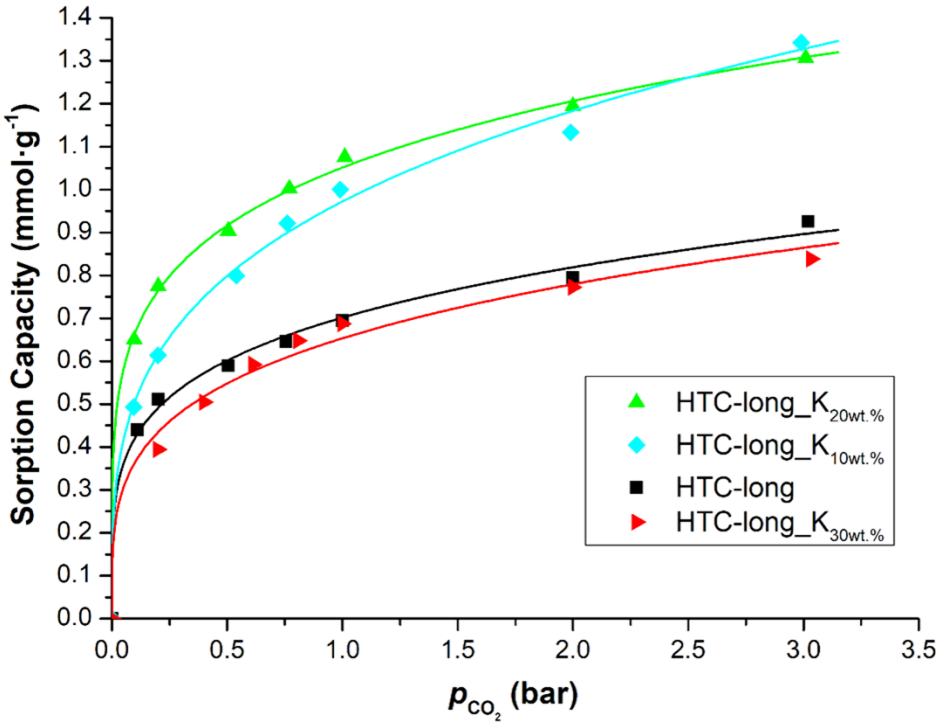

Fig. 5.17. Sorption equilibrium isotherms for different contents of K in the HTC-long_K series at 300 ºC - fitting with the Freundlich model.

Therefore, potassium impregnation affects the sorption capacity by changing the structure and the chemical properties of the HTC. Table 5.12 exhibits the surface areas of the different calcined HTC-long samples with different contents of potassium. As shown in Table 5.12, the surface area decreased with the potassium content. These results demonstrate that the sorption capacity increases with the content of basic sites (due to the impregnation of K_2CO_3), but such modification also blocked the pores (decrease of the surface area).

Therefore, the K_2CO_3 impregnation influenced the morphology, physical and chemical properties of the HTC, but there is an optimum value for the content of potassium for obtaining the highest performance.

Table 5.12 - Surface area for samples with different loading of potassium in HTC-long_K.

Sorbent	Surface Area ($m^2 \cdot g^{-1}$)	Total Pore Volume ($cm^3 \cdot g^{-1}$)
HTC-long	29	0.107
HTC-long_$K_{10\ wt.\%}^{dry}$	26	0.087
HTC-long_$K_{20\ wt.\%}^{dry}$	6	0.005
HTC-long_$K_{30\ wt.\%}^{dry}$	< 1	0.001

Determination of CO_2 uptake kinetics

The CO_2 uptake in the HTCs during the static tests can be described by a model based on the study of Du *et al*. [35], who proposes the formation of uni-, bi-, poly-dentate and bridged carbonate species. The formation of polydentate species is related to the slow irreversible CO_2 sorption while the other

species are related to the fast-reversible uptake. In another study [36], it has also been observed that these materials present two types of CO_2 sorption (slow/fast). Considering the mechanism proposed by Du *et al.* [35] and previous studies of the team [1, 2], the model described in Eq. (5.5) was used to describe the uptake of sorbed CO_2.

As already mentioned in the previous subchapter 5.1, the transient state model (Eq. (5.5)) assumes constant surface concentration in the particles, which are of spherical geometry, uniform initial concentration within the particles and two kinetic contributions occurring at the same time, one responsible for the fast uptake (mostly at the beginning) and, the other one, by the slow increase observed for longer times; the kinetics of these contributions is related with the $\frac{D_i}{r^2}$ parameters. As stated in subchapter 5.1, one should note that $q(\infty)$ is known, since it is the sorption capacity measured at the equilibrium, as well as is the initial value $(q(t=0))$, which is the sorption capacity measured in the initial time of the sorption tests. Moreover, F_1 and F_2 are the partial uptake fractions related to the two types of uptakes (fast and slow), respectively, $q(t)$ is the CO_2 sorption capacity measured at time t. $\frac{D_1}{r^2}$, $\frac{D_2}{r^2}$ and q_1 (related to the fast uptake; while q_2 is the sorption capacity related to the slow uptake) are model parameters that were obtained through non-linear fitting of Eq. (5.5) to the experimental data. Finally, as already indicated in the previous subchapter, it is worth noting that the quantity related to the slow uptake (q_2) is equal to the difference between q_∞ and q_1.

From Fig. 5.18 it is possible to see that the model predicts accurately the experimental data (doped-HTCs with the best performance for each interlayer anion series were selected to be illustrated), which is in line with the good fittings obtained in previous articles [1, 2]. The parameters calculated for each sorbent are shown in Table 5.13. Overall, the uptakes for samples with the anion CO_3^{2-} are faster than for samples prepared with the *long* anion - Fig. 5.19. On the other hand, data shown in Table 5.13 show that, in general, CO_2 adsorbs faster on base HTCs than on the K-doped samples, this meaning that impregnation with potassium slows down the sorption process; however, it enhances the CO_2 sorption capacity. This might be related to the previously mentioned pore blocking caused by the potassium impregnation (cf. Table 5.12), which probably slows the diffusion of CO_2 inside the particles. While in the HTCs derived from HTC-long it was possible to see that the substitution of Al^{3+} by Ga^{3+} enhanced the rate of the sorption, for the HTC-CO_3 series the effect was the opposite one.

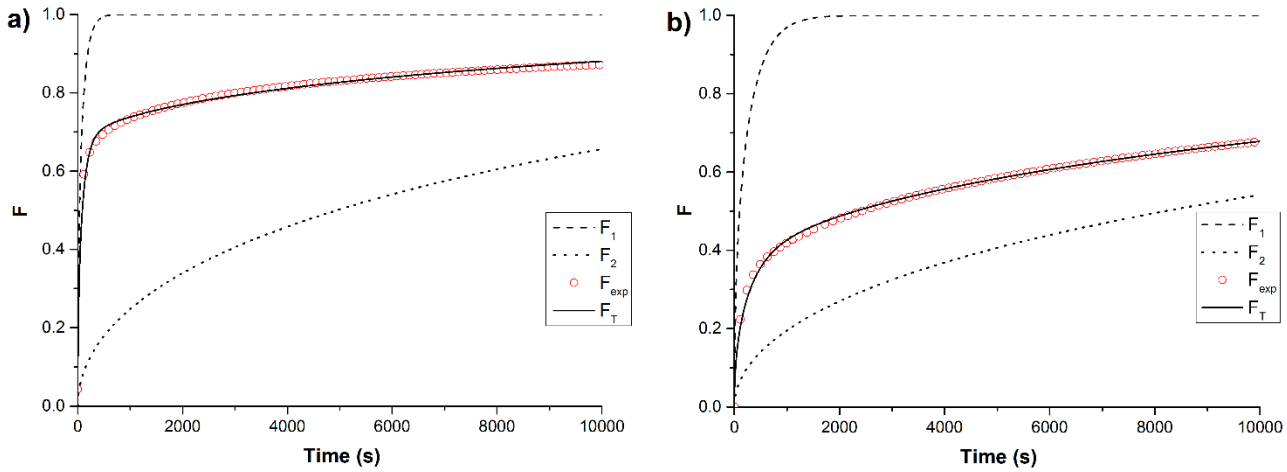

Fig. 5.18. Uptake curves for CO_2 sorption at 0.1 bar and 300 ºC for a) HTC-CO_3(Ga)_K and b) HTC-long_K.

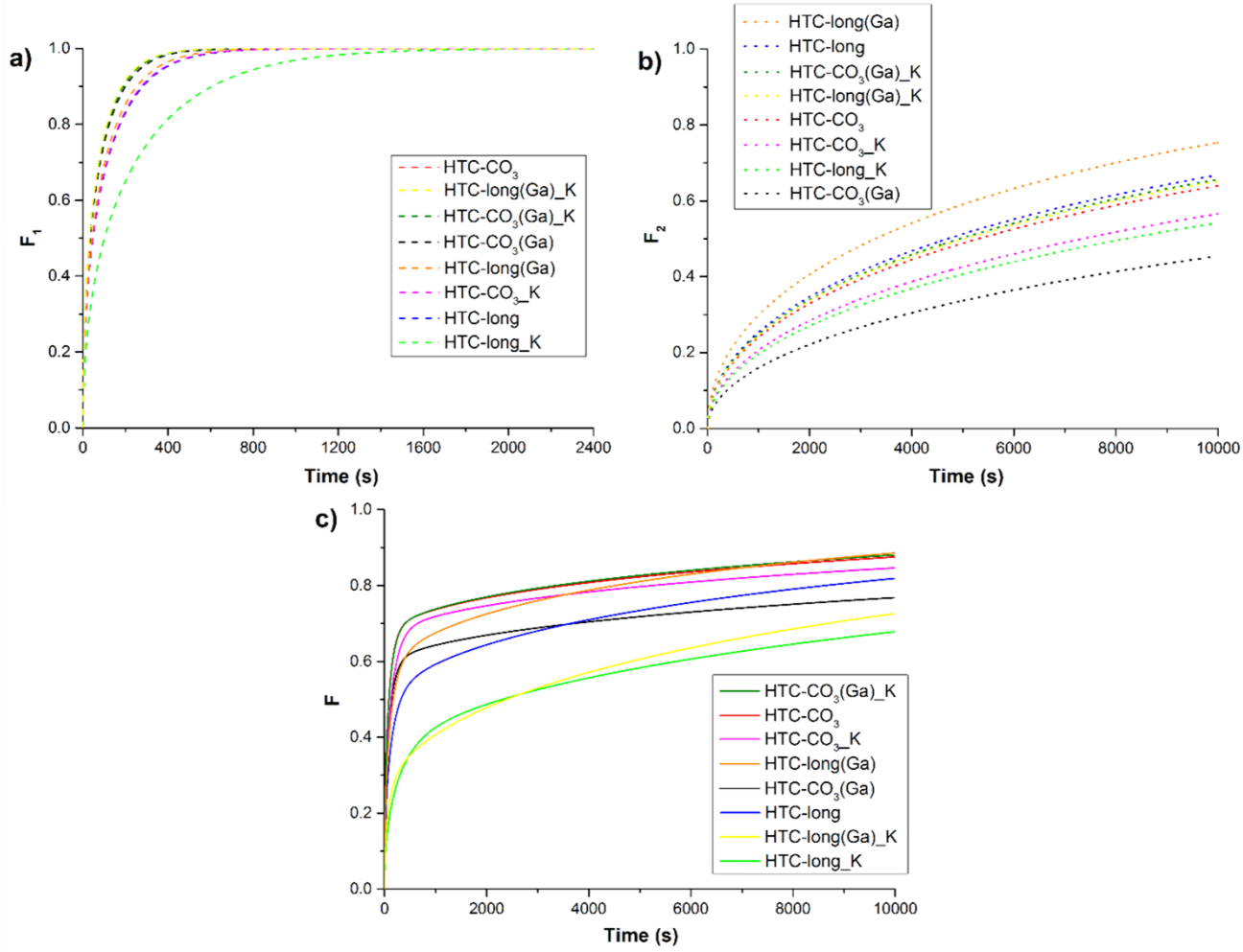

Fig. 5.19 Comparison of the uptake curves at 0.10 bar of CO_2 obtained through the model for the different samples: a) F_1, b) F_2 and c) F.

Table 5.13 - Parameters obtained through fitting of the experimental CO_2 uptakes for the samples at 0.10 bar and 300 ºC.

Sorbent	$\frac{D_1}{r^2}$ (s^{-1})	$\frac{D_2}{r^2}$ (s^{-1})	$\frac{q_1}{q_\infty} \times 100$
HTC-CO_3	1.00×10^{-3}	5.76×10^{-6}	65
HTC-CO_3(Ga)	9.15×10^{-4}	2.43×10^{-6}	58
HTC-CO_3_K	6.66×10^{-4}	4.16×10^{-6}	65
HTC-CO_3(Ga)_K	9.65×10^{-4}	6.19×10^{-6}	65
HTC-long	6.50×10^{-4}	6.50×10^{-6}	45
HTC-long(Ga)	7.24×10^{-4}	9.30×10^{-6}	54
HTC-long_K	3.02×10^{-4}	3.73×10^{-6}	30
HTC-long(Ga)_K	1.00×10^{-3}	6.06×10^{-6}	21

Breakthrough experiments

To determine the dynamic performance of several sorbents, sorption-desorption breakthrough cycles were carried out under different operation conditions.

The sorption capacities were calculated by Eq. (5.6) and the efficiency of the column (η) was calculated by Eq. (5.7). The values of $q_{\mathrm{CO_2 total}}$ used in the Eq. (5.7) were the sorption capacities obtained in the static tests to avoid very long breakthrough experiments. However, it was performed a test with a long sorption time (8 h) and the sorption capacity calculated for this dynamic test was very similar to the value taken from the equilibrium isotherm (differed only ≈ 5 %).

In the *Exp. 1.1* (see more details about this experimental run in Table 3.5), it was possible to observe that the first cycles show a higher CO_2 sorption capacity for all the samples analysed and none of the sorbents was completed saturated after 20 minutes of sorption ($\frac{y_{\mathrm{CO_2}}^{\mathrm{out}}}{y_{\mathrm{CO_2}}^{\mathrm{in}}}$ lower than 1 - data not shown). It can also be seen that the sorption capacities (Fig. 5.20c)), the breakthrough curves (Fig. 5.20a-b)) and the breakthrough/stoichiometric times were different for all the samples studied. As seen in this subchapter, the CO_2 sorption kinetics for the HTC-CO_3 samples series are faster than for the samples derived from HTC-long. Therefore, the efficiency of the column (η) should be higher for the HTC-CO_3 base formulation materials, as actually observed (Table 5.14), since the samples with base formulation HTC-long still sorb a large quantity of CO_2 after the breakthrough point. This behavior can be also seen in the shape of the breakthrough curves (samples with base formulation HTC-CO_3 present, in a general way, a steeper curve while for the HTC-long the dispersion is more notorious). Besides that, it was expected (and confirmed - Fig. 5.20c)) that the sorption performance should be higher for the samples with the base formulation HTC-CO_3, as also seen at the beginning of this subchapter. However, from the cycling tests, it was observed that the base formulation HTC-long samples present a lower absolute decrease in the sorption capacity in comparison with the samples with base formulation HTC-CO_3. Nevertheless, the relative decrease of the sorption capacity differed from sample to sample (see also Fig. 5.20d)). The decrease of the sorption capacity of the materials over the sorption-desorption cycles could be related to the formation of other phases like $MgCO_3$ (see

results of XRD in subchapter 5.2.2.1) that improve mechanical stability issues in doped-HTCs, as shown in previous work [46].

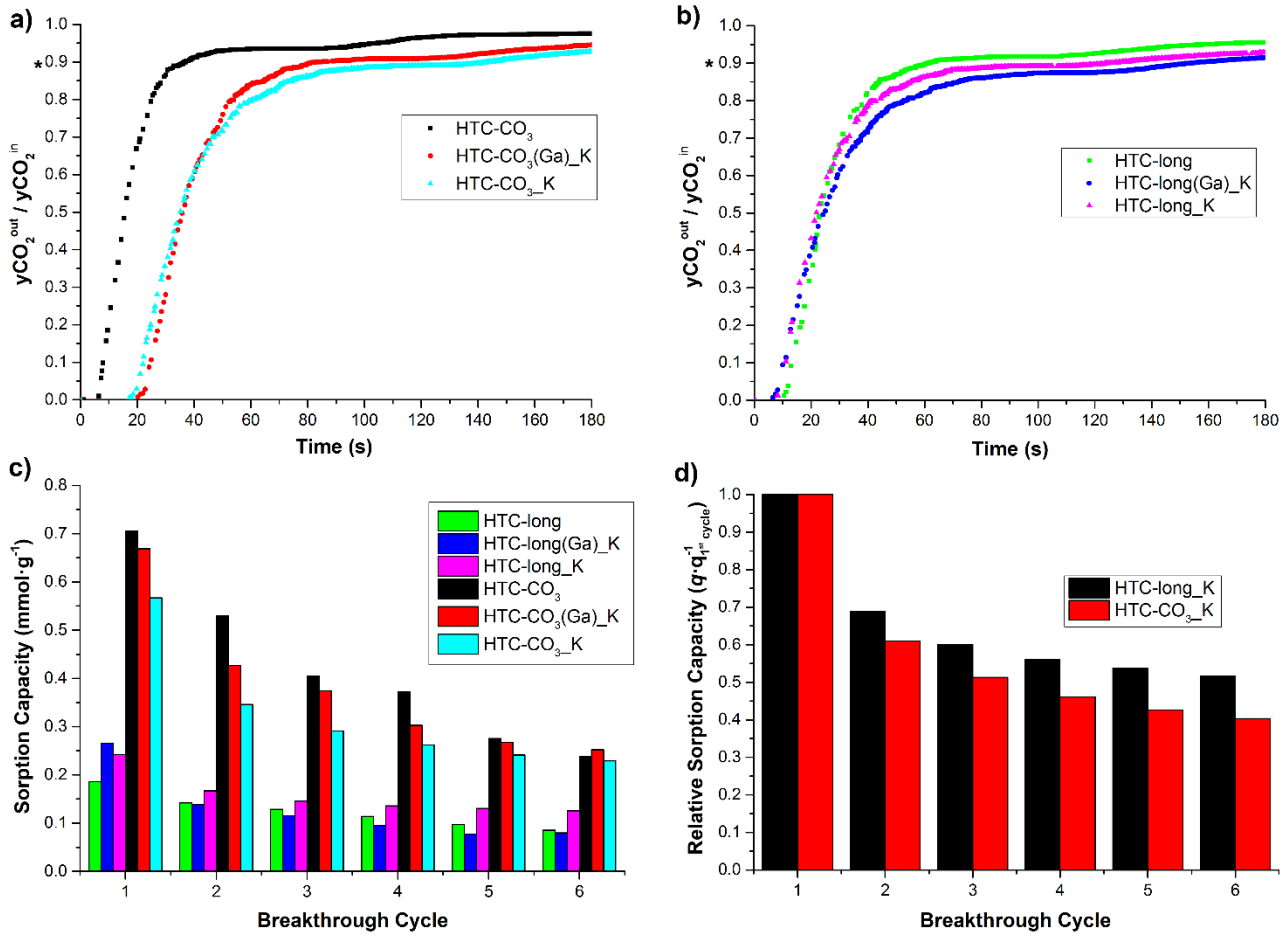

Fig. 5.20. Effect of the interlayer anion in the a-b) breakthrough curves, c) sorption capacities at 300 ºC and 1 bar and d) relative decrease of the sorption capacity over the sorption-desorption cycles for HTC-long_K and HTC-CO_3_K. Sorption step (20 min) carried out with 15 vol.% of CO_2 balanced in N_2 - total flow rate of 100 $mL_N \cdot min^{-1}$; pre-treatments were performed at 300 ºC (*Exp. 1.1*). Regeneration step carried out under 95 $mL_N \cdot min^{-1}$ of N_2 (30 min). * The mass was not kept constant (the samples had different densities).

Table 5.14 - Efficiencies of the column for different samples.

Sorbent	Efficiency, η (%)	Sorbent	Efficiency, η (%)
HTC-CO_3	20	HTC-long	9
HTC-CO_3_K	16	HTC-long_K	4
HTC-CO_3(Ga)_K	21	HTC-long(Ga)_K	4

It was possible to verify the effect of the initial state of the material after the pre-treatment (*Exp. 1.3*). It was concluded that the pre-treatment at 400 ºC of the calcined sorbent allowed to remove more efficiently the water and atmospheric CO_2 sorbed from the environment (see Fig. 5.21a)), in contrast with the pre-treatment at 300 ºC (as verified in the TG results - see Appendix D). Due to this reason, the sorption capacity of the HTC-CO_3_K was higher (0.66 $mmol \cdot g^{-1}$, for the same sorption time) - see Fig. 5.21a). The following sorption experiments were performed after a pre-treatment at 400 ºC.

The other effect studied in *Exp. 1.3* was the sorption time (Fig. 5.21b)). A sorption time of 20 min was not sufficient to capture CO_2 until the saturation of the sorbent. It can be seen that the sorption capacity increases with the sorption time. This behavior of the sorbent (HTC-CO_3_K) to continuously increase the CO_2 capture, even after long exposition times, has also been noted in the literature [35]. However, for a sorption time of 1 h, the sorption capacity of this HTC calculated from this dynamic test was nearly equal to the value determined from the static test (1.01 mmol·g^{-1} - a difference of only 0.04 %). The sorption capacity calculated when the sorption time was 8 h (1.06 mmol·g^{-1}) was very similar to the previous one and, for this reason, it was clear that the saturation of the sorbent was nearly reached after 1 h of sorption. The efficiencies for the HTC-CO_3_K were very similar for the different sorption times (16 %, 22 % and 14 % for sorption times of 20 min, 1 h and 8 h, respectively). In Fig. 5.21c) it is possible to see the two effects conjugated: higher sorption time and higher pre-treatment temperature allow to sorb a higher quantity of CO_2, however, the decrease (relative and absolute) of the performance over the cycles is also higher. A higher sorption time enhanced the formation of species related to the irreversible sorption [35].

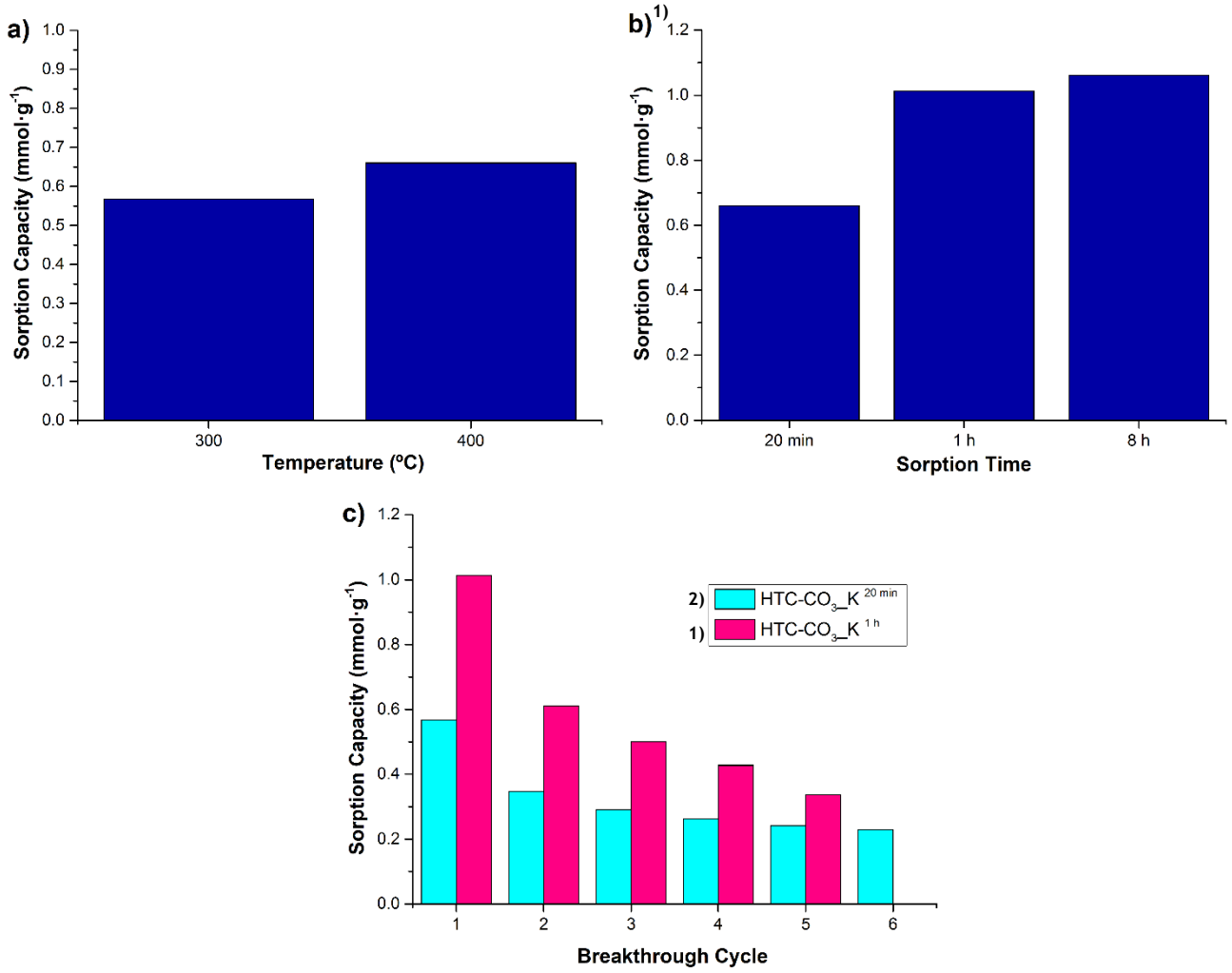

Fig. 5.21. Effect of a) the pre-treatment temperature (20 min of sorption time) and b) sorption time on the sorption capacity of the HTC-CO_3_K calculated in the dynamic tests at 300 ºC and 1 bar (*Exp. 1.3*); and c) simultaneous effect of the pre-treatment temperature and sorption time on the sorption capacity over the cycles of the HTC-CO_3_K at 300 ºC and 1 bar. Sorption step carried out with 15 vol.% of CO_2 balanced in N_2 - total flow rate of 100 mL·min^{-1}. Regeneration step carried out under 95 mL·min^{-1} of N_2 (30 min). Pre-treatments were performed at 400 ºC[1)] or 300 ºC[2)].

It was observed that steam negatively affects the sorption capacity of the sorbents with base formulation HTC-long (*Exp. 1.1* vs. *Exp. 1.4*) - see Fig. 5.22 (breakthrough curves in Fig. D.14 in Appendix D). Moreover, the presence of steam leads to the sorbents' loss of capacity over the cycles (Fig. 5.22b)). These results are in opposition to those reported in previous studies [20, 36, 38, 47, 48, 58-60] wherein it was concluded that the presence of steam enhanced the CO_2 sorption on HTC-based sorbents (with the CO_3^{-2} as an interlayer anion). So, it is possible to infer that the compensating anion affected the sorption mechanism of CO_2, once this anion changes the morphology, texture and chemical nature of the material (as seen in the characterization by XRD - the presence of different phases, BET - distinct areas - and TGA - different peaks -, respectively), so that H_2O and CO_2 compete for the same active sites in a different manner. In this way, the CO_2 sorption decreases possibly

because the active sites are occupied by the sorbed water molecules. However, further studies are required to better understand and explain in detail these results.

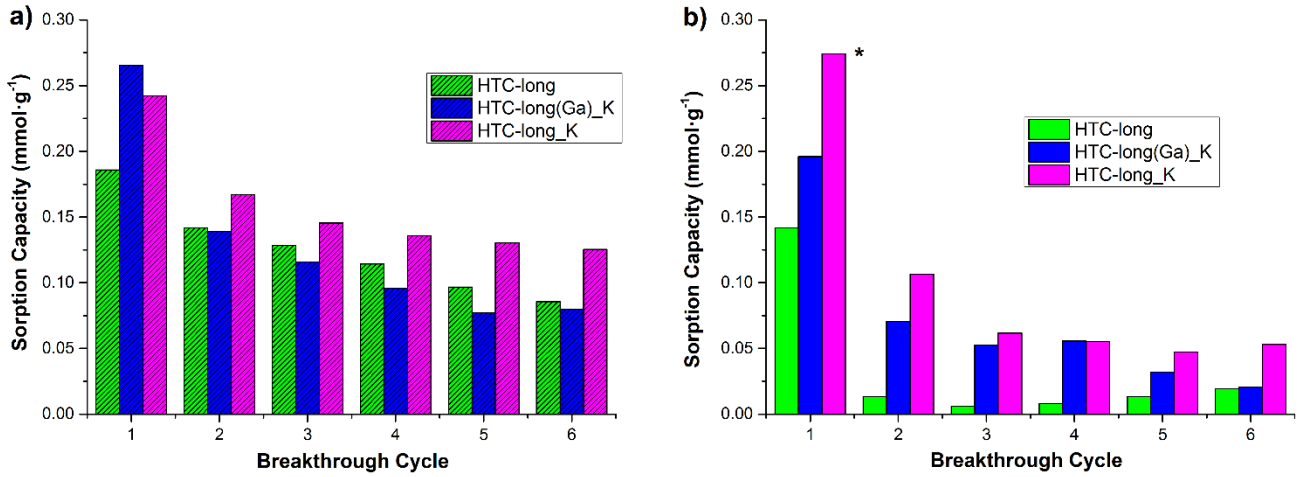

Fig. 5.22. Sorption capacities under a) dry conditions (*Exp. 1.1*) and b) in the presence of steam (*Exp. 1.4*), for the HTCs with base formulation HTC-long at 300 ºC and 1 bar. Sorption step (20 min) was carried out with 15 vol.% of CO_2 and 15 vol.% of steam balanced in N_2 - total flow rate of 100 $mL_N \cdot min^{-1}$; regeneration step carried out under 85 $mL \cdot min^{-1}$ of N_2 and 15 $mL_N \cdot min^{-1}$ of steam for 30 min (*Exp. 1.4*). Pre-treatments were performed at a) 300 ºC or b) 400 ºC. * Only in the 1st sorption cycle under wet conditions (*Exp. 1.4*), the sorption capacity of HTC-long_K was slightly higher than under dry conditions, because the pre-treatment was done at 400 ºC (while 300 ºC was employed for the dry tests - *Exp. 1.1*).

5.2.3. Conclusions

This work reports an investigation on how the interlayer anion influences the CO_2 sorption capacity of doped-HTCs sorbents. By doping HTC-CO_3 with 20 wt.% K, the CO_2 sorption capacity was increased, up to 1.43 $mmol \cdot g^{-1}$ (@p_{CO_2} = 1 bar and 300 ºC), and it was verified that the Ga^{3+} partial substitution in this HTC also slightly enhanced the sorption capacity (till 1.45 $mmol \cdot g^{-1}$ at p_{CO_2} = 1 bar and 300 ºC). However, the substitution of Al^{3+} by Ga^{3+} was not beneficial for the HTCs with the so-called *long* species (triacetoxyborohydride anion) as an interlayer precursor. For all the materials, the sorption equilibrium isotherm was well fitted using a Freundlich-type equation.

The sorption capacity of the sorbents was not related to their surface area but rather correlated with the chemical properties of the materials. In this way, the compensating anion influenced the sorption capacity of the HTCs and the impregnation with K always enhanced the sorption capacity. However, the effect of Ga^{3+} on the sorption performance depends on the interlayer anion used. It was observed that, in general, the sorption rates for samples with the anion CO_3^{2-} are higher than for the materials prepared with the *long* precursor. Moreover, a higher relative amount of CO_2 is sorbed on samples from the base formulation HTC-CO_3 than on samples derived from HTC-long during the fast uptake. Finally, it was possible to conclude that the compensating anion, the presence of K and the substitution of Al^{3+} by Ga^{3+} influence the sorption kinetic parameters.

Lastly, it was found that the sorbents from the base formulation HTC-long present a lower decrease in the sorption capacity (absolute decrease) in the dynamic cycles in dry conditions, as compared to the samples with base formulation HTC-CO_3. In addition, it was possible to verify that the interlayer anion affects the CO_2 sorption mechanism. For the sorbents with the base formulation HTC-long, the presence of steam has a negative effect on the performance. However, some of the sorbents prepared present a good performance to be subsequently used in a sorption-enhanced steam reforming process (HTC-CO_3 and HTC-CO_3_K).

Notation and Glossary

List of Variables

$\frac{D_1}{r^2}$	Kinetic parameter related to the fast uptake (s^{-1})
$\frac{D_2}{r^2}$	Kinetic parameter related to the slow uptake (s^{-1})
f	Number of fitting parameters (dimensionless)
F	Total CO_2 uptake fraction (dimensionless)
F_1	Partial uptake fraction related to fast uptake (dimensionless)
F_2	Partial uptake fraction related to slow uptake (dimensionless)
$\mathrm{F}_{\mathrm{CO_2}}$	CO_2 inlet molar flow rate ($mol \cdot min^{-1}$)
K_F	Freundlich constant ($mmol \cdot g^{-1} \cdot bar^{1/n}$)
m	Number of experimental points (dimensionless)
MSC	Model selection criterion (dimensionless)
$1/n$	Exponent constant of the Freundlich model (dimensionless)
$p_{\mathrm{CO_2}}$	Partial pressure of CO_2 (bar)
q_1	CO_2 sorption capacity related to the fast uptake ($mmol \cdot g^{-1}$)
q_2	CO_2 sorption capacity related to the slow uptake ($mmol \cdot g^{-1}$)
$q_{\mathrm{CO_2}}$	CO_2 sorption capacity ($mmol \cdot g^{-1}$)
q_{e}	CO_2 sorption capacity obtained from the experimental data ($mmol \cdot g^{-1}$)
$\overline{q_{\mathrm{e}}}$	Average of q_{e} ($mmol \cdot g^{-1}$)
q_{m}	CO_2 sorption capacity obtained from the isotherm model ($mmol \cdot g^{-1}$)
$q(\infty)$	Sorption capacity at the equilibrium ($mmol \cdot g^{-1}$)
R^2	Coefficient of determination (dimensionless)
t	Time (min)
T	Temperature (ºC)
$\mathrm{y}_{\mathrm{CO_2}}$	CO_2 molar fraction (dimensionless)
η	Efficiency of the column (dimensionless)
ΔH_{Ads}	Isosteric heat of adsorption ($kJ \cdot mol^{-1}$)

List of Acronyms

AAS	Atomic absorption spectrophotometry
BET	Brunauer-Emmett-Teller
DTG	Derivative thermogravimetric
FTIR	Fourier-transform infrared spectroscopy
HDMO	Hydrotalcite-derived mixed oxide
HTC	Hydrotalcite
HTC-A	Hydrotalcite with A as compensating anion

HTC(Ga)	Hydrotalcite with Ga^{3+} substitution
HTC_K	Hydrotalcite doped with K
SEM/EDS	Scanning electron microscopy / Energy dispersive spectroscopy
TGA	Thermogravimetric analysis
XRD	X-ray diffraction

References

[1] Silva, J.M., R. Trujillano, V. Rives, M.A. Soria and L.M. Madeira, High temperature CO2 sorption over modified hydrotalcites. Chemical Engineering Journal, 2017. 325: p. 25-34.

[2] Miguel, C.V., R. Trujillano, V. Rives, M.A. Vicente, A.F.P. Ferreira, A.E. Rodrigues, A. Mendes and L.M. Madeira, High temperature CO2 sorption with gallium-substituted and promoted hydrotalcites. Separation and Purification Technology, 2014. 127(Supplement C): p. 202-211.

[3] Khan, A.I. and D. O'Hare, Intercalation chemistry of layered double hydroxides: recent developments and applications. Journal of Materials Chemistry, 2002. 12(11): p. 3191-3198.

[4] Hutson, N.D. and B.C. Attwood, High temperature adsorption of CO2 on various hydrotalcite-like compounds. Adsorption, 2008. 14(6): p. 781-789.

[5] Brindley, G. and S. Kikkawa, A crystal-chemical study of Mg, Al and Ni, N hydroxy-perchlorates and hydroxycarbonates. American Mineralogist, 1979. 64(7-8): p. 836-843.

[6] Bhatta, L.K.G., S. Subramanyam, M.D. Chengala, S. Olivera and K. Venkatesh, Progress in hydrotalcite like compounds and metal-based oxides for CO2 capture: a review. Journal of Cleaner Production, 2015. 103(Supplement C): p. 171-196.

[7] Meyer, O., F. Roessner, R.A. Rakoczy and R.W. Fischer, Impact of Organic Interlayer Anions in Hydrotalcite Precursor on the Catalytic Activity of Hydrotalcite-Derived Mixed Oxides. ChemCatChem, 2010. 2(3): p. 314-321.

[8] Wang, Q., Z. Wu, H.H. Tay, L. Chen, Y. Liu, J. Chang, Z. Zhong, J. Luo and A. Borgna, High temperature adsorption of CO2 on Mg-Al hydrotalcite: Effect of the charge compensating anions and the synthesis pH. Catalysis Today, 2011. 164(1): p. 198-203.

[9] Velu, S., V. Ramjumar, A. Narayana and C.S. Swamy, Effect of interlayer anions on the physicochemical properties of zinc-aluminium hydrotalcite-like compounds. Journal of Materials Science, 1997. 32(4): p. 957-964.

[10] Li, S., Y. Shi, Y. Yang, Y. Zheng and N. Cai, High-Performance CO2 Adsorbent from Interlayer Potassium-Promoted Stearate-Pillared Hydrotalcite Precursors. Energy & Fuels, 2013. 27(9): p. 5352-5358.

[11] Yamamoto, T., T. Kodama, N. Hasegawa, M. Tsuji and Y. Tamaura, Synthesis of hydrotalcite with high layer charge for CO2 adsorbent. Energy Conversion and Management, 1995. 36(6): p. 637-640.

[12] Qin, Q., J. Wang, T. Zhou, Q. Zheng, L. Huang, Y. Zhang, P. Lu, A. Umar, B. Louis and Q. Wang, Impact of organic interlayer anions on the CO2 adsorption performance of Mg-Al layered double hydroxides derived mixed oxides. Journal of Energy Chemistry, 2017. 26(3): p. 346-353.

[13] Bhattacharyya, A. and D.B. Hall, New triborate-pillared hydrotalcites. Inorganic Chemistry, 1992. 31(18): p. 3869-3870.

[14] Li, L., S. Ma, X. Liu, Y. Yue, J. Hui, R. Xu, Y. Bao and J. Rocha, Synthesis and Characterization of Tetraborate Pillared Hydrotalcite. Chemistry of Materials, 1996. 8(1): p. 204-208.

[15] Rives, V., Layered Double Hydroxides: Present and Future. 2001: Nova Publishers.

[16] Shekoohi, K., F.S. Hosseini, A.H. Haghighi and A. Sahrayian, Synthesis of some Mg/Co-Al type nano hydrotalcites and characterization. MethodsX, 2017. 4: p. 86-94.

[17] Conterosito, E., L. Palin, D. Antonioli, D. Viterbo, E. Mugnaioli , U. Kolb, L. Perioli, M. Milanesio and V. Gianotti, Structural Characterisation of Complex Layered Double Hydroxides and TGA-GC-MS Study on Thermal Response and Carbonate Contamination in Nitrate- and Organic-Exchanged Hydrotalcites. Chemistry - A European Journal, 2015. 21(42): p. 14975-14986.

[18] Jang, S.-H., H.-C. Song, H.-C. Shin and J. Park. The characterization and synthesis of Mg-Al layered double hydroxides (LDHs). in Asian Pacific Confederation of Chemical Engineering congress program and abstracts Asian Pacific Confederation of Chemical Engineers congress program and abstracts. 2004. The Society of Chemical Engineers, Japan.

[19] Ram Reddy, M.K., Z.P. Xu, G.Q. Lu and J.C. Diniz da Costa, Layered Double Hydroxides for CO2 Capture: Structure Evolution and Regeneration. Industrial & Engineering Chemistry Research, 2006. 45(22): p. 7504-7509.

[20] Oliveira, E.L.G., C.A. Grande and A.E. Rodrigues, CO2 sorption on hydrotalcite and alkali-modified (K and Cs) hydrotalcites at high temperatures. Separation and Purification Technology, 2008. 62(1): p. 137-147.

[21] Halabi, M.H., M.H.J.M. de Croon, J. van der Schaaf, P.D. Cobden and J.C. Schouten, High capacity potassium-promoted hydrotalcite for CO2 capture in H2 production. International Journal of Hydrogen Energy, 2012. 37(5): p. 4516-4525.

[22] Yavuz, C.T., B.D. Shinall, A.V. Iretskii, M.G. White, T. Golden, M. Atilhan, P.C. Ford and G.D. Stucky, Markedly Improved CO2 Capture Efficiency and Stability of Gallium Substituted Hydrotalcites at Elevated Temperatures. Chemistry of Materials, 2009. 21(15): p. 3473-3475.

[23] Thommes, M., K. Kaneko, V. Neimark Alexander, P. Olivier James, F. Rodriguez-Reinoso, J. Rouquerol and S.W. Sing Kenneth, Physisorption of gases, with special reference to the evaluation of surface area and pore size distribution (IUPAC Technical Report), in Pure and Applied Chemistry. 2015. p. 1051.

[24] Magalhães, D., PhD Thesis: Síntese, caracterização e aplicação de sílica mesoporosa esférica como adsorvente. 2011, Instituto de Química, Universidade de São Paulo: São Paulo.

[25] Rodrigues, S.L., Remoção em fase líquida do fármaco Diclofenac por adsorção em biocarvão. 2015, Faculdade de Ciências e Tecnologia - Universidade Nova de Lisboa: Lisbon.

[26] Adhoum, N. and L. Monser, Decolourization and removal of phenolic compounds from olive mill wastewater by electrocoagulation. Chemical Engineering and Processing: Process Intensification, 2004. 43(10): p. 1281-1287.

[27] Ramaswamy, V., R. Vimalathithan and V. Ponnusamy, Synthesis and characterization of BaSO4nano particles using micro emulsion technique. Adv. Appl. Sci. Res, 2010. 1(3): p. 197-204.

[28] Kanagathara, N., M.K. Marchewka, M. Drozd, N.G. Renganathan, S. Gunasekaran and G. Anbalagan, FT-IR, FT-Raman spectra and DFT calculations of melaminium perchlorate monohydrate. Spectrochimica Acta Part A: Molecular and Biomolecular Spectroscopy, 2013. 112: p. 343-350.

[29] Chen, X., Modeling of Experimental Adsorption Isotherm Data. Information, 2015. 6(1): p. 14.

[30] Brandão, L., D. Fritsch, L.M. Madeira and A.M. Mendes, Kinetics of propylene hydrogenation on nanostructured palladium clusters. Chemical Engineering Journal, 2004. 103(1): p. 89-97.

[31] Soares, J., G.L. Casarin, H.J. José, R.D.F.P.M. Moreira and A.E. Rodrigues, Experimental and Theoretical Analysis for the CO2 Adsorption on Hydrotalcite. Adsorption, 2005. 11(1): p. 237-241.

[32] Gil, A., E. Arrieta, M.A. Vicente and S.A. Korili, Synthesis and CO2 adsorption properties of hydrotalcite-like compounds prepared from aluminum saline slag wastes. Chemical Engineering Journal, 2018. 334: p. 1341-1350

[33] Lee, K.B., A. Verdooren, H.S. Caram and S. Sircar, Chemisorption of carbon dioxide on potassium-carbonate-promoted hydrotalcite. Journal of Colloid and Interface Science, 2007. 308(1): p. 30-39.

[34] Jang, H.M., K.B. Lee, H.S. Caram and S. Sircar, High-purity hydrogen production through sorption enhanced water gas shift reaction using K2CO3-promoted hydrotalcite. Chemical Engineering Science, 2012. 73: p. 431-438.

[35] Du, H., C.T. Williams, A.D. Ebner and J.A. Ritter, In Situ FTIR Spectroscopic Analysis of Carbonate Transformations during Adsorption and Desorption of CO2 in K-Promoted HTlc. Chemistry of Materials, 2010. 22(11): p. 3519-3526.

[36] Coenen, K., F. Gallucci, P. Cobden, E. van Dijk, E. Hensen and M. van Sint Annaland, Chemisorption working capacity and kinetics of CO2 and H2O of hydrotalcite-based adsorbents for sorption-enhanced water-gas-shift applications. Chemical Engineering Journal, 2016. 293: p. 9-23.

[37] Crank, J., The Mathematics of Diffusion. 1975, London: Oxford University Press.

[38] Coenen, K., F. Gallucci, P. Cobden, E. van Dijk, E. Hensen and M.V. Annaland, Influence of material composition on the CO2 and H2O adsorption capacities and kinetics of potassium-promoted sorbents. Chemical Engineering Journal, 2018. 334: p. 2115-2123.

[39] Rocha, C., M.A. Soria and L.M. Madeira, Effect of interlayer anion on the CO2 capture capacity of hydrotalcite-based sorbents. Separation and Purification Technology, 2019. 219: p. 290-302.

[40] Bragg, W.L., The Crystalline State: Volume I. 1934, New York: The Macmillan Company.

[41] Patterson, A.L., The Scherrer Formula for I-Ray Particle Size Determination. Physical Review 1939. 56: p. 978.

[42] Pérez-Ramírez, J., S. Abelló and N.M. van der Pers, Memory Effect of Activated Mg-Al Hydrotalcite: In Situ XRD Studies during Decomposition and Gas-Phase Reconstruction. Chemistry - A European Journal, 2007. 13(3): p. 870-878.

[43] Chibwe, K. and W. Jones, Intercalation of organic and inorganic anions into layered double hydroxides. Journal of the Chemical Society, Chemical Communications, 1989(14): p. 926-927.

[44] Kwon, T. and T.J. Pinnavaia, Pillaring of a layered double hydroxide by polyoxometalates with Keggin-ion structures. Chemistry of Materials, 1989. 1(4): p. 381-383.

[45] Yong, Z., Mata and A.E. Rodrigues, Adsorption of Carbon Dioxide onto Hydrotalcite-like Compounds (HTlcs) at High Temperatures. Industrial & Engineering Chemistry Research, 2001. 40(1): p. 204-209.

[46] Coenen, K., F. Gallucci, B. Mezari, E. Hensen and M. van Sint Annaland, An in-situ IR study on the adsorption of CO2 and H2O on hydrotalcites. Journal of CO2 Utilization, 2018. 24: p. 228-239.

[47] Martunus, Z. Helwani, A.D. Wiheeb, J. Kim and M.R. Othman, Improved carbon dioxide capture using metal reinforced hydrotalcite under wet conditions. International Journal of Greenhouse Gas Control, 2012. 7: p. 127-136.

[48] Maroño, M., Y. Torreiro and L. Gutierrez, Influence of steam partial pressures in the CO2 capture capacity of K-doped hydrotalcite-based sorbents for their application to SEWGS processes. International Journal of Greenhouse Gas Control, 2013. 14(Supplement C): p. 183-192.

[49] Wu, Y.-J., P. Li, J.-G. Yu, A.F. Cunha and A.E. Rodrigues, K-Promoted Hydrotalcites for CO2 Capture in Sorption Enhanced Reactions. Chemical Engineering & Technology, 2013. 36(4): p. 567-574.

[50] Boon, J., P.D. Cobden, H.A.J. van Dijk, C. Hoogland, E.R. van Selow and M. van Sint Annaland, Isotherm model for high-temperature, high-pressure adsorption of CO2 and H2O on K-promoted hydrotalcite. Chemical Engineering Journal, 2014. 248: p. 406-414.

[51] Hanif, A., S. Dasgupta, S. Divekar, A. Arya, M.O. Garg and A. Nanoti, A study on high temperature CO2 capture by improved hydrotalcite sorbents. Chemical Engineering Journal, 2014. 236(Supplement C): p. 91-99.

[52] Walspurger, S., P.D. Cobden, O.V. Safonova, Y. Wu and E.J. Anthony, High CO2 Storage Capacity in Alkali-Promoted Hydrotalcite-Based Material: In Situ Detection of Reversible Formation of Magnesium Carbonate. Chemistry - A European Journal, 2010. 16(42): p. 12694-12700.

[53] Reijers, H.T.J., S.E.A. Valster-Schiermeier, P.D. Cobden and R.W. van den Brink, Hydrotalcite as CO2 Sorbent for Sorption-Enhanced Steam Reforming of Methane. Industrial & Engineering Chemistry Research, 2006. 45(8): p. 2522-2530.

[54] Yang, J.-I. and J.-N. Kim, Hydrotalcites for adsorption of CO2 at high temperature. Korean Journal of Chemical Engineering, 2006. 23(1): p. 77-80.

[55] Hufton, J., S. Mayorga, T. Gaffney, S. Nataraj, M. Rao and S. Sircar, Sorption enhanced reaction process (SERP). Proceedings of the 1998 USDOE Hydrogen Program Review, 1998. 2: p. 693-705.

[56] Maldonado-Hódar, F.J., L.M. Madeira, M.F. Portela, R.M. Martín-Aranda and F. Freire, Oxidative dehydrogenation of butane: changes in chemical, structural and catalytic behavior of Cs-doped nickel molybdate. Journal of Molecular Catalysis A: Chemical, 1996. 111(3): p. 313-323.

[57] Wang, X., Y. Kang, D. Cui, J. Li and D. Li, Influence of lanthanum promoter on vanadium catalyst for sulfur dioxide oxidation. Catalysis Communications, 2019. 118: p. 39-45.

[58] Ram Reddy, M.K., Z.P. Xu and J.C. Diniz da Costa, Influence of Water on High-Temperature CO2 Capture Using Layered Double Hydroxide Derivatives. Industrial & Engineering Chemistry Research, 2008. 47(8): p. 2630-2635.

[59] Coenen, K., F. Gallucci, G. Pio, P. Cobden, E. van Dijk, E. Hensen and M. van Sint Annaland, On the influence of steam on the CO2 chemisorption capacity of a hydrotalcite-based adsorbent for SEWGS applications. Chemical Engineering Journal, 2017. 314(Supplement C): p. 554-569.

[60] Soria, M.A., S. Tosti, A. Mendes and L.M. Madeira, Enhancing the low temperature water-gas shift reaction through a hybrid sorption-enhanced membrane reactor for high-purity hydrogen production. Fuel, 2015. 159: p. 854-863.

Chapter 6. Screening of Catalysts for Steam Reforming of Olive Mill Wastewater

This chapter is divided into two parts: in the first one (subchapter 6.1), several commercial catalysts were physicochemically characterized and tested in the olive oil mill wastewater steam reforming process. In the second (subchapter 6.2), similar characterization and catalytic tests to the first part were performed, but with prepared Ni-based catalysts.

Subchapter 6.1. Screening of commercial catalysts for steam reforming of olive mill wastewater *

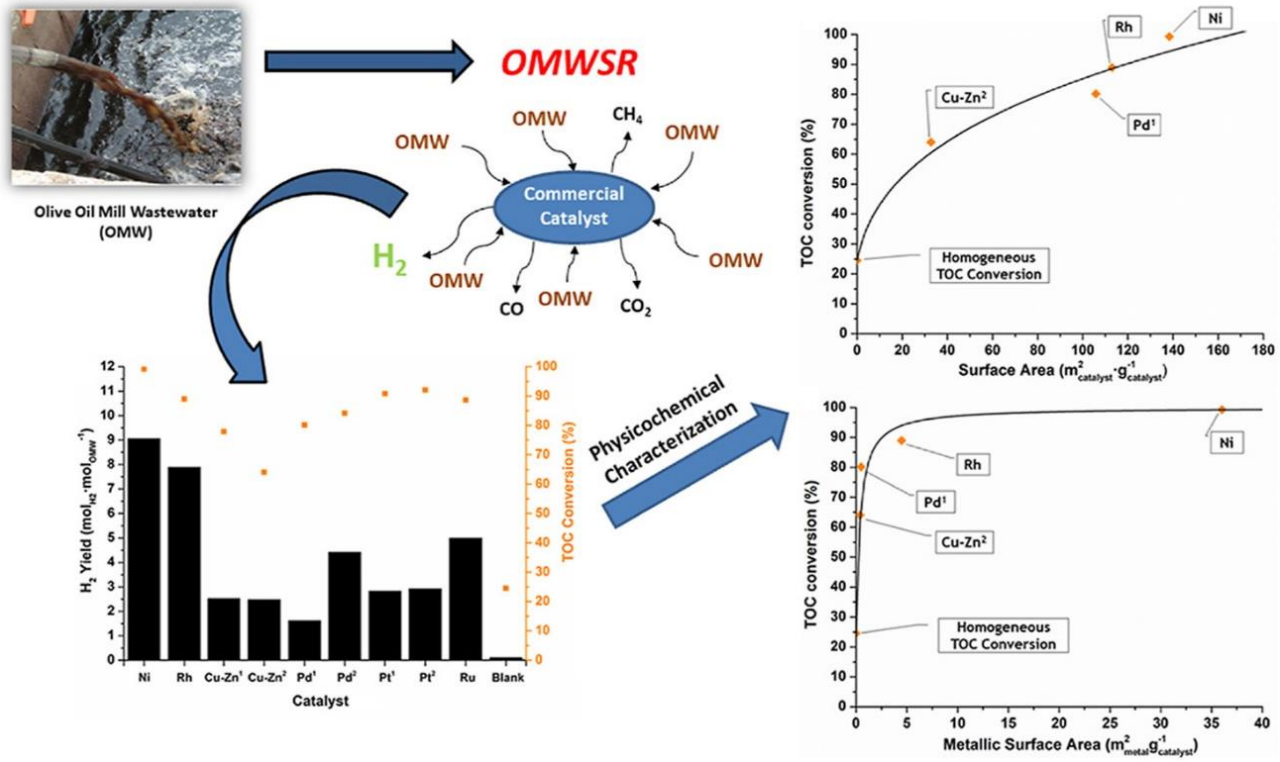

Highlights:

- A catalytic screening for the OMWSR using commercial catalysts was performed.
- The catalysts were physical-chemically characterized, tested and compared.
- High TOC conversion and H_2 yield are observed using Ni- and Rh-based catalysts.
- Catalysts' performance was correlated with their characterization.
- Rh-based sample showed high catalytic activity and stability during stability test.

* The contents of this subchapter were adapted from Rocha, C., M.A. Soria and L.M. Madeira, Screening of commercial catalysts for steam reforming of olive mill wastewater. Renewable Energy, 2021. 169: p. 765-779. (https://doi.org/10.1016/j.renene.2020.12.139)

Abstract:

Olive mill wastewater (OMW) is a pollutant effluent of olive oil production. To reduce the environmental impact of this agro-industrial sector, with the simultaneous valorization of such waste, the steam reforming of OMW was studied in this work. Besides the reduction of pollution resulting from OMW, the process allows producing "green" H_2. In this study, several commercial catalysts (Ni-, Cu-Zn- and noble metal-based) were tested to compare their performances. A catalytic screening study with all the commercial catalysts was performed, and stability tests were conducted with the material that demonstrated higher activity (Rh-based catalyst). The physicochemical characterization of the fresh and spent materials was realized through several techniques (temperature-programmed reduction (TPR), temperature-programmed oxidation (TPO), transmission electron microscopy (TEM), temperature-programmed desorption of CO_2 (TPD-CO_2), temperature-programmed desorption of NH_3 (TPD-NH_3), chemisorption of H_2/CO, scanning electron microscopy with energy dispersive spectroscopy (SEM/EDS) and physical adsorption of N_2 at -196 ºC). Although there are some materials with good catalytic performance, the Rh-based sample stood out during the tests, exhibiting high catalytic activity and high stability: at 400 ºC the H_2 yield (over 9 $mol_{H2} \cdot mol^{-1}_{OMW}$) and total organic carbon (TOC) conversion (> 98 %) were high along all the 24 h of the stability test.

6.1.1. Introduction

Taking into account the gap found in the literature, several commercial catalysts (Ni-, Cu-Zn- and noble metal-based) with different metals as active phase and different supports were herein screening for olive oil mill wastewater (OMW) steam reforming (OMWSR) for the first time, using a synthetic OMW effluent. The main aim was to find some promising materials with high catalytic performance (high H_2 yield with simultaneous reduction of the OMW organic load) and stability (low formation of coke).

The materials and methods used in this work are described in subchapter 3.3.

6.1.2. Results and discussion

6.1.2.1. Catalysts characterization

Besides the determination of the catalytic performance of several catalysts, this study aimed to correlate the catalytic activities with the physicochemical characterization of the materials. However, due to the high number of samples, only the catalysts that present the best and worst performances were selected for some characterization techniques.

Physical adsorption-desorption of nitrogen at -196 ºC and H_2 or CO Chemisorption

The specific Brunauer-Emmet-Teller (BET) surface area was determined for several catalysts that present the best (Ni and Rh) and the worst (Cu-Zn[2] and Pd[1]) catalytic activity in the experimental tests; data obtained are shown in Table 6.1, which range between 33 and 138 $m^2 \cdot g^{-1}$.

Table 6.1 - Textural properties of some selected catalysts.

Catalyst	BET surface area ($m^2_{catalyst} \cdot g^{-1}_{catalyst}$)	Total pore volume ($cm^3 \cdot g^{-1}_{catalyst}$)	Mean pore size (Å)
Cu-Zn[2]	33	0.15	160
Ni	138	0.25	55
Pd[1]	106	0.24	66
Rh	113	0.53	154

The total mesoporous volume follows the order: Rh > Ni > Pd[1] > Cu-Zn[2] while the mean pore size follows the order: Cu-Zn[2] > Rh > Pd[1] > Ni - see Table 6.1. For further details about the adsorption/desorption isotherms of N_2 over the catalysts, please see Appendix E, section 1.

The H_2 or CO chemisorption was determined to calculate the metal dispersion, using the theoretical metal(s) loading, already mentioned in Table 3.6.

The presence of Zn in the Cu-Zn[2] catalyst was not taken into account since in the conditions of reduction used before the chemisorption of H_2, this metal is not reduced [1]. In this way, the Zn present

in the material did not chemisorbed H_2. Besides that, only the metal dispersion of the Pd[1] was calculated using CO chemisorption, since the active phase (Pd) interacts/reacts with H_2 as verified in previous works [2, 3].

In Table 6.2 is verified that the metal dispersion and the metallic surface area per mass of metal were much higher for the Rh-based catalyst (Rh) and clearly lower for the Cu-Zn[2] catalyst. As expected, the metallic surface area per mass of metal followed the same trend of the metal dispersion, since a better metal distribution in the catalyst leads to a higher metallic surface area available for the reaction. Besides this, the metallic surface area per mass of sample was higher for the Ni catalyst; however, it is important to note that the metal loading in this sample is much higher than for the others - see Table 3.6.

Table 6.2 - Chemisorption results for some selected catalysts.

Catalyst	Metal Dispersion (%)	Metallic Surface Area ($m^2_{metal} \cdot g^{-1}_{catalyst}$)	Metallic Surface Area ($m^2_{metal} \cdot g^{-1}_{metal}$)
Cu-Zn[2]	0.15	0.39	0.97
Ni	8.2	36	55
Pd[1]	22*	0.49*	99*
Rh	55	4.5	240

* Obtained by CO chemisorption.

Temperature-programmed reduction-H_2

To determine an adequate pre-treatment temperature for the activation (reduction) of the catalysts, the reducibility of all samples was determined by temperature-programmed reduction (TPR). The results are shown in Fig. 6.1. For the commercial Ni-based catalyst, the reduction of NiO occurs mostly at lower temperatures (between 165 and 220 ºC).

The TPR profile of Cu-Zn[1] shows the presence of a single reduction peak (≈ 200-330 ºC), associated with the cupper species reduction, which is in line with that observed in other works [4, 5]. However, two different reduction peaks are shown in the TPR profile of Cu-Zn[2], also reported in previous works [6-8]. In this case, the peak at lower temperature (220 ºC) is specifically assigned to the reduction of isolated superficial Cu ions, which are more easily reduced, and the other peak (280 ºC) to the reduction of CuO particles [6, 7, 9]. In this way, since the peak detected in the TPR profile of Cu-Zn[1] was wide (with a shoulder at 220 ºC), it is likely to be the sum of two peaks identical to those considered in the TPR profile of Cu-Zn[2]. On the other hand, it was found that almost no significant H_2 consumption occurred for the noble metal-based catalysts (Rh, Pd[1], Pd[2], Pt[1], Pt[2] and Ru) reduction, as reported in previous studies [10, 11]. Of course, this is related to the much smaller metal content (cf. Table 3.6). Nevertheless, in the TPR profile of Ru, it was possible to see a small broad peak at ≈ 230 ºC. In opposition, a very well-defined small peak (at 250 ºC) is detected in the TPR profile of Rh. According to H_2 consumptions of Rh, only a small portion of RhO was reduced. Similar behavior

has been seen by Burch *et al.* [12] and Li *et al.* [13], who suggested that some RhO may spread over the Al_2O_3 support and diffuse into defect sites, becoming strongly bound and producing non-reducible species. Due to this issue, in previous works [13-15] only a small peak at ≈ 150 ºC was detected for a similar catalyst formulation. However, in this work, it was possible to see that some of the RhO species were reduced at temperatures near 250 ºC. Concerning the TPR profile of Ru (one reduction peak at ca. 230 ºC), a similar peak was detected (≈ 210 ºC) in the work of Mazzieri *et al.* [16].

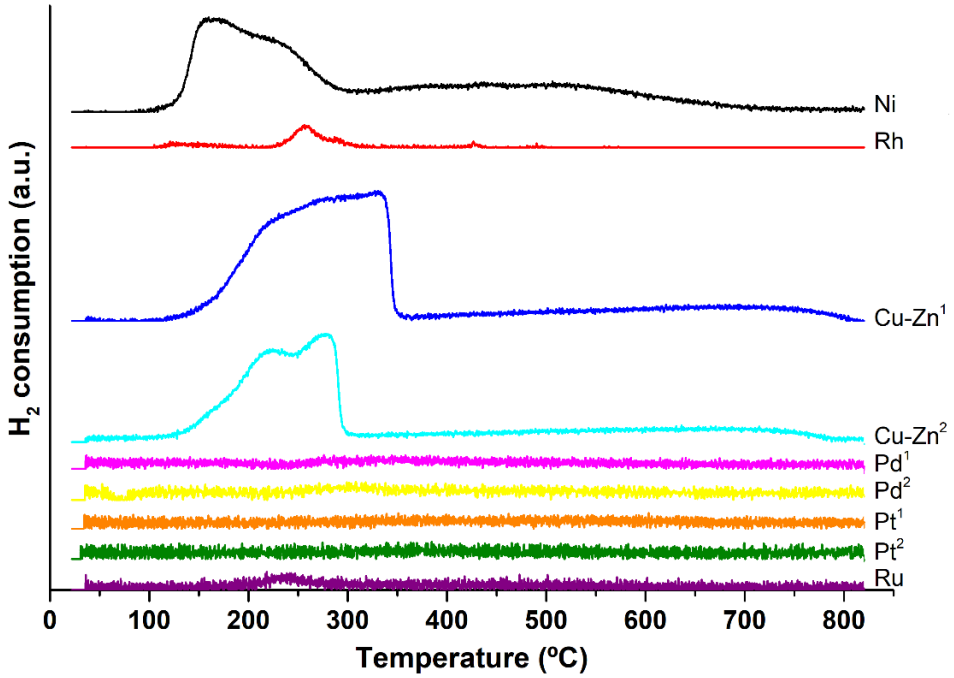

Fig. 6.1. TPR-H_2 profiles for all the catalysts.

Temperature-programmed desorption-CO_2/NH_3

To determine the basicity of the activated (reduced) catalysts, temperature-programmed desorption of CO_2 (TPD-CO_2) was conducted for the materials with best (Ni and Rh) and worst (Cu-Zn^2 and Pd^1) catalytic performance - see Fig. 6.2. From the TPD-CO_2 plots, it is possible to see that some catalysts have three types of basic sites, which, according to the literature, can be classified as weak, medium and strong. Peaks in the range of 23-250 ºC are attributed to weak basic sites, at 250-500 ºC to medium basic sites and above 500 ºC to strong basic sites [17].

The TPD-CO_2 results for the Ni sample show three distinct peaks, very well defined with maxima at 160, 440 and 670 ºC, associated with the three different basic sites. Small shoulders at 280 (medium basic sites), 500 and 560 ºC (strong basic sites) are also observed in the TPD-CO_2 analyses of this catalyst. The three types of basic sites were also verified for Cu-Zn^2; nevertheless, the desorption peaks were small and not very well defined (85, 490 and 700 ºC). Besides, in the TPD-CO_2 plot of Cu-$Zn^{2,}$ it is possible to see a shoulder at 200 ºC related to different weak basic sites. The TPD-CO_2 results for Rh show two broad desorption peaks in the range of 23-150 ºC (maximum at 80 ºC) - with

two shoulders at 30 and 130 ºC, demonstrating the presence of different weak basic sites -, and 420-690 ºC (maximum at 480 ºC), associated with three different basic sites (overlapping of desorption peaks of medium and strong basic sites). About Pd^1, the CO_2 desorption profile exhibits only one broad desorption peak in the range of 23-260 ºC (maximum at 95 ºC), with a shoulder at 240 ºC related to different weak basic sites.

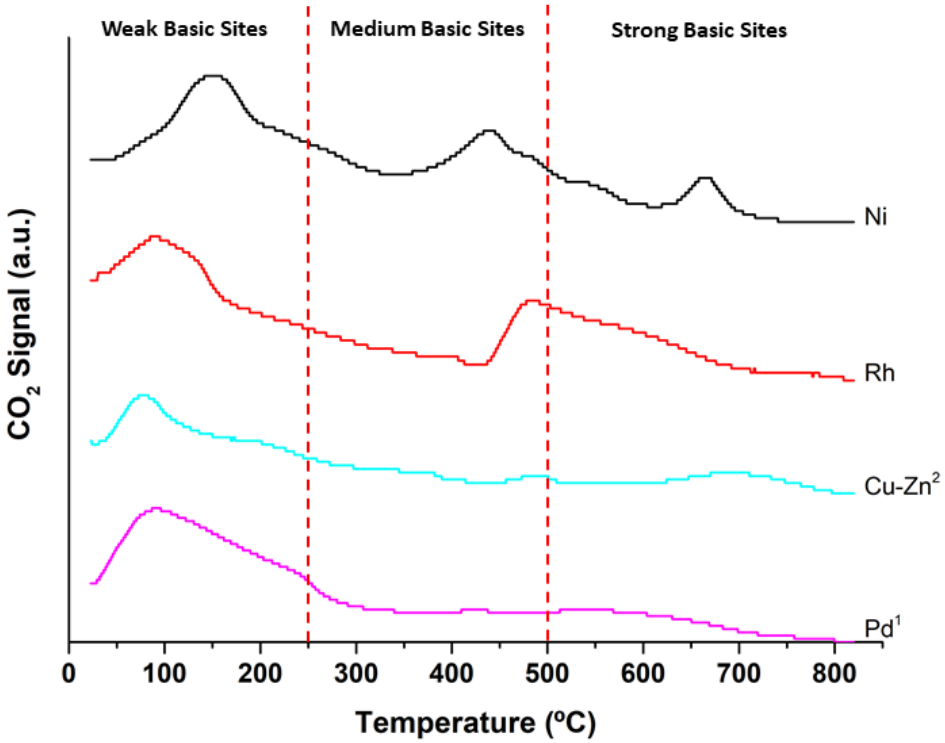

Fig. 6.2. TPD-CO_2 profiles for some selected catalysts.

Finally, in Table 6.3 it is possible to see the quantities of basic sites present in the catalysts, obtained by integration of the TPD-CO_2 curves. It is important to emphasize that despite the TPD-CO_2 data of the $Cu\text{-}Zn^2$ and Pd^1 catalysts did not present well-defined peaks at high temperatures (Fig. 6.2), these materials still desorbed CO_2 at these temperatures (cf. Table 6.3).

Results shown in Table 6.3 evidence that all catalysts have a high quantity of weak basic sites (in relation to the total quantity of basic sites). It can also be seen that the $Cu\text{-}Zn^2$ catalyst has a low quantity of medium and strong basic sites. Finally, it is worth noting that the Rh catalyst presents the highest quantities of strong basic sites.

Table 6.3 - Quantities of basic and acidic sites in some selected catalysts.

Catalyst	Weak Basic Sites ($mmol_{CO_2} \cdot g^{-1}_{catalyst}$)	Medium Basic Sites ($mmol_{CO_2} \cdot g^{-1}_{catalyst}$)	Strong Basic Sites ($mmol_{CO_2} \cdot g^{-1}_{catalyst}$)	Total Basic Sites ($mmol_{CO_2} \cdot g^{-1}_{catalyst}$)
Cu-Zn[2]	0.18	0.06	0.05	0.28
Ni	0.27	0.18	0.07	0.52
Pd[1]	0.28	0.09	0.07	0.44
Rh	0.28	0.11	0.12	0.50
	Weak Acidic Sites ($mmol_{NH_3} \cdot g^{-1}_{catalyst}$)	**Strong Acidic Sites ($mmol_{NH_3} \cdot g^{-1}_{catalyst}$)**	**Total Acidic Sites ($mmol_{NH_3} \cdot g^{-1}_{catalyst}$)**	
Cu-Zn[2]	0.02	0.04	0.06	
Ni	0.10	0.15	0.25	
Pd[1]	0.03	0.08	0.11	
Rh	0.11	0.10	0.22	

The basicity of a catalyst surface is dependent on the properties of the metals present in the material [18]. For instance, the presence of the rare-earth metal, used as a promoter of Al_2O_3 support, was manifested as strong basic sites in the Rh catalyst [19]. In addition, the utilization of Al_2O_3 as support allowed that the TPD-CO_2 profiles of all the catalysts exhibited basic sites with different strengths [20].

On the other hand, to determine the acidity of the activated catalysts, TPD-NH_3 was conducted for the same materials used in this work - see Fig. E.6 in Appendix E, section 1. From all TPD-NH_3 plots, it is possible to see that the catalysts have two types of acid sites, which, according to the literature, can be classified as weak (150-400 ºC) and strong (400-600 ºC) [21].

The TPD-NH_3 results for the Ni sample show three distinct peaks, with maxima at 250, 345 and 480 ºC. The other TPD-NH_3 plots only present two distinct peaks: Rh catalyst at 280 and 530 ºC, Cu-Zn[2] catalyst at 270 and 480 ºC and Pd[1] catalyst at 255 and 480 ºC. All samples showed peaks associated with the two different acid sites.

Finally, in Table 6.3, it is possible to see the quantities of acidic sites present in the catalysts, obtained by integration of the TPD-NH_3 curves. The results showed that the Ni and Rh catalysts have a higher quantity of acid sites than the others. Results shown in Table 6.3 evidence that all catalysts have a high quantity of strong acidic sites (in relation to the total quantity of acidic sites).

Temperature-programmed oxidation

Temperature-programmed oxidation (TPO) analyses were performed with the sample that was used in the stability tests (*Exp. 2.2*) - sample of Rh - and with four catalysts that were used in the initial catalytic screening - samples of Ni, Rh, Cu-Zn[2] and Pd[1]. The results confirm that the formation of coke on the catalysts occurred during OMWSR, which was completely oxidized into CO_2 during the TPO (Fig. 6.3). In these analyses, the formation of CH_4 and CO was also considered. However, none of these gases were detected during the TPO experiments.

It was observed that coke deposits in the Rh catalyst (used in the stability test) are gasified between approximately 250 and 550 ºC, with CO_2 peaks maxima at around 390 and 480 ºC. In several works [22-25] it was observed the existence of two different peaks during TPO of spent catalysts below and above 550 ºC, which were associated with the formation of amorphous and graphitic carbon, respectively. In this way, all the peaks detected in this study indicate that the coke deposits were mostly amorphous and graphitic carbon was almost not detected (< 3 %). It is important to point out that amorphous coke is considered to be more detrimental to catalyst performance than graphitic carbon [26-28]. The total amount of gasified carbon for the Rh catalyst used in the stability test was 0.081 $mg_C \cdot g_{catalyst}^{-1}$ (0.97 $mmol_C \cdot g_{catalyst}^{-1}$). Such low formation of coke deposits is related to the high quantity of steam in the reaction medium [29] and with the presence of a promoter in the material, as evidenced by the presence of basic sites (see TPD-CO_2 results), that induces the gasification of coke/inhibits the production of carbon [18, 30-32].

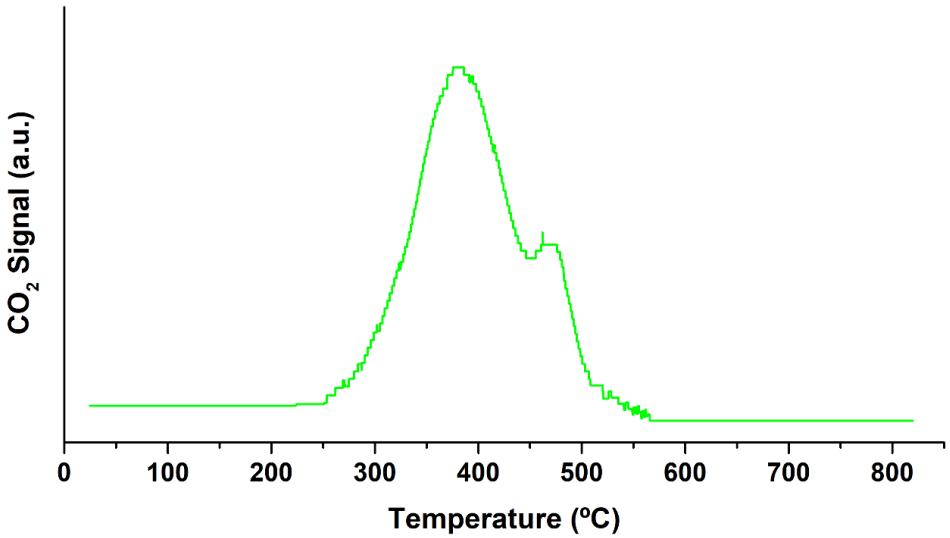

Fig. 6.3. TPO analysis for the spent Rh catalyst (used in the stability test - *Exp. 2.2*).

The TPO analyses (see Fig. E.7 in Appendix E, section 1) performed with the catalysts used in *Exp. 2.1* indicate that the Ni and Rh catalysts produced a low quantity of coke during the OMWSR, comparing with the amount of coke generated in the TPOs of catalysts Pd[1] and Cu-Zn[2] - see Table 6.4. It was also shown that coke deposits present in the Cu-Zn[2] catalyst gasified between 250 and 550 ºC but also above 550 ºC, evidencing the presence of graphitic coke.

Table 6.4 - Quantities of coke gasified in some selected spent catalysts.

Catalyst	Amorphous Coke ($mmol_C \cdot g^{-1}_{catalyst}$)	Graphitic Coke ($mmol_C \cdot g^{-1}_{catalyst}$)	Total Coke ($mmol_C \cdot g^{-1}_{catalyst}$)
Cu-Zn[2]	1.40	1.23	2.63
Ni	0.43	0.00	0.43
Pd[1]	2.04	0.00	2.04
Rh	0.45	0.00	0.45

Transmission electron microscopy

Transmission electron microscopy (TEM) analyses were performed with the fresh and spent catalysts that were used in the long-term experiments - Rh catalyst. Some micrographs are shown in Fig. 6.4. From Fig. 6.5, one can see that the average particle size of the fresh sample is lower than the one of the spent material. The calculated average particle size of the fresh and spent Rh catalyst is 2.35 and 3.02 nm, respectively. In this way, it was verified that the particles size of the catalyst practically did not change through the OMWSR reaction (increased very slightly) - see Fig. 6.5. So, since there is an error associated with the measurement of the particle size, it is not possible to firmly conclude that there was a sintering phenomenon in the catalyst. Either way, if sintering occurred, it was not very extensive for the Rh catalyst during the long-term stability test.

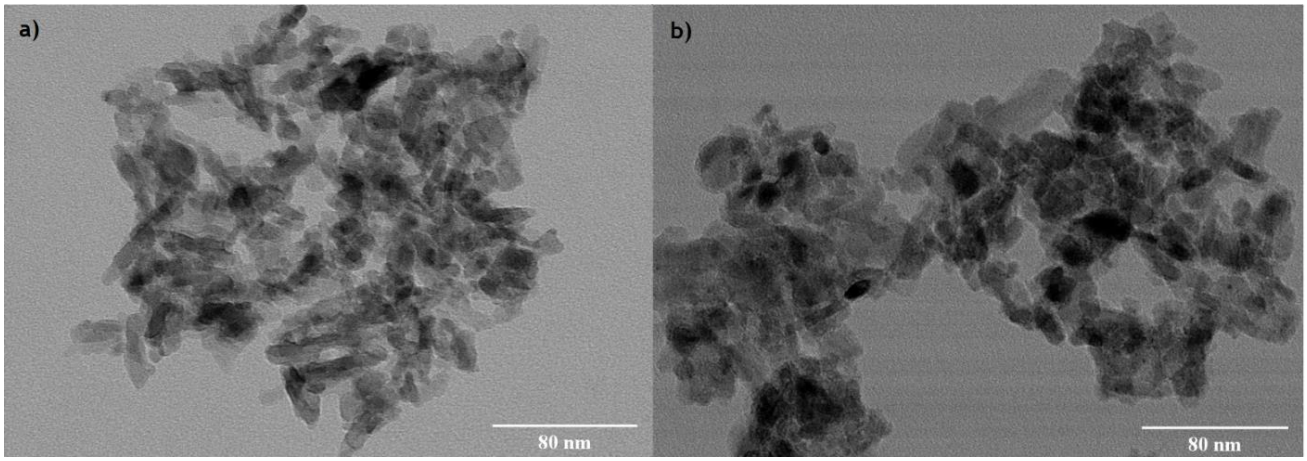

Fig. 6.4. TEM images of reduced fresh a) and spent b) samples of Rh catalyst.

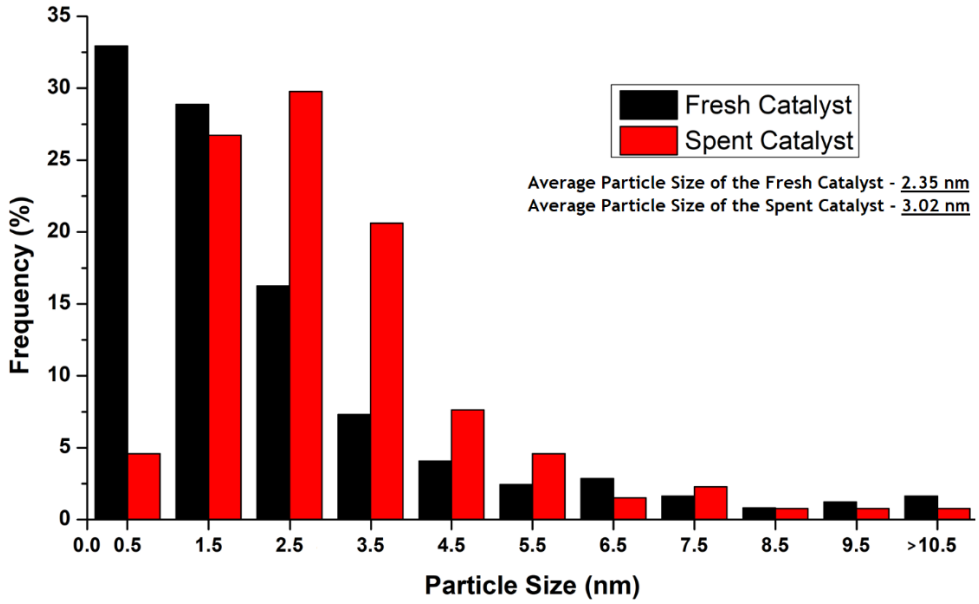

Fig. 6.5. Distribution of particle size of Rh sample.

6.1.2.2. Catalytic tests

Before the catalytic screening, blank tests (*Exp. 2.0*) were realized in the reactor packed with only SiC particles (particle size between 350-600 μm) at 350 and 400 ºC. Besides that, the yields of H_2, CO_2, CO, coke and CH_4 and the conversion of the OMW in terms of total organic carbon (TOC) in the thermodynamic equilibrium were determined in the Aspen Plus V.9® software using the same operating conditions - see details of the simulation elsewhere [29]. The results obtained are shown in Table 6.5.

Taking into account the molar fractions of the components present in the OMW stream (see subchapter 3.3.2), the maximum theoretical yield of H_2 (considering the complete conversion of OMW and assuming that no secondary reactions occurred - only the OMWSR reaction, Eq. (3.5)) is 12.182 mol of H_2 per mol of OMW fed. According to thermodynamics, excess H_2O promotes the steam reforming process and shifts the equilibrium producing a high quantity of H_2 and CO_2 (consuming nearly all the CO through the water-gas shift (WGS) reaction - Eq. (3.7)), while inhibiting the methanation reactions (Eq. (3.8) and reverse of Eq. (3.9)). For that reason, the H_2 yield - in the thermodynamic equilibrium - obtained in the simulations at 350 and 400 ºC (@ 1 bar) was close to the maximum theoretical yield of H_2 (Table 6.5), and the TOC conversions were complete. It is important to emphasize that the purity of H_2 in the thermodynamic equilibrium is affected by the presence of the CO_2 produced by the WGS reaction (Eq. (3.7)). The yields of the remaining gaseous products (also calculated by the Aspen Plus V.9® software) are also shown in Table 6.5, as well as the results obtained in the blank test. Since the OMWSR reaction was not catalyzed in this experimental run, H_2 and CO_2 yields were very low. The quantities of CH_4 and CO detected in this test were also very low for the two different temperatures, but higher than the ones obtained in the thermodynamic equilibrium. As expected, low H_2 selectivity and purity were obtained in the blank test, due to the presence of CH_4 and CO and the low extension of the steam reforming. TOC conversions were also low: only decomposition of the oxygenates occurred, with or without the presence of steam, as shown in Eqs. (3.6) and (3.16), respectively

.

Table 6.5 - Yields of all gaseous products and OMW TOC conversion in the thermodynamic equilibrium (obtained by Aspen Plus V.9® simulation) and in the blank experiment (*Exp. 2.0*).

Temperature (ºC)	H_2 Yield	CO Yield	CH_4 Yield	CO_2 Yield	H_2 Purity (%)	H_2 Selectivity (%)	TOC Conversion (%)
Thermodynamic Equilibrium (Aspen Plus V.9®)							
350	12.181	8.2×10^{-4}	7.6×10^{-6}	6.0	67	100	100
400	12.180	1.4×10^{-3}	5.7×10^{-7}	6.0	67	100	100
Blank Test (*Exp. 2.0*)							
350	0.10	8.8×10^{-3}	2.0×10^{-3}	0.14	40	33	24.5
400	0.18	1.5×10^{-2}	3.0×10^{-3}	0.18	47	45	25.1
Maximum Theoretical Yield of H_2	12.182						

Catalysts screening

In relation to *Exp. 2.1*, the mean of the results related to the production of H_2 (yield, purity and selectivity), and TOC conversion are shown in Fig. 6.6, for the tests performed at 350 and 400 ºC (data for the yields of the other gaseous components are shown in Fig. E.8 in Appendix E, section 2). Mean data were calculated from the results obtained over time. Transient data, for all the experimental runs (results along the time), are shown in Fig. 6.7.

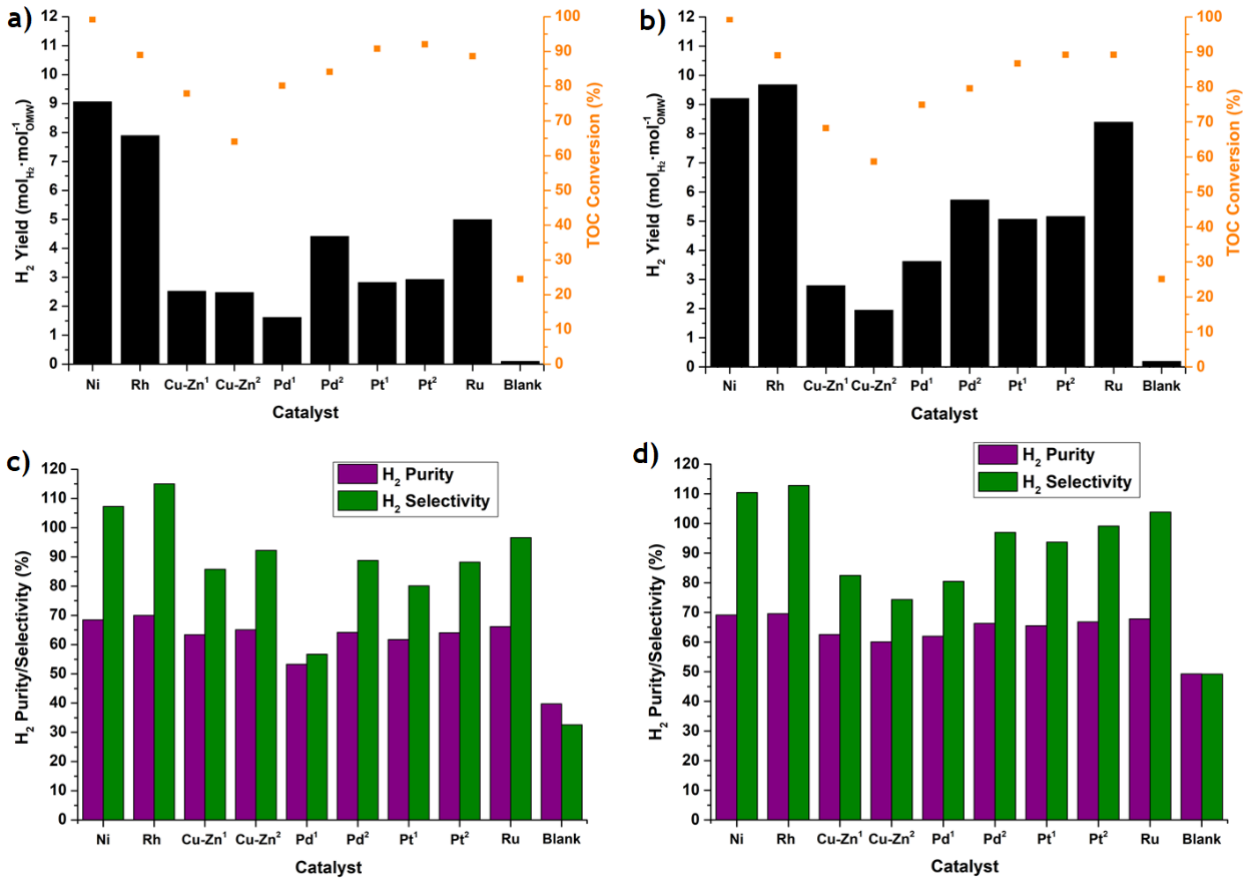

Fig. 6.6. Mean of H_2 yield and TOC conversion obtained in *Exp. 2.1* for all the catalysts at a) 350 ºC and b) 400 ºC. Mean of the H_2 purity/selectivity obtained in *Exp. 2.1* for all the catalysts at c) 350 ºC and d) 400 ºC.

Temperature significantly affects the performance of the catalysts. In a general way, the increase of temperature from 350 ºC to 400 ºC leads to an increase of H_2 and CO_2 yields due to the increase of the OMWSR reaction rate (exception goes for Cu-Zn^2 catalyst); the behavior of the production of H_2 and CO_2 along time was similar (Fig. 6.6a-b)), indicating that WGS (Eq. (3.7)) is the predominant reaction to produce these species. The yields of CO and CH_4 were very low in all the tests in line with the predominance of the WGS reaction in the process - see Fig. 6.7c-d). In all cases, the main products were H_2 and CO_2; for this reason, high H_2 purities and selectivities were obtained in these tests (Fig. 6.6c-d)). It is worth noting that the TOC conversion was high in practically all tests (Fig. 6.6e)), indicating that it is possible to reduce a significant fraction of the organic load from the OMW with the

majority of the catalysts employed. However, for Pd[1] and Cu-Zn[2] catalysts, it was observed a significant decrease of the TOC conversion along time, meaning that these samples lost catalytic activity with time-on-stream. Considering the results of the TPO analyses (subchapter 6.1.2.1), one can conclude that the catalysts with high and constant TOC conversion (Ni and Rh) produced low quantities of coke, in opposition to the higher amounts of coke detected in the TPO runs with the Pd[1] and Cu-Zn[2] samples, the ones that presented a decrease of the TOC conversion along time.

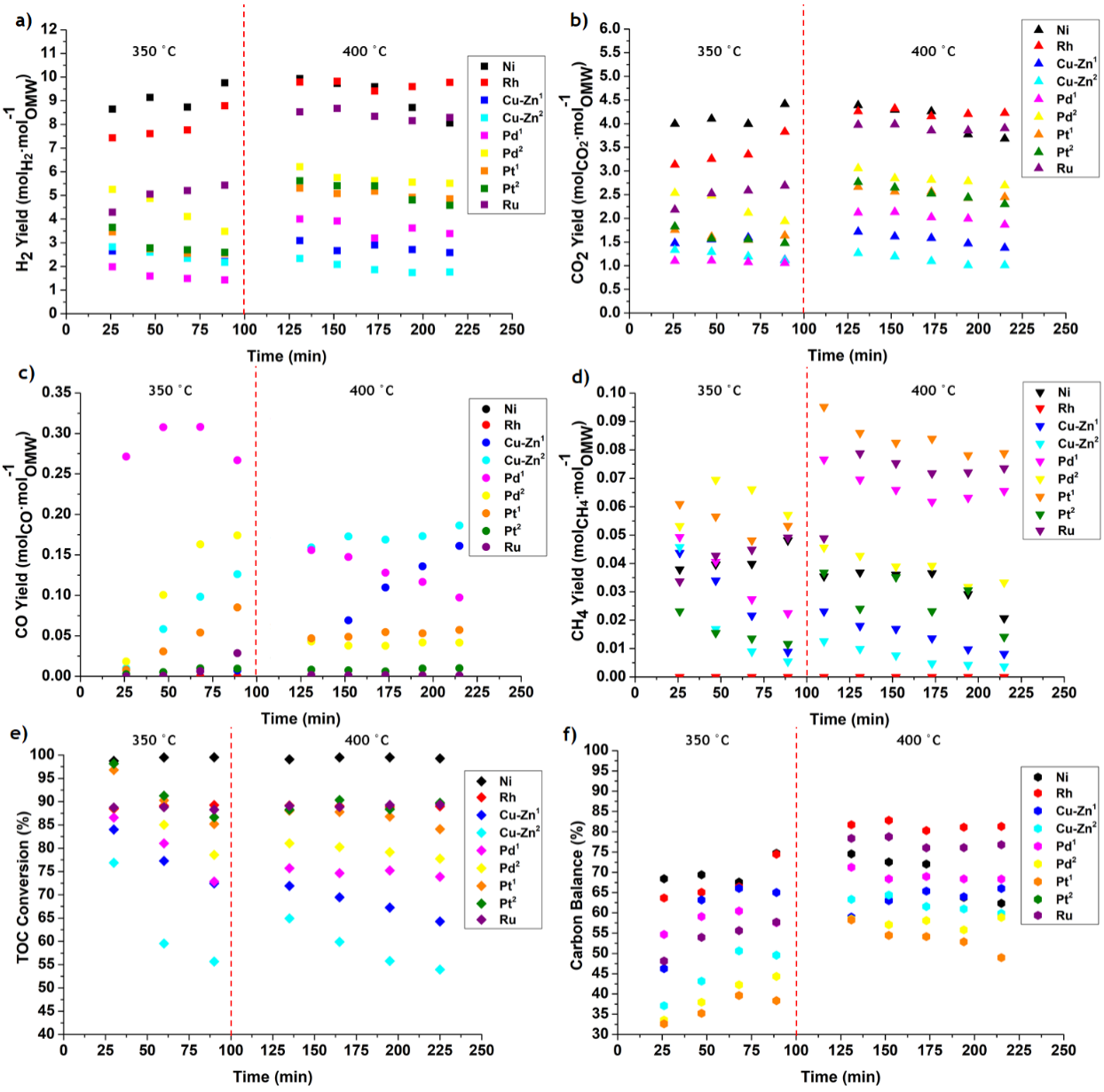

Fig. 6.7. Yields of a) H_2, b) CO_2, c) CO and d) CH_4, e) TOC conversion and f) carbon balance obtained in *Exp. 2.1* (catalytic screening) for all the catalysts as a function of time on stream at different temperatures.

For the Ni catalyst, the H_2 and CO_2 production (@ 400 ºC) started to progressively decrease until the end of the experimental test - see Fig. 6.7a-b); the other catalysts did not present a reduction of H_2

production or the decrease of the H_2 yield was not as accentuated as the one verified using the Ni-based catalyst.

High H_2 purities/selectivities were obtained in these tests, as mentioned above, except for the Pd^1 catalyst at 350 ºC (Fig. 6.6c)). At this temperature, this catalyst produced a low quantity of H_2 and has not converted all the CO through the WGS reaction (Eq. (3.7)); in addition, at 350 ºC, Pd^1 produces slight amounts of CH_4 - see Fig. 6.7d). For the Ni and Rh catalysts, the H_2 purity/selectivity keeps high and constant during all the experimental tests. Oppositely, for the $Cu\text{-}Zn^1$ catalyst, these parameters present oscillation during the screening test. For the $Cu\text{-}Zn^2$ sample, the H_2 purity/selectivity decreased along the time, in line with the catalyst deactivation mentioned above. Some catalysts presented a H_2 selectivity higher than 100 % (and H_2 purity higher than the value determined in the simulation with the *Aspen Plus V.9*® software - see Table 6.5) due to several reasons: formation of coke (decreasing the quantity of carbon products in the outlet stream), possible formation of other gaseous species not considered in Eq. (3.24) and not detected in the gas chromatograph (GC), and the cracking of the oxygenates/hydrocarbons (Eqs. (3.11) and (3.16) - dehydrogenation reactions) that can produce H_2 without the formation of other gaseous carbon products. Concerning the carbon balance (Eq. (3.26)), it did not close at 100 % for all the cases - see Fig. 6.7f). This indicates that the carbon eliminated from the liquid phase (difference between the carbon present in the initial effluent of OMW and the carbon present in the condensable phase obtained after the reaction) was not fully converted into CO, CO_2 or CH_4, meaning that the remaining carbon was probably present in the coke deposits and/or other possible gaseous species not quantified (e.g. ethane, propane, etc.). The presence of several hydrocarbons (C_1-$C_{>4}$) was confirmed in the catalytic test with the Rh catalyst at different temperatures - see Fig. E.9 in Appendix E, section 2. Besides, it was verified that the increase of the temperature favors the cracking of the long-chain hydrocarbons and enhances the appearance of smaller molecules (i.e. production of a higher quantity of CO, CO_2 and/or CH_4), thus more precisely closing the carbon mass balance (data not shown for brevity).

It was also verified that for all catalysts the carbon balance increased at 400 ºC, decreasing the coke formation / TOC conversion and/or increasing the cracking/hydrolysis/dehydrogenation of long-chain species (producing H_2, CO, CO_2 and CH_4). In the blank test, the carbon balance was ≈ 80 %.

For the Rh-based catalyst (Rh), Ni-based catalyst (Ni) and Ru-based catalyst (Ru), the TOC conversion was high and constant during all the experimental tests (Fig. 6.7e)). However, for the Cu-based catalysts ($Cu\text{-}Zn^1$ and $Cu\text{-}Zn^2$), Pd-based catalysts (Pd^1 and Pd^2) and Pt-based catalysts (Pt^1 and Pt^2), the TOC conversion decreased during the catalytic tests at 350 ºC, indicating that these catalysts lose the ability to crack/decompose the high molecular weight molecules along time. It was also observed the same behavior at 400 ºC for these materials, except for the catalysts Pd^1 and Pt^2.

In a general way, the catalysts with the worst catalytic performance (Pd-based catalysts - Pd^1 and Pd^2 - and Cu-based catalysts - $Cu\text{-}Zn^1$ and $Cu\text{-}Zn^2$) provided higher CO and CH_4 yields in comparison with the remaining catalysts, possibly as a consequence of the lower performance toward the WGS and methane steam reforming reactions (Eqs. (3.7) and (3.9) - see Fig. 6.7c-d)). Still, the low TOC conversion with the Cu-based materials ($Cu\text{-}Zn^1$ and $Cu\text{-}Zn^2$) showed that these catalysts do not present proper catalytic properties to crack/decompose the oxygenates/hydrocarbons (Eqs. (3.6), (3.11) and (3.16)).

Concerning the Pt-based catalysts (Pt^1 and Pt^2), despite the low formation of H_2, these materials reached high values of TOC conversion. Although these catalysts did not properly catalyze the WGS reaction, they present high performances to decompose and crack the oxygenates.

In conclusion, Rh-based catalysts (Rh) and the Ni catalyst (Ni) reached the highest values of H_2 yield (close to the stoichiometric value), TOC conversion and H_2 purity/selectivity at 350 and 400 ºC. These materials present a good performance to crack the oxygenates and properly catalyze the steam reforming reactions. As for the Ru-based catalyst, it was possible to see that such catalyst presented moderate performances among all the catalysts screened.

Catalytic activity vs. Physicochemical characterization

Despite the different metals (Rh, Pd, etc.) present in the catalysts, correlations of their activity with the respective characterization were assessed, focused on the catalysts with the best and worst performance. It was verified that some properties of the materials (for instance, mesoporous volume and the size of the pores) do not have any correlation with the catalytic performance (H_2 yield, TOC conversion, and H_2 purity/selectivity). However, the surface area of the catalysts seems to influence the TOC conversion - see Fig. 6.8a). The average TOC conversion was higher for the catalysts with a high surface area (Ni and Rh samples) at both temperatures considered. The results suggest that, despite the different active phases (and different metal loadings) existing in the catalysts, a high surface area allows to obtain high TOC conversion in this process. Still, it seems that the metallic surface area per mass of catalyst ($m^2_{metal} \cdot g^{-1}_{catalyst}$) is also correlated with the TOC conversion at both temperatures studied (see Fig. 6.8b)); the results suggest that the TOC conversion significantly increased until it reached a plateau at a certain value of the metallic surface area per mass of catalyst (ca. 7.5-10 $m^2_{metal} g^{-1}_{catalyst}$).

Finally, it is important to highlight that in both correlations (Fig. 6.8) it was represented a point called “Homogeneous TOC Conversion”, which corresponds to the TOC conversion determined in the blank test (*Exp. 2.0*); this value represents the conversion of TOC obtained in the gas phase of the reaction medium (i.e., without the presence of the catalyst).

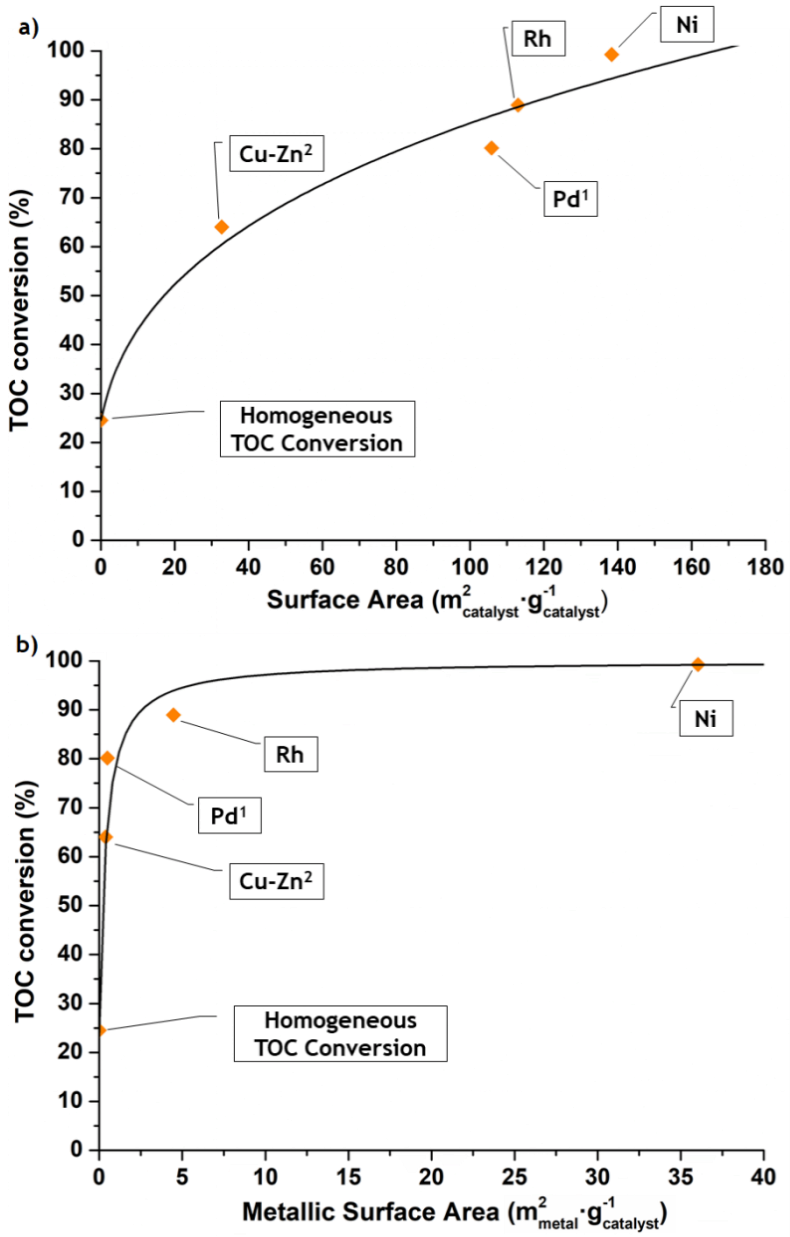

Fig. 6.8. Relation of TOC conversion with a) the surface area and b) the metallic surface area of the catalysts at 350 ºC. The lines represented in the graphs are only for better visualization.

The catalysts with the best performances (Ni and Rh) also presented a higher quantity of medium/strong basic sites than the catalysts with the worst performances (cf. Table 6.3). In this way, it was possible to verify that besides the high activity for the reactions present in the OMWSR process (related to the presence of strong acidic sites that promoted reactions like dehydration, hydrolysis and cracking [17, 33-36] - see Table 6.3 and the correlation between TOC conversion and density of acidic sites in Fig. 6.9), these materials also presented medium and strong basic sites. The existence of these strong basic sites for the Rh catalyst is explained by the presence of rare-earth metal in this material, as already mentioned in subchapter 6.1.2.1.

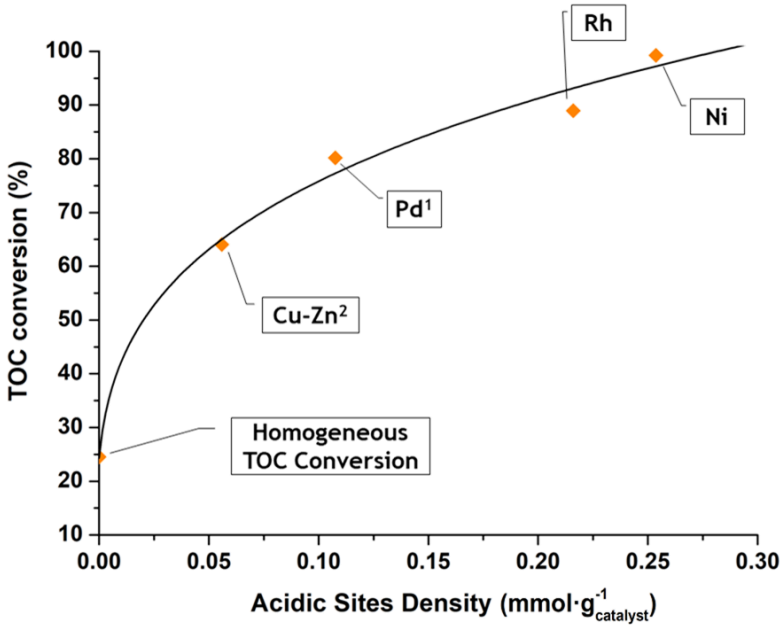

Fig. 6.9. Relation of TOC conversion with the acidic sites density of the catalysts at 350 ºC. The line represented in the graphs is only for better visualization.

Finally, in relation to the values of *TOF* calculated for these catalysts (see Fig. E.10 in Appendix E, section 2), it was possible to observe that the H_2 production per mol of metal available (on the surface of the catalyst) was higher for Cu-Zn[2] and Pd[1] catalysts. In this way, despite the higher H_2 yields obtained using the Ni and Rh, only the Rh sample has shown a high capacity for production of H_2 per mol of active metal available for the reaction. These results also indicate that if the Cu-Zn[2] and Pd[1] catalysts had a higher amount of active metal sites accessible to the reaction (higher dispersion or higher content of active metal) would probably produce a higher quantity of H_2 in the catalytic tests.

In this way, the conjugation of several properties makes the Rh catalyst promising for long-term tests: presence of a chemical species (rare-earth metal) in the catalyst that increases the resistance towards coke deposition on the material's surface - the addition of the promoter led to the formation of a high quantity of basic sites in the catalyst (Rh is the material with a higher quantity of strong basic sites - see Table 6.3) [18, 30-32]; high TOC conversion at 400 ºC (see Fig. 6.6); and higher *TOF* and H_2 yield than the Ni catalyst at 400 ºC (see Fig. 6.6 and Fig. E.10 in Appendix E, section 2). For these reasons, the Rh catalyst was selected to be tested in the *Exp. 2.2* (stability test - 24 h of time-on-stream) instead of Ni catalyst.

Stability test

The mass of catalyst used in this *Exp. 2.2* was lower than that for *Exp. 2.1*, to reach catalytic performances far away from the thermodynamic equilibrium; in this way, it is easier to detect a possible deactivation of the catalyst during the time-on-stream. The results of this experimental test can be

seen in Fig. 6.10 (complemented with data on Fig. E.11 in Appendix E, section 2). It is important to emphasize that due to technical and safety issues the stability test had to be stopped overnight (since there was a lot of liquid condensed that needs to be removed manually); for that reason, the system had some perturbations during the test (Fig. 6.10).

Once again, in this experimental run (*Exp. 2.2*, at 400 ºC) the behavior of the production of H_2 and CO_2 along time was similar among them. The yields of CO and CH_4 were very low and the main products were H_2 and CO_2, as expected. The steady-state was reached quickly and the H_2 yield almost did not change along the time, showing high stability. The Rh sample exhibited only a small loss of activity after 24 h of operation, as verified by the very slight decrease of H_2 production during the test (cf. Fig. 6.10a)). It is worth noting that the values of H_2 yield in the first hours were slightly higher than those obtained in *Exp. 2.1* at the same temperature (despite the lower mass used), probably because the catalyst in *Exp. 2.1* was tested firstly at 350 ºC and may have suffered a small deactivation (the formation of coke is more thermodynamically favorable at 350 than at 400 ºC [29, 37, 38]).

The TOC conversion was high and constant (between 98-100 %) during all the 24 h of operation - see Fig. 6.10a).

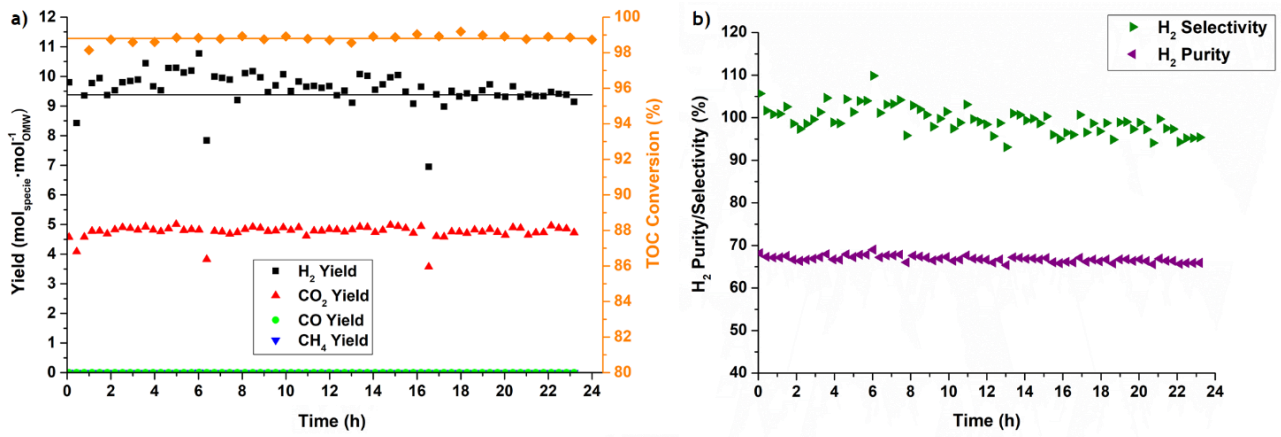

Fig. 6.10. a) Gaseous species yield and TOC conversion during *Exp. 2.2* (24 h time-on-stream) for the Rh catalyst. b) H_2 purity/selectivity obtained for the Rh catalyst. The mean of the H_2 yield in the last 4 hours is represented by the black line and the mean of the TOC conversion in the last 4 hours is represented by the orange line.

High H_2 purities/selectivities (for instance, H_2 selectivity higher than 100 %) were obtained again using this catalyst due to several reasons: formation of coke (therefore decreasing the number of carbon-containing gas products in the outlet stream), formation of other gaseous species not considered in Eq. (3.24) and not detected in the GC, and cracking of the oxygenates/hydrocarbons (Eqs. (3.11) and (3.16) - dehydrogenation reactions) that can produce H_2 without formation of other gaseous carbon products.

Concerning the carbon balance (Eq. (3.26)), it was possible to verify that the balance did not close at 100 % (as found in *Exp. 2.1*) - see Fig. E.11 in Appendix E, section 2. This indicates again that the

carbon eliminated from the liquid phase was not fully converted into the gaseous carbon species considered; thus, the remaining carbon could be present in coke deposits or/and in other gaseous species that were not considered (e.g. ethane, propane, etc.). Nevertheless, since the TPO analysis indicated that the formation of coke in this test was very low (see subchapter 6.1.2.1), the carbon balance below 100 % probably means that there were other carbon-containing gaseous species in the reactor outlet stream that were not considered in this study.

It was observed only a small amount of amorphous carbon formed in the Rh catalyst (0.97 $mmol_C \cdot g^{-1}_{catalyst}$, i.e., 0.081 $mg_C \cdot g^{-1}_{catalyst}$ - cf. subchapter 6.1.2.1), explaining, in this way, the presence of a very slight decrease of the H_2 yield in the stability test. As mentioned before, this low production of coke is related to the high quantity of water in the feed [29] and the presence of a chemical specie (rare-earth metal) in the material that promotes the gasification of coke/inhibits the production of carbon deposits - the addition of the promoter increased the basicity of the catalyst [18, 30-32]. In this way, the low formation of coke (and consequently, the high stability of the catalyst) can be explained by the presence of basic sites in these materials [18, 32]: the Rh-based catalyst presented the highest quantity of strong basic sites among all the catalysts examined in the TPD-CO_2 analysis - see results in subchapter 6.1.2.1. Moreover, the TOC conversion remains constant throughout the long-term test (only the H_2 yield decreases), demonstrating that coke could be deposited preferentially on the active sites that catalyzed the WGS reaction.

Finally, it was studied the effect of the stability test on the textural properties of the catalyst. By comparing the BET surface areas of the catalyst before and after the stability test (reduction of ≈ 6 % - see Table 6.6), it was observed only a small decrease of the surface area in the Rh sample. In this way, the small decrease of surface area in the stability test was not enough to deactivate the catalyst. In addition, it was noticed that the reduction of metal dispersion and metallic surface area per mass of catalyst (see Table 6.6) during the experimental test were not sufficient to deactivate the catalyst along the 24 h time-on-stream.

Table 6.6 - Morphological properties of the spent catalysts in the stability tests.

Catalyst	BET surface area ($m^2_{catalyst} \cdot g^{-1}_{catalyst}$)	Metal Dispersion (%)	Metallic S. Area ($m^2_{metal} \cdot g^{-1}_{catalyst}$)
Rh_{fresh}	113	55	4.5
Rh_{spent}	106	39	3.2

It is important to emphasize that the high stability of this catalyst may also be related to the operation conditions of the stability tests. In previous works, it was reported that the temperature used herein is not high enough to induce sintering of the Rh particles in the catalysts and, in this way, promote their deactivation [19, 39, 40]. In line with these studies, it was possible to verify that the average particle size of the Rh catalyst did not significantly change (TEM analyses, subchapter 6.1.2.1) during the 24 h time-on-stream stability test - in line with the chemisorption results. In addition, no major changes were

detected in the scanning electron microscopy with energy dispersive spectroscopy (SEM/EDS) analyses between the fresh and spent samples of the respective catalyst (see further details in Appendix E, section 2).

Finally, in Fig. E.12 in Appendix E, section 2, it is possible to verify the color difference between the condensed phase obtained in the blank test (at 400 ºC) and the condensed phase of the same stream after the OMWSR process in the stability test (after 12h of operating) using the Rh catalyst. The sample color of the blank test (yellow) was more intense since the TOC conversion was lower.

6.1.3. Conclusions

In this work, a catalyst screening study for the OMWSR was performed with commercial samples. It was verified that several, among the tested catalysts, have high catalytic performance for the OMWSR process towards "green" H_2 production. Among all the materials, it was possible to highlight the very good catalytic performance (in terms of H_2 yield, H_2 selectivity and TOC conversion) of the Ni, Rh and also Ru catalysts.

It seems that the metallic surface area per mass of catalyst correlates well with the TOC conversion obtained in the experimental tests: the performance of the catalysts significantly increased, but only until a certain value (ca. 7.5-10 $m_{metal}^2 \cdot g_{catalyst}^{-1}$); then, the TOC conversion appeared to reach a plateau, close to ca. 95% at 350 ºC. It was also suggested that, despite the different active phases (and different metal loadings) present in the commercial catalysts, high surface areas allow to obtain high TOC conversion during OMWSR, thus significantly decreasing the pollution load of the effluents of this agro-industrial activity. A similar correlation was also observed with the catalysts' acidity.

Concerning the stability test, it was possible to see that the Rh catalyst presented a high and relative stable H_2 yield (between 9-10 $mol_{H_2} \cdot mol^{-1}_{OMW}$) and TOC conversion (always between 98-100%) during the 24 h of the catalytic test. Moreover, the H_2 purity (≈ 67 %) and the H_2 selectivity (≈ 99 %) stay high and constant during all the experimental run and only a very slight deactivation was observed for this sample.

Subchapter 6.2. Use of Ni-containing catalyst for the olive mill wastewater steam reforming *

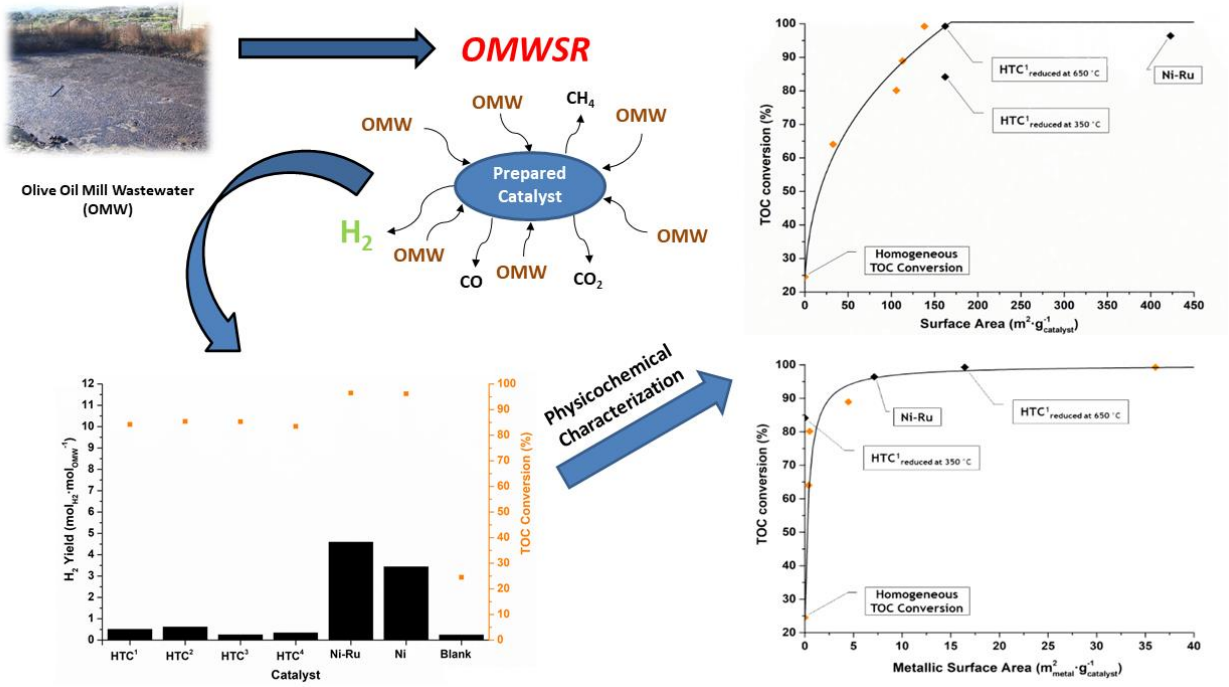

Highlights:

- A catalytic screening for the OMWSR using prepared Ni-based catalysts was performed.
- The catalysts were tested, physical-chemically characterized and compared.
- High TOC conversion and H_2 yield are observed using a Ni-Ru-based catalyst.
- Catalysts' performance was correlated with their characterization.
- Ni-Ru-based sample showed high catalytic activity and stability.

* The contents of this subchapter were adapted from Rocha, C., M.A. Soria and L.M. Madeira, Use of Ni-containing catalyst for the olive mill wastewater steam reforming. Submitted for publication.

Abstract:

Olive mill wastewater (OMW) is a pollutant stream produced in the olive oil industry. The OMW steam reforming (OMWSR) process was studied herein, aiming to reduce the negative environmental impact of such effluents; simultaneously, the waste is economically and energetically valorized with the production of green H_2. Several Ni-containing catalysts (with the metal species being incorporated/impregnated in hydrotalcite-based materials or silica) were prepared and tested to compare their performances for the OMWSR; still, stability tests with the two most promising materials were also carried out. The physicochemical characterization of the materials was realized through several techniques: thermogravimetric analysis (TGA), temperature-programmed reduction (TPR), temperature-programmed oxidation (TPO), temperature-programmed desorption of CO_2 (TPD-CO_2), temperature-programmed desorption of NH_3 (TPD-NH_3), chemisorption of H_2/CO, inductively coupled plasma optical emission spectrometry (ICP-OES) and physical adsorption-desorption of N_2 at -196 ºC. Although some catalysts showed good catalytic performance, the Ni-Ru/SiO_2 sample stood out, exhibiting high catalytic activity and stability: at 400 ºC the H_2 yield (> 8 $mol_{H_2} \cdot mol^{-1}_{OMW}$, i.e., > 67 % of the maximum theoretical yield of H_2) and total organic carbon (TOC) conversion (≈ 75 %) were high along all the 24 h of the stability test, with only a small deactivation being noticed. Despite the good catalytic performance of a hydrotalcite-based Ni-containing catalyst (sample HTC reduced at 650 ºC) in the first hours of the stability test, the material presented a high activity decrease during the long-term test, mostly due to the formation of amorphous coke.

6.2.1. Introduction

New and improved catalysts must be developed to achieve a high catalytic activity and stability in the catalytic reforming of the oxygenates present in the OMW composition. In this way, several Ni-based materials were prepared in this study, which were screened for the OMWSR process for the first time. These materials present a lower price than noble metal-based and good performance in reforming reactions due to their C-C bond rupture capability [41, 42]. Among the several possible Ni-based catalysts, Ni-based hydrotalcites (HTCs) as catalyst precursors are worth mentioning as they can exhibit high catalytic activity for the OMWSR reaction, since these materials are capable to generate mixed oxides with high surface area [43, 44]. Moreover, such catalysts were already tested for the steam reforming of different chemical species (acetic acid, toluene, benzene, and/or bio-oil), similar to those found in a typical OMW composition [45-49]. Still, the mixed oxides derived from HTCs were also used as support on Ni-based catalysts used in steam reforming processes [50, 51]. Finally, it was possible to verify in the literature that several Ni/SiO_2 catalysts were prepared for similar steam reforming processes [52-54].

In this way, this work aimed to study the potential of several Ni-based catalysts to be applied in the OMWSR process, aiming to obtain materials with high performance and stability. Six catalysts with different Ni loadings were prepared: three materials derived from HTCs and three samples prepared by Ni impregnation on SiO_2 or HTC supports.

The materials and methods used in this work are described in subchapter 3.3.

6.2.2. Results and discussion

6.2.2.1. Catalyst characterization

This study performed a correlation between the catalytic activity and the physical-chemical characterization of the in-house prepared catalysts, particularly for those with the best performance (HTC^1 and Ni-Ru catalysts). Catalysts characterization was performed employing several techniques such as XRD, TGA, BET, ICP, TPO, TPR, TPD-CO_2/NH_3 and chemisorption of H_2. In this way, only the main results obtained in this characterization are presented hereinbelow. For further information about the outcomes obtained in the characterization techniques, please refer to section 1 of Appendix F.

XRD

The crystalline phases detected in the XRD patterns of the dry, calcined, reduced and spent samples of HTC[1] and Ni-Ru (best catalysts, as shown hereinbelow) are shown in Table 6.7. The calcination treatment allowed the formation of the NiO phase in both catalysts. Besides that, it was also studied the effect of the reduction treatment in the crystal structure of the samples: it was possible to verify that the presence of H_2 at 350 ºC reduced completely the NiO phase to metallic Ni in the Ni-Ru catalyst. However, for the HTC[1] catalyst, a temperature of 650 ºC was required to reduce completely the NiO phase. Finally, it was analysed the XRD patterns of the spent samples of HTC[1] and Ni-Ru used in *Exp. 2.2* (stability tests); it was observed the formation of coke in both samples after 24 h of reaction.

Table 6.7 - XRD results for Ni-Ru and HTC[1] samples.

Catalyst	Identified phases
HTC[1] dry	HTC
HTC[1] calcined	NiO + Periclase
HTC[1] reduced at 350 ºC	NiO + Periclase
HTC[1] reduced at 650 ºC	Ni + Periclase
HTC[1] spent[a)]	Ni + Periclase + coke
Ni-Ru dry	Amorphous SiO_2
Ni-Ru calcined	NiO + Amorphous SiO_2
Ni-Ru reduced at 350 ºC	Ni + Amorphous SiO_2
Ni-Ru spent[b)]	Ni + Amorphous SiO_2 + coke

[a)] Spent catalyst that was reduced at 650 ºC previously of the catalytic test.
[b)] Spent catalyst that was reduced at 350 ºC previously of the catalytic test.

Physical adsorption-desorption of nitrogen -196 ºC, ICP and H_2/CO chemisorption

The specific surface area was determined for the HTC[1] and Ni-Ru samples. It was studied the effect of the calcination and reduction temperature in the morphological properties of these catalysts - see Table 6.8. These results showed that the calcination considerably influenced the morphology of the catalysts as it increased the surface area. However, it was observed that the reduction treatments did not significantly modify the morphological properties of both catalysts.

The ICP technique was applied to determine the actual loading of metals in the materials (Table 6.8). The metals content (and molar ratios of the cations in the HTCs) were close to the nominal values (see Table 3.7), except for the ruthenium loading in the Ni-Ru catalyst.

The H_2 or CO chemisorption over the catalysts with better catalytic performance (HTC[1] and Ni-Ru) was also determined to calculate the metal dispersion on these materials (Table 6.8). As expected, the metallic surface area followed the same metal dispersion trend as the higher the metal distribution, the larger the metal surface area accessible for the reaction. Finally, it was clear that a higher reduction temperature increased the dispersion of the metal in the HTC[1] catalyst.

Table 6.8 - BET, ICP and chemisorption results of some selected samples.

	BET Results		
Catalyst	**Surface Area BET ($m^2 \cdot g^{-1}_{catalyst}$)**	**Total pore volume ($cm^3 \cdot g^{-1}_{catalyst}$)**	**Mean Pore Size (Å)**
HTC^1 dry	105	0.265	65
HTC^1 calcined	162	0.433	80
HTC^1 reduced at 350 ºC	186	0.484	87
HTC^1 reduced at 650 ºC	171	0.494	95
HTC^1 spent[a)]	146	0.332	77
Ni-Ru dry	294	0.457	49
Ni-Ru calcined	423	0.621	49
Ni-Ru reduced at 350 ºC	426	0.636	49
Ni-Ru spent[b)]	381	0.588	52
	ICP Results		
	Metal(s) Loading (wt.%)	**Ni^{2+}/Mg^{2+}**	**$Al^{3+}/(Al^{3+}+Ni^{2+}+Mg^{2+})$**	**$(Ni^{2+}+Mg^{2+})/Al^{3+}$**
HTC^1 calcined	30	0.36	0.22	3.5
HTC^2 calcined	50	2.7	0.34	2.0
HTC^3 calcined	20	0.22	0.24	3.3
HTC^4 calcined	10	n.a.[c)]	0.30	2.3
Ni calcined	9	n.a.[c)]	n.a.[c)]	n.a.[c)]
Ni-Ru calcined	12-0.3	n.a.[c)]	n.a.[c)]	n.a.[c)]
	Chemisorption Results		
	Metal Dispersion (%)	**Metallic S. Area ($m^2_{metal} \cdot g^{-1}_{catalyst}$)**	**Metallic S. Area ($m^2_{metal} \cdot g^{-1}_{metal}$)**
HTC^1 reduced at 350 ºC	4.9×10^{-3}	9.8×10^{-3}	3.3×10^{-2}
HTC^1 reduced at 650 ºC	8.2	16	55
HTC^1 spent[a)]	4.7	9.3	31
Ni-Ru reduced at 350 ºC	9.0*	7.1*	59*
Ni-Ru spent[b)]	7.3*	5.8*	48*

[a)] Spent catalyst that was reduced at 650 ºC previously of the catalytic test.
[b)] Spent catalyst that was reduced at 350 ºC previously of the catalytic test.
[c)] Not applied.
* Obtained by CO chemisorption.

TPR-H_2, TPD-CO_2/NH_3 and TPO

The reducibility of all the catalysts was assessed by TPR. The calcined catalysts based on HTCs (HTC^1, HTC^2, HTC^3 and HTC^4) reduce completely only at very high temperatures, above the reaction temperature (> 400 ºC) - see Fig. 6.11. The TPR profiles obtained for the HTC samples are identical to those achieved in previous works for similar materials [45, 55, 56].

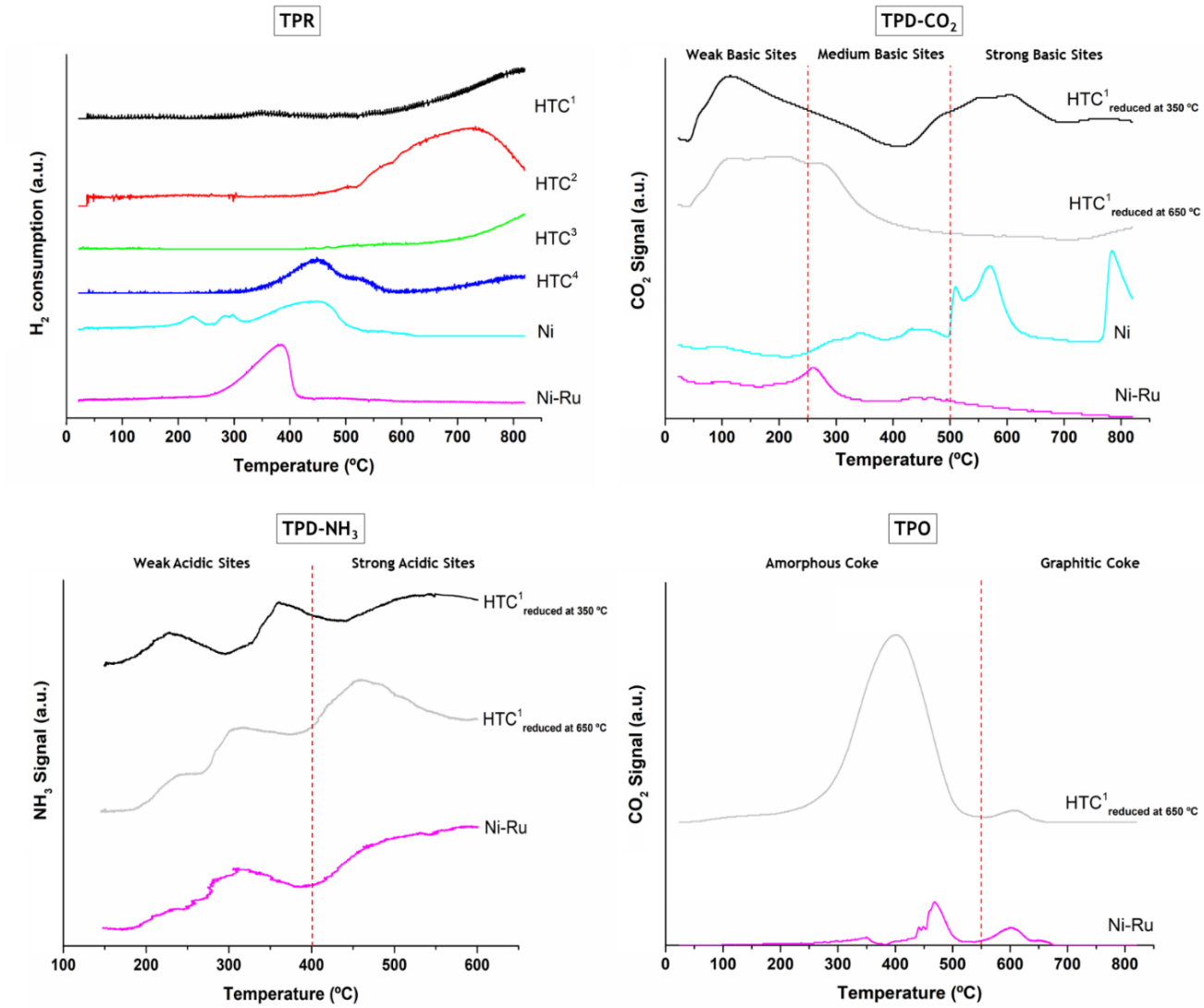

Fig. 6.11. TPR analyses for all the calcined catalysts; TPD-CO_2/NH_3 analyses for several prepared catalysts; and TPO analyses for the spent catalysts HTC^1 (activated at 650 ºC) and Ni-Ru (both used in the long-term tests - *Exp. 2.2*).

To determine the quantity of basic sites of the activated materials (after reduction), TPD-CO_2 was performed for the catalysts with the best catalytic performance in *Exps. 2.1* and *2.2* (HTC^1 and Ni-Ru) - see profiles in Fig. 6.11. Besides, it was studied the effect of the reduction temperature (350 ºC vs. 650 ºC) for HTC^1 (due to the results obtained in the catalytic tests). It is generally conceived that the materials can have three types of basic sites: peaks detected between 23-250 ºC are related to weak basic sites, in the range of 250-500 ºC due to medium strength basic sites while peaks above 500 ºC are associated with the stronger basic sites [17]. Upon integration of the TPD-CO_2 profiles, it was possible to verify that catalyst HTC^1 (reduced at 350 and 650 ºC) has a high quantity of weak basic sites (cf. Table 6.9). The catalyst HTC^1 reduced at 350 ºC presents a higher amount of total basic sites (particularly strong basic sites). Still, the increase of the reduction temperature for this sample leads to the formation of fewer strong basic sites, which are almost absent (cf. Table 6.9).

Besides that, to determine the quantity of acidic sites of the reduced catalysts, TPD-NH_3 analyses were performed for the HTC[1] and Ni-Ru samples - see Fig. 6.11. The catalysts present two kinds of acidic sites, which, according to previous works, can be categorized as strong (400-600 ºC) and weak (150-400 ºC) [21]. All samples showed peaks correlated with the two different acid sites. Table 6.9 shows the amounts of acidic sites present in the materials, obtained by integration of the TPD-NH_3 profiles. The results showed that the HTC[1] catalyst reduced at 350 ºC has a lower amount of acidic sites than the one reduced at higher temperatures, and also lower than the Ni-Ru material - see Table 6.9.

Table 6.9 - Amount of basic and acidic sites in some selected catalysts.

Catalyst	Weak Basic Sites ($mmol_{CO_2} \cdot g^{-1}_{catalyst}$)	Medium Basic Sites ($mmol_{CO_2} \cdot g^{-1}_{catalyst}$)	Strong Basic Sites ($mmol_{CO_2} \cdot g^{-1}_{catalyst}$)	Total Basic Sites ($mmol_{CO_2} \cdot g^{-1}_{catalyst}$)
HTC[1] reduced at 350 ºC	0.24	0.09	0.24	0.57
HTC[1] reduced at 650 ºC	0.34	0.12	0.03	0.49
Ni-Ru reduced at 350 ºC	0.18	0.10	0.04	0.32
	Weak Acidic Sites ($mmol_{NH_3} \cdot g^{-1}_{catalyst}$)	**Strong Acidic Sites ($mmol_{NH_3} \cdot g^{-1}_{catalyst}$)**	**Total Acidic Sites ($mmol_{NH_3} \cdot g^{-1}_{catalyst}$)**	
HTC[1] reduced at 350 ºC	0.11	0.07	0.18	
HTC[1] reduced at 650 ºC	0.10	0.19	0.29	
Ni-Ru reduced at 350 ºC	0.07	0.17	0.24	

The catalysts used in the long-term tests (*Exp. 2.2*) were subjected to TPO analyses - HTC[1] (reduced at 650 ºC) and Ni-Ru. Results obtained confirm coke production on the catalysts during the process, which was fully converted into CO_2 over the TPO experiments (see Fig. 6.11); neither CO nor CH_4 was detected. In several works [22-25], two different combustion peaks were reported during TPO of spent samples, below and above 550 ºC, which were related to the oxidation of amorphous and graphitic coke, respectively. So, the TPO results herein obtained indicate that the coke formed was mostly amorphous. However, minor amounts of graphitic coke were also detected in the two used catalysts, especially on the Ni-Ru one (Table 6.10). It was observed that the total quantity of gasified coke for the used HTC[1] catalyst reduced at 650 ºC was 1.44 $mmol_C \cdot g_{catalyst}^{-1}$ (1.40 $mmol_C \cdot g_{catalyst}^{-1}$ of amorphous coke, i.e. 97.2 % of the total coke deposit) while for the Ni-Ru sample was about 0.38 $mmol_C \cdot g_{catalyst}^{-1}$ (0.27 $mmol_C \cdot g_{catalyst}^{-1}$ of amorphous coke, i.e. 69.8 % of the total coke deposits). These relatively low amounts of coke deposits are associated with the high concentration of H_2O in the system [29] and the presence of basic sites.

Table 6.10 - Quantities of coke gasified in the used catalysts.

Catalyst	Amorphous Coke ($mmol_C \cdot g^{-1}_{catalyst}$)	Graphitic Coke ($mmol_C \cdot g^{-1}_{catalyst}$)	Total Coke ($mmol_C \cdot g^{-1}_{catalyst}$)
HTC[1] spent[a)]	1.40	0.04	1.44
Ni-Ru spent[b)]	0.27	0.11	0.38

[a)] Spent catalyst that was reduced at 650 ºC before the catalytic test.
[b)] Spent catalyst that was reduced at 350 ºC before the catalytic test.

6.2.2.2. Catalytic tests

Considering the initial composition of the synthetic OMW stream used in the chapter 6 (mentioned in subchapter 3.3.2) and the stoichiometry of Eq. (3.5), the maximum theoretical yield of H_2 is 12.182 mol of H_2 per mol of OMW_{feed}. Thermodynamic equilibrium calculations, performed with the *Aspen Plus V.9*® software, at 350 and 400 ºC and 1 bar (Table 6.5), show that H_2 yield is near the maximum theoretical and TOC conversion is complete at both temperatures. Table 6.5 also shows the results obtained in the blank tests (realized in the reactor filled with only silicon carbide); H_2 yield and TOC conversion are low, and are due to the thermal decomposition of the oxygenates through Eqs. (3.6) and (3.16).

Catalysts screening and effect of the reduction temperature

In relation to *Exp. 2.1* (wherein all the catalysts were reduced at 350 ºC), the average results of yield, selectivity and purity of H_2, and conversion of TOC are exhibited in Fig. 6.12 and Fig. F.5 in Appendix F, section 2; data concerning the yields for the other gaseous products are provided in Fig. 6.13. For further information about the production of all the gaseous species along time, please consult Fig. F.6 in Appendix F, section 2.

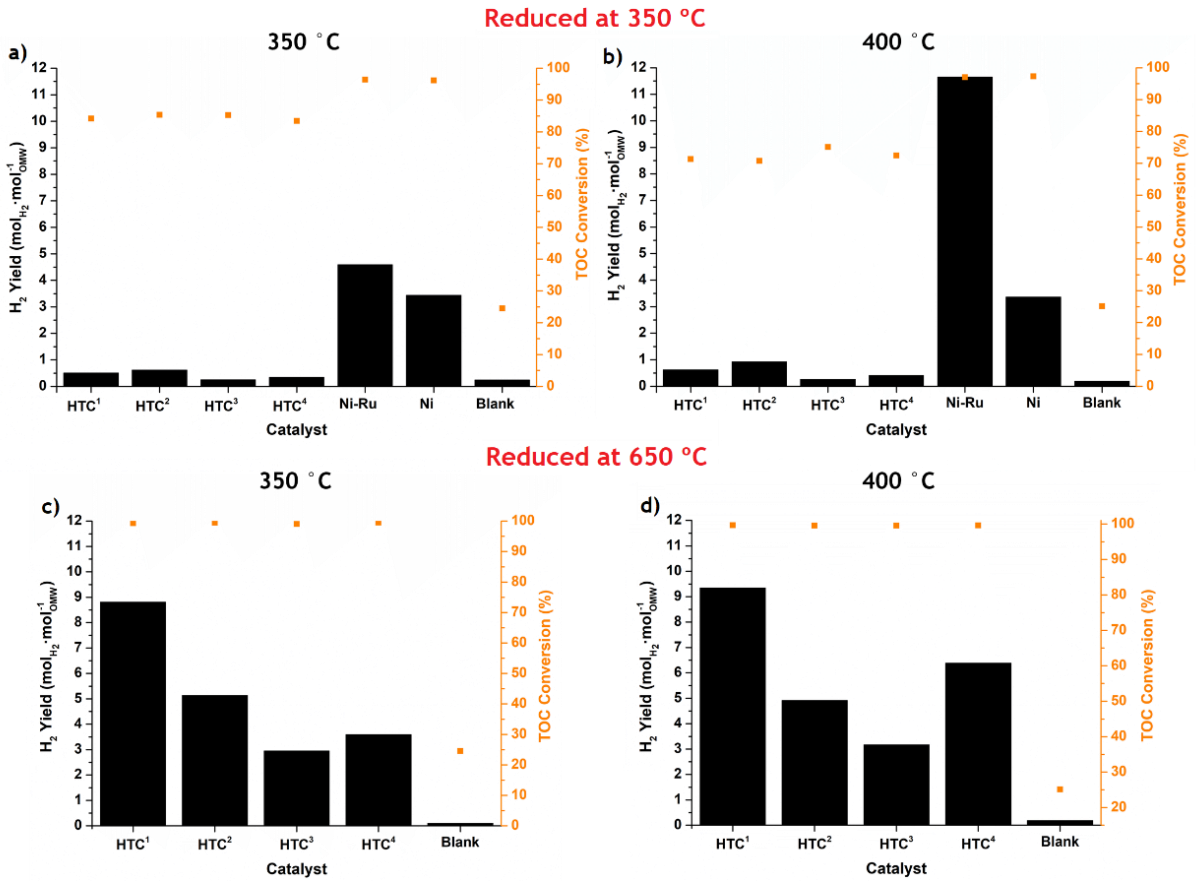

Fig. 6.12. Mean of the H_2 yield and TOC conversion obtained for all the catalysts activated at 350 ºC in the *Exp. 2.1* at a) 350 ºC and b) 400 ºC; and mean of H_2 yield and TOC conversion obtained for the HTC-based materials activated at 650 ºC in the *Exp. 2.1* at c) 350 ºC and d) 400 ºC.

In *Exp. 2.1*, the temperature rise, from 350 to 400 ºC, influences the catalytic performance, particularly for the Ni-Ru catalyst as the H_2 (and also CO_2) yield significantly increases due to the increase of the reaction rates; besides that, the evolutions in the formation of H_2 and CO_2 were very similar for all catalysts while the CO and CH_4 yields obtained were low (see Fig. 6.12 and Fig. 6.13).

During the catalytic tests with the HTC-based catalysts, the production of CO was relevant (Fig. 6.13). These catalysts produced a low quantity of H_2 (Fig. 6.12), meaning that the CO was not fully converted through WGS (Eq. (3.7)) and CO methanation (Eq. (3.8)) reactions. Inherently, the H_2 purity and selectivity obtained in HTC-based catalysts were low. Finally, in relation to the TOC conversion, these materials do not show an amazing capability to crack the oxygenates with high molecular weight - see Fig. 6.12. On the other hand, with the Ni-Ru and Ni catalysts, it was verified a high production of H_2 and CO_2 (main products) - Fig. 6.12 and Fig. 6.13. Low yields of CO and CH_4 at both temperatures were achieved for the Ni catalyst, however, for the Ni-Ru sample, the production of CH_4 was significant at 400 ºC and it was verified a slight increase of the CO yield along the time on stream at 400 ºC - see Fig. F.6 in Appendix F, section 2. The TOC conversions determined using the Ni-Ru and Ni catalysts were high, particularly at 400 ºC - Fig. 6.12. Finally, these results indicate that the impregnation with ruthenium increased significantly the performance of the catalyst: as compared to the Ni sample, similar values of TOC conversion were reached, but higher H_2 and CO_2 yields were attained, i.e., a higher ability to produce H_2 and CO_2 (short-chain species) along the decomposition of the OMW was obtained for the Ru-based sample (Fig. 6.12).

In the experimental tests with the Ni-Ru and Ni catalysts, the H_2 selectivity achieved values slightly above 100 % (and H_2 purities above the value determined in the thermodynamic equilibrium - Table 6.5) probably due to numerous causes: (i) production of coke and other carbon-containing gaseous products not considered in Eq. (3.24), and (ii) the decomposition of the oxygenates/hydrocarbons (Eqs. (3.11) and (3.16)) that can produce H_2 without producing other products. On the other hand, the carbon balance (Eq. (3.26)) does not close at 100 % for almost all catalysts (the exception goes for the Ni-Ru catalyst at 400 ºC). This shows that the carbon converted from the liquid was not completely transformed into gaseous carbon products: the remaining carbon was present on the catalyst surface as coke (confirmed by the TPO analyses) and in other carbon-containing gaseous species which were not analysed in this study (e.g. ethane, propane, etc.), as observed in a previous study [57]. It was verified that, in all experimental tests, the carbon balance at 400 ºC increased as compared to data obtained at 350 ºC, probably as a consequence of decreasing the coke production or/and increasing the production of short-chain species (CO, H_2, CO_2 and CH_4) with temperature. For further information about the H_2 selectivity/purity and carbon balance obtained in *Exp. 2.1*, see section 2 of Appendix F.

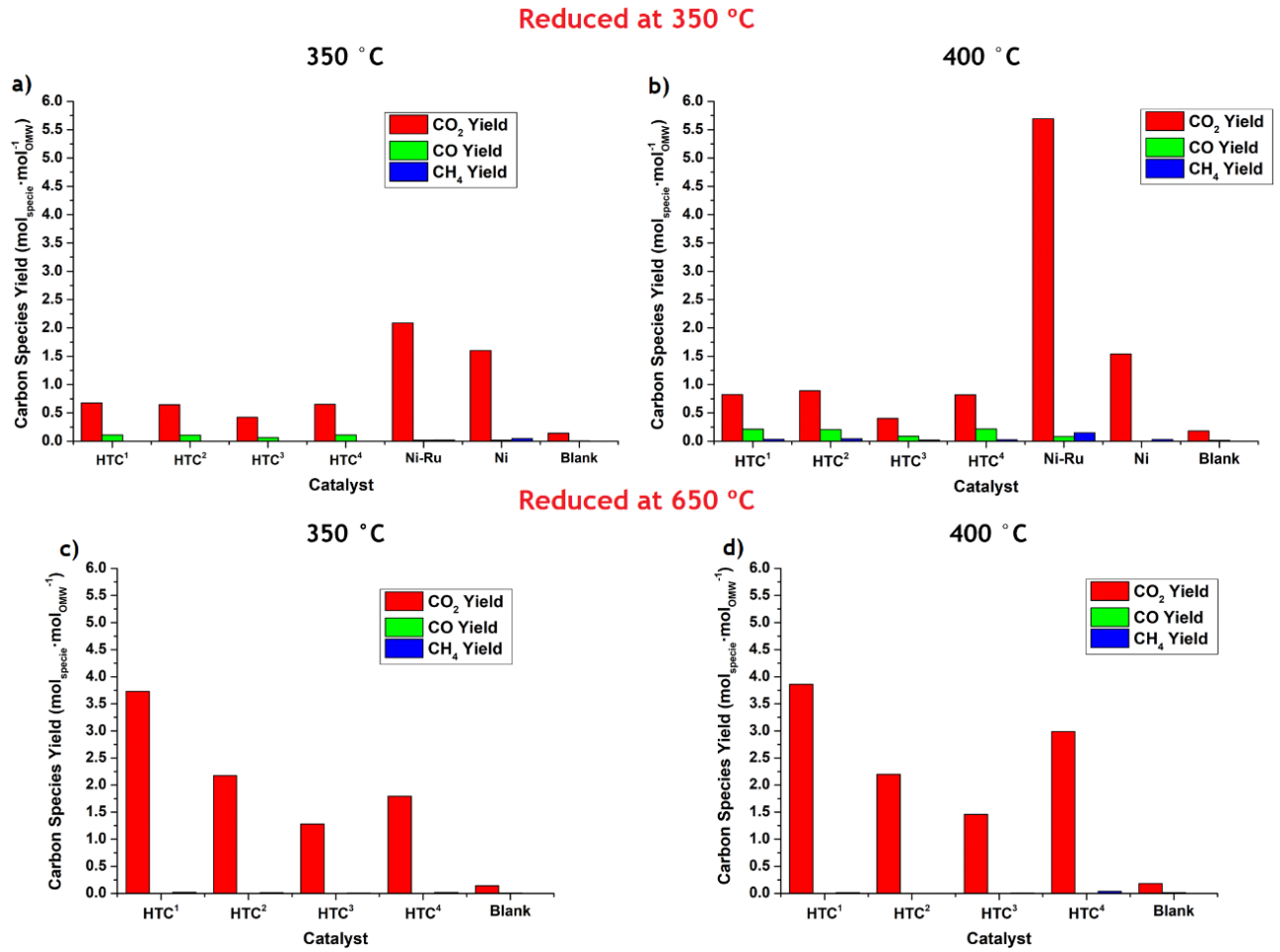

Fig. 6.13. Mean of carbon gaseous species yield obtained for all the catalysts activated at 350 ºC in the *Exp. 2.1* at a) 350 ºC and b) 400 ºC; and mean of carbon gaseous species yield obtained for the HTC-based materials activated at 650 ºC in the *Exp. 2.1* at c) 350 ºC and d) 400 ºC.

In a general way, for tests in *Exp. 2.1*, the catalysts with the worst catalytic activity (HTC-based) provided higher CO yields (Fig. 6.13) and, in this way, present lower performance to WGS reaction (Eq. (3.7)). In opposition, the Ni-Ru catalyst achieved the highest values of H_2 yield, TOC conversion and H_2 purity/H_2 selectivity at 350 and 400 ºC, the latter comparable to that of the Ni sample. Still, Ni-Ru produced low quantities of CH_4, properly catalyzed the WGS reaction (low CO yield) and decomposed efficiently the OMW. The conjugation of these results made the Ni-Ru material promising for the stability tests.

Since the TPR analyses of the hydrotalcites-derived catalysts presented high H_2 consumption at high temperatures (> 400 ºC), the effect of the reduction temperature (350 vs. 650 ºC) in the catalytic activity of these materials (HTC^1, HTC^2, HTC^3 and HTC^4) was also studied in *Exp. 2.1*. It was very clear that these materials, when reduced at 650 ºC, presented a higher catalytic performance: higher yield, selectivity and purity of H_2, and TOC conversion - cf. Fig. 6.12 and Fig. F.5 in Appendix F, section 2. Additionally, the reduction temperature affects the conversion of CO and the production of

CH_4. With the catalysts activated at 650 ºC, the CO yield was practically null, and, in general, the CH_4 yield was slightly lower than with the catalysts reduced at 350 ºC - see Fig. 6.13. Besides the higher catalytic activity of the materials reduced at 650 ºC, the catalyst reduced at 650 ºC presented higher H_2 purity/selectivity and carbon balance than the catalyst reduced at 350 ºC (c.f. section 2 of Appendix F).

Taking into account the results of this subchapter, catalyst HTC[1] activated at 650 ºC was also considered a promising material for long-term tests. Thus, this catalyst (reduced at 650 ºC) was selected to be tested in the 24 h of a long-term test, along with Ni-Ru.

Catalytic activity vs. Physicochemical characterization

First, it is worth mentioning that it was not possible to find any correlation between the Ni content in the catalysts (nor the Ni^{2+}/Mg^{2+} ratio in the HTC-based catalysts) and their catalytic performances.

In a previous study of the team, correlations between materials surface area (calcined catalysts) or metallic surface area per mass of catalyst and TOC conversion were found - the correlations (black line) and the data (orange symbols) obtained in the previous work [57] are presented in Fig. 6.14. As can be seen in Fig. 6.14a), the TOC conversion is higher for the materials with high surface area, reaching complete conversion for ca. 170 m^2/g; besides, TOC conversion significantly increased until reaching a certain value (plateau) of the metallic surface area per mass of catalyst (Fig. 6.14b)); such correlations are shown with the continuous lines in Fig. 6.14. In this way, it was aimed to verify if the correlations obtained in the previous work were valid for the two most promising catalysts prepared in this present work (the data obtained in the present work are represented with black symbols). As can be seen in Fig. 6.14, the correlations are also valid for these catalysts. The TOC conversion of the HTC[1] reduced at 350 ºC was lower than expected according to the correlations, which can be ascribed to the fact that the reduction with H_2 at 350 ºC is not enough to properly activate the catalyst (i.e., reduce all the NiO to metallic Ni); this was avoided with the reduction at 650 ºC, well in line with the correlations. In addition, it was also possible to verify that the correlation between TOC conversion and quantity of acidic sites present in the catalysts - also established in previous work [57] - was also valid for the materials herein analysed (see Fig. 6.15).

Finally, and in line with the last paragraph, it was verified that the temperature used in the reduction program (350 or 650 ºC) substantially affects the physicochemical characteristics of the HTC[1] catalyst: lower values of metallic dispersion and metallic surface areas and higher crystallite size were determined for the HTC[1] sample reduced at 350 ºC - see subchapter 6.2.2.1. Moreover, the XRD results revealed that only the reduction treatment at 650 ºC allowed the complete reduction of the NiO phase to metallic Ni. In this way, these different physicochemical properties justify the better catalytic performance of the HTC[1] catalyst reduced at 650 ºC.

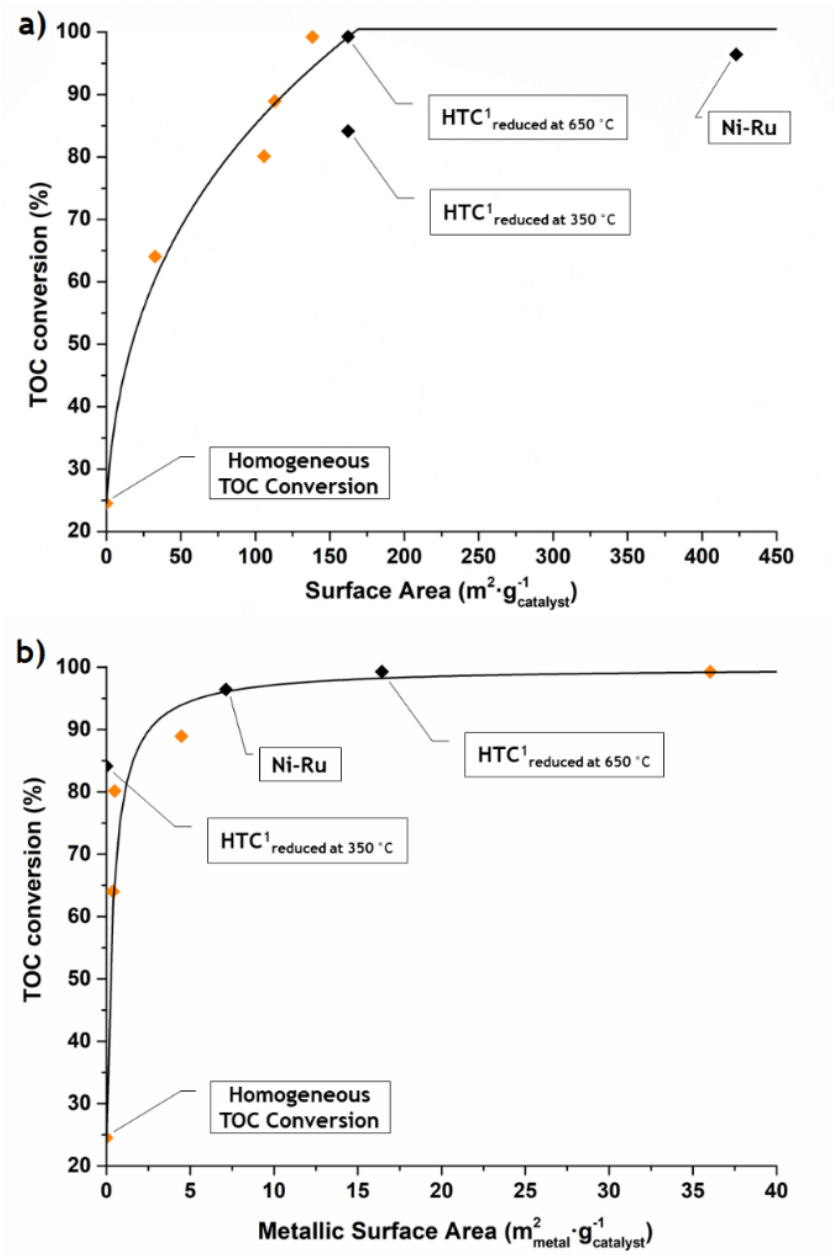

Fig. 6.14. Relation of TOC conversion at 350 ºC of the catalysts used in this work (black points) with a) their surface area (obtained for the calcined samples) and b) their metallic surface area. The orange points and black lines were obtained in previous work [57]. The lines represented in the graphs are just for clearer interpretation/guideline (no mathematical meaning). Data referring to homogeneous TOC conversion refer to the blank experiment reported in Table 6.5.

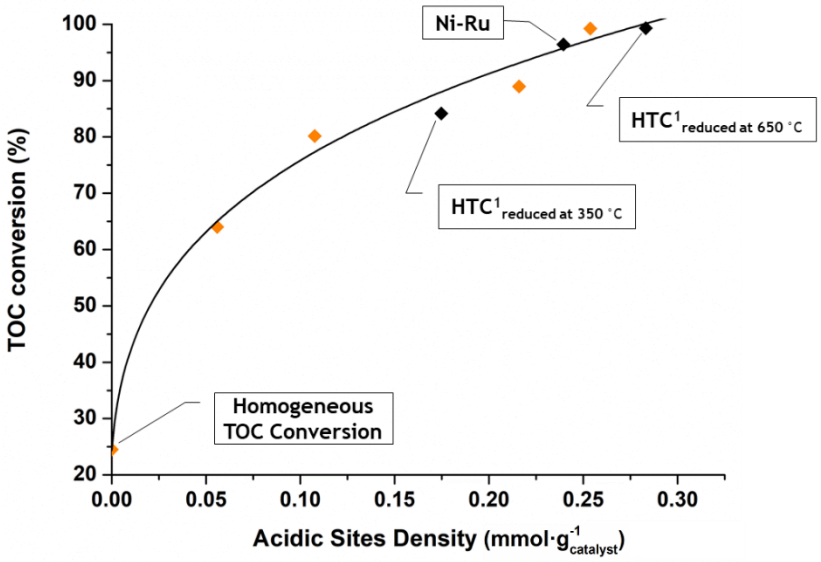

Fig. 6.15. Relation of TOC conversion at 350 °C for the catalysts used in this work (black points) with their density of acidic sites. The orange points and black line were obtained in previous work [57]. The line represented in the graph is just for clearer interpretation/guideline (no mathematical meaning). Data referring to homogeneous TOC conversion refers to the blank experiment reported in Table 6.5.

Stability tests

The catalysts utilized in the stability tests (*Exp. 2.2*) were HTC^1 (reduced 650 ºC) and Ni-Ru. The H_2 (and inherently CO_2) yields obtained in the stability tests follow distinct behavior in the HTC^1 and Ni-Ru catalysts. The Ni-Ru sample exhibits only a slight loss of catalytic performance during the 24 h of the reaction, as confirmed by the small decrease of the H_2 yield (always between 8-10 $mol_{H_2} \cdot mol^{-1}_{OMW}$, cf. Fig. 6.16a). However, for the experimental test with the HTC^1 catalyst, the H_2 yield is high and constant during the first 12 h of operation (> 8.5 $mol_{H_2} \cdot mol^{-1}_{OMW}$); then, the formation of H_2 drastically decreases until reaching similar values as the ones obtained in the blank test, indicating that the catalyst has no catalytic activity from that moment on - see Fig. 6.16b)).

It is possible to observe that the CH_4 yield remains nearly constant and low during the 24 h of the stability test for the HTC^1 catalyst and slightly increases during the first 7 h of reaction for the Ni-Ru catalyst - Fig. 6.16. On the other hand, the production of CO increases during the whole stability test for the Ni-Ru catalyst (in line with the continuous small deactivation), while for the HTC^1 catalyst the CO production only starts after 15 h of reaction (in line with the deactivation of the catalyst) - see Fig. 6.16. The increase of the CO yield in these two catalysts was related to the decreased extent of the WGS reaction (Eq. (3.7)), decreasing the production of H_2 and CO_2.

The TOC conversion remains constant along all the stability test for the Ni-Ru catalyst (≈ 75 % - see Fig. 6.16a)). For the HTC^1 catalyst, and as verified for the H_2 yield, the TOC conversion keeps high

and constant (≈ 99 %) during the first 14-15 h of operation; then, the value of TOC conversion drastically decreases until about 40 % (cf. Fig. 6.16b)).

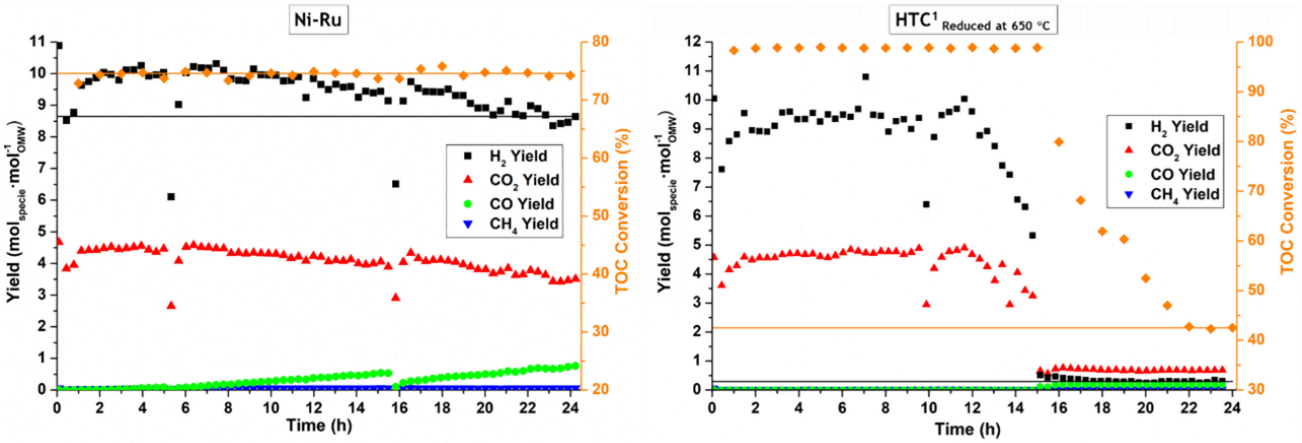

Fig. 6.16. Gaseous products yield and TOC conversion during the Exp. *2.2* (24 h of time-on-stream at 400 ºC) for the catalyst Ni-Ru and for the catalyst HTC[1] reduced at 650 ºC.

The behavior of the H_2 purity/selectivity for the Ni-Ru and HTC-based catalysts along time (Fig. F.8 in Appendix F, section 2) is similar to the behavior of the H_2 yield. Regarding the carbon balance (Eq. (3.26)), once again it does not close at 100 % in the stability tests using the HTC[1] catalyst - see Fig. F.9 in Appendix F, section 2. Since the TPO analyses after stability tests of the HTC-based catalysts indicated that the coke deposition was low (subchapter 6.2.2.1), the carbon balance below 100 % means that other gaseous carbon species were produced (e.g. ethane, propane, ethylene, etc.), which were not considered, as reported elsewhere [57].

It is important to take into consideration that Ni-based catalysts may suffer deactivation by carbon accumulation [20,21]. The differences in the catalyst's stability can be mostly related to the formation of amorphous coke on their surface throughout the experimental tests [23, 26-28]. By analyzing the formation of amorphous coke in the used catalysts (Table 6.10), it was observed that higher amounts of this type of carbon were formed on the surface of the HTC[1] catalyst, explaining, in this way, the high reduction of the H_2 yield in this catalytic test.

The effect of the stability tests on the textural properties of the catalysts was analysed. By comparing the catalysts surface area before and after the stability tests (see Table 6.8), and taking into account the correlation shown in Fig. 6.16a), it was concluded that the reduction of the surface area in the stability test with the Ni-Ru catalyst was not enough to justify the observed slight catalyst deactivation in terms of TOC conversion. Moreover, the reduction of the surface area in the long-term test of the HTC[1] sample also does not fully explain the high decrease of the OMW conversion. Besides, it was also observed that the decrease of metal dispersion and metallic surface area per mass of catalyst (see Table 6.8) was not sufficient to justify the slight deactivation of the Ni-Ru catalyst along all the

stability test, and does not completely explain the very high decrease of the TOC conversion using the catalyst HTC[1]. In this way, it was possible to conclude that the formation of amorphous coke is the main route for the deactivation of the HTC[1] catalyst and probably affects the performance of the Ni-Ru catalyst in terms of H_2 production.

Lastly, in Fig. F.15 in Appendix F, section 2, it is possible to verify the color difference between the condensed phases obtained in the stability test using the HTC[1] catalyst. The color of the samples (yellow) has become more intense as the TOC conversion decreased.

6.2.3. Conclusions

A catalytic screening for the OMWSR process was completed with in-house prepared Ni-containing catalysts. It was possible to emphasize the high catalytic performance (H_2 yield, TOC conversion and H_2 selectivity) of the Ni-Ru and HTC[1] (activated at 650 ºC) samples. Besides that, it was verified that the HTC-based material activated at 650 ºC presented a higher catalytic performance in comparison with the same material reduced at 350 ºC, because the reduction treatment at 650 ºC allowed the completely reduce the NiO phase to metallic Ni and to reach higher values of metallic dispersion and metallic surfaces areas.

It was found that the catalytic performances (TOC conversion) correlate well with metallic surface area and the surface area of the Ni-based catalysts.

Finally, it was verified that the Ni-Ru catalyst also presented the highest H_2 yield in 24 h time-on-steam tests (always > 8 $mol_{H_2} \cdot mol^{-1}_{OMW}$), constant TOC conversion (≈ 75 %) and low catalyst deactivation. Still, it was concluded that the catalyst HTC[1] reduced at 650 ºC presented a high H_2 yield (> 8.5 $mol_{H_2} \cdot mol^{-1}_{OMW}$) and TOC conversion (≈ 99 %) but only during the first 12 h of operation; then, the catalyst significantly deactivated due mostly to the amorphous coke produced.

Notation and Glossary

List of Symbols

D_{M}	Metal dispersion (dimensionless)
$D_{reactor}$	Internal diameter of the reactor (mm)
$d_{particle}$	Particle diameter (mm)
F_i	Molar flow rate of component *i* ($mol \cdot min^{-1}$)
M_{Metal}	Molecular weight of the metal ($g \cdot mol^{-1}$)
$\mathrm{N_A}$	Avogadro's number (mol^{-1})
n_{s}	Number of atoms at surface per unit area (m^{-2})
n_{m}	Quantity of chemisorbed molecules ($mol \cdot g^{-1}_{catalyst}$)
Q_{OMW}	Volumetric flow rate of OMW ($mL \cdot min^{-1}$)
s	Chemisorption stoichiometry (dimensionless)
S_{M}	Metallic surface area per mass of catalyst ($m^2 \cdot g^{-1}_{catalyst}$)
TOF	Turnover frequency (min^{-1})
W_{Catalyst}	Mass of catalyst (g)
y_{Metal}	Mass fraction of the metal in the catalyst (dimensionless)

List of Acronyms

BET	Brunauer-Emmet-Teller
GC	Gas chromatograph
HTC	Hydrotalcite
OMW	Olive oil mill wastewater
OMWSR	Olive oil mill wastewater steam reforming
SEM/EDS	Scanning electron microscopy / Energy dispersive spectroscopy
TEM	Transmission electron microscopy
TOC	Total organic carbon
TPD	Temperature-programmed desorption
TPO	Temperature-programmed oxidation
TPR	Temperature-programmed reduction
WGS	Water-gas shift

References

[1] Donphai, W., N. Piriyawate, T. Witoon, P. Jantaratana, V. Varabuntoonvit and M. Chareonpanich, Effect of magnetic field on CO2 conversion over Cu-ZnO/ZrO2 catalyst in hydrogenation reaction. Journal of CO2 Utilization, 2016. 16: p. 204-211.

[2] Oates, W.A. and T.B. Flanagan, The Reaction of Hydrogen Atoms with Palladium and its Alloys. Canadian Journal of Chemistry, 1975. 53(5): p. 694-701.

[3] Lischka, M. Hydrogen on palladium : A model system for the interaction of atoms and molecules with metal surfaces. 2003.

[4] Zhang, X.-R., L.-C. Wang, C.-Z. Yao, Y. Cao, W.-L. Dai, H.-Y. He and K.-N. Fan, A highly efficient Cu/ZnO/Al2O3 catalyst via gel-coprecipitation of oxalate precursors for low-temperature steam reforming of methanol. Catalysis Letters, 2005. 102(3): p. 183-190.

[5] Zhuang, Y., R. Currie, K.B. McAuley and D.S.A. Simakov, Highly-selective CO2 conversion via reverse water gas shift reaction over the 0.5wt% Ru-promoted Cu/ZnO/Al2O3 catalyst. Applied Catalysis A: General, 2019. 575: p. 74-86.

[6] Hajduk, Š., V.D.B.C. Dasireddy, B. Likozar, G. Dražić and Z.C. Orel, COx-free hydrogen production via decomposition of ammonia over Cu-Zn-based heterogeneous catalysts and their activity/stability. Applied Catalysis B: Environmental, 2017. 211: p. 57-67.

[7] Ding, W., Y. Liu, F. Wang, S. Zhou, A. Chen, Y. Yang and W. Fang, Promoting effect of a Cu-Zn binary precursor on a ternary Cu-Zn-Al catalyst for methanol synthesis from synthesis gas. RSC Advances, 2014. 4(58): p. 30677-30682.

[8] Gesmanee, S. and W. Koo-amornpattana, Catalytic hydrogenation of CO2 for methanol production in fixed-bed reactor using Cu-Zn supported on gamma-Al2O3. Energy Procedia, 2017. 138: p. 739-744.

[9] Córdoba, G., M. Viniegra, J.L.G. Fierro, J. Padilla and R. Arroyo, TPR, ESR, and XPS Study of Cu2+Ions in Sol-Gel-Derived TiO2. Journal of Solid State Chemistry, 1998. 138(1): p. 1-6.

[10] Cobo, M., A. Quintero and C.M.d. Correa, Liquid phase dioxin hydrodechlorination over Pd/γ-Al2O3. Catalysis Today, 2008. 133-135: p. 509-519.

[11] Kim, S.S., S.H. Choi, S.M. Lee and S.C. Hong, Enhanced catalytic activity of Pt/Al2O3 on the CH4 SCR. Journal of Industrial and Engineering Chemistry, 2012. 18(1): p. 272-276.

[12] Burch, R. and M.J. Hayes, The Preparation and Characterisation of Fe-Promoted Al2O3-Supported Rh Catalysts for the Selective Production of Ethanol from Syngas. Journal of Catalysis, 1997. 165(2): p. 249-261.

[13] Li, F., H. Ma, H. Zhang, W. Ying and D. Fang, Ethanol synthesis from syngas on Mn- and Fe-promoted Rh/γ-Al2O3. Comptes Rendus Chimie, 2014. 17(11): p. 1109-1115.

[14] Oliveira, R.L., I.G. Bitencourt and F.B. Passos, Partial oxidation of methane to syngas on Rh/Al2O3 and Rh/Ce-ZrO2 catalysts. Journal of the Brazilian Chemical Society, 2013. 24: p. 68-75.

[15] Sharma, P.K., N. Saxena, P.K. Roy and A. Bhatt, Hydrogen generation by ethanol steam reforming over Rh/Al2O3 and Rh/CeZrO2 catalysts: A comparative study. International Journal of Hydrogen Energy, 2016. 41(14): p. 6123-6133.

[16] Mazzieri, V., F. Coloma-Pascual, A. Arcoya, P.C. L'Argentière, Fı, x and N.S. goli, XPS, FTIR and TPR characterization of Ru/Al2O3 catalysts. Applied Surface Science, 2003. 210(3): p. 222-230.

[17] Singha, R.K., A. Yadav, A. Agrawal, A. Shukla, S. Adak, T. Sasaki and R. Bal, Synthesis of highly coke resistant Ni nanoparticles supported MgO/ZnO catalyst for reforming of methane with carbon dioxide. Applied Catalysis B: Environmental, 2016. 191: p. 165-178.

[18] Aziz, M.A.A., A.A. Jalil, S. Wongsakulphasatch and D.-V.N. Vo, Understanding the role of surface basic sites of catalysts in CO2 activation in dry reforming of methane: a short review. Catalysis Science & Technology, 2020. 10(1): p. 35-45.

[19] Silva, J.M., L.S. Ribeiro, J.J.M. Órfão, M.A. Soria and L.M. Madeira, Low temperature glycerol steam reforming over a Rh-based catalyst combined with oxidative regeneration. International Journal of Hydrogen Energy, 2019. 44(5): p. 2461-2473.

[20] Siva Kumar, V., B.M. Nagaraja, V. Shashikala, P. Seetharamulu, A.H. Padmasri, B. David Raju and K.S. Rama Rao, Role of acidic and basic sites of Al2O3 in predicting the reaction pathway of isophorone transformation. Journal of Molecular Catalysis A: Chemical, 2004. 223(1): p. 283-288.

[21] Fang, W.-W., M.-M. Mu, J. Tian, L.-G. Chen and Y. Li, Continuous synthesis of N-ethylethylenediamine over supported Cu-Zn-La catalysts. Chemical Papers, 2016. 70(4): p. 430-435.

[22] Wu, C., L. Dong, J. Huang and P.T. Williams, Optimising the sustainability of crude bio-oil via reforming to hydrogen and valuable by-product carbon nanotubes. RSC Advances, 2013. 3(42): p. 19239-19242.

[23] Tan, R., A. Alir, S. Mohamad, K. Md Isa, T. Amran and T.A. Tuan Abdullah, Ni-based catalysts for steam reforming of tar model derived from biomass gasification. 2019.

[24] Galetti, A.E., M.F. Gomez, L.A. Arrúa and M.C. Abello, Hydrogen production by ethanol reforming over NiZnAl catalysts: Influence of Ce addition on carbon deposition. Applied Catalysis A: General, 2008. 348(1): p. 94-102.

[25] Calles, J.A., A. Carrero, A.J. Vizcaíno and L. García-Moreno, Hydrogen production by glycerol steam reforming over SBA-15-supported nickel catalysts: Effect of alkaline earth promoters on activity and stability. Catalysis Today, 2014. 227: p. 198-206.

[26] Lu, P., Effect of Operating Conditions on the Coke Formation and Nickel Catalyst Performance During Cracking of Tar. Waste and biomass valorization, 2019. v. 10(no. 1): p. pp. 155-165-2019 v.10 no.1.

[27] He, L., S. Hu, L. Jiang, S.S.A. Syed-Hassan, Y. Wang, K. Xu, S. Su, J. Xiang, L. Xiao, H. Chiand X. Chen, Opposite effects of self-growth amorphous carbon and carbon nanotubes on the reforming of toluene with Ni/α-Al2O3 for hydrogen production. International Journal of Hydrogen Energy, 2017. 42(21): p. 14439-14448.

[28] Yao, D., H. Yang, H. Chen and P.T. Williams, Co-precipitation, impregnation and so-gel preparation of Ni catalysts for pyrolysis-catalytic steam reforming of waste plastics. Applied Catalysis B: Environmental, 2018. 239: p. 565-577.

[29] Rocha, C., M.A. Soria and L.M. Madeira, Thermodynamic analysis of olive oil mill wastewater steam reforming. Journal of the Energy Institute, 2019. 92(5): p. 1599-1609.

[30] Mi, J., Y. Cao, J. Zhang, C. Chen, D. Li, X. Lin, J. Chen and L. Jiang, Effects of Doping Rare Earth Elements (Y, La, and Ce) on Catalytic Performances of CoMo/MgAlM for Water Gas Shift Reaction. Industrial & Engineering Chemistry Research, 2018. 57(3): p. 833-844.

[31] Ozawa, M. and Y. Nishio, Thermal stability and microstructure of catalytic alumina composite support with lanthanum species. Applied Surface Science, 2016. 380: p. 288-293.

[32] Bu, K., S. Kuboon, J. Deng, H. Li, T. Yan, G. Chen, L. Shi and D. Zhang, Methane dry reforming over boron nitride interface-confined and LDHs-derived Ni catalysts. Applied Catalysis B: Environmental, 2019. 252: p. 86-97.

[33] Carlsson, M., Carbon Formation in Steam Reforming and Effect of Potassium Promotion. Johnson Matthey Technology Review, 2015. 59(4): p. 313-318.

[34] Faungnawakij, K., Y. Tanaka, N. Shimoda, T. Fukunaga, S. Kawashima, R. Kikuchi and K. Eguchi, Influence of solid-acid catalysts on steam reforming and hydrolysis of dimethyl ether for hydrogen production. Applied Catalysis A: General, 2006. 304: p. 40-48.

[35] Liu, Y., X. Guo, G.L. Rempel and F.T.T. Ng, The Promoting Effect of Ni on Glycerol Hydrogenolysis to 1,2-Propanediol with In Situ Hydrogen from Methanol Steam Reforming Using a Cu/ZnO/Al2O3 Catalyst. Catalysts, 2019. 9(5): p. 412.

[36] Zhong, Z., H. Ang, C. Choong, L. Chen, L. Huang and J. Lin, The role of acidic sites and the catalytic reaction pathways on the Rh/ZrO2 catalysts for ethanol steam reforming. Physical Chemistry Chemical Physics, 2009. 11(5): p. 872-880.

[37] Rocha, C., M.A. Soria and L.M. Madeira, Steam reforming of olive oil mill wastewater with in situ hydrogen and carbon dioxide separation - Thermodynamic analysis. Fuel, 2017. 207: p. 449-460.

[38] Rocha, C., M.A. Soria and L.M. Madeira, Thermodynamic analysis of olive oil mill wastewater steam reforming. Journal of the Energy Institute, 2018.

[39] Chiodo, V., S. Freni, A. Galvagno, N. Mondello and F. Frusteri, Catalytic features of Rh and Ni supported catalysts in the steam reforming of glycerol to produce hydrogen. Applied Catalysis A: General, 2010. 381(1): p. 1-7.

[40] Bulutoglu, P.S., Z. Say, S. Bac, E. Ozensoy and A.K. Avci, Dry reforming of glycerol over Rh-based ceria and zirconia catalysts: New insights on catalyst activity and stability. Applied Catalysis A: General, 2018. 564: p. 157-171.

[41] Silva, J.M., M.A. Soria and L.M. Madeira, Challenges and strategies for optimization of glycerol steam reforming process. Renewable and Sustainable Energy Reviews, 2015. 42: p. 1187-1213.

[42] Llorca, J., V.C. Corberán, N.J. Divins, Raquel O. Fraile and E. Taboada, Chapter 7 - Hydrogen from Bioethanol, in Renewable Hydrogen Technologies, L.M. Gandía, G. Arzamendi and P.M. Diéguez, Editors. 2013, Elsevier: Amsterdam. p. 135-169.

[43] Montañez, M.K., R. Molina and S. Moreno, Nickel catalysts obtained from hydrotalcites by coprecipitation and urea hydrolysis for hydrogen production. International Journal of Hydrogen Energy, 2014. 39(16): p. 8225-8237.

[44] Zeng, G., R. Gu and Y. Li, The preparation and catalytic behavior of a shell-core Ni/Mg-Al catalyst for ethanol steam reforming. International Journal of Hydrogen Energy, 2013. 38(26): p. 11256-11267.

[45] Borges, R.P., R.A.R. Ferreira, R.C. Rabelo-Neto, F.B. Noronha and C.E. Hori, Hydrogen production by steam reforming of acetic acid using hydrotalcite type precursors. International Journal of Hydrogen Energy, 2018. 43(16): p. 7881-7892.

[46] Pérez Zurita, M.J., M. Bartolini, T. Righi, G. Vitale and P. Pereira Almao, Hydrotalcite type materials as catalyst precursors for the Catalytic Steam Cracking of toluene. Fuel, 2015. 154: p. 71-79.

[47] Zhou, F., N. Pan, H. Chen, X. Xu, C. Wang, Y. Du, Y. Guo, Z. Zeng and L. Li, Hydrogen production through steam reforming of toluene over Ce, Zr or Fe promoted Ni-Mg-Al hydrotalcite-derived catalysts at low temperature. Energy Conversion and Management, 2019. 196: p. 677-687.

[48] Bimbela, F., J. Ábrego, R. Puerta, L. García and J. Arauzo, Catalytic steam reforming of the aqueous fraction of bio-oil using Ni-Ce/Mg-Al catalysts. Applied Catalysis B: Environmental, 2017. 209: p. 346-357.

[49] Josuinkas, F.M., C.P.B. Quitete, N.F.P. Ribeiro and M.M.V.M. Souza, Steam reforming of model gasification tar compounds over nickel catalysts prepared from hydrotalcite precursors. Fuel Processing Technology, 2014. 121: p. 76-82.

[50] Olivares, A.C.V., M.F. Gomez, M.N. Barroso and M.C. Abello, Ni-supported catalysts for ethanol steam reforming: effect of the solvent and metallic precursor in catalyst preparation. International Journal of Industrial Chemistry, 2018. 9(1): p. 61-73.

[51] Takehira, K., T. Shishido, P. Wang, T. Kosaka and K. Takaki, Steam reforming of CH4 over supported Ni catalysts prepared from a Mg-Al hydrotalcite-like anionic clay. Physical Chemistry Chemical Physics, 2003. 5(17): p. 3801-3810.

[52] Zhang, Y., W. Wang, Z. Wang, X. Zhou, Z. Wang and C.-J. Liu, Steam reforming of methane over Ni/SiO2 catalyst with enhanced coke resistance at low steam to methane ratio. Catalysis Today, 2015. 256: p. 130-136.

[53] Calles, J., A. Carrero, A. Vizcaíno and M. Lindo, Hydrogen Production by Ethanol Steam Reforming on Ni/SiO2 Catalysts: Effect of Ce and Zr Incorporation. 2010.

[54] Zhurka, M.D., A.A. Lemonidou, J.A. Anderson and P.N. Kechagiopoulos, Kinetic analysis of the steam reforming of ethanol over Ni/SiO2 for the elucidation of metal-dominated reaction pathways. Reaction Chemistry & Engineering, 2018. 3(6): p. 883-897.

[55] Dębek, R., M. Motak, M.E. Galvez, T. Grzybek and P. Da Costa, Promotion effect of zirconia on Mg(Ni,Al)O mixed oxides derived from hydrotalcites in CO2 methane reforming. Applied Catalysis B: Environmental, 2018. 223: p. 36-46.

[56] Park, K., K.Y. Kim, L. Lu, T.-H. Lim, S.-A. Hong and H.-I. Lee, Structural Characteristics of (NiMgAl)Ox Prepared from a Layered Double Hydroxide Precursor and its Application in Direct Internal Reforming Molten Carbonate Fuel Cells. Fuel Cells, 2007. 7(3): p. 211-217.

[57] Rocha, C., M.A. Soria and L.M. Madeira, Screening of commercial catalysts for steam reforming of olive mill wastewater. Renewable Energy, 2021. 169: p. 765-779.

Chapter 7. Olive Mill Wastewater Valorization through Steam Reforming using Hybrid Multifunctional Reactors for High-Purity H_2 Production *

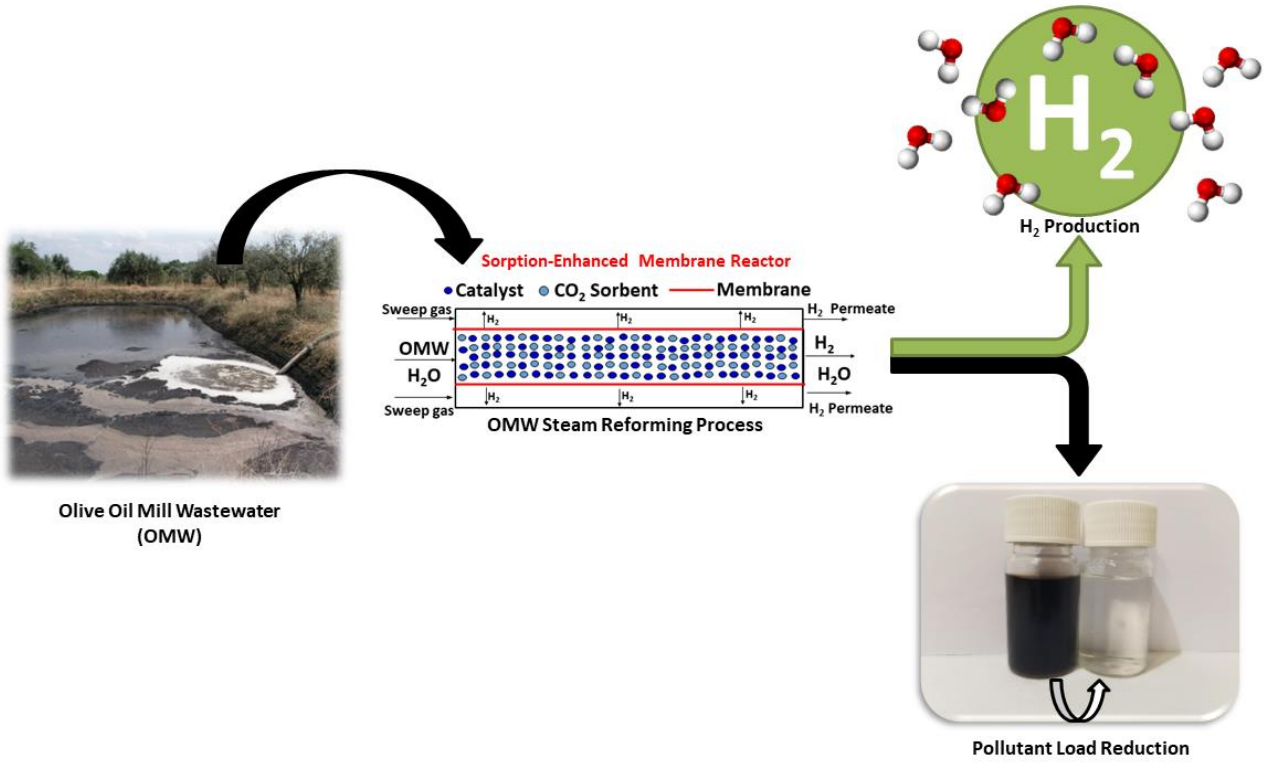

Highlights:

- The OMWSR was performed in several reactor configurations (TR, SER, MR and SEMR).
- CO_2 capture with a commercial sorbent increased the catalyst stability.
- During the pre-breakthrough in a SEMR, H_2 yield reached the maximum theoretical value.
- Use of a SEMR increases H_2 yield by 44 % in comparison with the results of the TR.
- OMWSR in a SEMR can efficiently treat real effluents with high H_2 yields.

* The contents of this subchapter were adapted from Rocha, C., M.A. Soria, and L.M. Madeira, Olive mill wastewater valorization through steam reforming using hybrid multifunctional reactors for high-purity H_2 production. Chemical Engineering Journal, 2021. (https://doi.org/10.1016/j.cej.2021.132651)

Abstract:

The main purpose of this study was to assess the benefits of different hybrid multifunctional reactors (sorption-enhanced reactor (SER), membrane reactor (MR) and sorption-enhanced membrane reactor (SEMR)) comparatively to a traditional reactor (TR) for H_2 production through olive oil mill wastewater steam reforming (OMWSR). In all reactor configurations, an in-house prepared Ni-Ru/Ce-SiO_2 catalyst was used, combined in the sorption-enhanced reactors with a potassium-promoted hydrotalcite-based sorbent to capture CO_2. Additionally, in the MR and SEMR configurations, a commercial Pd-Ag membrane was utilized to separate H_2 from the reaction medium.

It was verified an increase in both the H_2 production and catalyst stability using the SER (during the pre-breakthrough of CO_2) in comparison with the TR. However, a higher enhancement of the H_2 yield was observed using the SEMR (again during the pre-breakthrough period), which was less pronounced after the saturation of the sorbent (i.e., in the MR), due to the effect of the H_2 perm-selective membrane. Furthermore, pure H_2 can be obtained in the permeate side of the membrane reactors (in the absence of sweep gas).

It was also demonstrated that the use of such multifunctional reactors (and particularly the SEMR) in the steam reforming of real olive mill effluents allows reducing drastically the pollutant load of these streams, while economically valorizing this waste with the production of green H_2.

7.1. Introduction

The use of the multifunctional reactor concepts, with the aim of suppressing both thermodynamic and kinetic limitations, has been studied for several steam reforming processes [1, 2]. Since the main products of steam reforming processes are mostly H_2 and CO_2 and several of the reactions involved are reversible, the application of a sorption-enhanced reactor (SER) with CO_2 capture, a membrane reactor (MR) with selective H_2 permeation, or even a sorption-enhanced membrane reactor (SEMR), with simultaneous in-situ H_2 separation and CO_2 capture, could be promising in an olive oil mill wastewater (OMW) steam reforming (OMWSR) process, potentially yielding high-purity H_2 streams; this was already theoretically studied, from the thermodynamics point of view [3], but never experimentally tested (except the MR, as detailed above in this thesis).

The capture of CO_2 in a SER/SEMR can be carried out by combining, in the same bed, a catalyst and a CO_2 sorbent, such as CaO-based materials [4, 5], hydrotalcites (HTCs) [6, 7], lithium silicates [8, 9], lithium cuprate [10] or lithium zirconates [11, 12], among others. However, once the temperatures to be employed are foreseen to not exceed 400 ºC, due to the restrictions of materials compatibility (catalyst, CO_2 sorbent and H_2 perm-selective membrane), the best option for in situ CO_2 sorption are HTCs; actually, both sorption and regeneration steps can be carried out at such temperatures while maintaining reasonable working sorption capacities and kinetics [7, 13]. Besides, it has been widely reported that the presence of steam (a reagent in large excess in the OMWSR) increases the CO_2 sorption capacity and regenerability of HTCs, particularly potassium doped-HTCs [14-16].

For the operation of a SEMR, it is also necessary to use a H_2 perm-selective membrane, being the dense metallic membranes the most widely studied for H_2 selective permeation [17]. Pd-based membranes (especially Pd-Ag alloys) have been found as the most promising because of their higher permeability, stability against poisoning by CO_2, CO or H_2S, and compatibility with the operation conditions adopted in the OMWSR (300-500 ºC) [18-20].

The present work aims at evaluating the performance of four different reactor configurations (traditional reactor (TR) vs. the hybrid devices - SER, MR and SEMR) for the OMWSR. The catalytic tests were performed at different pressures and temperatures, using a Ni-Ru-based catalyst (Ni-Ru/CeO_2-SiO_2 - similar to the one already prepared in a previous work), which was combined with commercial and prepared hydrotalcites, in the SER/SEMR, and a commercial thin Pd-Ag membrane, in the MR/SEMR. The main novelty of this work is precisely the utilization of these hybrid multifunctional reactor configurations, never tested before for this application. To compare the performance of the different reactors, H_2 yield, total organic carbon (TOC) conversion and stability was assessed.

The methods and materials used in this work are described in subchapter 3.4.

7.2. Results and discussion

7.2.1. Thermodynamic results and blank tests

The initial synthetic effluent was characterized in terms of pH, TOC, TPh and chemical oxygen demand (COD) - see Table 7.1. Taking into account its composition (cf. Table 3.9 in subchapter 3.4.2), the maximum theoretical yield of H_2 for this OMW stream (considering complete conversion and that only the OMWSR reaction occurs (Eq. (3.5)) is 11.84 mol of H_2 per mol of OMW fed.

Before the catalytic tests, blank experimental runs (*Exp. 3.0*) at the two different operation conditions were performed in the TR with only SiC. Apart from that, the production of H_2, CO_2, CO, CH_4 and coke and the conversion of the OMW (assessed in terms of TOC conversion), in the thermodynamic equilibrium and for the operation conditions defined, were determined with the Aspen Plus V.9® software - see details elsewhere [21].

According to the thermodynamics, and due to the high quantity of H_2O in the feed, the steam reforming process is shifted towards the production of a high quantity of H_2 and CO_2 (consuming nearly all the CO through the water-gas shift (WGS) reaction - Eq. (3.7); besides that, the methanation reactions (Eq. (3.8) and reverse of Eq. (3.9)) is inhibited with the presence of a high amount of H_2O. For that reason, the H_2 yields obtained in the equilibrium at 350 ºC and 1 bar and 400 ºC and 4 bar were close to the maximum theoretical yield of H_2 (see Table 7.2), and the TOC conversions were complete. The yields achieved for the remaining gaseous products were very low and are also shown in Table 7.2.

Table 7.1 - Characterization of the liquid samples obtained in the experiments with the synthetic OMW.

Liquid Sample	TOC ($mg_C \cdot L^{-1}$)	TPh ($mg_{GA} \cdot L^{-1}$)	COD ($mg_{O_2} \cdot L^{-1}$)	pH
Initial Effluent	11 270	3 709	38 863	2.96
Condensable sample (7 min)[a)]	48	2.5	12	≈ 7
Condensable sample (34 min)[a)]	50	1.2	40	
Condensable sample (57 min)[a)]	48	2.4	17	
Condensable sample (77 min)[a)]	48	2.2	0	
Condensable sample (107 min)[a)]	53	1.5	14	
Condensable sample (122 min)[a)]	50	1.1	10	

[a)] Results obtained in a SEMR (subchapter 7.2.4) in the 4th cyle.

Table 7.2 also shows the results obtained in the blank test - *Exp. 3.0*. Since the process was not catalyzed in these experimental tests, the H_2 and CO_2 yields were very low. It was possible to verify that, at 400 ºC and 4 bar, the TOC conversion was higher as compared to the run at 350 ºC and 1 bar. Such conversion occurs mainly through thermal decomposition/cracking of OMW - Eqs. (3.6) and (3.16).

Table 7.2 - Yields of all gaseous products and OMW TOC conversion in the thermodynamic equilibrium (Aspen Plus V.9® simulation) and in the blank experiments (*Exp. 3.0*).

Operation Conditions	H_2 Yield	CO Yield	CH_4 Yield	CO_2 Yield	TOC Conversion (%)
Thermodynamic Equilibrium (Simulations in the Aspen Plus V.9® software)					
350 ºC, 1 bar (TR)	11.37	9.1×10^{-3}	0.11	5.8	100
400 ºC, 4 bar (TR)	11.29	1.6×10^{-2}	0.13	5.8	100
Blank Tests (*Exp. 3.0*)					
350 ºC, 1 bar	4.0×10^{-2}	0.00	0.00	0.25	25
400 ºC, 4 bar	6.0×10^{-2}	0.00	0.00	0.35	33
Maximum Theoretical Yield of H_2	11.84				

7.2.2. Traditional reactor

In the set of experiments with the TR (*Exp. 3.1*), the operating conditions chosen significantly affect the performance reached, namely the H_2 production and catalyst stability. Nevertheless, the behavior of the production of H_2 and CO_2 along time was similar (see Fig. 7.1), indicating that WGS (Eq. (3.7)) is the predominant reaction to produce these species. The yields of CO and CH_4 were very low in both tests, in line with the predominance of the WGS reaction (Eq. (3.7)) - see Fig. 7.1. It is worth noting that almost complete total conversion of the TOC (> 99 %) was obtained during all the tests in both operation conditions used, indicating that is possible to reduce nearly all the organic load from the OMW. In this way, it was observed a significant enhancement of the TOC conversion comparatively to the blank tests; so, the reactions were associated with the presence of the catalyst and not occurred in a significant extent in the gas phase. Accordingly, a change in the color from the fed OMW solution (yellow) to the liquid condensate at the outlet of the reactor (colorless) was clearly observed.

The H_2 yield observed at 350 ºC and 1 bar was always between 6.0-4.5 $mol_{H_2} \cdot mol^{-1}_{OMW}$ and always between 8.0-2.5 $mol_{H_2} \cdot mol^{-1}_{OMW}$ at 400 ºC and 4 bar (Fig. 7.1). The higher production of H_2 at 400 ºC and 4 bar in the first hours of the experiment is related to the favored kinetics under these conditions, which also allows producing a higher quantity of CH_4 (the methanation reactions are favorable at high pressures - Eq. (3.8) and reverse of Eq. (3.9). The CO yield obtained in the TR at 350 ºC and 1 bar was very low and only occurred in the first hours of the reaction, while this specie was not detected during all the catalytic cycles at 400 ºC and 4 bar. The high TOC conversion and relatively low formation of carbon-containing gaseous products indicate that the carbon eliminated from the liquid phase was not fully converted into CO, CO_2 or CH_4, meaning that the remaining carbon was probably present as coke deposits and/or other possible gaseous species not quantified (e.g. ethane, propane, etc.), as verified in previous work [22]. Consequently, the H_2 and CO_2 production, under both operating conditions but particularly for the test at 400 ºC and 4 bar, started to progressively decrease along the time-on-stream - see Fig. 7.1b). The difference in the performance between the two operating

conditions can be related to the formation of amorphous coke [23-25]. In fact, the temperature-programmed oxidation (TPO) results confirm the formation of carbon over the catalyst during OMWSR, which was oxidized up to CO_2 during the oxidative regeneration. It is important to emphasize that this type of coke is very detrimental to the catalytic performance [23, 26]. In this way, by comparing the coke content present in the catalyst (see in Table 7.3 the values corresponding to the TR), it was observed that higher amounts of amorphous carbon were formed at 400 ºC and 4 bar, explaining the highest decrease of catalytic activity in such experimental tests (in all 3 cycles). Such increased coking at 4 bar can be explained by Eqs. (3.12), (3.14) and (3.15), wherein coke production increases with pressure (the difference of temperatures between the operations conditions used in both sets of runs is small). Furthermore, it was observed that oxidative regeneration among periods (cf. vertical dashed lines in Fig. 7.1) allows a high recovery of the catalytic activity.

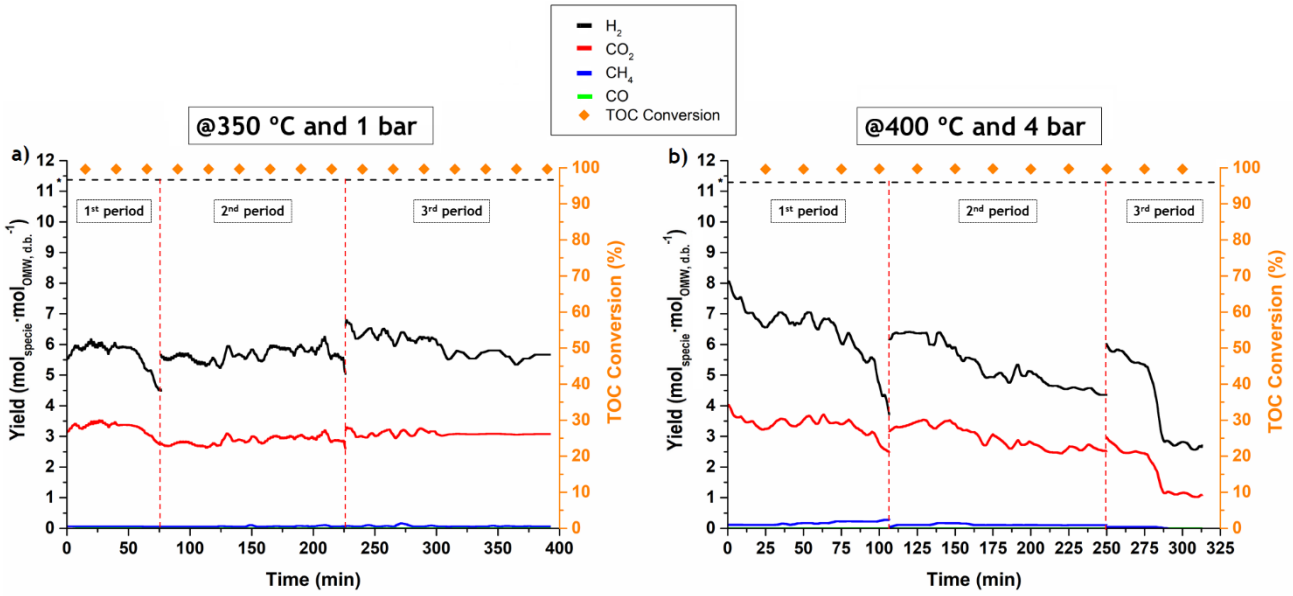

Fig. 7.1. Gaseous species yield and TOC conversion during *Exp. 3.1* (TR) at a) 350 ºC and 1 bar and at b) 400 ºC and 4 bar. * Thermodynamic equilibrium for the H_2 yield in a TR at the operations conditions used in the respective catalytic tests (dashed line).

Finally, it is worth mentioning that it was observed, in both runs, a higher catalyst deactivation in the periods where there was a higher coke production (see Table 7.3), namely in the 1st period of the experiment at 350 ºC and 1 bar and in the 1st and 3rd periods of the experiment at 400 ºC and 4 bar.

Table 7.3 - Quantities of coke produced in all experimental runs.

Cycle/Period	1st	2nd	3rd	4th
Experimental Run	**Amorphous Coke ($mmol_C \cdot g^{-1}_{catalyst} \cdot h^{-1}$)**			
TR (350 ºC, 1 bar)	3.0×10^{-2}	4.1×10^{-3}	3.2×10^{-3}	-
TR (400 ºC, 4 bar)	4.1×10^{-2}	1.5×10^{-2}	3.2×10^{-2}	-
SER (350 ºC, 1 bar)[a)]	8.0×10^{-2}	-	-	-
SER (350 ºC, 1 bar)[b)]	2.0×10^{-3}	1.7×10^{-3}	4.9×10^{-4}	-
SER (400 ºC, 4 bar)[a)]	2.3×10^{-1}	1.5×10^{-1}	8.6×10^{-2}	-
SER (400 ºC, 4 bar)[b)]	1.3×10^{-2}	1.2×10^{-2}	1.3×10^{-2}	6.0×10^{-3}
SEMR (350 ºC, 1 bar)[b)]	4.6×10^{-2}	3.3×10^{-2}	8.0×10^{-3}	-
SEMR (400 ºC, 4 bar)[b)]	9.6×10^{-2}	4.1×10^{-2}	2.4×10^{-2}	5.4×10^{-2}
	Graphitic Coke ($mmol_C \cdot g^{-1}_{catalyst} \cdot h^{-1}$)			
TR (350 ºC, 1 bar)	1.3×10^{-2}	2.9×10^{-3}	7.2×10^{-4}	-
TR (400 ºC, 4 bar)	3.1×10^{-2}	2.6×10^{-2}	3.6×10^{-2}	-
SER (350 ºC, 1 bar)[a)]	3.3×10^{-1}	-	-	-
SER (350 ºC, 1 bar)[b)]	9.6×10^{-2}	4.7×10^{-2}	3.3×10^{-2}	-
SER (400 ºC, 4 bar)[a)]	2.4×10^{-1}	1.9×10^{-1}	1.4×10^{-1}	-
SER (400 ºC, 4 bar)[b)]	8.4×10^{-2}	5.8×10^{-2}	7.3×10^{-2}	1.6×10^{-2}
SEMR (350 ºC, 1 bar)[b)]	-	-	-	-
SEMR (400 ºC, 4 bar)[b)]	-	-	-	-
	Total Coke ($mmol_C \cdot g^{-1}_{catalyst} \cdot h^{-1}$)			
TR (350 ºC, 1 bar)	4.3×10^{-2}	7.0×10^{-3}	3.9×10^{-3}	-
TR (400 ºC, 4 bar)	7.2×10^{-2}	4.2×10^{-2}	6.8×10^{-2}	-
SER (350 ºC, 1 bar)[a)]	4.1×10^{-1}	-	-	-
SER (350 ºC, 1 bar)[b)]	9.8×10^{-2}	4.8×10^{-2}	3.3×10^{-2}	-
SER (400 ºC, 4 bar)[a)]	4.7×10^{-1}	3.4×10^{-1}	2.3×10^{-1}	-
SER (400 ºC, 4 bar)[b)]	9.6×10^{-2}	7.0×10^{-2}	8.5×10^{-2}	2.2×10^{-2}
SEMR (350 ºC, 1 bar)[b)]	4.6×10^{-2}	3.3×10^{-2}	8.0×10^{-3}	-
SEMR (400 ºC, 4 bar)[b)]	9.7×10^{-2}	4.1×10^{-2}	2.4×10^{-2}	5.4×10^{-2}

[a)] Using the HTC-CO_3_K sorbent
[b)] Using the MG30_K sorbent.

7.2.3. Sorption-enhanced reactor

To overcome the shortcomings observed during the TR tests in the previous subchapter, namely in terms of limited H_2 production and deactivation due to coke formation, a SER was considered, being the only difference the inclusion of an HTC in the packed-bed together with the catalyst. The SER experiments were divided into two main sets: the first set of experiments using a commercial sorbent (MG30_K) and a second set with an in-house prepared sorbent (HTC-CO_3_K) [13]. Before those experiments, a blank test in which the reactor was filled with 1.6 g of MG30_K or HTC-CO_3_K (homogeneously diluted with SiC) was also performed to assess the catalytic activity of these materials. The production of gaseous products (H_2, CO_2, CO and CH_4) was noticed over the full duration of the experiment with MG30_K at 400 ºC and 4 bar, though to a very small extent (see Fig. G.2 in Appendix G). As seen before in the blank experiment where only SiC had been used, conversion of OMW into condensable products or large-chain gaseous products occurred, but not into small gaseous products. This means that the HTC was able to partly convert the large-chain compounds. The results herein observed are in line with a previous work where it was reported that a potassium-doped HTC catalyzes the WGS reaction [27]. Similar results were obtained for the

HTC-CO_3_K sorbent (data not shown). It was also verified that both materials produced low quantities of coke.

In *Exp. 3.2*, it was observed that the operating conditions and the sorbent chosen significantly affect the H_2 production and stability of the catalyst (Fig. 7.2). As verified in the previous subchapter for the TR, both CO and CH_4 yields were very low, and almost complete total TOC conversion (above 99 %) during all catalytic tests was reached. For all cases studied with this reactor configuration - both operation conditions and sorbents -, it was verified a slight increase of the CH_4 yield and a decrease of the H_2 yield after the CO_2 breakthrough; this is due to the presence of CO_2 in the reaction medium and the occurrence of the CO_2 methanation (reverse of Eq. (3.9)) - or of the CO methanation (Eq. (3.8)), since the WGS reaction in the pos-breakthrough zone is no longer promoted by the capture of CO_2, thus allowing the consumption of CO in other secondary reactions. The presence of CO was only detected in the last cycle at 350 ºC and 1 bar, using the MG30_K sorbent, probably due to a very slight deactivation of the catalyst for the WGS and CO methanation reactions (Eqs. (3.7) and (3.8)).

It was verified that at both operating conditions and using the MG30_K CO_2 sorbent (Fig. 7.2a) and Fig. 7.2c)), the H_2 yields obtained in the first cycle were higher than those achieved for the first hour in the TR. It can be clearly observed that, especially at 350 ºC and 1 bar, the SER was advantageous not only in the pre-breakthrough and breakthrough stages (shifting the reaction towards the production of more H_2 as a consequence of CO_2 capture) but also during the pos-breakthrough (i.e., when the MG30_K is saturated with CO_2), due to the catalytic activity of the HTCs towards both OMW decomposition and, more importantly, the WGS reaction. Accordingly, the H_2 yield observed in the SER with the commercial MG30_K at 350 ºC and 1 bar was always between 7-5 $mol_{H_2} \cdot mol^{-1}_{OMW}$ and always between 8.5-4.5 $mol_{H_2} \cdot mol^{-1}_{OMW}$ at 400 ºC and 4 bar, taking into account the results of all cycles. Still, it was noticed that the utilization of the MG30_K hydrotalcite as CO_2 sorbent increased the stability of the catalyst. In fact, the TPO results demonstrated that the utilization of the MG30_K in the fixed bed allowed to decrease the formation of the critical amorphous coke in comparison with the one produced in the TR, for both operation conditions - see Table 7.3. The removal of CO_2 from the reaction medium shifted the carbon dioxide reduction (Eq. (3.15)) to a lower formation of coke. These results also show that the carbon dioxide reduction (Eq. (3.15)) was predominant in comparison with the Boudouard reaction (Eq. (3.12)) for the formation of amorphous carbon deposits since, as already mentioned, the CO_2 capture decreased the formation of such coke type. Besides that, CH_4 cracking/decomposition (Eq. (3.13)) might have been considerably inhibited in the pre-breakthrough period, because CO and/or CO_2 methanation (Eq. (3.8) and reverse of Eq. (3.9)) were inhibited, as indicates the non-existence of CH_4 until the pre-breakthrough time observed in Fig. 7.2a) and Fig. **7.2**c). Comparing the amount of amorphous coke produced for the different operating conditions, the conclusions are in line with the results obtained for the TR (higher production at 400 ºC and 4 bar).

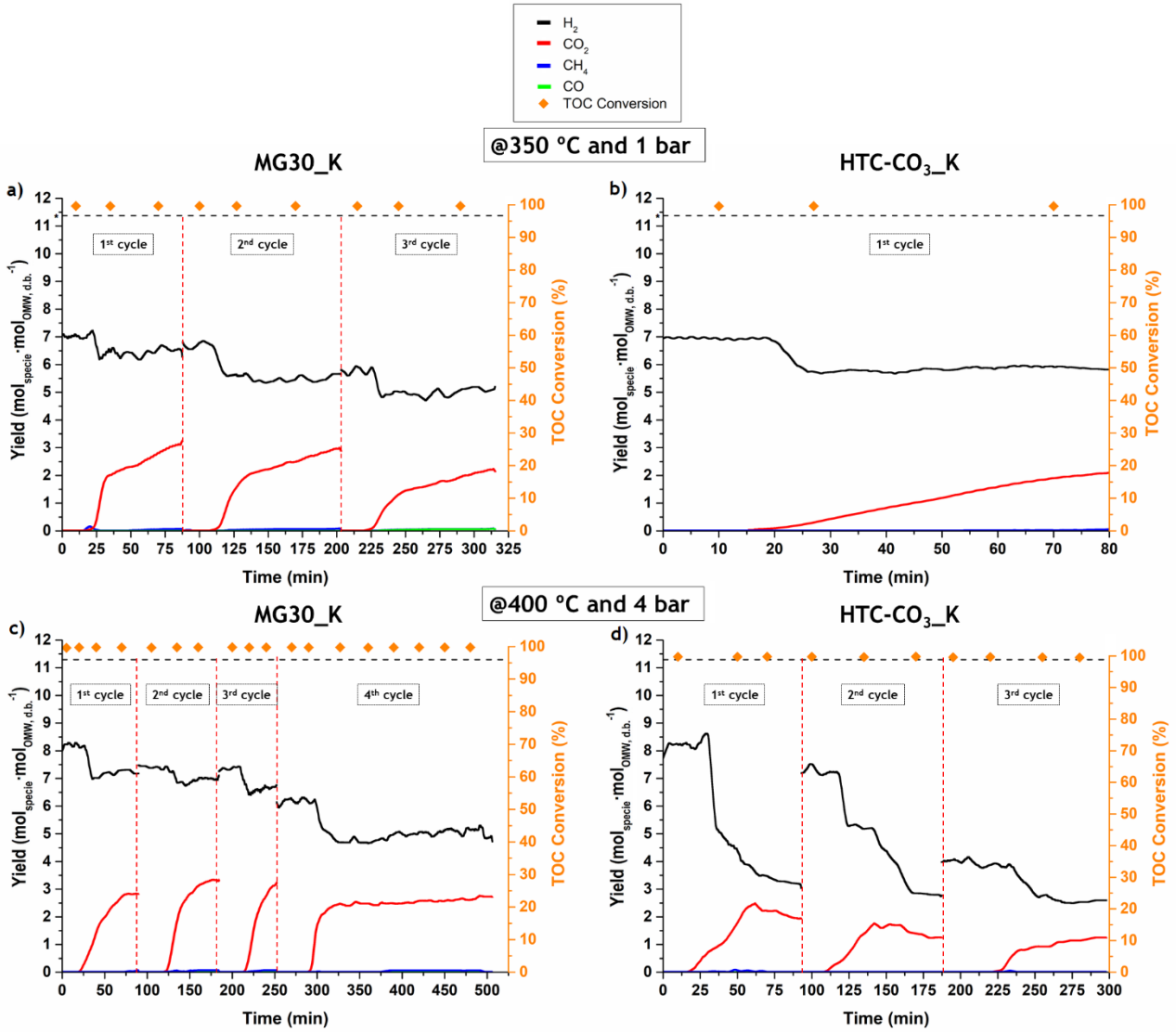

Fig. 7.2. Gaseous species yield and TOC conversion during *Exp. 3.2* (SER) at 350 ºC and 1 bar using as CO_2 sorbent a) MG30_K or b) HTC-CO_3_K; and at 400 ºC and 4 bar using as CO_2 sorbent c) MG30_K or d) HTC-CO_3_K. * Thermodynamic equilibrium for the H_2 yield in a TR at the operations conditions used in the respective catalytic tests (dashed line).

Despite the high stability during the tests, the performance of the catalyst slightly decreased over the cycles. In this context, a longer experiment was performed at 400ºC and 4 bar (4^{th} cycle; using the commercial sorbent). It was seen that the production of H_2 and TOC conversion remained constant after the CO_2 breakthrough for a long time of reaction and that the coke formation was very low - see Fig. 7.2c) and Table 7.3.

Data obtained in the SER with the prepared HTC-CO_3_K sorbent are shown in Fig. 7.2b) and Fig. 7.2d). It was found that the H_2 (and CO_2) production started to decrease significantly after the CO_2 breakthrough at 400 ºC and 4 bar - see Fig. 7.2d), so that the H_2 yield at the end of the cycles was even lower than the values verified for the TR, indicating that the catalyst was strongly deactivated.

As mentioned in the previous subchapter, the difference in the performance between the two operation conditions can be related to the formation of amorphous coke on the catalyst throughout the experiments. The TPO results confirm that a higher formation of coke occurred during the reaction in this case. In this way, by comparing the coke content present in the catalyst for the different scenarios (see Table 7.3), it was observed that higher amounts of amorphous carbon were formed when it was used a SER with the HTC-CO_3_K sorbent at 400 ºC and 4 bar, explaining the high decrease of the catalytic activity in such test. These results show that the presence of this sorbent increased the formation of coke deposits on the catalyst's surface, which can be due to the acidic sites present in the sorbent (responsible for the formation of coke precursors).

Despite these results, and in line with the higher catalyst stability verified in a TR at 350 ºC and 1 bar, the catalyst deactivation was not verified in the cycle that was carried out with the sorbent HTC-CO_3_K under such conditions. However, only one cycle was performed under these operation conditions due to the limitations verified at 400 ºC and 4 bar; therefore, it was considered that the use of this sorbent would have no further interest for this work.

7.2.3.1. Temperature-programmed desorption-CO_2/NH_3

Temperature-programmed desorption of CO_2 (TPD-CO_2) and TPD-NH_3 analyses were performed to chemically characterize and explain the behaviors of the sorbents used in the catalytic tests with the SER.

To determine the basicity of the sorbents, TPD-CO_2 was conducted - see Fig. 7.3a). According to the literature, the basic sites can be classified as weak (peaks in the range of 23-250 °C), medium (peaks in the range of 250-500 °C) and strong (peaks at temperatures > 500 °C) [28]. The TPD-CO_2 results for the two samples show the existence of all types of sites. In Table 7.4 it is possible to see the quantities of basic sites present in the materials, obtained by integration of the TPD-CO_2 curves. To determine the acidity of the sorbents, TPD-NH_3 was conducted for the same materials - see Fig. 7.3b). From the TPD-NH_3 plots, it is possible to see that the materials have practically only one type of acid sites, which, according to the literature, can be classified as strong (400-600 °C) [29]; Table 7.4 shows the quantities of acid sites present in the sorbents, obtained by integration of the TPD-NH_3 curves.

Table 7.4 - Quantities of basic and acidic sites in the sorbents.

Sorbent	**Weak Basic Sites ($mmol_{CO_2} \cdot g^{-1}_{catalyst}$)**	**Medium Basic Sites ($mmol_{CO_2} \cdot g^{-1}_{catalyst}$)**	**Strong Basic Sites ($mmol_{CO_2} \cdot g^{-1}_{catalyst}$)**	**Total Basic Sites ($mmol_{CO_2} \cdot g^{-1}_{catalyst}$)**
HTC-CO_3_K	0.05	0.02	0.89	0.96
MG30_K	0.05	0.07	0.50	0.62
Sorbent	**Weak Acidic Sites ($mmol_{NH_3} \cdot g^{-1}_{catalyst}$)**	**Strong Acidic Sites ($mmol_{NH_3} \cdot g^{-1}_{catalyst}$)**	**Total Acidic Sites ($mmol_{NH_3} \cdot g^{-1}_{catalyst}$)**	
HTC-CO_3_K	0.00	0.61	0.61	
MG30_K	0.01	0.46	0.47	

Results shown in Table 7.4 evidence that the two sorbents have a high quantity of strong basic sites being worth noting that HTC-CO_3_K presents the highest quantity of basic sites, which is in line with the higher CO_2 sorption capacity of this material [13]. In addition, the HTC-CO_3_K material also presents a higher quantity of acidic sites (though only strong acidic sites) that promote reactions like dehydration, hydrolysis and cracking [30, 31]. In this way, the higher quantity of acidic sites can explain the higher formation of amorphous coke during the catalytic tests, as a result of the production of coke precursors on the surface of HTC-CO_3_K.

Moreover, the high quantity of basic sites in both sorbents (coupled with the low catalytic activity of these materials) explain the low formation of coke in the blank tests with the sorbents - the basic sites inhibit the formation of coke deposits and promote the gasification of the carbon produced on the materials' surface [32, 33]. So, the production of coke in the experimental tests with the SER is practically only located on the surface of the catalyst.

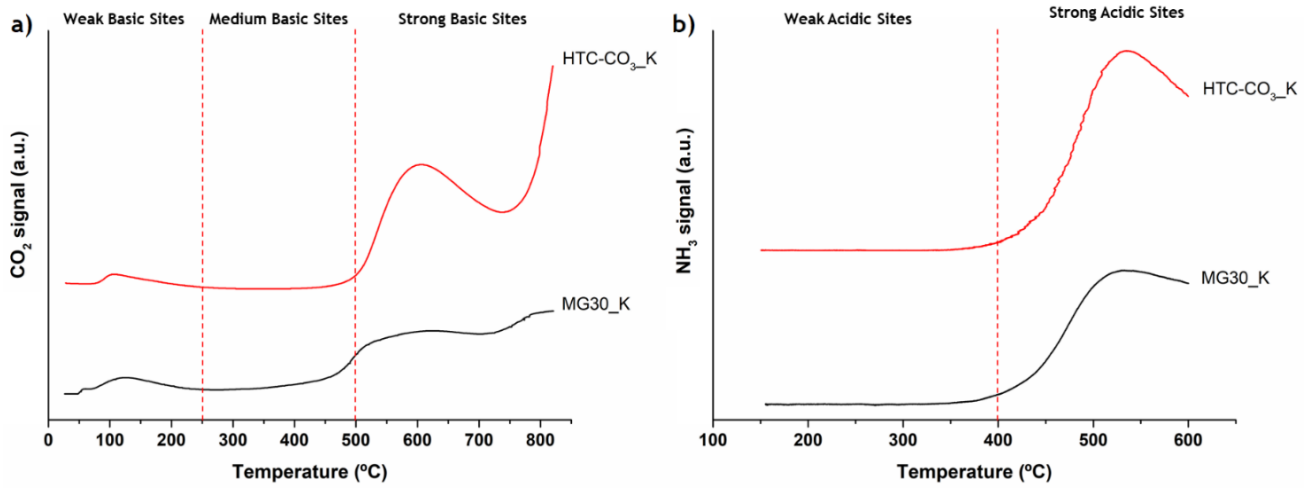

Fig. 7.3. a) TPD-CO_2 and b) TPD-NH_3 profiles for the sorbents used in the SER.

7.2.4. Sorption-enhanced membrane reactor

Before the catalytic runs in the SEMR (*Exp. 3.3*), permeation tests were carried out with pure H_2 under different driving-forces - see section 2 of Appendix G for further details and results.

In this set of experimental runs in the SEMR, only the commercial sorbent (MG30_K) was used due to the negative effects of the prepared material HTC-CO_3_K found in subchapter 7.2.3, inducing stronger catalyst deactivation.

In this *Exp. 3.3*, it was proved that the SEMR was able to shift the reactions present in the OMWSR process towards the production of higher quantities of H_2 in comparison with the TR and SER at both operations conditions. Similar to the other cases (using other reactor configurations), the behavior of the formation of H_2 and CO_2 along time was similar in the pos-breakthrough region (Fig. 7.4a-b)). A drastic change in the color from the fed OMW solution (yellow) to the liquid effluent (colorless) was

again observed. It was also verified that, for both operation conditions, after the CO_2 breakthrough (i.e., when the CO_2 sorbent is saturated) a decrease in performance in terms of H_2 production was observed, but higher H_2 and carbon-containing gaseous products production in comparison to the SER was still observed due to continuous H_2 removal (the system acts like a MR).

For both operation conditions with this reactor configuration (and similarly to the behavior found in the SER), it was verified a slight increase of the CH_4 yield after the CO_2 breakthrough due to the presence of CO_2 (as a consequence of CO_2 methanation - reverse of Eq. (3.9) - or CO methanation - Eq. (3.8)). The presence of CO was not detected at 400ºC and 4 bar in all cycles performed - complete consumption via WGS (promoted by the capture of CO_2 and separation of H_2) and methanation reactions (Eqs. (3.8) and (3.9)).

The difference between the H_2 yields obtained in the SER and SEMR is significant, even after saturation of the sorbent (at this point, the system started to behave like a MR), demonstrating that the effect of the membrane is very important in this multifunctional system - see Fig. 7.2 and Fig. 7.4a-b). Additionally, the yields of CO_2 observed after the breakthrough time in the SEMR were also higher than those obtained in the SER, which is clearly associated to an enhancement of the process due to the presence of the H_2 perm-selective Pd-Ag membrane. The H_2 yield observed in the SEMR at 350 ºC and 1 bar was always between 8.0-6.0 $mol_{H2} \cdot mol^{-1}_{OMW}$ and always between 11.5-9.0 $mol_{H2} \cdot mol^{-1}_{OMW}$ at 400 ºC and 4 bar (taking into account the results of all cycles during pre- and pos-breakthrough zones). So, during the pre-breakthrough, the H_2 yield achieved practically the maximum theoretical yield (11.84 $mol_{H2} \cdot mol^{-1}_{OMW}$) in all cycles at 400 ºC and 4 bar. In the first cycle, the H_2 yield inclusively exceeds the thermodynamic equilibrium yield (11.29 $mol_{H2} \cdot mol^{-1}_{OMW}$) defined for the TR in these operation conditions (cf. Fig. 7.4b)). The highest improvement in the H_2 production at 400 ºC and 4 bar is related with the highest permeation of H_2 and CO_2 capture under these experimental conditions; in this way, the reactions that involve the production of H_2 and/or CO_2 (for instance, the WGS reaction - Eq. (3.7) were strongly promoted in comparison with the situation at 350 ºC and 1 bar.

It was observed that the SEMR presents higher catalytic performance than MR and much better performance than both SER and TR. An H_2 yield enhancement of approximately 44 % was observed compared to the TR, approximately 39 % regarding the SEMR and about 16 % compared to the MR - see Fig. 7.5.

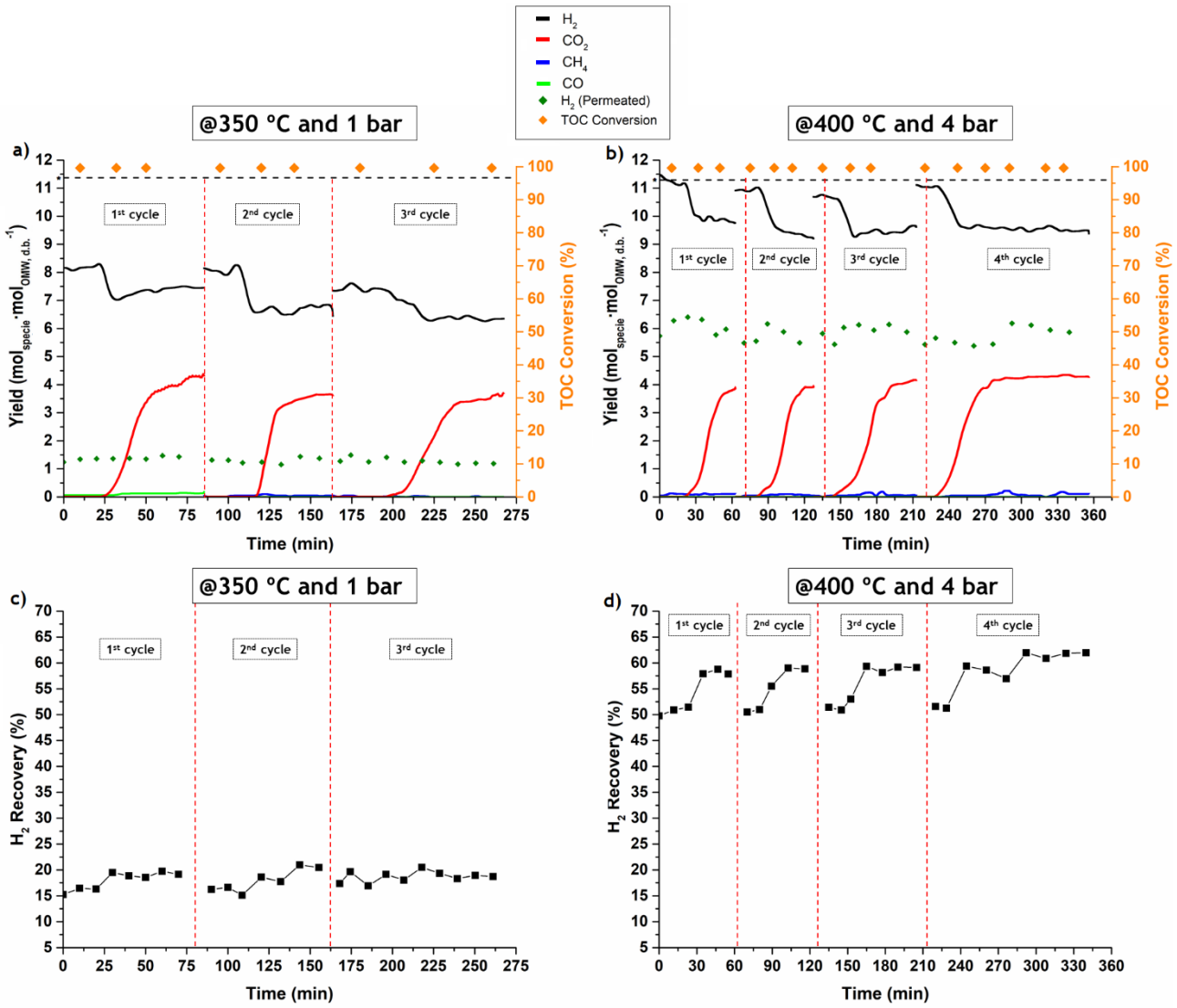

Fig. 7.4. Gaseous species yield and TOC conversion during *Exp. 3.3* (SEMR) at a) 350 ºC and 1 bar and at b) 400 ºC and 4 bar, and H_2 recovery in the permeate side at c) 350 ºC and 1 bar and at d) 400 ºC and 4 bar. Sweep gas = 100 $mL_{N2}·min^{-1}$ and $P_{permeate\ side}$ = 1 bar. * Thermodynamic equilibrium for the H_2 yield in a TR at the operations conditions used in the respective catalytic test (dashed line).

Moreover, as already mentioned, in the SEMR, CH_4 only started being observed at the reactor outlet at the beginning of CO_2 breakthrough, as verified in the SER (due to CO_2 and/or CO methanation - Eq. (3.8) and reverse of Eq. (3.9)). The quantity of CH_4 was higher at the catalytic test conducted at higher pressure (the methanations reactions are thermodynamically favored at higher pressures - Eq. (3.8) and reverse of Eq. (3.9)).

For the run at 400 ºC and 4 bar, a slightly longer experiment after the breakthrough time was performed to verify if the catalyst remained stable during all the cycle. Moreover, for this specific cycle (4^{th} cycle), besides the determination of TOC conversion, it was also determined the TPh and COD reductions of the outlet condensed stream, as well as the phenolic content in a HPLC-DAD apparatus. It was seen that the production of H_2 and TOC conversion remained constant after the CO_2

breakthrough for ca. 2 h - see Fig. 7.4b). Besides, the reduction of TPh and COD was practically complete during all the cycle (above 99 % - see Table 7.1), and the obtained chromatograms indicated that the compounds identified in the initial effluent were all converted - see Fig. H.3 in Appendix H, section 1.

In terms of coke production, the fact that both H_2 and CO_2 were removed from the reaction medium in the SEMR instead of only CO_2 (as occurs in the SER) could have played an important role in coke inhibition. First, it is important to emphasize that the CH_4 cracking/decomposition (Eq. (3.13)) might have been considerably inhibited in the pre-breakthrough period, since CO and/or CO_2 methanation (Eq. (3.8) and reverse of Eq. (3.9)) were inhibited (as indicated by the absence of CH_4 in the pre-breakthrough region - see Fig. 7.4a-b)). As verified in subchapter 7.2.3, the removal of CO_2 from the reaction medium shifted the carbon dioxide reduction (Eq. (3.15)) to a lower coke formation. However, the total quantity of amorphous coke produced in the catalytic tests using the SEMR was higher than in the SER (cf. Table 7.3). Therefore, despite the CO_2 sorption led to a decrease in the formation of amorphous coke, in the pos-breakthrough period the production of amorphous carbon is promoted due to the removal of H_2 from the retentate side. In this way, the CH_4 cracking (Eq. (3.13)) is predominant over the CO and CO_2 reduction (Eqs. (3.14) and (3.15)) for coke production, as already envisioned in previous thermodynamic work [3]. However, and despite the higher amorphous coke production in the SEMR, it was not verified catalytic deactivation during the cycles, probably due to the catalytic activity of the MG30_K towards the WGS reaction.

The percentage of H_2 recovered in the permeate side during the experimental tests with the SEMR is shown in Fig. 7.4c-d). It can be noticed that higher recoveries were obtained in the pos-breakthrough region and that, over the catalytic tests (pre- and pos-breakthrough time), it was obtained H_2 recoveries in the range of 15-21% in the experimental cycles at 350 ºC and 1 bar and in the range of 50-62 % in the experimental cycles at 400 ºC and 4 bar. The recovery of H_2 was higher for the later operation conditions because both variables (temperature and pressure) increase the quantity of H_2 permeating through the Pd-Ag membrane. In the permeate side, it was not detected any carbon-containing gaseous species along all the cycles.

Summarizing, the removal of H_2 and CO_2 allowed reaching higher H_2 yields in the SEMR during the pre-breakthrough period in comparison with all the other reactor configurations. An H_2 yield enhancement of approximately 44 % was observed compared to the TR, approximately 39 % regarding the SER and about 16 % compared to the MR - see Fig. 7.5. This allows simultaneous production of highly pure H_2 in the retentate and ultra-pure H_2 in the permeate side, considering the absence of sweep gas or an easily separable one (e.g. steam). Therefore, if the SEMR configuration is applied in a multi-column system that allows continuous operation in the pre-breakthrough region (so that while one column is in the production stage, the other is in the sorbent regeneration stage), a high quantity of pure H_2 would be continuously obtained in the permeate and retentate streams.

Another advantage of working continuously in the pre-breakthrough region is the fact that CH_4, CO and CO_2 are not present, thus avoiding the poisoning of the membrane and minimizing the coke production (particularly via CH_4 cracking). Additionally, the SEMR configuration operated at 400 ºC and 4 bar presented high stability over the consecutive cycles (the H_2 yields in the pre-breakthrough region remained nearly equal over the consecutive cycles, in opposition to what has been observed in the SER at the same operation conditions) - c.f. Fig. 7.2c) and Fig. 7.5b).

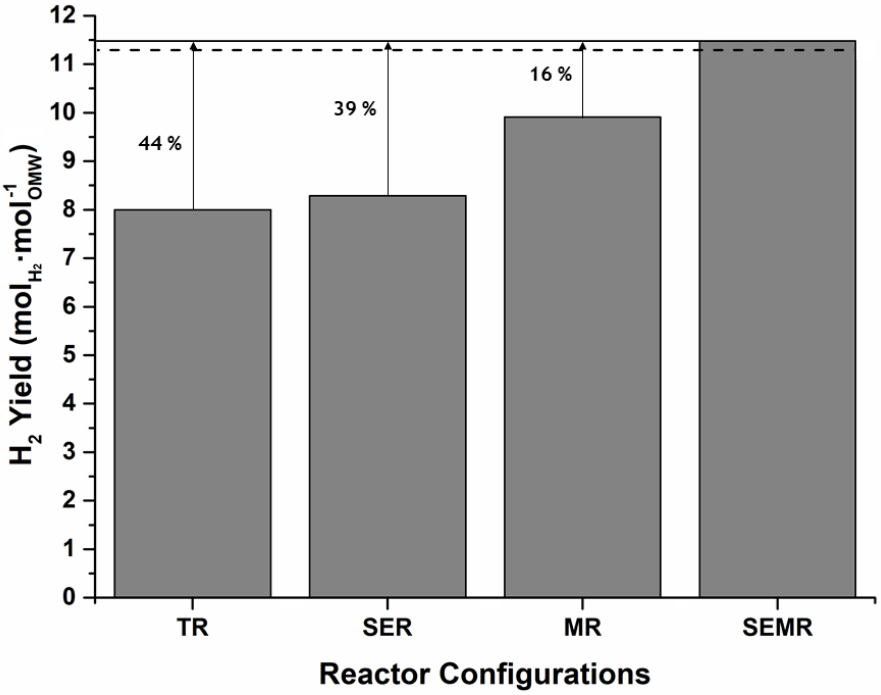

Fig. 7.5. Hydrogen yield with the different reactor configurations at 400 °C and 4 bar. The dashed line represents the thermodynamic equilibrium in a TR at 400 ºC and 4 bar and the continuous line represents the maximum theoretical value. Values in percentage indicate the improvement of the SEMR versus all other reactors.

7.2.4.1. Catalytic test with real effluent

Taking into account the promising results shown in subchapter 7.2.4, a catalytic test was performed in a SEMR with a real effluent, at 400 ºC and 4 bar. This effluent was characterized in terms of pH, TOC, TPh and COD - see Table 7.5. It was possible to verify that the values of TOC and COD determined for the real effluent were much higher than the ones obtained for the synthetic effluent. However, the phenolic content (TPh) was similar for both effluents - see Table 7.1 and Table 7.5.

Again, the yields of CO and CH_4 were very low and an almost complete total conversion of TOC (above 99 %) was obtained during all the test (Fig. 7.6). Besides that, the reduction of TPh and COD was also practically complete (above 99 %) - see Table 7.5. This level of pollutant charge reduction is exceptional and was also verified by the change in the color from the fed OMW effluent to the condensate effluent at the outlet of the reactor - see Fig. G.4 in Appendix G, section 1. It can be also noticed that high H_2 recoveries were obtained, with values in the range of 49-62 %.

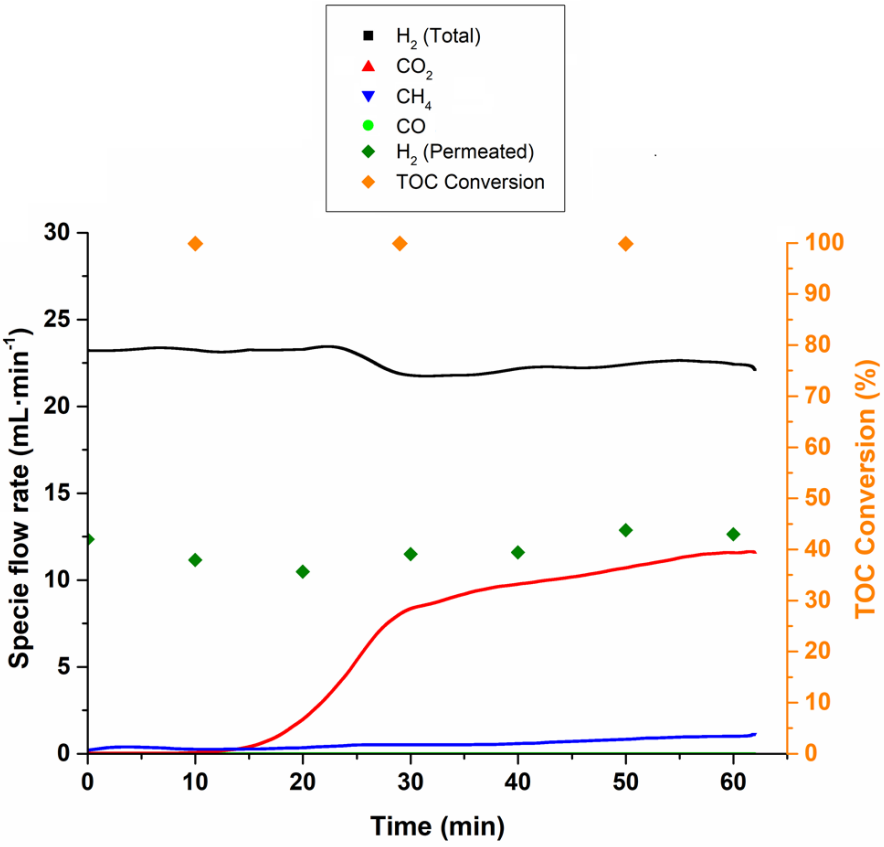

Fig. 7.6. Gaseous species flow rate and TOC conversion during *Exp. 3.4* (SEMR) for the real effluent of OMW.

With these catalytic results, it was proved that steam reforming, when carried in a SEMR, can efficiently handle real OMW effluents, with high productions of pure/ultra-pure H_2, with practically complete reduction of the pollutant load. Taking into account the limit values of various emission parameters for the discharge of wastewater in Portugal, it was verified that the condensable samples obtained during the catalytic test present suitable physicochemical characteristics, namely in terms of

pH (between 6.0-9.0), color (no visible color after a 1:20 vol. dilution), smell (no smell after a 1:20 vol. dilution) and COD (< 150 $mg_{O_2} \cdot L^{-1}$) [34] - cf. Table 7.5.

Table 7.5 - Characterization of the liquid samples obtained in the experiment with real OMW.

Liquid Sample	TOC ($mg_C \cdot L^{-1}$)	TpH ($mg_{AG} \cdot L^{-1}$)	COD ($mg_{O_2} \cdot L^{-1}$)	pH
Initial Effluent	41 279	3 636	88 633	4.95
Condensable sample (10 min)	50	1.6	0.0	≈ 7
Condensable sample (29 min)	52	1.4	1.8	
Condensable sample (50 min)	66	1.7	2.9	

7.3. Conclusions

In this work, a comparison of the performance between different reactor configurations (TR, SER, MR and SEMR) was performed for the OMWSR process. In a general way, it was observed that the TOC conversion remains practically complete along all the experiment tests and it was verified an enhancement of the H_2 production during the pre-breakthrough of CO_2 as compared to the TR, when using the SER or the SEMR. However, a higher improvement in terms of H_2 yield was observed when the MR and particularly the last multifunctional reactor configuration (i.e., the SEMR) was applied. The maximum H_2 yield was obtained using a SEMR at 400 ºC and 4 bar, close to the maximum attainable theoretical value, and above the thermodynamic limit for a TR. Besides that, it was observed that the HTCs catalyze the decomposition of OMW into gaseous products, tough to a low extent. Nevertheless, the utilization of the prepared K-doped HTC-CO_3 material, at 400 ºC and 4 bar, increases the formation of coke deposits and leads to a high deactivation of the catalyst due to the acidic sites present in the sorbent (which are responsible for the formation of coke precursors). Nevertheless, the utilization of the commercial MG30_K HTC as CO_2 sorbent increased the stability of the catalyst due to the stronger inhibition of coke formation, which is also beneficial for the Pd-Ag membrane.

The removal of H_2 and CO_2 allowed reaching higher H_2 yields in the SEMR during the pre-breakthrough time in comparison with the other reactor configurations. This allows simultaneous production of highly pure H_2 in the retentate and ultra-pure H_2 in the permeate side (in the absence of sweep gas). Therefore, if the SEMR configuration is applied in a multi-column system that allows continuous operation in the pre-breakthrough region, a high quantity of pure H_2 would be continuously obtained in both streams. It was also verified that after the CO_2 breakthrough, a decrease in performance was observed, but higher H_2 and carbon gaseous products production in comparison to the SER and TR was still observed due to continuous H_2 removal from the reaction medium (operation of the device as a MR).

Finally, it was proved that the steam reforming process, when implemented in a SEMR, can efficiently handle real OMW effluents, with high productions of H_2, with practically complete remotion of the pollutant load. Still, this approach opens the pave for valorizing other oxygenated wastes.

Notation and Glossary

List of Acronyms

COD	Chemical oxygen demand
HTC	Hydrotalcite
OMW	Olive oil mill wastewater
OMWSR	Olive oil mill wastewater steam reforming
SER	Sorption-enhanced reactor
SEMR	Sorption-enhanced membrane reactor
TOC	Total organic carbon
TPD	Temperature-programmed desorption
TPh	Total phenolic content
TPO	Temperature-programmed oxidation
TR	Traditional reactor
WGS	Water gas-shift

References

[1] Silva, J.M., M.A. Soria and L.M. Madeira, Thermodynamic analysis of Glycerol Steam Reforming for hydrogen production with in situ hydrogen and carbon dioxide separation. Journal of Power Sources, 2015. 273: p. 423-430.

[2] Rodrigues, A.E., L.M. Madeira, R. Faria and Y.J. Wu, Sorption Enhanced Reaction Processes. 2017: World Scientific Publishing Company Pte Limited.

[3] Rocha, C., M.A. Soria and L.M. Madeira, Steam reforming of olive oil mill wastewater with in situ hydrogen and carbon dioxide separation - Thermodynamic analysis. Fuel, 2017. 207: p. 449-460.

[4] Westbye, A., L. Di Felice, A. Aranda and P.D.C. Dietzel. Efficient calcination of CaCO3 by means of combined Ca-Cu materials for Sorption Enhanced Reforming. in 25th International Conference on Chemical Reaction Engineering. 2018. Florence, Italy.

[5] Guo, H., Z. Xu, T. Jiang, Y. Zhao, X. Ma and S. Wang, The effect of incorporation Mg ions into the crystal lattice of CaO on the high temperature CO2 capture. Journal of CO2 Utilization, 2020. 37: p. 335-345.

[6] Miguel, C.V., R. Trujillano, V. Rives, M.A. Vicente, A.F.P. Ferreira, A.E. Rodrigues, A. Mendes and L.M. Madeira, High temperature CO2 sorption with gallium-substituted and promoted hydrotalcites. Separation and Purification Technology, 2014. 127(Supplement C): p. 202-211.

[7] Silva, J.M., R. Trujillano, V. Rives, M.A. Soria and L.M. Madeira, Dynamic behaviour of a K-doped Ga substituted and microwave aged hydrotalcite-derived mixed oxide during CO2 sorption experiments. Journal of Industrial and Engineering Chemistry, 2019.

[8] Zhang, T., M. Li, P. Ning, Q. Jia, Q. Wang and J. Wang, K2CO3 promoted novel Li4SiO4-based sorbents from sepiolite with high CO2 capture capacity under different CO2 partial pressures. Chemical Engineering Journal, 2020. 380: p. 122515.

[9] Fang, Y., R. Zou and X. Chen, High-temperature CO2 adsorption over Li4SiO4 sorbents derived from different lithium sources. The Canadian Journal of Chemical Engineering, 2020. 98(7): p. 1495-1500.

[10] Labajos, F.M., V. Rives and M.A. Ulibarri, Effect of hydrothermal and thermal treatments on the physicochemical properties of Mg-Al hydrotalcite-like materials. Journal of Materials Science, 1992. 27(6): p. 1546-1552.

[11] Peltzer, D., J. Mùnera, L. Cornaglia and M. Strumendo, Characterization of potassium doped Li2ZrO3 based CO2 sorbents: Stability properties and CO2 desorption kinetics. Chemical Engineering Journal, 2018. 336: p. 1-11.

[12] Halabi, M.H., M.H.J.M. de Croon, J. van der Schaaf, P.D. Cobden and J.C. Schouten, Reactor modeling of sorption-enhanced autothermal reforming of methane. Part I: Performance study of hydrotalcite and lithium zirconate-based processes. Chemical Engineering Journal, 2011. 168(2): p. 872-882.

[13] Rocha, C., M.A. Soria and L.M. Madeira, Doping of hydrotalcite-based sorbents with different interlayer anions for CO2 capture. Separation and Purification Technology, 2020. 235: p. 116140.

[14] Coenen, K., F. Gallucci, G. Pio, P. Cobden, E. van Dijk, E. Hensen and M. van Sint Annaland, On the influence of steam on the CO2 chemisorption capacity of a hydrotalcite-based adsorbent for SEWGS applications. Chemical Engineering Journal, 2017. 314(Supplement C): p. 554-569.

[15] Coenen, K., F. Gallucci, P. Cobden, E. van Dijk, E. Hensen and M. van Sint Annaland, Chemisorption working capacity and kinetics of CO2 and H2O of hydrotalcite-based adsorbents for sorption-enhanced water-gas-shift applications. Chemical Engineering Journal, 2016. 293: p. 9-23.

[16] Coenen, K., F. Gallucci, P. Cobden, E. van Dijk, E. Hensen and M.V. Annaland, Influence of material composition on the CO2 and H2O adsorption capacities and kinetics of potassium-promoted sorbents. Chemical Engineering Journal, 2018. 334: p. 2115-2123.

[17] Gallucci, F., E. Fernandez, P. Corengia and M. van Sint Annaland, Recent advances on membranes and membrane reactors for hydrogen production. Chemical Engineering Science, 2013. 92(Supplement C): p. 40-66.

[18] Nooijer, N.d., A. Arratibel Plazaola, J. Meléndez Rey, E. Fernandez, D.A. Pacheco Tanaka, M.v. Sint Annaland and F. Gallucci, Long-Term Stability of Thin-Film Pd-Based Supported Membranes. Processes, 2019. 7(2): p. 106.

[19] Gallucci, F., J. Medrano, E. Fernandez, J. Melendez, M. van Sint Annaland and A. Pacheco, Advances on High Temperature Pd-Based Membranes and Membrane Reactors for Hydrogen Purification and Production. Journal of Membrane Science and Research, 2017. 3(3): p. 142-156.

[20] Miguel, C.V., A. Mendes, S. Tosti and L.M. Madeira, Effect of CO and CO2 on H2 permeation through finger-like Pd-Ag membranes. International Journal of Hydrogen Energy, 2012. 37(17): p. 12680-12687.

[21] Rocha, C., M.A. Soria and L.M. Madeira, Thermodynamic analysis of olive oil mill wastewater steam reforming. Journal of the Energy Institute, 2019. 92(5): p. 1599-1609.

[22] Rocha, C., M.A. Soria and L.M. Madeira, Screening of commercial catalysts for steam reforming of olive mill wastewater. Renewable Energy, 2021. 169: p. 765-779.

[23] Lu, P., Effect of Operating Conditions on the Coke Formation and Nickel Catalyst Performance During Cracking of Tar. Waste and biomass valorization, 2019. v. 10(no. 1): p. pp. 155-165-2019 v.10 no.1.

[24] Yao, D., H. Yang, H. Chen and P.T. Williams, Co-precipitation, impregnation and so-gel preparation of Ni catalysts for pyrolysis-catalytic steam reforming of waste plastics. Applied Catalysis B: Environmental, 2018. 239: p. 565-577.

[25] Tan, R., A. Alir, S. Mohamad, K. Md Isa, T. Amran and T.A. Tuan Abdullah, Ni-based catalysts for steam reforming of tar model derived from biomass gasification. 2019.

[26] He, L., S. Hu, L. Jiang, S.S.A. Syed-Hassan, Y. Wang, K. Xu, S. Su, J. Xiang, L. Xiao, H. Chiand X. Chen, Opposite effects of self-growth amorphous carbon and carbon nanotubes on the reforming of toluene with Ni/α-Al2O3 for hydrogen production. International Journal of Hydrogen Energy, 2017. 42(21): p. 14439-14448.

[27] Silva, J.M., L.S. Ribeiro, J.J.M. Órfão, S. Tosti, M.A. Soria and L.M. Madeira, From sorption-enhanced reactor to sorption-enhanced membrane reactor: A step towards H2 production optimization through glycerol steam reforming. Chemical Engineering Journal, 2019. 368: p. 795-811.

[28] Singha, R.K., A. Yadav, A. Agrawal, A. Shukla, S. Adak, T. Sasaki and R. Bal, Synthesis of highly coke resistant Ni nanoparticles supported MgO/ZnO catalyst for reforming of methane with carbon dioxide. Applied Catalysis B: Environmental, 2016. 191: p. 165-178.

[29] Fang, W.-W., M.-M. Mu, J. Tian, L.-G. Chen and Y. Li, Continuous synthesis of N-ethylethylenediamine over supported Cu-Zn-La catalysts. Chemical Papers, 2016. 70(4): p. 430-435.

[30] Liu, Y., X. Guo, G.L. Rempel and F.T.T. Ng, The Promoting Effect of Ni on Glycerol Hydrogenolysis to 1,2-Propanediol with In Situ Hydrogen from Methanol Steam Reforming Using a Cu/ZnO/Al2O3 Catalyst. Catalysts, 2019. 9(5): p. 412.

[31] Zhong, Z., H. Ang, C. Choong, L. Chen, L. Huang and J. Lin, The role of acidic sites and the catalytic reaction pathways on the Rh/ZrO2 catalysts for ethanol steam reforming. Physical Chemistry Chemical Physics, 2009. 11(5): p. 872-880.

[32] Aziz, M.A.A., A.A. Jalil, S. Wongsakulphasatch and D.-V.N. Vo, Understanding the role of surface basic sites of catalysts in CO2 activation in dry reforming of methane: a short review. Catalysis Science & Technology, 2020. 10(1): p. 35-45.

[33] Bu, K., S. Kuboon, J. Deng, H. Li, T. Yan, G. Chen, L. Shi and D. Zhang, Methane dry reforming over boron nitride interface-confined and LDHs-derived Ni catalysts. Applied Catalysis B: Environmental, 2019. 252: p. 86-97.

[34] Portugal, G.o., Decreto-Lei n.º 236/98. 1998. p. 3676 - 3722.

Chapter 8. Techno-Economic Analysis of the Olive Mill Wastewater Steam Reforming Process: a Case-Study in Portugal

Abstract:

Steam *reforming of olive oil mill wastewater (OMW) has been studied in several articles; however, there is no industrial installation to treat and valorize this effluent until now. In this way, to understand the economic impact of applying this technology in the olive oil industry, a techno-economic analysis of this process in a traditional reactor (TR) or in a sorption-enhanced reactor (SER - with in situ CO_2 removal) was performed. This study focused on key aspects of the process units, such as the reaction and heating/cooling zones. This analysis also considered the effect of different water contents in the OMW composition (60-90 wt.%) and the impact of the pressure (1-4 bar), at 400 ºC. To determine the outlet stream composition of the process and the heat released or required in the reaction, the Aspen Plus V.10® software was used. To calculate the cost of the heat exchanger, the Aspen Exchanger Design & Rating software was adopted.*

It was observed that the content of water in the feed, the pressure, the flow rate of the OMW fed and the reactor configuration used affect the economic benefit of the project over time: lower content of water in the feed, lower pressure, lower OMW flow rate and the utilization of a SER allows to obtain a most economically advantageous project.

8.1. Introduction

An economic evaluation for the olive oil mill wastewater (OMW) steam reforming (OMWSR) process has never been carried out. So, in this work, a preliminary techno-economic study of the OMWSR process was performed for the first time, considering the reaction in a traditional reactor (TR) or in a sorption-enhanced reactor (SER - with in situ CO_2 removal, to shift the thermodynamic equilibrium to a higher production of H_2 [1]). The temperature of the process was set at 400 ºC, based on the limitations and performance of the sorbents considered in this study [hydrotalcite (HTC) and CaO] [3-8] and due to the experimental conditions used in previous laboratory tests (never above 400 ºC) [9-11] - these experimental results were used in this techno-economic study.

In the thermodynamics simulations with the *Aspen Plus V.10*® software, the CO_2 sorption was represented/simulated through its interaction with CaO to produce calcium hydroxide ($Ca(OH)_2$) and calcium carbonate ($CaCO_3$) - Eqs. (3.17) and (3.18), respectively. However, for the determination of the cost of the materials used in the SERs it was considered the utilization of a K-promoted HTC as CO_2 sorbent.

This work was focused on the design and cost assessment of several key process units, such as the reactor and heat exchangers (HEs). Besides that, since the content of water in the effluent stream from the olive oil production is generally between 80-95 wt.% [12-15], this study also considered the effect of different water contents in the initial composition of the OMW (60-90 wt.%) - it was considered a pre-treatment of the initial OMW stream to reduce the content of water (for instance, by evaporation). Moreover, the effect of pressure (1-4 bar) and OMW flow rate was also studied (again, the maximum pressure considered in this study is related to the experimental conditions previously performed in laboratory tests). Factors such as cost of catalyst/sorbent, utilities and salaries of the employees were also considered.

8.2. General considerations

Before the specification and design of the process units and the determination of the initial investment, operation costs and revenues, some general considerations and assumptions have to be made. All such decisions will affect the OMWSR process implementation in an olive oil company, being the study herein presented based on Portuguese data (OMW production, salaries, etc.).

8.2.1. Olive oil/OMW production

To estimate the amount of OMW to be treated, it was necessary to define the daily amount of olive oil produced in a consolidated industry in Portugal. Oliveira da Serra (a large olive oil producer) has

facilities with a capacity for olive oil production up to 200 000 L per day [16]. Thus, it was considered for this study that the production of olive oil is fixed at 50 % of the maximum daily production (100 000 L). According to a previous study [17], wherein a relationship between the amount of OMW generated and the olive oil processing capacity is established (≈ 3 $L_{OMW} \cdot L^{-1}_{olive\ oil}$), it is possible to infer that the above-mentioned olive oil company would produce approximately a total amount of 257 075 L of OMW per day (10 711 $L \cdot h^{-1}$) during the olive oil production period (6 months, typically from November to March). This value will be used for all the design of the new process units. The phenolic species molar ratio (on a dry basis) used for simulating the wastewater was adjusted according to studies already reported [18-22]. The composition used in the simulation of this stream is shown in Table 8.1.

Table 8.1 - Composition of the OMW (dry basis).

Species	Molar Fraction	Mass Fraction
Vanillic acid	0.022	0.024
Tyrosol	0.054	0.048
Gallic acid	0.022	0.024
Cinnamic acid	0.025	0.024
Syringic acid	0.019	0.024
Veratric Acid	0.041	0.048
4-hydroxybenzoic acid	0.054	0.048
Protocatechuic acid	0.049	0.048
D-Arabinose	0.526	0.500
D-Galactose	0.188	0.214

8.2.2. Case-studies and reaction simulations

To evaluate the composition of the outlet stream of the process and the heat released or required in the reactor, it was assumed that equilibrium is reached in the reformer. The thermodynamic equilibrium was calculated using the *Aspen Plus V.10*® software for a TR and a SER at 400 ºC for different case-studies (considering the molar composition mentioned in Table 8.1 and the OMW total flow rate of 10 711 $L \cdot h^{-1}$ - only accounting for 6 months of operation - or 5 356 $L \cdot h^{-1}$ - for 12 months of operation). Table 8.2 exhibits the case-studies (and the different scenarios inside each case-study) considered in this work to analyze the impact of the different operating conditions on the economic balance. Each scenario was analyzed for different reactor configurations, TR and SER. It was always considered that the SER operated only until the breakthrough time (≈ 100 % of CO_2 removal).

As an example, the summary of the thermodynamic results of Case-study A (wherein the water content was changed) is presented in Table 8.3. The results for Case-studies B and C are presented in Appendix H, section 1. The quantity of H_2 produced is higher in the SERs in comparison with the production observed in the TRs, and in agreement with expectations and previous works [1]. The removal of CO_2 from the reaction medium with the CaO sorbent shifts the process towards the production of more H_2 and consumption of CO through the water-gas shift reaction (WGS - Eq. (3.7)) and promotes the inhibition of the methanation reactions (Eq. (3.8) and reverse of Eq. (3.9) - low

formation of CH_4) [1]. As expected from the thermodynamics, the total pressure affects the production of H_2 negatively (Eq. (3.8) and reverse of Eq. (3.9) - the methanation reactions are promoted at higher pressures), as verified in Case-study C [1, 23]. Besides that, a higher concentration of the OMW components (lower content of water in the feed) allows the formation of a higher quantity of gaseous products (by comparing Scenarios A.1 to A.3 and B.1 to B.7). Additionally, and as expected, it was observed that the molar flow rate of H_2 produced in Case-study A was higher than for Case-study B (for the same temperature and pressure) since the quantity of OMW fed was higher in Case-study A.

Table 8.2 - Reactor operating conditions studied for the different case-studies (and different scenarios).

Scenario	Temperature (ºC)	OMW Flow Rate ($L \cdot h^{-1}$)	Pressure (bar)	Content of Water (wt.%)
A.1	400	10 711	1	90
A.2				85
A.3				80
B.1		5 356		90
B.2				85
B.3				80
B.4				75
B.5				70
B.6				65
B.7				60
C.1			2	80
C.2			3	
C.3			4	

Table 8.3 - Molar flow rate of gaseous species and OMW conversion in the thermodynamic equilibrium for Case-study A.

Reactor Config.	H_2O inlet ($mol \cdot h^{-1}$)	H_2O outlet ($mol \cdot h^{-1}$)	Oxygenates intlet ($mol \cdot h^{-1}$)	H_2 outlet ($mol \cdot h^{-1}$)	CO outlet ($mol \cdot h^{-1}$)	CH_4 outlet ($mol \cdot h^{-1}$)	CO_2 outlet ($mol \cdot h^{-1}$)	Carbon outlet ($mol \cdot h^{-1}$)	CaO inlet* ($mol \cdot h^{-1}$)	$CaCO_3$ outlet ($mol \cdot h^{-1}$)	CO_2 Removal (%)	OMW Conversion (%)
Scenario A.1												
TR	595 056	553 665	7 548	65 009	364	6 643	38 354	0	0	0	0	100
SER		540 163		91 653	1	73	92	0	45 195	45 195	≈ 100	100
Scenario A.2												
TR	595 056	542 737	11 988	76 452	616	17 240	54 187	0	0	0	0	100
SER		509 331		142 651	4	844	172	0	71 024	71 024	≈ 100	100
Scenario A.3												
TR	595 056	533 338	16 982	83 525	892	30 615	70 555	0	0	0	0	100
SER		479 017		191 283	7	3897	232	0	97 926	97 926	≈ 100	100

* Minimum quantity of CaO to reach a nearly complete CO_2 capture in the SER.

8.2.3. Process diagram

This techno-economic study focuses only on constructing the main and essential units so that OMW effluent will be treated and valorized properly. The defined sequence of process units is shown in Fig. 8.1.

To apply the OMWSR process in an existing olive oil production plant, the following process units were defined: storage tank, pump, reactor, filter, boiler and condenser. Very briefly, the process can be described as follows: the OMW is firstly stored in a pond (this step is not represented in Fig. 8.1, since the companies, typically, have already ponds in their installations). Then, the liquid is fed (after being filtered or settled to remove large solids) to a storage tank, from where it is pumped into the rest of the process. After being filtered again (with a filter with low mesh size) to remove small solids, the OMW stream is heated and evaporated before being fed to the reactor, where the OMWSR occurs. The gaseous products are directed to a condenser, where the remaining water is condensed. The gases produced and the condensed water will be used later in the process in the boiler (see subchapter 8.3.3 for further details). Besides that, to have a good energy integration in the entire process, it is considered a utilization of several HEs - see Fig. 8.1. It was also considered a line in the process to feed air (or steam, alternatively) to the reactor in order to regenerate the catalyst (and the sorbent when it is used SERs) - it was assumed that the olive oil production installation already has compressed air points to be used in this technology. Table 8.4 presents the function of each unit provided for the OMWSR process.

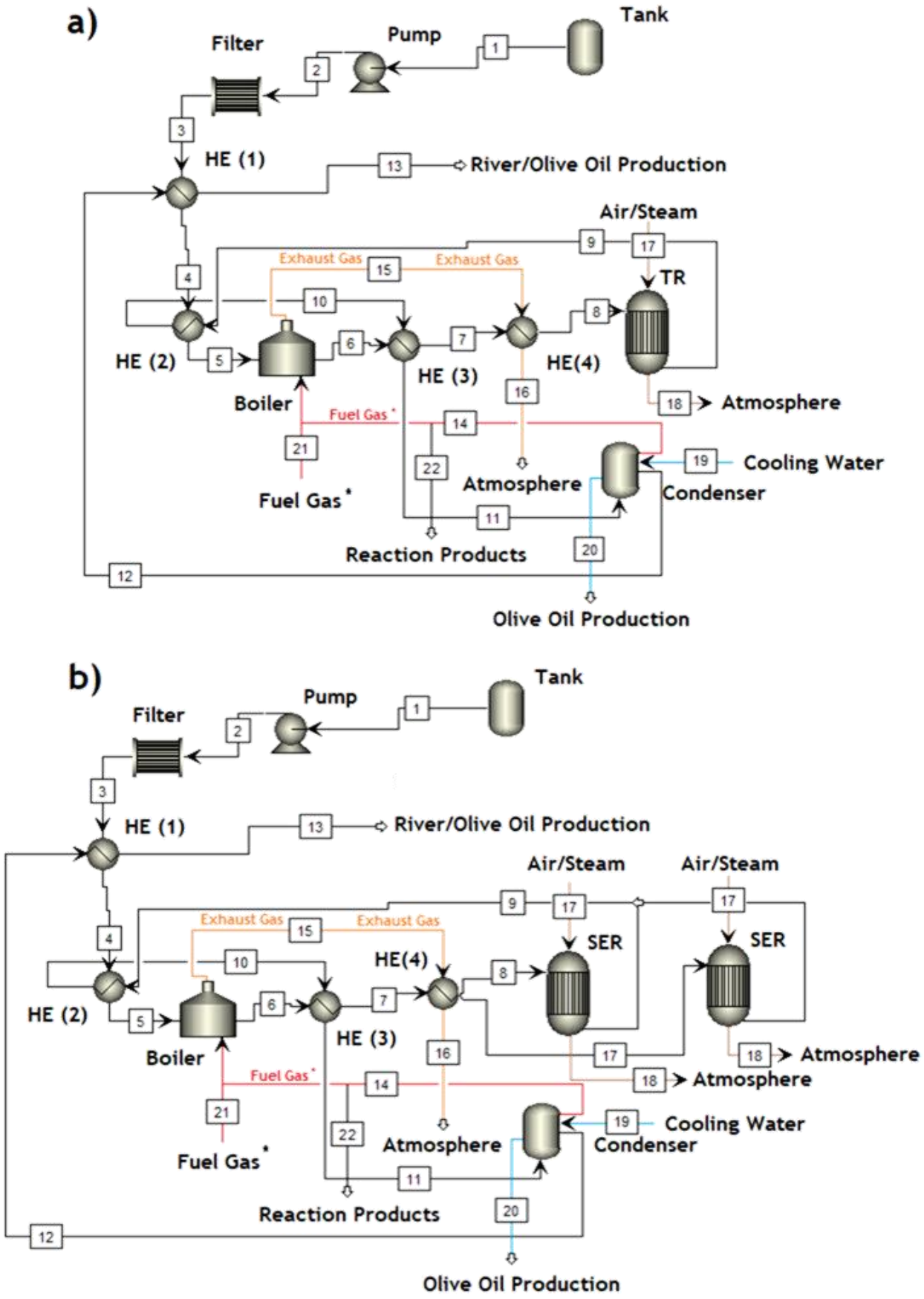

Fig. 8.1. Process diagram suggested for the application of the OMWSR process using a) a TR or b) SERs. * The *Fuel Gas* stream is composed of H_2+CH_4 (reaction products - stream 14) and natural gas (when necessary - stream 21).

Table 8.4 - Blocks used in Fig. 8.1.

Block	Description/Function
Tank	Stores the OMW
Pump	Pressurize liquid to be fed to the process units
Filter	Filters the OMW solid particles
Boiler	Vaporizes the OMW
HE	Heat exchange between different streams
TR/SER	Reactor where the OMWSR occurs
Condenser	Condenses the output stream from the reactor

8.2.4. Labor costs

The annual labor costs and the set of functions that will be necessary for the correct operation of the industrial unit are presented in Table 8.5. However, when hiring, it is important to take into account that the company that will use the technology already has an industrial unit for olive oil production. In this way, the number of new employees will be low (5 teams for 3 shifts) since the current employees will be able to assist in some tasks of this new effluent valorization line. However, the promotion of specific training for the tasks to be performed in the company should be provided to all collaborators. It was considered that regardless of the duration of the process (i.e., running the reforming plant for 6 months or 12 months every year, due to the seasonal nature of the olive oil industry), the employees will maintain their jobs and are allocated to other company functions when they are not needed in the steam reforming section.

As a general practice in the country, it was considered that the insurance for accidents at work for each employee has a cost equivalent to 5.1 % of their gross salary; besides that, it was defined a value of 7.20 € per day of food allowance (21 days per month, during 11 months of work) and it was considered the payment of the single social fee (23.75 % of the gross salary). All employees benefit from a shift allowance payment. To calculate these costs, it was considered 14 months of workers' income (holidays and Christmas), except for the payment of the food allowance.

Table 8.5 - Annual labor costs.

Category	Gross Salary (€·month^{-1})[a)]	Collaborators Number	Total Salaries (€·year^{-1})[b)]	Total Accident Insurance (€·year^{-1})[c)]
Operator	950	10	214 470	6 783
Supervisor	1 050	5	117 647	3 749
		Total (€·year^{-1})	342 648	

[a)] For each employee.

[b)] Includes single social fees, shift allowance, feed allowances and gross salaries - value calculated considering all the employees of the specific category.

[c)] Total cost of the accident insurance that covers all the employees of the specific category.

8.3. Design and costs of process units

To adjust/update the costs for a given year ($C_{updated}$), the Chemical Engineering Plant Cost Index (I) was applied, as shown in Eq. (8.3) [24]. In this study, the costs have been updated for the year 2018 that presented a I equal to 603.1 [25], and it was considered the $I_{reference}$ equal to 394.1 (2000 was considered the year of reference [26]) for all the equipment design, except for the boiler ($I_{reference}$ equal to 509.7 - 2007 was the reference year [27]).

$$C_{updated} = C_{reference} \times \frac{I}{I_{reference}} \quad (8.1)$$

Subchapters 8.3 and 8.4 present the results obtained in Case-study A, for brevity reasons. For further details about the results for Case-studies B and C, please consult the SI. However, all scenarios (from A to C) will be discussed hereinbelow and the profitability analysis of the Case-study B is also present in subchapter 8.4.5 (since it is the only case-study that presents profitable scenarios).

8.3.1. OMW tank

The tank used to store the OMW should be able to support the production capacity of OMW for 2 hours (10 711 $l \cdot h^{-1}$ for Case-study A, still with some security (10 % more) - see Table 8.6). It was considered the same tank for the Case-studies B and C (12 months of operation) since it was considered that the olive oil companies have ponds to store all the excess of the OMW produced. The vessel thickness (t_s) is given by Eq. (8.4) [28].

$$t_s = \frac{P\, r_i}{S\, E - 0.6\, P} + C_r \quad (8.2)$$

where P is the working pressure inside the process unit (psig), r_i is the intern radius (inches), S is the maximum tension allowed for the material (12 000 psig), E is the weld resistance (0.85) and C_r is the safety thickness relative to the corrosion effects, being considered 1/8 in (2 mm) [28]. The cost of the several parts of the storage tank was calculated from Eqs. (8.5), (8.6) and (8.7) in dollars (and then calculated in euros - 1 $ = 0.92 €). The total cost of the storage tank is given by Eq. (8.5) [28].

$$C_{Vessel} = F_M C_C + C_{PL} \quad (8.3)$$

where C_C is the carcass cost, F_M is the material factor and C_{PL} is the platforms and ladders costs. C_C for this vertical vessel is calculated by Eq. (8.6) (W is the weight (lb) of the unit) [28].

$$C_C = \exp\left(6.775 + 0.18255\,[\ln(W) + 0.02297(\ln(W))^2\right] \quad (8.4)$$

It was considered a value of F_M equal to 1 since it was used carbon steel in the design of the tank.

As it is a vertical vessel (L is the height (ft) and D_i is the internal diameter (ft) of the unit), the value of C_{PL} was determined by Eq. (8.7) [28]. In Table 8.6 the values are displayed in SI units.

$$C_{PL} = 285.1 \times {D_i}^{0.73960} \times L^{0.70684} \quad (8.5)$$

Table 8.6 - Design and cost of the OMW tank.

Design			
Temperature (ºC)	25	**Pressure (bar)**	1
Material	Stainless steel	**Geometry**	Cylinder
Volume (m^3)	24	**t_s (mm)**	5
Internal Diameter (m)	2.5	**Height (m)**	4.9
Weight (ton)	1.90	**Updated Cost (€)**	41 417

8.3.2. Reactor

The volume of the reactor was calculated based on the residence time of the fluid (τ - s), considered to be identical to the residence time determined in previous experimental tests (laboratory-scale experiments) [10, 29] - see Eq. (8.8), where the variable V (L) is the reactor volume, ϵ is the porosity (0.4) and Q (L·s^{-1}) is the OMW volume flow rate.

$$\tau = \frac{V \times \epsilon}{Q} \quad (8.6)$$

For the calculation of the internal diameter D_i and length L of the reformer (assumed to be a packed-bed tubular reactor), it was considered a quotient of L/D_i equal to that observed in the laboratory reactor (≈ 12.6) [9, 10, 29]. The reactor thickness (t_s) is given by Eq. (8.4) and the carcass cost was calculated from Eq. (8.9) [28]. Since the reactor is a horizontal vessel with a small diameter, it was assumed that C_{PL} = 0 €. The total cost of the reactor is given by Eq. (8.5), and it was also considered a value of F_M equal to 1 since it was used carbon steel in the design of the reactor.

$$C_C = \exp\left(8.717 - 0.23320\left[\ln(W) + 0.0433(\ln(W))^2\right]\right) \quad (8.7)$$

It is possible to observe the design and cost of the reactor for Case-study A in Table 8.7. Since the flow rate of OMW is lower in Case-studies B and C, the reformer should be smaller and cheaper (see Table H.3 in Appendix H, section 2, the features of the reactor designed for these case-studies and total cost).

Table 8.7 - Design and cost of the reactor used for Case-study A.

Design			
Temperature (ºC)	400	**Pressure (bar)**	4
Material	Stainless steel	**Geometry**	Cylinder
Volume (m^3)	3	**t_s (mm)**	5
Internal Diameter (m)	0.7	**Length (m)**	8.5
τ (s)	0.13		
Cost			
Weight (ton)	0.92	**Updated Cost (€)**	21 596*

* Includes an increase of 20 % for insulation and painting.

Despite the advantages of utilizing a SER in terms of quantity and purity of H_2, the drawback of this system is that the sorbent gets saturated at the CO_2 breakthrough time and then its regeneration is necessary. The system must therefore have two parallel reactors to run continuously (assuming that regeneration is no longer than the time required for the sorbent to get saturated), being that while one of them is used in the reaction stage, the other is being regenerated. These additional costs for the application of this technology will be discussed in the next subchapters.

Besides that, both reactor configurations need a temperature control system - an oven (a set of electric resistance heaters around the reactor) and a water-cooling system. The oven was included in the non-dimensioned equipment, while the refrigeration system was designed as a HE.

8.3.3. Energy integration and heat exchangers

To achieve a good energy integration in the entire plant, it was necessary to implement a HE network (HEN) using the process streams, as mentioned in subchapter 8.2.3. This energy integration has the objective of reducing the process expenses, as well as the environmental impact caused: the HEN integrates energetically the hot and the cold process streams, reducing the heating and cooling utilities required. Only one restriction was set in this energy integration: there should be a minimum temperature difference of 10 ºC between the streams that exchange heat.

The HEN of the streams presented in Fig. 8.1 is presented in Table 8.8 for Scenario A.1 (as an example) and in Tables H.4-H.15 for the remaining case-studies (in Appendix H, section 2). It is worth emphasizing that the utilization of utilities is required: it was selected the cooling water as cold utility and the H_2 and CH_4 produced in the OMWSR were considered to feed the boiler (hot utility - stream 14) together with natural gas (when necessary, i.e., when the amount of H_2 and CH_4 is not enough to keep the process energetically auto-sufficient - feed of natural gas by stream 21). It was also considered that the exhaust gas produced in the boiler is used in an exchanger (HE(4)) as a hot stream; and cooling water is used in the condenser to allow the condensation of the water present in the reactor outlet, as can be seen in Fig. 8.1.

The mass flow rates shown in the Table 8.8 and Tables H.4-H.15 (in Appendix H, section 2) are those calculated and defined previously in subchapter 8.2.2. For simplification, it was assumed that the feed and the outlet streams of the reactor are constituted only by water: it was possible to verify that the boiling point elevation due to the presence of solutes (comparison between water and OMW) is negligible since the molalities of the species present in the effluent are low in all case-studies and the ebullioscopic constant for water is also very low [30]. For the calculations, it was also assumed that the heats of combustion of H_2 and CH_4 are equal to 242 and 803 $kJ \cdot mol^{-1}$, respectively, the specific heats of water are 4.2 and 2.0 $kJ \cdot mol^{-1} \cdot {}^{o}C^{-1}$ (liquid and vapor state), respectively, and the vaporization heat of water is 40.7 $kJ \cdot mol^{-1}$ for all the pressures considered in scenarios [31].

Table 8.8 - Energy integration for Scenario A.1.

TR

HE	Streams	Inlet Temperature (ºC)	Outlet Temperature (ºC)	ΔT	Flow Rate ($kg \cdot h^{-1}$)	Heat exchanged (MW)
(1)	(3)	23	55	32	10 711	0.40
	(12)	100	65.5	-34.5	9 966	
(2)	(4)	55	95	40	10 711	0.50
	(9)	400	310.5	-89.5	9 966	
Boiler	(5)	95	100	5	10 711	6.78
	Fuel Gas* (14+21)	-	-	-	-	
(3)	(6)	100	195	95	10 711	0.57
	(10)	310.5	208.5	-102	9 966	
(4)	(7)	195	400	205	10 711	1.22
	Exhaust Gas (15)	-	-	-	-	
Condenser	(11)	208.5	100	-108.5	9 966	6.85
	Cooling Water (19)	23	90	67	88 002	

SER

HE	Streams	Inlet Temperature (ºC)	Outlet Temperature (ºC)	ΔT	Flow Rate ($kg \cdot h^{-1}$)	Heat (MW)
(1)	(3)	23	55	32	10 711	0.40
	(12)	100	64.5	-35.5	9 723	
(2)	(4)	55	95	40	10 711	0.50
	(9)	400	308	-92	9 723	
Boiler	(5)	95	100	5	10 711	6.78
	Fuel Gas* (14+21)	-	-	-	-	
(3)	(6)	100	195	95	10 711	0.57
	(10)	308	203.5	-104.5	9 723	
(4)	(7)	195	400	205	10 711	1.22
	Exhaust Gas (15)	-	-	-	-	
Condenser	(11)	203.5	100	-103.5	9 723	6.65
	Cooling Water (19)	23	90	67	85 532	

* Heat from the combustion of fuel gas (H_2+CH_4 + natural gas).

Table 8.9 - Utilities and utilization of the gaseous products (H_2 + CH_4).

TR			
Scenario	**Natural Gas (MW)**	**Cooling Water (kg·h^{-1})**	**Fraction of H_2+CH_4 used***
A.1	3.35	88 002	1.00
A.2	0.21	85 973	1.00
A.3	0.00	84 384	0.74
B.1	1.67	43 992	1.00
B.2	0.11	43 079	1.00
B.3	0.00	42 156	0.74
B.4	0.00	41 382	0.56
B.5	0.00	42 500	0.44
B.6	0.00	45 535	0.36
B.7	0.00	48 762	0.29
C.1	0.00	42 750	0.76
C.2	0.00	42 786	0.77
C.3	0.00	43 038	0.78
SER			
Scenario	**Natural Gas (MW)**	**Cooling Water (kg·h^{1})**	**Fraction of H_2+CH_4 used***
A.1	3.02	100 958	1.00
A.2	0.00	108 972	0.95
A.3	0.00	118 869	0.68
B.1	1.51	47 432	1.00
B.2	0.00	51 436	0.95
B.3	0.00	56 229	0.68
B.4	0.00	62 182	0.52
B.5	0.00	68 940	0.41
B.6	0.00	77 277	0.33
B.7	0.00	87 866	0.27
C.1	0.00	56 226	0.68
C.2	0.00	55 776	0.69
C.3	0.00	55 812	0.69

*Fraction of H_2 and CH_4 produced that was used in the boilers.

Table 8.9 presents the utilities needs to provide to the process (reaction stage). The quantity of water corresponds to the water necessary to supply to the condenser (e.g. Table 8.8) plus the required water to control the temperature of the reactor (@ 400 ºC - data not shown). In fact, depending on the conditions employed and feed composition, the reformer may need to be heated (the steam reforming is an endothermic process) or cooled (whenever other exothermic reactions prevail, like the water-gas shift or methanation). The latter is particularly relevant for the SER, when in the reaction stage (because CO_2 capture with the CaO sorbent is also an exothermal process), explaining the higher cooling water consumption in every case-study as compared to the TR. However, the consumption of electricity for heating the TR in the Scenarios A.1 and B.1 (only scenarios where the endothermic reactions prevail in reaction stage - data not shown) was residual in comparison with the total energy required for all the process. In the same way, in all case-studies, the energy for heating the SER in the sorbent regeneration step (also an endothermic process) was residual in comparison with the energy needed for the entire industrial plant. Moreover, it was assumed that the heat generated in the

coke oxidation in all case-studies (regeneration of the catalyst) was released to the air around the reactor - heat transfer through the reactor wall.

To determine the cost of the exchangers, the six-tenths rule was used, which consists of applying Eq. (8.10) [32] for the determination of a HE(*i*) cost (where *i* is the number of the HE in Fig 8.1), taking into account the heat exchanged in this unit and in the reference exchanger HE(R) - see Table 8.10 as an example for Scenario A.1 and Table H.16-H.27 in Appendix H, section 2, for the remaining case-studies. To implement this procedure, it was necessary to calculate the cost of the HE(R) through the *Aspen Exchanger Design & Rating software*. The results obtained with this HE(R) were used to estimate the purchase costs of the other exchangers used in this study - for further details, see Appendix H, section 2. Besides that, the condenser used in the process was designed as a HE and, in this way, the cost of this equipment was estimated also by Eq. (8.10) - see Table 8.10.

$$C_{\mathrm{HE}(i)} = C_{\mathrm{HE(R)}} \times \left(\frac{Heat_{\mathrm{HE}(i)}}{Heat_{\mathrm{HE(R)}}} \right)^{0.6} \tag{8.8}$$

The boiler cost has been estimated based on the flow rate of OMW evaporated (Eq. (8.11)) [28].

$$C_{\mathrm{Boiler}} = 106\,000 + 8.7 \times Q \tag{8.9}$$

Table 8.10 - Cost of HEs and boiler/condenser for Scenario A.1.

	TR		SER	
HE	**Heat (MW)**	**Cost (€)**	**Heat (MW)**	**Cost (€)**
(R) [a)]	0.50	28 502	0.50	28 502
(1)	0.40	24 855	0.40	24 855
(2)	0.50	28 415	0.50	28 415
(3)	0.57	30 739	0.57	30 739
(4)	1.22	48 765	1.22	48 765
Boiler	6.78	235 685*	6.78	235 685*
Condenser	6.85	137 045	6.65	134 702

[a)] HE used as reference.
* The boiler cost has not been calculated based on the heat exchanged but rather on the flow rate of OMW (Eq. (8.11)).

8.4 Economic evaluation

8.4.1. Fixed capital investment

Expenses related with the capital investment are considered in this subchapter. They include the purchase cost of equipment and their installation, as well as piping, instrumentation, among others. From Fig. 8.2, it is possible to observe the distribution of the contributions of the several costs associated with the fixed capital investment (FCI) [33].

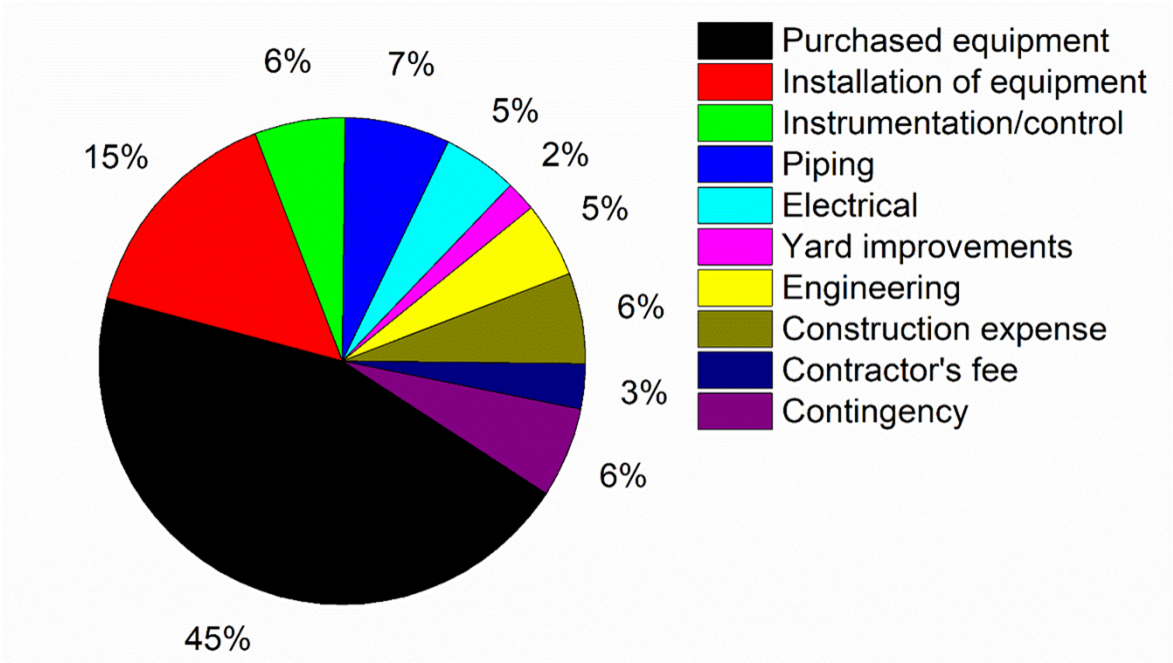

Fig. 8.2. Distribution of the contributions of the costs considered for the calculation of the FCI.

8.4.1.1. Purchase costs of the equipment

The purchase cost of the equipment dominates this category of expenses, representing almost half of FCI. It includes the cost of all designed equipment with an increase of 20 %, since all the equipment is subject to acidic conditions (due to the natural pH of OMW, in the range 3-6) [34]. It also has a 30 % additional cost to cover non-dimensioned equipment (filters, pumps, etc.). In Table 8.11, it is possible to consult the cost of the equipment for all Case-study A (for Case-studies B and C, see Table H.28 and Table H.29 in Appendix H, section 3).

Table 8.11 - Cost of the equipment for Case-study A.

Equipment	Purchase Cost (€)					
	TR			SER		
	A.1	A.2	A.3	A.1	A.2	A.3
Tank	41 417	41 417	41 417	41 417	41 417	41 417
Reactor	21 596	21 596	21 596	43 192	43 192	43 192
Exchangers	323 784	321 516	319 549	369 167	382 125	393 342
Boiler	282 823	282 823	282 823	282 823	282 823	282 823
Not designed	200 886	200 205	199 615	220 979	224 867	228 232
Total	870 505	867 556	865 000	957 577	974 422	989 005

Comparing the values for the different scenarios (Fig. 8.3), one can see that the cost of the equipment is practically independent of the content of water considered in the feed. However, the utilization of the SER technology slightly increases the initial cost of the equipment since two reactors are necessary compared with the TR-based technology (this applies for all scenarios, cf. Fig. 8.3). When it was considered the operation of the process only for 6 months, the price of the equipment is higher because the flow rate to be treated is higher (Scenario A.1 to A.3 vs. B.1 to B.3, respectively). Finally, in Scenarios B.3 (1 bar) and C.1 to C.3 (2 to 4 bar), it was observed that the utilization of higher pressures in the system practically did not influence the costs of the acquisition of the equipment.

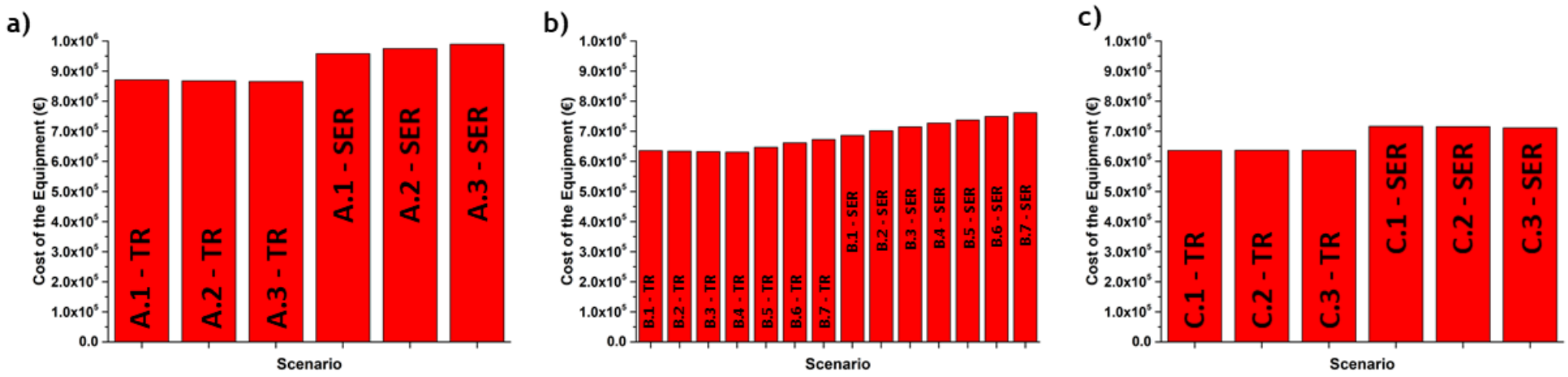

Fig. 8.3. Purchase cost of the equipment for the different Case-studies a) A, b) B and c) C using TRs or SERs.

8.4.1.2. Installation costs and total fixed capital investment

Table 8.12 shows the remaining costs that make up the investment in fixed capital for Case-study A. The working capital corresponds to 10 % of the FCI [33]. The total CI is then the sum of these two values. In SI, the process cost and the total CI for the Case-studies B and C are shown in Table H.30 and Table H.31, respectively, in Appendix H, section 3. In Fig. 8.4, it is possible to confirm that the total CI follows the same trend of the cost of the equipment already mentioned in subchapter 8.4.1.1.

Table 8.12 - Cost of the implementation of the process and total CI for Case-study A.

Component	Cost (€)					
	TR			SER		
	A.1	A.2	A.3	A.1	A.2	A.3
Purchased Equipment	870 505	867 556	865 000	957 577	974 422	989 005
Installation of Equipment	348 202	347 022	346 000	383 031	389 769	395 602
Instrumentation/Control	139 281	138 809	138 400	153 212	155 908	158 241
Piping	162 494	161 944	161 467	178 748	181 892	184 614
Electrical	96 723	96 395	96 111	106 397	108 269	109 889
Buildings	-	-	-	-	-	-
Yard Improvements	38 689	38 558	38 444	42 559	43 308	43 956
Service Facilities	-	-	-	-	-	-
Land*	-	-	-	-	-	-
Engineering	96 723	96 395	96 111	106 397	108 269	109 889
Construction Expense	116 067	115 674	115 333	127 677	129 923	131 867
Contractor's fee	58 034	57 837	57 667	63 838	64 961	65 934
Contingency	116 067	115 674	115 333	127 677	129 923	131 867
FCI	2 042 785	2 035 865	2 029 866	2 247 115	2 286 644	2 320 866
Working Capital	204 279	203 587	202 987	224 712	228 664	232 087
Total CI	2 247 063	2 239 451	2 232 852	2 471 826	2 515 309	2 552 952

* It is not necessary to acquire any land, as the technology is considered to be applied to an existing industry.

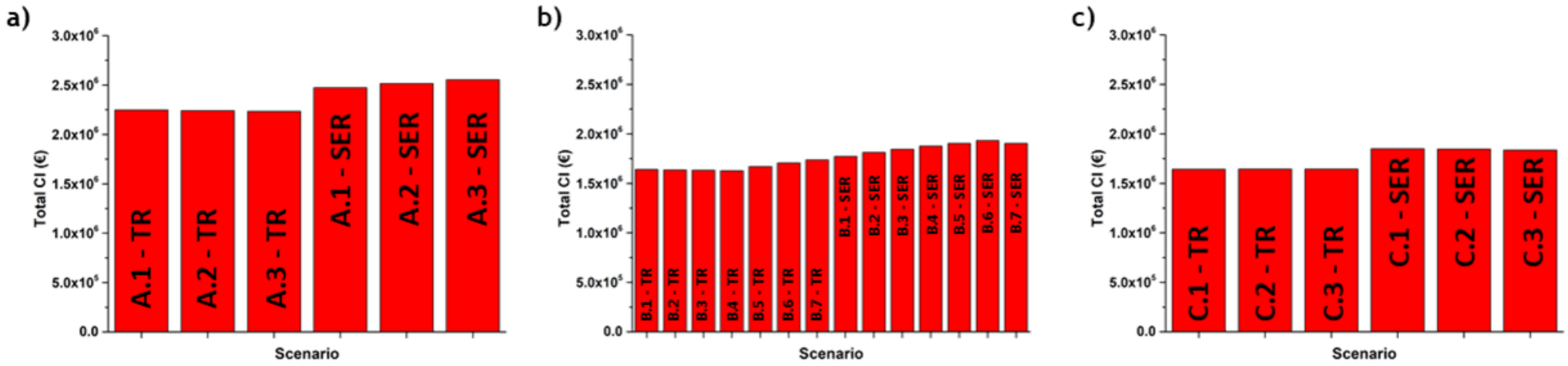

Fig. 8.4. Total CI calculated for Case-studies a) A, b) B and c) C using TRs or SERs.

8.4.2. Fixed Costs

The fixed costs associated with this project (depreciations are 10 % of the FCI, local taxes and insurances are 1 % each of the FCI [33]) are shown in Table 8.13 (for Case-study A, as an example) and Fig. 8.5. For further details about Case-studies B and C, please refer to, respectively, Table H.32 and Table H.33 in Appendix H, section 3. Since the calculation of the fixed costs was based on the cost of the equipment and FCI, the trend is equal to that observed in subchapters 8.4.1.1 and 8.4.1.2.

Table 8.13 - Fixed Costs for the Case-study A.

Component	Cost (€·year^{-1})					
	TR			SER		
	A.1	A.2	A.3	A.1	A.2	A.3
Depreciation	204 278	203 586	202 987	224 711	228 664	232 087
Local Taxes	20 428	20 359	20 299	22 471	22 866	23 209
Insurances	20 428	20 359	20 299	22 471	22 866	23 209
Total	245 134	244 304	243 584	269 654	274 397	278 504

8.4.3. Production costs

The estimate of the annual use of utilities, materials, salaries and maintenance (5 % of the FCI) are summarized in Table 8.14 for Case-study A. The direct production costs for the Case-studies B and C are provided in Appendix H (Table H.34 and Table H.35, respectively, in Appendix H, section 3). The definition of salaries was already explained in subchapter 8.2.4. The price of natural gas was estimated based on the selling price of this same source sold by a Portuguese energy company - 0.05 €·kWh^{-1} [35].

As already mentioned, the catalyst inside the TR will be periodically reactivated via regenerative oxidation with air or steam (for coke oxidation); this regenerative oxidation was also performed in a SER (removing, in this way, CO_2 from the sorbent and simultaneously promote oxidation of the coke deposited on the catalyst surface). It was considered that the steam required for the regeneration process of the catalyst/sorbent (if steam is selected to be the oxidizing agent) is obtained from the cooling water that is used in the condenser and in the reactor cooling system. The cost of the natural gas employed to produce steam was included in extra utilities costs (25 % of the total utilities expenses - data not shown but considered in the final value of the production costs). If the air is selected to be the oxidizing agent, it will not be necessary to contemplate any additional cost, since it was considered that the olive oil companies already have compressed air available to feed the SER in the regeneration stage.

Moreover, as mentioned in subchapter 8.3.3, the consumption of electricity for heating the TR in the Scenarios A.1 and B.1 (in the reaction stage) and to control the temperature of the SER in the sorbent regeneration step (for all case-studies) was also included in the extra utilities costs.

Table 8.14 - Production costs for the Case-study A.

Component	Cost (€·year^{-1})					
	TR			SER		
	A.1	A.2	A.3	A.1	A.2	A.3
Maintenance	102 139	101 793	101 493	112 356	114 332	116 043
Salaries	342 648	342 648	342 648	342 648	342 648	342 648
Materials	9 299	9 299	9 299	23 279	23 279	23 279
Utilities						
Colling Water	4228	4131	4054	4851	5236	5711
Natural Gas	730 608	46 469	0	659 122	0	0
Total Utilities	918 546	63 250	5 068	829 967	6 545	7 139
Total	1 372 633	516 991	458 509	1 308 250	486 804	489 110

Concerning the materials (SiC as inert + Ni/Mg-Al_2O_3 as catalyst + MG30 from SASOL as sorbent) - see Table 8.15 -, the quantity of catalyst was defined taking into account the value of W/F (mass of catalyst per flow rate of OMW) used in previous laboratory experimental tests [9, 10]. However, an adjustment of the W/F (+ 40 % in comparison with the experimental tests) was carried out in an attempt to approximate the catalytic results to the thermodynamic equilibrium. The cost of adding a higher amount of catalyst, if the additional % of catalyst considered is not sufficient to achieve thermodynamic equilibrium, is included in the extra utilities costs.

The selection of the catalyst was based on the low price of this type of catalyst (Ni-based) and the high performance for steam reforming processes: lower cost than noble metal-based ones and good activity in reforming reactions due to C-C bond rupture capability [36, 37]. It was defined that the materials were changed every year to maintain high performances, and a similar amount of sorbent and catalyst was assumed in the SERs ($m_{cat}/m_{sorbent}$ = 0.9) [11].

From Fig. 8.6 and Table 8.14, it was observed that for the situation with an initial water content of 90 wt.% in the OMW stream (Scenarios A.1 and B.1), the direct production costs are much higher than for the other scenarios. This is mainly related to the smaller amount of oxygenates in the feed, leading to a lower production of H_2 and CH_4; inherently, all the product gas stream is consumed to satisfy the process energy needs (cf. Table 8.14), being inclusively needed some natural gas. Finally, as expected, it is realized that the treatment of a higher volume of OMW makes the direct production costs higher (Fig. 8.6a) vs. Fig. 8.6b)).

Table 8.15 - Materials used in the TR and SER.

Materials Data			
Ni/Mg-Al_2O_3 Density ($kg \cdot m^{-3}$)	850	**Catalyst Price ($€ \cdot kg^{-1}$)**	14
MG30 Density ($kg \cdot m^{-3}$)	450	**MG30 Price ($€ \cdot kg^{-1}$)**	35
SiC Density ($kg \cdot m^{-3}$)	3 210	**SiC Price ($€ \cdot kg^{-1}$)**	1
Laboratory Reactor			
$Catalyst_{laboratory}$ (g)	0.94	**$W/F_{laboratory}$ ($g \cdot hr \cdot m^{-3}$)**	25.1
H_2 Yield obtained (mol_{H2}/mol_{oMW})	10.5	**H_2 Yield Maximum* (mol_{H2}/mol_{oMW})**	12.2
Case-study A			
TR			
Catalyst (kg)	475	**W/F ($g \cdot hr \cdot m^{-3}$)**	35.5
Reactor Volume (m^3)	3.05	**Porosity**	0.4
Catalyst Volume (m^3)	0.56	**Void Volume - inter-particle (m^3)**	1.22
Inert Volume (m^3)	1.27	**Inert (kg)**	4 086
Catalyst Cost ($€ \cdot year^{-1}$)	5 916	**Inert Cost ($€ \cdot year^{-1}$)**	3 383
Materials Cost ($€ \cdot year^{-1}$)	9 299		
SER			
Catalyst (kg)	475	**Catalyst/Sorbent (mass ratio)**	0.9
Sorbent (kg)	546	**Sorbent Volume (m^3)**	1.21
Inert Volume (m^3)	0.06	**Inert (kg)**	190
Catalyst Cost ($€ \cdot year^{-1}$)	5 916	**Sorbent Cost ($€ \cdot year^{-1}$)**	17 206
Inert Cost ($€ \cdot year^{-1}$)	157	**Materials Cost ($€ \cdot year^{-1}$)**	23 279
Case-studies B and C			
TR			
Catalyst (kg)	237	**W/F ($g \cdot hr \cdot m^{-3}$)**	35.5
Reactor Volume (m^3)	1.53	**Porosity**	0.4
Catalyst Volume (m^3)	0.28	**Void Volume - inter-particle (m^3)**	0.61
Inert Volume (m^3)	0.64	**Inert (kg)**	2 043
Catalyst Cost ($€ \cdot year^{-1}$)	2 958	**Inert Cost ($€ \cdot year^{-1}$)**	1 692
Materials Cost ($€ \cdot year^{-1}$)	4 650		
SER			
Catalyst (kg)	237	**Catalyst/Sorbent**	0.9
Sorbent (kg)	273	**Sorbent Volume (m^3)**	0.61
Inert Volume (m^3)	0.03	**Inert (kg)**	95
Catalyst Cost ($€ \cdot year^{-1}$)	2 958	**Sorbent Cost ($€ \cdot year^{-1}$)**	8 603
Inert Cost ($€ \cdot year^{-1}$)	79	**Materials Cost ($€ \cdot year^{-1}$)**	11 640

* At the thermodynamic equilibrium.

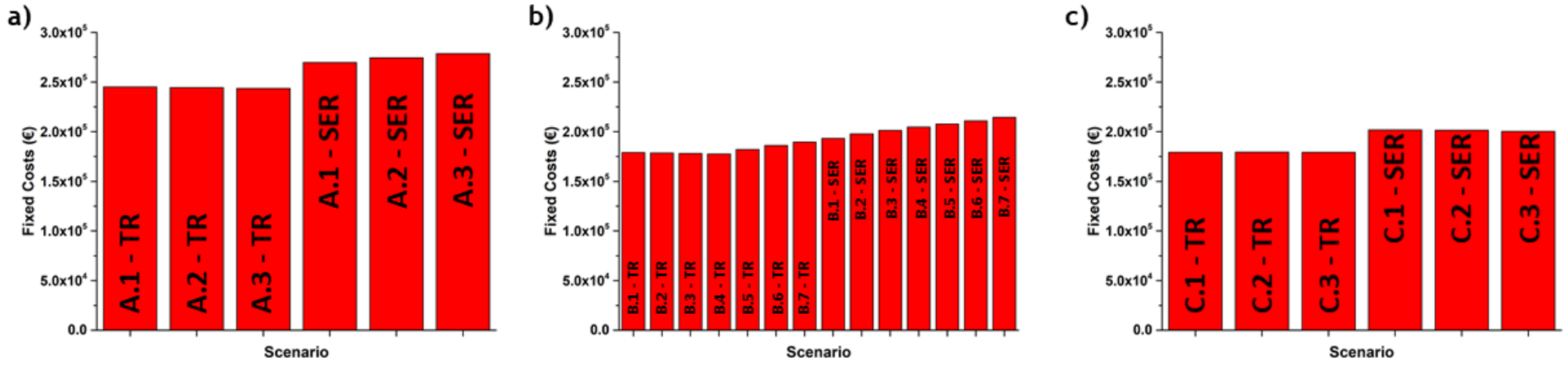

Fig. 8.5. Fixed Costs calculated for Case-studies a) A, b) B and c) C.

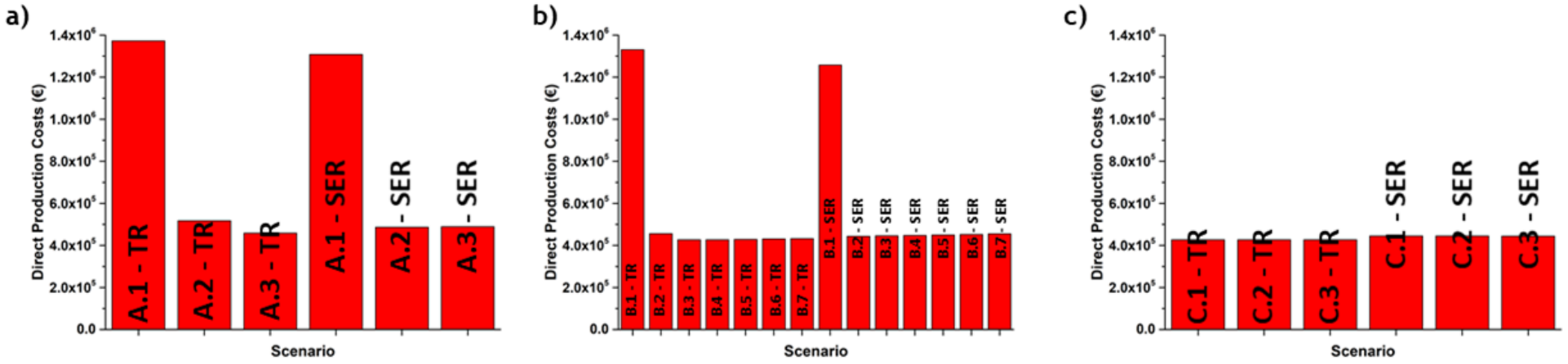

Fig. 8.6. Production Costs calculated for Case-studies a) A, b) B and c) C using TRs or SERs.

8.4.4. Revenues

The revenues generated depend on the quantity of H_2 and CH_4 yielded through the OMWSR. The production of these gases, as mentioned, depends on the initial composition of OMW and reactor configuration used. However, some fraction of these gases will be consumed in the boiler to guarantee the energy needs of the overall process (see subchapter 8.3.3, in Table 8.9). The values presented in Table 8.16 considered already the consumption of this fraction. It was assumed that the commercial value of these gases is two-thirds the value of natural gas (33 €·MWh^{-1}) [35].

Table 8.16 - Revenues of the OMWSR process for the Case-study A.*

Total Revenues (€·$year^{-1}$)					
TR			SER		
A.1	**A.2**	**A.3**	**A.1**	**A.2**	**A.3**
0	0	472 450	0	74 683	638 618

* The revenue comes from the net sale of H_2 and CH_4 produced in the process.

As mentioned in subchapter 8.2.2, the net production of CH_4 and H_2 is lower for higher contents of the water in the feed. In this way, as the water content decreases (e.g. from Scenarios A.1 to A.3, or from B.1 to B.7), the revenues increase (Fig. 8.7a) and Fig. 8.7b)); moreover, the utilization of the SER in either of the three case-studies analysed allows to produce more gaseous products and increase the revenues (Fig. 8.7). Lastly, and because the increase of the pressure in the system slightly decreases the production of CH_4 plus H_2 (reactors are under equilibrium conditions), this effect is negligible in Fig. 8.7.

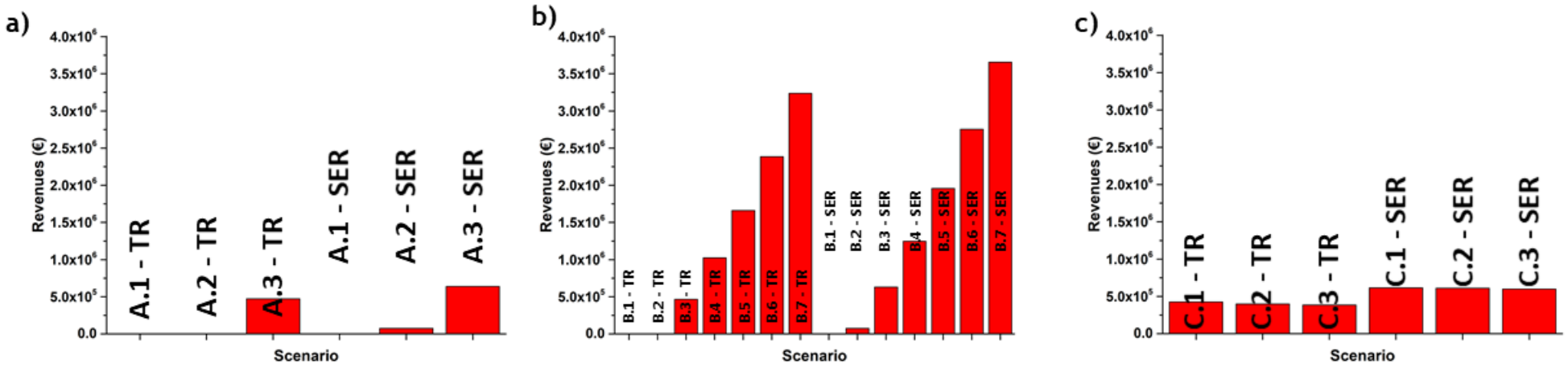

Fig. 8.7. Revenues calculated for Case-studies a) A, b) B and c) C using TRs or SERs.

8.4.5. Profitability analysis

For each case-study presented, a period of 10 years was considered for the profitability analysis, where the first year considered ("zero") is when the initial investment is carried out without the plant being in operation, starting the activity at the beginning of the year 1.

To calculate net results, it was considered a tax rate of 23 % (corporate income tax of 21 % plus other municipal taxes) and to determine the updated cash flows, it was used the inflation rate of 1.37 % [38]. It was also defined the value of 2 % to the minimum attractiveness rate of return.

For the analysis of the economic balance, several parameters such as the net present value (NPV - Eq. (8.18)), the internal rate of return (IRR - Eq. (8.19)) and the return time were considered.

Annual depreciation

$$\text{Depreciation} = \frac{\text{FCI}}{10 \text{ years}} \tag{8.10}$$

Tax-free results

$$\text{Tax\_free results} = \text{Revenues} - (\text{Fixed costs} + \text{Production costs}) \tag{8.11}$$

Net results

$$\text{Net results} = \text{Tax\_free results} \times (1 - \text{Tax rate}) \tag{8.12}$$

Cash flow

$$\text{Cash flow} = \text{Net results} + \text{Depreciation} \tag{8.13}$$

Updated cash flow

$$\text{Updated cash flow}_n = \text{Cash flow}_n \times (1 + \text{Cost of capital})^{-n} \tag{8.14}$$

where *n* is the number of years elapsed since the beginning of the project.

Accumulated cash flow

$$\text{Accumulated cash flow}_n = \text{Updated cash flow}_n + \text{Accumulated cash flow}_{n-1} \tag{8.15}$$

NPV

$$\text{NPV} = \sum_{n=0}^{N} \text{Updated cash flow}_n \tag{8.16}$$

where N is the total number of years of the project (in this study, N = 10).

IRR

$$\text{NPV} = 0 = \sum_{n=0}^{N} \frac{\text{Cash flow}_n}{(1 + \text{IRR})^n} \tag{8.17}$$

Fig. 8.8, Fig. 8.9 and Fig. 8.10 show the results of the profitability analyses (in terms of updated cash flow and accumulated cash flow) obtained for the several scenarios of the Case-studies A and B. It was verified that the project's profitability is favored when the process is carried out during all the year (Scenarios B.1 to B.3 vs. Scenarios A.1 to A.3, tough in all these scenarios profitability is negative), with lower content of water in the feed (Scenarios A.1 to A.3 and B.1 and B.7) and at lower pressure (Scenarios B.3 and C.1 to C.3 - the profitability analysis of the Case-study C can be seen in Fig. H.2 in Appendix H, section 3). Besides that, the utilization of SERs allows obtaining a more economically advantageous project.

Finally, it was also demonstrated that the Case-study B is the only one that presents profitable scenarios - for the other Case-studies A and C, it was concluded that the project would never be economically advantageous. In Table 8.17, it was presented the profitability indicators for the profitable scenarios of the Case-study B. The Scenario B.7-TR and the Scenario B.7-SER were the more profitable projects, presenting a return time of 1 year. For these scenarios, the IRR for the process with a TR is 126 % and for the process with SERs is 127 %; the NPVs are, respectively, approximately 19 million € and 21 million €.

Finally, it is important to emphasize several points in this techno-economic study:

- Some government and/or European financial support (national and/or European Union funds) may help in the initial investment of the technology as it is a solution to address an environmental problem;
- Although Case-studies A and C are economically unviable, it is worth taking into account the solution of the OMW problem. So, even if the technology works in a regime that is not economically viable, the resolution for this environmental problem will always be safeguarded;
- The cooling water used as a utility can be applied in olive oil production. In other words, it is possible to consider that this utility does not add an additional expense for the company. For instance, the cooling water that is heated in the HEs can be used in the process of the olive oil production (for instance, the cleaning of the olive oil mill);
- Only the main process units were designed, though more process units may need to be upgraded or added to the project. However, to eliminate these possible needs, a considerable percentage of capital was directed for the non-designed equipment (30 % of the designed equipment) and contingencies (6 % of the FCI) - see subchapter 8.4.1.1.

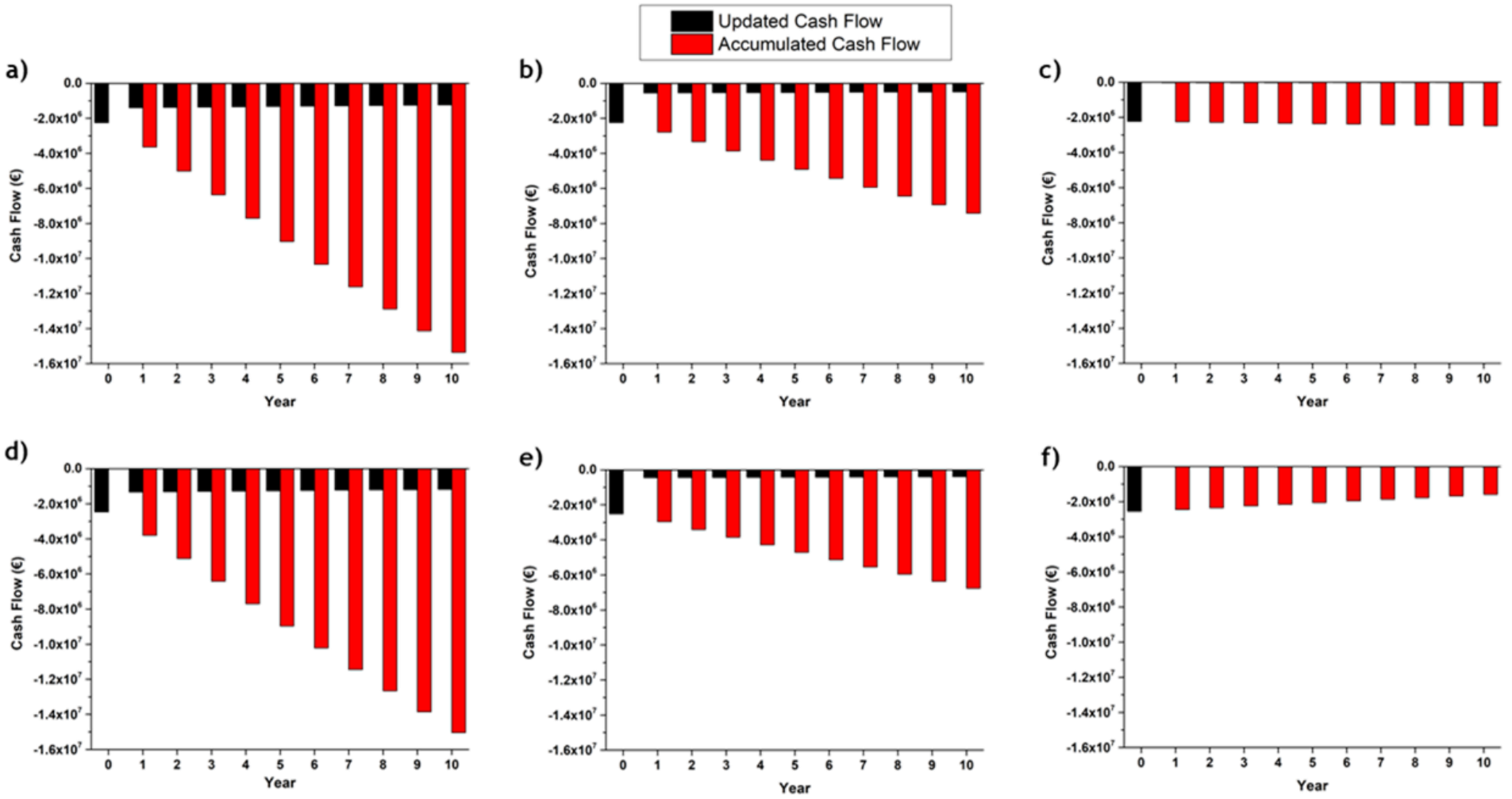

Fig. 8.8. Cash Flow Updated (red) and Accumulated Cash Flow (black) for Case-study A: a) A.1, b) A.2 and c) A.3 using a TR; d) A.1, e) A.2 and f) A.3 using a SER.

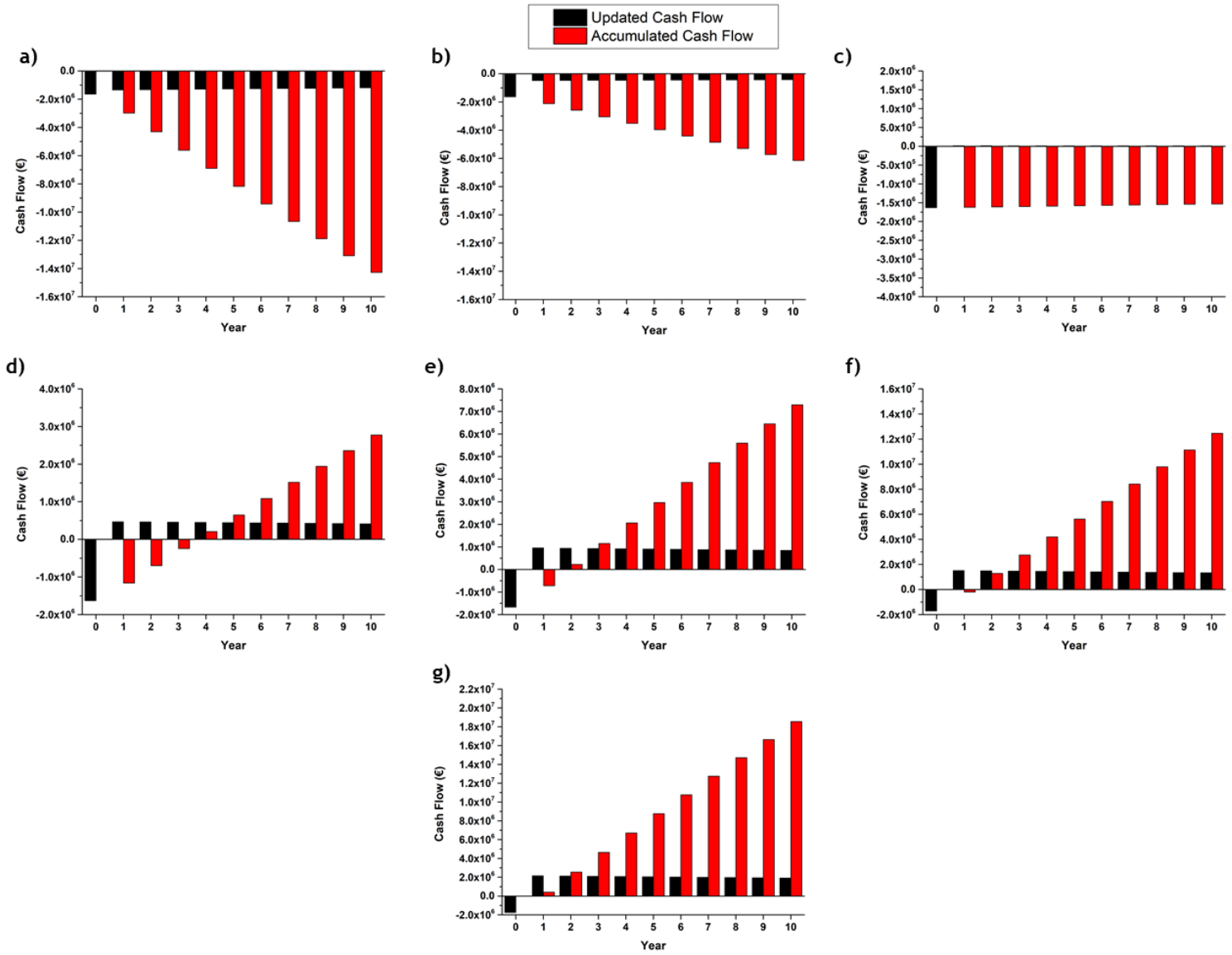

Fig. 8.9. Cash flow updated (red) and accumulated cash flow (black) for Case-study B using a TR: a) B.1, b) B.2, c) B.3, d) B.4, e) B.5, f) B.6 and g) B.7.

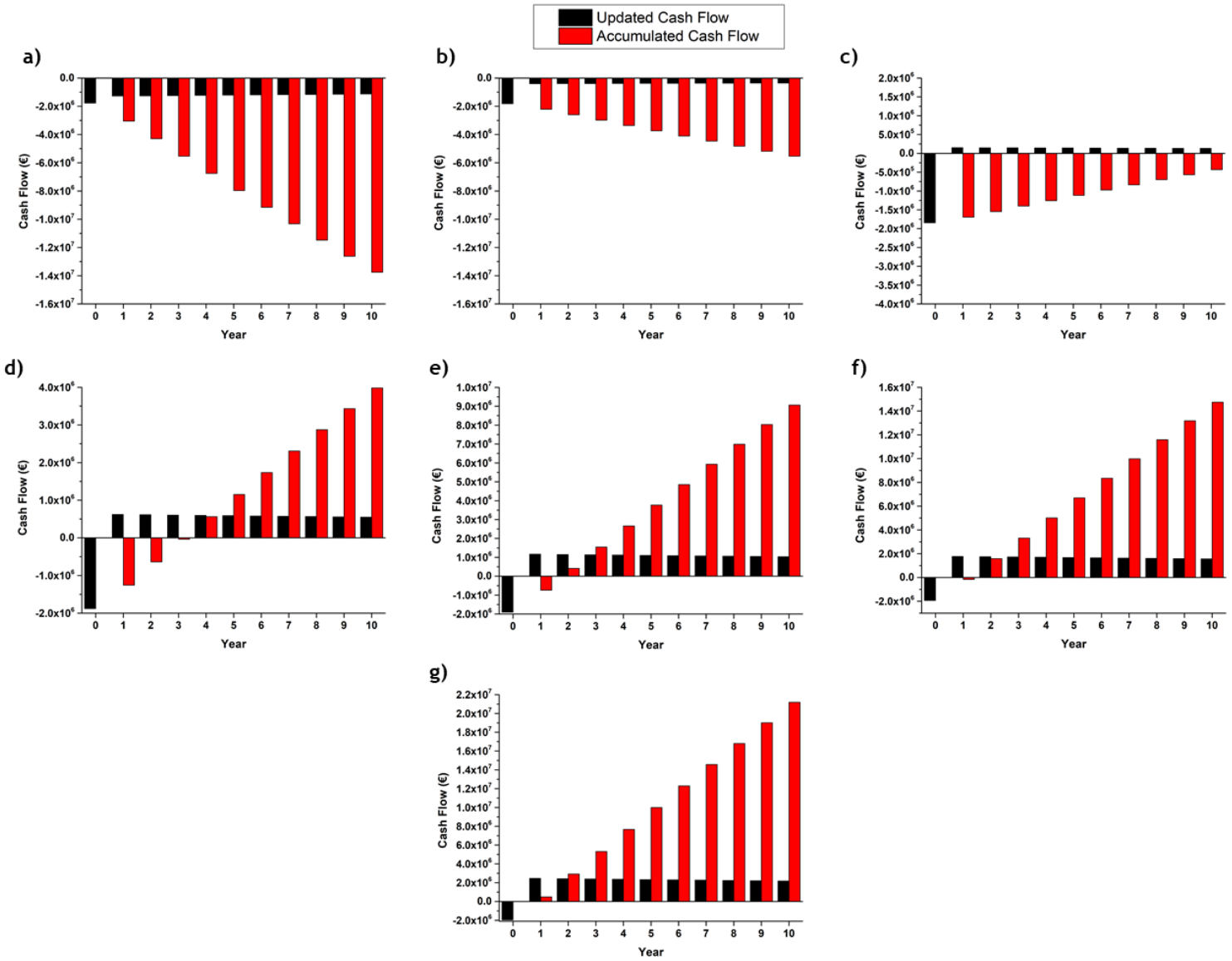

Fig. 8.10. Cash flow updated (red) and accumulated cash flow (black) for Case-study B using SERs: a) B.1, b) B.2, c) B.3, d) B.4, e) B.5, f) B.6 and g) B.7.

Table 8.17 - Determination of profitability indicators for Case-study B.

	TR							SER						
	B.1	**B.2**	**B.3**	**B.4**	**B.5**	**B.6**	**B.7**	**B.1**	**B.2**	**B.3**	**B.4**	**B.5**	**B.6**	**B.7**
Net Present Value (€)	-	-	-	2 773 770	7 292 928	12 463 080	18 542 988	-	-	-	3 982 891	9 061 228	14 751 295	21 184 894
IRR (%)	-	-	-	26	57	89	126	-	-	-	31	62	93	127
Return Time (years)	-	-	-	4	2	2	1	-	-	-	4	2	2	1

8.5. Conclusions

This work reports a techno-economic analysis of the OMWSR process in a TR or in SERs. It was verified that the quantity of water in the feed and the reactor configuration selected affect the economic state of the project over time: lower water contents in the OMW effluent and the utilization of SERs in parallel allow to obtain the most economically advantageous project. Moreover, the utilization of lower total pressures (in the range 1-4 bar) increases very slightly the project attractiveness from an economic point of view. Finally, it was also concluded that the project is more profitable when the process operates during all the year.

To sum up, Scenario B.7 (the OMWSR process occurs during all the year, at 400 ºC and 1 bar, and the content of water in the OMW feed is 60 wt.%) was the more profitable scenario, exhibiting a return time of only 1 year for both reactor configurations (TR or SERs). For this scenario, the IRR for the process with the TR is 126 % and with SERs is 127 %; the NPVs are, respectively, approximately 19 million € and 21 million €.

Notation and Glossary

List of Symbols

C_{Boiler}	Boiler cost ($)
C_{C}	Carcass cost ($)
C_{HE}	Heat exchanger cost ($)
C_{PL}	Platforms and ladders costs ($)
C_{r}	Safety thickness (in)
D_{i}	Internal diameter (ft)
E	Weld resistance (dimensionless)
F_{M}	Material factor (dimensionless)
I	Chemical engineering plant cost index (dimensionless)
L	Height or length (ft)
n	Number of years elapsed since the beginning of the project (dimensionless)
P	Pressure (psig)
Q	OMW volume flow rate ($L \cdot h^{-1}$)
r_{i}	Internal radius (in)
S	Tension (psig)
t_{s}	Vessel thickness (in)
V	Volume (L)
W	Weight (lb)
ϵ	Porosity (dimensionless)
τ	Residence time (h)

List of Acronyms

CI	Capital Investment
FCI	Fixed capital investment
HE	Heat Exchanger
HTC	Hydrotalcite
IRR	Internal rate of return
NPV	Net Present Value
OMW	Olive oil mill wastewater
OMWSR	Olive oil mill wastewater steam reforming
SER	Sorption-enhanced reactor
TR	Traditional reactor
WGS	Water-gas shift reaction

References

[1] Rocha, C., M.A. Soria and L.M. Madeira, Steam reforming of olive oil mill wastewater with in situ hydrogen and carbon dioxide separation - Thermodynamic analysis. Fuel, 2017. 207: p. 449-460.

[2] Leal, A.L., M.A. Soria and L.M. Madeira, Autothermal reforming of impure glycerol for H2 production: Thermodynamic study including in situ CO2 and/or H2 separation. International Journal of Hydrogen Energy, 2016. 41(4): p. 2607-2620.

[3] Ram Reddy, M.K., Z.P. Xu, G.Q. Lu and J.C. Diniz da Costa, Layered Double Hydroxides for CO2 Capture: Structure Evolution and Regeneration. Industrial & Engineering Chemistry Research, 2006. 45(22): p. 7504-7509.

[4] Wang, Q., H.H. Tay, D.J.W. Ng, L. Chen, Y. Liu, J. Chang, Z. Zhong, J. Luo and A. Borgna, The Effect of Trivalent Cations on the Performance of Mg-M-CO3 Layered Double Hydroxides for High-Temperature CO2 Capture. ChemSusChem, 2010. 3(8): p. 965-973.

[5] Reichle, W.T., S.Y. Kang and D.S. Everhardt, The nature of the thermal decomposition of a catalytically active anionic clay mineral. Journal of Catalysis, 1986. 101(2): p. 352-359.

[6] Yang, W., Y. Kim, P.K.T. Liu, M. Sahimi and T.T. Tsotsis, A study by in situ techniques of the thermal evolution of the structure of a Mg-Al-CO3 layered double hydroxide. Chemical Engineering Science, 2002. 57(15): p. 2945-2953.

[7] Avasthi, K.S., R.N. Reddy and S. Patel, Challenges in the Production of Hydrogen from Glycerol - A Biodiesel Byproduct Via Steam Reforming Process. Procedia Engineering, 2013. 51: p. 423-429.

[8] Dou, B., Y. Song, C. Wang, H. Chen and Y. Xu, Hydrogen production from catalytic steam reforming of biodiesel byproduct glycerol: Issues and challenges. Renewable and Sustainable Energy Reviews, 2014. 30: p. 950-960.

[9] Rocha, C., M.A. Soria and L.M. Madeira, Screening of commercial catalysts for steam reforming of olive mill wastewater. Renewable Energy, 2021. 169: p. 765-779.

[10] Rocha, C., M.A. Soria and L.M. Madeira, Use of Ni-containing catalysts for the Olive Mill Wastewater Steam Reforming (Submitted). Applied Catalysis B: Environmental, 2021: p. 765-779.

[11] Rocha, C., M.A. Soria and L.M. Madeira, Olive mill wastewater valorization through steam reforming using hybrid multifunctional reactors for high-purity H2 production (Submitted). Chemical Engineering Journal, 2021.

[12] Nasr, B., B. Ahmed and G. Abdellatif, Fenton treatment of olive oil mill wastewater-applicability of the method and parameters effects on the degradation process. Journal of Environmental Sciences, 2004. 16: p. 942-944.

[13] Katsoyannos, E., A. Hatzikioseyian, E. Remoundaki and M. Tsezos, Photocatalytic treatment of olive mill wastewaters (OMW) in pilot scale, in 13th International Symposium on Pollution and its Impact on Life in Mediterranean Region. 2005, National Technical University of Athens Greece.

[14] Tosti, S., C. Accetta, M. Fabbricino, M. Sansovini and L. Pontoni, Reforming of olive mill wastewater through a Pd-membrane reactor. International Journal of Hydrogen Energy, 2013. 38(25): p. 10252-10259.

[15] Gebreyohannes, A.Y., R. Mazzei and L. Giorno, Trends and current practices of olive mill wastewater treatment: Application of integrated membrane process and its future perspective. Separation and Purification Technology, 2016. 162: p. 45-60.

[16] Serra, O.d., Azeite de A a Z. 2020 14-05-2020]; Available from: https://www.oliveiradaserra.pt/pt/oliveira-da-serra/oliveira-da-serra/.

[17] Caputo, A.C., F. Scacchia and P.M. Pelagagge, Disposal of by-products in olive oil industry: waste-to-energy solutions. Applied Thermal Engineering, 2003. 23(2): p. 197-214.

[18] Allouche, N., I. Fki and S. Sayadi, Toward a High Yield Recovery of Antioxidants and Purified Hydroxytyrosol from Olive Mill Wastewaters. Journal of Agricultural and Food Chemistry, 2004. 52(2): p. 267-273.

[19] El-Abbassi, A., H. Kiai and A. Hafidi, Phenolic profile and antioxidant activities of olive mill wastewater. Food Chemistry, 2012. 132(1): p. 406-412.

[20] Daâssi, D., J. Lozano-Sánchez, I. Borrás-Linares, L. Belbahri, S. Woodward, H. Zouari-Mechichi, T. Mechichi, M. Nasri and A. Segura-Carretero, Olive oil mill wastewaters: Phenolic content characterization during degradation by Coriolopsis gallica. Chemosphere, 2014. 113: p. 62-70.

[21] Aggoun, M., R. Arhab, A. Cornu, J. Portelli, M. Barkat and B. Graulet, Olive mill wastewater microconstituents composition according to olive variety and extraction process. Food Chemistry, 2016. 209: p. 72-80.

[22] Esteves, B.M., C.S.D. Rodrigues and L.M. Madeira, Synthetic olive mill wastewater treatment by Fenton's process in batch and continuous reactors operation. Environmental Science and Pollution Research, 2018. 25(35): p. 34826-34838.

[23] Rocha, C., M.A. Soria and L.M. Madeira, Thermodynamic analysis of olive oil mill wastewater steam reforming. Journal of the Energy Institute, 2018.

[24] Mignard, D., Correlating the chemical engineering plant cost index with macro-economic indicators. Chemical Engineering Research and Design, 2014. 92(2): p. 285-294.

[25] S., J., Chemical engineering plant cost index: 2018 annual value. 2018; Available from: http://www.chemengonline.com/2019-cepci-updates-january-prelim-and-december-2018-final/.

[26] Vatavuk, W.M., Updating the CE plant cost index. Chemical Engineering, 2002. 109: p. 62-70.

[27] Sinnott, R. and G. Towler, Chapter 6 - Costing and Project Evaluation, in Chemical Engineering Design (Sixth Edition), R. Sinnott and G. Towler, Editors. 2020, Butterworth-Heinemann. p. 275-369.

[28] Seider, W.D., J.D. Seader and D.R. Lewin, Product and Process design principles: synthesis, analysis, and evaluation. 2004, New York: John Wiley & Sons, Limited.

[29] Coutinho, M.M., Characterization and scale-down of flow reactors for applications at small-scale manufacturing. 2017, Instituto Superior Técnico.

[30] Boiling-point elevation, in Encyclopedic Dictionary of Polymers, J.W. Gooch, Editor. 2007, Springer New York: New York, NY. p. 120-120.

[31] Perry, R.H. and D.W. Green, Perry's chemical engineers' handbook. 8th edition ed. 2008, New York: McGraw-Hill.

[32] Turton, R., R.C. Bailie, W.B. Whiting and J.A. Shaeiwitz, Analysis, synthesis and design of chemical processes. 2008: Pearson Education.

[33] Peters, M.S. and K.D. Timmerhaus, Plant Design and Economics for Chemical Engineers. 4th ed. 1991, New York: McGraw-Hill.

[34] Borja, R., F. Raposo and B. Rincón, Treatment technologies of liquid and solid wastes from two-phase olive oil mills. Grasas y Aceites, 2006. 57(1): p. 32-46.

[35] Galp, Tarifário Gás Natural 2020 18-05-2020]; Available from: https://www.galpenergia.com/PT/ProdutosServicos/GasNatural/Mercado-Regulado/Tarifario/Paginas/Tarifario.aspx?tipoUtilizacao=1.

[36] Silva, J.M., M.A. Soria and L.M. Madeira, Challenges and strategies for optimization of glycerol steam reforming process. Renewable and Sustainable Energy Reviews, 2015. 42: p. 1187-1213.

[37] Llorca, J., V.C. Corberán, N.J. Divins, Raquel O. Fraile and E. Taboada, Chapter 7 - Hydrogen from Bioethanol, in Renewable Hydrogen Technologies, L.M. Gandía, G. Arzamendi and P.M. Diéguez, Editors. 2013, Elsevier: Amsterdam. p. 135-169.

[38] Portugal, G.o., Imposto sobre o Rendimento das Pessoas Coletivas (IRC) em Portugal. 2021 23-06-2021]; Available from: https://eportugal.gov.pt/cidadaos-europeus-viajar-viver-e-fazer-negocios-em-portugal/impostos-para-atividades-economicas-em-portugal/imposto-sobre-o-rendimento-das-pessoas-coletivas-irc-em-portugal.

Chapter 9. Conclusions and Future Work

This chapter presents the general conclusions of this PhD thesis, some of its limitations and perspectives of future work.

9.1. Conclusions

This PhD thesis was focused on the valorization of olive oil mill wastewater (OMW), by means of H_2 production through OMW steam reforming (OMWSR), particularly envisaging to assess the potential of using a hybrid multifunctional sorption-enhanced membrane reactor (SEMR). OMW is a polluting effluent derived from the production of olive oil. To reduce this environmental problem, several treatment/valorization methods are used, but these processes have in general low efficiency and cost problems. Due to this, OMWSR seems to be a good solution, since it decreases the pollutant load of the OMW and, at the same time, the waste is valorized with the production of H_2.

A thermodynamic analysis was first performed to study the effects of several variables on the OMWSR process with in situ H_2 and/or CO_2 separation; such variables include the temperature, the pressure, the content of water in the feed, the initial OMW composition and the removal fractions of H_2 and/or CO_2. For this analysis, it was considered the utilization of a traditional reactor (TR), a sorption-enhanced reactor (SER), a membrane reactor (MR) or a SEMR. It was found that the H_2 yield increases with the temperature up to a maximum value and then decreases, while it continuously decreases with the pressure. In opposition, higher water content in the feed and an improved H_2 removal or CO_2 removal allow reaching a higher yield of H_2. The best operating conditions for each OMW composition were determined, being also found that coke formation increases with decreasing temperature and water content in the feed. At 500 °C, 1 bar, 60 wt.% of water in the feed, fCO_2 = 0.99 and fH_2 = 0.80, the H_2 yield was 13.42 (close to the maximum theoretical value of 13.54, for a certain OMW composition). Even though the SEMR presents a higher H_2 yield than the SER and the MR, the improvement is not very high at 500 ºC; an increase of 31 and 15% respectively. At the same operation conditions, in comparison with the TR, the H_2 production increases by 141%. However, these differences become much bigger at lower operation temperatures, where the benefits of the SEMR become even more notorious.

Then, it was investigated the effect of the compensating anions used in the synthesis of hydrotalcites (HTCs) on the CO_2 sorption performance. It was found that the sorption capacities are related with the interlayer distance (determined by X-ray powder diffraction) of the HTCs. Besides that, the effects on the CO_2 sorption capacity of the Al^{3+} partial substitution with Ga^{3+} and of the impregnation with potassium were studied. It was verified that, by doping the HTC-CO_3 with 20 wt.% of potassium, the sorption capacity was increased, up to 1.43 mmol·g^{-1} (@p_{CO_2}= 1 bar and 300 ºC); additionally, it was also confirmed that the Ga^{3+} partial substitution also slightly enhanced the sorption capacity of this material. Despite these results, the substitution of Al^{3+} by Ga^{3+} was not positive for the HTCs with the *long* species (triacetoxyborohydride) as interlayer anion precursor. Furthermore, it was possible to verify that the compensating anion affects also the CO_2 sorption mechanism, and that the presence of steam has a negative effect on the performance of all sorbents with the base formulation HTC-long.

Lastly, the sorption kinetics for all the samples was evaluated considering a model which includes two kinetic contributions (slow and fast) being concluded that the interlayer anion, the presence of K and the substitution of Al^{3+} by Ga^{3+} influence the sorption kinetic parameters.

A catalyst screening study for the OMWSR was performed with commercial and prepared samples. Among all the materials, it was possible to emphasize the very high catalytic performance (in terms of H_2 yield, H_2 selectivity and total organic carbon (TOC) conversion) of the Ni-, Rh- and Ru-based catalysts. Besides that, it was confirmed that the HTC-based catalysts (in-house prepared - e.g. HTC[1]) activated at 650 ºC presented a higher performance in comparison with the same samples reduced at 350 ºC. It was found that the metallic surface area per mass of catalyst or surface area correlates well with the TOC conversion obtained in the experimental tests during OMWSR; a similar correlation was also observed with the quantity of acidic sites in the samples. Concerning the stability tests, it was possible to see that the commercial Rh catalyst presented a high and stable H_2 yield (9-10 $mol_{H2} \cdot mol^{-1}_{OMW}$) and TOC conversion (98-100%) during the 24 h of the experiment. The Ni-Ru catalyst also presented high H_2 yield in the 24 h long-term tests (always > 8 $mol_{H2} \cdot mol^{-1}_{OMW}$), constant TOC conversion (≈ 75 %) and low catalyst deactivation. Still, it was concluded that the HTC[1] catalyst reduced at 650 ºC presented a high H_2 yield (always > 8.5 $mol_{H2} \cdot mol_{OMW}^{-1}$) and TOC conversion (≈ 99 %) but only during the first 12 h; then, the material significantly deactivated due mostly to the amorphous coke produced. In this way, a strategy with periodic oxidative regeneration was revealed to be feasible to restore, completely or at least partially, the activity of the catalysts that suffered from coking.

A comparison of the performance between the different reactor configurations (TR, SER, MR and SEMR) was performed for the OMWSR process. It was observed that the TOC conversion remains practically complete along all the catalytic tests and it was verified an enhancement of the H_2 production during the CO_2 pre-breakthrough as compared to the TR, when using the sorption-enhanced reactors (SER/SEMR). However, a higher improvement in terms of H_2 yield was observed when the last multifunctional reactor configuration was applied. Actually, the maximum H_2 yield (11.50) was obtained using a SEMR at 400 ºC and 4 bar, close to the maximum attainable theoretical value (11.84), and above the thermodynamic limit for a TR (11.29). Besides, it was observed that the HTCs (used as CO_2 sorbents) catalyze the decomposition of OMW, tough to a low extent. Moreover, the utilization of the prepared K-doped HTC-CO_3 material, at 400 ºC and 4 bar, increases the formation of coke deposits on the catalyst surface and leads to a high deactivation due to the acidic sites present in the sorbent (responsible for the production of coke precursors). Nevertheless, the utilization of the commercial HTC MG30_K as CO_2 sorbent increased the stability of the catalyst due to the stronger inhibition of coke deposition. The removal of H_2 (with a commercial Pd-Ag-based perm-selective membrane) and CO_2 allowed to reach higher H_2 productions in the SEMR during the pre-breakthrough region in comparison with the other two reactor configurations. This allowed a simultaneous production

of highly pure H_2 in the retentate side and ultra-pure H_2 in the permeate side (in absence of the sweep gas). Therefore, in such conditions, if the SEMR is applied in a system with multiple columns that allows continuous operation in the pre-breakthrough region, a high amount of pure H_2 would be constantly achieved in both sides. It was also verified that after the CO_2 breakthrough, a decrease in performance was observed, but higher H_2 and CO_2 production in comparison to the SER and TR was still noticed due to continuous H_2 removal from the reaction medium (operation of the device as a MR). Lastly, it was demonstrated that the steam reforming technology, when applied in a SEMR, can efficiently handle real OMW streams, with high H_2 production, with practically complete remotion of the organic load. Still, this approach opens the pave for other oxygenated effluents.

Finally, this PhD work reports a techno-economic analysis of the OMWSR process in a TR or in SERs. It was verified that the quantity of water in the feed and the reactor configuration selected affect the economic state of the project over time: lower water contents in the OMW effluent and the utilization of SERs in parallel allow to obtain the most economically advantageous project. Moreover, the utilization of lower total pressures (in the range 1-4 bar) increases the project attractiveness from an economic point of view. Finally, it was also concluded that the project is more profitable when the process operates during all the year. To sum up, the Scenario B.7 was the more profitable scenario, exhibiting a return time of only 1 year for both reactor configurations (TR or SERs). For this case, the internal rate of return (IRR) for the process with the TR is 126 % and with SERs is 127 %; the net present values (NPVs) are, respectively, approximately 19 million € and 21 million €.

9.2. Limitations

In Chapter 4 it was observed that the potassium-doped gallium-substituted hydrotalcite presented higher sorption capacity than several hydrotalcites reported in the literature, especially commercial sorbents. However, the quantity of material that can be prepared per cycle is quite limited considering the amounts normally required to perform experiments in the SER and SEMR modules. It is necessary to create a proper preparation method to increase the amount of sorbent produced and establish a collaboration with companies acting in the field (e.g. Sasol) to circumvent this drawback. Still, a techno-economic analysis is suggested, particularly because the use of gallium provided minor improvements in terms of CO_2 sorption capacity.

In Chapters 5 and 6 was not possible to identify and quantify, in detail, the long-chain gaseous products produced during the steam reforming of the olive oil mill wastewater, due to equipment limitations. This is important to be complemented with an in-depth analysis of the liquid phase. Therefore, in subsequent studies, more elaborated analysis systems should be employed to identify

all the carbon-containing gaseous and liquid products to understand the mechanism of the reactions and to quantify the yield of these components, allowing also to close the mass balances.

In Chapter 6 it was used a total flowrate of olive oil mill wastewater of only 0.5 $mL \cdot min^{-1}$ due to limitations of the evaporation system, which is not prepared to evaporate a higher quantity of effluent. Still, the evaporation system presents several problems due to the production of solid residues on the walls of the pipes, leading to the clogging of the installation. Consequently, it was not possible to perform stability tests for longer periods, as the system stopped the evaporation. Therefore, the evaporation system needs to be improved, to evaporate a higher quantity of effluent in a stable manner and without creating operational problems.

Since there was not enough time to prepare a Pd-based membrane (COVID-19 crisis), a commercial membrane supplied by Tecnalia was used in Chapter 6. The use of in-house prepared membranes is a topic that could be further explored.

9.3. Perspectives

Following the limitations pointed in the previous subchapter, several perspectives of work to be developed in the near future might be considered.

For modeling and simulation of the OMWSR process, the kinetics of the reactions that occur in this process are necessary to be determined (for instance, the determination of the kinetics of the decomposition of the major oxygenate species). It will be necessary the study of the steam reforming of the individual components present in the OMW composition, or at least the major and more representative. Alternatively, and due to the complexity of such effluents, one may consider to follow only lumped parameters during the kinetic tests (e.g. TOC).

For future work, it is proposed the possibility of using organic anions as interlayer anions in the interlayer space of the HTCs (with long chain and stable in water), in order to increase the sorption capacity. Besides that, it is necessary to perform a cost-benefit analysis in order to select the most interesting HTC to use in CO_2 capture processes.

A deeper study to find an OMWSR catalyst more stable (less formation of amorphous coke) should be carried out, as this is a crucial issue for the successful implementation of these technologies. Besides that, it is important to study the relationship between price and performance of the catalysts. Finally, the utilization of hybrid dual-function materials (materials that catalyze the OMWSR reaction and, simultaneously, capture CO_2) should be considered as well, for the application in a SER or SEMR.

Furthermore, it will be interesting to prepare, characterize and test other Pd-based membranes to be applied in a MR or SEMR. Permeation tests and catalytic tests should be carried out in these reactor

configurations without sweep gas (to avoid the mass transfer resistance of the support) and downstream separation units; alternatively, it would be interesting to use steam as sweep gas in the permeation/catalytic tests.

Finally, the results obtained in this PhD thesis demonstrated that the tested multifunctional reactors seem to be promising for the valorization of OMW and potentially other oxygenated-containing streams, which of course should be tested as well. But, quite important, is also the test of the technologies at a higher TRL (technology readiness level), complemented with a deeper techno-economic and LCA (life cycle assessment) analysis.

Appendix A. Supporting Information for subchapter 4.1

1. Thermodynamic results

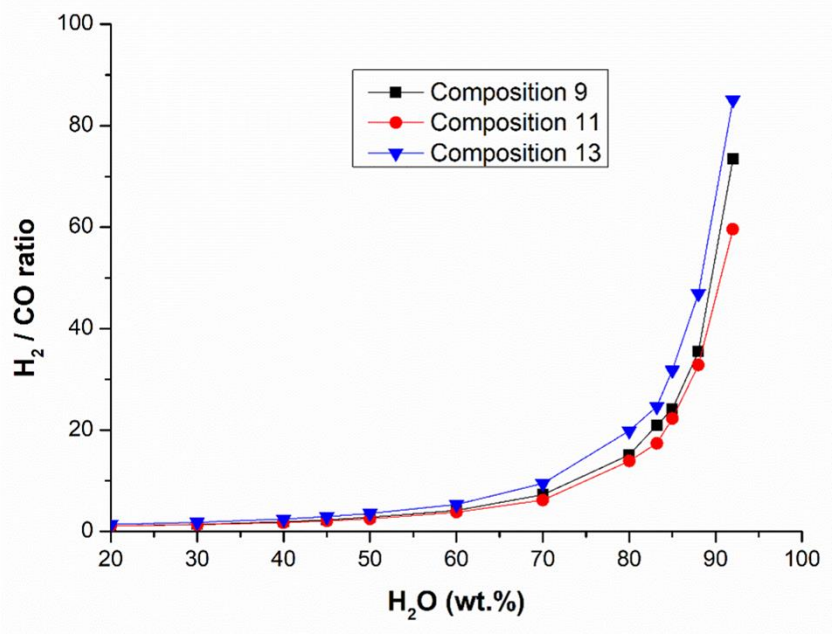

Fig. A.1. H_2/CO ratio in the thermodynamic equilibrium at 1 bar for different contents of water in the feed (wt.%) at operation temperatures that correspond to the maximum H_2 yield for Compositions #9, #11 and #13.

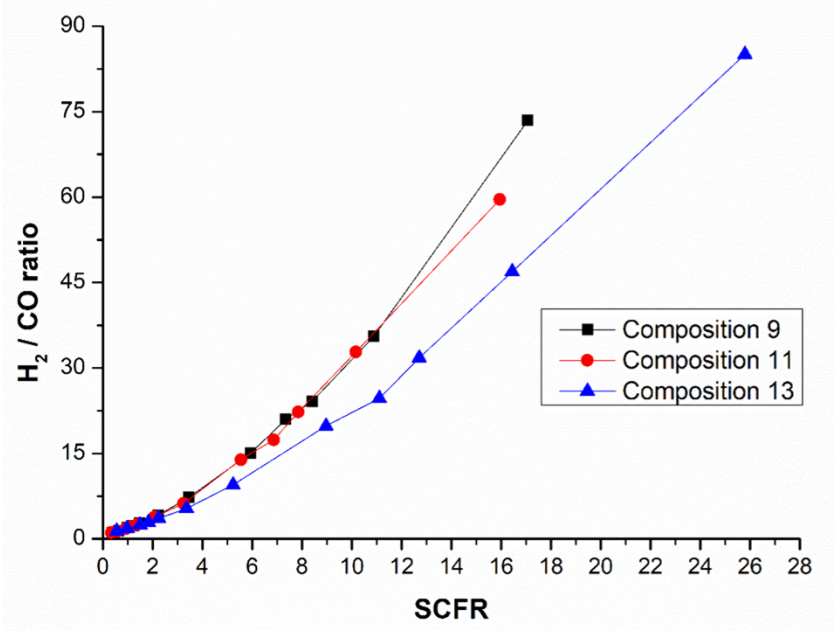

Fig. A.2. H_2/CO ratio in the thermodynamic equilibrium at 1 bar for different steam-to-carbon feed ratios (SCFRs) at operation temperatures that correspond to the maximum H_2 yield for Compositions #9, #11 and #13.

Appendix B. Supporting Information for subchapter 4.2

1. Thermodynamic results

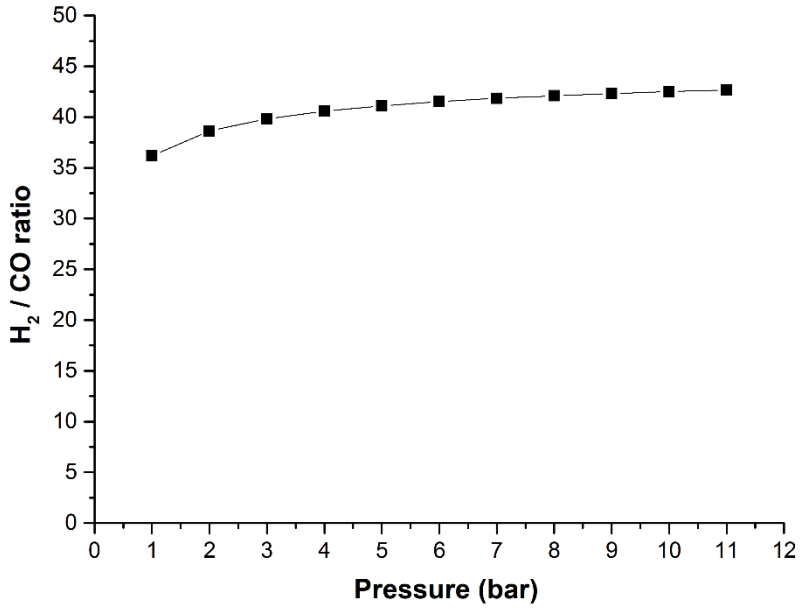

Fig. B.1. Molar ratio of H_2/CO as function of pressure, at 400 ºC with a content of water in the feed of 60 wt.% (SCFR = 2.1) - TR.

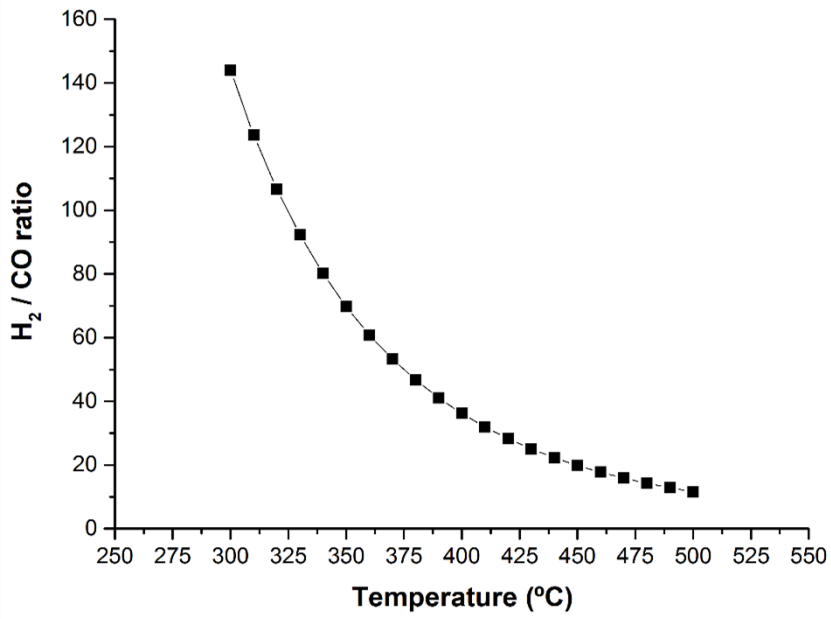

Fig. B.2. Molar ratio of H_2/CO as function of temperature, at 1 bar with a content of water in the feed of 60 wt.% (SCFR = 2.1) - TR.

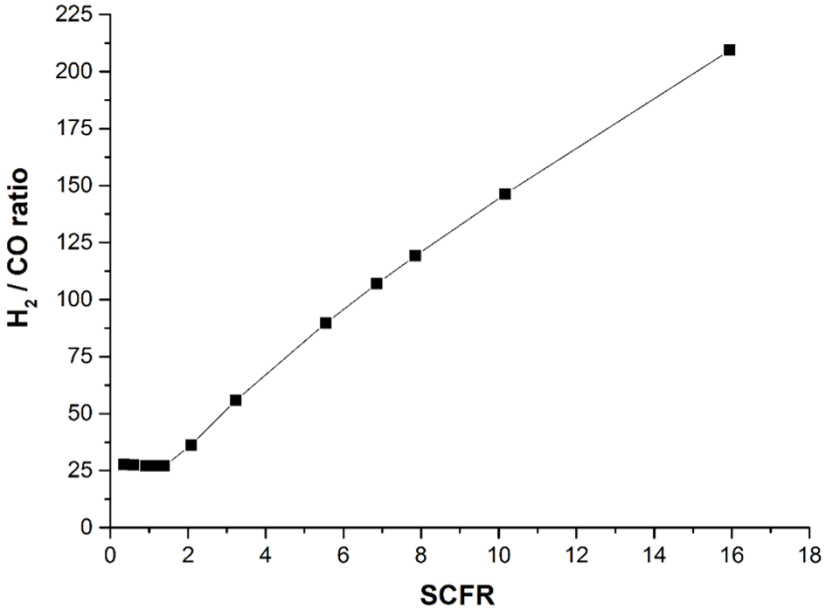

Fig. B.3. Molar ratio of H_2/CO as function of content of water in the feed (SCFR), at 1 bar and 400 ºC - TR.

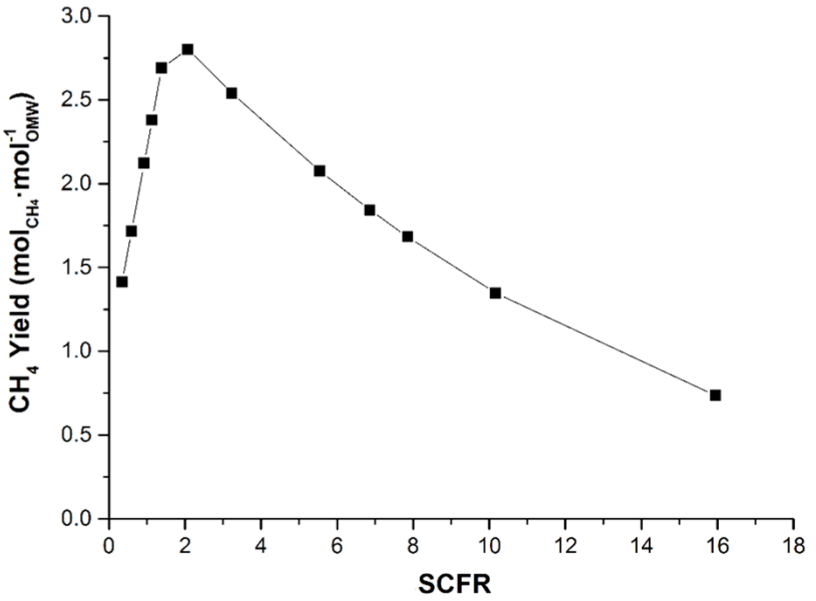

Fig. B.4. Yield of CH_4 as function of content of water in the feed (SCFR), at 1 bar and 400 ºC - TR.

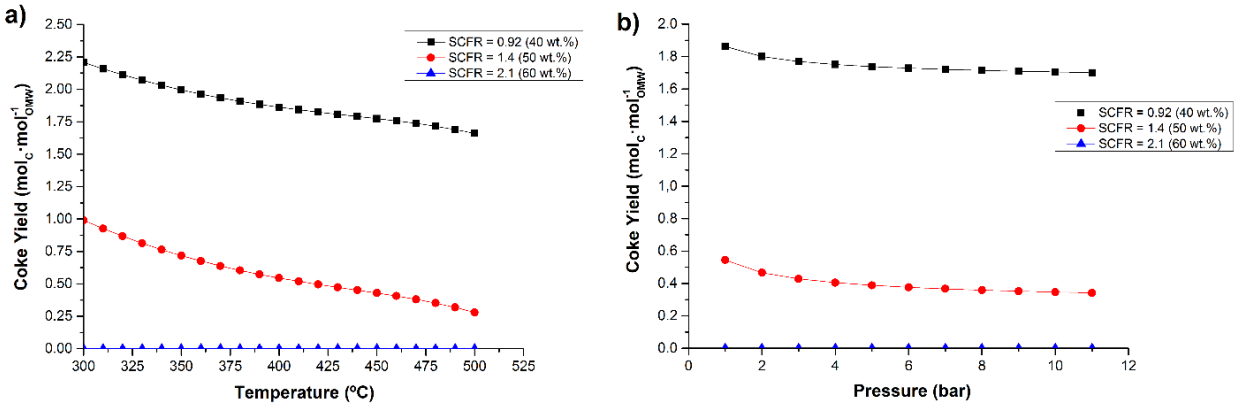

Fig. B.5. Yield of coke as a function of content of water in the feed (SCFR) and temperature, at 1 bar a) and as a function of content of water in the feed (SCFR) and pressure, at 400 ºC b) - TR.

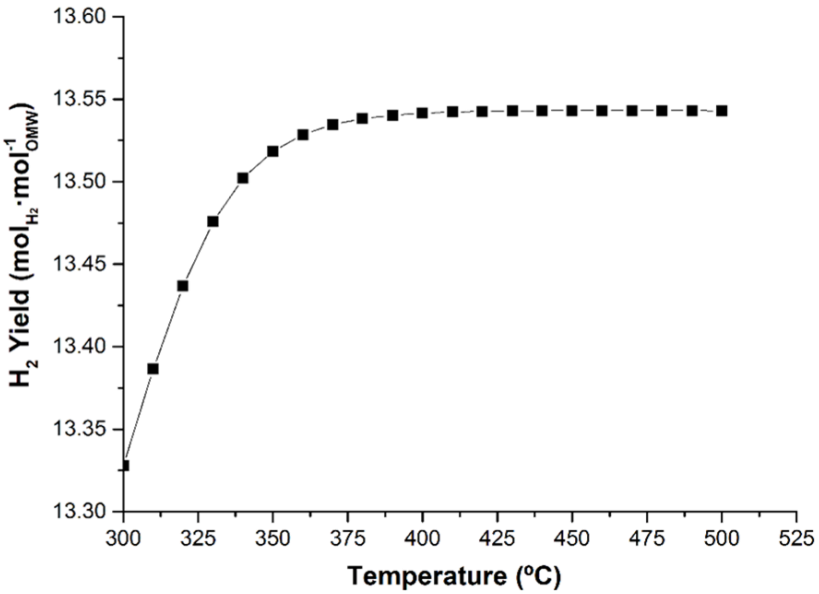

Fig. B.6. Yield of H_2 as function of temperature in a SEMR (fH_2 = 0.8 and fCO_2 = 0.99; CaO/OMW = 6.5), at 1 bar with 88 wt.% of water in the feed (SCFR = 10.2).

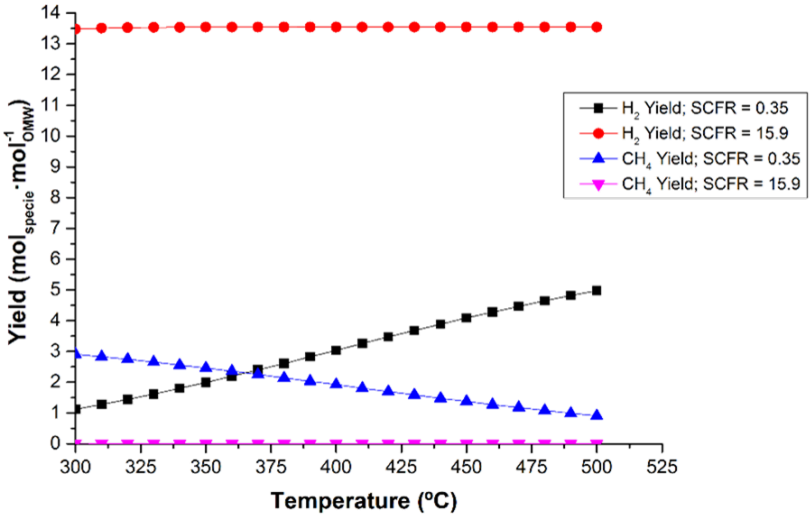

Fig. B.7. Yield of H_2 and yield of CH_4 as function of temperature and content of water in a SEMR (fH_2 = 0.8 and fCO_2 = 0.99; CaO/OMW = 3.5/6.5), at 1 bar.

Appendix C. Supporting Information for subchapter 5.1

1. Sorbent characterization

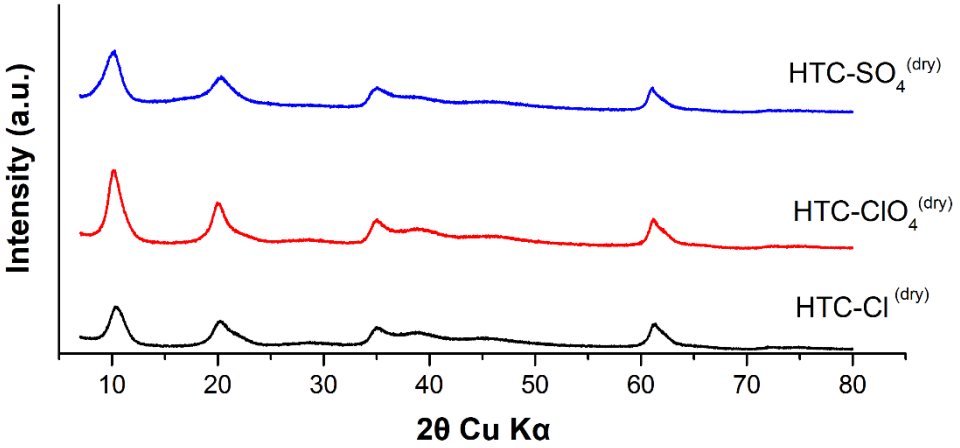

Fig. C.1. XRD patterns of dry samples of HTC-Cl, HTC-ClO_4 and HTC-SO_4. The curves have been vertically displaced for clarity.

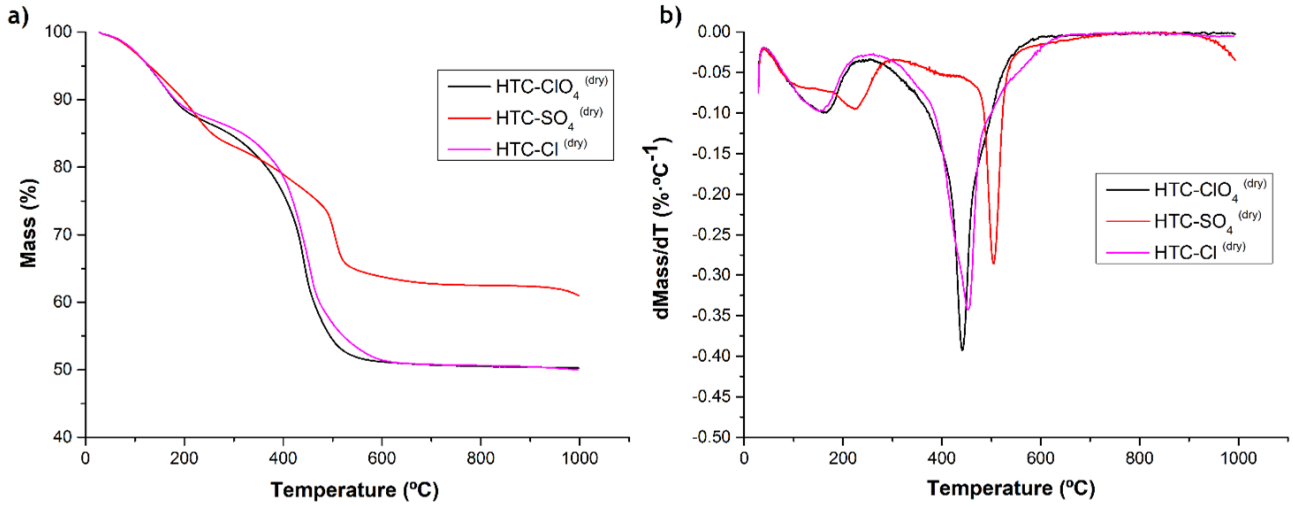

Fig. C.2. Thermogravimetric a) and derivative thermogravimetric b) analysis of the dry samples HTC-Cl, HTC-SO_4 and HTC-ClO_4.

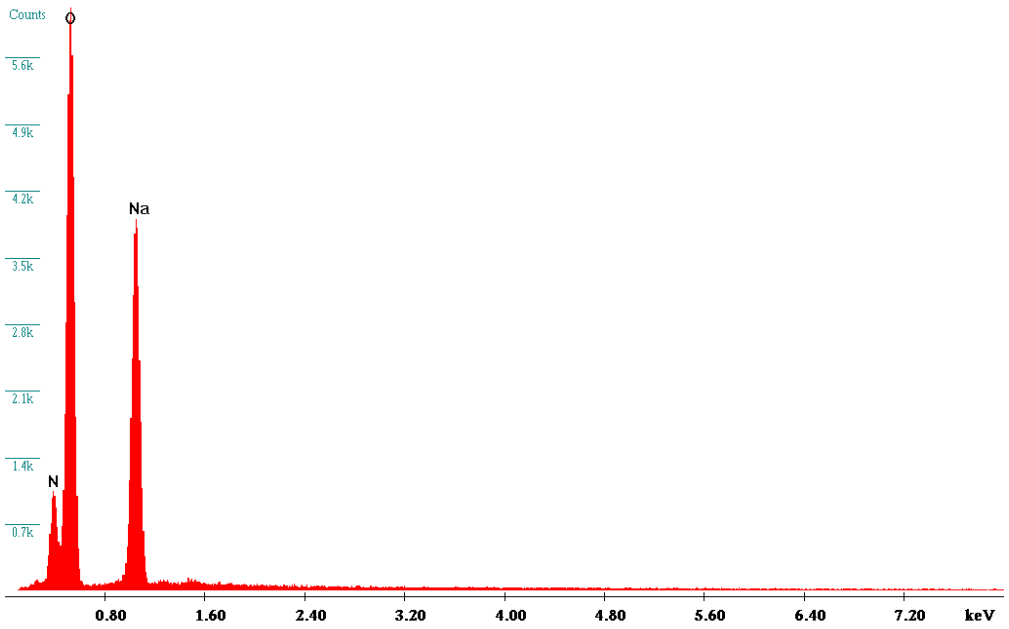

Fig. C.3. EDS analysis for the dry samples of HTC-long in the Z1 zone.

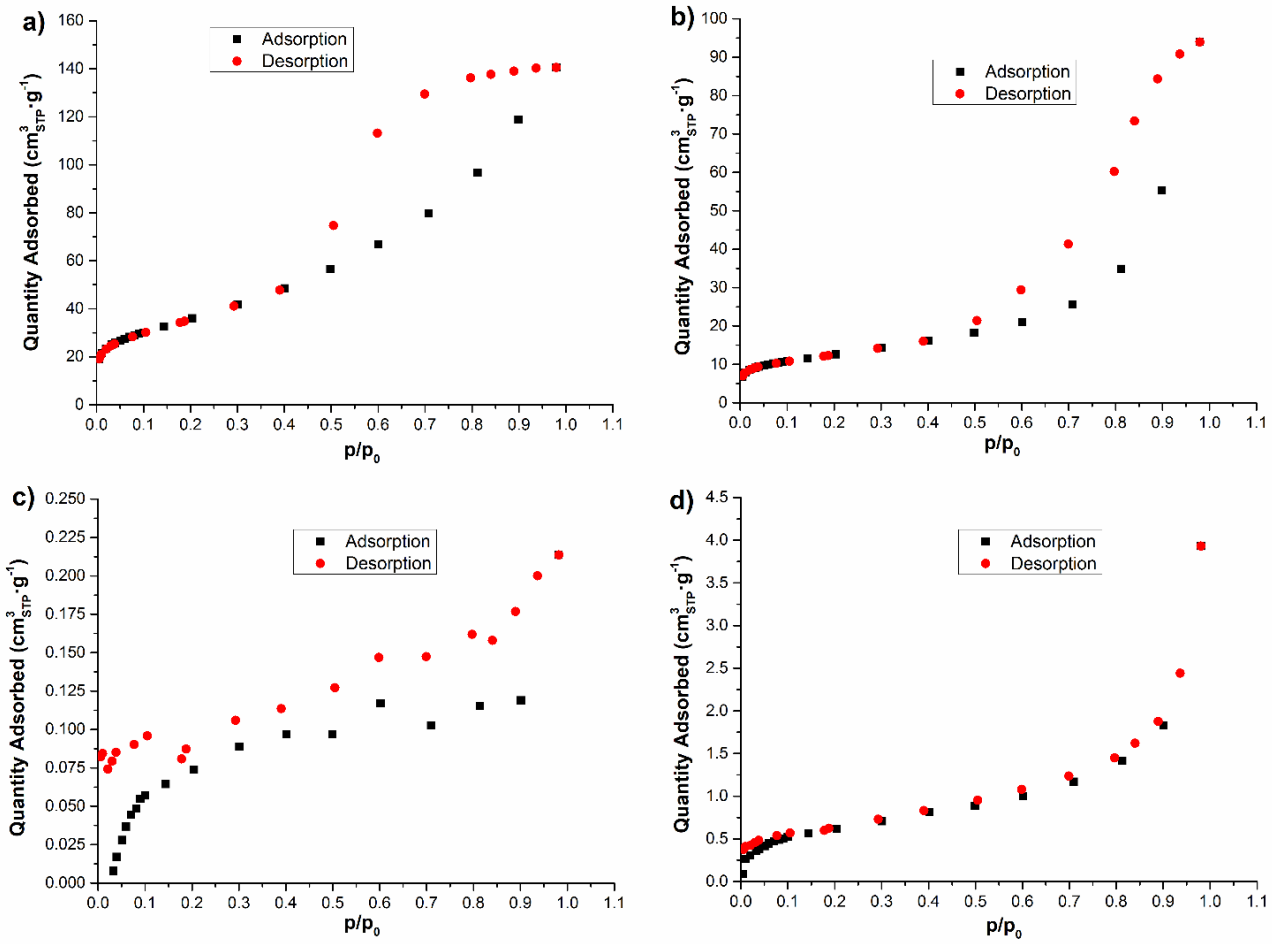

Fig. C.4. Adsorption/desorption isotherms of nitrogen over calcined samples: a) HTC-BrO3, b) HTC-Cl, c) HTC-ClO_4 and d) HTC-SO_4.

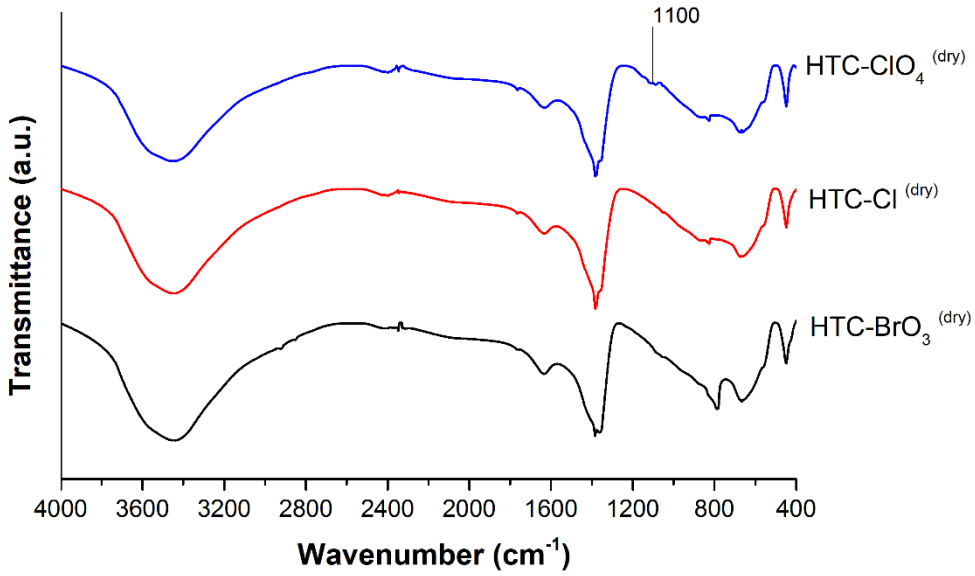

Fig. C.5. FTIR spectras for dry samples of HTC-ClO_4, HTC-Cl and HTC-BrO_3.

2. Adsorption tests

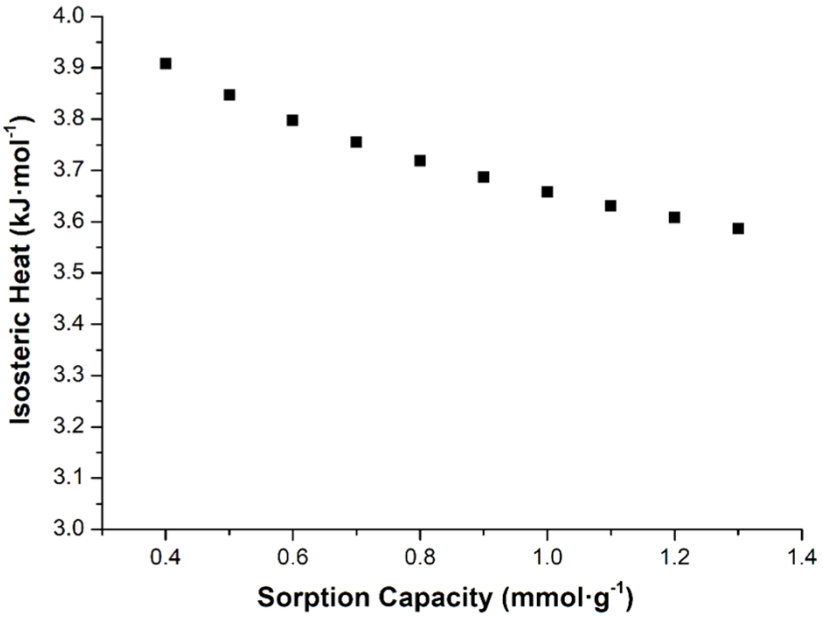

Fig. C.6. Isosteric heat of adsorption for different sorption capacities for HTC-CO_3.

Appendix D. Supporting Information for subchapter 5.2

1. Sorbent characterization

1.1. TG/DTG

The study of the mass variation in these runs was important, since the final mass of the sorbent in the packed-bed (in the dynamic tests) was used for the calculation of the sorption capacity.

In temperature program 1), it was analysed the decomposition of the dried samples in the range of 30-1000 ºC, to determine the optimum calcination temperature to use - Fig. D.1. The total mass loss in this temperature program is displayed in Table D.1, together with the temperatures at which DTG peaks appear. All samples present at least 2 types of DTG peaks related to the removal of water (close to 100 ºC), hydroxyl groups (in the range of 100-250 ºC) and peaks related to the removal of interlayer anions (higher than 250 ºC), as discussed in detail elsewhere [1, 2]. Depending on the compensating anion used, the DTG peak related to its removal was shifted to high or low temperatures (in the range of 380-560 ºC) - see Table D.1. For the HTC-long sample it was possible to identify a weak peak at 440 ºC, probably due to the small presence of CO_3^{2-} (anions with more affinity than the ones derived from the *long* anion to form this type of material in the preparation). As mentioned before, the dry samples were calcined at 400 ºC before the CO_2 sorption experiments, as this pre-treatment removes water and the interlayer anions obtaining hydrotalcite-derived mixed oxides (HDMOs).

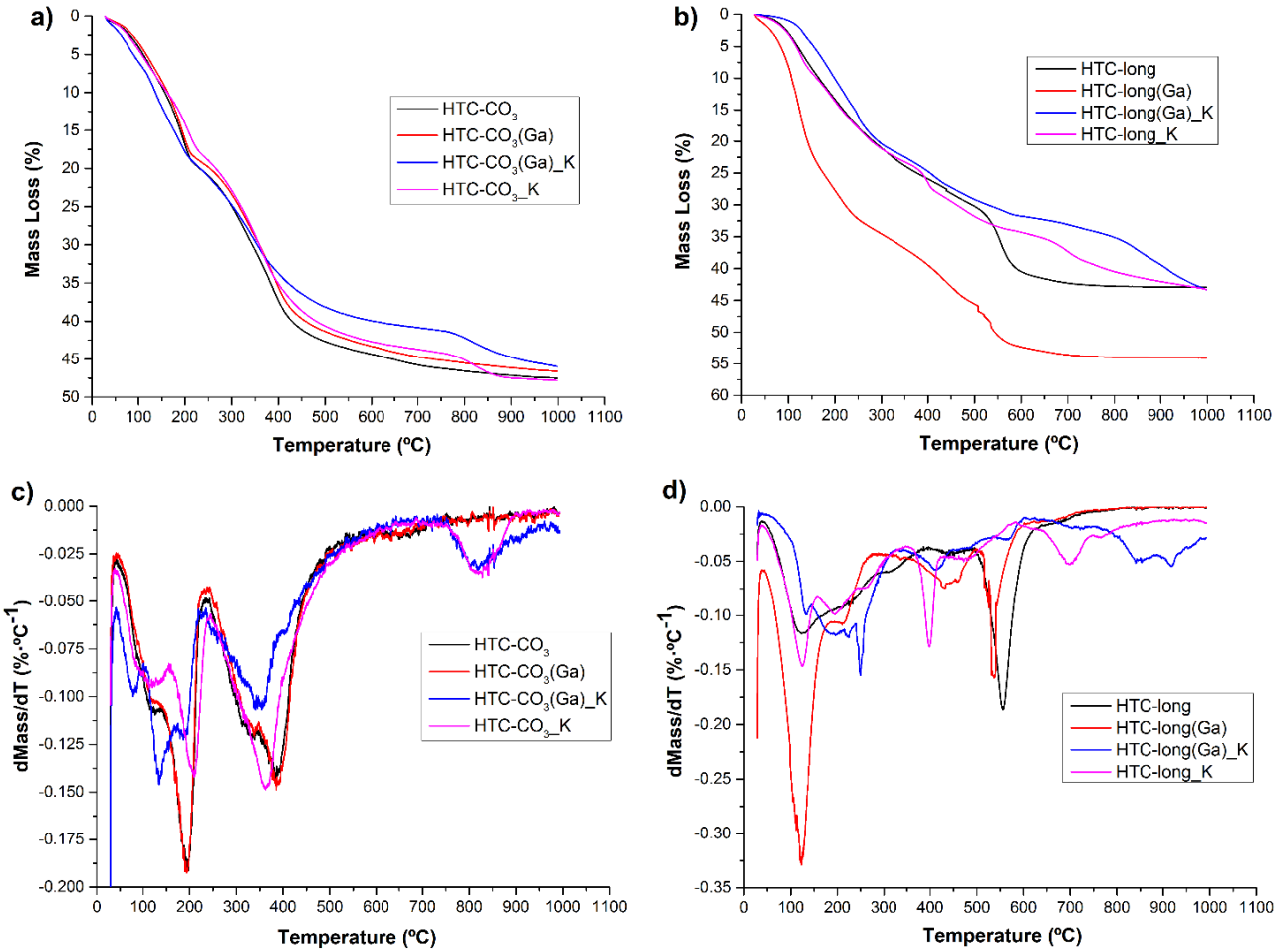

Fig. D.1. Thermogravimetric analysis a) of the dry samples with base formulation HTC-CO_3 and b) dry samples with base formulation HTC-long. Derivative thermogravimetric analysis c) of the dry samples with base formulation HTC-CO_3 and d) of the dry samples with base formulation HTC-long.

In the temperature program 2), it was verified if 2 h of calcination at 400 ºC is enough to obtain the derived mixed oxides, i.e., if the loss of mass is negligible after this time - for instance, for the HTC-long_K_{dry} sample (Fig. D.2), it was verified that the loss of mass after 2 h of calcination is almost negligible (< 2 %). Similar conclusions were obtained for the other samples.

In temperature program 3), it was analysed the loss of mass in the pre-treatments realized (at 300 and 400 ºC) in the calcined samples before the breakthrough experiments (dynamic tests). It was possible to verify that the total loss of mass was higher (increase between 1-5 %) at 400 ºC, since at this temperature all water and atmospheric CO_2 are removed from the sorbent (data not shown).

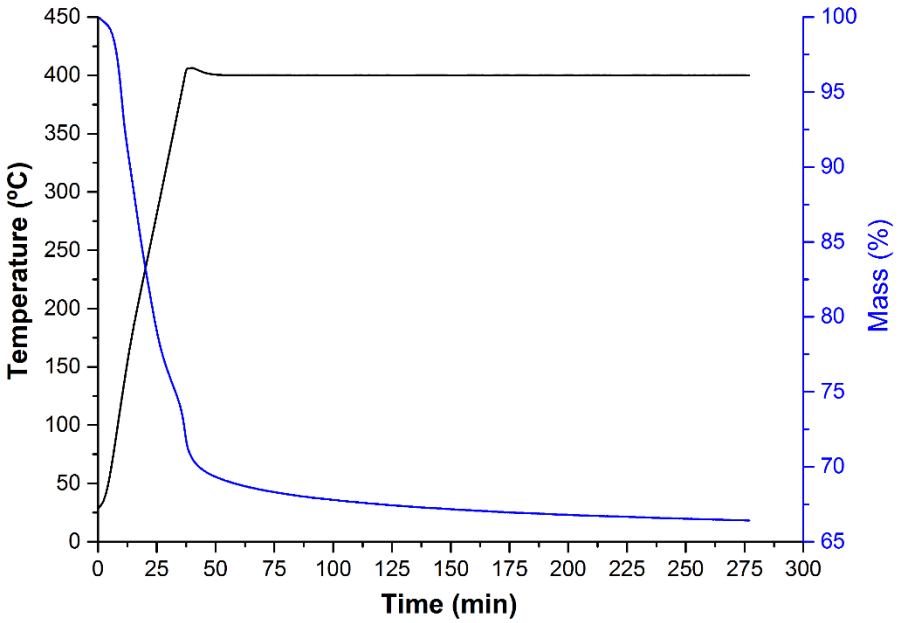

Fig. D.2. Thermogravimetric analysis of the dry samples for the HTC-long_K - calcination program.

Table D.1 - TG/DTG results for the prepared samples.

Sorbent	Total Mass Loss (%)	Temperature DTG Peaks (ºC)
HTC-CO_3 dry	47	115 / 190 / 380
HTC-CO_3_K dry	48	115 / 205 / 360
HTC-CO_3(Ga) dry	47	115 / 185 / 380
HTC-CO_3(Ga)_K dry	46	80 / 135 / 190 / 350 / 810
HTC-long dry	43	125 / 440/ 555
HTC-long_K dry	43	125 / 195 / 400 / 700
HTC-long(Ga) dry	54	122 / 430 / 530
HTC-long(Ga)_K dry	43	135 / 200 / 250 / 410 / 850 / 920

1.2. XRD

To verify if the materials prepared present the typical structures of HTCs and analyze the crystalline differences among them, the powder X-ray diffraction patterns (Fig. D.3) of several samples were made. While dry HTC-CO_3 series present typical structures of HTCs (lattice parameters: $a = b = 3.034 \pm 0.002$ Å and $c = 22.78 \pm 0.02$ Å), for the HTC-long sample the presence of different phases may be considered (with the same lattice parameters: $c = 32.0 \pm 0.5$ Å) related with the presence of triborate $[B_3O_3(OH)_4]^-$ and/or tetraborate $[B_4O_5(OH)_4]^{2-}$ anions), because both compensating anions exhibit characteristics peaks in the XRD patterns at the same 2θ values: ≈ 9, 16 and 24º [3, 4]; in this way, it was not possible to discard the presence of any of such anions.

In what concerns the dry HTC-long_K sample, several weak peaks recorded (at ≈ 20, 30 and 40 º) might be due to the formation of small amounts of K_2CO_3 - see Fig. D.3.The XRD pattern of the calcined HTC-long_K corresponds to mostly amorphous materials, where only weak and broad (at ≈ 30, 35 and 40 º) signals due to MgO and $Mg_{0.4}Al_{2.4}O_4$ were observed. After CO_2 sorption (in the static

tests), the XRD patterns (for HTC-long_K spent and HTC-CO_3(Ga)_K spent) showed important differences in comparison with both dry and calcined samples - Fig. D.3. Some peaks observed in the calcined HTC-long_K disappear when the sample was used. In addition, it was possible to verify that the XRD patterns of the spent samples (HTC-long_K and HTC-CO_3(Ga)_K) were different (especially at 2θ Cu Kα ≈ 45 º - see Fig. D.3b)) and present different phases. Despite the presence of CO_2 in the sorption tests, the original structure of the HTCs was not totally recovered, because the experiments with these samples were carried out in the absence of water, and thus the HTC-like structure could not be recovered.

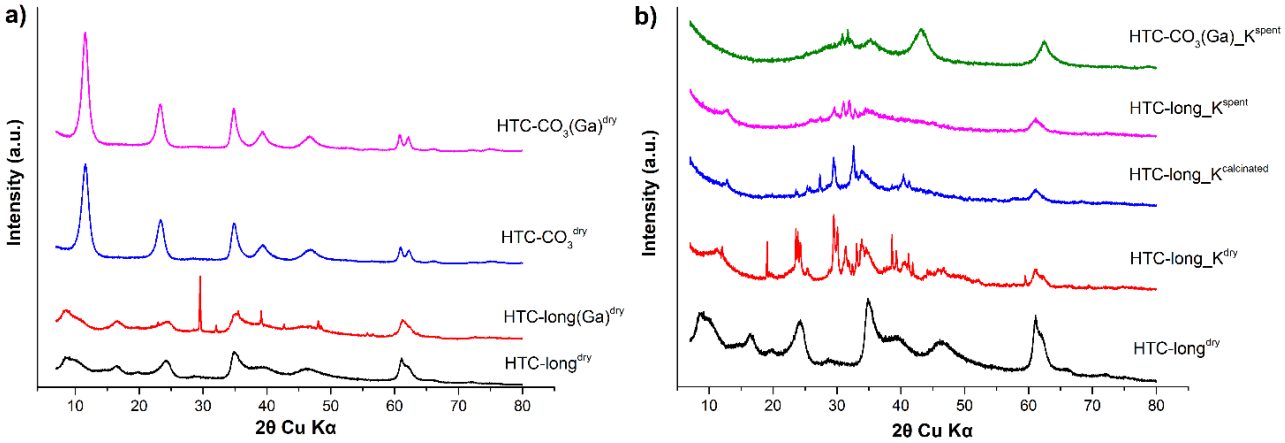

Fig. D.3. XRD patterns for a) dry samples of base formulations and for b) HTC-long_K and spent HTC-CO_3(Ga)_K samples in different states. The curves have been vertically displaced for clarity.

1.3. FTIR

FTIR analysis was performed to assess the presence of different interlayer anions in the dry samples and the effects resulting from the substitution of Al^{3+} by Ga^{3+} and the impregnation with potassium (see spectra in Fig. D.4). All spectra show an intense typical and broad band centered at 3455 cm^{-1}, due to the stretching mode of the hydroxyl groups, both from the brucite-like layers and the water molecules present in the interlayer, as well as on the external surface of the sorbent, as seen in previous works [1, 2]. The shoulder at 2900-3000 cm^{-1}, present mostly in the samples with base formulation HTC-CO_3, has been attributed [2, 5] to the stretching mode of interlayer hydroxyl groups hydrogen-bonded to carbonate species. In the samples with base formulation HTC-long, this shoulder was not very pronounced. The bending mode of the H_2O molecules is responsible for the weak band at ca. 1630 cm^{-1}, recorded for all samples. The v_3 mode of interlayer anions was responsible for the unique intense band recorded at 1350-1390 cm^{-1} for all samples.

Like in previous works [2], it can be observed for the samples with base formulation HTC-CO_3 that the band at 1380 cm^{-1} shows a shoulder at 1500 cm^{-1}, which can be related to the presence of carbonate species in two different sites with different interactions. However, it is not clear if the spectra for the samples with base formulation HTC-long present this shoulder. The other weaker bands below

1000 cm^{-1} correspond to the presence of the lattice bonds (Al-OH, Mg-OH, etc.). Interlayer anions slightly influence the peak intensity and positions of Al-O and Mg-O vibrations [6].

In the spectra of the samples with base formulation HTC-long, there are no traces of methyl group vibrations in the range 2750-3000 cm^{-1}, which proves that no acetate anions have been retained by the sorbent and, in this way, the only interlayer anion(s) present in the HTC-long samples was(were) $[B_3O_3(OH)_4]^-$ and/or $[B_4O_5(OH)_4]^2$. The presence of the anion(s) is noticed in some defined bands (e.g. at ≈ 1494, 1380 and 1150 cm^{-1}); however, in some samples, there are some characteristic bands associated with this species that are not very well defined (e.g. ≈ 950 cm^{-1}) [4]. Moreover, other characteristic bands of the interlayer anion(s) located below 1000 cm^{-1} (e.g at ≈ 450 cm^{-1}) could be overlapped with one of the bands related to the presence of lattice bonds [4]. Finally, it is worth mentioning that the substitution of Al^{3+} by Ga^{3+} did not change the spectra of the materials - see Fig. D.4. However, for the samples impregnated with potassium, several differences in the bands in the vicinity of 1000 cm^{-1} were observed (between 1220 and 600 cm^{-1}). This difference can be due to the higher surface basicity in these samples, allowing the sorption of CO_2 from the environment, leading to the formation of surface carbonate species. The weakness and the closeness of the bands expected for these different species make it difficult to identify the sorbed species.

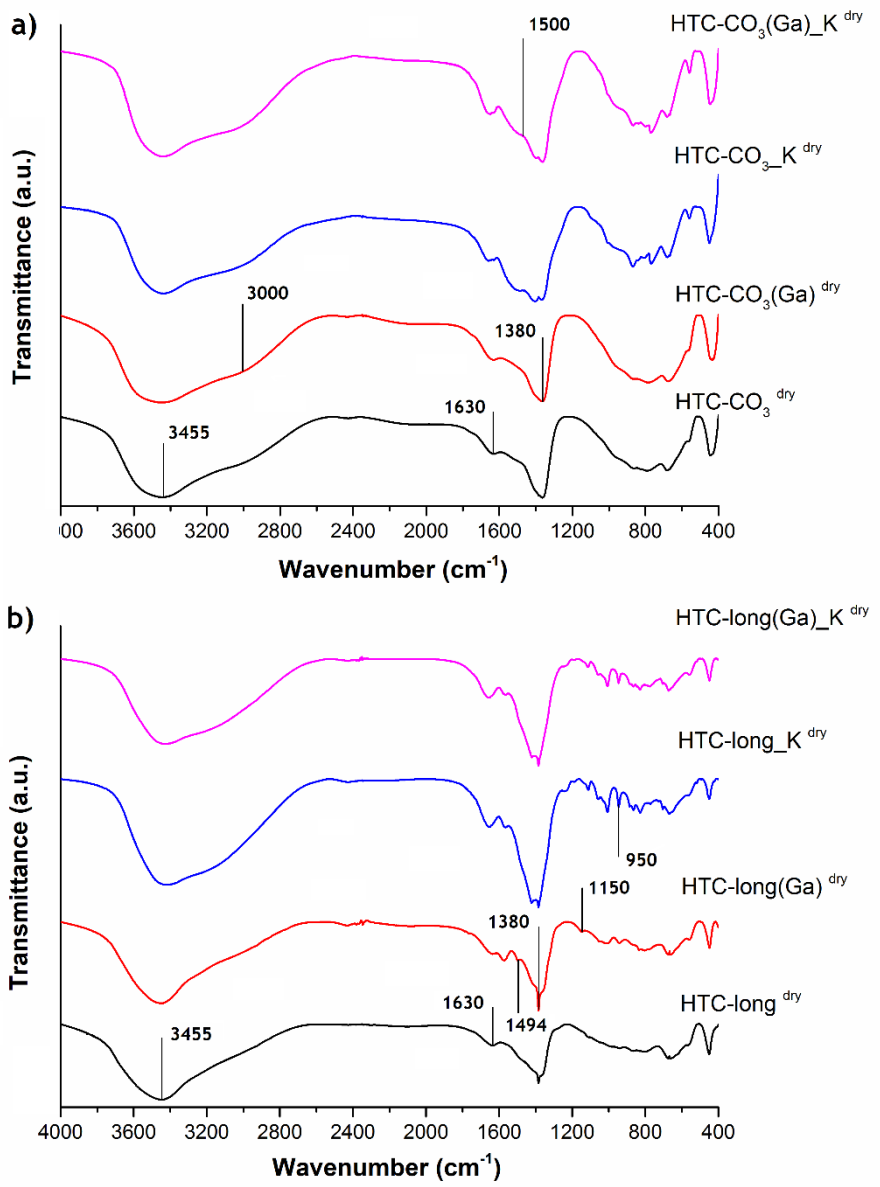

Fig. D.4. FTIR spectra of dry samples derived from the base formulation of a) HTC-CO_3 and b) HTC-long.

1.4. Physical adsorption of nitrogen at -196 ºC

Type II isotherms (HTC-CO_3 ^{calcined}, HTC-CO_3(Ga) ^{calcined}, HTC-CO_3(Ga)_K ^{calcined}, HTC-CO_3(Ga)_K ^{spent}, HTC-long_K ^{calcined}, HTC-long_K ^{spent}, HTC-long_$K_{10wt.\%}$ ^{calcined}) and Type IV isotherms (HTC-long ^{calcined}, HTC-long(Ga) ^{calcined}, HTC-CO_3(Ga)_K ^{dry}, HTC-long_K ^{dry} and HTC-long_$K_{30wt.\%}$ ^{calcined}) were obtained for the samples (Fig. D.5, Fig. D.6 and Fig. D.7), which means that the resulting materials are macroporous/mesoporous solids; and the volume of microporous (< 0.003 $cm^3 \cdot g^{-1}$ - determined by t-plot method) can be neglected. As expected for the Type II isotherms, the sorbents have macroporous and the sorption mechanism involves the production of multilayers [7-9]. For the Type IV(a) isotherms, the mechanism of sorption-desorption was not reversible, occurring hysteresis. In

these materials, capillary condensation/evaporation was present in the mesoporous filling mechanism in these materials [7-9].

For the HTC-long(Ga) ^{calcined} the hysteresis that occurred was the H2(b), linked with the existence of not well-defined pores [8, 9]. The Type H2(b) hysteresis is related to the block of the pores, where the size distribution of neck widths is larger [8]. For the HTC-CO_3(Ga)_K ^{dry}, HTC-long_K ^{calcined}, HTC-long_K ^{spent} and HTC-long_$K_{30wt.\%}$ ^{calcined} the hysteresis that occurred was the H4, associated with the presence of narrow slit-shaped pores [8, 9]. However, for HTC-CO_3(Ga)^{calcined}, HTC-long ^{calcined} and HTC-long_K ^{dry} the hysteresis that occurred was the H3, related to the occurrence of slit-shaped pores [8, 9]. Loops of this type are produced by non-rigid aggregates of plate-like particles, but also if the pore network consists of macropores that are not completely filled with condensate [8].

The total volume of mesoporous and macroporous, for the analysed HTCs, follows the next order: HTC-$CO_3^{calcined}$ ≈ HTC-CO_3(Ga)^{calcined} > HTC-CO_3(Ga)_K ^{dry} > HTC-CO_3(Ga)_K ^{calcined} ≈ HTC--CO_3(Ga)_K ^{spent} > HTC-long(Ga) ^{calcined} > HTC-long ^{calcined} > HTC-long_$K_{10wt.\%}$ ^{calcined} > HTC-long_K ^{dry} > HTC-long_K ^{spent} ≈ HTC-long_K ^{calcined} > HTC-long_$K_{30wt.\%}$ ^{calcined} (data not shown).

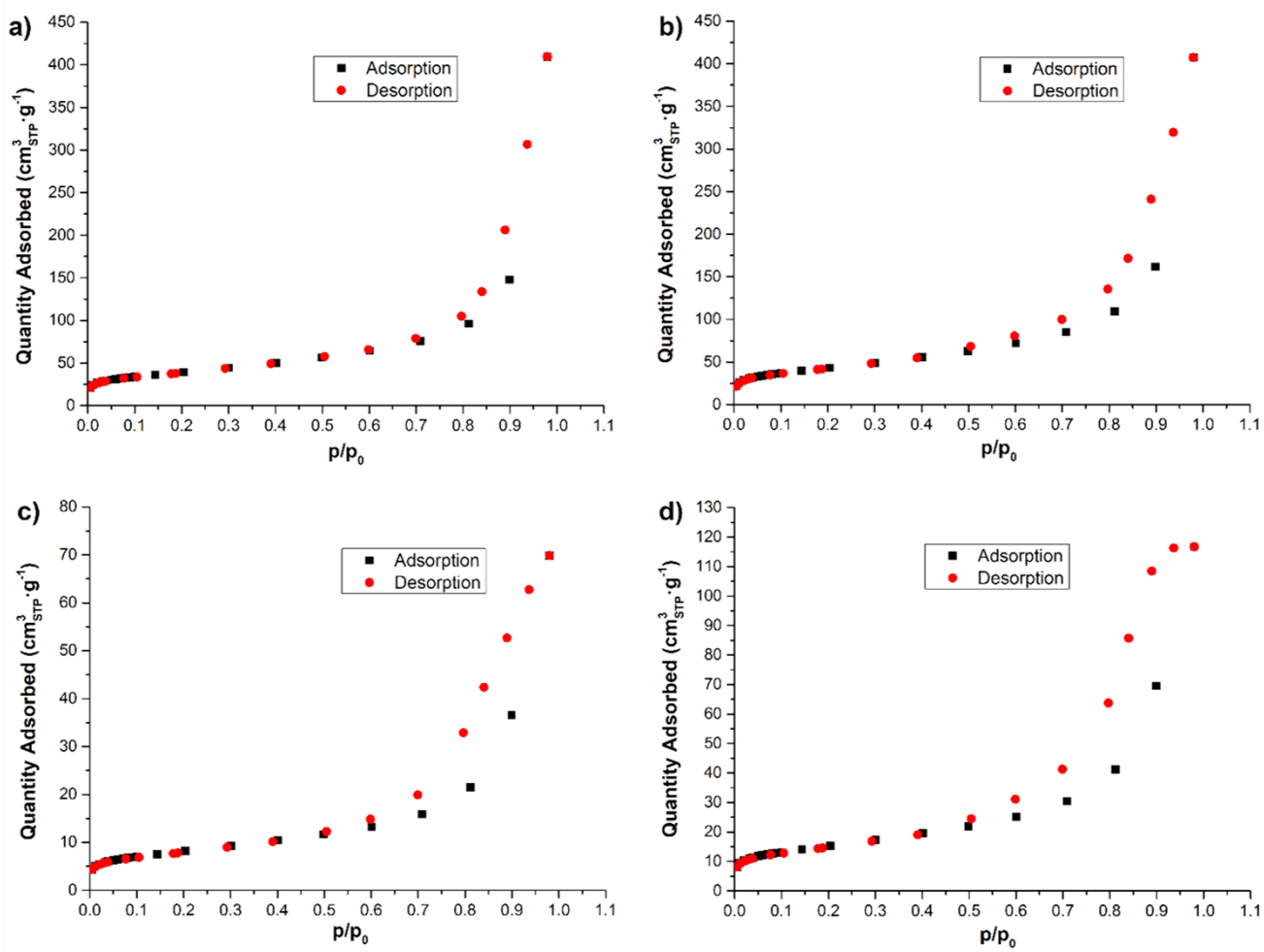

Fig. D.5. Adsorption/desorption isotherms of N_2 over the calcined samples: a) HTC-CO_3, b) HTC-CO_3(Ga), c) HTC-long and d) HTC-long(Ga).

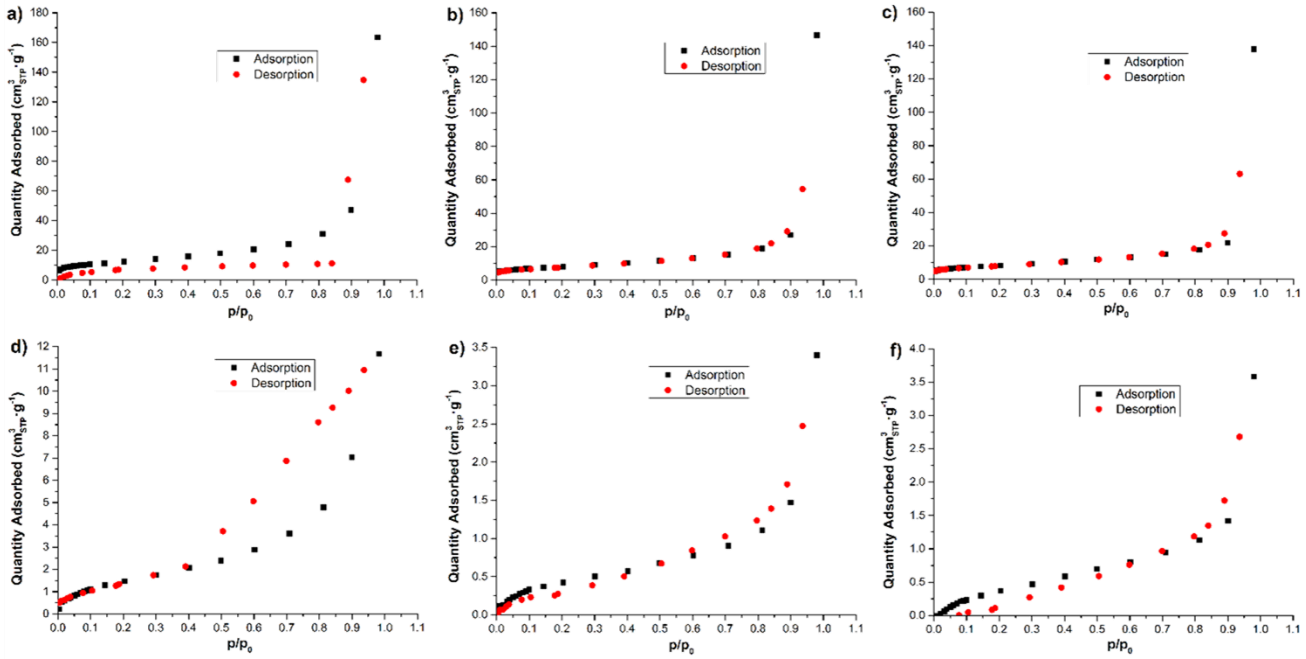

Fig. D.6. Adsorption/desorption isotherms of N_2 over the samples: a) HTC-CO_3(Ga)_K ^{dry}, b) HTC-CO_3(Ga)_K ^{calcined}, c) HTC-CO_3(Ga)_K ^{spent}, d) HTC-long_K ^{dry}, e) HTC-long_K ^{calcined} and f) HTC-long_K ^{spent}.

The specific surface area of HTC-CO_3(Ga)_K decreases after calcination. This is related to the collapse of the structure (decrease of the porosity) and related to the modification of the potassium species morphology in the HTC (from honey to needle - seen in the SEM analysis), which leads to a pore blocking caused by the K_2CO_3 phase. Besides that, the modification with K decreases the specific surface area of the hydrotalcites, being that the surface area for the calcined HTC-CO_3(Ga)_K is very close to the value reported for a similar calcined HCT [1].

For the HTC-long_K series, the specific surface area also decreases after calcination, related, again, to the collapse of the structure and the pore blocking caused by the K_2CO_3 phase (from a layer to a cubic structure - seen in the SEM analysis), being that in this case a very low value was obtained (only 2 $m^2 \cdot g^{-1}$). The surface area of the spent sorbent was slightly higher than that obtained for the calcined sample, which was also observed for the HTC-CO_3 series. This is probably due to the "memory effect" that this type of sorbents present [10-12]; in this way, the structure of the dry HTC-long_K was partially recovered after the tests (contact with CO_2 in the experiments and water from the atmosphere).

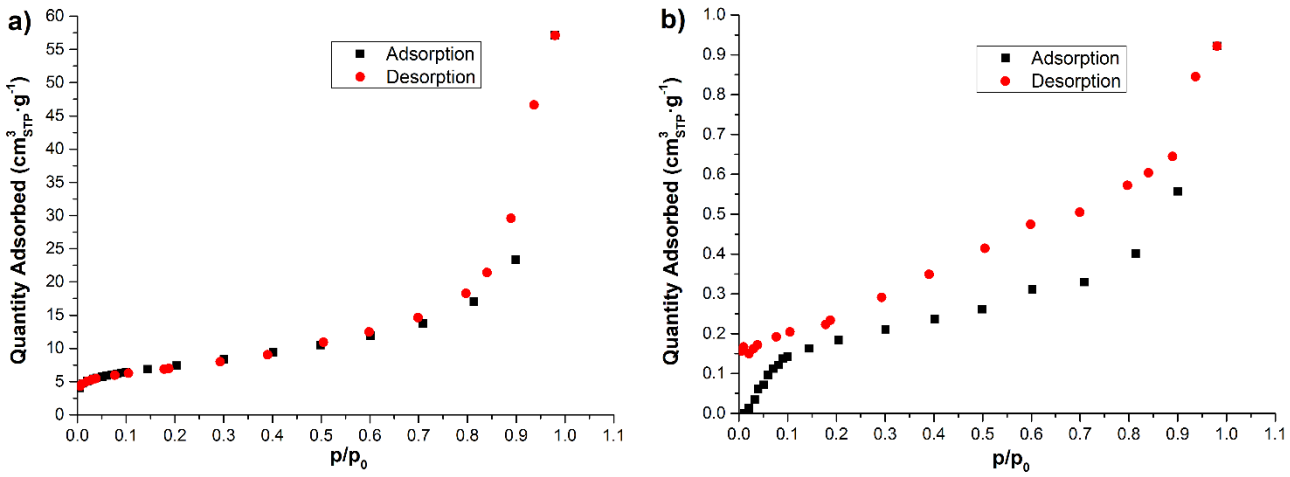

Fig. D.7. Adsorption/desorption isotherms of N_2 over the calcined samples: a) HTC-long_$K_{10wt.\%}$, b) HTC-long_$K_{30wt.\%}$.

1.5. SEM/EDS

None of the dry samples shows a defined morphology in the SEM images, although the presence of thin slabs is clearly verified (for instance, see Fig. D.8a)). The existence of these structures had already been reported in other works - for HTC with CO_3^{2-} as interlayer anion [1, 2, 13].

For the dry HTC-CO_3_K and dry HTC-CO_3(Ga)_K samples it was possible to see the presence of agglomerates of potassium (like honey structures), meaning that potassium deposits preferentially on certain zones (Fig. D.8c-d)) For the calcined and spent sample HTC-CO_3(Ga)_K (data not shown for the spent sample), the potassium assumed a needle structure, as seen in previous works [1, 2, 13] - see Fig. D.8e). The calcined and spent materials are fully converted into the mixed metal oxide structure as can be seen by the absence of thin slabs in the SEM images. Lastly, it was possible to observe by SEM (Fig. D.8a) and Fig.8e)) that the porosity (intra-particular) decreases with the impregnation of potassium in the samples with base formulation HTC-CO_3, since this component blocks the pores, which is in agreement with the results of the physical adsorption of N_2 at -196 ºC reported below and other studies [1, 2].

The surface of the HTC-long material is smooth and the porosity was very low - see Fig. D.8f). For the dry HTC-long_K and dry HTC-long(Ga)_K samples it was possible to verify, in several particles, the presence of a layer of potassium on the surface of the materials (see Fig. D.8h) and Fig. D.8k). However, for some particles in the dry sample of HTC-long_K, it was possible to verify the presence of isolated particles of potassium (data not shown). For the calcined and spent sample of HTC-long_K, the potassium assumed a cubic structure and was more dispersed in the particles - Fig. D.8i). However, in a few particles (for calcined and spent samples), it was possible to see that some potassium presents a honey structure, probably an intermediate state before the formation of the cubic structures - zone Z1 in Fig. D.8 j).

EDS analysis for the materials with the base formulation HTC-CO_3 showed that the $Mg^{2+}/(Al^{3+}+Ga^{3+})$ ratio for all samples was not constant in the particles (it varies from zone to zone, but is close to 2). Besides that, it was found that several zones exist without Ga^{3+} on the surface. For example, for the dry HTC-CO_3(Ga)_K sample, it was defined a zone Z1 without Ga^{3+} and a zone Z2 with a ratio of $Al^{3+}/Ga^{3+} \approx 10$ - see Fig. D.8d) and Fig. D.9. Analyzing one global particle of the dry HTC-CO_3(Ga)_K, it was seen a ratio of $Al^{3+}/Ga^{3+} \approx 11$. The analysis of the sample HTC-CO_3(Ga)_K calcined and spent allows to conclude that the calcination removes water, CO_3^{2-} and OH^- (the content of O and C decreases) and after the sorption test (spent sample), a few quantity of atmospheric CO_2 is irreversibly sorbed (the content of O and C increases in comparison with the calcined sample). From EDS analysis of the dry HTC-CO_3_K, it was possible to obtain information about the impregnation of potassium. Analyzing one particle in a global view, it was seen a ≈ 10 wt.% of K in the sample, but it varies depending on the zone of analysis. The content of potassium is very large in Z1 (≈ 29 wt.%) and Z3 (≈ 20 wt.%) zones, and low in Z2 (≈ 13 wt.%) and Z4 (8 wt.%) zones, meaning that potassium deposits preferentially on certain zones of the particles - Fig. D.8b-c) and Fig. D.10. Although incipient wetness impregnation usually leads to a homogeneous distribution of the active phase, it is clear that K was not well distributed in the material and has a preference to deposit in certain zones, as observed in previous works [1, 2].

Since the surface of dry HTC-long had low porosity, the content of Mg^{2+} and Al^{3+} detected (by EDS) was very low in the samples impregnated with potassium (HTC-long_K and HCT-long(Ga)_K) - results for dry HTC-long_K in Fig. D.8h) and Fig. D.11. In the Z1 and Z2 zones (Fig. D.8j)) of the calcined sample of HTC-long_K, the content of potassium was higher, independent of the zone - > 25 wt. % (EDS results in Fig. D.12).

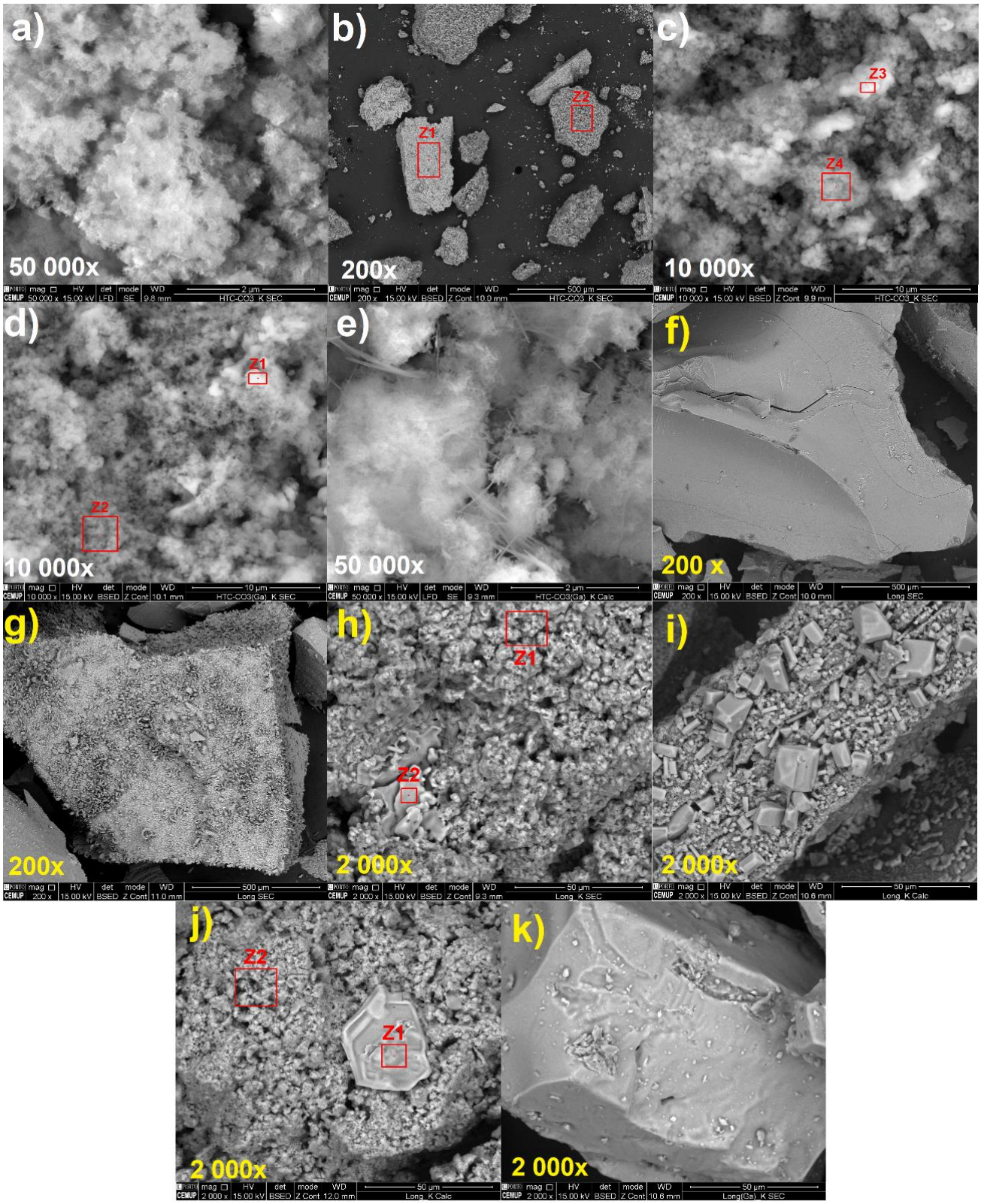

Fig. D.8. SEM images for HTC-CO_3_K ^{dry} [a), b) and c)], HTC-CO_3(Ga)_K ^{dry} [d)], HTC-CO_3(Ga)_K ^{calcined} [e)], HTC-long ^{dry} [f) and g)], HTC-long_K^{dry} [h)], HTC-long_K ^{calcined} [i) and j)] and HTC-long(Ga)_K^{dry} [k)].

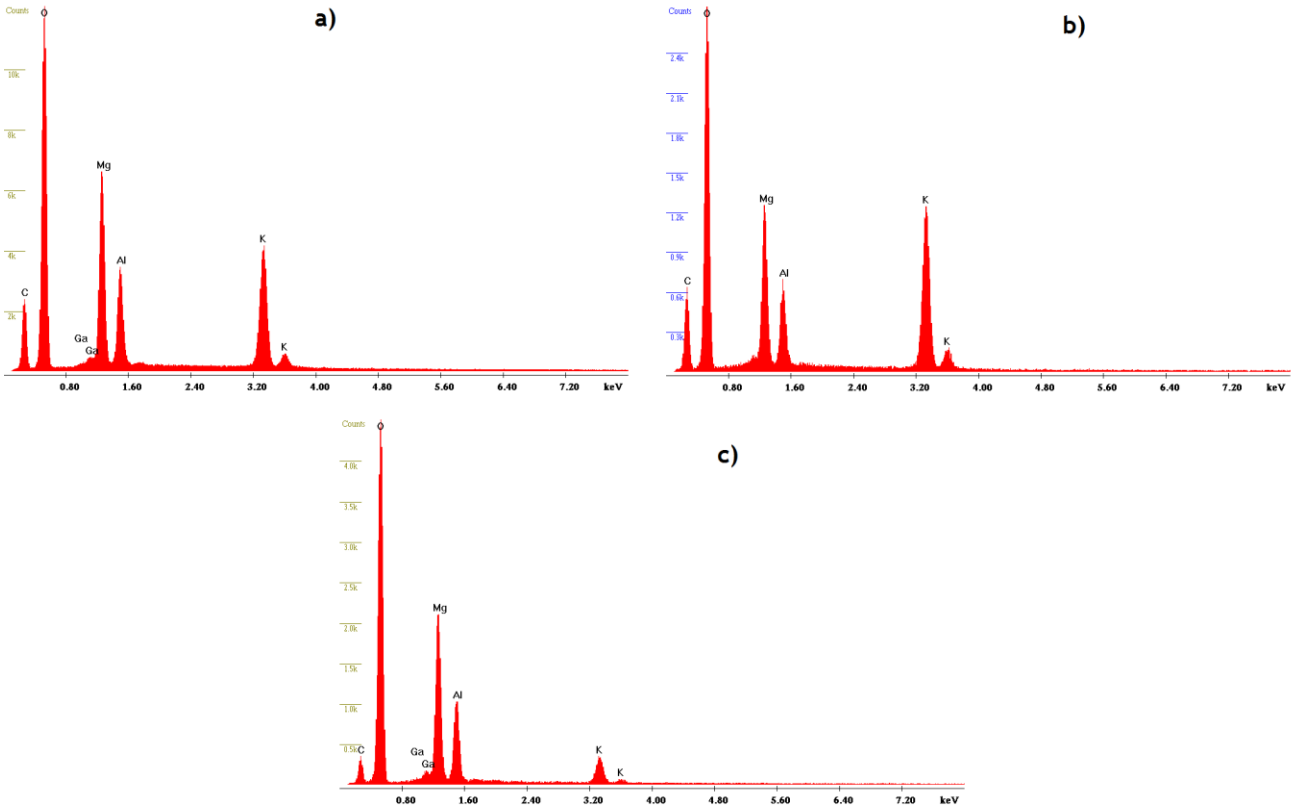

Fig. D.9. EDS analysis for the dry samples of HTC-CO_3(Ga)_K a) in a global way, in b) Z1 and c) Z2 zone.

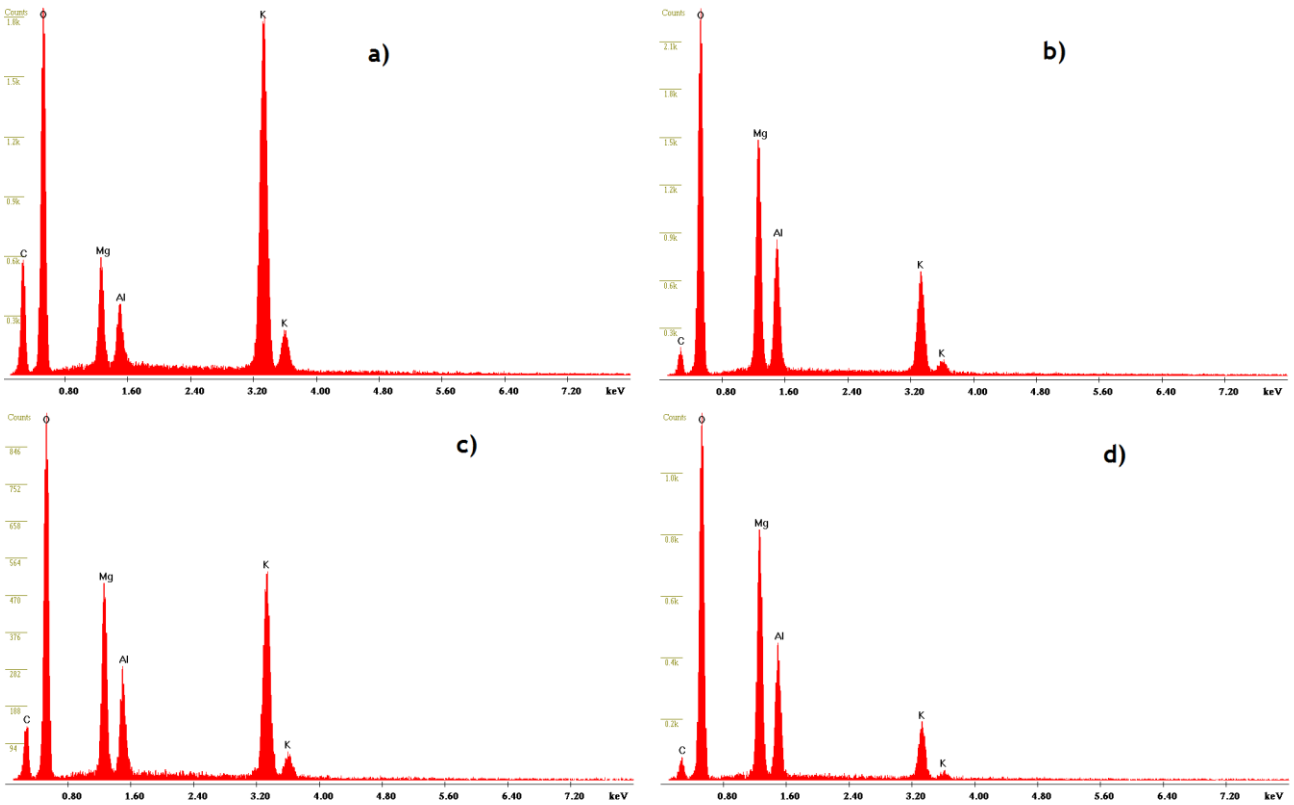

Fig. D.10. EDS analysis for the dry samples of HTC-CO_3_K in a) Z1, b) Z2, c) Z3, d) Z4 zone.

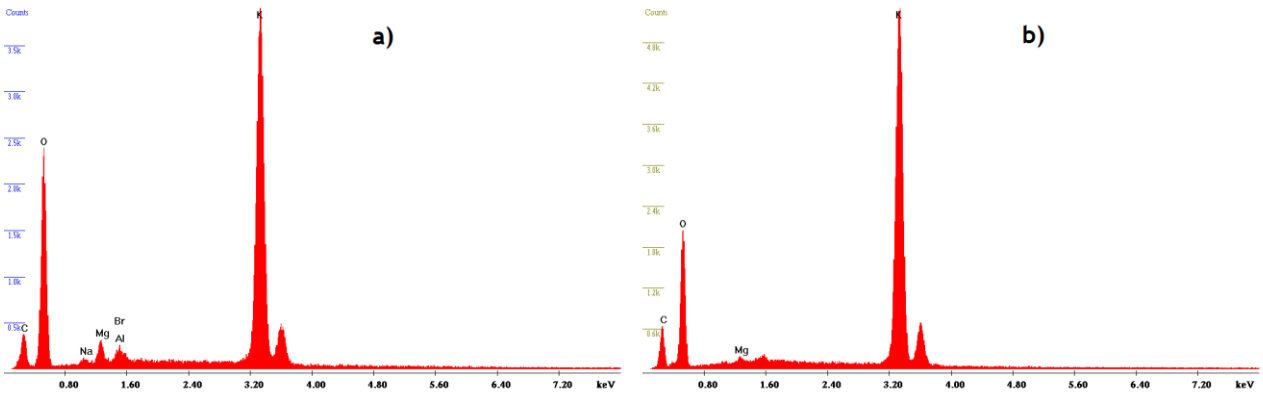

Fig. D.11. EDS analysis for the dry sample of HTC-long_K in a) Z1 and b) Z2 zone.[3]

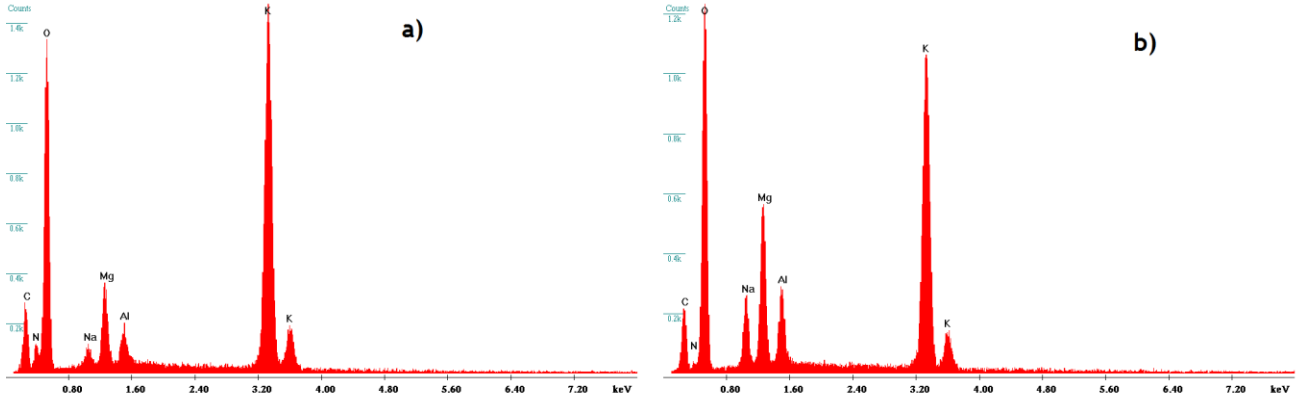

Fig. D.12. EDS analysis for the calcined samples of HTC-long_K in a) Z1 and b) Z2 zone.[3]

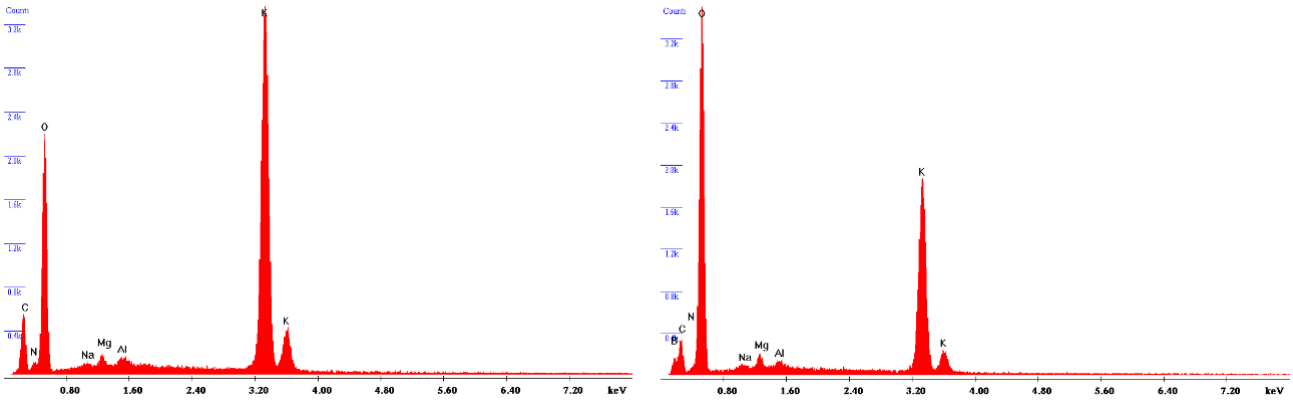

Fig. D.13. EDS analysis for the dry sample of HTC-long(Ga)_K in two different zones. [3]

[3] The presence of Na^{2+} in the EDS data results from the fact that these samples were not washed sufficiently with water before drying (it is noteworthy that the samples are not the same as in the XRD diffraction patterns). However, the content of the cation in the materials is very low and does not affect CO_2 sorption capacity (data not shown).

2. Adsorption tests

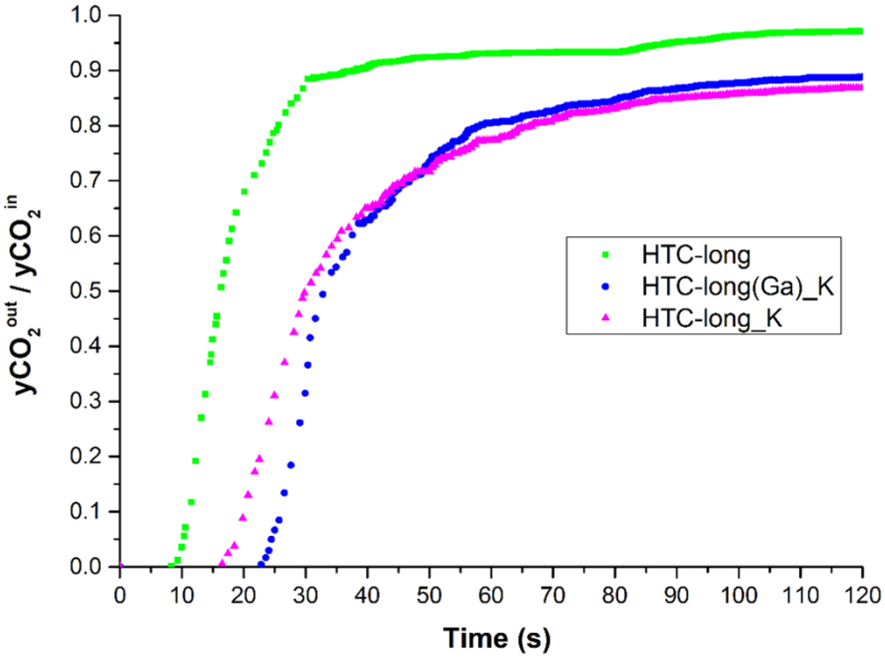

Fig. D.14. Breakthrough curves in the presence of steam. Sorption step (20 min) was carried out with 15 vol.% of CO_2 and 15 vol.% of steam balanced in N_2 - total flow rate of 100 $mL_N \cdot min^{-1}$. Regeneration step carried out under 85 $mL \cdot min^{-1}$ of N_2 and 15 $mL_N \cdot min^{-1}$ of steam (30 min). Pre-treatments were performed at 400 ºC.

References

[1] Silva, J.M., R. Trujillano, V. Rives, M.A. Soria and L.M. Madeira, High temperature CO2 sorption over modified hydrotalcites. Chemical Engineering Journal, 2017. 325: p. 25-34.

[2] Miguel, C.V., R. Trujillano, V. Rives, M.A. Vicente, A.F.P. Ferreira, A.E. Rodrigues, A. Mendes and L.M. Madeira, High temperature CO2 sorption with gallium-substituted and promoted hydrotalcites. Separation and Purification Technology, 2014. 127(Supplement C): p. 202-211.

[3] Bhattacharyya, A. and D.B. Hall, New triborate-pillared hydrotalcites. Inorganic Chemistry, 1992. 31(18): p. 3869-3870.

[4] Li, L., S. Ma, X. Liu, Y. Yue, J. Hui, R. Xu, Y. Bao and J. Rocha, Synthesis and Characterization of Tetraborate Pillared Hydrotalcite. Chemistry of Materials, 1996. 8(1): p. 204-208.

[5] Kruissink, E.C., L.L. van Reijen and J.R.H. Ross, Coprecipitated nickel-alumina catalysts for methanation at high temperature. Part 1.—Chemical composition and structure of the precipitates. Journal of the Chemical Society, Faraday Transactions 1: Physical Chemistry in Condensed Phases, 1981. 77(3): p. 649-663.

[6] Wang, Q., Z. Wu, H.H. Tay, L. Chen, Y. Liu, J. Chang, Z. Zhong, J. Luo and A. Borgna, High temperature adsorption of CO2 on Mg-Al hydrotalcite: Effect of the charge compensating anions and the synthesis pH. Catalysis Today, 2011. 164(1): p. 198-203.

[7] Magalhães, D., PhD Thesis: Síntese, caracterização e aplicação de sílica mesoporosa esférica como adsorvente. 2011, Instituto de Química, Universidade de São Paulo: São Paulo.

[8] Thommes, M., K. Kaneko, V. Neimark Alexander, P. Olivier James, F. Rodriguez-Reinoso, J. Rouquerol and S.W. Sing Kenneth, Physisorption of gases, with special reference to the evaluation of surface area and pore size distribution (IUPAC Technical Report), in Pure and Applied Chemistry. 2015. p. 1051.

[9] Rodrigues, S.L., Remoção em fase líquida do fármaco Diclofenac por adsorção em biocarvão. 2015, Faculdade de Ciências e Tecnologia - Universidade Nova de Lisboa: Lisbon.

[10] Pérez-Ramírez, J., S. Abelló and N.M. van der Pers, Memory Effect of Activated Mg-Al Hydrotalcite: In Situ XRD Studies during Decomposition and Gas-Phase Reconstruction. Chemistry - A European Journal, 2007. 13(3): p. 870-878.

[11] Chibwe, K. and W. Jones, Intercalation of organic and inorganic anions into layered double hydroxides. Journal of the Chemical Society, Chemical Communications, 1989(14): p. 926-927.

[12] Kwon, T. and T.J. Pinnavaia, Pillaring of a layered double hydroxide by polyoxometalates with Keggin-ion structures. Chemistry of Materials, 1989. 1(4): p. 381-383.

[13] Oliveira, E.L.G., C.A. Grande and A.E. Rodrigues, CO2 sorption on hydrotalcite and alkali-modified (K and Cs) hydrotalcites at high temperatures. Separation and Purification Technology, 2008. 62(1): p. 137-147.

Appendix E. Supporting Information for subchapter 6.1

1. Catalyst characterization

1.1. Physical adsorption of nitrogen at -196 ºC

According to the IUPAC classification, isotherms of the Type IV(a) were obtained for all catalysts - see Fig. E.1. The volume of micropores (< 0.007 $cm^3 \cdot g^{-1}$) can be neglected for all samples. The isotherms obtained for these materials mean that they are mesoporous solids, which was confirmed with the diameter of the pores determined by the Density Functional Theory method (data not shown) [1]. For the N_2 adsorption isotherms, the process of adsorption-desorption of N_2 was irreversible (presence of hysteresis). Besides the production of multilayers, capillary condensation is present in the mesoporous filling mechanism in these materials. When the capillary condensation is different from the capillary evaporation, hysteresis occurs [1-3]. For Rh and Cu-Zn[2] catalysts, the hysteresis observed is of the H2(b) type, connected with the existence of not well-defined pores [1, 3]. For Ni and Pd[1] samples, it is possible to see the co-existence of two types of hysteresis (H2(b) and H3), indicating the presence of two types of pores. The hysteresis H3 is related to the occurrence of slit-shaped pores [1, 3].

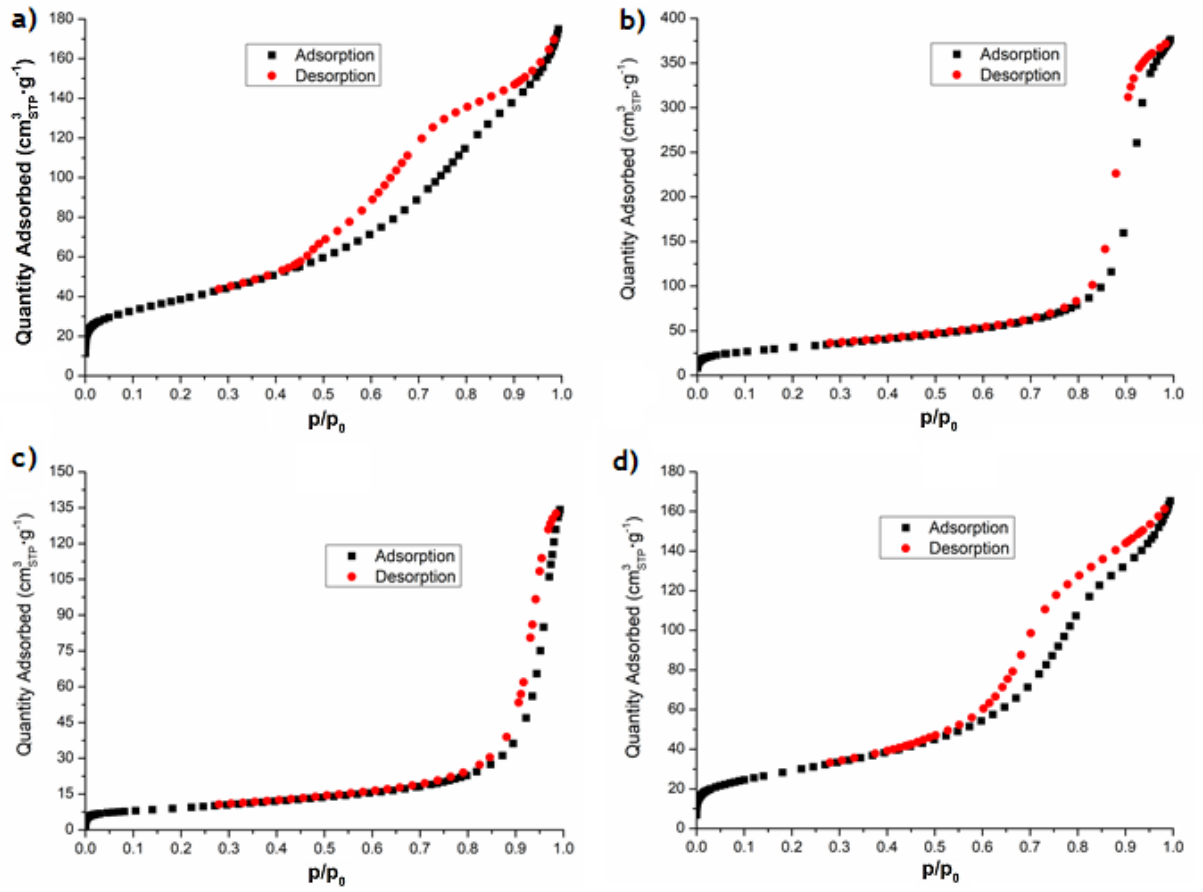

Fig. E.1. Adsorption/desorption isotherms of N_2 over different catalysts: a) Ni, b) Rh, c) Cu-Zn[2] and d) Pd[1].

1.2. SEM/EDS analyses

SEM/EDS analyses were performed to inspect the morphology of the fresh catalysts (namely the distribution of the active phase) and to understand the changes that the materials suffered during the stability tests. The SEM images and the EDS analyses were performed for one catalyst (the sample tested in the stability test): fresh and spent samples of Rh-based catalyst.

In a preliminary analysis, it was confirmed that the fresh sample shows a defined morphology (see Fig. E.2a)) and the fresh and spent catalyst presents an irregular surface (Fig. E.2c)). Additionally, for the fresh and spent catalyst, it was possible to verify, in some particles, the presence of two different morphological structures: one porous/irregular structure and another part which is non-porous/honey-type (Fig. E.2c-d)).

EDS analyses (and EDS mapping) showed that the Rh content in the samples of the catalyst was not homogeneous in the surface of some particles (it varies from zone to zone). For instance, it was possible to define a zone Z1 and a zone Z2 on the surface of a fresh catalyst particle with different Rh loadings (higher loading of Rh in zone Z1) - see Fig. E.2b), Fig. E.3d) and Fig. E.4. The same happened for the spent sample - see Fig. E.2d) and Fig.E.5.

Finally, differences between fresh and spent catalysts (in SEM images and EDS analyses) were not found, which can be related to the fact that the production of coke was very low (as already mentioned in TPO results).

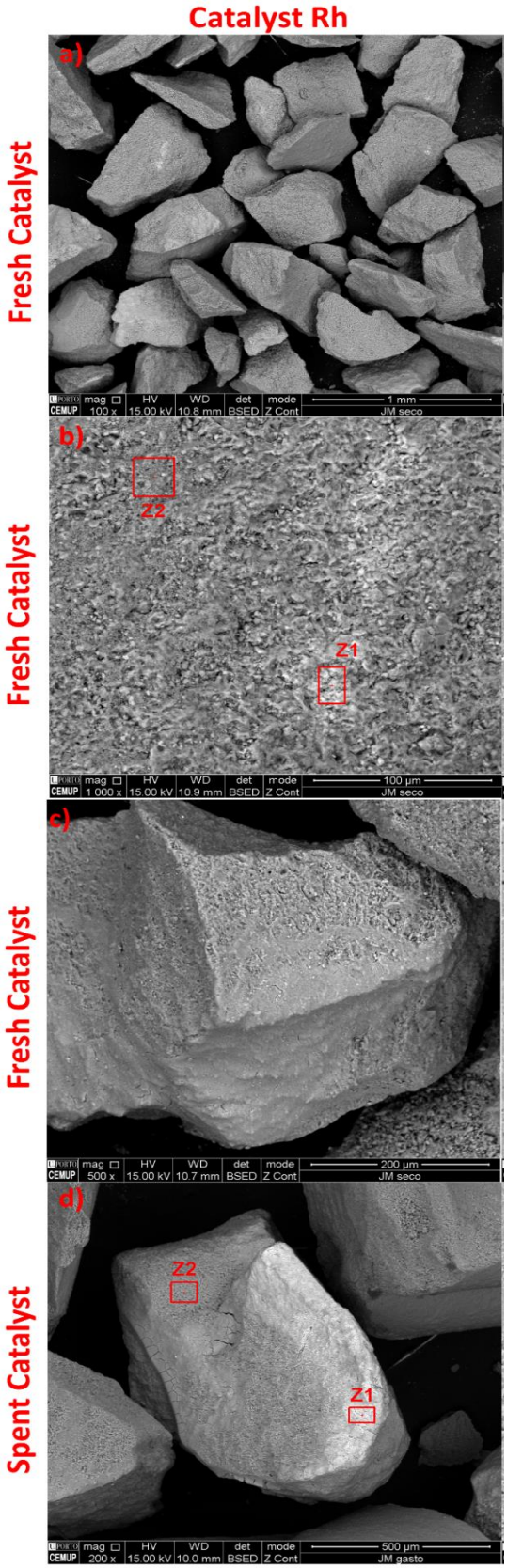

Fig. E.2.. SEM images of a-c) fresh sample and d) spent sample of catalyst Rh.

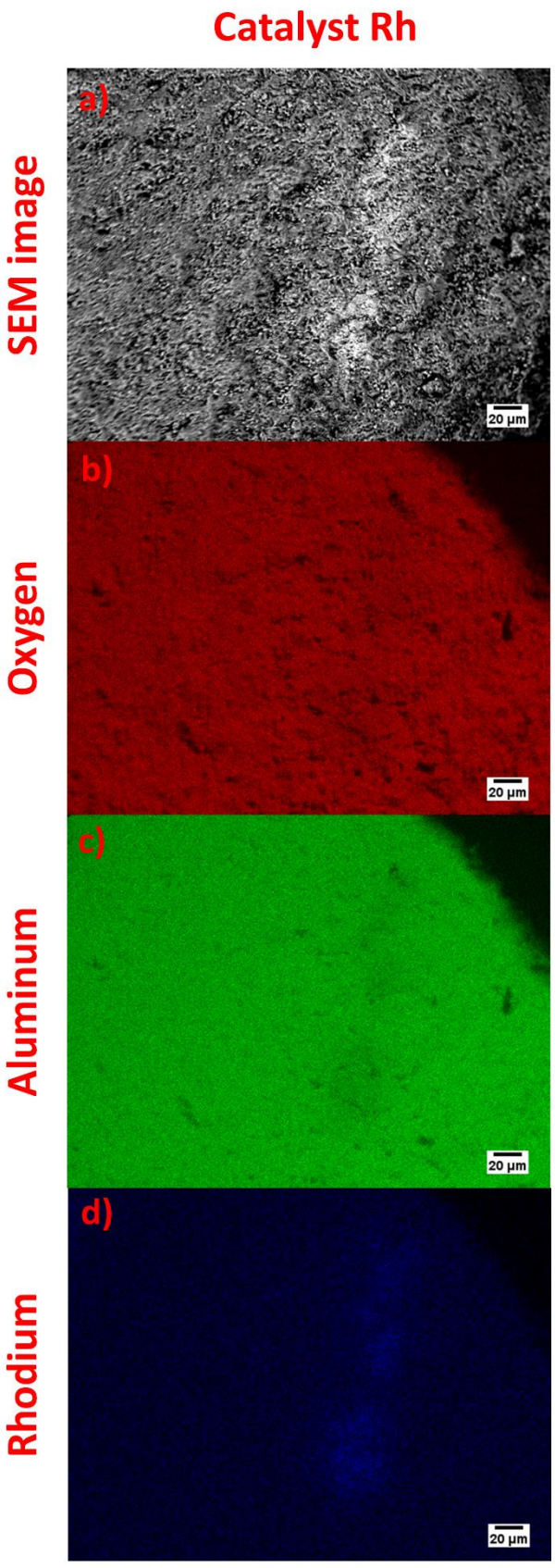

Fig. E.3. SEM images of a) dry samples of catalyst Rh, along with EDS mapping of b) - Oxygen, c) Aluminum and d) Rhodium for the Rh sample.

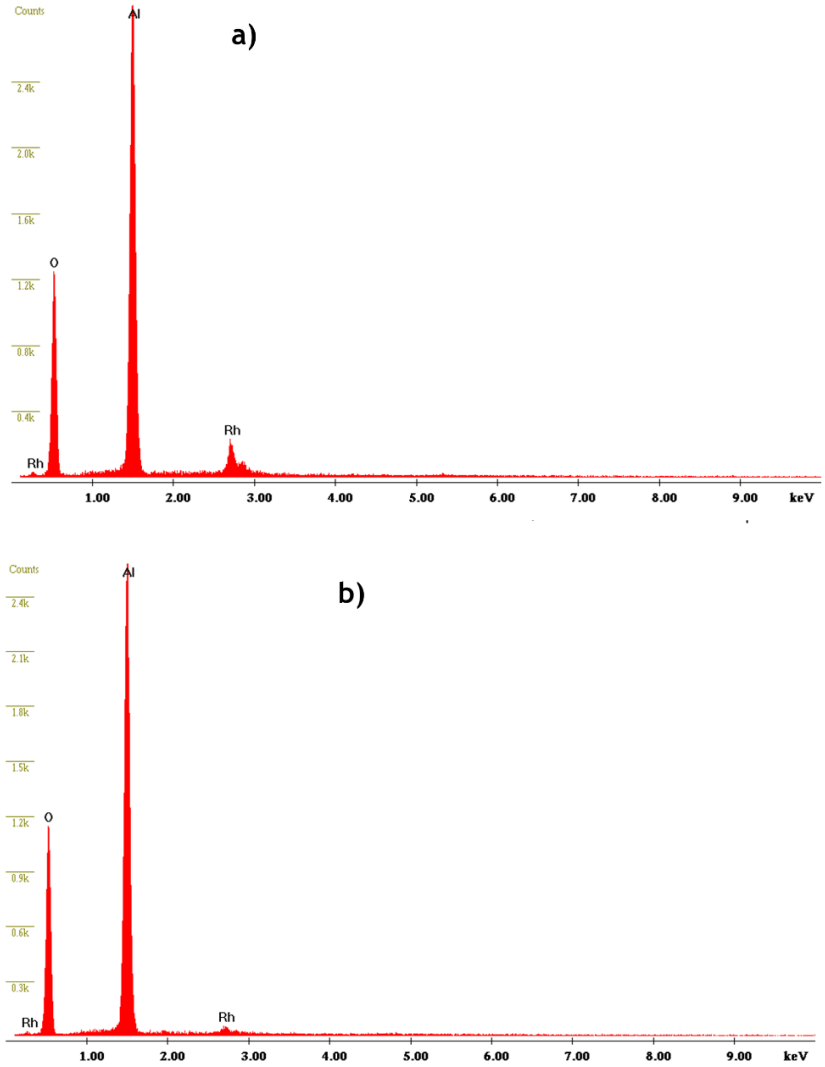

Fig. E.4. EDS analysis for the fresh sample of catalyst Rh in a) Z1 and b) Z2 zone of Fig. E.2b).

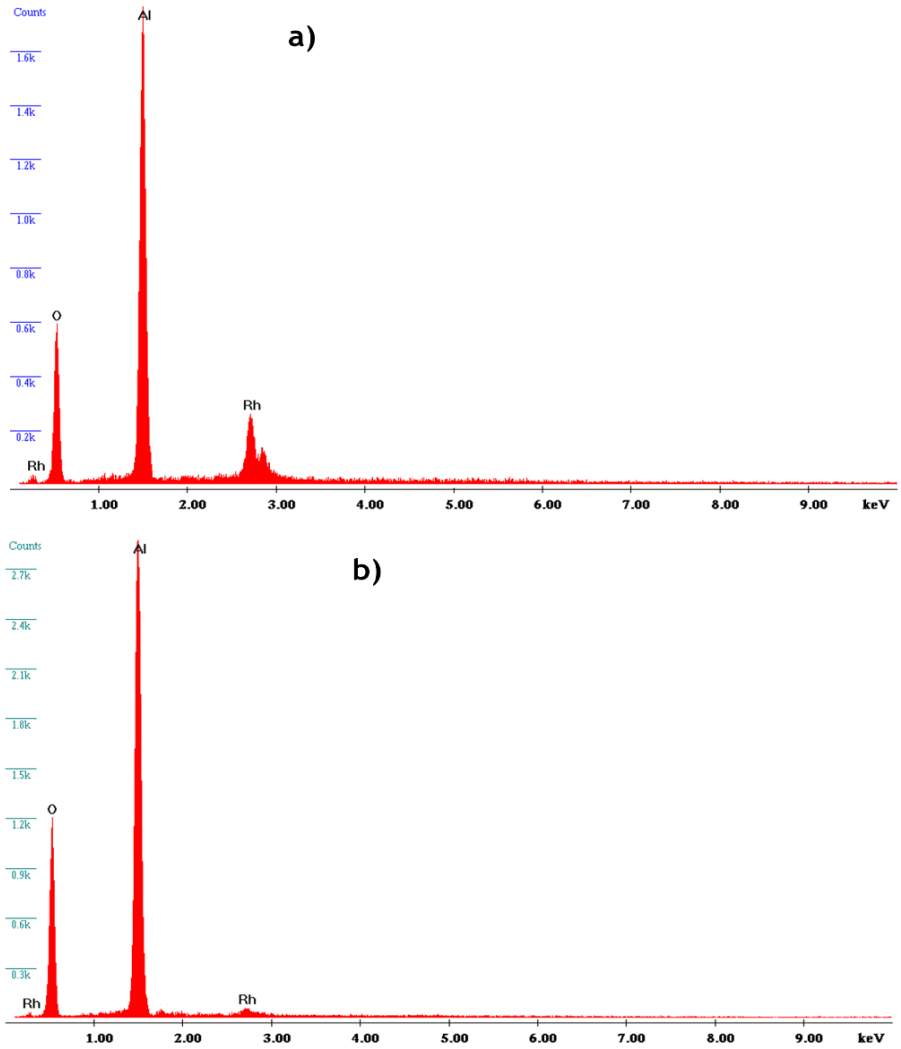

Fig. E.5. EDS analysis for the spent sample of catalyst Rh in a) Z1 and b) Z2 zone of Fig. E.2d).

1.3. TPD-NH_3 and TPO analyses

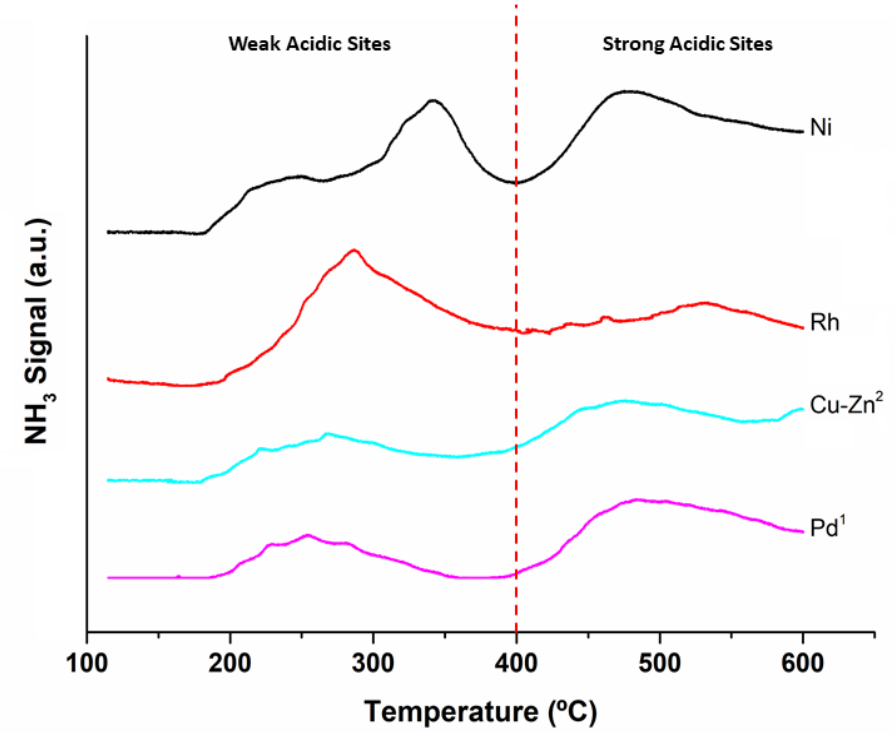

Fig. E.6. TPD-NH_3 profiles for some selected catalysts.

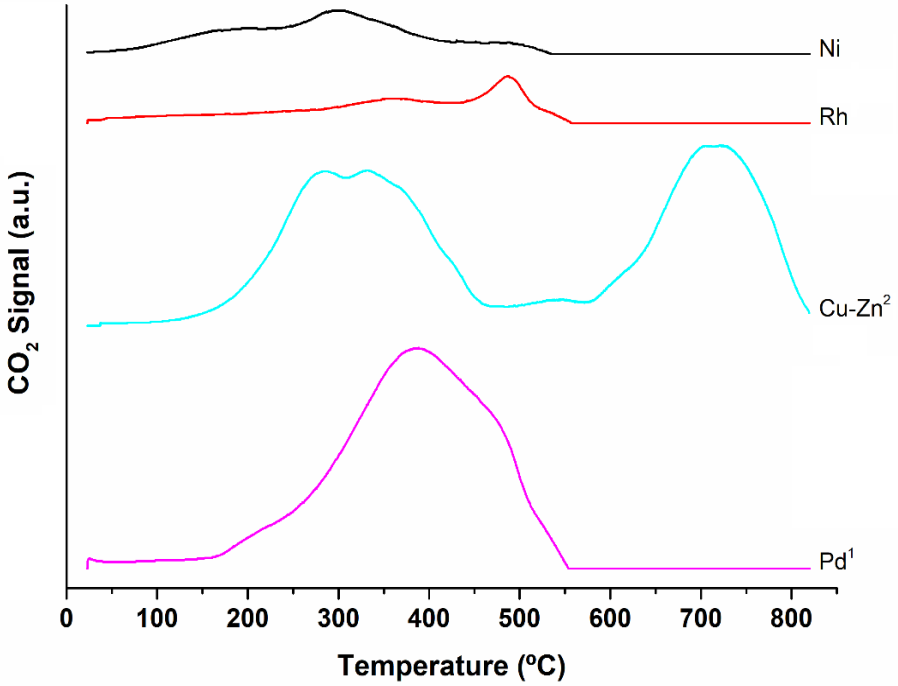

Fig. E.7. TPO analyses for the spent catalysts Ni, Rh, Cu-Zn[2] and Pd[1] (used in *Exp. 2.1*).

2. Catalytic tests

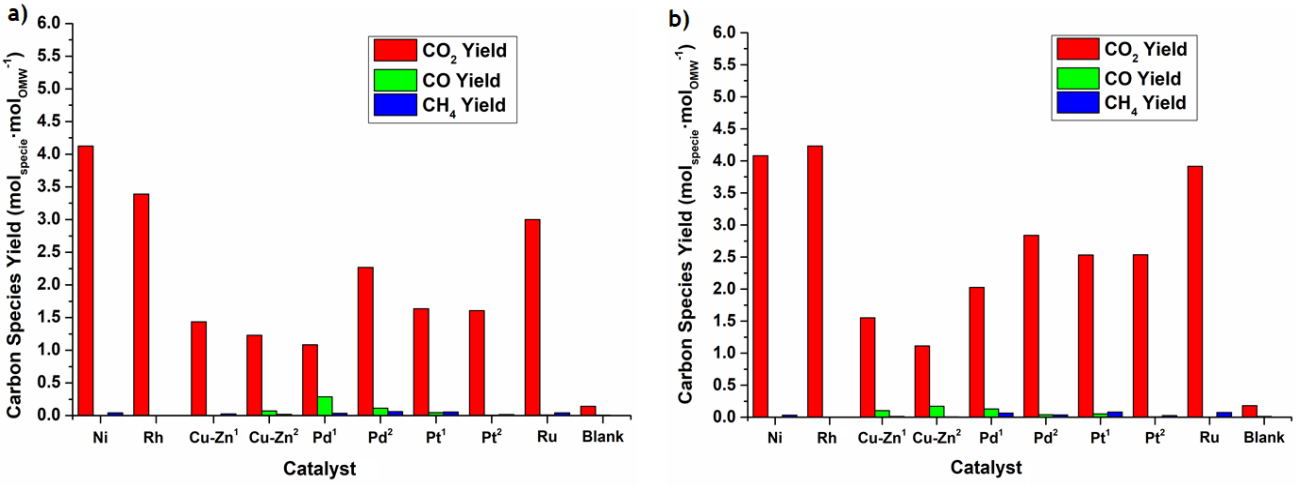

Fig. E.8. Mean of carbon gaseous species yield obtained in *Exp. 2.1* for all the catalysts at a) 350 ºC and b) 400 ºC.

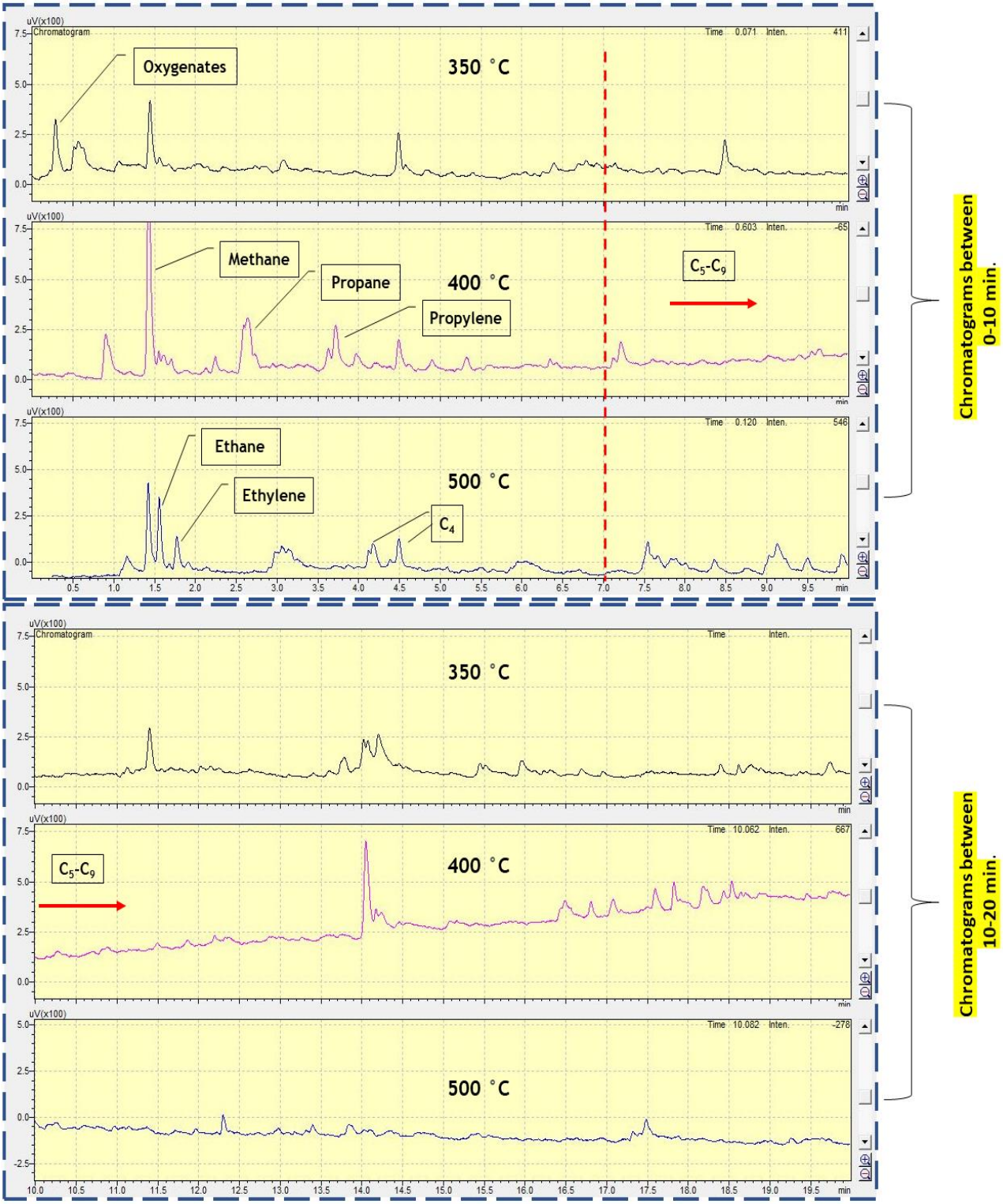

Fig. E.9. Identification of the hydrocarbons present in the outlet stream of the OMWSR reactor with the Rh catalyst at different temperatures.

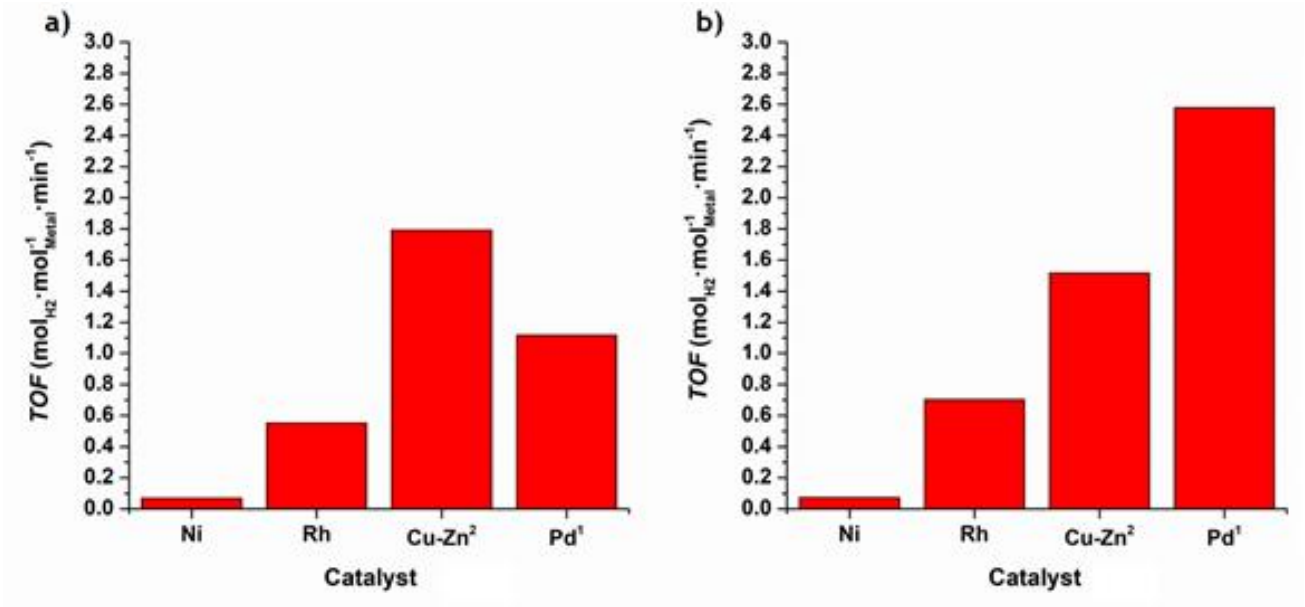

Fig. E.10. *TOF* for several catalysts concerning the H_2 production at a) 350 and b) 400 ºC.

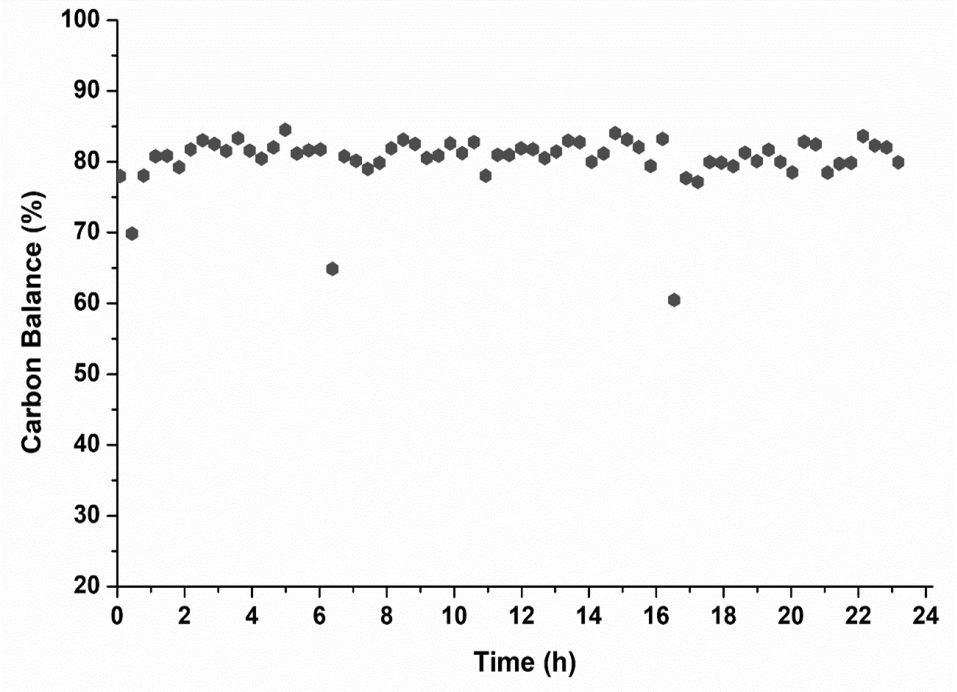

Fig. E.11. Carbon balance calculated in *Exp. 2.2* (stability tests) for the most promising catalyst Rh.

Fig. E.12. Color difference between the condensed phase obtained in the blank test (on the left side) and the condensed phase of the same stream after the OMWSR process in the stability test (on the right side).

References

[1] Thommes, M., K. Kaneko, V. Neimark Alexander, P. Olivier James, F. Rodriguez-Reinoso, J. Rouquerol and S.W. Sing Kenneth, Physisorption of gases, with special reference to the evaluation of surface area and pore size distribution (IUPAC Technical Report), in Pure and Applied Chemistry. 2015. p. 1051.

[2] Magalhães, D., PhD Thesis: Síntese, caracterização e aplicação de sílica mesoporosa esférica como adsorvente. 2011, Instituto de Química, Universidade de São Paulo: São Paulo.

[3] Rodrigues, S.L., MSc Dissertation: Remoção em fase líquida do fármaco Diclofenac por adsorção em biocarvão. 2015, Faculdade de Ciências e Tecnologia - Universidade Nova de Lisboa: Lisbon.

Appendix F. Supporting Information for subchapter 6.2

1. Catalyst characterization

1.1. TG/DTG

The loss of mass and thermal decompositions during calcination of several prepared materials were determined by thermogravimetric (TG) analysis and derivative thermogravimetric (DTG) analysis and accounted to prepare the impregnated sample (HTC[4]) and to select the calcination temperature for Ni-Ru/SiO_2 and Ni/SiO_2.

In Fig. F.1 it was possible to verify the TGA/DTG for the HTC that it was used as support of HTC[4]. The dry sample was heated at 10 ºC·min^{-1} up to 500 ºC and maintained at this temperature for 5 h, in a N_2 atmosphere. This temperature (500 ºC) was also selected in the calcination of this catalyst allows to destroy completely the typical structure of the HTC and obtains only a mixed oxide material [1-3]. Due to that, this characterization was essential to prepare the impregnated sample with the correct loading of Ni. The sample presents several peaks in the DTG analysis related to the removal of water (shoulder close to 100 ºC), hydroxyl groups (peak at 190 ºC) and interlayer anion CO_3^{2-} (peak at 360 ºC) - see Fig. F.1. The total mass loss during the calcination program was 43 %.

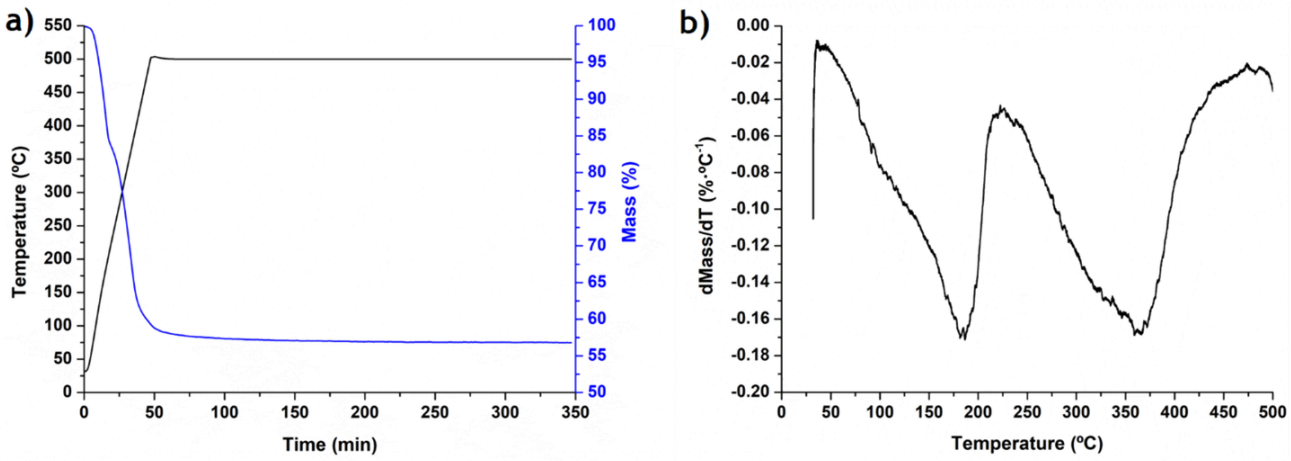

Fig. F.1. Thermogravimetric a) and derivative thermogravimetric b) analysis of the dry sample the support of the HTC[4] catalyst.

In Fig. F.2 it was also analysed the decomposition of the dried sample of Ni-Ru/SiO_2 in the range of 30-1000 ºC (in a N_2 atmosphere), to determine the optimum calcination temperature (Fig. F.2). The sample of Ni-Ru/SiO_2 presents 2 DTG peaks: one related to the removal of water (water at surface and interlayer water - in the range of 100-200 ºC) and hydroxyl groups, and the other related to the

decomposition of Ru (between 270 and 300 ºC). It was possible to verify that at high temperatures (> 270 ºC), the catalyst decomposed due to the volatilization of Ru (formation of volatile oxides during the calcination under oxidizing atmosphere) [4-8]; In this way, the calcination temperature of Ni-Ru/SiO_2 must be lower than 270 ºC.

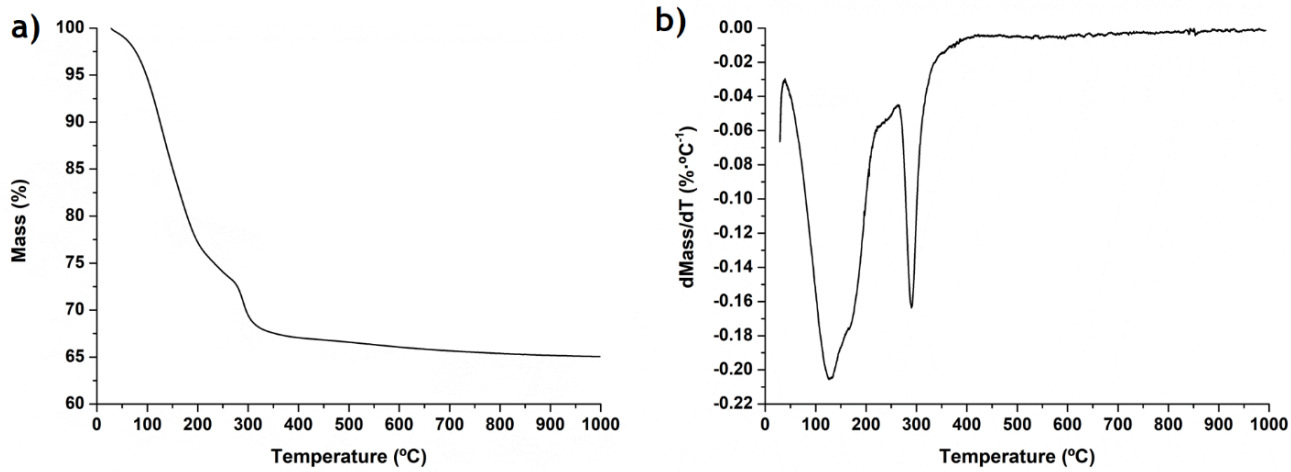

Fig. F.2. Thermogravimetric a) and derivative thermogravimetric b) analysis of the dry sample of Ni-Ru.

1.2. XRD

It was verified that the dry samples of HTC^x present typical structures of HTCs (see diffractograms in Fig. F.3 and identified phases in Table F.1), similar to previous studies [9, 10]. However, for the HTC^4 dry sample, more than one phase was observed and residual content of a salt (probably nickel (II) nitrate) was verified - see Fig. F.3. The additional phase of HTC was obtained due to the anion exchange (CO_3^{2-} by NO_3^-) [11, 12] in the interlayer of the HTC during the impregnation [13]. The dry sample of Ni-Ru is a very amorphous material and, for this reason, it was only possible to detect the SiO_2 phase in the corresponding pattern [14].

Concerning the calcined materials, it was observed that all samples presented NiO. That is, the calcination treatment allowed the formation of the NiO phase in all the catalysts (XRD patterns peaks at 37º, 43º, 63º, 76º and 80º). Besides that, it is also necessary to emphasize that the positions of several peaks like NiO, MgO, Al_2O_3, $MgNiO_2$, $NiAl_2O_4$ and the spinel phase of $MgAl_2O_4$ are very similar being difficult to distinguish the phases formed during the calcination in the XRD patterns [15, 16]. Therefore, the existence of these phases in the materials was never excluded, even if not very well detected in the analyses; for instance, despite not being detected, it was also expectable the presence of MgO (periclase) in the calcined catalysts HTC^2 and HTC^4, as verified in other similar calcined samples prepared in this study (HTC^1 and HTC^3). Besides that, since the content of Ni and Mg in these catalysts was very high, the detection of other possible phases (e.g. Al_2O_3) may have been inhibited. In the Ni-Ru sample, the phases related to Ru were not detected, since the content of this

element in the catalysts was very low. The absence of Ru reflection indicates that the sizes of the particles are small and below the detection limit of the equipment.

Table F.1 - XRD results for all the prepared catalysts.

Catalyst	Identified phases
HTC^1_{dry}	HTC
$HTC^1_{calcined}$	NiO + Periclase
$HTC^1_{reduced\ at\ 350\ ºC}$	NiO + Periclase
$HTC^1_{reduced\ at\ 650\ ºC}$	Ni + Periclase
HTC^1_{spent} [a)]	NiO + Periclase + Al_2O_3 + Mg_3CO_6 + coke
HTC^1_{spent} [b)]	Ni + Periclase + coke
$HTC^2_{calcined}$	NiO
$HTC^3_{calcined}$	NiO + Periclase
HTC^4_{dry}	2 phases of HTC + $NiNO_3$
$HTC^4_{calcined}$	NiO
Ni-Ru $_{dry}$	Amorphous SiO_2
Ni-Ru $_{calcined}$	NiO + Amorphous SiO_2
Ni-Ru $_{reduced\ at\ 350\ ºC}$	Ni + Amorphous SiO_2
Ni-Ru $_{spent}$ [a)]	Ni + Amorphous SiO_2 + coke

[a)] Spent catalyst that was reduced at 350 ºC previously of the catalytic test.
[b)] Spent catalyst that was reduced at 650 ºC previously of the catalytic test.

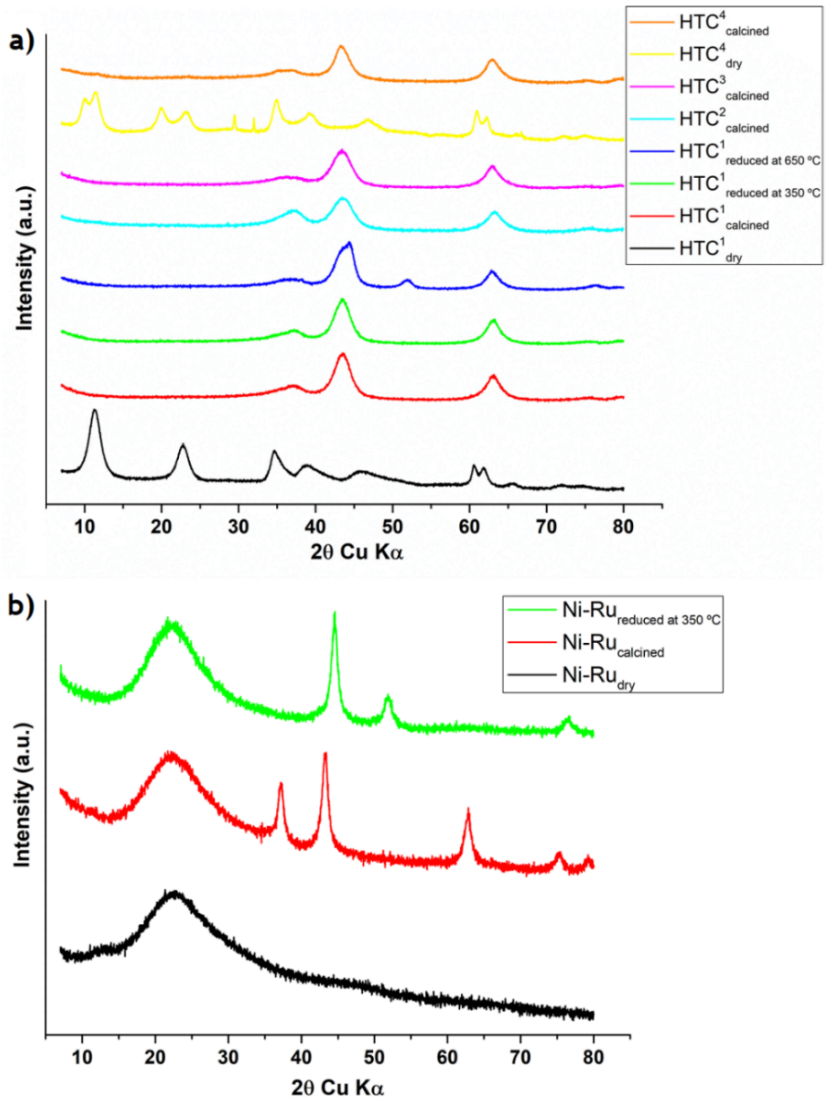

Fig. F.3. XRD patterns of different prepared catalysts. The curves have been vertically displaced for clarity.

1.3. Physical adsorption of nitrogen at -196 ºC

According to the IUPAC classification, isotherms of Type IV(a) were obtained for all the samples - see Fig. F.4. The volume of micropores (< 0.04 $cm^3 \cdot g^{-1}$) can be neglected for all the materials in comparison with the mesoporous volume. The isotherms obtained mean that the materials are mesoporous, which was confirmed with the diameter of the pores determined by the Density Functional Theory method (data not shown) [17].

For the N_2 adsorption isotherms obtained, it was possible to verify that the process of sorption-desorption of N_2 was irreversible (presence of hysteresis): the capillary condensation is different from the capillary evaporation and the hysteresis occurs [17, 18] - the type of hysteresis is indicated close to the isotherm in the Fig. F.4.

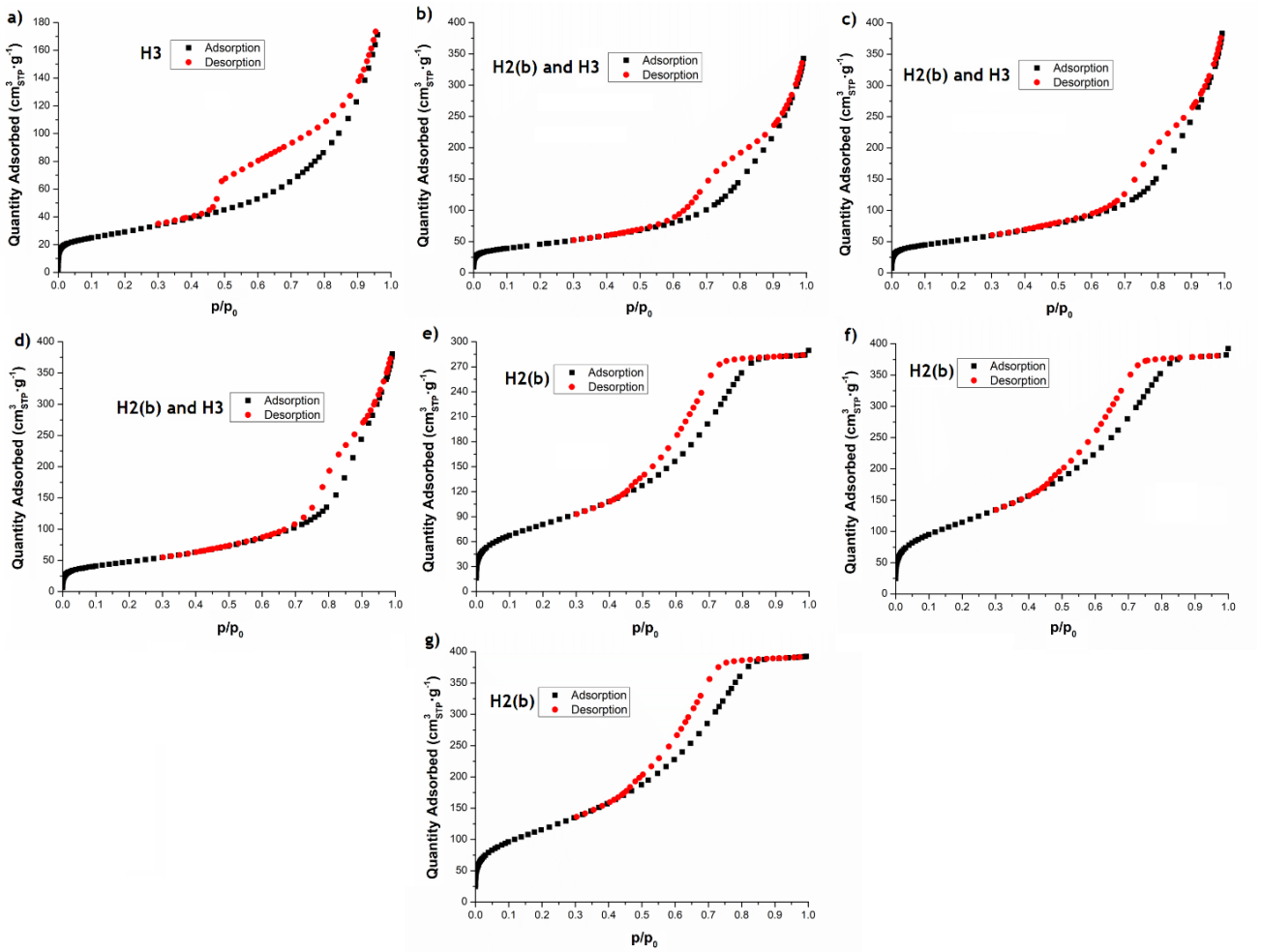

Fig. F.4. Adsorption/desorption isotherms of N_2 over catalysts HTC[1] a) dry, b) calcined, c) reduced at 350 ºC and d) reduced at 650 ºC) and Ni-Ru e) dry, f) calcined and g) reduced at 350 ºC).

1.4. TPR-H_2

TPR profile of calcined catalyst HTC[4] shows two distinct types of reduction: the first peak of H_2 consumption at lower temperatures (450 ºC) is mainly related to the reduction of oxygen species adsorbed on the catalyst surface (leading, for instance, to NiO particles that remained outside the Mg-Al oxide lattice) while the second wide zone occurs at higher temperatures (> 600 ºC) and is associated with the reduction of bulk NiO to metallic Ni [19, 20]. Besides that, analyzing the TPR profiles of all HTC-based catalysts, it was possible to verify a high interaction between NiO species and MgO in these materials; the reduction peaks of Ni species indicate the presence/formation of a NiO-MgO solid solution (reduction at temperatures above 750 ºC) [21-24].

The TPR profile of the calcined sample of Ni/SiO_2 presents three different peaks related to the reduction of surface NiO present in the SiO_2 support to metallic Ni. The existence of several peaks evidenced the inhomogeneity of nickel in this material - i.e., NiO particles with different interactions with the SiO_2 support [25-27]. The Ni-Ru catalyst only one broad peak was detected in the TPR analysis related to the reduction of NiO; it was not seen any peak related with the reduction of RuO_2, probably due to the low content of ruthenium in the sample (as seen in the ICP analysis). Contrasting with the Ni catalyst, the existence of only one broad reduction peak in the TPR results of the Ni-Ru catalyst demonstrated that the interactions of the NiO particles with the SiO_2 support are more similar in this material [25-27].

1.5. TPD-CO_2

The TPD-CO_2 results of the Ni-Ru sample did not show a very well-defined peak related to weak basic sites. In addition, two desorption peaks related to medium basic sites (a defined peak at 260 ºC and a small peak at 450 ºC) were detected. Nevertheless, it was not possible to verify the presence of strong basic sites in this catalyst. About the Ni sample, it was seen that this material does not present defined peaks in the region of the weak basic sites. The TPD profile of this catalyst presents two small peaks (at 350 and 430 ºC - with a shoulder in the first peak at 310 ºC) connected with the existence of medium basic sites, and two overlapped desorption peaks (associated to medium and strong basic sites) in the temperature range of 490-650 ºC - maximums at 500 and 575 ºC - and a narrow peak at 790 ºC related with strong basic sites.

For the material HTC[1] reduced at 650 ºC it was possible to identify 2 desorption peaks - one broad peak between 50 and 350 ºC (weak and medium basic sites), with high and nearly constant desorption of CO_2 in this range, and another small peak at >750 ºC (strong basic sites). However, when the HTC[1] material was activated at 350 ºC, also one broad desorption peak related to medium and strong basic sites was detected in the range of 430-680 ºC (maximum at 600 ºC, with a shoulder at 480 ºC). Besides that, it was detected a broad peak between 50-400 ºC related to the existence of weak and medium

basic sites (with maximum CO_2 desorption at 115 ºC) and a small peak at 760 ºC associated with the presence of strong basic sites.

1.6 SEM/EDS

SEM/EDS analyses were performed to understand the morphology of the catalysts and to inspect the changes that they suffered during the stability tests. The SEM images and the EDS analyses were performed for the HTC[1] and Ni-Ru catalysts.

In a preliminary analysis, it was confirmed that none of the samples shows a well-defined morphology. The presence of thin slabs and irregular porous surface was clearly observed for HTC[1] (cf. Fig. F.5a), Fig. F.5c) and Fig. F.5e) for the dry, calcined and reduced samples of HTC[1], respectively - even though the SEM image for the sample reduced to 650 ºC is not shown, it has the same morphology as the others). The EDS analyses (and EDS mapping) of these materials indicated homogenous distribution of the chemical elements in different samples of HTC[1] and the content of coke at the surface of the used materials was very low - see Fig. F.5 and Fig. F.6.

Additionally, for the dry catalyst Ni-Ru, it was possible to observe large flat surfaces with high contents of ruthenium and nickel - Z1 zone represented in Fig. F.5b)). However, after the calcination, the ruthenium in all Ni-Ru samples (calcined, reduced and spent) was detected in small particles.

EDS analyses (and EDS mapping) showed that the nickel and ruthenium content of the calcined, reduced and spent samples of the Ni-Ru catalyst was not homogeneous on the surface of the particles - see Fig. F.6. It was possible to find zones Z1, Z2 and Z3 on the surface of the particles of these samples with different loadings of nickel and ruthenium. For all the samples of this catalyst, it was verified that only in the zones Z3 ruthenium was detected - see Fig. F.5 and Fig. F.8.

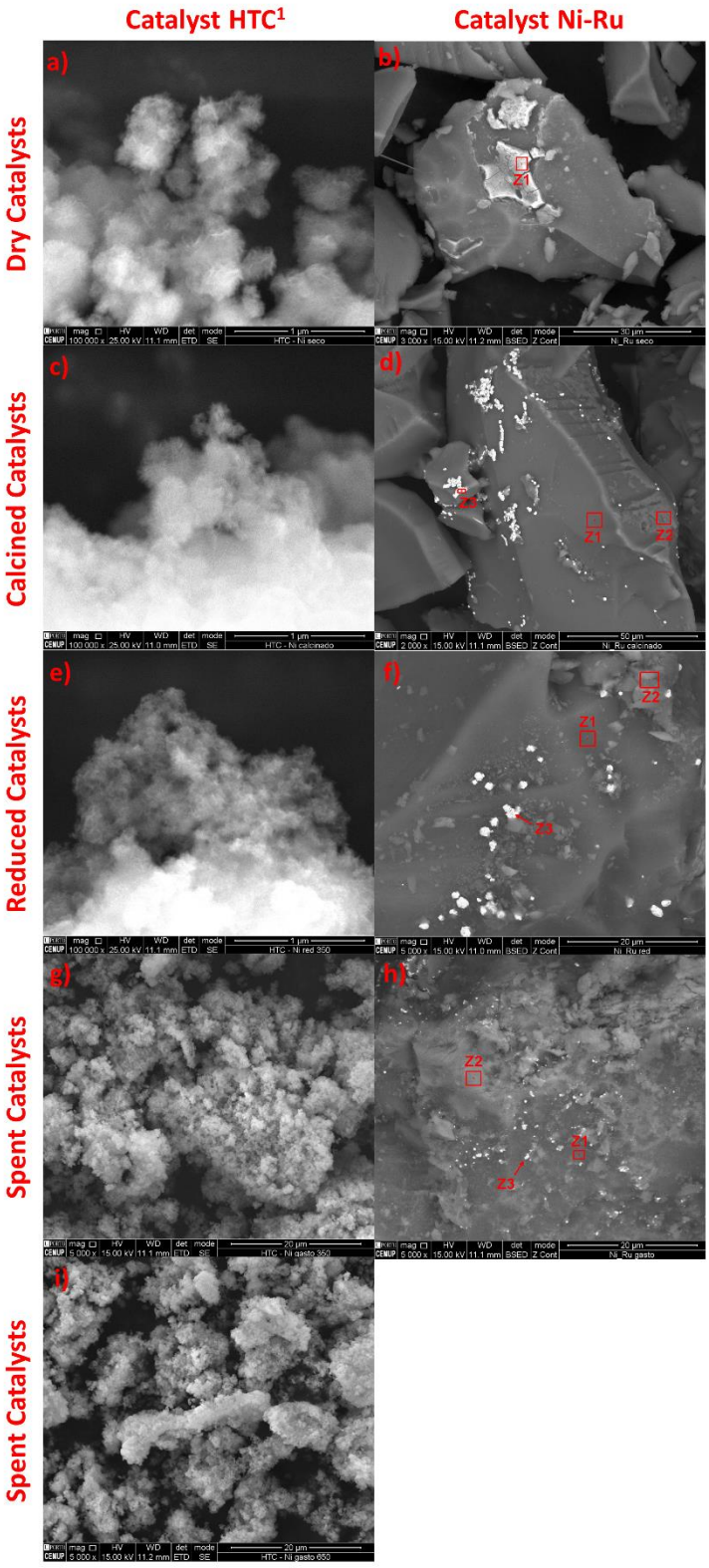

Fig. F.5. SEM images of samples of HTC[1] and Ni-Ru catalysts: a) and b) - dry samples; c) and d) calcined samples; e) and f) reduced samples at 350 ºC; and spent catalysts that were previously activated at g-h) 350 ºC or i) 650 ºC.

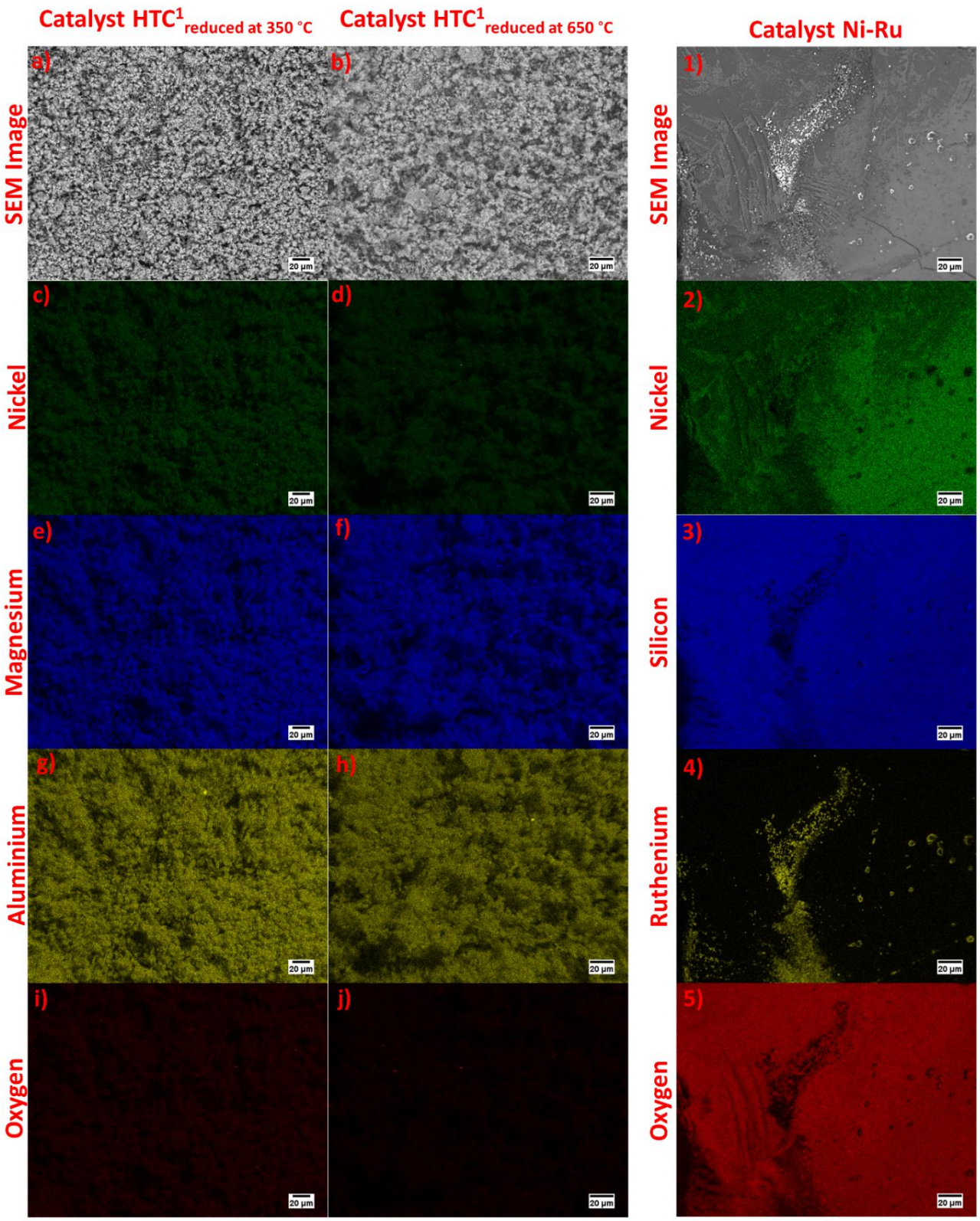

Fig. F.6. EDS mapping of reduced samples of catalyst HTC[1] (reduced at a) 350 ºC or b) 650 ºC) and 1) catalyst Ni-Ru.

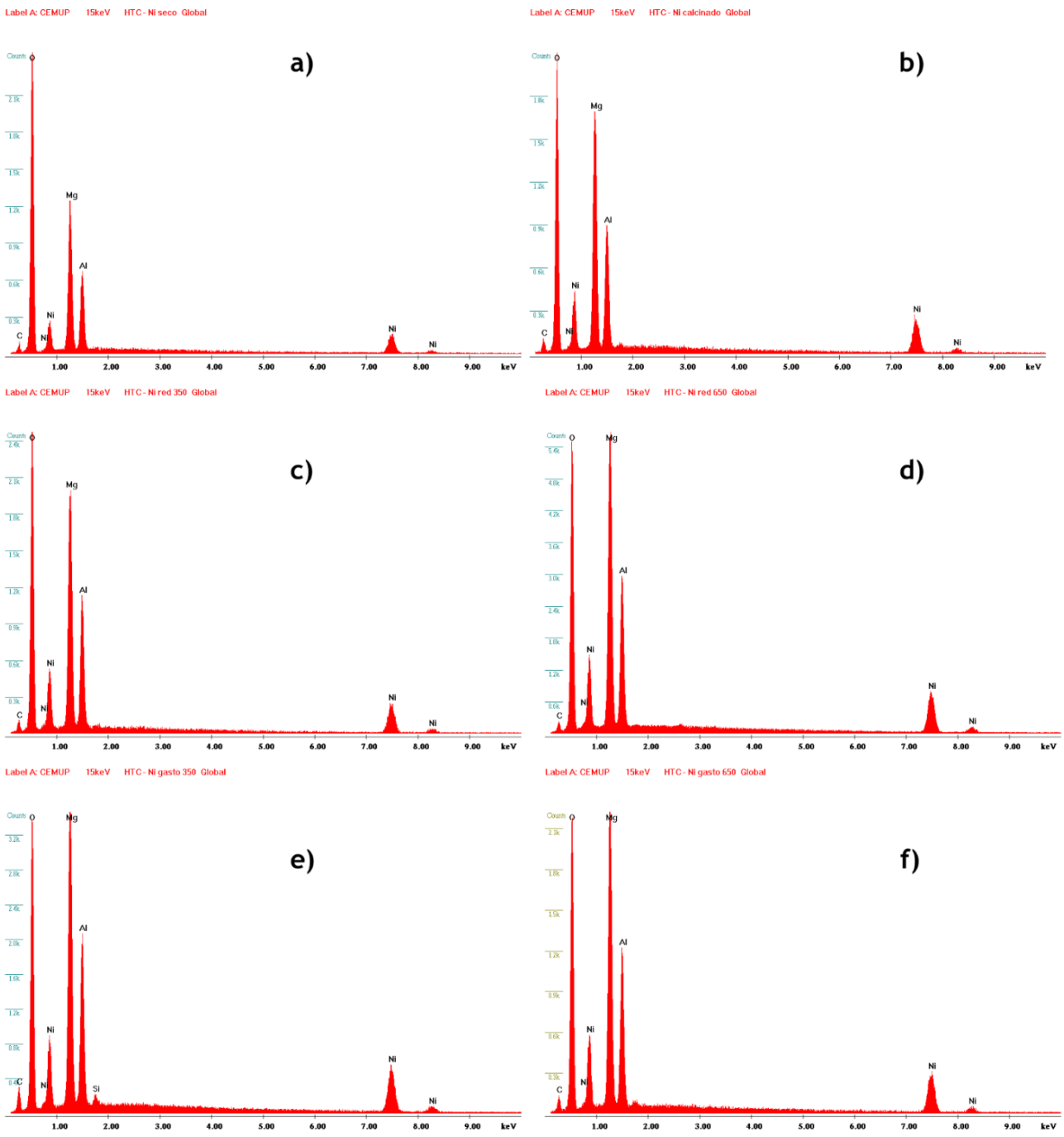

Fig. F.7. EDS analyses for different samples of HTC[1]: a) dry, b) calcined, reduced (activated at c) 350 ºC or d) 650 ºC) and spent catalyst (previously activated at e) 350 ºC or f) 650 ºC).

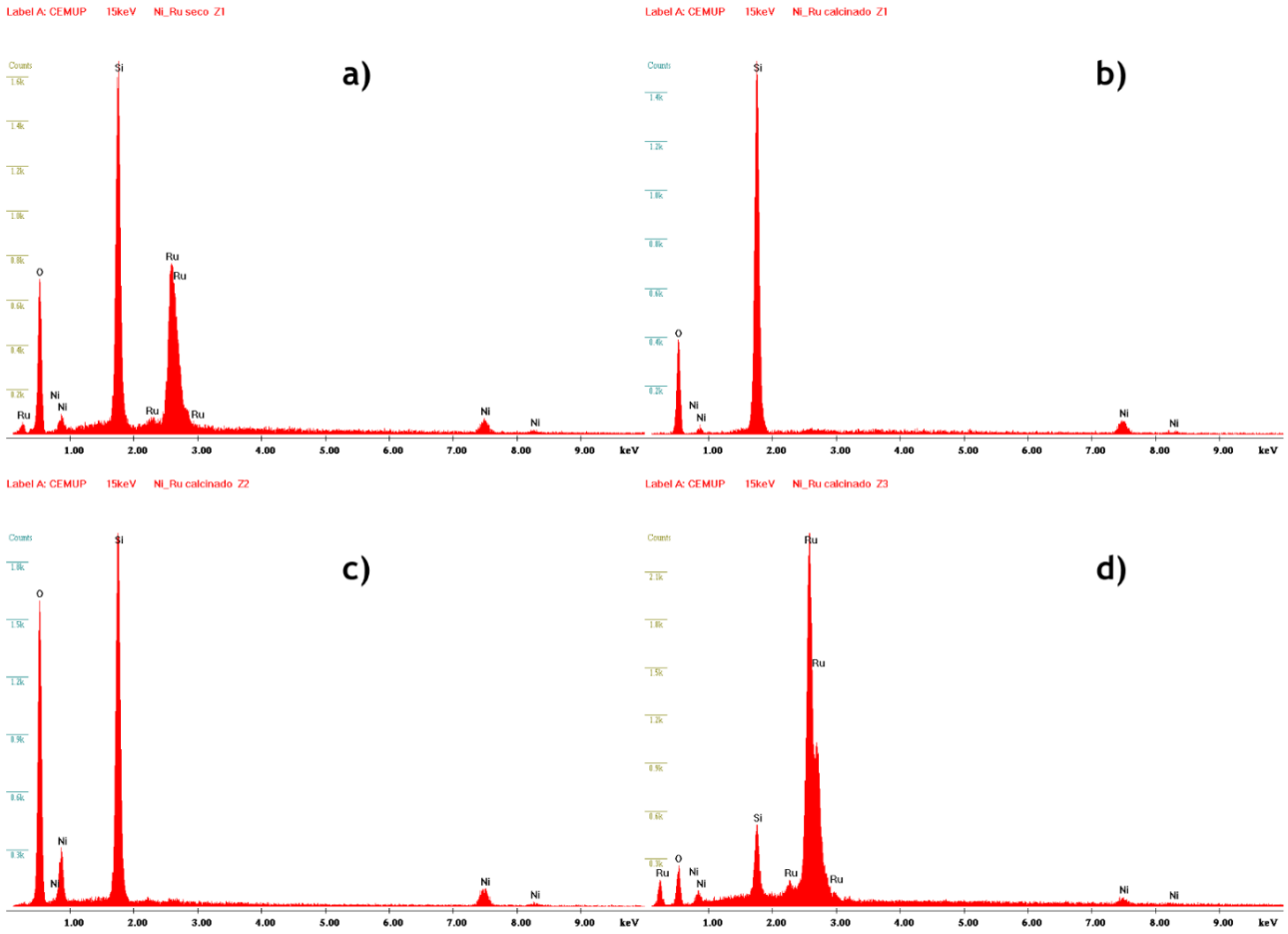

Fig. F.8. EDS analysis for the dry sample of Ni-Ru catalyst in a) Z1 zone and for the calcined sample of Ni-Ru catalyst in b) Z1 zone, c) Z2 zone and d) Z3 zone.

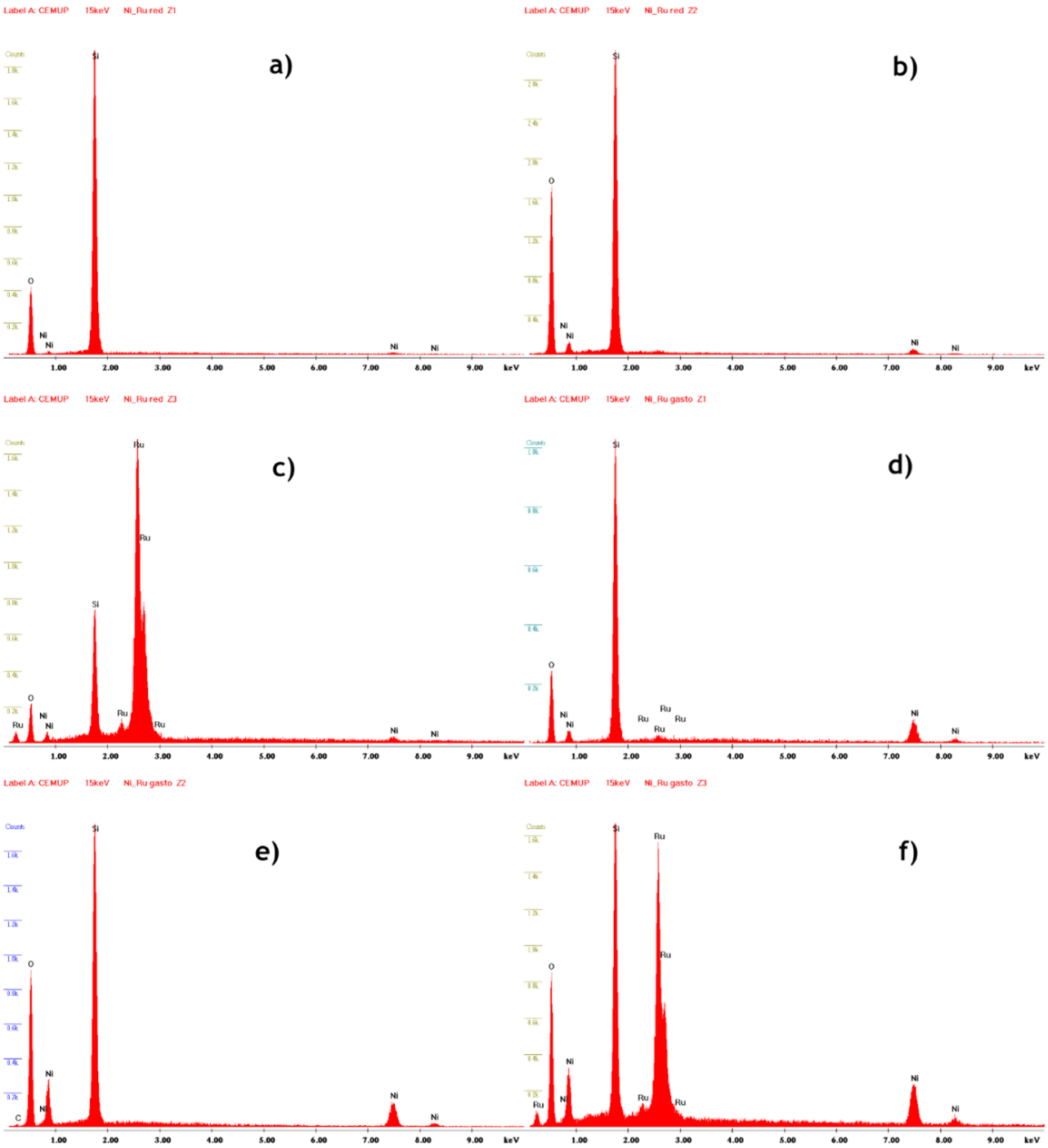

Fig. F.9. EDS analysis for the sample of Ni-Ru catalyst reduced at 350 ºC in a) Z1 zone, b) Z2 zone and c) Z3 zone and for the spent sample of Ni-Ru catalyst in d) Z1 zone, e) Z2 zone and f) Z3 zone.

2. Catalytic tests

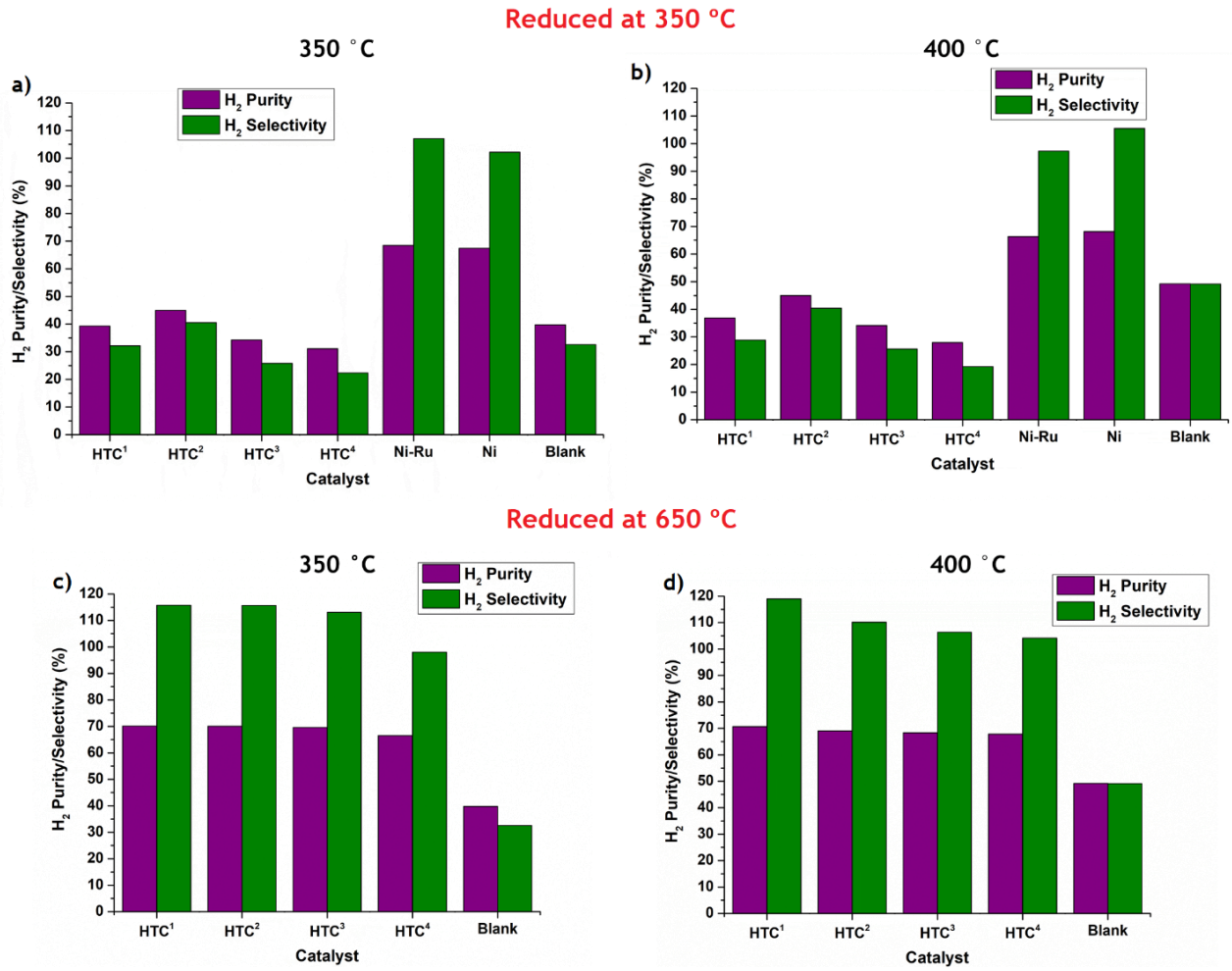

Fig. F.10. Mean of the H_2 purity/selectivity obtained for all catalysts activated at 350 ºC in *Exp. 2.1* at a) 350 ºC and b) 400 ºC; and mean of the H_2 purity/selectivity obtained for the HTC-based materials activated at 650 ºC in *Exp. 2.1* at c) 350 ºC and d) 400 ºC.

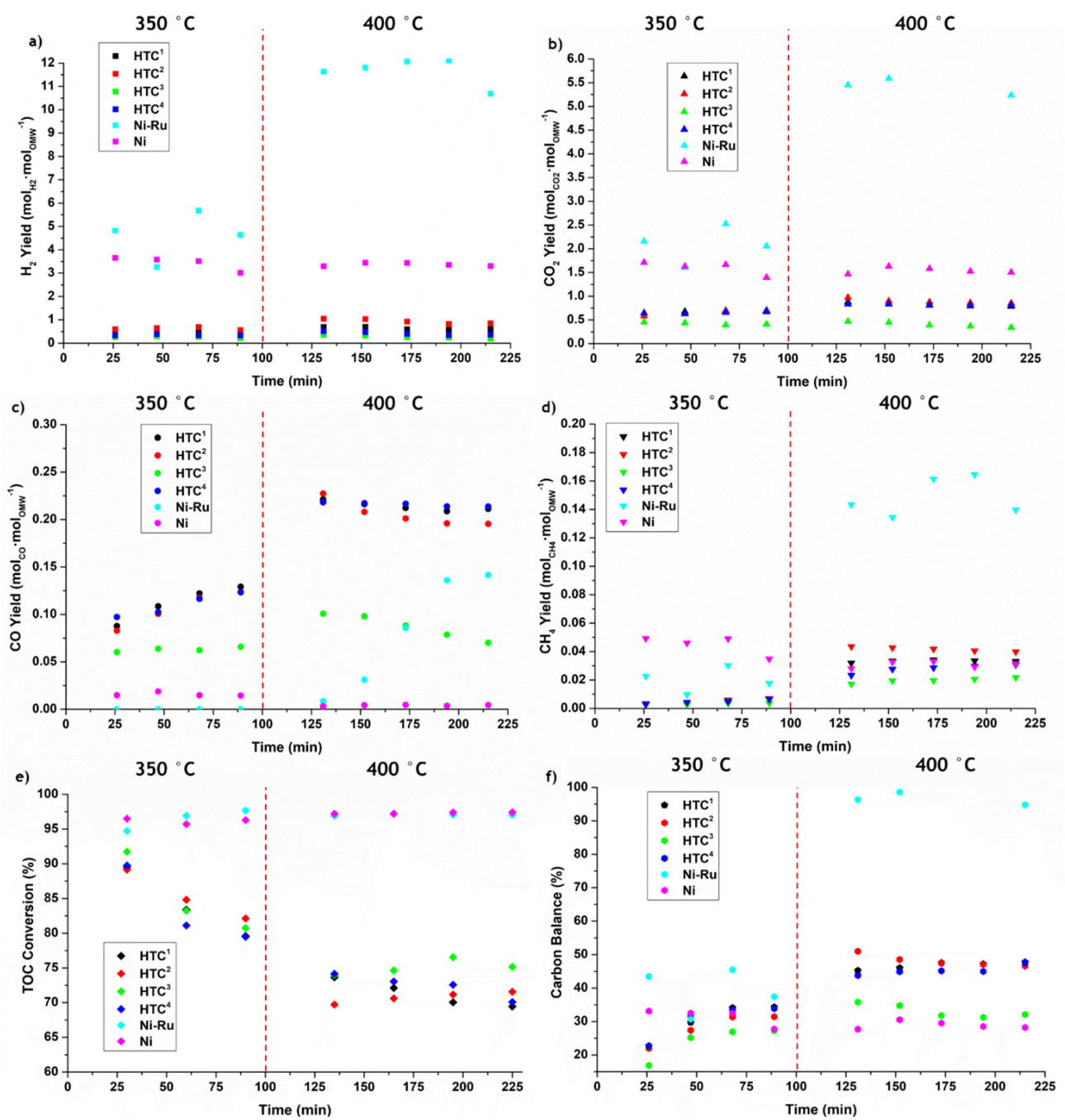

Fig. F.11. Yields of a) H_2, b) CO_2, c) CO and d) CH_4, e) TOC conversion and f) carbon balance obtained in *Exp. 2.1* (catalytic screening) for all the catalysts activated at 350 ºC as a function of time on stream at different temperatures.

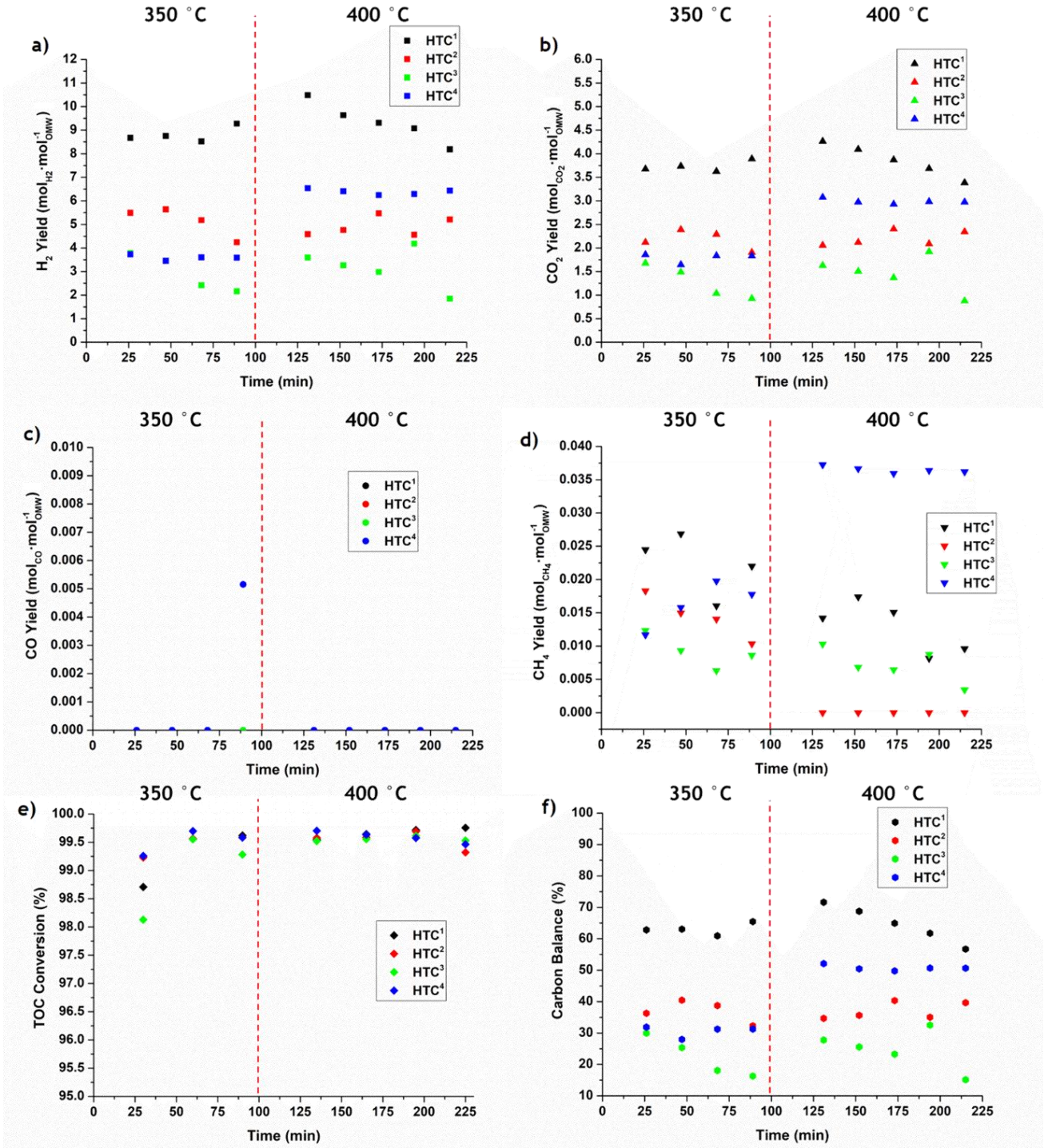

Fig. F.12. Yields of a) H_2, b) CO_2, c) CO and d) CH_4, e) TOC conversion and f) carbon balance obtained in *Exp. 2.1* for the HTC-based catalysts activated at 650 ºC as a function of time on stream at different temperatures.

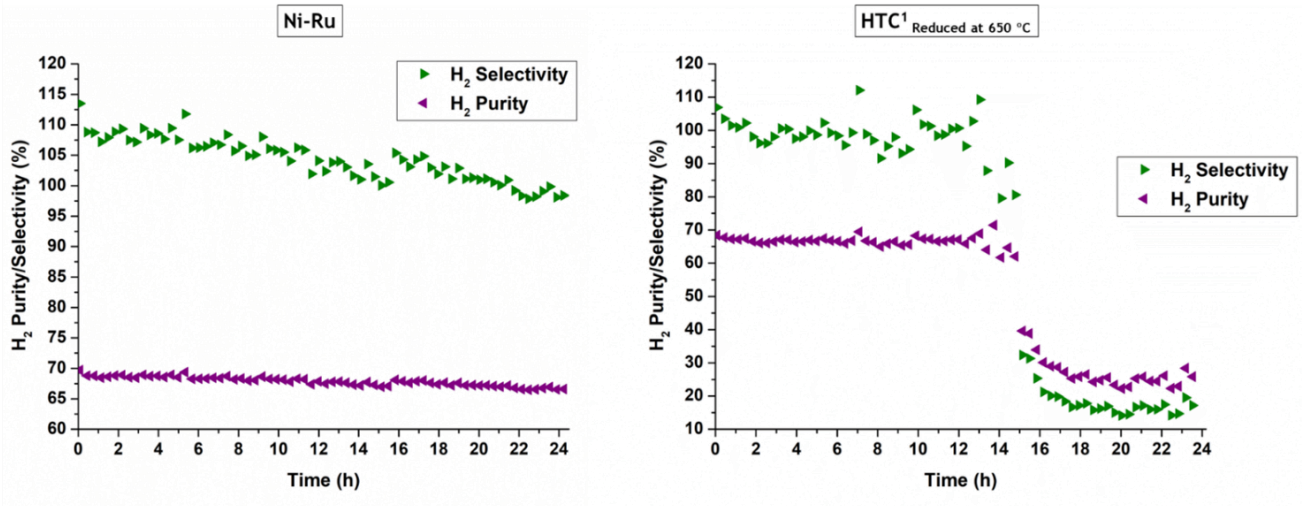

Fig. F.13. H_2 purity/selectivity obtained for the catalysts Ni-Ru and HTC^1 during the stability tests (*Exp. 2.2*).

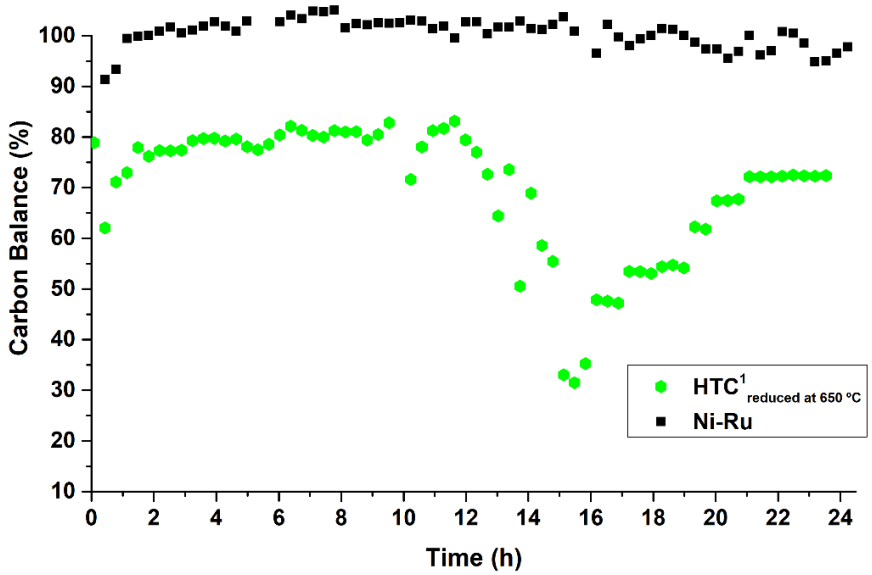

Fig. F.14. Carbon balance calculated in *Exp. 2.2* (stability tests) for the two catalysts studied in the stability tests.

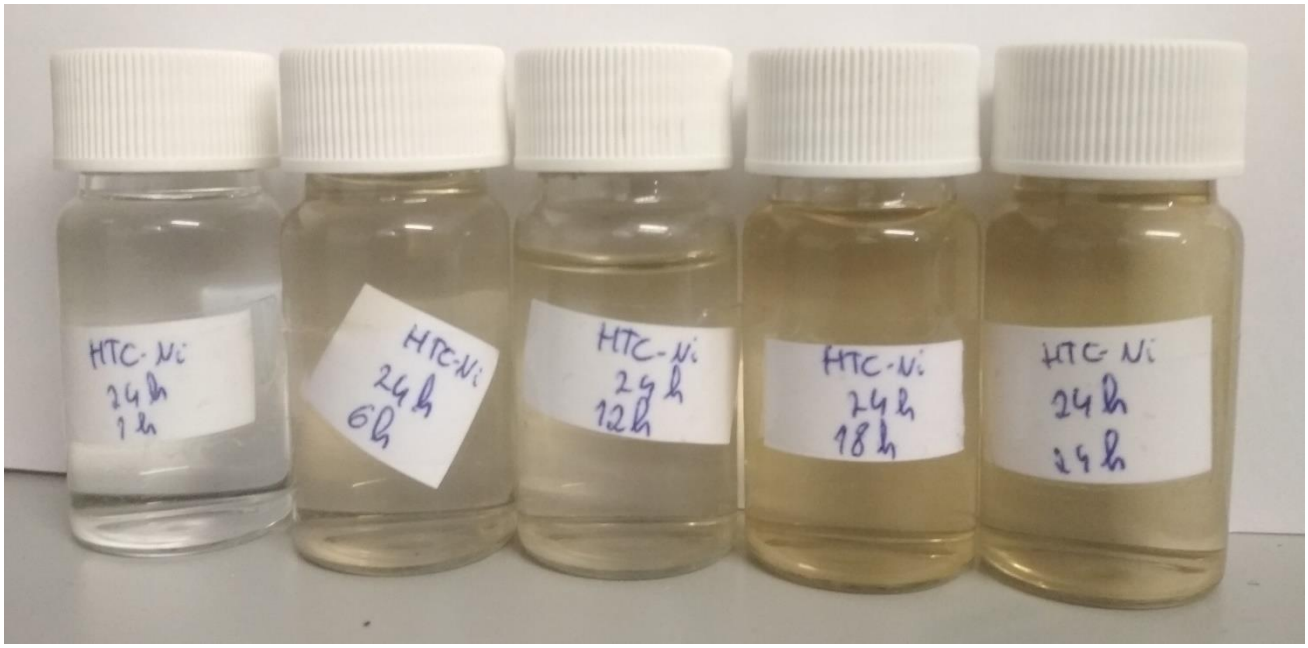

Fig. F.15. Color difference between the condensed phases obtained along the stability test using the HTC[1] catalyst (samples were collected over time from left to right).

References

[1] Ram Reddy, M.K., Z.P. Xu, G.Q. Lu and J.C. Diniz da Costa, Layered Double Hydroxides for CO2 Capture: Structure Evolution and Regeneration. Industrial & Engineering Chemistry Research, 2006. 45(22): p. 7504-7509.

[2] van Bokhoven, J.A., J.C.A.A. Roelofs, K.P. de Jong and D.C. Koningsberger, Unique Structural Properties of the Mg-Al Hydrotalcite Solid Base Catalyst: An In Situ Study Using Mg and Al K-Edge XAFS during Calcination and Rehydration. Chemistry - A European Journal, 2001. 7(6): p. 1258-1265.

[3] Miyata, S. and A. Okada, Synthesis of Hydrotalcite-like Compounds and their Physico-Chemical Properties - The Systems Mg2+-Al3+-SO2- and Mg2+-Al3+-CrO2- Clays and Clay Minerals, 1977. 25(1): p. 14-18.

[4] Ragaini, V., C. Pirola, S. Vitali, G. Bonura, C. Cannilla and F. Frusteri, Stability of Metallic Ruthenium in Ru-Co Supported Silica Catalysts. Catalysis Letters, 2012. 142(12): p. 1452-1460.

[5] Zou, W. and R.D. Gonzalez, The chemical anchoring of noble metal amine precursors to silica. Catalysis Today, 1992. 15(3): p. 443-453.

[6] Goodwin, J.G., D.O. Goa, S. Erdal and F.H. Rogan, Reactive metal volatilization from Ru/Al2O3 as a result of ruthenium carbonyl formation. Applied Catalysis, 1986. 24(1): p. 199-209.

[7] Girardon, J.S., A. Constant-Griboval, L. Gengembre, P.A. Chernavskii and A.Y. Khodakov, Optimization of the pretreatment procedure in the design of cobalt silica supported Fischer-Tropsch catalysts. Catalysis Today, 2005. 106(1): p. 161-165.

[8] Argyle, M.D. and C.H. Bartholomew, Heterogeneous Catalyst Deactivation and Regeneration: A Review. Catalysts, 2015. 5(1): p. 145-269.

[9] Cunha, A.F., Y.J. Wu, F.A. Díaz Alvarado, J.C. Santos, P.D. Vaidya and A.E. Rodrigues, Steam reforming of ethanol on a Ni/Al2O3 catalyst coupled with a hydrotalcite-like sorbent in a multilayer pattern for co2 uptake. The Canadian Journal of Chemical Engineering, 2012. 90(6): p. 1514-1526.

[10] Park, K., K.Y. Kim, L. Lu, T.-H. Lim, S.-A. Hong and H.-I. Lee, Structural Characteristics of (NiMgAl)Ox Prepared from a Layered Double Hydroxide Precursor and its Application in Direct Internal Reforming Molten Carbonate Fuel Cells. Fuel Cells, 2007. 7(3): p. 211-217.

[11] Tsujimura, A., M. Uchida and A. Okuwaki, Synthesis and sulfate ion-exchange properties of a hydrotalcite-like compound intercalated by chloride ions. Journal of Hazardous Materials, 2007. 143(1): p. 582-586.

[12] Ingram, L. and H.F.W. Taylor, The crystal structures of sjögrenite and pyroaurite. Mineralogical Magazine and Journal of the Mineralogical Society, 1967. 36(280): p. 465-479.

[13] Nejati, K., A. Mokhtari, F. Khodam and Z. Rezvani, Syntheses of Mg-Al-NO3 layered double hydroxides with high crystallinity in the presence of amines. Canadian Journal of Chemistry, 2015. 94(1): p. 66-71.

[14] Waseem, M., S. Mustafa, A. Naeem, K. Shah, I. Shah and Ihsan-Ul-Haque, Synthesis and characterization of silica by sol-gel method. Vol. 3. 2009. 19-21.

[15] Nawfal, M., C. Gennequin, M. Labaki, B. Nsouli, A. Aboukaïs and E. Abi-Aad, Hydrogen production by methane steam reforming over Ru supported on Ni-Mg-Al mixed oxides prepared via hydrotalcite route. Vol. 40. 2015. 1269-1277.

[16] Wang, C., B. Dou, H. Chen, Y. Song, Y. Xu, X. Du, T. Luo and C. Tan, Hydrogen production from steam reforming of glycerol by Ni-Mg-Al based catalysts in a fixed-bed reactor. Chemical Engineering Journal, 2013. 220: p. 133-142.

[17] Thommes, M., K. Kaneko, V. Neimark Alexander, P. Olivier James, F. Rodriguez-Reinoso, J. Rouquerol and S.W. Sing Kenneth, Physisorption of gases, with special reference to the evaluation of surface area and pore size distribution (IUPAC Technical Report), in Pure and Applied Chemistry. 2015. p. 1051.

[18] Rodrigues, S.L., Remoção em fase líquida do fármaco Diclofenac por adsorção em biocarvão. 2015, Faculdade de Ciências e Tecnologia - Universidade Nova de Lisboa: Lisbon.

[19] Wu, H.-p., Z.-y. Qian, X.-l. Xu and X.-f. Xu, N2O decomposition over K-promoted NiAl mixed oxides derived from hydrotalcite-like compounds. Journal of Fuel Chemistry and Technology, 2011. 39(2): p. 115-121.

[20] Borges, R.P., R.A.R. Ferreira, R.C. Rabelo-Neto, F.B. Noronha and C.E. Hori, Hydrogen production by steam reforming of acetic acid using hydrotalcite type precursors. International Journal of Hydrogen Energy, 2018. 43(16): p. 7881-7892.

[21] Song, C. and W. Pan, Tri-reforming of methane: a novel concept for catalytic production of industrially useful synthesis gas with desired H2/CO ratios. Catalysis Today, 2004. 98(4): p. 463-484.

[22] Djaidja, A., S. Libs, A. Kiennemann and A. Barama, Characterization and activity in dry reforming of methane on NiMg/Al and Ni/MgO catalysts. Catalysis Today, 2006. 113(3): p. 194-200.

[23] Li, D., Y. Nakagawa and K. Tomishige, Methane reforming to synthesis gas over Ni catalysts modified with noble metals. Applied Catalysis A: General, 2011. 408(1): p. 1-24.

[24] Zanganeh, R., M. Rezaei and A. Zamaniyan, Dry reforming of methane to synthesis gas on NiO-MgO nanocrystalline solid solution catalysts. International Journal of Hydrogen Energy, 2013. 38(7): p. 3012-3018.

[25] Yao, N., H. Ma, Y. Shao, C. Yuan, D. Lv and X. Li, Effect of cation-oligomer interactions on the size and reducibility of NiO particles on NiRu/SiO2 catalysts. Journal of Materials Chemistry, 2011. 21(43): p. 17403-17412.

[26] Yan, X., Y. Liu, B. Zhao, Z. Wang, Y. Wang and C.-j. Liu, Methanation over Ni/SiO2: Effect of the catalyst preparation methodologies. International Journal of Hydrogen Energy, 2013. 38(5): p. 2283-2291.

[27] Liu, B., N. Yao, S. Li, J. Wang, D. Lv and X. Li, Methanation of CO in hydrogen-rich gas on Ni-Ru/SiO2 catalyst: The type of active sites and Ni-Ru synergistic effect. Chemical Engineering Journal, 2016. 304: p. 476-484.

Appendix G. Supporting Information for Chapter 7

1. Catalytic tests

Fig. G.1. Module and tube/membrane used in the experimental tests.

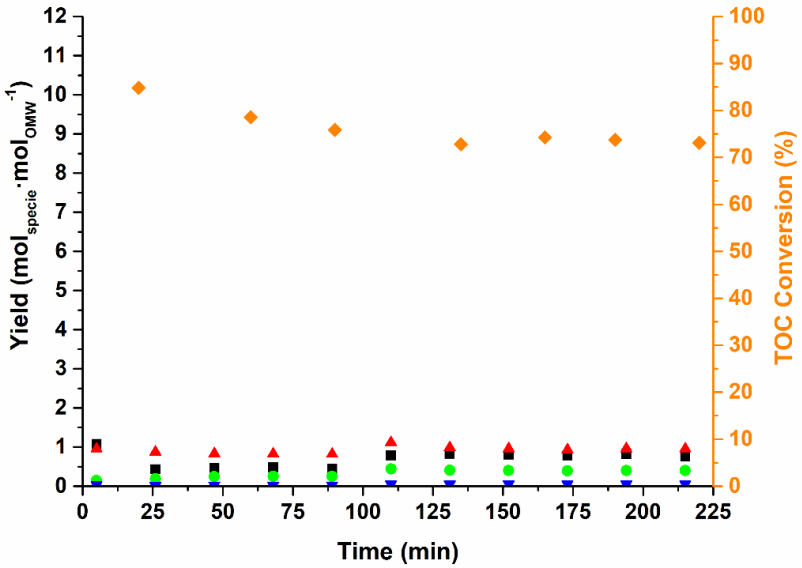

Fig. G.2. Gaseous carbon-containing products yields and TOC conversion at 400 ºC and 4 bar, obtained in the blank catalytic test with the commercial CO_2 sorbent MG30_K.

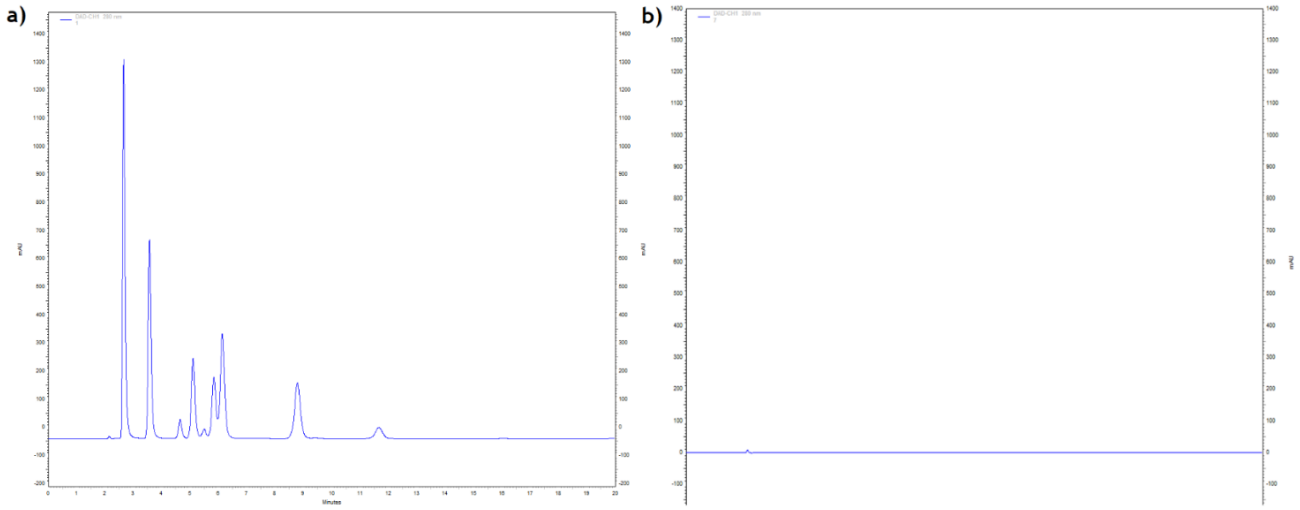

Fig. G.3. Identification of the organic content in a) the initial synthetic OMW effluent and in b) the outlet stream of the SEMR during the 4th cycle, at 400 ºC and 4 bar.

Fig. G.4. Color difference between the real effluent (on the left side) and the condensed phase of the same stream after the OMWSR process in the SEMR, at 400 ºC and 4 bar (on the right side).

2. Permeation tests

The simplest model typically used to describe the mass transport of H_2 through a Pd-based membrane assumes that the H_2 diffuses through the membrane according to Fick's first law [1-3]. In the H_2 permeation through this type of membrane is commonly assumed that the diffusion coefficient is constant along the membrane thickness and the mass transport is controlled by the diffusion step. In the case of Pd-based membranes, the sorption isotherm is generally described by Sieverts' law [4]. In this way, the flux of H_2 that is obtained in the permeate side can be determined by integration of Fick's first law of diffusion along all the membrane thickness - Eq. (G.1) [4]:

$$J_{H_2} = \frac{L_{H_2}}{\delta} \times \left(p_{H_2,feed}^{0.5} - p_{H_2,permeate}^{0.5} \right) \quad \text{(G.1)}$$

where J_{H_2} is the H_2 permeating flux, L_{H_2} is the permeability of the membrane, δ is the membrane thickness, p_{H_2} is the partial pressures of H_2 on the retentate or the permeate side. The ratio $\frac{L_{H_2}}{\delta}$ is normally called permeance.

However, despite the widespread use of Eq. (G.1) for several Pd-based membranes, it is necessary to highlight that this equation is only valid for certain operation conditions; for instance, as already mentioned, the equation is only applicable when the resistance in the diffusion along the membrane is the rate-determining step [5]. In this way, due to the several possible phenomena that occur in the membrane, it is common to use a global empirical equation for the flux of permeated H_2 through the membrane (Eq. (G.2)). Typically, the pressure exponent (*n*) takes values between 0.5 and 1 (for instance, due to the presence of external mass transfer resistances); however, higher values for the pressure exponent have been determined in previous works [6, 7].

$$J_{H_2} = \frac{L_{H_2}}{\delta} \times \left(p_{H_2,feed}^{n} - p_{H_2,permeate}^{n} \right) \quad \text{(G.2)}$$

Moreover, taking into consideration the variation of the driving-force along the membrane length, it was considered a logarithmic mean driving-force, defined as $\Delta P_{ln}{}^{n} = \frac{{p_{H_2,feed}}^{n} - \left({p_{H_2,feed}}^{n} - {p_{H_2,permeate}}^{n} \right)}{\ln\left(\frac{{p_{H_2,feed}}^{n}}{{p_{H_2,feed}}^{n} - {p_{H_2,permeate}}^{n}} \right)}$, considering that the H_2 partial pressure in the inlet of the permeate side is equal to 0 and that the H_2 partial pressure in the retentate side is equal to the H_2 partial pressure in the feed [8]. Then, replacing the expression of the driving-force present in Eq. (G.2) by the logarithmic mean driving-force, Eq. (G.3) is obtained.

$$J_{H_2} = \frac{L_{H_2}}{\delta} \times (\Delta P_{ln}{}^{n}) = \frac{L_{H_2}}{\delta} \times \left(\frac{{p_{H_2,feed}}^{n} - \left({p_{H_2,feed}}^{n} - {p_{H_2,permeate}}^{n} \right)}{\ln\left(\frac{{p_{H_2,feed}}^{n}}{{p_{H_2,feed}}^{n} - {p_{H_2,permeate}}^{n}} \right)} \right) \quad \text{(G.3)}$$

Before performing the OMWSR reaction in the SEMR, the 5 µm-thick Pd-Ag membrane was activated in situ at 400 ºC by feeding 200 $mL_N \cdot min^{-1}$ of pure H_2 at 1 bar. The H_2 collected in the permeate side was continuously swept in counter-current mode with 100 $mL_N \cdot min^{-1}$ of N_2 at atmospheric pressure. The membrane activation procedure was carried out until the H_2 flux stabilized for 1 h. Afterwards, pure H_2 permeation tests were performed under a wide range of driving-forces (Fig. G.5).

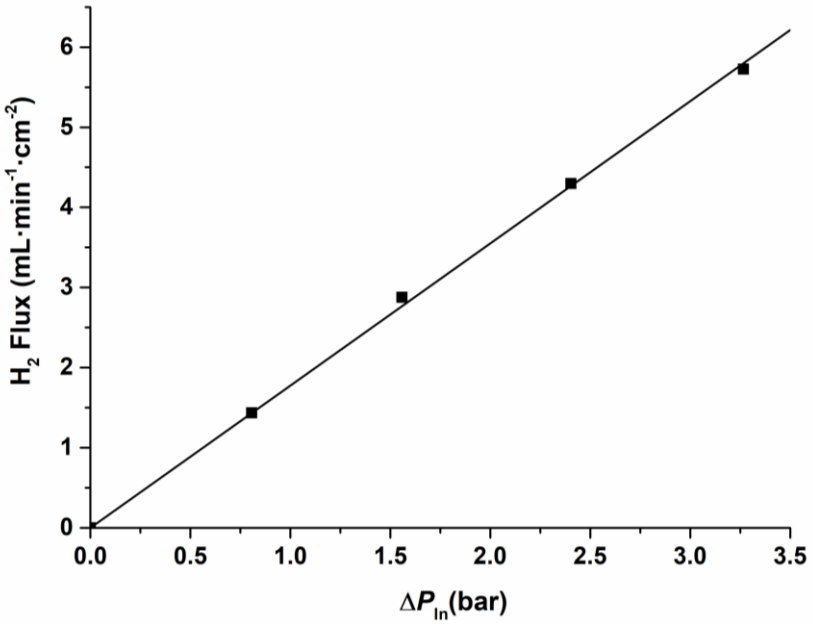

Fig. G.5. H_2 permeating flux as a function of the logarithmic mean driving-force for hydrogen permeation through the Pd-Ag membrane.

In this work, it was verified that the pressure exponent did not take the value of 0.5 (the *n* value determined was equal to 1) by fitting the experimental data with Eq. (G.3), due to the mass transport resistance that exists in the permeate side as a consequence of the presence of sweep gas - feeding sweep gas in the permeate side induces mass transfer limitation in the porous support, and thus a decrease of the H_2 flux [9]. The permeance obtained for this Pd-Ag membrane was equal to 1.32 x 10^{-7} $mol \cdot m^{-2} \cdot s^{-1} \cdot Pa^{-1}$, lower than the values determined for similar membranes (differ by one order of magnitude**)** [10], due to the mass transfer resistance imposed by the support.

Besides that, it was observed that the temperature influenced the performance of the membrane towards H_2 permeation. In Fig. G.6a) it is possible to verify the increase of the H_2 flux with the increase of the temperature for 2 different driving-forces ($\Delta P_{ln} \approx 1$ or 2 bar). Since the permeability of the membrane follows an Arrhenius-type equation (Eq. (G.4)), the apparent activation energy was determined from the linear fit between L_{H_2} and the inverse of the absolute temperature (see Fig. G.6b)).

$$L_{H_2} = {L_{H_2}}^0 \times e^{\left(-\frac{E_a}{RT}\right)} \quad \text{(G.4)}$$

In Eq. (G.4), ${L_{H_2}}^0$ is the pre-exponential factor, T is the absolute temperature, R is the molar ideal gas constant and E_a is the apparent activation energy of the permeation process. In this case, an activation energy of 38.75 kJ·mol^{-1} was obtained; according to the literature [11], activation energy values higher than 30 kJ·mol^{-1} indicate that diffusion is not the limiting step, as previously verified by the value determined for the pressure exponent n (≠ 0.5).

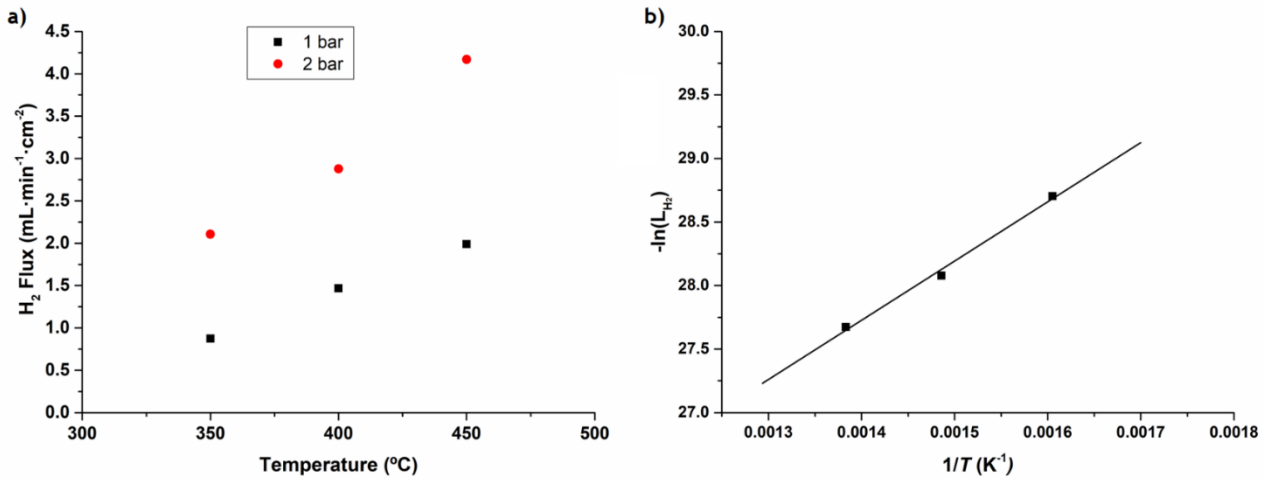

Fig. G.6. a) H_2 permeating flux as a function of the temperature at different driving-forces (ΔP_{ln} ≈ 1 and 2 bar) and b) hydrogen permeability as a function of the inverse of the absolute temperature (determined at ΔP_{ln} ≈ *1*).

Lastly, it was verified that a N_2 sweep gas flow rate higher than 100 $mL_N \cdot min^{-1}$ almost did not influence the quantity of H_2 permeated - see Fig. G.7. So, in the experimental tests with a SEMR, it was used a N_2 sweep gas flow rate of 100 $mL_N \cdot min^{-1}$ in the permeate side.

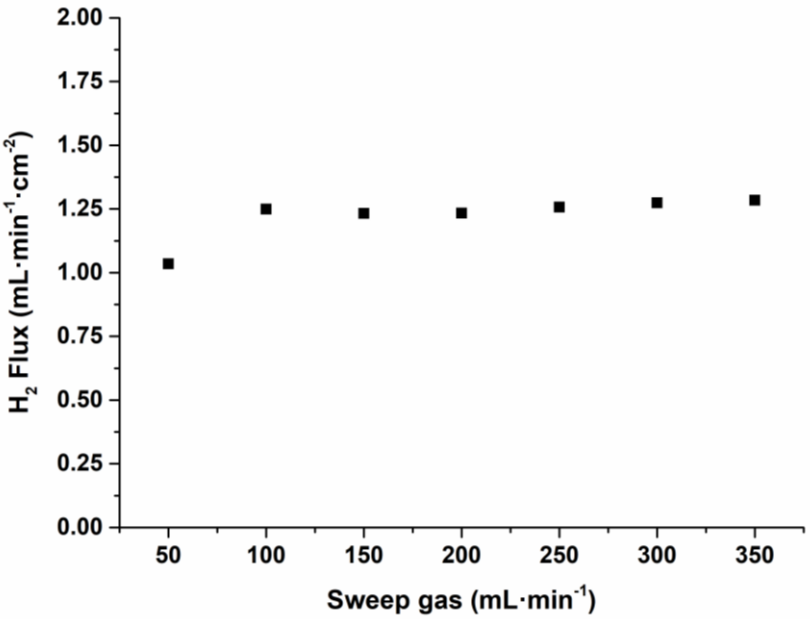

Fig. G.7. Effect of the flowrate of sweep gas in the H_2 permeating flux with $\Delta P_{ln} \approx 1$ bar.

References

[1] Barrie, J.A. and K. Munday, Gas transport in heterogeneous polymer blends: I. Polydimethylsiloxane-g-polystyrene and polydimethylsiloxane-b-polystyrene. Journal of Membrane Science, 1983. 13(2): p. 175-195.

[2] Shah, M.R., R.D. Noble and D.E. Clough, Analysis of transient permeation as a technique for determination of sorption and diffusion in supported membranes. Journal of Membrane Science, 2006. 280(1): p. 452-460.

[3] Koros, W.J., A.H. Chan and D.R. Paul, Sorption and transport of various gases in polycarbonate. Journal of Membrane Science, 1977. 2: p. 165-190.

[4] Campo, M., A. Tanaka, A. Mendes and J.M. Sousa, 3 - Characterization of membranes for energy and environmental applications, in Advanced Membrane Science and Technology for Sustainable Energy and Environmental Applications, A. Basile and S.P. Nunes, Editors. 2011, Woodhead Publishing. p. 56-89.

[5] Pizzi, D., R. Worth, M. Giacinti Baschetti, G.C. Sarti and K.-i. Noda, Hydrogen permeability of 2.5μm palladium-silver membranes deposited on ceramic supports. Journal of Membrane Science, 2008. 325(1): p. 446-453.

[6] Keurentjes, J.T.F., F.C. Gielens, H.D. Tong, C.J.M. van Rijn and M.A.G. Vorstman, High-Flux Palladium Membranes Based on Microsystem Technology. Industrial & Engineering Chemistry Research, 2004. 43(16): p. 4768-4772.

[7] Gielens, F.C., H.D. Tong, C.J.M. van Rijn, M.A.G. Vorstman and J.T.F. Keurentjes, Microsystem technology for high-flux hydrogen separation membranes. Journal of Membrane Science, 2004. 243(1): p. 203-213.

[8] Miguel, C.V., A. Mendes, S. Tosti and L.M. Madeira, Effect of CO and CO2 on H2 permeation through finger-like Pd-Ag membranes. International Journal of Hydrogen Energy, 2012. 37(17): p. 12680-12687.

[9] Nordio, M., S. Soresi, G. Manzolini, J. Melendez, M. Van Sint Annaland, D.A. Pacheco Tanaka and F. Gallucci, Effect of sweep gas on hydrogen permeation of supported Pd membranes: Experimental and modeling. International Journal of Hydrogen Energy, 2019. 44(8): p. 4228-4239.

[10] Fernandez, E., A. Helmi, J.A. Medrano, K. Coenen, A. Arratibel, J. Melendez, N.C.A. de Nooijer, V. Spallina, J.L. Viviente, J. Zuñiga, M. van Sint Annaland, D.A. Pacheco Tanakaand F. Gallucci, Palladium based membranes and membrane reactors for hydrogen production and purification: An overview of research activities at Tecnalia and TU/e. International Journal of Hydrogen Energy, 2017. 42(19): p. 13763-13776.

[11] Yun, S. and S. Ted Oyama, Correlations in palladium membranes for hydrogen separation: A review. Journal of Membrane Science, 2011. 375(1): p. 28-45.

Appendix H. Supporting Information for Chapter 8

1. Thermodynamic analysis results

Table H.1 - Flow of gaseous species and OMW conversion in the thermodynamic equilibrium for Case-study B.

Reactor Config.	H_2O inlet ($mol \cdot h^{-1}$)	H_2O outlet ($mol \cdot h^{-1}$)	Oxygenates intlet ($mol \cdot h^{-1}$)	H_2 outlet ($mol \cdot h^{-1}$)	CO outlet ($mol \cdot h^{-1}$)	CH_4 outlet ($mol \cdot h^{-1}$)	CO_2 outlet ($mol \cdot h^{-1}$)	Carbon outlet ($mol \cdot h^{-1}$)	CaO inlet* ($mol \cdot h^{-1}$)	$CaCO_3$ outlet ($mol \cdot h^{-1}$)	CO_2 Removal (%)	OMW Conversion (%)
	Scenario B.1											
TR	297 541	276 845	3 774	32 506	182	3 322	19 178	0	0	0	0	100
SER		270 093		45 828	1	36	46	0	22 599	22 599	≈ 100	100
	Scenario B.2											
TR	297 541	271 380	5 994	38 228	308	8 621	27 095	0	0	0	0	100
SER		254 676		71 329	2	422	86	0	35 514	35 514	≈ 100	100
	Scenario B.3											
TR	297 541	266 681	8492	41 764	446	15 308	35 279	0	0	0	0	100
SER		240 643		93 399	5	2 510	165		48 965	48 965	≈ 100	100
	Scenario B.4											
TR	297 541	262 072	11 322	44 338	604	23 246	44 195	0	0	0	0	100
SER		227 167		113 552	7	6 091	174	0	61 773	61 773	≈ 100	100
	Scenario B.5											
TR	297 541	257 243	14 577	46 410	789	32 533	54 164	0	0	0	0	100
SER		210 092		139 927	6	9 349	106	0	78 024	78 024	≈ 100	100
	Scenario B.6											
TR	297 541	251 976	18 290	48 198	1012	43 397	65 508	0	0	0	0	100
SER		194 328		162 488	6	15 076	86	0	94 749	94 749	≈ 100	100
	Scenario B.7											
TR	297 541	246 070	22 644	49 820	1 285	56 185	78 618	0	0	0	0	100
SER		180 288		180 106	7	23 934	83	0	112 065	112 065	≈ 100	100

* Minimum quantity of CaO to reach a nearly complete CO_2 capture in the SER.

Table H.2 - Flow of gaseous species and OMW conversion in the thermodynamic equilibrium for Case-study C.

Reactor Config.	H_2O inlet ($mol \cdot h^{-1}$)	H_2O outlet ($mol \cdot h^{-1}$)	Oxygenates intlet ($mol \cdot h^{-1}$)	H_2 outlet ($mol \cdot h^{-1}$)	CO outlet ($mol \cdot h^{-1}$)	CH_4 outlet ($mol \cdot h^{-1}$)	CO_2 outlet ($mol \cdot h^{-1}$)	Carbon outlet ($mol \cdot h^{-1}$)	CaO inlet* ($mol \cdot h^{-1}$)	$CaCO_3$ outlet ($mol \cdot h^{-1}$)	CO_2 Removal (%)	OMW Conversion (%)
	Scenario C.1											
TR	297 541	271 810	8 492	31 364	305	17 943	32 784	0	0	0	0	100
SER	297 541	240 888		92 904	1	2 634	44	0	48 353	48 353	≈ 100	100
	Scenario C.2											
TR	297 541	274 300	8 492	26 324	245	19 219	31 570	0	0	0	0	100
SER	297 541	240 938		92 804	1	2 659	20	0	48 353	48 353	≈ 100	100
	Scenario C.3											
TR	297 541	275 853	8 492	23 182	209	20 013	30 811	0	0	0	0	100
SER	297 541	240 955		92 769	0	2 668	11	0	48 353	48 353	≈ 100	100

* Minimum quantity of CaO to reach a nearly complete CO_2 capture in the SER

2. Design and Costs of Process Units

Reactor

Table H.3 - Design and cost of the reactor used for Case-studies B and C.

Design			
Temperature (ºC)	400	**Pressure (bar)**	4
Material	Stainless steel	**Geometry**	Cylinder
Volume (m^3)	2	**t_s (mm)**	5
Internal Diameter (m)	0.5	**Lenght (m)**	6.8
		τ (s)	0.13
Cost			
Weight (ton)	0.54	**Updated Cost (€)**	17 323*

* Includes an increase of 20 % for insulation and painting.

Energy Integration

Table H.4 - Energy integration for Scenario A.2.

TR

HE	Streams	Inlet Temperature (ºC)	Outlet Temperature (ºC)	ΔT	Flow Rate (kg·h^{-1})	Heat (MW)
(1)	(3)	23	55	32	10 711	0.40
	(12)	100	65	-35	9 769	
(2)	(4)	55	95	40	10 711	0.50
	(9)	400	308.5	-91.5	9 769	
Boiler	(5)	95	100	5	10 711	6.78
	Fuel Gas* (14+21)	-	-	-	-	
(3)	(6)	100	195	95	10 711	0.57
	(10)	308.5	204.5	-104	9 769	
(4)	(7)	195	400	205	10 711	1.22
	Exhaust Gas (15)	-	-	-	-	
Condenser	(11)	204.5	100	-104.5	9 769	6.69
	Cooling Water (19)	23	90	67	85 973	

SER

HE	Streams	Inlet Temperature (ºC)	Outlet Temperature (ºC)	ΔT	Flow Rate (kg·h^{-1})	Heat (MW)
(1)	(3)	23	55	32	10 711	0.40
	(12)	100	62.5	-37.5	9 168	
(2)	(4)	55	90	35	10 711	0.44
	(9)	400	314.5	-85.5	9 168	
Boiler	(5)	90	100	10	10 711	6.84
	Fuel Gas* (14+21)	-	-	-	-	
(3)	(6)	100	195	95	10 711	0.57
	(10)	314.5	203.5	-111	9 168	
(4)	(7)	195	400	205	10 711	1.22
	Exhaust Gas (15)	-	-	-	-	
Condenser	(11)	203.5	100	-103.5	9 168	6.28
	Cooling Water (19)	23	90	67	80 692	

* Heat from the combustion of fuel gas ((H_2+CH_4) + natural gas).

Table H.5 - Energy integration for Scenario A.3.

TR

HE	Streams	Inlet Temperature (ºC)	Outlet Temperature (ºC)	ΔT	Flow Rate (kg·h^{-1})	Heat (MW)
(1)	(3)	23	55	32	10 711	0.40
	(12)	100	64.5	-35.5	9 600	
(2)	(4)	55	95	40	10 711	0.50
	(9)	400	307	-93	9 600	
Boiler	(5)	95	100	5	10 711	6.78
	Fuel Gas* (14+21)	-	-	-	-	
(3)	(6)	100	195	95	10 711	0.57
	(10)	307	201	-106	9 600	
(4)	(7)	195	400	205	10 711	1.22
	Exhaust Gas (15)	-	-	-	-	
Condenser	(11)	201	100	-101	9 600	6.56
	Cooling Water (19)	23	90	67	84 384	

SER

HE	Streams	Inlet Temperature (ºC)	Outlet Temperature (ºC)	ΔT	Flow Rate (kg·h^{-1})	Heat (MW)
(1)	(3)	23	53	30	10 711	0.37
	(12)	100	63	-37	8 622	
(2)	(4)	53	84.5	31.5	10 711	0.39
	(9)	400	318	-82	8 622	
Boiler	(5)	84.5	100	15.5	10 711	6.91
	Fuel Gas* (14+21)	-	-	-	-	
(3)	(6)	100	195	95	10 711	0.57
	(10)	318	200	-118	8 622	
(4)	(7)	195	400	205	10 711	1.22
	Exhaust Gas (15)	-	-	-	-	
Condenser	(11)	200	100	-100	8 622	5.88
	Cooling Water (19)	23	90	67	75 550	

* Heat from the combustion of fuel gas ((H_2+CH_4) + natural gas).

Table H.6 - Energy integration for Scenario B.1.

TR

HE	Streams	Inlet Temperature (ºC)	Outlet Temperature (ºC)	ΔT	Flow Rate (kg·h^{-1})	Heat (MW)
(1)	(3)	23	55	32	5 356	0.20
	(12)	100	65.5	-34.5	4 983	
(2)	(4)	55	95	40	5 356	0.25
	(9)	400	310.5	-89.5	4 983	
Boiler	(5)	95	100	5	5 356	3.39
	Fuel Gas* (14+21)	-	-	-	-	
(3)	(6)	100	195	95	5 356	0.28
	(10)	310.5	208.5	-102	4 983	
(4)	(7)	195	400	205	5 356	0.61
	Exhaust Gas (15)	-	-	-	-	
Condenser	(11)	208.5	100	-108.5	4 983	3.42
	Cooling Water (19)	23	90	67	43 992	

SER

HE	Streams	Inlet Temperature (ºC)	Outlet Temperature (ºC)	ΔT	Flow Rate (kg·h^{-1})	Heat (MW)
(1)	(3)	23	55	32	5 356	0.20
	(12)	100	65	-35	4 862	
(2)	(4)	55	95	40	535	0.25
	(9)	400	308	-92	4 862	
Boiler	(5)	95	100	5	5 356	3.39
	Fuel Gas* (14+21)	-	-	-	-	
(3)	(6)	100	194	94	5 356	0.28
	(10)	308	204	-104	4 862	
(4)	(7)	194	400	206	5 356	0.61
	Exhaust Gas (15)	-	-	-	-	
Condenser	(11)	204	100	-104	4 862	3.33
	Cooling Water (19)	23	90	67	42 804	

* Heat from the combustion of fuel gas ((H_2+CH_4) + natural gas).

Table H.7 - Energy integration for Scenario B.2.

TR

HE	Streams	Inlet Temperature (ºC)	Outlet Temperature (ºC)	ΔT	Flow Rate (kg·h^{-1})	Heat (MW)
(1)	(3)	23	55	32	5 356	0.20
	(12)	100	65	-35	4 885	
(2)	(4)	55	95	40	5 356	0.25
	(9)	400	308.5	-91.5	4 885	
Boiler	(5)	95	100	5	5 356	3.39
	Fuel Gas* (14+21)	-	-	-	-	
(3)	(6)	100	195	95	5 356	0.28
	(10)	308.5	204.5	-104	4 885	
(4)	(7)	195	400	205	5 356	0.61
	Exhaust Gas (15)	-	-	-	-	
Condenser	(11)	204.5	100	-104.5	4 885	3.35
	Cooling Water (19)	23	90	67	43 079	

SER

HE	Streams	Inlet Temperature (ºC)	Outlet Temperature (ºC)	ΔT	Flow Rate (kg·h^{-1})	Heat (MW)
(1)	(3)	23	54	31	5 356	0.19
	(12)	100	63.5	-36.5	4 584	
(2)	(4)	54	95	41	5 356	0.25
	(9)	400	300.5	-99.5	4 584	
Boiler	(5)	95	100	5	5 356	3.39
	Fuel Gas* (14+21)	-	-	-	-	
(3)	(6)	100	186.5	86.5	5 356	0.26
	(10)	300.5	199	-101.5	4 584	
(4)	(7)	186.5	400	213.5	5 356	0.64
	Exhaust Gas (15)	-	-	-	-	
Condenser	(11)	199	100	-99	4 584	3.13
	Cooling Water (19)	23	90	67	40 253	

* Heat from the combustion of fuel gas ((H_2+CH_4) + natural gas).

Table H.8 - Energy integration for Scenario B.3.

TR

HE	Streams	Inlet Temperature (ºC)	Outlet Temperature (ºC)	ΔT	Flow Rate (kg·h^{-1})	Heat (MW)
(1)	(3)	23	55	32	5 356	0.20
	(12)	100	64.5	-35.5	4 800	
(2)	(4)	55	95	40	5 356	0.25
	(9)	400	307	-93	4 800	
Boiler	(5)	95	100	5	5 356	3.39
	Fuel Gas* (14+21)	-	-	-	-	
(3)	(6)	100	195	95	5 356	0.28
	(10)	307	201	-106	4 800	
(4)	(7)	195	400	205	5 356	0.61
	Exhaust Gas (15)	-	-	-	-	
Condenser	(11)	201	100	-101	4 800	3.28
	Cooling Water (19)	23	90	67	42 156	

SER

HE	Streams	Inlet Temperature (ºC)	Outlet Temperature (ºC)	ΔT	Flow Rate (kg·h^{-1})	Heat (MW)
(1)	(3)	23	53	30	5 356	0.19
	(12)	100	63	-37	4 332	
(2)	(4)	53	95	42	5 356	0.26
	(9)	400	291	-109	4 332	
Boiler	(5)	95	100	5	5 356	3.39
	Fuel Gas* (14+21)	-	-	-	-	
(3)	(6)	100	180	80	5 356	0.24
	(10)	291	190	-101	4 332	
(4)	(7)	180	400	220	5 356	0.66
	Exhaust Gas (15)	-	-	-	-	
Condenser	(11)	190	100	-90	4 332	2.93
	Cooling Water (19)	23	90	67	37 719	

* Heat from the combustion of fuel gas ((H_2+CH_4) + natural gas).

Table H.9 - Energy integration for Scenario B.4.

TR

HE	Streams	Inlet Temperature (ºC)	Outlet Temperature (ºC)	ΔT	Flow Rate (kg·h^{-1})	Heat (MW)
(1)	(3)	23	55	32	5 356	0.20
	(12)	100	64	-36	4 717	
(2)	(4)	55	95	40	5 356	0.25
	(9)	400	306	-94	4 717	
Boiler	(5)	95	100	5	5 356	3.39
	Fuel Gas* (14+21)	-	-	-	-	
(3)	(6)	100	193	93	5 356	0.28
	(10)	306	201	-105	4 717	
(4)	(7)	193	400	207	5 356	0.62
	Exhaust Gas (15)	-	-	-	-	
Condenser	(11)	201	100	-101	4 717	3.22
	Cooling Water (19)	23	90	67	41 382	

SER

HE	Streams	Inlet Temperature (ºC)	Outlet Temperature (ºC)	ΔT	Flow Rate (kg·h^{-1})	Heat (MW)
(1)	(3)	23	52	29	5 356	0.18
	(12)	100	62	-38	4 089	
(2)	(4)	52	95	43	5 356	0.27
	(9)	400	282	-118	4 089	
Boiler	(5)	95	100	5	5 356	3.39
	Fuel Gas* (14+21)	-	-	-	-	
(3)	(6)	100	175	75	5 356	0.22
	(10)	282	184	-98	4 089	
(4)	(7)	175	400	225	5 356	0.67
	Exhaust Gas (15)	-	-	-	-	
Condenser	(11)	184	100	-84	4 089	2.75
	Cooling Water (19)	23	90	67	35 316	

* Heat from the combustion of fuel gas ((H_2+CH_4) + natural gas).

Table H.10 - Energy integration for Scenario B.5.

TR

HE	Streams	Inlet Temperature (ºC)	Outlet Temperature (ºC)	ΔT	Flow Rate (kg·h^{-1})	Heat (MW)
(1)	(3)	23	54	31	5 356	0.19
	(12)	100	64	-36	4 630	
(2)	(4)	54	95	41	5 356	0.25
	(9)	400	303.5	-96.5	4 630	
Boiler	(5)	95	100	5	5 356	3.39
	Fuel Gas* (14+21)	-	-	-	-	
(3)	(6)	100	192	92	5 356	0.27
	(10)	303.5	200	-103.5	4 630	
(4)	(7)	192	400	208	5 356	0.62
	Exhaust Gas (15)	-	-	-	-	
Condenser	(11)	200	100	-100	4 630	3.16
	Cooling Water (19)	23	90	67	40 572	

SER

HE	Streams	Inlet Temperature (ºC)	Outlet Temperature (ºC)	ΔT	Flow Rate (kg·h^{-1})	Heat (MW)
(1)	(3)	23	51	28	5 356	0.17
	(12)	100	61	-39	3 782	
(2)	(4)	51	95	44	5 356	0.27
	(9)	400	270	-130	3 782	
Boiler	(5)	95	100	5	5 356	3.39
	Fuel Gas* (14+21)	-	-	-	-	
(3)	(6)	100	166	66	5 356	0.20
	(10)	270	177	-93	3 782	
(4)	(7)	166	400	234	5 356	0.70
	Exhaust Gas (15)	-	-	-	-	
Condenser	(11)	177	100	-77	3 782	2.53
	Cooling Water (19)	23	90	67	32 562	

* Heat from the combustion of fuel gas ((H_2+CH_4) + natural gas).

Table H.11 - Energy integration for Scenario B.6.

TR

HE	Streams	Inlet Temperature (ºC)	Outlet Temperature (ºC)	ΔT	Flow Rate (kg·h^{-1})	Heat (MW)
(1)	(3)	23	54	31	5 356	0.19
	(12)	100	64	-36	4 536	
(2)	(4)	54	95	41	5 356	0.25
	(9)	400	300	-100	4 536	
Boiler	(5)	95	100	5	5 356	3.39
	Fuel Gas* (14+21)	-	-	-	-	
(3)	(6)	100	185	85	5 356	0.25
	(10)	300	200	-100	4 536	
(4)	(7)	185	400	215	5 356	0.64
	Exhaust Gas (15)	-	-	-	-	
Condenser	(11)	200	100	-100	4 536	3.10
	Cooling Water (19)	23	90	67	39 879	

SER

HE	Streams	Inlet Temperature (ºC)	Outlet Temperature (ºC)	ΔT	Flow Rate (kg·h^{-1})	Heat (MW)
(1)	(3)	23	50	27	5 356	0.17
	(12)	100	59	-41	3 498	
(2)	(4)	50	95	45	5 356	0.28
	(9)	400	257	-143	3 498	
Boiler	(5)	95	100	5	5 356	3.39
	Fuel Gas* (14+21)	-	-	-	-	
(3)	(6)	100	158	58	5 356	0.17
	(10)	257	168	-89	3 498	
(4)	(7)	158	400	242	5 356	0.72
	Exhaust Gas (15)	-	-	-	-	
Condenser	(11)	168	100	-68	3 498	2.32
	Cooling Water (19)	23	90	67	29 844	

* Heat from the combustion of fuel gas ((H_2+CH_4) + natural gas).

Table H.12 - Energy integration for Scenario B.7.

TR

HE	Streams	Inlet Temperature (ºC)	Outlet Temperature (ºC)	ΔT	Flow Rate ($kg \cdot h^{-1}$)	Heat (MW)
(1)	(3)	23	53.5	30.5	5 356	0.19
	(12)	100	63	-37	4 429	
(2)	(4)	53.5	95	41.5	5 356	0.26
	(9)	400	295	-105	4 429	
Boiler	(5)	95	100	5	5 356	3.39
	Fuel Gas* (14+21)	-	-	-	-	
(3)	(6)	100	183	83	5 356	0.25
	(10)	295	193	-102	4 429	
(4)	(7)	183	400	217	5 356	0.65
	Exhaust Gas (15)	-	-	-	-	
Condenser	(11)	193	100	-93	4 429	3.01
	Cooling Water (19)	23	90	67	38 736	

SER

HE	Streams	Inlet Temperature (ºC)	Outlet Temperature (ºC)	ΔT	Flow Rate ($kg \cdot h^{-1}$)	Heat (MW)
(1)	(3)	23	49	26	5 356	0.16
	(12)	100	57	-43	3 245	
(2)	(4)	49	95	46	5 356	0.29
	(9)	400	241	-159	3 245	
Boiler	(5)	95	100	5	5 356	3.39
	Fuel Gas* (14+21)	-	-	-	-	
(3)	(6)	100	149	49	5 356	0.15
	(10)	241	159	-82	3 245	
(4)	(7)	149	400	251	5 356	0.75
	Exhaust Gas (15)	-	-	-	-	
Condenser	(11)	159	100	-59	3 245	2.14
	Cooling Water (19)	23	90	67	27 450	

* Heat from the combustion of fuel gas ((H_2+CH_4) + natural gas).

Table H.13 - Energy integration for Scenario C.1.

TR

HE	Streams	Inlet Temperature (ºC)	Outlet Temperature (ºC)	ΔT	Flow Rate ($kg \cdot h^{-1}$)	Heat (MW)
(1)	(3)	23	55	32	5 356	0.20
	(12)	100	64.5	-35.5	4 893	
(2)	(4)	55	115	60	5 356	0.37
	(9)	400	265	-135	4 893	
Boiler	(5)	115	120	5	5 356	3.39
	Fuel Gas* (14+21)	-	-	-	-	
(3)	(6)	120	185	65	5 356	0.19
	(10)	265	195	-70	4 893	
(4)	(7)	185	400	215	5 356	0.64
	Exhaust Gas (15)	-	-	-	-	
Condenser	(11)	195	100	-95	4 893	3.33
	Cooling Water (19)	23	90	67	42750	

SER

HE	Streams	Inlet Temperature (ºC)	Outlet Temperature (ºC)	ΔT	Flow Rate ($kg \cdot h^{-1}$)	Heat (MW)
(1)	(3)	23	53	30	5 356	0.19
	(12)	100	63	-37	4 336	
(2)	(4)	53	115	62	5 356	0.39
	(9)	400	240	-160	4 336	
Boiler	(5)	115	120	5	5 356	3.39
	Fuel Gas* (14+21)	-	-	-	-	
(3)	(6)	120	165	45	5 356	0.13
	(10)	240	185	-55	4 336	
(4)	(7)	165	400	235	5 356	0.70
	Exhaust Gas (15)	-	-	-	-	
Condenser	(11)	185	100	-93	4 336	2.92
	Cooling Water (19)	23	90	67	37 588	

* Heat from the combustion of fuel gas ((H_2+CH_4) + natural gas).

Table H.14 - Energy integration for Scenario C.2.

TR

HE	Streams	Inlet Temperature (ºC)	Outlet Temperature (ºC)	ΔT	Flow Rate (kg·h^{-1})	Heat (MW)
(1)	(3)	23	55	32	5 356	0.20
	(12)	100	65.5	-34.5	4 937	
(2)	(4)	55	130	75	5 355	0.47
	(9)	400	230	-170	4 937	
Boiler	(5)	130	135	5	5 356	3.39
	Fuel Gas* (14+21)	-	-	-	-	
(3)	(6)	135	175	40	5 356	0.12
	(10)	230	185	-45	4 937	
(4)	(7)	175	400	225	5 355	0.67
	Exhaust Gas (15)	-	-	-	-	
Condenser	(11)	185	100	-85	4 937	3.33
	Cooling Water (19)	23	90	67	42 786	

SER

HE	Streams	Inlet Temperature (ºC)	Outlet Temperature (ºC)	ΔT	Flow Rate (kg·h^{-1})	Heat (MW)
(1)	(3)	23	53	30	5 356	0.19
	(12)	100	63	-37	4 337	
(2)	(4)	53	130	77	5 356	0.48
	(9)	400	200	-200	4 337	
Boiler	(5)	130	135	5	5 356	3.39
	Fuel Gas* (14+21)	-	-	-	-	
(3)	(6)	135	160	25	5 356	0.07
	(10)	200	170	-30	4 337	
(4)	(7)	160	400	240	5 356	0.72
	Exhaust Gas (15)	-	-	-	-	
Condenser	(11)	170	100	-70	4 337	2.89
	Cooling Water (19)	23	90	67	37 138	

* Heat from the combustion of fuel gas ((H_2+CH_4) + natural gas).

Table H.15 - Energy integration for Scenario C.3.

TR

HE	Streams	Inlet Temperature (ºC)	Outlet Temperature (ºC)	ΔT	Flow Rate (kg·h^{-1})	Heat (MW)
(1)	(3)	23	55	32	5 356	0.20
	(12)	100	65.5	-34.5	4 965	
(2)	(4)	55	140	85	5 356	0.53
	(9)	400	210	-190	4 965	
Boiler	(5)	140	145	5	5 356	3.39
	Fuel Gas* (14+21)	-	-	-	-	
(3)	(6)	145	170	25	5 356	0.07
	(10)	210	185	-25	4 965	
(4)	(7)	170	400	230	5 356	0.69
	Exhaust Gas (15)	-	-	-	-	
Condenser	(11)	185	100	-85	4 965	3.35
	Cooling Water (19)	23	90	67	43 038	

SER

HE	Streams	Inlet Temperature (ºC)	Outlet Temperature (ºC)	ΔT	Flow Rate (kg·h^{-1})	Heat (MW)
(1)	(3)	23	53	30	5 356	0.19
	(12)	100	63	-37	4 337	
(2)	(4)	53	140	87	5 356	0.54
	(9)	400	175	-225	4 337	
Boiler	(5)	140	145	5	5 356	3.39
	Fuel Gas* (14+21)	-	-	-	-	
(3)	(6)	145	150	5	5 356	0.01
	(10)	175	170	-5	4 337	
(4)	(7)	150	400	250	5 356	0.75
	Exhaust Gas (15)	-	-	-	-	
Condenser	(11)	170	100	-70	4 337	2.89
	Cooling Water (19)	23	90	67	37 174	

* Heat from the combustion of fuel gas ((H_2+CH_4) + natural gas).

Heat Exchanger

For the design of the HE of reference, it was necessary to define some inputs in the simulator *Exchanger Design & Rating* software: HE type (AES), inlet and outlet temperatures of each stream and heat exchanged. The volume flow of each current was estimated for the software. The most important results of the simulation (from design to equipment cost) are presented in Fig. H.1.

Aspen Exchanger Design and Rating Shell & Tube V12

File: C:\Users\eq11051\Desktop\Simulador Permutador.EDR Printed: 26/03/2021 at 11:33:20

TEMA Sheet

Heat Exchanger Specification Sheet

1	Company: FEUP							
2	Location: Porto							
3	Service of Unit:		Our Reference:					
4	Item No.:		Your Reference:					
5	Date: 26/03/2021		Rev No.:		Job No.:			
6	Size: 0,6 - 4	m	Type: AES	Horizontal		Connected in: 1	parallel	1 series
7	Surf/unit(eff.)	70,4	m²	Shells/unit 1		Surf/shell(eff.)	70,4	m²
8	**PERFORMANCE OF ONE UNIT**							
9	Fluid allocation			Shell Side		Tube Side		
10	Fluid name			Quente		Fria		
11	Fluid quantity, Total		kg/h	9896		10747		
12	Vapor (In/Out)		kg/h	9896	9896	0	0	
13	Liquid		kg/h	0	0	10747	10747	
14	Noncondensable		kg/h	0	0	0	0	
15								
16	Temperature (In/Out)		°C	400	310,49	55	95	
17	Bubble / Dew point		°C	/	/	/	/	
18	Density Vapor/Liquid		kg/m³	0,32 /	0,33 /	/ 988,23	/ 962,76	
19	Viscosity		cp	0,0244 /	0,0206 /	/ 0,5106	/ 0,296	
20	Molecular wt, Vap			18,01	18,01			
21	Molecular wt, NC							
22	Specific heat		kJ/(kg-K)	2,058 /	2,007 /	/ 4,186	/ 4,193	
23	Thermal conductivity		W/(m-K)	0,0548 /	0,0444 /	/ 0,6377	/ 0,6742	
24	Latent heat		kcal/kg					
25	Pressure (abs)		bar	1	0,9	1	0,97645	
26	Velocity (Mean/Max)		m/s	91,55 / 116,32		0,06 / 0,06		
27	Pressure drop, allow./calc.		bar	0,1	1,52256	0,2	0,02355	
28	Fouling resistance (min)		m²-K/W	0		0	0 Ao based	
29	Heat exchanged 0,5		MW			MTD (corrected) 279,65		°C
30	Transfer rate, Service 25,4			Dirty 243,9		Clean 243,9		W/(m²-K)
31	**CONSTRUCTION OF ONE SHELL**					**Sketch**		
32				Shell Side		Tube Side		
33	Design/Vacuum/test pressure		kgf/cm²	3,059 / /		3,059 / /		
34	Design temperature / MDMT		°C	435 /		130 /		
35	Number passes per shell			1		1		
36	Corrosion allowance		mm	3,18		3,18		
37	Connections	In	mm	1 457,2 / -		1 50,8 / -		
38	Size/Rating	Out		1 457,2 / -		1 38,1 / -		
39	Nominal	Intermediate		/ -		/ -		
40	Tube #: 313	OD: 19,05	Tks. Average 2,11	mm	Length: 4	m	Pitch: 23,81	mm Tube pattern:30
41	Tube type: Plain		Insert:None		Fin#:	#/m	Material:Carbon Steel	
42	Shell Carbon Steel		ID 600	OD 620	mm	Shell cover	Carbon Steel	
43	Channel or bonnet	Carbon Steel				Channel cover	Carbon Steel	
44	Tubesheet-stationary	Carbon Steel	-			Tubesheet-floating	Carbon Steel	
45	Floating head cover	Carbon Steel				Impingement protection	None	
46	Baffle-cross Carbon Steel		Type Single segmental		Cut(%d) 26,5	Horiz	Spacing: c/c 0,3	m
47	Baffle-long -		Seal Type			Inlet	830,21	mm
48	Supports-tube	U-bend	0		Type			
49	Bypass seal		Tube-tubesheet joint		Expanded only (2 grooves)(App.A 'i')			
50	Expansion joint -		Type None					
51	RhoV2-Inlet nozzle 1033		Bundle entrance 1363		Bundle exit 1608			kg/(m-s²)
52	Gaskets - Shell side	Flat Metal Jacket Fibe	Tube side	Flat Metal Jacket Fibe				
53	Floating head	Flat Metal Jacket Fibe						
54	Code requirements	ASME Code Sec VIII Div 1		TEMA class R - refinery service				
55	Weight/Shell 2620	Filled with water 3792,1		Bundle 1371,9	kg			
56	Remarks							
57								
58								

Fig. H.1. HE specification sheet (TEMA sheet).

Table H.16 - Cost of HEs and boiler/condenser for Scenario A.2.

	TR		SER	
HE	**Heat (MW)**	**Cost (€)**	**Heat (MW)**	**Cost (€)**
(R) [a)]	0.50	28 502	0.50	28 502
(1)	0.40	24 855	0.40	24 855
(2)	0.50	28 415	0.44	26 227
(3)	0.57	30 739	0.57	30 739
(4)	1.22	48 765	1.22	48 765
Boiler	-	235 685*	-	235 685*
Condenser	6.69	135 155	6.28	130 072

[a)] HE used as reference.
* The boiler cost has not been calculated based on the heat exchanged but rather on the flow rate of OMW.

Table H.17 - Cost of HEs and boiler/condenser for Scenario A.3.

	TR		SER	
HE	**Heat (MW)**	**Cost (€)**	**Heat (MW)**	**Cost (€)**
(R) [a)]	0.50	28 502	0.50	28 502
(1)	0.40	24 855	0.37	23 910
(2)	0.50	28 415	0.39	24 621
(3)	0.57	30 739	0.57	30 739
(4)	1.22	48 765	1.22	48 765
Boiler	-	235 685*	-	235 685*
Condenser	6.56	133 516	5.88	125 123

[a)] HE used as reference.
* The boiler cost has not been calculated based on the heat exchanged but rather on the flow rate of OMW.

Table H.18 - Cost of HEs and boiler/condenser for Scenario B.1.

	TR		SER	
HE	**Heat (MW)**	**Cost (€)**	**Heat (MW)**	**Cost (€)**
(R) [a)]	0.50	28 502	0.50	28 502
(1)	0.20	16 398	0.20	16 398
(2)	0.25	18 748	0.25	18 748
(3)	0.28	20 281	0.28	20 153
(4)	0.61	32 174	0.61	32 268
Boiler	-	180 557*	-	180 557*
Condenser	3.42	90 404	3.33	88 946

[a)] HE used as reference.
* The boiler cost has not been calculated based on the heat exchanged but rather on the flow rate of OMW.

Table H.19 - Cost of HEs and boiler/condenser for Scenario B.2.

	TR		SER	
HE	**Heat (MW)**	**Cost (€)**	**Heat (MW)**	**Cost (€)**
(R) [a)]	0.50	28 502	0.50	28 502
(1)	0.20	16 398	0.19	16 089
(2)	0.25	18 748	0.25	19 027
(3)	0.28	20 281	0.26	19 172
(4)	0.61	32 174	0.64	32 968
Boiler	-	180 557*	-	180 557*
Condenser	3.35	89 173	3.13	85 712

[a)] HE used as reference.
* The boiler cost has not been calculated based on the heat exchanged but rather on the flow rate of OMW.

Table H.20 - Cost of HEs and boiler/condenser for Scenario B.3.

	TR		SER	
HE	**Heat (MW)**	**Cost (€)**	**Heat (MW)**	**Cost (€)**
(R) [a)]	0.50	28 502	0.50	28 502
(1)	0.20	16 398	0.19	15 775
(2)	0.25	18 748	0.26	19 304
(3)	0.28	20 281	0.24	18 294
(4)	0.61	32 174	0.66	33 567
Boiler	-	180 557*	-	180 557*
Condenser	3.28	88 063	2.93	82 342

[a)] HE used as reference.
* The boiler cost has not been calculated based on the heat exchanged but rather on the flow rate of OMW.

Table H.21 - Cost of HEs and boiler/condenser for Scenario B.4.

	TR		SER	
HE	**Heat (MW)**	**Cost (€)**	**Heat (MW)**	**Cost (€)**
(R) [a)]	0.50	28 502	0.50	28 502
(1)	0.20	16 398	0.18	15 458
(2)	0.25	18 748	0.27	19 579
(3)	0.28	20 024	0.22	17 599
(4)	0.62	32 362	0.67	34 022
Boiler	-	180 557*	-	180 557*
Condenser	3.22	87 101	2.75	79 334

[a)] HE used as reference.
* The boiler cost has not been calculated based on the heat exchanged but rather on the flow rate of OMW.
.

Table H.22 - Cost of HEs and boiler/condenser for Scenario B.5.

	TR		SER	
HE	**Heat (MW)**	**Cost (€)**	**Heat (MW)**	**Cost (€)**
(R) [a)]	0.50	28 502	0.50	28 502
(1)	0.19	16 089	0.17	15 136
(2)	0.25	19 027	0.27	19 851
(3)	0.27	19 894	0.20	16 300
(4)	0.62	32 456	0.70	34 832
Boiler	-	180 557*	-	180 557*
Condenser	3.16	86 081	2.53	75 392

[a)] HE used as reference.
* The boiler cost has not been calculated based on the heat exchanged but rather on the flow rate of OMW.

Table H.23 - Cost of HEs and boiler/condenser for Scenario B.6.

	TR		SER	
HE	**Heat (MW)**	**Cost (€)**	**Heat (MW)**	**Cost (€)**
(R) [a)]	0.50	28 502	0.50	28 502
(1)	0.19	16 089	0.17	14 809
(2)	0.25	19 027	0.28	20 120
(3)	0.25	18 972	0.17	15 084
(4)	0.64	33 107	0.72	35 542
Boiler	-	180 557*	-	180 557*
Condenser	3.10	85 103	2.32	71 618

[a)] HE used as reference.
* The boiler cost has not been calculated based on the heat exchanged but rather on the flow rate of OMW.

Table H.24 - Cost of HEs and boiler/condenser for Scenario B.7.

	TR		SER	
HE	**Heat (MW)**	**Cost (€)**	**Heat (MW)**	**Cost (€)**
(R) [a)]	0.50	28 502	0.50	28 502
(1)	0.19	15 933	0.16	14 477
(2)	0.26	19 166	0.29	20 387
(3)	0.25	18 703	0.15	13 632
(4)	0.65	33 291	0.75	36 329
Boiler	-	180 557*	-	180 557*
Condenser	3.01	83 711	2.14	68 204

[a)] HE used as reference.
* The boiler cost has not been calculated based on the heat exchanged but rather on the flow rate of OMW.

Table H.25 - Cost of HEs and boiler/condenser for Scenario C.1.

	TR		SER	
HE	**Heat (MW)**	**Cost (€)**	**Heat (MW)**	**Cost (€)**
(R) [a)]	0.50	28 502	0.50	28 502
(1)	0.20	16 398	0.19	15 775
(2)	0.37	23 911	0.39	24 386
(3)	0.19	16 151	0.13	12 953
(4)	0.64	33 107	0.70	34 922
Boiler	-	180 557*	-	180 557*
Condenser	3.33	88 843	2.92	82 241

[a)] HE used as reference.
* The boiler cost has not been calculated based on the heat exchanged but rather on the flow rate of OMW.

Table H.26 - Cost of HEs and boiler/condenser for Scenario C.2.

	TR		SER	
HE	**Heat (MW)**	**Cost (€)**	**Heat (MW)**	**Cost (€)**
(R) [a)]	0.50	28 502	0.50	28 502
(1)	0.20	16 398	0.19	15 775
(2)	0.47	27 337	0.48	27 772
(3)	0.12	12 070	0.07	9 104
(4)	0.67	34 022	0.72	35 366
Boiler	-	180 557*	-	180 557*
Condenser	3.33	88 888	2.89	81 649

[a)] HE used as reference.
* The boiler cost has not been calculated based on the heat exchanged but rather on the flow rate of OMW.

Table H.27 - Cost of HEs and boiler/condenser for Scenario C.3.

	TR		SER	
HE	**Heat (MW)**	**Cost (€)**	**Heat (MW)**	**Cost (€)**
(R) [a)]	0.50	28 502	0.50	28 502
(1)	0.20	16 398	0.19	15 775
(2)	0.53	29469	0.54	2 983
(3)	0.07	9 104	0.01	3 466
(4)	0.69	34474	0.75	36 242
Boiler	-	180 557*	-	180 557*
Condenser	3.35	89 202	2.89	81 696

[a)] HE used as reference.
* The boiler cost has not been calculated based on the heat exchanged but rather on the flow rate of OMW.
.

3. Economic Balance

Purchase costs of the equipment

Table H.28 - Cost of the equipment for Case-study B.

Equipment	Purchase Cost (€)													
	TR							SER						
	B.1	B.2	B.3	B.4	B.5	B.6	B.7	B.1	B.2	B.3	B.4	B.5	B.6	B.7
Tank	41 417	41 417	41 417	41 417	41 417	41 417	41 417	41 417	41 417	41 417	41 417	41 417	41 417	41 417
Reactor	17 323	17 323	17 323	17 323	17 323	17 323	17 323	34 646	34 646	34 646	34 646	34 646	34 646	34 646
Exchangers	213 606	212 128	210 797	209 558	222 096	233 155	242 182	235 218	247 300	256 906	266 424	274 456	283 169	292 970
Boiler	216 669	216 669	216 669	216 669	216 669	216 669	216 669	216 669	216 669	216 669	216 669	216 669	216 669	216 669
Not designed	146 704	146 261	145 862	145 490	149 251	152 569	155 277	158 385	162 009	164 891	167 747	170 156	172 770	175 710
Total	635 719	633 797	632 067	630 457	646 756	661 132	672 868	686 335	702 041	714 528	726 902	737 343	748 670	761 412

Table H.29 - Cost of the equipment for Case-study C.

Equipment	Purchase Cost (€)					
	TR			SER		
	C.1	C.2	C.3	C.1	C.2	C.3
Tank	41 417	41 417	41 417	41 417	41 417	41 417
Reactor	17 323	17 323	17 323	34 646	34 646	34 646
Exchangers	214 093	214 458	214 376	258 323	257 589	254 466
Boiler	216 669	216 669	216 669	216 669	216 669	216 669
Not designed	146 850	146 960	146 935	165 316	165 096	164 159
Total	636 351	636 826	636 719	716 371	715 416	711 356

Total CI

Table H.30 - Cost of the implementation of the process and total CI for Case-study B.

Component	Cost (€)													
	TR							SER						
	B.1	B.2	B.3	B.4	B.5	B.6	B.7	B.1	B.2	B.3	B.4	B.5	B.6	B.7
Purchased Equipment	635 719	633 797	632 067	630 457	646 756	661 132	672 868	686 335	702 041	714 528	726 902	737 343	748 670	761 412
Installation of Equipment	254 287	253 519	252 827	252 183	258 702	264 453	269 147	274 534	280 816	285 811	290 761	294 937	299 468	304 565
Instrumentation/Control	101 715	101 408	101 131	100 873	103 481	105 781	107 659	109 814	112 327	114 325	116 304	117 975	119 787	121 826
Piping	118 667	118 309	117 986	117 685	120 728	123 411	125 602	128 116	131 048	133 379	135 688	137 637	139 752	142 130
Electrical	70 635	70 422	70 230	70 051	71 862	73 459	74 763	76 259	78 005	79 392	80 767	81 927	83 186	84 601
Buildings	-	-	-	-	-	-	-	-	-	-	-	-	-	-
Yard Improvements	28 254	28 169	28 092	28 020	28 745	29 384	29 905	30 504	31 202	31 757	32 307	32 771	33 274	33 841
Service Facilities	-	-	-	-	-	-	-	-	-	-	-	-	-	-
Land	-	-	-	-	-	-	-	-	-	-	-	-	-	-
Engineering	70 635	70 422	70 230	70 051	71 862	73 459	74 763	76 259	78 005	79 392	80 767	81 927	83 186	84 601
Construction Expense	84 762	84 506	84 276	84 061	86 234	88 151	89 716	91 511	93 605	95 270	96 920	98 312	99 823	101 522
Contractor's Fee	42 381	42 253	42 138	42 030	43 117	44 075	44 858	45 756	46 803	47 635	48 460	49 156	49 911	50 761
Contingency	84 762	84 506	84 276	84 061	86 234	88 151	89 716	91 511	93 605	95 270	96 920	98 312	99 823	101 522
FCI	1 491 820	1 487 311	1 483 250	1 479 472	1 517 721	1 551 456	1 578 996	1 610 598	1 647 456	1 676 760	1 705 796	1 730 299	1 756 879	1 786 780
Working Capital	149 182	148 731	148 825	147 947	151 772	155 146	157 900	161 060	164 746	167 676	170 580	173 030	175 688	178 678
Total CI	1 641 002	1 636 042	1 631 576	1 627 419	1 669 493	1 706 602	1 736 896	1 771 658	1 812 202	1 844 436	1 876 375	1 903 328	1 932 567	1 965 457

Table H.31 - Cost of the implementation of the process and total CI for Case-study C.

Component	Cost (€)					
	TR			SER		
	C.1	C.2	C.3	C.1	C.2	C.3
Purchased Equipment	636 351	636 826	636 719	716 371	715 416	711 356
Installation of Equipment	254 540	254 730	254 688	286 548	286 166	284 543
Instrumentation/control	101 816	101 892	101 875	114 619	114 467	113 817
Piping	118 786	118 874	118 854	133 723	133 544	132 787
Electrical	70 706	70 758	70 747	79 597	79 491	79 040
Buildings	-	-	-	-	-	-
Yard Improvements	28 282	28 303	28 299	31 839	31 796	31 616
Service Facilities	-	-	-	-	-	-
Land	-	-	-	-	-	-
Engineering	70 706	70 758	70 747	79 597	79 491	79 040
Construction Expense	84 847	84 910	84 896	95 516	95 389	94 848
Contractor's Fee	42 423	42 455	42 448	47 758	47 694	47 424
Contingency	84 847	84 910	84 896	95 516	95 389	94 848
FCI	1 493 304	1 494 418	1 494 167	1 681 084	1 678 843	1 669 316
Working Capital	149 330	149 442	149 417	168 108	167 884	166 932
Total CI	1 642 634	1 643 860	1 643 584	1 849 193	1 846 727	1 836 248

Fixed Costs

Table H.32 - Fixed costs for Case-study B.

Component	Cost (€·year^{-1})													
	TR							SER						
	B.1	B.2	B.3	B.4	B.5	B.6	B.7	B.1	B.2	B.3	B.4	B.5	B.6	B.7
Amortizations	149 182	148 731	148 325	147 947	151 772	155 146	157 900	161 060	164 746	167 676	170 580	173 030	175 688	178 678
Local Taxes	14 918	14 873	14 833	14 795	15 177	15 515	15 790	16 106	16 475	16 768	17 058	17 303	17 569	17 868
Insurances	14 918	14 873	14 833	14 795	15 177	15 515	15 790	16 106	16 475	16 768	17 058	17 303	17 569	17 868
Total	179 018	178 477	177 990	177 537	182 127	186 175	189 480	193 272	197 695	201 211	204 696	207 636	210 825	214 414

Table H.33 - Fixed costs for Case-study C.

Component	Cost (€·year^{-1})					
	TR			SER		
	C.1	C.2	C.3	C.1	C.2	C.3
Amortizations	149 330	149 442	149 417	168 108	167 884	166 932
Local Taxes	14 933	14 944	14 942	16 811	16 788	16 693
Insurances	14 933	14 944	14 942	16 811	16 788	16 693
Total	179 196	179 330	179 300	201 730	201 461	200 318

Production Costs

Table H.34 - Production costs for Case-study B.

Component	Cost (€·year^{-1})													
	TR							SER						
	B.1	B.2	B.3	B.4	B.5	B.6	B.7	B.1	B.2	B.3	B.4	B.5	B.6	B.7
Maintenance	74 591	74 366	74 163	73 974	75 886	77 573	78 950	80 530	82 373	83 838	85 290	86 515	87 844	89 339
Salaries	342 64	342 648	342 648	342 648	342 648	342 648	342 648	342 648	342 648	342 648	342 648	342 648	342 648	342 648
Materials	4 650	4 650	4 650	4 650	4 650	4 650	4 650	11 640	11 640	11 640	11 640	11 640	11 640	11 640
Utilities														
Colling Water	4 561	4 466	4 371	4 290	4 406	4 721	5 056	4 918	5 333	5 830	6 447	7 148	8 012	9 110
Natural Gas	722 604	23 236	0	0	0	0	0	653 383	0	0	0	0	0	0
Total Utilities	908 956	34 628	5 463	5 363	5 508	5 901	6 320	822 876	6 320	7 287	8 059	8 935	10 015	11 387
Total	1 330 846	456 291	426 924	426 635	428 692	430 772	432 568	1 257 695	443 327	445 414	447 637	449 738	452 147	455 015

Table H.35 - Production costs for Case-study C.

Component	Cost (€·year^{-1})					
	TR			SER		
	C.1	C.2	C.3	C.1	C.2	C.3
Maintenance	74 665	74 721	74 708	84 054	83 942	83 466
Salaries	342 648	342 648	342 648	342 648	342 648	342 648
Materials	4 650	4 650	4 650	11 640	11 640	11 640
Utilities						
Colling Water	4063	4066	4090	5344	5301	5304
Natural Gas	0	0	0	0	0	0
Total Utilities	5 079	5 083	5 113	6 680	6 626	6 631
Total	427 042	427 102	427 119	445 022	444 857	444 385

Revenues

Table H.36 - Revenues of the OMWSR process for the Case-study B.*

Total Revenues (€·year^{-1})													
TR							SER						
B.1	**B.2**	**B.3**	**B.4**	**B.5**	**B.6**	**B.7**	**B.1**	**B.2**	**B.3**	**B.4**	**B.5**	**B.6**	**B.7**
0	0	467 278	1 024 831	1 660 341	2 385 682	3 236 261	0	75 760	630 943	1 246 394	1 957 670	2 754 555	3 655 692

* The revenue comes from the net sale of H_2 and CH_4 produced in the process.

Table H.37 - Revenues of the OMWSR process for the Case-study C.*

Total Revenues (€·year^{-1})					
TR			SER		
C.1	**C.2**	**C.3**	**C.1**	**C.2**	**C.3**
425 123	399 481	384 680	614 531	609 270	599 270

* The revenue comes from the net sale of H_2 and CH_4 produced in the process.

Profitability Analysis

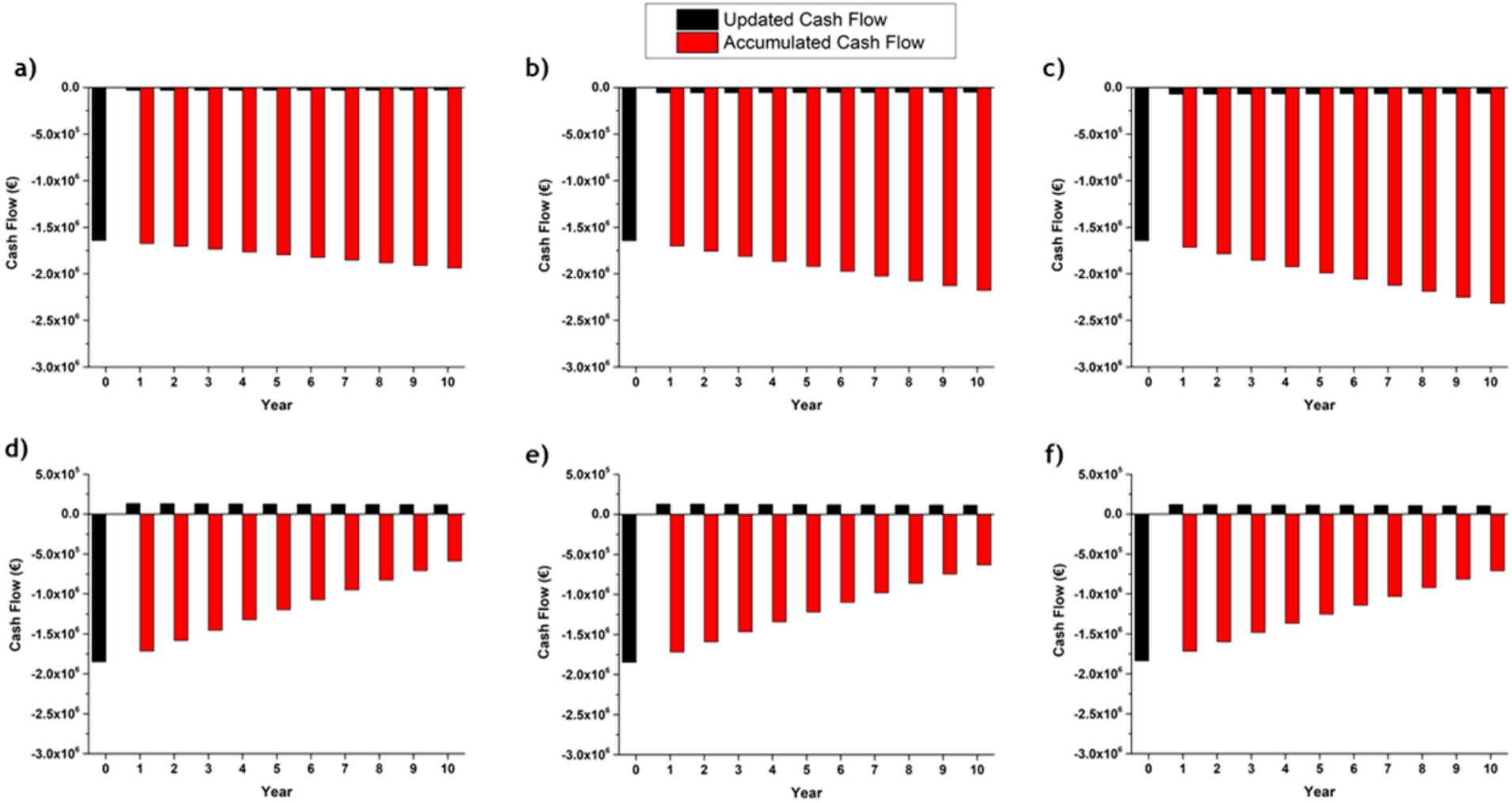

Fig. H.2. Cash flow updated (red) and accumulated cash flow (black) for Case-study C: a) C.1, b) C.2 and c) C.3 using a TR; d) C.1, e) C.2 and f) C.3 using SERs

Appendix I. Publications and Communications

1. Scientific publications in peer reviewed international scientific journals

1. **Rocha, C.**, M.A. Soria and L.M. Madeira, Steam reforming of olive oil mill wastewater with in situ hydrogen and carbon dioxide separation - Thermodynamic analysis. Fuel, 2017. 207: p. 449-460.
2. **Rocha, C.**, M.A. Soria and L.M. Madeira, Effect of interlayer anion on the CO2 capture capacity of hydrotalcite-based sorbents. Separation and Purification Technology, 2019. 219: p. 290-302.
3. **Rocha, C.**, M.A. Soria and L.M. Madeira, Thermodynamic analysis of olive oil mill wastewater steam reforming. Journal of the Energy Institute, 2019. 92(5): p. 1599-1609.
4. Soria, M.A., **C. Rocha**, S. Tosti, A. Mendes and L.M. Madeira, COx free hydrogen production through water-gas shift reaction in different hybrid multifunctional reactors. Chemical Engineering Journal, 2019. 356: p. 727-736.
5. **Rocha, C.**, M.A. Soria and L.M. Madeira, Doping of hydrotalcite-based sorbents with different interlayer anions for CO2 capture. Separation and Purification Technology, 2020. 235: p. 116140.
6. **Rocha, C.**, M.A. Soria and L.M. Madeira, Screening of commercial catalysts for steam reforming of olive mill wastewater. Renewable Energy, 2021. 169: p. 765-779.
7. **Rocha, C.**, M.A. Soria, and L.M. Madeira, Use of Ni-containing catalysts for the Olive Mill Wastewater Steam Reforming (Submitted for publication).
8. **Rocha, C.**, M.A. Soria, and L.M. Madeira, Olive mill wastewater valorization through steam reforming using hybrid multifunctional reactors for high-purity H_2 production. Chemical Engineering Journal, 2021.

2. Oral communications in scientific meetings

1. Soria, M.A., **C. Rocha**, S. Tosti, A. Mendes and L.M. Madeira, COx free hydrogen production through water-gas shift reaction in different hybrid multifunctional reactors. 13th International Conference on Catalysis in Membrane Reactors, 10th to 13th June, 2017, Houston, USA.
2. **Rocha, C.**, M.A. Soria and L.M. Madeira, Olive Mill Wastewater Valorisation through Steam Reforming using a Hybrid Sorption-Enhanced Membrane Reactor. 11th International Symposium on Catalysis in Multiphase Reactors - 10th International Symposium on Multifunctional Reactors, 21st to 24th March, 2021, Milan, Italy.

3. Poster communications in scientific meetings

1. **Rocha, C.,** M.A. Soria and L.M. Madeira, Thermodynamic Analysis of Olive Mill Wastewater Steam Reforming with in Situ H2 and CO2 Separation. 13th International Conference on Catalysis in Membrane Reactors, 10th to 13th June, 2017, Houston, USA.
2. **Rocha, C.,** M.A. Soria and L.M. Madeira, Effect of interlayer anion on the CO2 capture capacity of hydrotalcite-based sorbents. 25th International Conference on Chemical Reaction Engineering, 20th to 23rd May, 2018, Florence, Italy.
3. **Rocha, C.,** M.A. Soria and L.M. Madeira, Study of the effect of the compensating anion on the CO2 sorption capacity of hydrotalcite based sorbents. 13th International Chemical and Biological Engineering Conference, 2nd to 4th October, 2018, Aveiro, Portugal.